# Suspicious Minds: A Molecular Taphonomic Approach to Preservation of the Central Nervous System




ALEXANDRA L. SEVIOUR

Merton College

University of Oxford

A thesis submitted for the degree of

*Doctor of Philosophy*

Trinity Term, 2026

Supervised by Prof.s R. Fischer, G. Larson, & E. Saupe

# Declaration

I hereby declare that this thesis has never been submitted, either in the same or a different form, to this or any other university for a degree or any other qualification. All the work presented in this thesis is my own unless otherwise stated in the author contributions, and was conducted while I was registered as a graduate student at the Department of Earth Sciences, University of Oxford, and the Nuffield Department of Medicine, University of Oxford, under the supervision of Prof.s Roman Fischer, Greger Larson, and Erin Saupe.

This work is dedicated to W.E.D. Evans (1920–1964), the unacknowledged father of molecular taphonomy. His 1963 monograph, *The Chemistry of Death*, laid the foundations of modern thanatochemistry: though too often forgotten by those who build upon it, his influence endures quietly in all that followed.

And to the late Professor Tony Waldron, who placed in my hands my first ancient spinal cord – and with it the question that became this thesis.

# Abstract

Brains decompose rapidly after death, yet are frequently recovered in the archaeological record, often as the only surviving soft tissue. This paradox exposes a major gap in our current understanding of soft tissue preservation: existing models treat decay and preservation as opposing, antithetical outcomes, and do not adequately account for inter-organ divergence during decomposition. This thesis resolves that paradox by integrating a global archaeological synthesis with deep palaeoproteomic profiling and experimental decay.

An archive of $> 4,400$ preserved human brains spanning $\sim 12,000$ years was compiled, of which $> 1,300$ derived from otherwise skeletonised remains in wet, oxygen-poor environments. These cases define a previously undescribed preservation type consistent with an organ-specific taphonomic trajectory. To determine the molecular composition of brains of this type, an optimised palaeoproteomic workflow was developed using high-resolution mass spectrometry: $> 1,200$ proteins were recovered from a single archaeological brain, demonstrating that ancient soft tissues can preserve high-dimensional proteomes far richer than those typically retrievable from hard tissues. To identify the mechanism underpinning the unknown taphonomic trajectory, mice carcasses were experimentally decayed for six months under varied water–oxygen regimes, and $> 1.26$ million peptide-specific decay profiles modelled to distinguish decay-prone from decay-resistant brain peptides.

Different burial environments yielded reproducible divergence in molecular fate: waterlogged, hypoxic conditions favour the selective persistence of structurally ordered, redox-active, membrane-associated brain peptides, bearing modification patterns consistent with radical-mediated oxidation followed by local termination and crosslinking, rather than with chain-propagating fragmentation. Decomposition is shown to be a branching chemical process in which intrinsic tissue chemistry and

early *post-mortem* environmental conditions jointly determine whether stabilising or destabilising reactions prevail. Soft tissue preservation is thus reframed as a potential outcome of decay itself, and a molecular framework established for predicting when complex biomolecular information is likely to be retained in the archaeological record.

# Acknowledgements

My deepest debt of gratitude goes to my principal advisor, Professor Roman Fischer. By the time Roman became the eighth person entrusted with supervising this project, I had grown accustomed to finding (and having) my own way. But Roman welcomed me into his group, and offered me something I had been missing for a long time: an academic home. He gave me complete intellectual freedom to pursue every question that captured my imagination, supported every new experiment and analysis I dreamt up, and – annoyingly – always managed to be right whenever he persuaded me to try it his way. Even as the only palaeoproteomics researcher in his clinical proteomics group, I was always treated as a colleague whose insights and expertise were equally valued and respected. His easy, infectious laughter, and refusal to take himself (or anything) too seriously, made science joyful again. This thesis is immeasurably stronger for his guidance, and I will always be grateful that he chose to take me on.

That gratitude extends to my co-advisors, Professors Greger Larson and Erin Saupe, who were unfailingly generous with their time and advice throughout my doctorate. Whether managing the many DPhil milestones, navigating the publication process, or planning the next stage of my academic journey, they made time to listen, advise, and encourage. Greger's willingness to help at a moment when my future as a researcher hung in the balance changed the course of my career: I would not be writing these Acknowledgements without his intervention.

Over the last four years, I have had the privilege of working alongside countless excavators, conservators, curators, and scientists across the globe whose curiosity, generosity, and willingness to share resources made this thesis possible. Closest to home, I owe heartfelt thanks to those at the Centre for Medicines Discovery – especially Benedikt, Iolanda, Simon, Jasmine, Darragh, Andreas, Robyn, Svenja,

George, and Hannah – not only for sharing their knowledge and expertise, but most of all for sharing laughs. Amongst researchers curing cancer and eliminating Alzheimer's, it would have been easy to feel like the comic relief story at the end of the evening news. Instead, they met each of my improbable archaeological samples with genuine fascination and enthusiasm, and, more than once, their excitement carried me through the moments when my own inevitably faltered.

Above all these wonderful colleagues, I owe particular thanks to Dr. Sarah Flannery. Sarah taught me almost everything I know about practical proteomics, and knows this thesis more intimately than anyone else. Her kindness, patience, encouragement, and endless capacity for mischief transformed even the most frustrating of long days in the lab into peals of laughter. More than a collaborator, she has become one of those rare friends with whom I can simply be my whole, flawed self. I cannot imagine having completed this work without her beside me.

To my office mates – Hannah, Harri, Lewis, Lot, and Kate – thank you for making these years unforgettable. Whether an experiment had failed, the mass spectrometer had other ideas, or somebody had spent an entire afternoon making perfectly good code considerably worse, there was always someone ready with a hug, a listening ear, or a reason to laugh. Sharing this journey with you, from that very first day onwards, has been the greatest privilege of my PhD.

To my parents, Diane and Graham, thank you for first nurturing the curiosity that led me here. I doubt either of you imagined that would become quite such a long-term commitment, through diplomas, an undergraduate degree, a Master's degree, a PhD – and next a medical degree, well into my 30s. You remain my strongest foundation, reminding me always to try hard, but try even harder to enjoy it. Mum, you are my inspiration. Dad, you are my strength.

And to my husband, Richard. You have been my greatest champion, and my fiercest protector. Where Roman gave me an academic home, and my friends and colleagues made the work joyful, you gave me the most valuable thing of all: a life outside it, filled with love and laughter. The path that brought me

to Oxford was unimaginably difficult, yet it also brought me to you. For that, I would not change a single step.

Last, and very much least: while many earn gratitude, a few are remembered only for the obstacles they placed in the path of others. To those who believed power would outlast perseverance – who abused authority, abandoned professional responsibility, or protected reputation over truth – this thesis is, in every sense, about persistence.

# Contents

**List of Figures** **xiv**

**List of Tables** **xvi**

**Abbreviations** **xviii**

**1 Introduction** **1**
1.1 Research Problem . . . . . 1
1.2 Molecular Taphonomy . . . . . 2
1.2.1 Biostratinomy and diagenesis . . . . . 2
1.2.2 Experimental taphonomy . . . . . 4
1.2.3 Biomolecular preservation . . . . . 7
1.3 Death & Decomposition . . . . . 18
1.3.1 Autolysis . . . . . 20
1.3.2 Putrefaction . . . . . 24
1.3.3 Environmental modifiers . . . . . 28
1.4 Soft-Tissue Preservation . . . . . 35
1.4.1 Dehydration . . . . . 36
1.4.2 Freezing . . . . . 41
1.4.3 Tanning . . . . . 44
1.4.4 Saponification . . . . . 47
1.4.5 Exceptional soft-tissue preservation on geological timescales 50
1.5 The Brain . . . . . 57
1.5.1 Nervous tissue structure and composition . . . . . 57
1.5.2 Age-related changes *in vivo* . . . . . 61
1.5.3 Early *post-mortem* decomposition . . . . . 74
1.6 Palaeoproteomics . . . . . 78
1.6.1 Applications and advantages . . . . . 78
1.6.2 Sample preparation . . . . . 81
1.6.3 Mass spectrometric analysis . . . . . 85
1.6.4 Sequence identification . . . . . 89
1.7 Research Aims & Thesis Overview . . . . . 94
1.8 References . . . . . 96

**2 Human Brains Preserve in Diverse Environments for at least 12,000 Years** **179**
2.1 Author Contributions . . . . . 179

2.2 Abstract . . . 179
2.3 Background . . . 180
2.4 Results . . . 182
2.5 Discussion . . . 188
2.5.1 Geographic, palaeoclimatic, and temporal trends in brain preservation . . . 188
2.5.2 Mechanisms of brain preservation on geological timescales 192
2.5.3 Palaeobiological applications of preserved brains . . . 196
2.6 Conclusions . . . 199
2.7 Methods . . . 199
2.8 Acknowledgements . . . 200
2.9 References . . . 200

**3 Deep Palaeoproteomic Profiling of Archaeological Human Brains 208**
3.1 Author Contributions . . . 208
3.2 Abstract . . . 209
3.3 Introduction . . . 209
3.4 Materials & Methods . . . 213
3.4.1 Archaeological brain material . . . 213
3.4.2 In-solution . . . 213
3.4.3 In-gel . . . 215
3.4.4 On-filter . . . 216
3.4.5 On-bead . . . 218
3.4.6 Data acquisition . . . 218
3.4.7 Data analysis . . . 219
3.5 Results . . . 222
3.5.1 Benchmarking protocol performance with ion mobility spectrometry . . . 222
3.5.2 Identifying biases in modification, hydropathy, isoelectric point, and contamination . . . 227
3.5.3 Limitations . . . 236
3.6 Discussion . . . 236
3.7 Acknowledgements . . . 239
3.8 References . . . 240

**4 Molecular Solution to the Paradox of Ancient Brain Preservation 245**
4.1 Author Contributions . . . 245
4.2 Abstract . . . 246
4.3 Introduction . . . 246
4.4 Methods . . . 248
4.4.1 Experimental taphonomy . . . 248
4.4.2 Proteomics . . . 250
4.4.3 Data analysis . . . 250
4.5 Results . . . 252
4.5.1 Divergent taphonomic trajectories under oxic and hypoxic burial . . . 252

4.5.2 *Post-mortem* shifts in brain proteome composition . . . . 254
4.5.3 Peptide-specific decay profiles in different environments . . 255
4.5.4 Environmental controls on recalcitrant peptide classes . . 257
4.5.5 Physicochemical, sequence, and structural predictors of peptide recalcitrance . . . . . 257
4.5.6 Protein features and modifications associated with recalcitrance . . . . . 260
4.6 Discussion . . . . . 261
4.7 Conclusions . . . . . 265
4.8 Limitations . . . . . 266
4.9 Supporting Information . . . . . 267
4.10 Data Availability . . . . . 268
4.11 Acknowledgements . . . . . 268
4.12 References . . . . . 268

**5 Discussion & Conclusions 273**
5.1 From Destruction to Divergence: Reframing Decomposition . . . 273
5.1.1 Brain preservation is systematic, not anomalous . . . . . 273
5.1.2 Molecular persistence is probabilistic, not random . . . . . 276
5.1.3 Environmental constraint redirects decay chemistry . . . . 280
5.1.4 Long-term preservation is established early *post-mortem* . 282
5.1.5 Preservation is a permissible outcome of decay . . . . . 284
5.2 Limitations . . . . . 285
5.2.1 Of the archaeological archive . . . . . 285
5.2.2 Of the experimental design . . . . . 287
5.2.3 Of the molecular evidence . . . . . 288
5.3 Further Work . . . . . 289
5.3.1 Experimental resolution of organ-specific taphonomic divergence . . . . . 290
5.3.2 Direct characterisation of crosslinked products . . . . . 291
5.3.3 Validation of the palaeoproteomic workflow across preserved brains . . . . . 292
5.4 Future Directions . . . . . 293
5.4.1 Peptide-level decay profiling as a method of predictive taphonomy . . . . . 293
5.4.2 Preserved brains as a new archive for molecular palaeobiology and palaeopathology . . . . . 294
5.5 Conclusions . . . . . 295
5.6 References . . . . . 296

**Appendices**

**Glossary 302**

**A Supplementary: Human Brains Preserve in Diverse Environments for at least 12,000 Years** **330**
A.1 Co-Author Permissions . . . 330
A.2 Dataset . . . 332
A.3 Methods . . . 332
A.4 Figures . . . 335
A.5 Tables . . . 336
A.6 References . . . 340

**B Supplementary: Deep Palaeoproteomic Profiling of Archaeological Human Brains** **342**
B.1 Co-Author Permissions . . . 342
B.2 Methods . . . 343
B.2.1 In-solution . . . 343
B.2.2 In-gel . . . 350
B.2.3 On-filter . . . 352
B.2.4 On-bead . . . 358
B.3 Results . . . 360
B.4 Figures . . . 361
B.5 Tables . . . 363
B.6 References . . . 368

**C Supplementary: Molecular Solution to the Paradox of Ancient Brain Preservation** **369**
C.1 Co-Author Permissions . . . 369
C.2 Results . . . 371
C.2.1 Divergent taphonomic trajectories under oxic and hypoxic burial . . . 371
C.2.2 *Post-mortem* shifts in brain proteome composition . . . 373
C.2.3 Environment-specific peptide decay trajectories and recalcitrance . . . 374
C.2.4 Environmental controls on recalcitrant peptide classes . . . 375
C.2.5 Physicochemical, sequence, and structural predictors of peptide recalcitrance . . . 376
C.2.6 Protein topology, domains, and modifications associated with recalcitrance . . . 379
C.3 Discussion . . . 380
C.3.1 Role of water in enabling radical-mediated oxidative crosslinking under hypoxia . . . 380
C.3.2 Role of reactive residues in radical-mediated oxidative crosslinking . . . 382
C.4 Methods . . . 384
C.4.1 Experimental taphonomy . . . 384
C.4.2 Proteomics . . . 387
C.4.3 Data analysis . . . 389
C.5 Figures . . . 397

C.6 Tables . . . . . 414
C.7 References . . . . . 430

# List of Figures


1.1 Differential preservation potential of biomolecular classes . . . . . 8

2.1 Distribution and frequency of preserved human brains by type, compared with soft tissues in the IsoArcH repository . . . . . 183
2.2 Five mechanisms of brain preservation . . . . . 185
2.3 Relationships between depositional context and preservation type 186
2.4 Relationships between geographic location and unknown preservation type . . . . . 189
2.5 Chemical processes of molecular crosslinking and metal complexation potentially underpinning the unknown preservation mechanism . . 193

3.1 Overview of the study design . . . . . 212
3.2 Total numbers of proteins retrieved with each protocol . . . . . 223
3.3 Unsupervised data clustering and multivariate ordination analyses 225
3.4 Measures of extraction efficiency . . . . . 226
3.5 Nature and extent of deamidation . . . . . 228
3.6 Discovery of covalent modifications . . . . . 229
3.7 Distribution of GRAVY scores by protocol . . . . . 230
3.8 Hydropathic profiles retrieved with each protocol . . . . . 231
3.9 Distribution of isoelectric point by protocol . . . . . 233
3.10 Isoelectric profiles retrieved with each protocol . . . . . 234
3.11 Abundance of common laboratory contaminants . . . . . 235

4.1 Overview of experimental and analytical workflow . . . . . 249
4.2 Divergent taphonomic trajectories under oxic and hypoxic burial . 253
4.3 Peptide-specific decay profiles in different environments . . . . . 256
4.4 Protein features associated with recalcitrance . . . . . 258

A.1 Search strategy employed . . . . . 335
A.2 Co-occurrence of tissue types . . . . . 335

B.1 Proteins retrieved with each search strategy, and impact of FAIMS on protein identification . . . . . 361
B.2 Nature of non-tryptic peptides . . . . . 362

C.1 Protein concentration during decomposition . . . . . 397
C.2 Proteomic profiles by burial environment . . . . . 398
C.3 Proteomic profiles by time point . . . . . 399
C.4 Complex heatmap of scaled protein iBAQ data with integrated linear modelling, $k$-means and hierarchical clustering of proteins globally 400
C.5 Complex heatmap of scaled protein iBAQ data with integrated linear modelling, $k$-means and hierarchical clustering of proteins in wet–oxic conditions . . . . . 401
C.6 Complex heatmap of scaled protein iBAQ data with integrated linear modelling, $k$-means and hierarchical clustering of proteins in wet–hypoxic conditions . . . . . 402
C.7 Complex heatmap of scaled protein iBAQ data with integrated linear modelling, $k$-means and hierarchical clustering of proteins in dry–oxic conditions . . . . . 403
C.8 Complex heatmap of scaled protein iBAQ data with integrated linear modelling, $k$-means and hierarchical clustering of proteins in dry–hypoxic conditions . . . . . 404
C.9 Biological process enrichment of proteins at early and late PMI . 405
C.10 Molecular function enrichment of proteins at early and late PMI . 406
C.11 Cellular component enrichment of proteins at early and late PMI 407
C.12 Precision–recall for early- and late-peaking peptide classifiers across conditions . . . . . 408
C.13 Calibration and discrimination of the peptide-level recalcitrance classifier . . . . . 409
C.14 Hydropathy by burial environment . . . . . 410
C.15 Sequence coverage distributions by preservation category within burial environments . . . . . 411
C.16 Odds of modification at late *vs.* early PMI by burial environment 412
C.17 Determination of optimal number of clusters for hierarchical clustering analysis of iBAQ data . . . . . 413

# List of Tables


1.1 Decomposition stages with associated *post-mortem* phenomena . . 19

2.1 Author contributions . . . . . 179

3.1 Author contributions . . . . . 208

4.1 Author contributions . . . . . 245

A.1 Selection (inclusion and exclusion) criteria applied in the literature search. . . . . 336
A.2 Types of brain preservation . . . . . 336
A.3 Per-site frequency of brain preservation . . . . . 336
A.4 Summary statistics by preservation type . . . . . 337
A.5 Statistical testing by preservation type . . . . . 337
A.6 Archaeological age by preservation type . . . . . 338
A.7 Elevation by preservation type . . . . . 338
A.8 Latitude by preservation type . . . . . 339
A.9 Maximum temperature by preservation type . . . . . 339
A.10 Precipitation by preservation type . . . . . 339

B.1 Reagents required for the PreOmics® BeatBox iST method . . . . 343
B.2 Reagents required for the urea with SPE method . . . . . 345
B.3 Reagents required for the urea with SPE + iST method . . . . . 346
B.4 Reagents required for the sodium laurate with SPE method . . . 348
B.5 Reagents required for the SDS–PAGE method . . . . . 350
B.6 Reagents required for the PreOmics® BeatBox with S-Trap micro method . . . . . 352
B.7 Reagents required for the SDS with S-Trap micro method . . . . 354
B.8 Reagents required for the urea with FASP method . . . . . 355
B.9 Reagents required for the SDS with FASP method . . . . . 357
B.10 Reagents required for the SP3 method . . . . . 358
B.11 DDA and DIA search strategies . . . . . 363
B.12 DIA identification results by protocol . . . . . 363
B.13 Statistical over-representation of protein classes . . . . . 363
B.14 Nature of dependent peptides . . . . . 364

B.15 Summary of hydropathy by protocol . . . . . 364
B.16 Hydropathic profiles retrieved by each protocol . . . . . 365
B.17 Summary of isoelectric point by protocol . . . . . 366
B.18 Isoelectric profiles retrieved by each protocol . . . . . 366

---

C.1 Proteins recovered by experimental condition and time point . . . 414
C.2 Protein abundance at different time points . . . . . 414
C.3 Protein abundance in different burial environments . . . . . 415
C.4 Protein classes recalcitrant in wet–hypoxic conditions . . . . . 415
C.5 Protein classes recalcitrant in dry–oxic conditions . . . . . 415
C.6 Protein classes recalcitrant in dry–hypoxic conditions . . . . . 416
C.7 Hydropathy by preservation category . . . . . 416
C.8 Net charge by preservation category . . . . . 417
C.9 Isoelectric point by preservation category . . . . . 417
C.10 Mean peptide length and sequence coverage by preservation category 418
C.11 Mean peptide length by preservation category . . . . . 418
C.12 Sequence coverage by preservation category . . . . . 419
C.13 Secondary structure by preservation category . . . . . 419
C.14 Weighted $\alpha$-helix fraction by preservation category and burial environment . . . . . 420
C.15 Weighted $\beta$-sheet fraction by preservation category and burial environment . . . . . 420
C.16 Predicted secondary structure model confidence by preservation category . . . . . 421
C.17 Intrinsic disorder by preservation category . . . . . 421
C.18 Mean IUPred score by preservation category and burial environment 422
C.19 Fraction disordered by preservation category and burial environment 422
C.20 UniProt feature section by preservation category . . . . . 423
C.21 UniProt feature type by preservation category . . . . . 423
C.22 Dominant radical oxidation pathways under contrasting hydration and oxygen regimes . . . . . 424
C.23 Reactivity and preservation potential of key amino-acid residues . 426
C.24 Sample mass and protein concentration for the DDA dataset . . . 427
C.25 Sample mass and protein concentration for the DIA dataset . . . 429

# Abbreviations

| | |
|---|---|
| **4-HNE** | 4-Hydroxynonenal |
| **A** | Adenine |
| **ACN** | Acetonitrile |
| **AD** | Alzheimer's disease |
| **aDNA** | Ancient deoxyribonucleic acid |
| **ADP** | Adenosine diphosphate |
| **AGC** | Automatic gain control |
| **AGE** | Advanced glycation end product |
| **Ala** | Alanine |
| **ALE** | Advanced lipoxidation end product |
| **ALS** | Amyotrophic lateral sclerosis |
| **Arg** | Arginine |
| **Asn** | Asparagine |
| **Asp** | Aspartic acid |
| **ATP** | Adenosine triphosphate |
| **ATR–FTIR** | Attenuated total reflectance–Fourier transform infrared spectroscopy |
| **BCA** | Bicinchoninic assay |
| **BPI** | Base peak intensity |
| **BSA** | Bovine serum albumin |
| **C** | Cytosine |
| **CI** | Confidence interval |
| **CID** | Collision-induced dissociation |
| **CNS** | Central nervous system |
| **CSF** | Cerebrospinal fluid |
| **CV** | Compensation voltage |
| **Cys** | Cysteine |
| **DDA** | Data-dependent acquisition |
| **DEA** | Differential expression analysis |
| **DIA** | Data-independent acquisition |
| **diaPASEF** | Parallel accumulation–serial fragmentation combined with data-independent acquisition |
| **DNA** | Deoxyribonucleic acid |
| **DTT** | Dithiothreitol |
| **ECDF** | Empirical cumulative distribution function |
| **ECM** | Extracellular matrix |
| **EDTA** | Ethylenediaminetetraacetic acid |
| **EI** | Electron ionisation |
| **ESI** | Electrospray ionisation |
| **ETC** | Electron transfer chain |
| **ETD** | Electron transfer dissociation |
| **FA** | Formic acid |
| **$FADH_2$** | Flavin adenine dinucleotide |
| **FAIMS** | High-field asymmetric-waveform ion mobility spectrometry |
| **FASP** | Filter-aided sample preparation |
| **FDR** | False discovery rate |

| | |
|---|---|
| **FE** | Fold enrichment |
| **FT–ICR** | Fourier-transform ion cyclotron resonance |
| **FTD** | Frontotemporal dementia |
| **G** | Guanine |
| **Gln** | Glutamine |
| **Glu** | Glutamic acid |
| **Gly** | Glycine |
| **GO** | Gene Ontology |
| **GRAVY** | GRand AVerage of hydropathY |
| **GuHCl** | Guanidine hydrochloride |
| **HCD** | Higher-energy collisional dissociation |
| **His** | Histidine |
| **HPLC** | High-performance liquid chromatography |
| **IAA** | Iodoacetamide |
| **iBAQ** | Intensity-based absolute quantification |
| **ICP–MS** | Inductively coupled plasma–mass spectrometry |
| **IDP** | Intrinsically disordered protein |
| **Ile** | Isoleucine |
| **iST** | In-StageTip method |
| **LC** | Liquid chromatography |
| **LC–MS/MS** | Liquid chromatography–tandem mass spectrometry |
| **Leu** | Leucine |
| **LOESS** | Locally estimated scatterplot smoothing |
| **$\log_2$FC** | $\text{Log}_2$-fold change |
| **Lys** | Lysine |
| ***m/z*** | Mass-to-charge ratio |
| **MBP** | Myelin basic protein |
| **MBR** | Match-between-runs |
| **MDA** | Malondialdehyde |
| **Met** | Methionine |
| **micro-XRF** | Micro-X-ray fluorescence |
| **MS** | Mass spectrometry |
| **MS/MS** | Tandem mass spectrometry |
| **MWCO** | Molecular-weight cut-off |
| **$NAD^+$** | Oxidised nicotinamide adenine dinucleotide |
| **NADH** | Reduced nicotinamide adenine dinucleotide |
| **NADPH** | Reduced nicotinamide adenine dinucleotide phosphate |
| **NCE** | Normalised collision energy |
| **NDD** | Neurodegenerative disease |
| **NPV** | Negative predictive value |
| **OR** | Odds ratio |
| **PANTHER** | Protein ANalysis THrough Evolutionary Relationships |
| **PC** | Principal component |
| **PCA** | Principal component analysis |
| **PD** | Parkinson's disease |
| **PEG** | Polyethylene glycol |
| **PEP** | Posterior error probability |
| **Phe** | Phenylalanine |
| **pI** | Isoelectric point |
| **pLDDT** | Predicted local distance difference test |
| **PLP1** | Myelin proteolipid protein |
| **PMI** | *Post-mortem* interval |
| **PPV** | Positive predictive value |
| **Pro** | Proline |
| **PSM** | Peptide-spectrum match |

| | |
|---|---|
| **PTM** | Post-translational modification |
| **PUFA** | Polyunsaturated fatty acid |
| **py–GC–MS** | Pyrolysis–gas chromatography–mass spectrometry |
| **QRILC** | Quantile regression imputation of left-censored data |
| **RAGE** | Receptor for advanced glycation end product |
| **RCS** | Reactive carbonyl species |
| **RF** | Radio frequency |
| **RNA** | Ribonucleic acid |
| **RNS** | Reactive nitrogen species |
| **ROC–AUC** | Receiver operating characteristic–area under the curve |
| **ROS** | Reactive oxygen species |
| **S-Trap** | Suspension trapping |
| **SD** | Standard deviation |
| **SDS** | Sodium dodecyl sulfate |
| **SDS–PAGE** | In-gel purification with sodium dodecyl sulfate–polyacrylamide gel electrophoresis |
| **SEM** | Standard error of the mean |
| **Ser** | Serine |
| **SL** | Sodium laurate |
| **SP3** | Single-pot solid-phase-enhanced sample preparation |
| **SPE** | Solid-phase extraction |
| **T** | Thymine |
| **TCEP** | Tris(2-carboxyethyl)phosphine |
| **TDP-43** | TAR DNA-binding protein 43 |
| **TEAB** | Triethylammonium bicarbonate |
| **TFA** | Trifluoroacetic acid |
| **Thr** | Threonine |
| **TIMS** | Trapped ion mobility spectrometry |
| **TOF** | Time-of-flight |
| **Trp** | Tryptophan |
| **Tyr** | Tyrosine |
| **U** | Uracil |
| **UHPLC** | Ultra-high-performance liquid chromatography |
| **UMAP** | Uniform manifold approximation and projection |
| **Val** | Valine |
| **XAS** | X-ray absorption spectroscopy |
| **y BP** | Years Before Present (AD 1950) |

# 1 Introduction

## 1.1 Research Problem

Archaeologists have long treated ancient, preserved human brains as isolated curiosities, frequently employing the singular language of anomaly, rarity, or uniqueness in their reports on such finds; yet the existence of multiple such reports renders that framing inherently untenable. The more significant (though overlooked) observation is that these brains are often preserved in the absence of other soft tissues, despite the brain being among the organs most vulnerable to rapid *post-mortem* decomposition. That this pattern has been documented across centuries of archaeology without attracting mechanistic explanation is itself telling: it points to a systematic phenomenon whose causes have been consistently overlooked rather than merely missed. This paradox exposes a major gap in our current understanding of soft-tissue preservation: existing taphonomic models explain persistence primarily in terms of the depositional environment and a limited set of canonical preservation types (such as dehydration and freezing), which do not adequately account for inter-organ divergence within the same body – whereby one exceptionally decay-prone tissue remains while others are lost.

Resolving this paradox requires a molecular-level framework that begins with the chemistry of biomolecular decomposition and preservation, considers how

environmental conditions regulate those processes, examines how the distinctive molecular architecture of nervous tissue conditions its *post-mortem* fate, and then asks how that fate can be investigated through the study of ancient proteins.

## 1.2 Molecular Taphonomy

The term *taphonomy* – from the Greek *taphos* ('grave') and *nomos* ('law') – was first introduced by Efremov [1] to describe the 'laws of burial'; that is, the scientific study of organic remains as they transition from the biosphere to the lithosphere [2, 3]. Behrensmeyer and Kidwell [4] subsequently refined the concept specifically to include 'the study of processes of preservation and how they affect information in the fossil record'; such that 'molecular taphonomy' may be understood as the study of these processes at the level of biomolecules [5, 6]. Although formalised only recently [7], the discipline has been practised for centuries [2]: among the earliest taphonomists was Leonardo da Vinci (AD 1452–1519), whose experiments on living and dead bivalves led him to conclude that fossils found at high elevation in the nearby Apennine mountains had not been transported there by the Biblical Flood, but rather lived and died *in situ* [8]. Da Vinci's observations on molluscs anticipated the central taphonomic distinction between the depositional circumstances in which remains are accumulated, and the later processes by which they are altered after burial.

### 1.2.1 Biostratinomy and diagenesis

An organism's taphonomic history – that is, its journey from the moment of death to the moment of its recovery from the archaeological or fossil record [9] – is conventionally divided into two phases that together describe the transfer of remains into the burial environment, and their subsequent alteration within it [10, 11]. Biostratinomy encompasses the interval between death and burial, during which remains are exposed at or near the surface and subject to physical redistribution, biological interaction, and early chemical modification [12, 13]. Diagenesis begins once remains are incorporated into a sedimentary or depositional context, and comprises the suite of physicochemical and biological processes that alter their

composition and structure over time [12, 14]. These phases are causally linked: processes initiated during biostratinomy condition the state in which remains enter the burial environment, and thereby constrain the taphonomic trajectories available during subsequent diagenesis [15].

During the biostratinomic interval, remains are subjected to processes that redistribute tissues within the surrounding environment and regulate the extent of exchange with it [16]. Mechanical processes such as disarticulation, fragmentation, and transport alter anatomical relationships and expose new tissue surfaces [17–19], whether driven by physical agents such as wind, water flow, or gravity [20], or by biological activity including scavenging, trampling, and bioturbation [13, 21]. Vertebrate scavenging [22–24] and invertebrate and microbial activity [25, 26] also contribute to selective tissue loss and carcass dispersal, accelerating the removal of labile soft tissues and increasing the surface area of remaining material. Increased surface area enhances interaction with atmospheric oxygen and liquid water, accelerating oxidative and hydrolytic reactions at exposed interfaces [27]. Repeated cycles of hydration and desiccation, thermal stress, and solar irradiation promote shrinkage and progressive loss of structural cohesion in soft tissues [28, 29], and induce cracking and delamination of bone [30, 31]. Disruption of tissue structure reduces the degree of compartmentalisation that would otherwise limit enzymatic degradation and microbial colonisation of sequestered substrates [32]. Biostratinomy thus governs the chemical state in which biomolecules enter the burial environment by controlling surface accessibility, exposure time, and the integrity of structural barriers.

Following burial, diagenesis encompasses the progressive alteration of remains within the sedimentary matrix, mediated by interactions between decaying organic matter, microbial communities, pore fluids, and mineral phases [14, 33]. These interactions are governed by a set of interrelated physicochemical parameters, including temperature [34], water activity [35], pH [36], redox potential [37], and ionic strength [38], which together define the local reaction environment (i.e., the ‘microenvironment’). Hydrolysis cleaves susceptible covalent bonds within

biomolecules [39], while dissolution mobilises mineral and organic constituents into pore waters, facilitating their redistribution or loss from decaying remains [40]. Once in solution, ions and organic molecules may participate in exchange reactions and complexation processes that alter the composition of both organic and inorganic phases through the incorporation, sequestration, or release of dissolved species [41]. These changes in pore-water chemistry can in turn promote recrystallisation of existing minerals or precipitation of new mineral phases, modifying the structure and composition of mineral-associated tissues [42]; such mineral transformations may occlude pore spaces or encapsulate organic material, thereby altering accessibility to fluids and microorganisms [43]. These processes do not operate in isolation, but as components of a coupled and evolving system in which multiple reactions proceed concurrently, compete for substrates, and modify the local chemical environment, thereby influencing the direction and rate of subsequent reactions [44].

Accordingly, biostratinomy conditions the physicochemical state in which remains enter the burial environment, while diagenesis governs their subsequent transformation within it. The material ultimately recovered from the archaeological and fossil records therefore reflects the cumulative effects of both phases, overprinted by any subsequent modification during excavation, handling, and storage [45]. As a result of this superimposition, the contributions of individual processes cannot be resolved directly from the end product alone; rather, they must be inferred by reconstructing the sequence of transformations and the conditions under which they occurred [46].

### 1.2.2 Experimental taphonomy

Experimental taphonomy is the field's actualistic branch [47], which reconstructs taphonomic trajectories – that is, the chemical pathways by which biological tissues are altered, degraded, or preserved from the moment of death to their eventual recovery – by observing the transformation of extant organisms, isolated tissues, or tissue analogues under controlled laboratory conditions [47]. It serves two related aims: (i) the reconstruction of the processes that generate preservation, on timescales that can be observed directly, manipulated experimentally, and then used to infer

longer-term trajectories, and (ii) the resolution of the sequence of morphological transformation and data loss that occurs during decomposition [48].

Experimental taphonomy can be separated into two complementary approaches: decay experiments, which track the early *post-mortem* breakdown of tissues under biologically and environmentally realistic conditions [49], and maturation experiments, which subject organic materials to elevated temperatures and pressures in order to accelerate diagenetic reactions that would otherwise occur over geological timescales [50]. The latter, widely employed in both palaeontology and organic geochemistry, typically involve enclosing samples within sealed metal capsules and heating them under controlled pressure regimes, thereby promoting chemical transformation, condensation, and polymerisation reactions associated with long-term burial [51–54]. These approaches provide a means of experimentally approximating the later stages of diagenesis [55], and assessing the stability of biomolecules under conditions of thermal maturation [56–58]. However, because maturation experiments necessarily impose physicochemical conditions that exceed those encountered in most archaeological contexts, their outputs are most directly applicable to deep-time fossilisation [59], rather than to the shorter-term, 'shallow-time' burial environments characteristic of archaeology. By contrast, decay experiments operate on timescales and under conditions that more closely approximate the early *post-mortem* interval (PMI) [60], during which the principal biochemical transformations that govern subsequent taphonomic trajectories are established [47].

The methodological premise is that complex taphonomic systems can be reduced to a set of experimentally tractable variables while preserving the relationship between the decaying organic remains and depositional environment, that together governs the rate and mode of degradation [47, 49, 61]. Confounding biological variables include phylogenetic affinity [62], ontogenetic stage [63], tissue type [64], and physiological condition at death [65], while confounding environmental variables include temperature [66], water activity [67], oxygen availability [68], pH [69], salinity [70], sedimentary matrix [71], burial depth [72], and the composition and activity of associated microbial communities [73]. Moreover, the means by which

decay is observed and quantified constitute additional, analytical variables, given different measurements capture different aspects of the taphonomic process and may therefore yield different estimates of decay progression. Common metrics include anatomical loss [74], mass loss [75], histological alteration [76], and molecular change [77]. This design logic has remained a constant across the development of experimental taphonomy, while the analytical emphasis has evolved from descriptive staging to quantitative, process-based measurement [78].

A further strength of experimental decay is that it allows the physicochemical environment of decomposition to be characterised directly, rather than inferred from end products. Decomposition is accompanied by rapid and spatially heterogeneous shifts in physicochemical parameters that collectively define the microenvironment in which biomolecular transformation proceeds [79, 80]. For example, recent work has shown that carcasses of different taxa generate measurably different redox conditions even when placed in ostensibly identical depositional contexts [37, 68], suggesting that body size and bulk organic composition influence how rapidly reducing conditions develop around decaying remains [81]. As a consequence, identical depositional settings can support divergent chemical regimes at the scale of individual carcasses [64, 82–85], leading to differences in rates of degradative processes (such as hydrolysis, oxidation, and microbial consumption), as well as in the likelihood of stabilising transformations (such as polymerisation, crosslinking, and mineral interaction). Experimental decay therefore provides a means of connecting the intrinsic properties of biological tissues to the microenvironmental conditions that govern their subsequent taphonomic trajectories [36].

The principal methodological challenge for experimental taphonomy is translation rather than replication. Laboratory experiments isolate individual controls, whereas natural depositional systems superimpose multiple interacting variables across space and time [60, 61]; accordingly, experimental decay is most informative when interpreted as a framework for causal inference, rather than as a direct simulation of the fossil record [44]. The most robust recent studies address this by integrating controlled decay experiments with advanced quantitative analytical

approaches spanning molecular, microbiological, geochemical, and physicochemical domains, enabling high-resolution characterisation of biomolecular composition and environmental conditions through time. This shift has moved experimental taphonomy from purely descriptive observation toward measurement-driven reconstruction of taphonomic trajectories, with the goal of constraining which biological and environmental variables can plausibly generate the exceptional preservation observed in archaeological and palaeontological material. These constraints, however, operate on organic substrates that differ fundamentally in their chemical composition and structure; consequently, identical taphonomic conditions do not yield uniform outcomes across all biomolecular classes.

### 1.2.3 Biomolecular preservation

The preservation of organic matter after death is intrinsically selective, reflecting systematic differences in the chemical stability of constituent biomolecules [86, 87]. A consistent hierarchy is observed in which nucleic acids are rapidly degraded, proteins and carbohydrates evidence intermediate and variable survival, and lipids and structurally complex biopolymers exhibit the greatest persistence (Figure 1.1) [86]. This pattern arises from fundamental aspects of molecular architecture and reactivity. Labile molecules such as ribo- and deoxyribo-nucleic acids (RNA and DNA, respectively) contain hydrolysable backbones and are highly susceptible to depurination, strand cleavage, and oxidative damage, leading to rapid fragmentation and loss [88, 89]. Proteins, while also prone to hydrolysis and oxidation, may partially persist where structural features or intermolecular interactions limit accessibility or promote stabilising modifications [90–92]. By contrast, many lipids and structurally complex biopolymers are characterised by hydrophobicity, repetitive or crosslinked architectures, and reduced functional group reactivity, which together confer resistance to aqueous degradation and favour long-term survival [93]. Importantly, preservation does not necessarily entail the retention of intact biomolecules: while

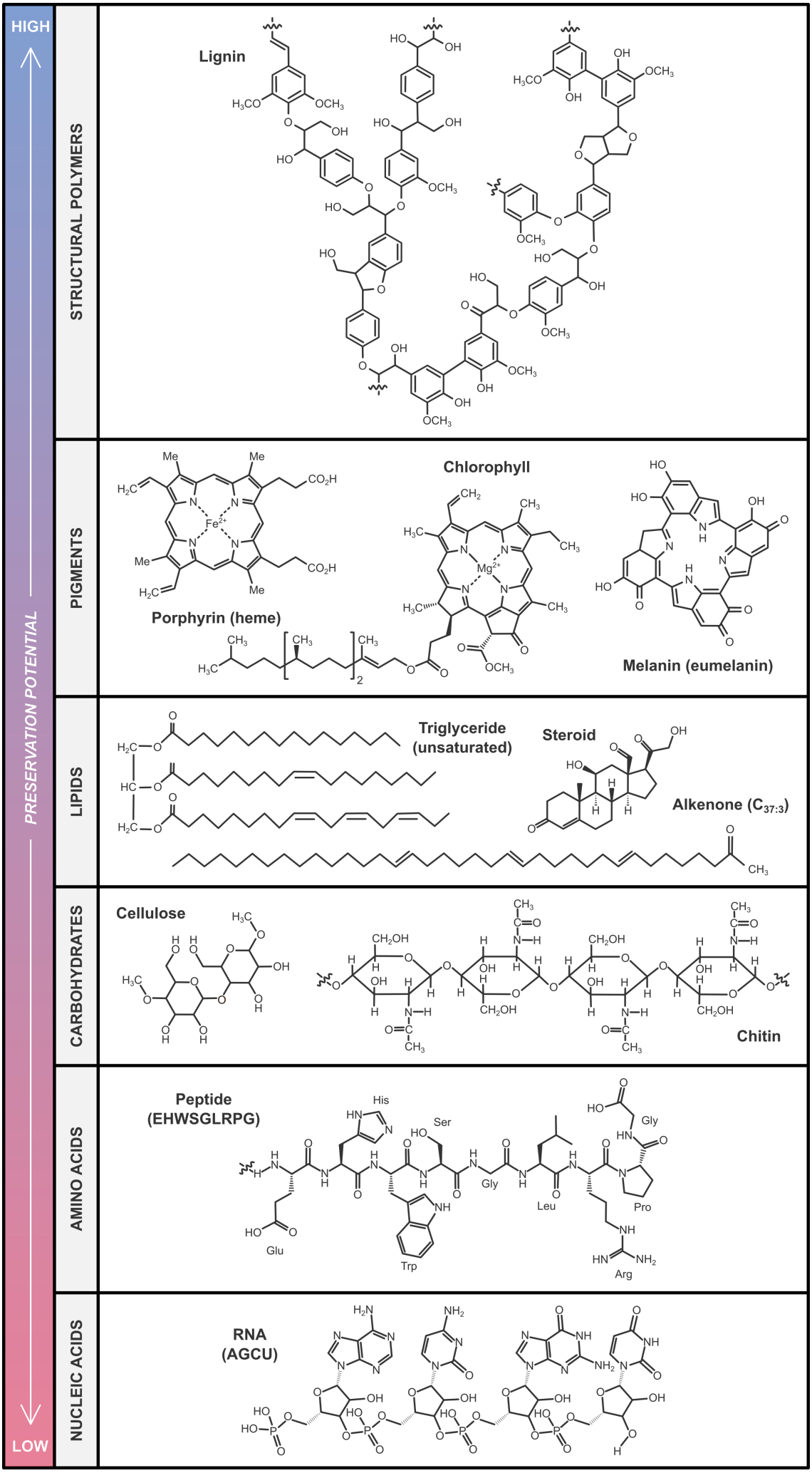



**Figure 1.1 | Differential preservation potential of biomolecular classes.**

some molecules may retain aspects of their native architecture, original structures are frequently altered by diagenetic transformation, yielding modified derivatives that preserve information about their biological precursors [86]. The following sections examine each biomolecular class in turn, relating their chemical properties to their differential preservation potential.

#### 1.2.3.1 Structural polymers and pigments

Structural polymers and pigments comprise distinct classes of biomolecules that nonetheless converge on physicochemical properties associated with high preservation potential. Structural polymers are predominantly extracellular, network-forming biopolymers that strengthen cell walls or protective envelopes, and form barriers to water, solutes, and pathogens [94–96]; they are generated by enzymatic or oxidative polymerisation of precursor molecules into irregular, crosslinked macromolecular assemblies [97, 98]. Unlike sequence-defined biopolymers such as proteins (Section 1.2.3.4) or nucleic acids (Section 1.2.3.5), structural polymers exhibit heterogeneous connectivity, variable bond types, and extensive three-dimensional crosslinking, producing insoluble matrices in which reactive functional groups are unevenly distributed and often sterically shielded [99, 100]. Their resistance to degradation arises from relatively low solubility, restricted molecular mobility, and limited access to susceptible bonds [100], such that decay proceeds through spatially heterogeneous hydrolysis and oxidation [101, 102], with secondary condensation and crosslinking increasing recalcitrance over time [51, 103, 104]. Sporopollenin, an exceptionally inert, heavily crosslinked polymer incorporating both aliphatic and aromatic domains [105, 106], has been reported diagenetically unaltered from the Late Carboniferous ($\sim$ 310 Ma) [107].

Pigments, by contrast, are chemically diverse biomolecules defined by their visible-light absorption, which commonly arises from extended $\pi$-conjugated systems [108] or electron-delocalised chromophores [109]. Pigments include low-molecular-weight compounds such as carotenoids [110] and porphyrins [111], and macromolecular assemblies such as melanins [112]. Low-molecular-weight pigments

**Box 1.1 | *Melanin***

Melanin provides a well characterised example of a pigment that illustrates the chemical basis of their persistence in soft tissues [128]. Eumelanin consists of a heterogeneous assembly of indole-derived units (principally 5,6-dihydroxyindole and related structures) linked through carbon–carbon (C–C) and carbon–oxygen (C–O) bonds into an amorphous, $\pi$-conjugated network [129]. This architecture confers resistance to degradation through several mechanisms. First, the absence of a periodic backbone containing uniform hydrolysable bonds removes a dominant, repeatable site of cleavage. Second, extensive conjugation stabilises radical intermediates [130], favouring electron delocalisation over bond scission during oxidative stress. Third, strong chelation of transition metals (e.g., Fe, Cu) facilitates redox cycling [131] that can drive further oxidative coupling and condensation reactions. During diagenesis, melanin therefore undergoes progressive oxidation and covalent rearrangement within an already crosslinked network, yielding a chemically modified but structurally persistent residue [118].

commonly undergo fragmentation, oxidation, cyclisation, and aromatisation during diagenesis, yielding more stable derivatives that preserve diagnostic structural motifs [113–116]. Melanins (Box 1.1) form through oxidative polymerisation of phenolic or indolic precursors into heterogeneous, crosslinked, largely insoluble networks [117]: the resulting aromatic, electronically delocalised architecture resists complete depolymerisation and instead undergoes progressive oxidative crosslinking, metal chelation, and secondary condensation during diagenesis [58, 118, 119], yielding insoluble residues that retain elements of the original molecular structure [120, 121]. Porphyrins have been recovered from Proterozoic sediments ($\sim$ 1.1 Ga) [115], and melanin-derived residues from Palaeozoic ($\sim$ 325 Ma) [122], Jurassic ($\sim$ 200 Ma) [123–125], Cretaceous ($\sim$ 130 Ma) [126], and Palaeogene ($\sim$ 50 Ma) [120, 127] fossil organisms.

#### 1.2.3.2 Lipids

Lipids comprise a diverse class of relatively low-molecular-weight, amphiphilic compounds characterised by a hydrocarbon-based hydrophobic core and a polar head group [132, 133]. In contrast to proteins, which are assembled from 20 amino acids (Section 1.2.3.4), and nucleic acids, which derive from four nucleotide bases (Section 1.2.3.5), lipids are biosynthesised from two principal precursor types: acetate-derived units (acetogenic lipids, formed *via* acetyl-CoA) and isoprene units (polyisoprenoids) [134]. Given the wide range of compounds encompassed, their preservation potential varies as a function of bond type and molecular architecture

[86, 134], which determine the dominant degradation pathways to which lipids are susceptible. Lipids in which functional groups are linked by ester bonds – such as triacylglycerols and many phospholipids – contain hydrolysable ester and phosphate ester/phosphodiester linkages that are readily cleaved under aqueous and enzymatic conditions [135], yielding free fatty acids, glycerol, and deacylated phospholipid products [136, 137]. Unsaturated fatty acids undergo autoxidation initiated at allylic positions [138], forming hydroperoxides that decompose to shorter-chain acids, aldehydes (R−CHO), ketones (R−C[=O]−R′), and related secondary oxidation products [139].

By contrast, lipids dominated by C−C and carbon–hydrogen (C−H) bonds, particularly those incorporating cyclic or polycyclic frameworks (such as sterols and their derivatives; Box 1.2), lack equivalent labile linkages and therefore exhibit greater resistance to hydrolytic breakdown [140, 141]. These hydrocarbon-rich lipids undergo progressive loss or modification of functional groups, including dehydration, isomerisation, reduction, and, in some pathways, side-chain oxidation or decarboxylation [142]; such reactions simplify the molecule while preserving the underlying carbon framework [134]. As a result, lipid preservation is typically expressed as a suite of diagenetic derivatives that retain the carbon skeleton of the original biomolecule, but lack its original functionalisation [93, 143]. Such derivatives have been recovered from sediments dating as far back as the Proterozoic ($\sim$ 1.6 Ga), where aryl isoprenoid biomarkers (breakdown products of aromatic carotenoid pigments) provide molecular evidence for the redox-associated ecological niches of ancient microbial communities [144].

#### 1.2.3.3 Carbohydrates

Carbohydrates comprise a chemically broad class of polyhydroxy aldehydes and ketones and their derivatives, but preserved polysaccharides dominate in taphonomic contexts [6, 151]. These polymers exhibit substantial structural diversity [152], arising from both the range of constituent monosaccharides – exceeding 20 common types when distinct sugar identities and their pyranose (six-membered) and furanose

**Box 1.2 | *Cholesterol***

Cholesterol is the principal sterol of animal cell membranes [145]. It comprises a rigid tetracyclic (cyclopentanoperhydrophenanthrene) nucleus, a $\beta$-oriented hydroxyl ($-$OH) group at C3, a $\Delta^5$ double bond within the ring system, and an eight-carbon aliphatic side chain at C17 [146]. The molecule is dominated by a polycyclic hydrocarbon framework in which C$-$C bonds are arranged in a conformationally constrained structure, while functionalisation is limited to a small number of substituents [146]. This architecture confers relative resistance to degradation: cholesterol lacks repeating, readily hydrolysable linkages, and its fused tetracyclic ring system promotes retention of the carbon skeleton during diagenesis and thermal maturation, as observed for sterols more generally in the fossil record [134, 147]. As a result, diagenetic reactions act primarily on the peripheral functional groups – removing the C3 hydroxyl group by dehydration, followed by isomerisation and hydrogenation of unsaturations, and structural rearrangement or reduction of the steroid skeleton [148] – while the polycyclic core is retained. During diagenesis, these modifications progressively simplify the molecule, yielding sterenes, diasterenes, and ultimately steranes that preserve the carbon skeleton and aspects of the original stereochemistry [149, 150]. Cholesterol therefore illustrates a broader principle of lipid preservation: chemical transformation proceeds through selective loss of functionalisation while conserving a structurally robust hydrocarbon framework [134, 147].

(five-membered) forms are considered – and the variability of the glycosidic linkages that connect them [153]. Unlike the chemically uniform backbones of nucleic acids and proteins, glycosidic bonds vary in stereochemistry ($\alpha$- or $\beta$-type), position, and branching, and monosaccharide residues can participate in multiple linkage points [153]. Additional complexity arises from covalent association with proteins and lipids (glycoconjugates) and from the capacity to form higher-order and, in some cases, crystalline structures [153, 154].

Polysaccharide stability is governed primarily by the accessibility of glycosidic linkages to hydrolytic attack [155], which is in turn controlled by molecular architecture; specifically linkage stereochemistry, degree of branching, and supramolecular organisation [156]. Storage polysaccharides (such as glycogen and starch) are highly branched and largely amorphous, presenting exposed glycosidic bonds that are readily hydrolysed and therefore tend to be short-lived [157, but see 158]. In contrast, structural polysaccharides (such as cellulose and chitin) adopt extended $\beta$-linked conformations that promote dense interchain hydrogen bonding and ordered packing [159], limiting solvent penetration and enzymatic access to the backbone [160, 161]. The dominant degradative pathways of carbohydrates are hydrolysis of glycosidic bonds and enzymatic depolymerisation [156], followed by microbial attack [162] and, where reducing ends are present, oxidation reactions that further destabilise the polymer [163]. Chitin (Box 1.3) is one of the best-documented examples of

**Box 1.3 | *Chitin***

Chitin is a linear polymer composed of N-acetyl-D-glucosamine linked by 1,4-$\beta$-glycosidic bonds [168], and constitutes the principal structural aminopolysaccharide in fungal cell walls, arthropod cuticles, and many molluscan and sponge tissues [169]. Its persistence arises from a combination of molecular and supramolecular features: the extended $\beta$-linked backbone supports dense interchain hydrogen bonding, while the acetamido group ($-NH-C[=O]-CH_3$) at C2 facilitates additional intra- and intermolecular hydrogen bonding *via* its N–H donor and carbonyl (C=O) oxygen acceptor [159], promoting the formation of highly ordered crystalline polymorphs ($\alpha$-, $\beta$-, and $\gamma$-chitin) [170]. This organisation reduces accessibility of glycosidic linkages to hydrolytic enzymes and limits solvent penetration [160, 161]. In extant organisms, chitin is frequently incorporated into composite materials in which it is associated with proteins [171] and, in some taxa, mineral phases [172]; these associations further restrict molecular mobility and reduce accessibility of the glycosidic backbone to enzymatic and chemical attack [161]. Degradation proceeds through selective cleavage of glycosidic, amide, and ester linkages, with preferential loss of amorphous domains and chain ends, while crystalline regions remain comparatively resistant [166]. Early diagenesis involves partial depolymerisation accompanied by deacetylation of N-acetyl groups ($N-C[=O]-CH_3$) and dehydration of the polysaccharide backbone, generating unsaturated (ene–ketone) structures and reducing hydroxyl functionality [173, 174]. Concurrently, breakdown of associated proteins and lipids releases fatty acids that become covalently incorporated into the residual chitin scaffold *via* ester linkages, forming an increasingly aliphatic, crosslinked macromolecular network [174]. Nitrogen is retained within this modified framework in altered forms (e.g., amides [$R-C(=O)-NR'$], imines [C=N], and oxidised species such as nitro groups [$-NO_2$]), reflecting transformation rather than wholesale loss of the original aminopolysaccharide [166].

long-term carbohydrate preservation, having been detected in Proterozoic ($\sim 1$ Ga) fungal cell walls [164] and Cambrian ($\sim 500$ Ma) sponges [165], as well as a range of Palaeozoic (540–250 Ma) arthropods [103, 104, 166, 167].

#### 1.2.3.4 Proteins

Proteins are linear heteropolymers of amino acids linked by peptide bonds [175]. Each amino acid consists of a central ($\alpha$-) carbon atom covalently bonded to four substituents: an amino group ($-NH_2$, protonated as $-NH_3^+$ under physiological conditions), a carboxyl group ($-COOH$, typically deprotonated to $-COO^-$), a hydrogen atom, and a variable side chain (R group) that defines its chemical properties [175]. The 20 canonical proteinogenic amino acids are commonly grouped by side-chain chemistry into aliphatic (Ala, Gly, Ile, Leu, Pro, Val), hydroxylic (Ser, Thr), aromatic (Phe, Trp, Tyr), amidic (Asn, Gln), sulfur-containing (Cys, Met), acidic (Asp, Glu), and basic (Arg, His, Lys) classes [176]. These side chains differ in charge state, polarity, hydrogen-bonding capacity, metal coordination behaviour, and redox reactivity, and therefore determine the distribution of nucleophilic, electrophilic, and metal-binding sites within a protein (Box 1.4) [176]. With the

**Box 1.4 | *An example peptide sequence: EHWSGLRP***

The peptide sequence EHWSGLRP (Figure 1.1) illustrates how residue-specific chemistry interacts with local structure to influence preservation [178]. For clarity, each residue is considered individually here; however, it is important to recognise that the reactivity of each residue in a folded protein depends on local secondary structure and interactions with neighbouring residues, such that modifications at one site can alter the chemical reactivity and microenvironment of others [179].

E (Glu) contains a $\gamma$-carboxylate group that is negatively charged at physiological pH and participates in salt bridges and metal coordination [180]. When involved in stabilising interactions or buried within a folded structure, it can reduce local solvent access [181]; when exposed, its polarity promotes hydration of the local environment and can increase the exposure of nearby peptide bonds to hydrolytic attack [182].

H (His) bears an imidazole ring ($C_3H_7N$) with a p$K_a$ near physiological pH, enabling reversible protonation and strong coordination of transition metals [183]. This capacity promotes metal-catalysed oxidation reactions, which can locally destabilise structure and accelerate both backbone cleavage and side-chain modification [184].

W (Trp) contains an electron-rich indole ring that is highly susceptible to oxidative attack [185], which disrupts aromatic stacking and hydrophobic interactions, destabilising local structure and increasing exposure of neighbouring residues [186].

S (Ser) bears a primary alcohol ($-CH_2-OH$) capable of hydrogen bonding and, *in vivo*, O-phosphorylation or O-glycosylation [187]. *Post-mortem*, loss of these labile substituents can alter local hydrogen-bonding interactions and increase accessibility of the underlying protein surface [187].

G (Gly), whose side chain is hydrogen, does not itself host side-chain PTMs. However, it imparts conformational flexibility to the backbone, which can reduce local structural order and expose adjacent peptide bonds [188].

L (Leu) is a hydrophobic aliphatic residue that contributes to non-polar core packing [189]. When buried, it limits water penetration and stabilises adjacent peptide bonds; when exposed, it offers little intrinsic chemical protection [189].

R (Arg) contains a positively charged guanidinium group ($-NH-C[=NH_2^+]-NH_2$) that forms strong electrostatic and hydrogen-bonding interactions, stabilising local structure [190]. It is susceptible to non-enzymatic glycation and oxidative carbonylation, both of which alter charge and disrupt interactions [191].

P (Pro) is unique in that its side chain forms a covalent bond with the backbone nitrogen, constraining backbone geometry and reducing conformational freedom [192]. This constraint can modulate the hydrolytic susceptibility of adjacent peptide bonds, depending on sequence context and environment [193], while Pro itself can still undergo oxidation and cis–trans isomerisation [194].

The absence of Asn, Gln, Cys, and Met removes several of the most labile deamidation and sulfur-oxidation sites [195, 196]. At eight residues in length, EHWSGLRP lies within the size range routinely detected by mass spectrometry (MS) [197]; if recovered intact or with limited modification, it may still retain enough sequence information for confident assignment to a protein.

exception of Gly, whose side chain is hydrogen, all proteinogenic amino acids are chiral at the $\alpha$-carbon and L-configured in extant biology [177].

Peptide-bond formation links the $\alpha$-carboxyl group of one residue to the $\alpha$-amino group of the next by condensation, yielding an amide linkage ($-CO-NH-$) with substantial resonance stabilisation, partial double-bond character, and restricted rotation about the C–N bond [175]. This planarity constrains backbone conformation and underpins the hierarchical organisation of protein structure: primary structure is the linear amino-acid sequence; secondary structure comprises regular backbone

hydrogen-bonding motifs (most commonly $\alpha$-helices and $\beta$-sheets); tertiary structure is the three-dimensional fold of a single polypeptide chain; and quaternary structure is the association of multiple polypeptide chains into higher-order assemblies [175]. This hierarchical organisation produces a heterogeneous distribution of solvent accessibility, local dielectric environment, conformational flexibility, and steric constraint, such that identical residues can exhibit markedly different chemical reactivity depending on their structural context [179].

Proteins support a very large and still-expanding repertoire of post-translational modifications (PTMs) *in vivo*, with more than 600 PTM types and on the order of $10^6$ mapped sites reported in current databases [198], although annotation remains uneven and strongly biased toward a subset of species and PTM types [199–201]. By contrast, the *post-mortem* modification space is much less completely mapped, despite the principal degradative pathways being well established [202]. In aqueous environments, peptide bonds undergo hydrolysis, leading to chain scission and progressive fragmentation [203, 204]. Side-chain reactions then dominate the surviving fragments: deamidation of Asn and Gln [205]; oxidation of sulfur-containing [195, 196, 206, 207] and aromatic residues [208–210]; carbonylation of susceptible side chains [211, 212]; racemisation and isomerisation at the $\alpha$-carbon [213]; and non-enzymatic glycation reactions (Section 1.4.5.2) [214]. Disulfide bonds (–S–S–), formed by oxidation of paired Cys residues, act as covalent crosslinks that stabilise tertiary and quaternary structure by lowering conformational entropy in the unfolded state [215]; reduction, oxidation, or exchange of these links can destabilise folded conformations, increase solvent access, and facilitate subsequent hydrolysis [216].

These *post-mortem* processes – collectively termed diagenetic PTMs – are generally non-enzymatic, sequence-dependent, and effectively irreversible on diagenetic timescales, and the resulting modified states are often described as ‘diagenetiforms’, in contrast to *in vivo* proteoforms [217]. Recent work indicates that endogenous peptide sequences can persist well into the Miocene ($\sim 20\,\mathrm{Ma}$) under favourable conditions [218], particularly within mineral-bound or otherwise closed systems [219].

Claims of substantially greater antiquity – most notably Cretaceous ($> 65\,\mathrm{Ma}$) 'dinosaur' peptides [220, 221] – are contested [222, 223], and remain unresolved. Nonetheless, continued improvements in extraction protocols and high-resolution tandem mass spectrometry (MS/MS) are progressively extending the temporal limits of protein recovery [202, 224], suggesting that the current upper bound reflects both preservational constraints and analytical sensitivity.

#### 1.2.3.5 Nucleic acids

Nucleic acids are linear polymers of nucleotides, each of which consists of three components: a nitrogenous base (nucleobase), a pentose sugar (deoxyribose in DNA, ribose in RNA), and one or more phosphate groups [225]. The nucleobase may be either a purine (adenine [A] or guanine [G]) or a pyrimidine (cytosine [C] or thymine [T] in DNA, and cytosine or uracil [U] in RNA) [225]. In DNA, complementary bases (A – T and C – G) form hydrogen-bonded pairs that stabilise the characteristic double-helical structure [226]; RNA is typically single-stranded but can form local secondary structures through intramolecular base pairing [227]. Nucleotides are linked by $3', 5'$-phosphodiester bonds, in which the phosphate group connects the $3'$-hydroxyl of one sugar to the $5'$-phosphate group of the next, forming a repeating sugar–phosphate backbone with inherent directionality ($5' \rightarrow 3'$) [225]. Each linkage consists of the same phosphodiester functional group, such that the backbone presents a continuous series of equivalent hydrolysable bonds: this structural regularity renders nucleic acids susceptible to systematic backbone cleavage, in contrast to the heterogeneous bonding patterns of many other biomolecular classes.

The chemical stability of nucleic acids is strongly influenced by the structure of the sugar moiety. RNA contains a $2'$-hydroxyl group on the ribose ring, which can act as an intramolecular nucleophile, attacking the adjacent phosphate group to form a cyclic $2', 3'$-phosphate intermediate in a transesterification reaction [228]. This reaction results in backbone scission and fragmentation as one phosphodiester bond is cleaved and another is formed, and can proceed spontaneously under a wide range of aqueous conditions [229], rendering RNA intrinsically less stable than DNA

**Box 1.5 | *An example RNA sequence: AGCU***

The RNA sequence AGCU illustrates how the chemical structure of ribonucleotides governs instability and fragmentation. Each nucleotide contains a ribose sugar bearing a 2′-hydroxyl group positioned to attack the adjacent phosphodiester linkage [228]. Cleavage can therefore occur at any position along the backbone *via* intramolecular transesterification, in which the 2′-hydroxyl acts as a nucleophile, forming a cyclic 2′,3′-phosphate intermediate and breaking the chain [228]. This non-enzymatic reaction leads to rapid fragmentation into shorter nucleic acid fragments (oligonucleotides, typically $<$ 20 nucleotides in length) [235].

The nucleobases introduce additional, parallel degradation pathways. Adenine and guanine, as purines, are susceptible to depurination, generating apurinic sites that destabilise the backbone and promote strand cleavage [236]. Cytosine undergoes deamination to uracil, altering base identity and introducing miscoding lesions [237, 238]. Uracil is not subject to further deamination but remains susceptible to oxidative modification [239]. These base-level reactions act in concert with backbone cleavage to produce progressive shortening and chemical alteration of the sequence [240], such that RNA is rarely preserved beyond short, highly degraded fragments, even under favourable conditions [241, 242].

[228]. DNA, lacking a 2′-hydroxyl group on its pentose sugar, does not undergo this intramolecular cleavage pathway and is therefore comparatively more stable [230], although it remains chemically labile on diagenetic timescales.

The dominant degradative pathways of DNA are hydrolytic and involve both the sugar–phosphate backbone and the attached bases (Box 1.5) [231]. Depurination – the hydrolytic cleavage of the N-glycosidic bond linking purine bases to the deoxyribose sugar – results in the loss of the base and the formation of an abasic (apurinic/apyrimidinic) site [231]. Depyrimidination, the analogous loss of cytosine or thymine, proceeds *via* the same mechanism but at a lower rate [231]. These abasic sites destabilise the backbone and promote strand cleavage through $\beta$-elimination reactions [232]. In parallel, cytosine residues undergo spontaneous deamination, in which the exocyclic amino group at C4 is hydrolytically replaced by a carbonyl group, converting cytosine to uracil [233]. During high-throughput DNA sequencing, this chemical change is detected as an apparent cytosine-to-thymine (C $\rightarrow$ T) substitution on one strand, and a complementary guanine-to-adenine (G $\rightarrow$ A) substitution on the opposite strand: a characteristic signature of *post-mortem* DNA damage [234]. Additional reactions, including oxidative modification of bases and covalent crosslinking between strands or with proteins, further contribute to molecular degradation [234].

As a result of these processes, nucleic acids are typically preserved as highly fragmented, chemically modified molecules rather than intact sequences [89, 231]. Preservation depends primarily on environmental conditions that limit hydrolysis and oxidative damage [243]: low temperature, reduced water activity, and chemical sequestration – particularly adsorption to mineral surfaces or encapsulation within protective matrices [244, 245] – reduce reaction rates by limiting molecular mobility and water-mediated reactions, as well as restricting interactions with oxidants and other reactive species. Under favourable conditions such as these, ancient DNA has been recovered from permafrost sediments dating to the Pleistocene ($\sim$ 2 Ma) [246], representing the current upper limit of authenticated sequence recovery; by contrast, authenticated RNA sequences are currently limited to late Quaternary contexts ($\sim$ 50 ka) [247, 248].

## 1.3 Death & Decomposition

The preservation potential of any biomolecule is realised only through its interaction with the physicochemical changes initiated after death. From a biological perspective, death is a process; from the medical perspective, however, it is necessary to define a point in the process at which death can be diagnosed and confirmed in an accurate and systematised manner [249, 250]. Thus, in the UK death is defined as 'the permanent loss of the capacity for consciousness, combined with permanent loss of the capacity to breathe' [251]. Three diagnostic criteria – somatic, circulatory, and neurological – may be used depending on the circumstances in which death is suspected; circulatory criteria, for instance, are likely to be applied following cardiorespiratory arrest [252]. Of greatest relevance to molecular taphonomists are the somatic criteria, which, being macroscopically observable signs of decomposition (such as *livor* or *rigor mortis*), are most often applied when death is suspected to have occurred some time previously. The term 'somatic death' denotes the irreversible loss of integrated physiological function (specifically the vital functions of the brain, heart, and lungs) [253]; it does not, however, imply instantaneous failure of every constituent cell. Cellular death, which refers to a biological cell ceasing to

carry out its function(s) due to an irreversible loss of plasma membrane integrity [254, 255], is temporally and mechanistically heterogeneous: some cell populations lose viability within minutes of circulatory arrest, while others remain metabolically competent for hours [256, 257]. It is from this progressive, tissue-specific loss of cellular function [258] that the observable processes of decomposition arise.

The decomposition of a corpse is conventionally divided into five stages – fresh, bloated, active decay, post-decay and skeletonised – which are characterised by macroscopic changes in colour, odour, and texture (Table 1.1) [259, 260]. Although nominal time intervals are often quoted, there may be considerable variation in terms of how quickly a corpse enters and occupies each stage, depending principally on environmental factors (such as temperature, moisture, pH, burial or submersion, scavenging, and insect activity) and tissue-specific properties [261]. At the molecular level, the principal organising distinction is between two biochemical processes – autolysis (endogenous enzymatic self-digestion; Section 1.3.1) and putrefaction (microbially driven degradation; Section 1.3.2) – that together account for the major biochemical and morphological transformations observed during these stages [261].

**Table 1.1 | Decomposition stages with associated *post-mortem* phenomena.** Adapted from Powers [259] and after Galloway *et al.* [262]. Approximate time intervals (days) are included here as a tentative guide for terrestrial contexts; however, there is considerable variation in the time course of decomposition with an array of endogenous and exogenous factors, particularly in terms of the initiation and cessation of the post-decay stage. Note that stage boundaries are heuristic: macroscopic indicators overlap and may be asynchronous between body regions.

| Stage | Approx. PMI | Description |
|---|---|---|
| **Fresh** | 0–3 d | Begins at the moment of death and ends as putrefaction begins. During this stage, autolytic processes are active; readily observable macroscopic changes may include *pallor mortis* (paleness of the skin due to cessation of blood circulation) [263], *algor mortis* (equilibration of the body temperature with the environment) [264], *livor mortis* (lividity caused by gravitational pooling of the blood) [265], and *rigor mortis* (stiffening of the corpse due to contraction of the muscle fibres) [266].<br>Marbling may appear in the skin as oxygen dissociates from haemoglobin within gravitationally pooled blood, increasing the proportion of deoxyhaemoglobin and imparting a blue-purple hue (cyanosis); subsequent intravascular haemolysis (autolysis of red blood cells) releases haemoglobin that later participates in pigmentary and sulfide-mediated discolouration [267]. |

*Continued on next page*

| Stage | Approx. PMI | Description |
|---|---|---|
| | | Skin slippage may take place, as release of hydrolytic enzymes from cells at the dermal–epidermal junction causes loosening of the epidermis from the underlying dermis [267]. This can also produce bullae (fluid-filled blisters) on the skin. Insect activity is generally minimal at this stage [267]. |
| **Bloated** | 3–6 d | Begins with bloating of the corpse (a swelling characteristically crepitant to palpation), as putrefactive processes produce sufficient gaseous byproducts to inflate the abdominal cavity and other soft tissue [268]. A major component of this gas is hydrogen sulfide ($H_2S$): a small molecule readily diffused through decaying tissues, it reacts with haemoglobin in the red blood cells to form sulfhaemoglobin, a pigmented molecule that may cause the skin to adopt a green discolouration [269].<br>Other components include the breakdown products of microbially driven biomolecular degradation, such as hydrogen ($H_2$), carbon dioxide ($CO_2$), methane ($CH_4$), and ammonia ($NH_3$) [270]. This stage is characterised by geometric growth rates of, in the first instance, endogenous anaerobic bacteria of the gastrointestinal tract [271].<br>Latterly, invasive/opportunistic xenobiota colonising the corpse compete for the rich nutrient resource that decaying tissues represent [272]. Insect activity may be extensive, and accelerated as dark, malodorous fluids begin to leak from the body (purging) [273]. |
| **Active decay** | 5–11 d | Begins with abdominal rupture and/or other soft-tissue breaching, permitting the escape of trapped putrefactive gases. This process is both facilitated by and promotes insect activity and/or other scavenger feeding [273]. During this stage, there may be a substantial loss of soft-tissue mass (primarily as a consequence of maggot infestation) [274].<br>The corpse may appear blackened due to the accumulation of darkly pigmented breakdown products (such as ferrous sulfide [FeS] and melanoidins) [261].<br>Toward the end of this stage, as water continues to be lost from the ever-decreasing tissue mass, the corpse typically begins to dry, triggering a shift in insect population toward scavenging and predatory beetles [275]. |
| **Post-decay** | 10–25 d | The nature of this stage is highly dependent on the nature of the depositional environment; first and foremost whether the context is aquatic or terrestrial, and additionally the temperature, pH, indoor/outdoor location, burial/submersion depth, humidity/aridity, precipitation, circulating air/water currents, and the like. |
| **Skeletonised** | $\gtrsim$ 25 d | Conventionally defined as the stage at which only bones and, potentially, keratinous tissues (i.e., hair, nail) remain. |

### 1.3.1 Autolysis

Before considering the biochemical cascade that follows death, it is necessary to acknowledge the degree of structural organisation that characterises the living cell. A vertebrate cell is a highly organised, energy-dependent system in which lipid membranes maintain spatial segregation of otherwise reactive components [276].

Phospholipid bilayers define both the cell boundary and the membranes of internal organelles, delineating discrete microenvironments in which distinct metabolic processes occur [277]. Within these membrane-bound compartments, enzymes, substrates, and ions are maintained at carefully controlled concentrations [278]. Among these compartments are lysosomes, which sequester hydrolytic enzymes; peroxisomes, which mediate oxidative metabolism; and mitochondria, which generate energy to power the cell [278].

The bulk interior of the cell consists of an aqueous cytoplasmic matrix (the cytosol) enriched in dissolved ions, small metabolites, proteins, and ribonucleic complexes [279]. Interwoven throughout this space is the cytoskeleton: a dynamic network of filamentous proteins that confers mechanical stability, organises intracellular transport, and anchors membrane systems in place [280]. Genetic material – the millions to billions of polymerised nucleotide bases comprising the genome – is segregated within the nucleus, itself enclosed by a double membrane (the nuclear envelope) that regulates molecular traffic between nucleoplasm and cytoplasm [281]. Mitochondria, likewise membrane-bound, sustain cellular energetics by maintaining electrochemical gradients across their inner membranes, enabling adenosine triphosphate (ATP) synthesis through oxidative phosphorylation (Box 1.6) [282]. In life, this architecture is sustained by continuous energy input and by strict control of ionic and redox conditions [283]. The integrity of membranes, the sequestration of hydrolytic enzymes within acidic endolysosomal compartments, and the maintenance of electrochemical gradients are therefore active processes rather than passive states [284–286]; and it is precisely this dependence on metabolic regulation that renders cellular organisation inherently unstable once circulation and oxygen supply cease.

Within minutes of the onset of systemic hypoxia, cellular autolysis begins [293]. Autolysis refers to the 'self-digestion' of the cell; that is, the process by which endogenous catabolic enzymes act on cellular and molecular components that would not normally serve as substrates [259]. Compartmentalisation of these

**Box 1.6 | *Oxidative phosphorylation***

Under aerobic conditions, most cellular ATP is generated by oxidative phosphorylation at the inner mitochondrial membrane, from which energy is released by hydrolysis of phosphate ester linkages [287]. This process is driven by the electron transfer chain (ETC), in which electrons derived from reduced metabolic intermediates (principally nicotinamide adenine dinucleotide [NADH] and flavin adenine dinucleotide [$FADH_2$]) are passed along a sequence of membrane-associated protein complexes [287]. As electrons move through these complexes, they undergo a series of controlled oxidation–reduction reactions: the energy released during these reactions is used to pump protons ($H^+$) from the mitochondrial matrix across the inner membrane into the intermembrane space [288].

This proton movement creates both a chemical gradient (the difference in proton concentration) and an electrical gradient (the difference in charge, *aka.* the cellular membrane potential) across the otherwise proton-impermeable inner membrane. Together, these form an electrochemical gradient – the proton motive force – between the intra- and extracellular spaces that stores potential energy, which is maintained by the sodium–potassium ($Na^+$–$K^+$)-ATPase pump [289]. Protons can return to the matrix only by passing through ATP synthase, an enzyme embedded in the membrane: as protons flow down their gradient through ATP synthase, the enzyme harnesses this energy to attach a phosphate group to adenosine diphosphate (ADP), forming ATP [290].

Molecular oxygen ($O_2$) serves as the terminal electron acceptor at the end of the chain. When oxygen is unavailable – as occurs following circulatory arrest – electron flow ceases, proton pumping stops, the gradient dissipates, and ATP synthesis rapidly declines [291]. Disruption of any component of the chain, or damage to the inner mitochondrial membrane itself, similarly compromises ATP production [292].

enzymes – most notably within lysosomes, and more broadly within membrane-bound organelles including peroxisomes – protects the cellular machinery *in vivo* [278, 294], and their activity is constrained under physiological conditions by the near-neutral cytosolic pH ($\sim 7.2$), relative to the acidic lumen of the lysosome ($\sim 5.0$) [295]. When oxidative phosphorylation fails *post-mortem*, ATP production declines rapidly, disabling ATP-dependent ion transport and biosynthetic processes [291]. Failure of the $Na^+$–$K^+$-ATPase pump leads to intracellular accumulation of $Na^+$ and $Cl^-$ with diffusion of $K^+$ outward [289]; osmotic influx of water follows, producing organellar and cellular swelling (cytotoxic oedema) [296]. Simultaneously, ATP-dependent $Ca^{2+}$ pumps (including plasma membrane and sarcoplasmic/endoplasmic reticulum $Ca^{2+}$-ATPases) cease to function, and mitochondrial $Ca^{2+}$ buffering fails, resulting in elevated intracellular $Ca^{2+}$ concentrations [297]. Increased cytosolic $Ca^{2+}$ activates $Ca^{2+}$-dependent proteases (such as calpains [298] and phospholipases), promotes mitochondrial dysfunction and oxidative damage, and accelerates breakdown of membrane lipids, cytoskeletal linkages, and structural proteins [299, 300]. Progressive membrane destabilisation increases permeability and sets the stage for leakage of lysosomal hydrolases into the cytoplasm [294, 301, 302].

**Box 1.7 | *Rigor mortis***

*Rigor mortis* refers to the stiffening of muscle groups *post-mortem*, which imparts rigidity to the corpse [261]. Sarcomeres, the contractile units of muscle cells, comprise parallel filaments of the proteins actin and myosin, between which crosslinks form to effect muscle contraction [311]. The process is tightly regulated by both ATP and $Ca^{2+}$ availability [312]. The initial flaccidity of muscles several hours *post-mortem* is due to continued formation of ATP by anaerobic glycolysis [313–316]; however, once ATP levels decrease below $\sim 85\%$ of their *in vivo* value, $Ca^{2+}$ pumps in the sarcoplasmic reticulum cease to function [267]. $Ca^{2+}$ ions leak into the cytoplasm where they bind troponin, a regulatory protein that inhibits actinomyosin interaction [317]: troponin is itself bound to tropomyosin, a protein that wraps around actin, blocking its myosin binding sites [318]. The resulting conformational change pulls tropomyosin away from actin, exposing its myosin binding sites and triggering muscle contraction [318]. Without ATP available to break the actinomyosin complex, the muscle cannot relax [317]. While the corpse generally returns to a flaccid state $\lesssim 48$ hours after death, the precise cause of the breakdown of actinomyosin crosslinks has not been resolved [319].

To partially compensate for the loss of mitochondrial ATP, cells shift to anaerobic glycolysis: a metabolic pathway in which glycogen is converted to glucose, which is metabolised to pyruvate and ultimately to lactic acid [303]. This fermentative process yields limited ATP and causes progressive cytoplasmic acidification, as elevated pyruvic and lactic acid concentrations decrease intracellular pH (Box 1.7) [303, 304]. The increasing acidity causes nuclear chromatin to aggregate [305], suppressing RNA transcription and further restricting protein synthesis, including that of enzymes required for cellular maintenance [306]. Acidification also enhances the activity of lysosomal hydrolases once they escape their membrane-bound compartments [307], bringing substrates and catabolic enzymes into contact under increasingly permissive conditions, and amplifying enzymatic degradation of cellular and molecular components [308]. Morphologically, increasing membrane permeability and cytoskeletal disruption are characterised by vacuolisation and membrane blebbing (irregular 'blistering' of the membrane caused by localised decoupling from the cytoskeleton) [309, 310].

These biochemical events correspond to the well-described ultrastructural progression of acute lethal cell injury [261, 293]. An initial, potentially reversible phase is characterised by (i) abrupt reduction in ATP and failure of ATP-driven biosynthesis; (ii) dysfunction of membrane-bound enzyme systems; (iii) osmotic imbalance with swelling of the cytocavitary network; (iv) a transient shift to fermentative metabolism with lactic acidosis; and (v) condensation of nuclear

chromatin [261]. If energetic collapse persists, the process enters an irreversible phase in which (i) mitochondrial matrix proteins denature and aggregate, forming fluffy clumps known as 'flocculent densities' [320]; (ii) the protein portion of the cytoplasm denatures and appears as granular densities; (iii) permeability of membrane-bound organelles increases, leading to leakage; (iv) potent hydrolases released from damaged lysosomes are activated at lowered pH, invading the nucleus and irreversibly degrading chromatin (karyolysis) and other intracellular structures, resulting in loss of cell–cell adhesion; and finally, as membranes are progressively destroyed, (v) phospholipids released from disintegrating bilayers reorganise into visible concentric lamellar (myelin-like) bodies, a cardinal sign of end-stage autolysis [261]. These chemical and ultrastructural effects result in two distinct kinds of observable necrosis [261]. In enzyme-rich tissues such as the brain, extensive proteolytic activity produces liquefactive necrosis, often resulting in cavitation [261, 293]. In other tissues, where structural proteins denature more rapidly than they are hydrolysed, coagulative necrosis predominates [293]; in this type, gross architecture may be preserved for some time, despite loss of cellular detail [321].

### 1.3.2 Putrefaction

Whereas autolytic processes are aseptic, involving the breakdown of a cell by its own machinery, putrefaction describes the digestion of a cell by the diverse biota that colonises a decomposing body *post-mortem* [259]. As autolysis reaches its terminal stages, the internal environment of the body becomes increasingly hypoxic, favouring the rapid proliferation of the endogenous bacterial flora of the large intestine and, to a lesser extent, bacteria present in surrounding tissues [271, 322–327]. This transition marks not only a microbial shift, but a fundamental redox shift: as oxygen is depleted, oxidative catabolic pathways give way to fermentative and other reductive pathways that reconfigure the chemical state of tissues [328, 329].

The adult human gut hosts a microbiota comprising trillions of members represented by thousands of species-level phylogenetic types [330]. These organisms consist primarily of obligate anaerobes belonging to the classes *Clostridia* (phylum

*Bacillota*) and *Bacteroidia* (phylum *Bacteroidota*) – together amounting to > 90% of all gut microbes [331] – with smaller proportions of facultative aerobes (particularly the *Enterobacteriaceae* family, phylum *Pseudomonadota*) [332, 333]. In addition to the body's various endogenous microbial communities, invasive/opportunistic xenobionts from the surrounding environment (including animals, plants, and fungi) also play a role [81, 272, 334, 335]. The most prolific of these xenobionts are bacteria that, once host tissues begin to lose structural integrity, rapidly exploit cellular substrates in their immediate environment by secreting exoenzymes to degrade organic matter, which at once provides a nutrient source for the bacterium, and expedites its further invasion of host tissue [324, 336]. At the molecular level, exoenzymatic digestion transforms complex biomolecules into reduced substrates and volatile byproducts [337]; these metabolites reflect microbial electron transfer reactions occurring under oxygen-limited conditions [338] and form the chemical basis of the macroscopic changes characteristic of bloated and active decay stages (Table 1.1), such as abdominal distension, tissue discolouration, and the unmistakable malodour of putrefactive decomposition.

Enteric flora generate a range of organic acids (including lactic, acetic, acetoacetic, and propionic acids) and alcohols (such as ethanol and butanol), as well as acetone [329, 339]. These products arise from microbial fermentative pathways that regenerate oxidised cofactors (e.g., oxidised nicotinamide adenine dinucleotide [$NAD^+$]) under hypoxic conditions [340], thereby sustaining ATP production in the absence of molecular oxygen as a terminal electron acceptor. Collectively, these fermentation products contribute to the acidic environment created early within the decomposing body [261]. In the fertile milieu provided by autolysis – slightly acidic, hypoxic, and nutrient-rich, devoid of defensive cells and protective mechanisms – protein degradation emerges as a major chemical component of putrefaction [341–345].

Proteins are denatured and hydrolysed by bacterial exoenzymes into their constituent amino acids, which are transported into bacterial cells where endoenzymes remove amino groups through deamination, or remove carboxyl groups

through decarboxylation [346]. Phe, for example, undergoes deamination to form phenylpyruvic acid and ammonia [347], which, in acidic conditions, may be converted to ammonium ($NH_4^+$) [27], releasing reduced nitrogen species that further alter the redox chemistry of decomposing tissues. The amino acids ornithine and Lys, on the other hand, are readily decarboxylated to produce carbon dioxide and the foul-smelling compounds putrescine (1,4-butanediamine) and cadaverine (1,5-pentanediamine), respectively [348]. These diamines are members of a group of toxic compounds called ptomaines, and accumulate within the body cavity during the bloated stage (Table 1.1) alongside gaseous products of bacterial carbohydrate fermentation, such as methane, hydrogen, and hydrogen sulfide [261, 349]. Production of these compounds reflects terminal reductive processes in which carbon and protons serve as alternative electron acceptors in the absence of oxygen [349], and their accumulation contributes to the overall reducing potential of the putrefying microenvironment [261]. The bloated stage of putrefaction can therefore be understood not merely as microbial digestion, but as a progressive reduction of tissue chemistry in which electron flow is redirected from oxygen-dependent oxidative pathways toward fermentative and sulfide-generating pathways that reconfigure the chemical and visual landscape of the corpse (Box 1.8).

The bloated stage ends with abdominal rupture, which releases trapped putrefactive gases and marks the transition to the active decay stage (Table 1.1). Rupture exposes internal tissues to atmospheric oxygen, driving a shift from obligate anaerobic bacteria to aerobic and facultative anaerobic decomposers [322, 356]. The latter include those already present within the corpse – notably the orders *Pseudomonadales* (phylum *Pseudomonadota*) and *Bacillales* (phylum *Bacillota*) – whose relative abundance increases sharply once oxygen tension rises [356], alongside aerobic taxa recruited from the surrounding burial substrate (particularly the phylum *Proteobacteria*) [357–359]. Although grave-associated microbial communities evidence conserved similarity across diverse soil types [335, 360], their composition varies with burial depth and saturation [361].

**Box 1.8 | *Tissue discolouration***

The cumulative effect of fermentative and reductive reactions *post-mortem* is a progressive lowering of tissue redox potential, the consequences of which are most visibly expressed in pigment chemistry. Colour changes accompanying putrefaction arise from at least two principal chemical processes, both governed fundamentally by oxidation–reduction reactions: (i) the transformation of heme to bile pigments [350], and (ii) the reaction of acidic and reduced breakdown products with heme and liberated iron [351].

Bile pigments exhibit a range of colours, reflective of their oxidation state. Following lysis of erythrocytes, haemoglobin is degraded and the heme moiety is converted to biliverdin, a green pigment; biliverdin is subsequently reduced to bilirubin, which is yellow [350]. Under anoxic, microbially active conditions, bilirubin can be reduced to urobilinogen; where oxidising conditions are available, subsequent oxidation of urobilinogen yields urobilin, imparting a brown colouration [352].

Alongside the interconversion of bile pigments, putrefactive metabolites generate further discolouration through reactions with heme-bound or liberated iron. Phenylpyruvic acid, produced *via* microbial deamination of Phe, can combine with oxidised (ferric, $Fe^{3+}$) iron to form a green ferric–phenylpyruvate complex [261]. Hydrogen sulfide, generated through bacterial metabolism of the sulfur-containing amino acids Cys and Met [353], and, in strongly anoxic settings, by sulfate-reducing microorganisms [354], modifies the heme porphyrin of haemoglobin to form green sulfhaemoglobin [351, 354], while reaction with reduced (ferrous, $Fe^{2+}$) iron mobilised from heme proteins, ferritin, transferrin, and other cellular reservoirs forms insoluble ferrous sulfide, a black precipitate [351, 355]. Green and brown-black discolouration may therefore develop concurrently or sequentially according to the local availability and chemical state of haemoglobin, sulfide, and iron [261]. These visible colour changes – particularly evident in superficial vessels [267] – thus reflect shifting oxidation states within a spatially variable, progressively reducing biochemical system.

This anaerobic-to-aerobic transition is accompanied – and in part driven – by the arrival of necrophagous insects [362, 363], whose access to the corpse is itself contingent on the physical properties of the burial environment. Exposed or shallowly buried remains are colonised rapidly by ovipositing Diptera (principally the families *Calliphoridae* [364] and *Sarcophagidae* [365]), whereas burial at depth, enclosure, or submersion may alter, delay, or exclude insect access altogether [366, 367]. Where access is possible, insect colonisation follows a broadly predictable successional sequence, with early dipteran taxa supplemented and later succeeded by coleopteran taxa (such as the families *Histeridae*, *Silphidae*, *Cleridae*, and *Dermestidae*) as the tissue substrate is depleted and its chemical composition changes [368–371]. Each insect taxon transfers its own associated microbial communities – both gut-resident and across other tissues [372] – to the corpse during colonisation, which integrate with the existing decomposer community to impact the rate of tissue breakdown [373, 374]. Insect activity, therefore, actively shapes the progression of decomposition during putrefaction [363].

### 1.3.3 Environmental modifiers

The decomposition of organic matter is ultimately mediated by three primary factors: (i) the decomposer community that has access to the remains, (ii) the physicochemical environment in which decomposition occurs, and (iii) the bio-physicochemical properties of the organic material itself [375]. The present section focuses on the second of these controls. Within the environmental context of decomposition, numerous extrinsic factors regulate the nature and rate of chemical reactions within and around the corpse [72, 376]; such as ambient temperature [66, 377, 378], atmospheric and soil oxygen [379, 380], moisture and humidity [35, 80, 381, 382], pH [383, 384], soil composition and texture [79, 385–387], burial or immersion depth [388–391], and air movement [262, 392]. Many of these influences, however, ultimately act by modifying a smaller set of physicochemical conditions: the temperature-dependent kinetics of chemical reactions, the availability of oxygen as a terminal electron acceptor, and the presence (or absence) of water as both solvent and hydrolytic reactant. The discussion that follows therefore examines three key environmental modifiers of decomposition – temperature, oxygen, and water – which together shape the chemical trajectories available to decaying tissues.

#### 1.3.3.1 Temperature

Ambient temperature is one of the most powerful physical regulators of decomposition because it governs the kinetics of both autolysis and putrefaction. The relationship is commonly expressed by the temperature coefficient $Q_{10}$, which describes the multiplicative change in reaction rate for every 10 °C change in temperature; for many biological and chemical processes, $Q_{10} \approx 2$–3, corresponding to the empirical van 't Hoff 'rule of ten' [261]. $Q_{10}$ values for enzyme-catalysed reactions typically lie between 1.1–3.0, such that a 10 °C change may alter the reaction rate by approximately one- to three-fold, depending on the system and assuming that enzymes remain intact [393]. As decomposition proceeds through enzyme-mediated pathways – initially endogenous and subsequently exogenous – the overall tempo of decay reflects the thermal regime to which the body is

exposed. Temperature also affects the 'dwell time' spent in each decomposition stage (Table 1.1) [382]: warmer conditions accelerate catalytic turnover and microbial growth, thus typically shortening stage durations and increasing the overall velocity of decay, whereas cooler conditions progressively retard these processes and may prolong stage duration [66, 394].

This temperature dependence arises from the thermodynamic and structural properties of proteins. Mammalian enzyme systems are adapted to operate optimally near physiological temperature ($\sim$ 37 °C), and deviations from this range alter catalytic efficiency [395–397]. Cooling reduces molecular motion and slows reaction rates without necessarily denaturing enzymes, whereas sustained high temperatures promote protein unfolding, aggregation, and loss of enzymatic activity [398]. At sufficiently high temperatures (e.g., sustained heat approaching 60 °C for many intracellular mammalian proteins [but see 399]) enzyme denaturation becomes prevalent and – given a protein's function is intimately tied to its folded structure – enzyme-mediated catalytic pathways fail [400]. Thus temperature exerts a non-linear influence on decay: moderate increases enhance autolytic and microbial breakdown, but sufficiently elevated temperatures can denature critical enzymes and restructure tissue proteins, altering the subsequent trajectory of decomposition.

Temperature also governs the metabolic pathways that predominate during putrefaction, beyond merely the rate at which they proceed. As oxygen becomes depleted and microbial communities proliferate, fermentative and other anaerobic pathways dominate [380]. The rate at which organic substrates are reduced to acids, alcohols, methane, hydrogen, and hydrogen sulfide is temperature-dependent, because the underlying enzymatic reactions and electron-transfer processes are themselves thermally sensitive [401]. Warmer environments favour rapid turnover of reduced end products and, under anaerobic metabolism, accelerate shifts in tissue redox potential toward increasingly reducing conditions; cooler environments slow these transformations and prolong the persistence of intermediate compounds [402, 403]. In this way, temperature modulates the balance between oxidative and reductive chemistries within the decomposing corpse.

Finally, the effective temperature experienced by decaying tissues depends on the thermal properties of the surrounding environment. Burial depth [404, 405], soil properties and moisture [35, 406], and enclosure within media that modify heat exchange (e.g., clothing, wrapping materials, sealed containers, water) [407] can buffer or amplify temperature fluctuations, while the body's finite thermal mass delays equilibration, and decomposition itself can generate endogenous heat [408]. Indeed, heat generated by microbial metabolism during the bloated stage and by maggot masses during active decay can raise internal carcass temperatures well above ambient levels, frequently by 10–20 °C [378, 408, 409] and, in cases of substantial maggot infestation, to more than 50 °C [384]. Thermal conditions thus alter enzyme kinetics and microbial proliferation [410, 411]; under sustained cold or intense heat, these effects may suppress putrefactive breakdown and, in some contexts, contribute to preservation (Section 1.4).

#### 1.3.3.2 Oxygen

Oxygen availability exerts a primary control on whether decomposition proceeds predominantly *via* oxidative or reductive pathways [412]. Molecular oxygen is a high-energy terminal electron acceptor, and its depletion drives a shift toward alternative electron acceptors (e.g., nitrate [$NO_3^-$], Fe[III], sulfate [$SO_4^{2-}$], $CO_2$) associated with anaerobic metabolisms (e.g., denitrification, iron reduction, sulfate reduction, methanogenesis), thereby changing both the energetic landscape and reaction network of *post-mortem* decomposition [261]. Following death, circulation ceases and residual dissolved oxygen within tissues is rapidly consumed by remaining oxidative enzymes and proliferating microbes [327, 413]. As a consequence, even in atmospherically exposed bodies, the local partial pressure of oxygen ($pO_2$, or oxygen availability) declines steeply within internal tissues [414], and hypoxic conditions develop relatively early in the autolytic phase [27, 37, 68].

The rate and extent of this decline depend on both intrinsic and extrinsic controls on oxygen diffusion. Internally, tissue architecture, cellular compartmentalisation, and metabolic heterogeneity (i.e., variable oxygen demand) create steep oxygen

gradients [414]; externally, burial depth, soil compaction, water saturation, and enclosure regulate the rate at which oxygen can diffuse into tissues [27]. Waterlogged soils and submerged environments are characteristically oxygen-deficient because diffusion is slow and microbial consumption is rapid, resulting in low redox potential (Eh) [415, 416]. By contrast, dry, well-aerated soils maintain higher oxygen availability and therefore higher Eh values [417]. Given oxygen diffusion in water is approximately four orders of magnitude slower than in air, immersion or high soil moisture can restrict oxygen penetration into tissues even when the surrounding environment is nominally oxygenated [418], thereby promoting reducing conditions within the corpse. As a result, oxygen availability within a corpse is neither uniform nor static [419]: bodies develop fine-scale redox heterogeneity in which oxidising and reducing microenvironments coexist over millimetre scales [420–423]. The gut lumen, for example, rapidly becomes hypoxic and supports sulfate reduction and methanogenesis [271, 424, 425], whereas superficial vessels or tissues intermittently exposed to air may remain relatively oxidising for longer periods. These microgradients create divergent chemical niches within the same corpse, and thereby set the scene for different molecular fates across tissues.

As oxygen is depleted, two interrelated biochemical consequences follow. In host tissues, the cessation of oxidative phosphorylation causes rapid ATP depletion and loss of ATP-dependent functions [291], precipitating autolysis (Section 1.3.1); and in parallel, microbial communities shift toward anaerobic respiration and fermentation (Section 1.3.2) [328, 329]. Many enteric and soil bacteria are facultative or obligate anaerobes able to exploit alternative terminal electron acceptors as Eh falls [426, 427]. Once oxygen is exhausted, microbial respiration proceeds through a redox cascade of successively lower-potential acceptors [428], with each step generating distinct reduced end products and further altering tissue chemistry.

These redox shifts directly govern the chemical trajectories of major biomolecular classes. Lipids (Section 1.2.3.2) are particularly sensitive to oxygen availability: in oxygenated microenvironments they undergo oxidative reactions (including peroxidative chain processes) that fragment unsaturated fatty acids into smaller, more polar

compounds [429], whereas under oxygen-limited conditions these oxidative pathways are curtailed and lipids instead follow reductive pathways, including hydrogenation [430], fermentative breakdown [431], or, under specific physicochemical regimes, participation in saponification (Section 1.4.4) [432]. Proteins (Section 1.2.3.4) respond differently but no less decisively. In oxygenated microenvironments, reactive oxygen species (ROS) drive side-chain oxidation, backbone cleavage, and oxidative crosslink formation (yielding carbonylated residues and high-molecular-weight aggregates) [433–437]. In reducing, anoxic microenvironments, microbial metabolism predominates: proteins are hydrolysed to amino acids, which are subsequently catabolised *via* deamination and coupled redox reactions to yield ammonium and volatile fatty acids, with terminal conversion of the latter to methane [438, 439]. Thus local oxygen availability determines whether biomolecules are oxidatively fragmented, reductively transformed, or structurally modified in ways that shape downstream taphonomic trajectories.

#### 1.3.3.3 Water

Water exerts multiple, interdependent physicochemical controls on decomposition. As a solvent, it governs the concentration, mobility, and interaction of ions and organic molecules across intra- and extracellular compartments [440–442]; as a reactant, it participates directly in hydrolytic cleavage of biopolymers [443, 444]; and as a thermal buffer, its high specific heat moderates temperature fluctuations and therefore reaction kinetics [445]. Since both autolysis and putrefaction proceed largely by enzyme-catalysed hydrolysis, the presence, distribution, and behaviour of water strongly influence both the rate and the mode of *post-mortem* molecular breakdown [396, 446].

At the molecular level, water is a necessary reagent for hydrolysis: ester, peptide, and glycosidic bonds in lipids, proteins, and carbohydrates respectively are cleaved by nucleophilic attack in aqueous media [87, 204, 447], and hydrolase enzymes require an aqueous environment to maintain their hydration shell, permit the conformational flexibility necessary for substrate binding, and support catalytic

turnover [448–450]. Given approximately 60% of an adult human body is water ($\sim$ 40% intracellular and $\sim$ 20% extracellular) [446], aqueous fluids within tissues act as the principal transport medium for soluble and volatile products of decomposition. Many small metabolites of autolysis and putrefaction – including short-chain fatty acids, alcohols, ammonia/ammonium, organic acids, hydrogen sulfide and other reduced sulfur species – partition into tissue fluids, where they diffuse through interstitial spaces and redistribute within and between cells [451–453].

This redistribution afforded by an aqueous phase alters local concentrations of reactants, and modulates pH and Eh at the cellular level. The same aqueous transport processes extend into the surrounding burial environment, as dissolved metabolites diffuse into soil pore waters, or adjacent aqueous phases in the case of immersion [80, 376, 379, 454–456]. In moist or saturated conditions, catalysts and substrates are mobile and hydrolysis proceeds efficiently [457, 458]; whereas in desiccating conditions, limited water availability reduces enzyme mobility and substrate accessibility, slowing bond cleavage and allowing competing non-hydrolytic reactions to predominate [459–461]. Water simultaneously regulates molecular mobility, enzymatic activity, and oxygen diffusion both within and beyond the corpse, thus governing whether organic matter undergoes rapid hydrolytic fragmentation, or alternative pathways that either promote further degradation or facilitate stabilisation.

Hydrodynamics – that is, whether water is flowing (lotic) or stagnant (lentic) – influence how aqueous transport interacts with oxygen supply [462]. In flowing systems, bulk water movement (advection) replenishes dissolved oxygen and removes soluble decomposition products, sustaining relatively oxidising conditions at tissue–water interfaces and diluting labile metabolites [463]. Penetration of oxygen into tissues, however, remains diffusion-limited even under advective flow [464]. In stagnant water or poorly drained, waterlogged soils, oxygen supply is governed almost entirely by molecular diffusion through water, which is slow relative to microbial oxygen consumption [465, 466]. As a result, oxygen is rapidly depleted; persistent hypoxia develops; anaerobic, microbially-mediated metabolic pathways

are favoured, and reduced metabolites accumulate *in situ* [467–471]. Hydrodynamics thus impacts whether oxidative or reductive chemistries prevail, by regulating the balance between advective oxygen renewal (as in lotic systems) and diffusion-limited oxygen depletion (as in lentic systems) [472, 473].

In addition to its flow regime, the chemical composition of the aqueous environment further shapes decomposition processes. Salinity and dissolved ions impose osmotic constraints on cells and enzymes, alter the solubility and speciation of (in)organic compounds, and select for microbial communities adapted to particular ionic regimes [474–479]. Elevated ionic strength, as in brackish or marine environments, can suppress some enzymatic activities while favouring halotolerant or sulfate-reducing groups [480, 481]; it also modifies metal complexation and precipitation equilibria [482–484]. Freshwater environments, by contrast, tend to support different assemblages of fermentative and iron- or sulfate-reducing microbes, depending on the available electron acceptors [485, 486]. These shifts in microbial ecology have direct chemical consequences. Waterlogged, anoxic environments tend to favour functional guilds with reducing metabolisms: fermentative bacteria that generate organic acids and alcohols [487]; iron-reducing bacteria that convert ferric to ferrous iron [488]; sulfate-reducing bacteria that reduce sulfate to hydrogen sulfide [489]; and, under strongly reducing conditions, methanogenic archaea that yield methane [490]. The metabolic products of these guilds further entrench the redox heterogeneity established by oxygen availability (Section 1.3.3.2).

Finally, temperature interacts with water in ways that amplify these effects. Water's thermal inertia dampens diurnal and seasonal fluctuations in temperature, such that submerged or deeply waterlogged remains experience reduced thermal variability relative to exposed carcasses [491]. This buffering slows the kinetics of temperature-sensitive reactions (Section 1.3.3.1) [492] and can delay or alter microbial succession: cold, oxygen-poor aqueous environments tend to retard catalytic and microbial turnover, whereas warm, oxygenated waters generally accelerate metabolic rates [493, 494]. Water is therefore best understood not merely as a medium for decomposition chemistry, but as a conditional regulator

of it: by controlling oxygen transport, solute mobility, and microbial ecology, it influences whether tissues undergo rapid breakdown or are diverted toward alternative taphonomic trajectories. The mechanistic consequences of these divergent trajectories – including dehydration, freezing, tanning and saponification – are examined in detail in the following section.

## 1.4 Soft-Tissue Preservation

Hard tissues, such as bone and teeth, are frequently recovered in the archaeological and fossil records. Their long-term persistence is primarily a consequence of their composite mineral–organic nature, and the relative thermodynamic stability of their constituent phases [495–501]. Bone, for example, consists of an organic matrix dominated ($> 90\%$) by type I collagen – a highly ordered protein comprising triple-helical tropocollagen molecules packed together into twisted fibrils – interpenetrated by a poorly crystalline, carbonate-substituted hydroxyapatite ($Ca_{10}[PO_4]_6[OH]_2$) mineral phase [502–504]. The proteinaceous phase provides a hierarchically organised template that may be retained at the fibrillar and tissue scale [505, 506], even as its primary structure is progressively cleaved, modified, or replaced during diagenesis [33, 77, 507, 508]; whereas the mineral phase constitutes a low-solubility, pervasive inorganic fraction that physically restricts access of water, enzymes, and microorganisms to the proteinaceous phase, while also buffering local pH and redox conditions through dissolution–precipitation equilibria [40, 509–512].

Although extensive degradation or complete loss can occur under unfavourable conditions, such as prolonged exposure to acidic environments, high temperatures, or intense microbial activity [33, 513], hard tissues typically undergo diagenetic alteration rather than wholesale destruction. The hydroxyapatite component of bone may recrystallise, incorporate exogenous ions (particularly $Fl^-$ and $Sr^{2+}$), and undergo modification of its carbonate content through dissolution–reprecipitation and ion-exchange processes [514–517]), while pore spaces become infilled with secondary minerals (permineralisation) [518, 519]. As a result, morphological and microstructural features may be retained even where the original organic

components are substantially altered or lost [520]. Preservation of hard tissues is therefore achieved not by preventing chemical change, but by maintaining a mineral-supported framework that constrains and mediates that change [521].

Soft tissues, by contrast, lack an intrinsic mineral scaffold and are composed predominantly of water-rich, chemically labile biopolymers, including proteins, lipids, and carbohydrates [522]. In life, these molecules are maintained through metabolic regulation and cellular compartmentalisation [523]; following death, this control collapses, and they become susceptible to hydrolytic, enzymatic, and oxidative degradation [304]. Because they are not embedded within a stabilising mineral phase, soft tissues remain fully accessible to these forms of chemical attack, and are therefore rapidly broken down under most environmental conditions [524]. Their persistence over extended timescales cannot be explained by the same mechanisms that govern hard-tissue preservation; instead, their long-term persistence requires either suppression of degradative processes, or transformation of labile biomolecules into more chemically recalcitrant forms, depending on local physicochemical conditions (such as temperature, water activity, and oxygen availability) [44, 525]. The following sections describe the distinct physicochemical pathways by which such stabilisation may be achieved, and the environmental conditions in which each is most likely to occur.

### 1.4.1 Dehydration

Dehydration preserves soft tissues principally by lowering water activity ($A_w$) – that is, the fraction of water that is thermodynamically available to solvate molecules and participate in chemical reactions – thereby removing the aqueous medium required for hydrolytic reactions, enzyme catalysis, and sustained microbial metabolism [526, 527]. In reflecting the chemical potential of water, rather than simply its bulk quantity, water activity is an informative measure of hydration state in biochemical systems [528]: it determines key solvent properties including ion solvation, diffusivity of dissolved species, and the availability of water to act as a nucleophile in hydrolytic bond cleavage [529]. These properties collectively govern

both the stoichiometry and the kinetics of hydrolytic reactions, which – whether enzyme-mediated or spontaneous – require water both as a reactant and as the solvent medium for enzymatic catalysis (Section 1.3.3.3) [530]. Immediately *post-mortem*, water activity in soft tissues is expected to be close to unity ($A_w \approx 1.0$), reflecting the high water content of the living body [531]; however, as water is progressively lost through evaporation, sorption, or diffusion into surrounding media, water activity declines, suppressing the bond-cleavage reactions that normally drive early decomposition [532].

Proteins (Section 1.2.3.4) respond strongly to decreasing water activity *post-mortem* because their structure and function depend on interactions with surrounding water molecules [533]. In hydrated tissues, a layer of bound water – the hydration shell – surrounds protein surfaces and forms hydrogen bonds and electrostatic interactions with polar amino-acid residues [449, 534]. This shell stabilises the folded structure and permits the limited conformational flexibility required for substrate binding and catalysis [535]. As tissues lose water, the hydration shell is progressively disrupted, reducing molecular flexibility and promoting structural rearrangement, while the mobility of both proteins and surrounding solutes declines [536]. Continued dehydration can induce partial or complete denaturation [537], as proteins form aberrant intermolecular interactions (e.g., hydrogen bonds, salt bridges) in the absence of their normal hydration environment [538]; this process is facilitated by increasing intracellular solute and ion concentrations as water is removed [539, 540]. Concomitantly, reduced solvent shielding enhances hydrophobic interactions, exposing non-polar residues normally buried in the protein core, and promoting aggregation [537, 541]. These aggregates are typically non-functional and may further perturb cellular chemistry by disrupting membrane organisation and cellular compartmentalisation [542], which releases redox-active metal ions (e.g., $Fe^{2+}$, $Cu^{+}$) from controlled pools that, under oxidising conditions, promote ROS generation [538, 543].

Dehydrated proteins become increasingly susceptible to non-enzymatic glycation *via* the Maillard reaction, in which carbonyl groups of reducing sugars react with nuc-

leophilic amino groups on proteins (and, more broadly, other biomolecules), forming covalent adducts that can subsequently rearrange and polymerise (Section 1.4.5.2) [538, 544]. This process, which is favoured by elevated solute concentrations and oxidative conditions that generate reactive carbonyl intermediates [545], yields heterogeneous, often crosslinked aggregates and contributes to the progressive loss of native macromolecular structure [546]. In parallel, oxidative modification of proteins generate carbonyl functionalities directly on amino-acid side chains (protein carbonylation), while also producing reactive carbonyl species (RCS) that can further drive glycation [211, 547]; consequently, oxidative damage and Maillard-type reactions become increasingly coupled under low-water conditions [544]. Carbonylated species are relatively resistant to proteolytic degradation, owing to conformational alteration and crosslinking that limit protease accessibility [211], and may therefore accumulate in desiccating microenvironments [543, 547]. As dehydration proceeds further, the combined effects of macromolecular crowding, partial unfolding, and elevated solute concentration can drive the system toward physical immobilisation [537]: under sufficiently low water activity, the intracellular milieu may transition into an amorphous, glass-like state (vitrification; Box 1.9) [548].

Lipids (Section 1.2.3.2) respond to dehydration differently from proteins because their dominant degradation pathways diverge once hydrolytic reactions are suppressed [547]. In hydrated tissues, triglycerides and phospholipids are degraded primarily through enzymatic and abiotic ester hydrolysis [569]; however, as water activity declines, these reactions slow markedly, permitting persistence of intact lipid structures [570]. At the same time, dehydration directly alters lipid organisation: reduced hydration of polar headgroups promotes tighter acyl-chain packing, driving transitions from fluid liquid-crystalline bilayers to more ordered gel phases and, under severe dehydration, to non-bilayer structures [571–573]. These phase changes decrease membrane fluidity and integrity, facilitating loss of compartmentalisation and enhancing contact between lipids, proteins, and reactive species [574–576]. By contrast, unsaturated fatty acyl chains remain susceptible to autoxidation, a radical chain process that can proceed at low water activity provided oxygen and initiation

**Box 1.9 | *Vitrification***

Vitrification occurs when dehydration concentrates cellular solutes and macromolecules sufficiently that the remaining aqueous phase solidifies into an amorphous, glass-like matrix in which molecular motion is severely restricted [548]: translational diffusion of enzymes, substrates, and small metabolites slows dramatically, and viscous flow of the surrounding medium effectively ceases [549, 550]. As a result, enzymes are unable to access substrates efficiently, and hydrolytic degradation is strongly inhibited [551]. The propensity for this transition depends strongly on matrix composition, particularly the abundance of low-molecular-weight solutes capable of stabilising amorphous phases [552]. Sugars and polyols – including glucose, trehalose, glycerol, and sorbitol – promote glass formation by replacing hydrogen bonds normally provided by water and by increasing the viscosity of the surrounding solution [553, 554]. Because such solutes are present in intracellular fluids and extracellular matrices of biological tissues, they can facilitate the formation of vitrified matrices during dehydration [555–557]. Consequently, tissues rich in disaccharides (like trehalose and sucrose) may vitrify at relatively higher water activities than those dominated by proteins [558].

Protein composition further modulates this behaviour [559]. Structured globular proteins generally have dense, strongly perturbed hydration shells and tend to partially unfold or aggregate as hydration shells collapse [560]; whereas intrinsically disordered proteins (IDPs) typically have weaker hydration shells, and adopt increasingly ordered (mostly helical) structures upon dehydration due to forming intramolecular hydrogen bonds in the absence of water [560, 561]. In a range of extremotolerant organisms (including bacteria and tardigrades), IDPs are known to stabilise amorphous phases and contribute to desiccation tolerance by helping to maintain the integrity of vitrified matrices during anhydrobiosis [537, 562, 563]). Thus the relative abundance of small solutes, structured globular proteins, and IDPs influences how readily vitrification occurs in dehydrating tissues [564].

Vitrification may occur once water activity falls below the level required for microbial growth, typically $A_w \lesssim 0.6$–$0.9$ [565], although the precise threshold depends on species physiology, solute composition, drying rate, and temperature [566–568]. Vitrification should therefore be understood as a conditional stabilising mechanism whose onset and effectiveness are determined by the chemical composition and microstructure of the desiccating tissue matrix [537].

sources are available [577]. Lipid peroxidation yields hydroperoxides that decompose into RCS (e.g., aldehydes such as malondialdehyde [MDA] and 4-hydroxynonenal [4-HNE]) [429], alongside ketones and shorter-chain acids, and can also promote crosslinking and polymerisation [578]. These reactions may be enhanced during partial dehydration in some model systems, where increased oxygen diffusion and reduced antioxidant capacity may favour radical propagation [579–583], but may become kinetically constrained by limited molecular mobility (as observed in low-diffusivity membrane environments [584]) under extreme desiccation. As a result, lipid degradation in drying tissues shifts from hydrolytic cleavage toward oxidative transformation and structural reorganisation, progressively altering both membrane architecture and the molecular composition of lipid residues.

Low water activity also constrains microbial activity [585]. Microbial metabolism requires a hydrated cellular environment that maintains membrane fluidity, supports aqueous cytoplasmic enzymatic reactions, and preserves osmotic balance between

the cytoplasm and the surrounding medium [586]. As water activity declines, water is drawn out of microbial cells, generating osmotic stress that dehydrates cellular components and disrupts membrane structure, ion gradients, and enzyme function [587–589]. Dehydration also slows diffusion of nutrients and metabolites through the surrounding medium, limiting the supply of substrates available for microbial growth [590]. These constraints set practical limits on microbial proliferation: most non-extremophilic bacteria cease growth once water activity falls below approximately $A_w \lesssim 0.90$ [526, 565], whereas many fungi remain metabolically active at somewhat lower values (typically $A_w \approx .0.70$–$0.75$) because their cell walls and osmotic regulation systems better tolerate concentrated environments [539, 591]. Specialised xerophilic microorganisms, however, can grow at still lower water activities by accumulating compatible solutes that maintain intracellular hydration and stabilise enzyme function under osmotic stress [591].

At tissue and organ scales, the molecular consequences of dehydration produce characteristic morphological changes. Tissues undergo volumetric contraction as water is lost from cells and extracellular spaces [28, 29], as well as mechanical stiffening as structural proteins such as collagen lose bound water and become less flexible [592–594]. The resulting appearance is typical of natural mummification: skin becomes dry and leathery, while internal organs shrink and collapse, becoming increasingly friable as their water content depletes [595]. While there is considerable variation in terms of the contexts yielding mummified remains [596–599], environmental settings that favour dehydration are those in which the rate of water loss from tissues exceeds the rate at which moisture can be replenished from the surrounding environment [28, 381]. Such conditions arise where relative humidity is low and air circulation promotes evaporation (i.e., high vapour-pressure deficit) [600]; where elevated temperatures accelerate evaporative water loss [262]; or where surrounding materials act as hygroscopic sinks that absorb moisture from decaying remains [601]. Natural examples include hyper-arid deserts, exposed high-altitude environments with low atmospheric moisture, and well-ventilated crypts or burial chambers

[602]. Comparable conditions may also be produced artificially through deliberate desiccation during embalming [603], or controlled drying of remains [604, 605].

### 1.4.2 Freezing

Unlike dehydrating conditions, in which water is progressively removed from tissues, freezing preserves soft tissues by immobilising water within an ice lattice, alongside the temperature-dependent suppression of chemical kinetics [606]. As tissues cool below 0 °C, ice formation segregates pure water into a solid phase and excludes solutes into the residual unfrozen fraction, increasing ionic strength and altering pH and viscosity [606, 607]. This cryoconcentrated phase can approach highly viscous or glassy states at sufficiently low temperature, constraining molecular diffusion [608], while reaction rates decline in accordance with Arrhenius behaviour [607]. Together, reduced solvent mobility and low temperature limit enzyme–substrate interactions and microbial activity. These combined effects suppress the hydrolytic and microbial processes underpinning autolysis and putrefaction, allowing tissues to persist with comparatively limited biochemical alteration while they remain frozen [609].

The preservation of microstructure in frozen tissues depends strongly on the rate of freezing [606, 609, 610]. During slow cooling, ice forms predominantly in the extracellular space, concentrating solutes in the unfrozen fraction and driving osmotic dehydration of cells [611]; this reduces intracellular water content and suppresses intracellular ice formation, but exposes cells to injury from high solute concentrations and associated physicochemical stresses [612]. At higher cooling rates, cellular dehydration is kinetically limited, such that water is retained within the cell with subsequent intracellular ice formation [613]; the resulting crystals physically disrupt membranes, displace and fracture organelles, and compromise subcellular compartmentalisation [614–617]. It appears that only under conditions that achieve extremely fine-scale ice formation ($< 20$ crystals per $\mu m^2$), [618] or vitrification using concentrated cryoprotectants [619], might rapid cooling preserve cellular architecture.

Proteins (Section 1.2.3.4) are affected by freezing through both kinetic suppression and cryoconcentration-driven destabilisation under natural, solute-excluding conditions [620]. Lower temperature reduces backbone and side-chain mobility and therefore catalytic turnover, while diffusion-limited substrate delivery in the frozen microenvironment further restricts enzymatic activity [620]. Concurrently, ice formation excludes solutes into the unfrozen aqueous phase, generating highly concentrated, spatially heterogeneous microenvironments that impose ionic and osmotic stresses on proteins [621, 622]. These conditions selectively destabilise polypeptides: labile globular enzymes with marginal thermal stability, many signalling and metabolic proteins, and membrane-associated proteins that depend on bilayer fluidity for proper folding are particularly prone to denaturation or irreversible aggregation [623–625], as well as to mechanical damage during ice crystal growth. By contrast, structurally ordered proteins such as mature collagen fibrils are generally more resistant to unfolding and may retain gross mechanical integrity despite freezing [626]. IDPs exhibit variable responses to cryoconcentration, in some cases increasing susceptibility to aggregation through enhanced intermolecular interactions [627].

Lipids (Section 1.2.3.2) behave differently from proteins under freezing conditions. Hydrolytic cleavage of triglycerides and phospholipids requires liquid water and active lipases; as such, when water is immobilised and enzymatic activity suppressed, hydrolysis is inhibited [570, 628]. At the same time, membrane lipids undergo phase transitions on cooling: bilayers become more tightly packed and less fluid, increasing susceptibility to cracking when ice crystals grow through or adjacent to membranes [629, 630]. Ice-induced membrane rupture contributes to the release of lipid contents, lipases, and pro-oxidant metal ions into the unfrozen aqueous phase [631]. Autoxidation of unsaturated acyl chains (lipid peroxidation) is temperature-dependent and therefore slowed at low temperatures, but is not eliminated: radical-mediated peroxidation can proceed within the unfrozen aqueous phase and at exposed surfaces where oxygen persists, albeit at reduced rates [632–634]. These reactions generate lipid hydroperoxides that subsequently decompose into RCS

and shorter-chain fatty acids [429]: because these electrophilic products can react with proteins and other biomolecules, significant molecular alteration may occur during prolonged cold storage [635–638], and particularly during thaw, when oxygen availability increases and previously concentrated reactants regain mobility [639].

Microbial activity is greatly reduced in frozen environments, but rarely eliminated [640–642]. Many bacteria and fungi shift into dormant or low-metabolic states as temperature declines [643, 644], particularly during prolonged or deep freezing [645], yet a fraction of the community can sustain maintenance metabolism [640] – and in some cases slow growth [643, 646–648] – within unfrozen aqueous microenvironments at subzero temperatures. Reported activity spans a continuum from active growth near the freezing point to ultra-low maintenance metabolism at temperatures well below −20 °C, with rates many orders of magnitude lower than under temperate conditions [640, 649]. Freezing also influences extracellular enzyme dynamics [621, 650], although effects are often modest: enzyme activities may be transiently reduced during freezing or freeze–thaw cycles [651, 652], but frequently recover upon thaw and can persist in partially frozen systems [653, 654]. The overall effect is therefore predominantly bacteriostatic rather than bactericidal: microbial communities commonly survive freezing and can rapidly resume activity when conditions permit, such that long-term preservation depends on sustained low temperatures and limited thawing.

At macroscopic scales, sustained freezing commonly yields widespread retention of soft-tissue morphology, including preservation of internal organs [655–661]. Histological organisation has been documented in specimens recovered from permafrost (i.e., permanently frozen) environments, with identifiable collagenous extracellular matrices [659, 662, 663], muscle fascicle architecture [664], and vascular and neural structures [660, 661, 665], whereas fine intracellular detail – particularly nuclei and labile cytoplasmic components – is commonly degraded or absent [659, 666]. If thawing occurs, however, tissues damaged by ice recrystallisation and solute-concentrated microenvironments [615, 667] frequently become fluid-rich, and undergo rapid liquefactive necrosis as enzymatic and microbial activity resumes [657, 668].

Environmental contexts that favour preservation by freezing include permafrost regions, glacial or subglacial environments, high-latitude tundras, high-altitude alpine settings, and deep, thermally stable caves.

### 1.4.3 Tanning

Peat-bog preservation (commonly termed 'bog tanning') arises under conditions of persistent waterlogging, low oxygen availability, and sustained acidity, together with the accumulation of chemically reactive organic matter derived from peat-forming vegetation [669, 670]. In temperate and boreal peatlands, this vegetation is typically dominated by *Sphagnum* moss, a genus of bryophytes whose partially decomposed remains release polyuronic acids (sphagnan) from degrading cell walls – the primary Sphagnum-specific tanning agent [669] – alongside phenolic compounds, humic and fulvic substances, and other acidic polysaccharides into pore waters [671, 672]. These dissolved and colloidal components generate an acidic, metal-binding aqueous phase that suppresses microbial decay while promoting direct chemical modification of proteins (Section 1.2.3.4) and other biomolecules (Section 1.2.3) [673, 674].

The organic fraction of peat waters comprises three components. First, polyphenols (including phenolic acids and tannin-like oligomers) provide multiple hydroxyl groups capable of hydrogen bonding with proteins [675, 676], supplemented by hydrophobic and $\pi$–$\pi$ interactions that promote protein aggregation [677] and lipid association [678]. Second, humic and fulvic substances consist of heterogeneous, partially oxidised organic matter containing aromatic, aliphatic, and functionalised domains (including carboxyl, carbonyl, and phenolic groups [Ar – OH]) [679–681]. Third, acidic polysaccharides derived from *Sphagnum* cell walls (collectively referred to as sphagnan) are rich in uronic acids and carry a high density of negative charge [682]. Together, these components define the reactive chemical milieu of peat pore waters.

Initial interactions between peat solutes and tissues are predominantly non-covalent [683]. Polyphenols bind proteins through hydrogen bonding to peptide backbone amide and carbonyl groups, with additional contributions from side-chain

interactions (particularly hydroxyl-bearing residues such as Ser, Thr, and Tyr), and $\pi$–$\pi$ interactions with aromatic residues [675, 683]. Because polyphenols are multivalent (i.e., capable of forming multiple simultaneous interactions), a single tannin-like molecule can bridge multiple binding sites [684], promoting precipitation of insoluble protein–polyphenol complexes [685, 686]; these reversible interactions reduce protein solubility and limit protease accessibility [675, 687]. The effect is most pronounced in collagen-rich tissues [688], whose extended fibrillar structure bears a high density of regularly exposed peptide-backbone amide and carbonyl groups [689, 690], representing a large and repetitive binding surface for polyphenols [691–694].

Humic and fulvic substances, together with sphagnan, reinforce polyphenol-mediated stabilisation *via* pH-dependent physicochemical processes [695]. Under acidic conditions, humic and fulvic substances exist as amphiphilic supramolecular aggregates [696–698] that undergo protonation-driven coiling, aggregation, and partial precipitation [695]. These aggregates associate with proteins *via* hydrogen bonding, as well as other electrostatic and hydrophobic interactions [699, 700], and can physically entrap biomolecules within their matrices [698, 701, 702]. Their adsorption generates heterogeneous organic coatings that constrain diffusion and further restrict enzymatic access [701, 703]. Sphagnan, by contrast, is a highly anionic, water-retentive polymer with strong cation-exchange capacity, maintaining low ionic activity and regulating the distribution and availability of dissolved ions within the microenvironment [672, 674]. Both sphagnan and humic and fulvic substances bind divalent and transition metal ions [704, 705], thereby reducing the bioavailability of cofactors required for microbial metabolism and extracellular enzymatic activity.

Further stabilisation, which is largely irreversible, arises through covalent modification of tissue proteins [669]. In peat environments, reactive carbonyl groups – particularly $\alpha$-keto-carboxylate moieties derived from sphagnan [669, 706] – condense with primary amines on proteins, especially Lys $\varepsilon$-amino groups and, to a lesser extent, N-terminal $\alpha$-amines [706]. Initial formation of Schiff bases (a class of imines formed by condensation of a carbonyl group with a primary

amine) may be reversible, but these intermediates can undergo rearrangement and condensation reactions to yield more stable products [707], including crosslinked and polymeric structures analogous to Maillard-derived melanoidins [706]. This carbonyl–amine chemistry produces a tanning-like effect in which proteins become covalently crosslinked [708], less soluble, and more resistant to enzymatic hydrolysis, while also contributing to metal sequestration [669, 706].

A second covalent pathway involves oxidation of phenolic compounds derived from peat (rather than from the tissue itself) to reactive electrophilic quinones [709]. These species react rapidly *via* nucleophilic addition [710], particularly Michael-type addition of thiols and intramolecular attack by side-chain amino groups [711], forming irreversible C–N and C–S linkages within and between proteins, and between proteins and phenolic molecules [712]. The resulting crosslinking promotes formation of large protein aggregates with increased thermal stability and altered digestibility [713, 714]. Quinone formation requires at least limited oxidation [709, 713] and may thus be favoured in microenvironments where small amounts of oxygen are available, such as at tissue–water interfaces or during the early stages of burial.

Together, carbonyl–amine condensation and quinone-mediated addition constitute complementary covalent pathways to protein stabilisation during tanning. These organic stabilising processes, however, occur concurrently with inorganic reactions that promote demineralisation [670]. Acidic conditions promote dissolution of mineral phases, particularly the hydroxyapatite component of bone, through proton-mediated demineralisation and removal of calcium ions [40, 715, 716]. The combined effect is typically selective preservation: collagen-rich soft tissues are chemically stabilised, whereas mineralised tissues are progressively lost [688]. This selectivity may be spatially structured, as reactions are expected to be most intense at tissue surfaces in direct contact with peat pore water, while penetration into deeper tissues depends on diffusion of reactive species, local oxygen availability, and early *post-mortem* disruption [717].

Peat tanning is therefore a time-dependent process that – like dehydration and freezing – requires prolonged exposure to stable environmental conditions [718].

Sustained water saturation, low oxygen availability, and acidity are required for crosslinking reactions to proceed [669, 670]; if conditions change (e.g., through drainage or drying), the chemical pathways that stabilise tissues may be interrupted, and alternative degradative processes may dominate [719]. The environments in which bog tanning occurs are concentrated in low-lying temperate and boreal regions, particularly across northern Europe (including Scandinavia, the British Isles, the Netherlands, northern Germany, and Denmark), where waterlogged peat deposits are widespread [720]. Within the archaeological record, peat-preserved human remains (so-called 'bog bodies') are overwhelmingly of Holocene age [721], most commonly dating to the later prehistoric period (particularly the Bronze and Iron Ages) [722–724], reflecting the expansion of peatlands under post-glacial climatic conditions [725], as well as excavation biases [721].

### 1.4.4 Saponification

*Sensu stricto*, saponification refers to the hydrolysis of triglycerides to yield glycerol and fatty-acid salts. In *post-mortem* contexts, however, the term is used more broadly to describe the transformation after death of body fat into adipocere – a waxy, soap-like residue more commonly known as 'grave wax' [726]. This represents a related but more complex lipid transformation pathway than classical saponification: whereas the latter is driven by strong base-catalysed (alkaline) hydrolysis and produces fatty-acid salts directly, adipocere formation proceeds primarily through enzyme-mediated hydrolysis of triglycerides followed by secondary transformation of the liberated fatty acids, with salt formation occurring only as a later (and often incomplete) step [727, 728]. Unlike dehydration and freezing, then, which preserve soft tissues by removing and immobilising water respectively, saponification involves its consumption.

The process is initiated by the breakdown of lipids (Section 1.2.3.2) *post-mortem* [729]. Endogenous lipases released during autolysis [260, 730], together with bacterial esterases secreted during putrefaction (particularly *Clostridium perfringens* and *Micrococcus luteus* [731, 732]) [259, 733], catalyse the hydrolysis of triglycerides,

cleaving their ester bonds to yield glycerol and free fatty acids. The subsequent fate of these breakdown products depends strongly on local oxygen availability [734] and microbial metabolism [735]. Unsaturated free fatty acids, such as oleic (C18:1), palmitoleic (C16:1), and linoleic (C18:2) acids, which contain carbon–carbon double bonds (C=C), are particularly vulnerable to secondary transformation [732, 736]. Under aerobic conditions, these compounds are readily and progressively oxidised through microbial $\beta$-oxidation to acetyl-CoA, and are ultimately fully mineralised to carbon dioxide and water [737, 738]; thus the lipid substrate is effectively consumed, and adipocere formation is limited [734].

By contrast, under oxygen-limited conditions, microbial $\beta$-oxidation cannot proceed to completion [739]. Lipid degradation remains incomplete, and fatty acids are chemically modified rather than fully mineralised, leading to the accumulation of intermediate products within the tissue [735]. Under these conditions, unsaturated free fatty acids are characteristically transformed *via* microbial hydration of double bonds, followed by oxidation of the hydroxyl group to a ketone (oxo) group (C=O), thus yielding 10-hydroxy and subsequently 10-oxo fatty acids [731, 732, 736]. Partial hydrogenation or isomerisation of double bonds may also occur, but is less consistently documented than hydration–oxidation pathways [740–742]. In parallel, microbial degradation of proteins and amino acids generates basic products such as ammonia, which can shift the pH from mildly acidic to increasingly alkaline [743]. Under these conditions, saturated fatty acids deprotonate to form carboxylate ions, which then co-ordinate with cations (e.g., $Ca^{2+}$, $Mg^{2+}$, $Na^{+}$, $K^{+}$), whether naturally present in pore waters or burial matrices, or leached from surrounding tissues [729, 744]. These interactions generate fatty-acid salts ('soaps') that, being hydrophobic and poorly soluble, tend to precipitate or crystallise, completing the transformation of initially liquid lipid reserves into a solid, wax-like matrix [745].

Adipocere formation is thus strongly controlled by the burial environment. It is most commonly associated with wet, oxygen-poor depositional contexts in which moisture is retained and gas exchange is restricted, such as submerged remains, waterlogged graves, sealed coffins, tombs, and other enclosed environments

[746–748]. Once formed, adipocere is relatively resistant to further decomposition while these conditions are maintained [749, 750]. Its persistence derives first from its composition, which is typically enriched in 10-hydroxystearic and 10-hydroxypalmitic acids [732, 736, 751], as well as long-chain, even-carbon saturated fatty acids; most notably palmitic (C16:0), stearic (C18:0), and myristic (C14:0) acids [728, 730, 747, 752]. Oxygenated derivatives (such as 10-oxostearic and 10-oxopalmitic acids) may also constitute a minor component in low-oxygen environments where partial oxidation occurs [731, 751, 753]. These compounds have higher melting points than their unsaturated precursors and are less readily metabolised by microbes, promoting their retention and progressive enrichment [732, 736]. Persistence derives second from adipocere's physical structure: the low solubility and (semi-)crystalline organisation of fatty acids and their salts [745] reduce water penetration and limit enzyme accessibility, while the solid matrix they form restricts microbial diffusion into underlying tissues. This stability is, however, conditional: exposure to abundant oxygen promotes microbial degradation of adipocere [754], while drying causes cracking and fragmentation of the matrix, reopening routes for microbial colonisation and putrefactive degradation of an increased surface area [755].

Given that adipocere formation depends on the availability of a triglyceride-rich substrate, it is strongly tissue-selective. It occurs most readily in subcutaneous adipose tissue [664, 756–760], which consists of densely packed adipocytes filled with neutral lipid [761], but may also develop in visceral fat deposits [756] and bone marrow [762], both of which likewise contain substantial lipid stores dominated by triglycerides [761]. By contrast, tissues with low lipid content, such as muscle or collagenous connective tissue, are not primary substrates for this process. Thus, although geographically widespread, adipocere formation is nonetheless unevenly distributed within the corpse [759, 763, 764], allowing preservation of certain body contours and external morphology even where the underlying tissues have been substantially altered chemically.

### 1.4.5 Exceptional soft-tissue preservation on geological timescales

Exceptional soft-tissue preservation in the fossil record requires stabilisation mechanisms capable of operating over geological timescales, far exceeding those typically invoked in archaeological contexts [524]. Processes such as dehydration, freezing, tanning, and saponification act primarily by suppressing enzymatic and microbial degradation, and are therefore effective over years to millennia; however, they do not, in most cases, substantially and permanently reduce the intrinsic chemical reactivity of biomolecules, or prevent subsequent abiotic transformation. Over extended burial intervals, ranging from thousands to millions of years, intrinsic chemical lability (such as susceptibility to hydrolysis and oxidation) persists [86, 765], and, coupled with diagenetic conditions such as elevated temperature, pressure, and fluctuating redox environments, continues to drive molecular transformation [766]. Rather than prolonged inhibition of decay, preservation on geological timescales therefore involves conversion of labile biomolecules into more chemically recalcitrant forms [525]. The mechanisms considered in this section – oxidative polymerisation [767] and carbonyl-driven crosslinking *via* advanced lipoxidation and glycation reactions [768] – provide plausible pathways for such transformation.

#### 1.4.5.1 Oxidative polymerisation

The role of oxidative chemistry in long-term preservation was first proposed by Schweitzer *et al.* [767] on the basis of a model in which haemoglobin, upon death, releases iron that catalyses free-radical reactions in the presence of dioxygen – and in which the greatest tissue stabilisation is observed when both haemoglobin and oxygen are present. The mechanism described here thus derives from a framework developed for, and tested under, aerobic conditions. The question of whether radical-mediated crosslinking of this type can also operate in oxygen-poor environments – and the conditions under which it does so – falls outside the scope of this section.

Oxidative polymerisation encompasses a set of radical-mediated reactions in which biomolecules – particularly unsaturated lipids and proteins – are transformed

into crosslinked, high-molecular-weight networks through partial oxidation [769–771]. In lipid systems, the process is typically initiated by the abstraction of a hydrogen atom from an oxidisable site (R–H) on an unsaturated fatty acid, yielding a carbon-centred lipid radical ($R\cdot$) [772]:

$$R{-}H + \cdot OH \longrightarrow R\cdot + H_2O \tag{1}$$

This abstraction is mediated by highly reactive species such as hydroxyl radicals (·OH) [773], which are generated through redox-active transition metal chemistry (notably $Fe^{2+}/Fe^{3+}$ *via* Fenton-type reactions; Section 1.5.2.3) [774, 775], or by decomposition of pre-existing ROS [776]. Hydrogen abstraction is strongly favoured at allylic – particularly bis-allylic – positions in polyunsaturated lipids (e.g., linoleic acid, arachidonic acid) [138, 777], where the resulting radical is resonance-stabilised through delocalisation of the unpaired electron across adjacent $\pi$-bonds [778]. The resulting carbon-centered lipid radical reacts rapidly with molecular oxygen to form a lipid peroxyl radical ($ROO\cdot$) [779]:

$$R\cdot + O_2 \longrightarrow ROO\cdot \tag{2}$$

which can in turn abstract hydrogen from a neighbouring oxidisable lipid site, propagating the chain reaction and generating a lipid hydroperoxide (ROOH) alongside a new lipid radical ($R'\cdot$) [779]:

$$ROO\cdot + R{-}H \longrightarrow ROOH + R'\cdot \tag{3}$$

Lipid hydroperoxides are relatively unstable and act as key branching points in the reaction network [779, 780]. Their decomposition – *via* homolytic cleavage or metal-catalysed reduction – produces alkoxyl ($RO\cdot$) and hydroxyl radicals [781]:

$$ROOH \longrightarrow RO\cdot + \cdot OH \tag{4}$$

Alkoxyl radicals can then participate in several competing pathways [782]. One possibility is propagation of the radical chain *via* hydrogen abstraction (analogous to Equation 3), producing an alcohol (ROH) and a new lipid radical ($R''\cdot$) [783]:

$$RO\cdot + R{-}H \longrightarrow ROH + R''\cdot \tag{5}$$

Alternatively, alkoxyl radicals may undergo $\beta$-scission, resulting in cleavage of the carbon chain that yields a carbonyl fragment ($R'{=}O$) and a smaller alkyl radical ($R'''\cdot$), thereby contributing to molecular fragmentation and the generation of diffusible carbonyl species [784]:

$$RO\cdot \longrightarrow R'{=}O + R'''\cdot \tag{6}$$

These competing pathways determine whether alkoxyl radicals undergo chain cleavage to form smaller, diffusible products, or remain available for subsequent recombination and crosslinking reactions [782]. In addition to generating secondary oxidation products – including RCS such as aldehydes and ketones, as well as short-chain carboxylic acids, epoxides, and alcohols [785] – they also attack neighbouring biomolecules [786, 787].

When recombination predominates, crosslinking proceeds *via* several complementary mechanisms operating across both lipid- and protein-derived intermediates [788]. Radical–radical coupling produces covalent C–C and C–O crosslinks from peroxyl and alkoxyl intermediates [789, 790], terminating the chain reaction [787]:

$$R\cdot + R'\cdot \longrightarrow R{-}R \tag{7}$$

Protein oxidation proceeds *via* the same radical framework defined above (Equations 1–7), but with broader reaction pathways reflecting the chemical diversity of amino-acid side chains [770, 791]. Hydroxyl radicals, generated *via* hydroperoxide decomposition (Equation 4) [792] or metal-catalysed reactions [793], can react with proteins through three principal mechanisms. First, hydrogen atom abstraction from aliphatic C–H bonds in the peptide backbone or amino-acid side chains ($R{-}CH_2{-}$) produces carbon-centred protein radicals ($R{-}CH\cdot{-}$) [770, 794]:

$$R{-}CH_2{-} + \cdot OH \longrightarrow R{-}CH\cdot{-} + H_2O \tag{8}$$

These abstraction reactions occur preferentially at residues with relatively weak or activated C–H bonds, broadly following the order aliphatic > basic > sulfurous > amidic and acidic residues [795–798]. Second, hydroxyl radicals can undergo

rapid addition to electron-rich $\pi$ systems and heteroatom centres within amino-acid side chains (R–C=C–R′) [791, 799, 800]. This pathway is often kinetically competitive with, or faster than, hydrogen abstraction at aromatic and sulfur-containing residues [770, 796, 801], reflecting the stabilisation of the resulting radicals by delocalisation or heteroatom participation [778]. In aromatic residues, for instance, hydroxyl radicals add to the ring to yield resonance-stabilised hydroxylated radical intermediates (R–CHOH–C$\cdot$–R′) [800]:

$$\mathrm{R{-}C{=}C{-}R' + \cdot OH \longrightarrow R{-}CHOH{-}C\cdot{-}R'} \tag{9}$$

Third, in sulfurous residues, hydroxyl radicals react preferentially *via* one-electron oxidation of the sulfur atom to generate thiyl (RS$\cdot$) or sulfur-centred radical cation intermediates [798, 802], which can subsequently rearrange or participate in crosslinking reactions [770].

The initially formed radicals – whether carbon-centred, hydroxylated, or sulfur-centred – readily react with molecular oxygen to generate peroxyl radicals, undergo secondary hydrogen abstraction, or fragment to yield stable oxidation products including hydroxylated aromatics, carbonyl derivatives, and ring-opened species [770, 791]. Newly formed protein-derived radicals can then follow the same reaction pathways defined for lipid-derived radicals; namely recombination to form intermolecular linkages (such as dityrosine [803], ditryptophan [209] and Tyr–Trp crosslinks [804]) (Equation 7) [770, 805], or reaction with oxygen to yield peroxyl radicals (Equation 2) that further propagate oxidation [806].

Electrophilic carbonyl products of lipid peroxidation provide an additional, non-radical pathway for covalent modification and crosslinking. Aldehydes react with nucleophilic amino-acid side chains *via* two principal mechanisms. Simple aldehydes, including dialdehydes such as MDA, react preferentially with Lys $\epsilon$-amines (R′–$NH_2$) to form Schiff bases, which are intrinsically reversible and persist primarily when stabilised by subsequent chemical transformation [807, 808]:

$$\mathrm{R{-}CHO + R'{-}NH_2 \longrightarrow R{-}CH{=}N{-}R' + H_2O} \tag{10}$$

By contrast, $\alpha,\beta$-unsaturated aldehydes (such as 4-HNE, acrolein, or 4-oxo-2-nonenal) react predominantly *via* Michael addition [809], in which nucleophilic residues – particularly Cys, His, and Lys [810] – attack the electrophilic $\beta$-carbon of the conjugated system [811, 812]:

$$\alpha,\beta\text{-unsaturated aldehyde} + \text{nucleophile} \longrightarrow \text{Michael adduct} \tag{11}$$

Crosslink formation arises when bifunctional aldehydes, or sequential reactions of initial adducts, bridge two nucleophilic sites, yielding intra- and intermolecular linkages [812]: these processes extend modification beyond the initial site of radical formation by introducing diffusible intermediates capable of modifying distal biomolecules [813, 814]. Together with radical recombination reactions, these carbonyl-mediated processes define the principal routes by which partially oxidised biomolecules may be converted into covalently stabilised products, exhibiting increased heterogeneity, reduced susceptibility to proteolysis, and a propensity for aggregation [770, 815, 816].

The persistence of these reactions over geological timescales presumably requires conditions under which radical chemistry can continue, albeit at low rates, during prolonged burial. Continued sedimentation progressively isolates remains from atmospheric oxygen while exposing them to increasing temperature and pressure [50]: under these conditions, radical formation need not depend solely on oxidative processes, but may arise through thermally induced bond cleavage, including homolytic scission of C–H and C–C bonds [817–819]. The cumulative effect of such reactions over extended timescales may be sufficient to sustain low concentrations of reactive intermediates, allowing continued crosslinking and chemical transformation of organic matter [767]. In this way, oxidative polymerisation converts partial oxidation into long-term stabilisation, transforming labile biomolecules into recalcitrant, crosslinked macromolecular residues capable of persisting on geological timescales.

#### 1.4.5.2 ALE/AGE formation

Wiemann *et al.* [768] demonstrated that ALE- and AGE-type N-heterocyclic polymers are the principal product of soft-tissue fossilisation in vertebrate hard tissues, and that this transformation requires oxidative depositional conditions: specimens from reducing environments release no soft tissue on decalcification, and their experimental maturation protocol explicitly promotes oxidative crosslinking by sustained exposure to air. The carbonyl-driven crosslinking chemistry described in this section is therefore grounded in evidence from – and interpreted within – aerobic burial contexts. Whether analogous carbonyl chemistry can arise and yield stable products under oxygen-poor conditions is a separate question, not addressed in the sources reviewed here.

As established in Section 1.4.5.1, radical-mediated lipid peroxidation generates a range of reactive intermediates, including carbonyl-containing products formed through $\beta$-scission of alkoxyl radicals (Equation 6) [784]. These species – encompassing aldehydes, ketones, and $\alpha$-dicarbonyl compounds – are not terminal degradation products, but remain chemically reactive and capable of further transformation [785, 820]. They react readily with nucleophilic amino-acid side chains [820] *via* general carbonyl–nucleophile mechanisms, including Schiff base formation (Equation 10) [807, 808] and Michael addition (Equation 11) [812, 821], yielding stable covalent adducts and intermolecular crosslinks [788, 812] that contribute to the chemical stabilisation of degraded tissues [768]. When such reactions arise from lipid-derived carbonyl intermediates, they are described as advanced lipoxidation end product (ALE) formation [808, 816].

However, carbonyl-driven stabilisation can also arise through a fundamentally different route that does not depend on radical-mediated oxidation [822–824]. Under oxygen-limited conditions, reducing sugars provide an independent source of reactive carbonyl intermediates, giving rise to advanced glycation end product (AGE) formation [214, 823]. In this pathway, the carbonyl group of a reducing sugar

(such as glucose) reacts with a primary amine – most commonly the $\varepsilon$-amino group of Lys residues or N-terminal $\alpha$-amino groups – to form a reversible Schiff base [544]:

$$\text{reducing sugar} + \text{amine} \rightleftharpoons \text{Schiff base} + \text{H}_2\text{O} \tag{12}$$

This intermediate then undergoes an Amadori rearrangement to yield a more stable ketoamine (Amadori product) [825, 826], which may subsequently degrade through dehydration, fragmentation, and secondary oxidation reactions to generate highly reactive $\alpha$-dicarbonyl species such as glyoxal, methylglyoxal, and 3-deoxyglucosone [214, 544]. These dicarbonyl intermediates are potent crosslinking agents [827]: owing to their bifunctional electrophilic character, they react with multiple nucleophilic sites, particularly thiols and primary amines. Cys residues often react most rapidly [828, 829], whereas Lys and Arg dominate in the formation of stable AGE adducts and intermolecular crosslinks [830, 831]:

$$\alpha\text{-dicarbonyl} + \text{nucleophile} \longrightarrow \text{AGE adduct/crosslink} \tag{13}$$

Additional oxygen-limited processes may further contribute to carbonyl generation. Microbial metabolism of carbohydrates under reducing conditions primarily converts sugars to carboxylates, alcohols, and gases [832], but proceeds *via* central metabolic intermediates that include carbonyl species, providing a potential indirect source of RCS [833, 834]. In parallel, hydrolytic depolymerisation of polysaccharides yields carbonyl-bearing fragments that can undergo dehydration, isomerisation, and retro-aldol-type fragmentation to generate low-molecular-weight aldehydes and related intermediates [835].

Carbonyl-driven stabilisation thus proceeds *via* two mechanistically distinct but chemically convergent pathways: ALE formation from lipid-derived carbonyls generated during oxidative polymerisation, and AGE formation from sugar-derived carbonyls generated independently under oxygen-limited conditions. [525]. Despite these differences in origin, both pathways ultimately generate covalently crosslinked, chemically heterogeneous macromolecular assemblages with reduced solubility and increased resistance to enzymatic hydrolysis and microbial degradation [767, 768, 836].

## 1.5 The Brain

The following section summarises those aspects of brain structure, *in vivo* molecular change, and early *post-mortem* transformation that are required to interpret patterns of decomposition and preservation in nervous tissue. The emphasis is therefore on features that control molecular composition, spatial heterogeneity, and reaction pathways, rather than presenting a comprehensive account of neurobiology.

### 1.5.1 Nervous tissue structure and composition

The human central nervous system (CNS) is an exceptionally complex organ, comprising on the order of $10^{11}$ neurons [837–839] interconnected through an estimated $10^{14}$–$10^{15}$ synapses [840, 841], and supported by a comparably abundant and functionally diverse population of non-neuronal cells [842–844]. Its primary function – information processing and the integration and transmission of signals – is achieved through tightly regulated electrochemical processes [845] operating across highly specialised cellular and subcellular architectures [846]. This functional complexity is mirrored in the brain's structural [847] and biochemical heterogeneity [848, 849], comprising multiple distinct cell types, subcellular compartments, and molecular microenvironments, each with characteristic compositions and properties [850–852].

At the macroscopic scale, the brain is organised into anatomically and functionally distinct regions. The largest component, the cerebrum, is divided into two left and right hemispheres connected by commissural fibre tracts (principally the corpus callosum) [853, 854], and further subdivided into four lobes (frontal, parietal, temporal, and occipital) associated with different domains of sensory processing, motor control, and higher cognitive function [855–857]. Inferior to the cerebrum lies the diencephalon, comprising the thalamus, hypothalamus, epithalamus, and subthalamus: the thalamus relays and modulates sensory and motor signals to the cortex [858–860]; the hypothalamus regulates endocrine activity, autonomic function, and homeostatic processes *via* its connections with the pituitary gland [861–863]; the epithalamus (including the pineal gland) is involved in circadian

regulation and neuroendocrine signalling [864]; and the subthalamus contributes to motor control through its integration within basal ganglia circuits [865].

Inferior to the diencephalon, the brainstem is divided into the midbrain, pons, and medulla oblongata [866, 867]: the midbrain integrates visual and auditory reflexes and contributes to motor control [868, 869]; the pons contains major ascending and descending tracts and coordinates communication between the cerebrum and the cerebellum [870, 871]; and the medulla oblongata houses centres essential for cardiovascular, respiratory, and visceral autonomic regulation [872, 873]. Posteriorly, the cerebellum is specialised for motor coordination and balance [874], and is distinguished by a highly regular laminar architecture and dense neuronal packing [875]. The brain is bathed in cerebrospinal fluid (CSF), which occupies the ventricular system and subarachnoid space, providing mechanical protection, facilitating waste clearance, and contributing to chemical homeostasis [876–878]. Finally, the brain is enclosed by three concentric meningeal layers – the dura mater, arachnoid mater, and pia mater – that provide structural support, and which compartmentalise intracranial spaces while enclosing the cerebral vasculature [879]. This hierarchical anatomical organisation establishes large-scale compartmental boundaries that constrain fluid movement, vascular supply, and tissue connectivity, and thereby influence the spatial distribution of metabolites, solutes, and signalling molecules within the brain [880–882].

At the cellular level, nervous tissue is composed of neurons and several classes of non-neuronal cells. Neurons are electrically excitable, exceptionally long-lived cells (Box 1.10) specialised for the generation and propagation of action potentials; they are morphologically polarised [883, 884], with dendrites receiving synaptic input [885], a soma integrating signals [886], and an axon conducting action potentials to presynaptic terminals, where neurotransmitter release mediates communication at synapses [887]. Non-neuronal cells include multiple glial cell types, whose abundance relative to neurons varies by region [851] but is broadly comparable at the whole-brain scale [837, 888]. Astrocytes regulate extracellular ion balance [889], neurotransmitter recycling [890], and metabolic support [891]; oligodendrocytes

**Box 1.10 | *Neuronal longevity and limited regenerative capacity of the CNS***

In many tissues of the human body – particularly epithelial and haematopoietic systems – cells are maintained through continuous or periodic renewal driven by resident stem and progenitor cell populations [899, 900]. This process of cell turnover, whereby damaged, senescent, or apoptotic cells are replaced by newly generated cells, contributes to tissue homeostasis and limits the long-term accumulation of cellular damage [901, 902]. In such systems, damage may be mitigated either by intracellular repair mechanisms [903], or by removal and replacement of affected cells [904].

Neurons in the human CNS, however, are predominantly post-mitotic [905]: following differentiation during development, they exit the cell cycle and do not normally undergo further division [906, 907]. As a result, most neurons exhibit negligible turnover and persist for decades [908], often for the lifetime of the individual [909–912], and must maintain structural and functional integrity without the opportunity for replacement through cell division [913–917]. This cellular longevity is coupled to the limited regenerative capacity of the adult CNS: although a degree of neurogenesis has been demonstrated in specific regions (notably the dentate gyrus of the hippocampus [918–920] and the subventricular zone [921–923]), its extent in humans is limited, and insufficient to replace neuronal populations lost through ageing, injury, or disease. In most cortical, subcortical, and brainstem regions, neuronal loss is therefore effectively permanent [924].

The persistence of neurons reflects both developmental constraints and functional requirements. Neural circuits are defined by highly specific patterns of synaptic connectivity often extending over long distances [925, 926], established during development and early life [927, 928], with subsequent activity-dependent refinement and pruning [929]. Replacement of individual neurons requires not only cell generation, but also accurate re-establishment of these connectivity patterns, including synapse-specific connectivity, strength, timing, and network integration [930–933]. In the mature adult brain, this level of reconstruction is generally not achievable, and maintenance of existing cells predominates over replacement [934].

Consequently, neurons rely on sustained activity of intracellular maintenance systems – including proteostasis [935, 936], mitochondrial quality control [937–939], and DNA repair [917] – to preserve cellular integrity over extended timescales. Progressive decline or dysregulation of these systems leads to the accumulation of molecular damage, including protein misfolding (Section 1.5.2.1) [940, 941], and non-enzymatic (Section 1.5.2.2) [942, 943] and oxidative modification (Section 1.5.2.3). In contrast to tissues with ongoing cell turnover, such changes in neurons are retained and accumulate over time, contributing to age-related functional decline and increased susceptibility to degeneration [944, 945].

This combination of post-mitotic state, limited regenerative capacity, and long-term maintenance underlies a central feature of brain biology: the ageing CNS is composed of cells that have experienced decades of metabolic activity and cumulative molecular stress. This property distinguishes nervous tissue from other tissue types and organ systems, and provides the biological context in which the molecular processes described in Section 1.5.2 operate.

ensheath axons with myelin and enable saltatory conduction [892, 893]; and microglia act as resident immune cells mediating immune surveillance and phagocytosis [894]. Endothelial and associated perivascular cells form the structural and functional basis of the blood–brain barrier, regulating molecular exchange between the circulating blood and neural tissue [895, 896]. Ependymal cells, which line the ventricular system and contribute to CSF production and circulation, are derived from the neuroepithelium and exhibit both glial and epithelial characteristics [897, 898].

The above cell populations are organised into defined anatomical and functional domains, and a fundamental anatomical distinction is that between grey matter

and white matter. Grey matter, concentrated in the cerebral cortex and subcortical nuclei, is enriched in neuronal cell bodies, dendritic arbours, synapses, and associated glial processes [946, 947]. Relative to white matter, it contains a higher proportion of protein ($\sim$ 60% by dry weight) associated with synaptic and cytoskeletal machinery [948], alongside substantial lipid contributions ($\sim$ 40% by dry weight) from cellular membranes [949]. White matter, by contrast, consists predominantly of myelinated axons organised into fibre tracts that connect spatially separated regions of grey matter [950]. Due to the abundance of myelin, it contains a higher lipid fraction than grey matter [951]; typically on the order of 50–65% by dry weight [949]. Myelin itself is a specialised multilamellar membrane structure in which lipids comprise $\sim$ 70–85% of the dry weight, and proteins $\sim$ 15–30% [949, 952, 953]. The lipid fraction includes cholesterol, phospholipids, and glycolipids (notably galactocerebrosides and sulfatides) [952, 954], while the protein fraction is dominated by a small number of specialised components, including myelin basic protein (MBP) and myelin proteolipid protein (PLP1) [955].

At the subcellular level, the brain is further partitioned into discrete compartments that differ in both composition and function. These include neuronal soma, dendrites, axons, and presynaptic and post-synaptic elements at synapses [956]; glial processes, including astrocytic endfeet that ensheath blood vessels [957]; and intracellular organelles such as mitochondria, lysosomes, and the endoplasmic reticulum [958]. Each compartment maintains a distinct proteomic and lipidomic profile: synapses, for example, are enriched in neurotransmitter receptors, scaffolding proteins organising signalling complexes, and vesicle-associated machinery [959–961]; whereas axons are characterised by filament-forming cytoskeletal proteins [962–964] and membrane specialisations associated with conduction [965]. This nano- to micro-metre scale partitioning constrains the spatial distribution of biomolecules, and creates microenvironments with differing accessibility to water, ions, enzymes, and reactive species [966–968].

The extracellular matrix (ECM) of the brain is compositionally distinct from that of most other tissues. Whereas ECM is typically dominated by fibrillar collagens

in other organs [969], in the brain it is characterised by a hydrated network of hyaluronic acid and associated proteoglycans [970, 971], including chondroitin sulfate proteoglycans that form specialised structures such as perineuronal nets [972, 973]. This matrix occupies the extracellular space – estimated to comprise $\sim 20\%$ of brain volume [974] – and contributes to the regulation of diffusion, ion homeostasis, and synaptic stability [975–977]. In contrast to the mechanically reinforcing, collagen-rich ECMs of most tissues [978], the brain's glycosaminoglycan-dominated, sparsely fibrillar ECM supports a compliant, highly hydrated microenvironment that facilitates molecular exchange, rather than providing tensile strength [971].

In sum, the above features define the brain as a chemically and structurally heterogeneous organ in which lipids, proteins, and carbohydrates are unevenly distributed across well defined cellular and subcellular compartments. This intrinsic heterogeneity establishes a mosaic of molecular microenvironments within the same organ, providing the physicochemical context within which both *in vivo* ageing and *post-mortem* degradation processes operate.

### 1.5.2 Age-related changes *in vivo*

Normal and pathological brain ageing (manifesting as neurodegenerative diseases [NDDs]) lie on a continuum of shared molecular processes [979–983], such that differences are expressed primarily in their rate, extent, and anatomical distribution rather than in fundamentally distinct pathoetiology [984–986]. Across this continuum, the human brain undergoes progressive chemical and structural change, characterised by the accumulation of modified biomolecules, declining efficiency of intracellular maintenance systems, and alteration of cellular and extracellular organisation [987–989]. Neuronal and glial populations do not age uniformly: instead, intrinsic differences in connectivity and metabolic activity, as well as in local microenvironments, give rise to regional and cell type-specific patterns of molecular damage and functional decline [990–995]. Given most neurons are post-mitotic and adult CNS regeneration is limited (Box 1.10) [905], these changes are retained within cells and tissues over extended timescales, rather than mitigated

by cell turnover [909]; brain tissue at death therefore comprises a chemically modified and structurally altered molecular assemblage, in which proteins, lipids, carbohydrates, and nucleic acids have already undergone varying degrees of damage and degradation [996]. These processes can be grouped into a broad set of interacting molecular and cellular mechanisms that collectively reshape the biochemical and microenvironmental landscape of nervous tissue over the lifespan.

#### 1.5.2.1 Proteostatic failure and protein aggregation

Proteostasis, or protein homeostasis, is maintained in eukaryotic cells by an integrated network of molecular chaperones and protein degradation systems, including the ubiquitin–proteasome system, autophagy–lysosomal pathways, and mitochondrial quality-control mechanisms [997, 998]. This network is under particular strain in neurons [999], which are long-lived, post-mitotic, and highly polarised cells with extensive axonal and dendritic arbourisations [1000]. This large surface area imposes sustained demands for protein turnover across spatially segregated compartments, including distal processes and synapses [1001–1003]. As a result, even modest perturbations in proteostatic capacity can have disproportionately large effects in the brain, where cellular longevity and structural complexity limit opportunities for renewal [1000, 1004, 1005].

In the healthy brain, these systems limit the accumulation of damaged, misfolded, and aggregation-prone proteins, while preserving the proteome required for synaptic transmission and plasticity [1006, 1007]. With ageing, however, proteostatic capacity declines, and the balance between protein synthesis, folding, trafficking, and degradation becomes progressively less efficient [1008, 1009]. In the non-diseased ageing brain, this is associated with reduced autophagic flux, impaired lysosomal function, and increased neuronal and glial senescence [1010–1012], creating conditions in which damaged proteins are less effectively cleared and more likely to persist or accumulate [1013].

The same proteostatic failure underlies the major age-related proteinopathies of the CNS [944]. NDDs such as Alzheimer's disease (AD), Parkinson's disease

(PD), frontotemporal dementia (FTD), and amyotrophic lateral sclerosis (ALS) are characterised by the disease-specific accumulation of misfolded and aggregated proteins, including amyloid-$\beta$ and hyperphosphorylated tau in AD [1014–1016], $\alpha$-synuclein in PD [1017, 1018], and TAR DNA-binding protein 43 (TDP-43) in ALS and many FTD cases [1019–1021]. Protein aggregation in this context reflects defined shifts in protein chemistry and cellular environment, including altered proteolytic processing [1022–1024], aberrant PTMs [1025, 1026], disrupted metal ion homeostasis [1027–1029], and changes in membrane association that promote misfolding and nucleation [1030–1032]. From a molecular taphonomic perspective, this implies that brain tissue at death may already contain proteins that are chemically modified, partially unfolded, or primed for aggregation, preconditioning the molecular substrate on which *post-mortem* transformation and preservation processes act. This preconditioning is not contingent on overt neuropathology: as the preceding paragraph establishes, proteostatic decline and the accumulation of damaged proteins are features of the normal ageing brain, with NDDs representing the far end of a continuous spectrum rather than a categorically distinct state.

#### 1.5.2.2 Non-enzymatic molecular damage and spontaneous modification

A further dimension of age-related change in the human brain is that of spontaneous, non-enzymatic PTMs [1033], which alter residue charge, backbone geometry, and intermolecular interaction potential without enzymatic mediation [1034, 1035]. Unlike regulated modifications associated with cellular signalling, these reactions arise from the intrinsic chemical reactivity of proteins and small metabolites, and accumulate as a function of time, protein turnover rate, and local physicochemical environment [1035, 1036]. Median protein lifetimes are longer in the brain than in other organs [1012, 1037–1039], increase by $\sim$ 20% with ageing [1040], and coincide with an abundance of 'long-lived' and 'extremely long-lived' proteins [1041–1043]. Myelin-associated proteins, for instance, exhibit slow turnover with residence times of several months [1038, 1044], such that, once incorporated into compact myelin, they experience prolonged exposure to the local chemical

environment, and can accumulate spontaneous modifications over extended periods [1045, 1046]. Degenerative protein modifications of this kind include deamidation, isomerisation and racemisation, glycation and glycoxidation, and related carbonyl-driven processes, all of which contribute to progressive chemical remodelling of the CNS proteome with age.

Deamidation is among the best-characterised of these processes, producing alterations in local charge, backbone geometry, and protein function [1047]. It involves the spontaneous conversion of the neutral amide side chains of Asn and Gln residues to negatively charged carboxylates: Gln deamidation proceeds predominantly through direct hydrolysis to Glu [1048], whereas Asn deamidation more commonly proceeds *via* intramolecular cyclisation to a cyclic succinimide intermediate, the subsequent hydrolysis of which yields either Asp or isoAsp [1049]. In long-lived brain proteins, deamidation accumulates over time and can promote structural destabilisation, aggregation, and altered susceptibility to proteolysis [1047, 1050]. In dementia-affected brain tissue, amyloid-associated material is enriched for deamidated proteins, suggesting that this modification alters charge state and ion-binding capacity in ways that promote amyloid aggregation [1050, 1051]; consequently, deamidation has been implicated in the pathoetiology of several NDDs [1047, 1052–1054].

Racemisation (interconversion of L- and D-protein configurations) and isomerisation (conversion of a residue to an alternative isomeric form) are closely linked spontaneous modifications that occur predominantly at Asn and Asp residues [213]. Both Asp isomerisation and Asn deamidation proceed *via* intramolecular attack of the backbone amide nitrogen on the side-chain carbonyl group to form a cyclic succinimide intermediate [213, 1055]. This intermediate can undergo racemisation prior to hydrolysis, and subsequent ring opening at either carbonyl yields mixtures of L- and D-Asp together with L- and D-isoAsp [1056]. Formation of isoAsp results from rearrangement of the peptide backbone attachment from the $\alpha$-carboxyl group of Asp to the $\beta$-carboxyl group. Consequently, an additional methylene group ($-CH_2-$) is effectively incorporated into the peptide backbone [1057, 1058],

introducing a local kink that perturbs backbone geometry, protein folding, molecular recognition, and proteolytic turnover [1057, 1059–1061]. These spontaneous changes in stereochemistry (L → D) and backbone connectivity (Asp → isoAsp) accumulate in long-lived, aggregation-prone proteins implicated in NDDs – including amyloid-$\beta$, tau, $\alpha$-synuclein, huntingtin, and prion protein – modifying their structural and functional properties over time [1051, 1060, 1062–1067].

Non-enzymatic glycation represents a complementary pathway of chemical modification yielding AGEs that is particularly consequential in long-lived neural proteins. In the human brain, AGEs accumulate progressively with normal ageing [1068–1070] and are disproportionately enriched in amyloid plaques and neurofibrillary tangles in AD-type pathology [1071–1075], consistent with the selective involvement of long-lived, aggregation-prone proteins as both substrates and targets. AGEs engage cell-surface receptors such as the receptor for AGEs (RAGE), activating downstream signalling cascades including NF-$\kappa$B-mediated inflammatory pathways that further alter the redox and proteomic environment of the tissue [1076–1078]. RAGE activation also increases ROS *via* reduced nicotinamide adenine dinucleotide phosphate (NADPH) oxidase and mitochondria [1079, 1080], creating oxidative stress that further activates NF-$\kappa$B and augments AGE formation, forming a self-amplifying loop [1081, 1082]. The primary detoxification route for reactive dicarbonyls – glyoxalase I and II, which convert methylglyoxal to D-lactate [1083] – declines in activity with age, reducing the capacity of nervous tissue to limit carbonyl stress [1084, 1085]. As a result, the combination of long protein residence times, elevated RCS flux, and declining glyoxalase activity allows glycation reactions to proceed slowly but continuously *in vivo*, even in the absence of acute metabolic disturbance [1086–1088], yielding proteins that are crosslinked, carbonyl-enriched, and partially resistant to proteolytic turnover [544, 1089].

Collectively, these spontaneous modifications alter amino-acid residues, charge distributions, backbone geometry, and crosslinking potential within proteins [1035]. They destabilise native conformations in some cases [1090], and promote the persistence of structurally altered or chemically resistant forms in others [1033]. As

a result, long-lived proteins within the ageing brain differ from their newly synthesised counterparts in both chemical composition and structural state, providing a heterogeneous substrate upon which subsequent degradative and transformative processes operate. In archaeological contexts, the same spontaneous reactions are interpreted as diagenetic signatures: site-specific deamidation of Asn and Gln is widely used to authenticate ancient proteins and assess their degradation [1091–1099], whereas amino-acid racemisation provides a longer-established – but strongly context-dependent – geochronological tool across $10^3$–$10^5$-year timescales [1100–1106].

#### 1.5.2.3 Oxidative damage and mitochondrial dysfunction

Oxidative stress is a pervasive feature of brain ageing, arising from the continuous production of ROS and reactive nitrogen species (RNS) during aerobic metabolism [1107–1109], and the secondary generation of RCS during biomolecular oxidation [1110]. The brain is particularly susceptible to oxidative damage because of its high and sustained rate of oxygen consumption [1111], its use of transition metals [1112], and its enrichment in polyunsaturated fatty acids (PUFAs) within neuronal and myelin membranes [1113]; coupled with its relatively modest antioxidant defences [1114, but see 1115], and its limited metabolic flexibility and dependence on mitochondrial oxidative phosphorylation to meet neuronal ATP demand [1116]. However, susceptibility to oxidative damage in the ageing human brain is not uniformly distributed. At the regional level, the hippocampus and frontal cortex accumulate substantially greater oxidative burden with age than the cerebellum [1117], paralleling their higher metabolic demands and comparatively limited antioxidant defences [991].

Lipid peroxidation constitutes a major route by which oxidative damage propagates within nervous tissue [1118–1120]. PUFAs contain bis-allylic methylene groups that are especially prone to hydrogen abstraction, rendering membrane lipids a primary target for radical-mediated attack [1121]. Initiated by ROS, peroxidation of PUFAs proceeds *via* chain-propagating reactions that generate lipid radicals, lipid hydroperoxides, and a range of secondary breakdown products (Section 1.4.5.1) [429].

Among these are reactive aldehydes (e.g., 4-HNE, MDA), which can diffuse from their site of origin and react with nucleophilic residues in proteins to form covalent adducts [785]: such modifications alter protein conformation, impair enzymatic activity, and promote the formation of crosslinked, aggregated, or aggregation-prone structures, extending the effects of oxidative damage beyond the lipid phase in which it is initiated [810, 1122–1124]. As a result, membrane-associated proteins and other components embedded within lipid-rich environments are exposed to both primary radical attack, and secondary modification by lipid-derived electrophiles [1122]. Proteins involved in energy metabolism, synaptic transmission, and cytoskeletal organisation are also recurrent targets [1125–1127], reflecting their proximity to mitochondrial ROS sources and membrane-rich environments [1128].

Oxidative damage of this kind is not confined to proteins and lipids, however. Neurons are exceptionally long-lived cells [909] and maintain high levels of transcriptional and metabolic activity throughout their lifetime [1129], such that their DNA is continuously subject to endogenous damage arising from ROS [1130, 1131], spontaneous base hydrolysis and deamination [1132], and strand breakage associated with transcriptional activity [1133]. In addition, neuronal activity itself induces transient DNA strand breaks through the action of topoisomerases, which relieve torsional stress during rapid gene expression associated with synaptic activity [1134–1136]; these breaks are normally rapidly repaired, but represent an additional source of cumulative genomic stress [1137, 1138]. Indeed, it is estimated that human neurons experience on the order of $10^4$–$10^5$ DNA lesions per day, and over a billion repairs throughout life [917]. However, the efficiency of repair pathways – including base excision repair [1139, 1140], single-strand break repair [1141, 1142], and double-strand break repair *via* non-homologous end joining and homologous recombination [1143] – declines with age [1144]. As a result, unrepaired or misrepaired lesions persist, altering local chromatin structure and transcriptional regulation, and, in some cases, activating DNA damage response pathways that promote cellular senescence or inflammatory signalling [1145–1147]. Genome maintenance thus

becomes a limiting factor in neuronal longevity, influencing both cell survival and the functional state of surviving neurons over time [1148, 1149].

Mitochondria occupy a central position in these processes, acting as both a major intracellular source of ROS – primarily through electron leakage from the ETC [1150, 1151] – and as targets of oxidative damage [1152, 1153]. With ageing, mitochondrial function declines, reflected in reduced efficiency of electron transport [1154], accumulation of mitochondrial DNA lesions [1155, 1156], and impaired mitophagy [1157]; together, these changes both promote increased ROS production, and diminish the cell's capacity to maintain redox balance [1158]. Neurons are particularly sensitive to such changes [1159, 1160], especially within distal axonal and synaptic compartments where mitochondrial turnover and transport are constrained [1161]. Mitochondrial dysfunction is further implicated in pathological ageing – including in AD, PD, and ALS [1162, 1163] – where it tends to co-localise with protein aggregation and glial activation [1164, 1165]. However, even in the absence of overt disease, oxidative damage and mitochondrial dysfunction together ensure that brain tissue at death is likely to contain proteins, lipids, and nucleic acids that have already undergone substantial chemical modification [981, 988], particularly within membrane-rich compartments and metabolically active regions [1166, 1167].

#### 1.5.2.4 Metal and calcium dyshomeostasis

Metal ions – such as iron, copper, and zinc – are required for normal brain function, but their behaviour depends on tightly regulated uptake, intracellular trafficking, compartmental sequestration, storage, and export [1028, 1168–1170]. In the healthy brain, these metals are imported by specialised transporter proteins [1171–1173], distributed to target proteins by chaperone systems [1174, 1175], buffered by metal-binding proteins and small molecules [1176, 1177], and either sequestered within intracellular compartments or exported from the cell [1178–1180]. As a result, labile concentrations of iron, copper, and zinc are carefully controlled, limiting inappropriate metal-catalysed reactions while ensuring availability for essential cellular processes. With ageing, these systems become less tightly compartmentalised as a

consequence of oxidative damage to transporters and membranes, impaired vesicular trafficking, and disruption of protein-mediated metal sequestration [1181–1183]. Metal ions are therefore redistributed into labile intracellular and extracellular pools rather than remaining bound to storage proteins or chaperoned pathways [1170].

Iron differs from copper and zinc in that $Fe^{2+}$ readily participates in one-electron redox cycling under physiological conditions [1184] and is not maintained at vanishingly low free concentrations [1185]; consequently, even modest increases in the labile $Fe^{2+}$ pool have direct chemical consequences [1186, 1187]. In healthy ageing, iron accumulation is most evident in deep grey matter, especially the putamen and other basal ganglia nuclei [1188–1190]; some studies also report deposition in cortical regions, though this is more variable and typically of lower magnitude than subcortical accumulation [1188, 1191–1193]. Neuromelanin-rich nuclei such as the substantia nigra and locus coeruleus are also classical iron-accumulating sites [1194–1196], with deposition more pronounced in PD-type neurodegeneration [1197–1199].

The behaviour of iron in these environments is governed by Fenton chemistry [1200]. $Fe^{2+}$ reacts with hydrogen peroxide ($H_2O_2$) produced continuously during aerobic metabolism – particularly through dismutation of superoxide ($\cdot O_2^-$) generated by mitochondrial ETC leakage, a reaction catalysed principally by mitochondrial superoxide dismutase [1201, 1202] – to generate hydroxyl radicals [1203]:

$$Fe^{2+} + H_2O_2 \longrightarrow Fe^{3+} + OH^- + \cdot OH \tag{14}$$

Hydroxyl radicals are highly reactive and non-selective, reacting with lipids [773], proteins [1204], carbohydrates [1205], and nucleic acids [1206]; they initiate lipid peroxidation, oxidise protein backbones and side chains, and induce strand breaks and base modifications in DNA [1207–1209]. Redistribution of iron into labile pools therefore increases the rate and spatial extent of radical-mediated oxidation within the tissue [1210, 1211]. Peroxidation of membrane phospholipids is also a key trigger of ferroptosis, an iron-dependent, non-apoptotic form of regulated cell death [1212]. Under conditions of iron overload, failure of antioxidant systems – which

normally reduce lipid hydroperoxides to non-toxic alcohols, thereby preserving membrane integrity [1213, 1214] – permits accumulation of lipid-derived ROS, initiating a ferroptotic cascade culminating in membrane rupture, mitochondrial dysfunction, and neurodegeneration [1215–1218].

Oxidative attack on proteins by iron-catalysed hydroxyl radicals likewise promotes carbonylation, an irreversible oxidative modification in which aldehyde or ketone groups are introduced into amino-acid side chains, generating primary carbonyls [211, 1219]. Residues such as Lys, Arg, Pro, and Thr are particularly susceptible [1220, 1221] because their side chains are readily oxidised by metal-catalysed ROS to primary carbonyls [1222], while Lys also reacts with lipid-derived aldehydes like 4-HNE and MDA to yield secondary carbonyl adducts [1222, 1223]. Extensive carbonylation destabilises local structure, increases hydrophobicity and aggregation propensity, and, concomitantly, decreases solubility, thereby impairing the function and turnover of metal-binding proteins and reinforcing metal dyshomeostasis [1224–1226].

Copper possesses higher intrinsic redox reactivity than iron, and its intracellular speciation is thus even more tightly constrained [1227]. Free copper is maintained at exceptionally low concentrations (typically femtomolar to attomolar) [1228, 1229], with almost all copper held in high-affinity complexes or chaperone-bound pools [1230, 1231]. In the brain, disruption of this system can arise from oxidative damage to or downregulation of transport proteins, failure of P-type ATPase-mediated efflux, or release of copper from metalloproteins under conditions of cellular stress [1175, 1231–1233]. Under these circumstances, $Cu^{+}/Cu^{2+}$ redox cycling can generate ROS in a manner analogous to iron, contributing to lipid peroxidation, protein oxidation, and mitochondrial dysfunction [436, 1203]; and, as with iron, the chemical effects of copper are largely determined by the size and localisation of the labile pool relative to its protein-bound fraction [1234]. Finally, excess intracellular copper is implicated in a copper-dependent, non-apoptotic cell death pathway known as cuproptosis [1235], in which copper binds lipoylated mitochondrial proteins, whose subsequent aggregation promotes the destabilisation

and loss of iron–sulfur cluster proteins involved in mitochondrial respiration, which in turn triggers proteotoxic stress [1235–1237].

Zinc differs from iron and copper in that it does not undergo redox cycling under physiological conditions [1238]; its effects are therefore mediated through binding interactions rather than radical generation [1239]. $Zn^{2+}$ is abundant in the brain and is concentrated in synaptic vesicles of certain glutamatergic neurons [1240, 1241], from which it is released in an activity- and $Ca^{2+}$-dependent manner to modulate ionotropic receptors and ion channels [1242], thereby influencing both excitatory and inhibitory synaptic activity [1243, 1244]. With ageing, altered expression of zinc-regulatory proteins perturbs the balance between vesicular, protein-bound, and extracellular pools [1245], which in turn can modify the metal-binding state of receptors and structural proteins [1246], favour misfolding and aggregation (notably in AD) [1247–1250], and disrupt synaptic plasticity and signalling [1251, 1252]; ultimately contributing to age-related cognitive decline [1253]. These effects are particularly evident in zinc-enriched regions such as the cortex and hippocampus, where synaptic zinc plays a prominent role in neurotransmission [1241, 1254, 1255].

Calcium, like zinc, does not participate in redox cycling; however, its age-related dysregulation, like that of iron and copper, involves the deterioration of tightly regulated intracellular compartmentalisation [1256, 1257]. In the living brain, intracellular $Ca^{2+}$ concentrations are maintained at low nanomolar levels relative to the extracellular space by a coordinated system of plasma-membrane $Ca^{2+}$-ATPases, $Na^{+}/Ca^{2+}$ exchangers, sequestration within the endoplasmic reticulum, mitochondrial uptake, and cytosolic buffering proteins [1258–1260]. With ageing, the efficiency of these systems declines, leading to elevated basal intracellular $Ca^{2+}$ concentrations and delayed clearance following activity-dependent influx [1261, 1262]. These changes are particularly evident in neurons with high firing rates and extensive synaptic connectivity, where repeated $Ca^{2+}$ influx through voltage- and ligand-gated channels places sustained demand on buffering and extrusion systems [1263, 1264]. Elevated intracellular $Ca^{2+}$ activates calcium-dependent enzymes, including calpains, phospholipases, and endonucleases: calpains

cleave cytoskeletal and membrane-associated proteins [1265, 1266]; phospholipases hydrolyse membrane phospholipids, generating lysophospholipids and free fatty acids [1267, 1268]; and endonucleases fragment nuclear DNA [1269]. In parallel, mitochondrial $Ca^{2+}$ overload disrupts oxidative phosphorylation, promotes further ROS generation, and can trigger opening of the mitochondrial permeability transition pore, leading to loss of membrane potential and release of pro-apoptotic factors [1270–1273]. Consequently, neurons with chronically elevated intracellular $Ca^{2+}$ concentrations and impaired calcium buffering at the time of death may undergo more rapid *post-mortem* calcium dysregulation once ATP-dependent ion homeostasis collapses, accelerating membrane destabilisation and lysosomal enzyme release during autolysis (Section 1.3.1) [1274, 1275].

In sum, age-related metal dyshomeostasis produces regionally disparate patterns of metal reactivity within the brain, generating chemically distinct microenvironments with different capacities for oxidation, carbonylation, and protein aggregation [1276, 1277]. Regions containing elevated labile $Fe^{2+}$ or $Cu^{2+}$ support hydroxyl-radical generation and downstream oxidative and carbonyl chemistry [1028], whereas zinc-rich synaptic compartments influence protein conformation and aggregation without direct redox involvement [1203], and poorly buffered intracellular $Ca^{2+}$ primes affected neurons for rapid autolytic degradation [1275]. Equally, some compartments effectively sequester metals in relatively inert and conditionally mobilised stores [1278–1280], while others harbour labile metal pools that, when expanded or mislocalised, promote neurodegeneration [1112, 1281]. The ageing brain thus enters the PMI with pre-existing gradients in metal distribution and reactivity – and, for calcium, a pre-existing propensity for rapid *post-mortem* enzymatic autolysis – which contribute to the spatial variability of subsequent chemical transformation within the tissue.

#### 1.5.2.5 Cellular and tissue-level remodelling

The preceding sections describe molecular changes within brain cells. These processes, however, do not occur in isolation: they are embedded within a structured

tissue environment that constrains the movement, interaction, and persistence of molecules. Age-related change in the brain therefore reflects not only the accumulation of intracellular damage, but also progressive remodelling of the cellular and extracellular context in which that damage occurs.

Glial cells are principal mediators of this environmental remodelling. The brain's resident immune cells, microglia are chronically exposed to damage-associated molecular patterns – such as extracellular ATP, mitochondrial components, oxidised lipids, and misfolded proteins [1282, 1283] – released from stressed and dying cells, accumulating oxidative damage and generating neurotoxic ROS and nitric oxide (NO) in response [1165, 1284]. With age, the result is a shift toward reduced phagocytic capacity and elevated basal production of pro-inflammatory cytokines [1285–1287], which progressively alters the chemical composition of the extracellular space [1288]. Astrocytes are affected in parallel: Glu uptake becomes less efficient [1289, 1290], metabolic shuttling of energy substrates to neurons is impaired [891, 1291], and extracellular ion homeostasis is disrupted [889]. Extracellular Glu and $K^+$ consequently rise while local energy supply becomes less tightly controlled, modifying pH, redox balance, and the availability of enzymatic cofactors throughout the tissue [1292, 1293]. Glial dysfunction therefore translates intracellular damage into measurable changes in the reactivity and composition of the microenvironment, and the two processes are mutually reinforcing: a more pro-inflammatory, redox-perturbed milieu accelerates cellular deterioration, which in turn sustains and amplifies glial activation [1286, 1294, 1295].

White matter is particularly vulnerable to age-related remodelling because myelin integrity depends on continued oligodendrocyte function, which declines with age [1296, 1297]. Existing myelin undergoes structural degradation – including lamellar disruption, lipid redistribution, and partial breakdown of myelin-associated proteins [1298–1300] – that exposes previously sequestered lipid domains to water, oxygen, and reactive species [1301]. The result is increased susceptibility to lipid peroxidation and secondary carbonyl formation, with lipid-derived reactive intermediates diffusing into surrounding compartments [1302, 1303].

The ECM also undergoes reorganisation. Altered expression of matrix-synthesising enzymes, increased protease activity, and the accumulation of oxidative and carbonyl-mediated crosslinks modify the polymer length, charge density, and crosslinking state of the neural ECM [1304, 1305], including the perineuronal nets that surround subsets of neurons [1306, 1307]. A stiffer, more crosslinked matrix impedes molecular mobility, altering the effective diffusion of ions and small molecules through the extracellular space [1308, 1309], with consequences for synaptic chemistry and the susceptibility of the matrix to further oxidative and carbonyl-mediated modification [1310].

Finally, the blood–brain barrier becomes progressively less effective with age [1311]. Structural changes in the neurovascular unit – such as reduced tight junction integrity, altered pericyte coverage, and disrupted astrocytic endfoot organisation, driven in part by oxidative stress and vascular ageing [1312–1314] – increase transcellular permeability [1315–1317]. Plasma-derived proteins, ions, and other solutes enter the parenchyma, introducing new substrates and disrupting osmotic balance [1318, 1319]; at the same time, impaired metabolite clearance allows reactive species to accumulate locally [1320, 1321]. Together, these changes erode the concentration gradients that normally separate intravascular, extracellular, and intracellular compartments, increasing solute mobility and altering the redox and ionic conditions throughout the tissue [1322, 1323]. These remodelling processes ensure that, by the time of death, decades of glial dysfunction, myelin remodelling, ECM crosslinking, and barrier deterioration may together have shaped a tissue whose chemical composition, structural organisation, and reactive potential differ substantially from those of a younger brain.

### 1.5.3 Early *post-mortem* decomposition

Decomposition of the brain in the immediate PMI remains incompletely characterised. Observations are distributed across a heterogeneous literature that differs substantially in experimental design, species, preservation conditions, time course, and analytical methodology [310], such that reports on the nature and rate of

structural deterioration vary widely, and in some cases yield apparently conflicting interpretations of structural persistence. The synthesis presented here therefore represents an attempt to integrate these disparate observations, while recognising that substantial uncertainty remains regarding the precise decay trajectory of many brain structures.

Morphological alteration begins within minutes of the cessation of circulation, and progresses over a timescale of hours to days [1324, 1325]. The earliest consistently reported microscopic changes are perivascular and pericellular rarefactions, together with intracellular and extracellular vacuolisation [310]. Perivascular rarefactions – regions of reduced staining density appearing as optically clear spaces on histological sections – develop around blood vessels [1326, 1327], while pericellular rarefactions surround neuronal and glial somata [1328]. Although some have interpreted these features as arising from cytoplasmic contraction or retraction of the surrounding neuropil [1328], they are thought predominantly to reflect the swelling of astrocytic processes and perivascular endfeet, which take up water following failure of ion homeostasis in the immediate *post-mortem* period [310, 1329–1332]. Vacuoles – that is, rounded, non-staining inclusions within cells or neuropil – may be observed from as early as 30 minutes after death under certain conditions [1333], though this timing is temperature-dependent, and their appearance may be delayed to several hours *post-mortem* under cooler conditions [1326, 1334–1337]. Vacuolisation has been attributed to organelle swelling, fluid accumulation, and separation of cellular components [1338, 1339], particularly swollen mitochondria and dilated endoplasmic reticulum or Golgi apparatus [310]. Together, these changes reflect redistribution of water and solutes within the tissue, and can mechanically distort or compress surrounding structures [1340, 1341].

At the cellular level, a broad hierarchy of vulnerability has been described, though the available evidence is heterogeneous and in several respects unresolved [310]. Synaptic ultrastructure appears to be among the more labile features: changes in synaptic morphometry (such as reduced concavity and thickening of the post-synaptic membrane) have been documented within minutes of death [1342–1345],

and vesicle redistribution has been reported within the first hour [1346–1351]. However, whether these morphometric changes translate into loss of identifiable synaptic contacts is considerably less clear: some studies report substantial decreases in visualisable synapse numbers within the first several hours *post-mortem* [1338, 1344, 1352], while others find no significant reduction over several days [840, 1353, 1354]. It has been argued that much of the apparent loss likely reflects compression of synaptic profiles by swollen astrocytic processes, or degradation of specific synaptic markers used for identification, rather than structural disintegration *per se* [1338]. The persistence of intact synaptic contacts therefore remains uncertain, and is strongly dependent on the visualisation method employed [310].

Dendrites and axons evidence morphological alteration over a somewhat longer timescale, though again the evidence is highly method-dependent. Studies have documented beading, varicosity formation, and moniliform changes in dendrites with attendant loss in immunoreactivity from several hours *post-mortem* [1326, 1328, 1344, 1355–1360], while others have reported retention of dendritic spine morphology beyond 24 hours [1361–1367], and as long as five days after death [1368]. As with synaptic morphometric changes, it is difficult to reconcile these divergent findings; however, the evidence suggesting longer stability is harder to dismiss as systematically flawed than that reporting faster degradation [310], and apparent early loss may partly reflect the sensitivity of particular staining methods rather than true structural disintegration [310]. Axons exhibit broadly similar patterns – such as segmental swelling and varicosity formation [1344, 1355, 1356, 1369] – and there is some suggestion that they may degrade more slowly than dendrites [310], though this remains uncertain given the same method-dependent caveats apply. In contrast to these processes, neuronal somata tend to retain their overall outline for relatively longer periods, a reflection of the general observation that cell membranes are more resistant to decomposition than intracellular organelles [310]; as such, significant intracellular deterioration can occur while gross cell shape remains recognisable [1326, 1352, 1367, 1370]. In this respect, myelin appears to be the most resistant major structural component [310]: whereas separation of individual

lamellae can be observed within hours of death [1334, 1367, 1371–1373], this reflects delamination rather than destruction of the myelin sheath. As a consequence, white matter architecture may be retained after other neural structures have deteriorated, and myelinated fibre tracts appear to be among the most stable anatomical features of the decomposing brain [1342, 1351, 1352, 1372, 1374–1377].

This hierarchy of structural persistence is further modulated by regional and cellular context, although the evidence for many specific patterns is limited and not always consistent across studies [310]. The cerebellum – and particularly its granule cell layer – is the most consistently and robustly identified region of selective vulnerability [310]: morphological change is detectable within minutes [1378], typically manifesting as disintegration of granule cells without equivalent change in adjacent Purkinje cells [1326, 1379–1381]. The susceptibility of the cerebellum to rapid dissolution has been attributed to high local enzyme content and tissue acidity [1326, 1382–1384]. While the cerebral cortex tends to be better preserved than subcortical regions (such as the basal ganglia and thalamus) [1385], one study [1364] reported that superficial cortical layers (I–III) were less well preserved than deeper layers (IV–VI) at 30 days *post-mortem*. White matter, by contrast, is comparatively persistent, reflecting the relative stability of myelinated axons [1385].

These observations collectively indicate that early *post-mortem* decomposition of the brain is characterised by rapid deformation of cellular morphology within minutes to hours, followed by progressive and spatially variable loss of fine structural detail over hours to days, while larger-scale organisation – particularly of somata and myelinated tracts – persists for longer [310]. Critically, however, observations in terms of the nature, extent, and rate of these changes are strongly modulated by the method used to visualise them, the specific feature (or marker[s] of that feature) under examination, the cell type, and the brain region [310]. The *post-mortem* brain therefore comprises a compositionally and structurally diverse tissue whose various components retain differing and often poorly characterised degrees of integrity soon after death: this uncertainty is a fundamental feature of the field of

neuropathology, and constrains both the interpretation of observed morphology as well as the trajectory of subsequent molecular and morphological change.

## 1.6 Palaeoproteomics

### 1.6.1 Applications and advantages

Palaeoproteomics is the study of proteins (Section 1.2.3.4) preserved in forensic, archaeological, and fossil materials [1386]. In practice, this entails the recovery and mass spectrometric analysis of peptide sequences derived from proteins that have undergone partial degradation and chemical modification after death [202]. The object of study is therefore not the intact *in vivo* proteome, but a surviving peptide assemblage ('palaeoproteome') whose composition and associated modification state has been filtered by life, death, decomposition, burial, excavation, extraction, analysis, and interpretation, and from which the presence of source proteins, and the chemical transformations they have undergone, must be inferred [202]. The goal of palaeoproteomics is to recover, identify, and study these proteins long after their natural lifespan has ended, often after extensive taphonomic alteration over centuries, millennia, or, in some cases, millions of years [202]. Proteins are particularly valuable as bioarchives in this context [1387, 1388] because they occur in all tissues, are typically present in many more copies per cell than the genome, and, relative to nucleic acids, tend to persist in a wider range of depositional contexts and over longer timescales [202, 1389]. Further, their amino-acid sequences can preserve variation informative at several biological levels: taxonomically diagnostic peptides can support species identification [1390–1392], genetically variant peptides can reveal underlying non-synonymous variation useful for human identification [1393–1395], and sex-specific peptides (notably X- and Y-chromosome-derived amelogenin preserved in dental enamel) can support biological sex estimation [1396, 1397].

Protein preservation is, however, intrinsically more complex than the preservation of DNA or other ancient biomolecules (Section 1.2.3) [91, 1387], precisely because of their diversity in terms of composition (possessing 20 amino-acid building blocks

*vs.* four nitrogenous bases in nucleic acids), modification state, biochemical properties (e.g., hydrophobicity, isoelectric behaviour), folded structure, size, function, and complexation with other biomolecules and inorganics [202]. Moreover, the progression from intact proteome to palaeoproteome is governed by an array of interacting variables beyond the nature of proteins themselves [343, 344], including the composition and structure of the surrounding matrix [219, 1398–1404], the physicochemical properties of the wider burial environment (e.g., water availability, pH, redox conditions, and sediment chemistry) [38, 519, 1405–1407], and local thermal conditions such as temperature and humidity [1408–1412]. These variables jointly influence the rates and modes of diagenetic reactions (such as hydrolysis, oxidation, deamidation, racemisation, and isomerisation), and they do so differently not only for different proteins, but for different regions within the same protein [90, 342, 1413]. As such, protein degradation after death has been called the 'black box' of taphonomy [202]: the effects of individual taphonomic processes cannot be resolved at the level of whole proteins, but require analysis at the level of constituent peptide sequences and their modification states [1414].

The consequences of this heterogeneity become apparent during the biostratinomic interval, when endogenous and microbial proteases progressively hydrolyse intact proteins through sequential endopeptidase- and exopeptidase-mediated cleavage, generating progressively smaller peptide fragments and free amino acids [77, 1415, 1416]; they continue to manifest after burial, when non-enzymatic hydrolysis and diagenetic PTMs further alter peptide sequence and structure [217]. Structural accessibility and residue chemistry together govern which parts of proteins are most vulnerable to decay [342]: peptide bonds in flexible, solvent-exposed regions are generally more accessible to hydrolytic and enzymatic attack than those in buried or structurally constrained regions [1417–1420], while individual residues differ in reactivity according to side-chain chemistry and local sequence context [179, 1421]. Residue-specific modifications likewise vary in response to physicochemical conditions: oxidation of Met and Trp, for example, requires ROS and is therefore

promoted under oxidising conditions [1422, 1423]; deamidation of Asn and Gln proceeds through hydrolytic mechanisms whose rates increase with temperature, water availability, and alkaline pH, and also vary with neighbouring residues [1424–1427]. As a result, patterns of peptide persistence and modification reflect the interaction between residue chemistry, protein structure, and environmental conditions, and can be related to the chemical processes responsible for their transformation [1428, 1429]. Deamidation of Asn and Gln is employed in this context as an indicator of protein degradation and relative antiquity [1091, 1092, 1094, 1096–1099, 1430], although its dependence on sequence context and environmental conditions, together with potential artefactual deamidation during sample preparation [1431], makes it most defensible as a contextual marker rather than a chronological measure [1432].

Recovery and analysis impose additional filters on the palaeoproteome. Protein extraction solubilises only those peptides that remain chemically accessible within the burial matrix [202]; highly crosslinked, mineral-bound, aggregated, or otherwise insoluble fractions may not enter the workflow [1414, 1433, 1434]. Enzymatic digestion (Section 1.6.2) introduces a further sequence-dependent constraint: the proteases used in the analytical workflow generate peptides according to residue-specific cleavage preferences, such that the peptides available for analysis are partly determined by the distribution of surviving residues [1435–1437]. Liquid chromatography (LC) and electron ionisation [EI] (Section 1.6.3) then favour peptides within particular ranges of hydrophobicity, mass, and charge state, while MS/MS detects most readily those peptides that ionise and fragment efficiently under the selected acquisition conditions [1438–1440]. Database searching (Section 1.6.4) narrows the dataset further by identifying only those spectra that can be matched to sequences represented in the reference database, and to modifications permitted in the search parameters [1440, 1441]. The reported palaeoproteome thus reflects both taphonomic history and analytical filtering: it is the subset of surviving peptides that is simultaneously preserved, extractable, digestible, detectable, and identifiable [202]. Interpretation must therefore distinguish between patterns arising from taphonomic processes, and those imposed by analytical selection.

Despite these considerable challenges, palaeoproteomics has developed rapidly over the past decade into a powerful tool for investigating both biological and cultural aspects of the past [1388]. The first large-scale palaeoproteome – comprising 126 proteins from a 43 ka mammoth bone, published in 2012 [1442] – marked a transition from the analysis of individual proteins to the characterisation of complex proteomes, demonstrating that peptide-level data could be used to reconstruct biological information preserved for millennia. Subsequent studies have expanded both the range of substrates and the scope of inference, establishing that palaeoproteomes can directly inform the study of life and death in the past [1388]. At the species level, ancient proteins have been used to resolve phylogenetic relationships in cases where DNA is absent or degraded, placing extinct taxa within the tree of life and extending the molecular evolutionary record far beyond the limits of ancient genomics [218, 1443–1454]. At the individual level, palaeoproteomes preserve evidence of physiology [1455–1462], ageing [1463–1465], and disease [1466–1476], since tissue-specific protein expression, abundance, and modification patterns [1477, 1478] reflect both normal biological processes and pathological responses, including metabolic stress [1479, 1480], immune activity [1481, 1482], and host–microbiome interactions [1483, 1484]. The palaeoproteome may also record how death unfolded and how the body was altered thereafter [345, 665, 1485–1487], since the pattern of protein survival – that is, which molecules persist, in which tissues, and in what modified forms – is shaped by the biochemical events of decomposition and the conditions of burial [202]. Together, these applications demonstrate that palaeoproteomes encode information spanning the full arc of an organism's life history to its taphonomic fate, and that this information can be recovered when interpreted within a rigorous analytical and taphonomic framework [1488].

### 1.6.2 Sample preparation

Proteomic analyses can be broadly divided into 'top-down' and 'bottom-up' approaches [but see 1489]. Top-down proteomics analyses intact proteins, preserving information on proteoforms, including covalent modification states and, in specialised

implementations (e.g., native top-down proteomics [1490]), aspects of higher-order structure and protein–protein interactions [1491]. Bottom-up proteomics, by contrast, analyses peptides generated by proteolytic cleavage [1492]. In palaeoproteomics, the latter is effectively predetermined: diagenetic reactions *post-mortem* fragment proteins prior to analysis, such that the surviving molecular entities are predominantly peptides rather than intact proteins. Extraction, digestion, and clean-up of the palaeoproteome are therefore constrained and informed by the chemical state of the material, and must accommodate the extent of fragmentation and modification imposed by its taphonomic history.

Ancient protein sample preparation is designed to maximise recovery of endogenous peptides from material that has already been altered by backbone fragmentation (e.g., hydrolysis, proteolysis), side-chain modification (e.g., oxidation, deamidation), and differential loss of sequence regions governed by residue chemistry, protein architecture, and structural accessibility, while minimising the introduction and propagation of exogenous protein contamination [202]. Contamination is a central concern in palaeoproteomics because proteins are ubiquitous, readily transferred, and their comparatively low sequence variability relative to DNA limits the ability to discriminate endogenous from exogenous sources [1488], particularly when contaminant proteins derive from phylogenetically related organisms [1468, 1493–1495]. As a result, contaminant proteins may be incorrectly assigned as endogenous, leading to erroneous interpretations of proteome composition, modification patterns, and downstream biological inference. Alternatively, modern contaminants – being typically abundant, intact proteins that generate high-intensity mass spectral signals – might mask fragmented, low-abundance, ancient peptides [202, 1488]; similarly, non-protein contaminants (e.g., polymers, salts, metal ions) can interfere with chromatographic separation or suppress ionisation, reducing detectability and hampering identification of the endogenous fraction [1496–1498]. Exogenous protein contamination may be introduced at multiple stages prior to and during analysis, and mitigation therefore requires control at each stage of the workflow (Box 1.11).

**Box 1.11 | *Best practices in palaeoproteomics***

Palaeoproteomic analyses require explicit consideration of both contamination and data authenticity at every stage of the workflow, from sample selection through to interpretation [202]. While the field remains methodologically heterogeneous, with substantial variation in reporting standards and laboratory practices, Hendy *et al.* [1488] emphasise the need for transparent, reproducible protocols that allow independent evaluation of results. Rather than prescribing rigid criteria, they advocate a framework in which multiple, complementary lines of evidence are used to support protein identification and authentication, recognising that no single indicator is sufficient in isolation.

Sample selection is a critical first step [1488]. The choice of material should be guided by an informed assessment of its biomolecular preservation potential, taking into account both the intrinsic properties of the substrate and its depositional context and taphonomic history [1488]. Mineralised tissues such as bone, enamel, and dental calculus are often preferred because their inorganic matrices can protect biomolecules from degradation [1404, 1499], although preservation remains highly variable even within similar contexts [507, 1095, 1097, 1398]. Where possible, non-invasive screening or small-scale pilot studies should be undertaken prior to more extensive destructive sampling to evaluate protein preservation and avoid unnecessary damage to valuable specimens [1500–1503]. Sampling itself should be minimised and carefully controlled [1504–1507]: archaeological and palaeontological specimens are often unique and irreplaceable, and destructive analysis should therefore be limited to the smallest quantity necessary to achieve analytical objectives [1508]. Researchers must also be aware of post-excavation treatments, as conservation materials such as glues, consolidants, and resins can introduce exogenous proteins or interfere with mass spectrometric analysis [1509, 1510]. Such treatments are widespread in museum collections and may not always be documented, particularly for older material [1511].

Contamination is a pervasive issue and can be introduced at multiple stages [1488]. Modern proteins may be introduced to an archaeological sample from handling during excavation and curation [1512], where proteins from skin, hair, and clothing (especially keratins) are readily transferred [1513]. Burial and storage environments may also contribute microbial proteins [1514, 1515]. Conservation treatments represent an additional source of exogenous material, often introducing proteins derived from animal collagen or plant resins [1516, 1517]. Within the laboratory, contamination can arise from reagents (e.g., bovine serum albumin, proteases), consumables (e.g., latex gloves, plastic films), airborne particulates, and carry-over between analytical runs [1497, 1518, 1519]. Cross-contamination between samples is also a risk, particularly when reagents, equipment, or workspaces are shared [1488].

Mitigating these risks requires strict laboratory practices [1488]. Sample preparation should be conducted in dedicated clean laboratory environments using sterilised equipment and high-purity reagents, with physical separation of ancient and modern protein workflows wherever possible [1488]. Personnel-derived contamination can be reduced by wearing appropriate protective clothing, including lab coats, gloves, and face coverings [1520], and by avoiding materials derived from animal fibres such as wool or leather [1488]. Exposed skin should be minimised, and handling procedures should be designed to reduce direct contact with samples [1488]. Laboratory surfaces and equipment should be regularly decontaminated using chemical agents such as bleach or 70% v/v ethanol [1521], or by ultraviolet irradiation [1522, 1523], and single-use consumables should be employed wherever feasible to prevent carry-over [1524]. Fresh reagents should be prepared for each batch of extractions, and care should be taken to avoid aerosol formation or sample mixing during handling [1488]. Blank extractions should be processed alongside samples to monitor background contamination, and injection blanks should be run during mass spectrometric analysis to detect carry-over within the instrument [1525]. Replicate analyses – either repeated extractions or multiple mass spectrometric runs – are recommended to assess reproducibility and to identify spurious signals [1526].

The palaeoproteome is further shaped by the chemistry of extraction, digestion, and clean-up, which together recover only those peptides that are chemically accessible and sufficiently soluble under the chosen conditions [202]. For mineralised tissues, extraction commonly begins with a demineralisation step, which removes

the inorganic phase restricting solvent access to proteins occluded within, or tightly associated with, the mineral matrix [1434]. Ethylenediaminetetraacetic acid (EDTA)-based protocols are widely used for osteological tissues because they chelate $Ca^{2+}$ ions and effect dissolution of the hydroxyapatite mineral phase under relatively mild conditions, thereby releasing proteinaceous material while limiting additional chemical modification [1527–1529]. Stronger acid-based protocols (e.g., hydrochloric acid [HCl]) may be employed for more degraded or mineral-bound substrates where rapid dissolution or recovery of acid-insoluble fractions is required [1434, 1530]; however, these conditions are more aggressive and can promote additional hydrolysis and side-chain modification, such that the choice between EDTA-based chelation and strong acid-based dissolution reflects a trade-off between maximising yield and preserving endogenous chemical information [1531, 1532].

In contrast to mineralised tissues, non-mineralised tissues are relatively under-explored in palaeoproteomics. Studies to-date have focused largely on keratinised [1533, 1534] and collagenous tissues [1469, 1504, 1534–1536], and method optimisation for internal soft tissues is lacking. In modern proteomics, solubilisation of non-mineral-bound proteins relies on chaotropic agents (e.g., urea, guanidine hydrochloride [GuHCl]) and detergents (e.g., sodium dodecyl sulfate [SDS]), which disrupt hydrogen bonding, hydrophobic interactions, and protein aggregation [1537]; however, in archaeological contexts, their effectiveness is expected to depend on the nature and extent of diagenetic alteration [1414].

Once proteins or peptides (whether once mineral-bound or not) are in solution, samples are typically subjected to reduction and alkylation to cleave disulfide bonds and prevent their reforming, reducing disulfide-mediated structural constraints that may hinder proteolytic access, and thereby improving peptide recovery [1538]. Where enzymatic digestion is required, it is most commonly performed using trypsin, which cleaves peptide bonds on the C-terminal side of Lys and Arg residues [1539] (generally with the exception of circumstances where either is followed by Pro [1540]), producing peptides with defined termini and charge states that are well suited to MS (typically, though not exclusively, in the range of $\sim$ 7–25 amino acids, depending on

sequence context and missed cleavages) [1541]. In highly degraded or particularly ancient samples, however, the digestion step may be shortened (i.e., by reducing the enzyme concentration or incubation time) [1434, 1542] or omitted entirely [1543, 1544], as endogenous peptides generated by diagenetic hydrolysis may already fall within the detectable mass range. Under such conditions, additional digestion risks generating fragments that are too short for confident protein assignment.

The digested peptide mixture is subsequently desalted and concentrated, most commonly by reversed-phase solid-phase extraction (C18) [1545–1548], although alternative methods such as bead-based capture (e.g., single-pot solid-phase-enhanced sample preparation [SP3]) are also widely used [1549, 1550]. This clean-up step removes salts, detergents, chaotropes, and other components that interfere with chromatographic separation and ionisation [1551], but introduces further selectivity: peptides that are highly hydrophilic (and therefore weakly retained on the hydrophobic stationary phase) [1552, 1553], or very short (typically $< 5$–6 amino acids, depending on composition and charge state) [1554], may not be efficiently retained and can be lost during elution. The final analyte therefore represents the intersection of multiple constraints: peptides that have survived taphonomic transformation, remained chemically accessible during extraction, been retained through digestion and clean-up, and fall within the physicochemical space detectable by MS [202]. Interpretation of palaeoproteomic data must therefore account for this cumulative filtering when relating observed peptide populations to underlying biological and taphonomic processes [202].

### 1.6.3 Mass spectrometric analysis

Liquid chromatography–tandem mass spectrometry (LC–MS/MS) is the principal analytical method used in palaeoproteomics to identify peptide sequences from complex biological mixtures [202]. Its goal is to convert a heterogeneous population of peptides into mass spectra – in which the $x$-axis represents mass-to-charge ratio ($m/z$) and the $y$-axis ion intensity (relative abundance) – from which peptide sequence information and protein identity can be inferred [1555]. This is achieved

through a series of coupled processes: chromatographic separation, ionisation, mass analysis of intact ions (MS1), isolation and fragmentation of selected precursor ions, and mass analysis of the resulting fragment ions (MS2) [1555, 1556]. The key distinction is that MS1 provides $m/z$ and intensity measurements of intact peptide ions (precursors), whereas MS2 fragments selected precursors to generate sequence-informative spectra used for peptide identification and downstream protein inference [1557, 1558]. The instrument itself comprises three core components [1559]: an ion source (which generates gas-phase ions), a mass analyser (which separates ions by $m/z$), and a detector (which records ion abundance) [1560]. Together, these stages transform a complex peptide mixture into a set of spectra encoding peptide identity.

Separation is first achieved by LC, most commonly reversed-phase LC [1561]. Here, a high-pressure pump drives the sample through a column packed with a hydrophobic (non-polar) stationary phase (typically C18-bonded silica) [1562] using a mobile (polar) phase composed of water and an organic solvent (usually acetonitrile or methanol) [1563]. The composition of this mobile phase is varied over time as a gradient, increasing the proportion of organic solvent [1564]. Peptides partition between the mobile and stationary phases according to their hydrophobicity: hydrophilic peptides remain preferentially solvated in the aqueous mobile phase and elute early, whereas more hydrophobic peptides interact more strongly with the stationary phase and require higher organic solvent concentrations to be displaced [1565]. The purpose of this step is to separate peptides in time, so that fewer species enter the mass spectrometer simultaneously: minimising co-elution reduces competition for charge during ionisation (*aka.* ion suppression), improves signal-to-noise ratios, and increases the likelihood that low-abundance ions will be sampled for MS/MS analysis when only a limited number of precursors can be fragmented in a given acquisition cycle [1561].

Following chromatographic separation, peptides must be converted from solvated molecules in liquid into gas-phase ions, so that they can be manipulated and detected by the mass analyser, which operates under high vacuum [1560]. This is achieved using an ion source, most commonly electrospray ionisation (ESI) [1566].

In ESI, the LC effluent passes through a charged capillary held at high voltage, generating a spray of charged droplets [1566, 1567]. As the solvent evaporates, charge density within the droplets increases until electrostatic repulsion exceeds surface tension, leading to Coulombic fission into progressively smaller droplets; continued evaporation ultimately yields gas-phase peptide ions [1566, 1567]. ESI typically produces multiply protonated ions ($[M + zH]^{z+}$), which lowers their $m/z$ and enables large peptides to be detected within the operating range of the mass analyser [1568, 1569]. ESI is considered a 'soft' ionisation technique because it transfers peptides into the gas phase without extensive fragmentation, preserving the intact precursor ions required for subsequent MS/MS analysis [1570]. In contrast, 'hard' ionisation methods (e.g., EI) deposit sufficient energy during ionisation to induce extensive fragmentation and are therefore suited to small, volatile molecules rather than intact peptides; for this reason, they are generally not used in proteomics [1571, 1572]. Although negative-ion mode may be employed in specific contexts (e.g., for analysis of highly acidic peptides [1573]), positive-ion mode is most commonly used due to the relative scarcity of efficiently ionising acidic residues in average peptides, coupled with the instability of negative sprays under common source conditions [1574, but see 1575].

Once ionised, peptides enter the mass analyser, where the first stage of measurement (MS1) occurs. A mass analyser separates ions based on their $m/z$ using electric and/or magnetic fields [1576]; common types include quadrupoles (which transmit ions within a defined $m/z$ window), time-of-flight (TOF) analysers (which separate ions based on flight time), ion traps (which confine ions within and sequentially eject them from oscillating fields), and Orbitrap™ (Thermo Fisher Scientific) or Fourier-transform ion cyclotron resonance (FT–ICR) instruments (which trap ions and measure their oscillation or cyclotron frequencies, respectively, with high mass accuracy and resolution) [1559, 1560, 1577]. The MS1 spectrum records the $m/z$, isotopic distribution, and relative abundance of ions at a given retention time during chromatographic separation, thereby defining the pool of precursor ions available for MS/MS analysis [1578].

At this stage, different acquisition strategies may be employed. In data-dependent acquisition (DDA), the instrument selects the most intense precursors from the MS1 scan for fragmentation in real time, resulting in stochastic sampling biased toward higher-abundance species [1579]. In data-independent acquisition (DIA), by contrast, the instrument systematically fragments all ions within pre-defined $m/z$ windows, generating multiplexed MS2 spectra in which fragments from many co-eluting peptides share each scan; thus, DIA data requires computational deconvolution and specialised scoring tools [1579, 1580]. DDA is widely used in palaeoproteomics because it produces cleaner, more easily interpretable spectra for individual peptides [202]. DIA, however, has been little explored as a strategy for ancient proteins [but see 1391], despite offering improved reproducibility and quantitative coverage at the cost of increased analytical complexity [1581].

Given different amino-acid sequences, isobaric residues (such as Leu and Ile), and many combinations of PTMs can yield the same or very similar $m/z$, precursor mass alone is insufficient to uniquely identify peptides [1582]; thus selected precursors are isolated and fragmented, producing a product-ion spectrum that encodes sequence information and permits peptide identification. Fragmentation is most commonly achieved by collision-based methods such as collision-induced dissociation (CID) or higher-energy collisional dissociation (HCD), in which ions are accelerated by electric fields and collide with an inert gas (e.g., nitrogen), converting kinetic energy into internal energy [1583]. According to the mobile proton model, this energy redistributes protons within the peptide ion, promoting cleavage of the peptide bond linking the $\alpha$-carboxyl group of one amino-acid residue to the $\alpha$-amino group of the next (C–N), thereby generating characteristic $b$- and $y$-type fragment ions (the former retaining the N-terminus, and the latter the C-terminus) [1584]. However, labile PTMs – particularly phosphorylation – can introduce competing, energetically favourable fragmentation pathways: phosphopeptides commonly undergo preferential cleavage of the phosphoester bond, resulting in characteristic 'neutral loss' ions through elimination of phosphoric acid or related species [1585, 1586]. An alternative fragmentation method, electron transfer

dissociation (ETD), proceeds *via* electron transfer to multiply charged cations, promoting cleavage of the bond between the amide nitrogen of one residue and the $\alpha$-carbon of the next (N$-$C$\alpha$), producing mainly *c*- and *z*-type fragment ions (the former retaining the N-terminus, and the latter the C-terminus) while preserving labile modifications [1584]. CID and HCD remain dominant in palaeoproteomics because they are compatible with a wide range of instrument platforms, produce abundant and predictable fragment ions, and are well supported by existing database-search algorithms [1587, 1588]; ETD, while valuable for preserving labile modifications, is less effective for low-charge or short peptides [1589], and is thus ill-suited to ancient, highly degraded material.

The resulting fragment ions are then measured in the second stage of analysis (MS2), producing a tandem mass spectrum whose pattern of fragment masses encodes peptide sequence information. Because the mass differences between adjacent fragment ions correspond to individual amino-acid residues, series of *b*-, *y*-, *c*-, or *z*-type ions form partial or complete sequence ladders from which peptide identity can be inferred [1590]. The LC–MS/MS pipeline described therefore yields not a fully characterised proteome, but a body of spectral evidence – each spectrum an indirect, probabilistic fingerprint of a peptide – whose identity and biological meaning must be decoded computationally [1591].

### 1.6.4 Sequence identification

The bioinformatic stage of palaeoproteomics converts tandem mass spectra into peptide identifications and, subsequently, protein-level inferences [1488]. The experimental output of LC–MS/MS is a set of MS2 spectra, each consisting of peaks defined by $m/z$ values and intensities, which represent indirect measurements of peptide fragmentation behaviour: the central task at this stage is therefore to assign each spectrum to a peptide sequence, quantify the confidence of that assignment, and then integrate peptide-level evidence into protein-level interpretations [1592]. The appropriate computational strategy depends in part on the data acquisition strategy [1593]: DDA generates MS2 spectra derived predominantly from individually isolated

precursor ions, making the data well suited to database searching and *de novo* sequencing [1594, 1595], whereas DIA generates multiplexed MS2 spectra across predefined *m/z* windows and therefore typically requires spectral library searching, spectrum reconstruction, and library-free DIA workflows [1581, 1596].

In database searching, experimental spectra are compared against *in silico* predicted fragmentation spectra derived from peptide sequences in a reference database [1597]. Candidate peptides are generated under user-defined constraints, including protease specificity, number of missed cleavages allowed, precursor and fragment mass tolerances, and permitted fixed or variable modifications; theoretical fragment patterns are then matched against observed spectra and scored [1594, 1598, 1599]. The logic behind this approach also underpins many library-free DIA workflows, in which predicted fragment-ion patterns are used to query multiplexed MS2 spectra directly without reliance on an empirical spectral library, typically through targeted extraction of fragment-ion traces or scoring against predicted spectral intensities [1596].

In spectral library searching, experimental spectra are matched directly against reference spectra that have been previously acquired and curated from known peptide sequences, typically in prior DDA experiments [but see 1600], and stored together with their associated peptide annotations and fragmentation patterns [1596, 1597]. Since both query and reference spectra are empirical, this approach can improve sensitivity and scoring accuracy, particularly for DIA data in which fragmentation patterns are reproducible across runs [1601]; the method is therefore central to many DIA workflows, but its performance depends on the completeness, taxonomic relevance, and acquisition context of the library [1602, 1603]. In palaeoproteomics, this remains a constraint; although one that should lessen as curated libraries expand.

In *de novo* sequencing, no reference spectra are required; rather, peptide sequences are inferred directly from the fragment-ion series by reconstructing residue masses from observed *m/z* differences [1590, 1597]. This approach is especially valuable when reference databases are incomplete, as is often the case for extinct taxa, poorly represented lineages, peptides bearing unexpected sequence

variation, or heavily diagenetically modified sequences [202, 1440]. Despite recent advances afforded by deep learning-based methods [1604–1606], *de novo* sequencing remains computationally demanding: it requires combinatorial exploration of possible residue sequences consistent with the observed fragment-ion ladder, and, being more sensitive to incomplete or noisy spectra [1607, 1608], is generally less robust than database search [1609, 1610]. Nonetheless, it is increasingly useful as a complementary strategy, particularly where database coverage is poor or where sequence variants are of specific interest [1611]. In DIA, *de novo* methods are more challenging because MS2 spectra are multiplexed [1612], but they can contribute within spectrum-reconstruction workflows [1613], in which DIA spectra are computationally deconvolved into pseudo-DDA spectra representing individual precursors [e.g., 1614]; or within hybrid approaches [1613] that combine *de novo* inference with database or library searching [e.g., 1615].

Regardless of the strategy used, spectrum interpretation proceeds by scoring candidate peptide-spectrum matches (PSMs). Each PSM is assigned a score reflecting the degree of agreement between observed and predicted fragmentation patterns, typically incorporating the number and intensity of matched fragment ions, mass accuracy of precursor and fragments [1616], and, increasingly, expected fragmentation intensity patterns [1617–1619]. Different search engines implement distinct scoring schemes – such as binomial [1620], probabilistic [1621], multivariate hypergeometric [1622], cross-correlation [1623], or machine-learning [1624] types – meaning that scores are not directly comparable between platforms. The identification process is therefore fundamentally statistical: each spectrum is compared against a large set of candidate peptide sequences derived from the search space, and the best-scoring matches are retained as PSMs [1616].

Confidence in PSMs is typically controlled using a target–decoy strategy to estimate the false discovery rate (FDR). In this framework, spectra are searched against a combined database containing both true ('target') sequences and artificial ('decoy') sequences (typically reversed or shuffled versions of target proteins) [1625]. Since decoy matches represent false positives by construction, the proportion of

decoy hits among accepted identifications provides an empirical estimate of the expected false discovery proportion [1625]. FDR is therefore best understood as the expected proportion of false positives among the accepted identifications, rather than as a probability assigned to any individual match [1626]. In practice, typically a 1% FDR threshold is applied which means that, on average, approximately 1% of accepted identifications are expected to be incorrect. This estimate, however, may depend on score calibration, database size, and search-space definition [1627–1629]; consequently, FDR control is sensitive to implementation and can be mis-estimated if not carefully applied [1630, 1631]. FDR thresholds are usually enforced at the PSM level and then propagated to peptide- and protein-level identifications [1632], although these levels are not directly equivalent.

Related but distinct confidence metrics include the posterior error probability (PEP) and the $q$-value. The PEP represents the probability that a given PSM is incorrect, conditional on its score and the estimated score distributions of correct and incorrect matches [1633]. The $q$-value, by contrast, is the minimum FDR threshold at which a given PSM would be accepted, and thus provides a rank-based measure of confidence across the dataset [1634]. Although FDR, PEP, and $q$-value are derived from score distributions, they operate at different levels of inference – population-level expectation, individual match, and ranked list, respectively – and are therefore not interchangeable [1635].

Protein inference is a separate and non-trivial step. Once peptides have been identified with a quantified measure of confidence, they must be mapped back to proteins; however, many peptides are degenerate, meaning they are shared among multiple proteins in the form of homologues, paralogues, or isoforms [1636]. As a result, identifications are often reported as 'protein groups' rather than individual proteins, defined as the minimal set of proteins that can explain the observed peptides [1637, 1638]. Unique peptides exist in only one protein of a proteome, and thus provide direct evidence for that specific protein, whereas shared peptides support only the group [1639]. 'One-hit' identifications – that is, those supported by a single unique peptide – are generally considered weak [1488] because a single PSM

provides limited statistical support, and is more susceptible to random matches or ambiguous assignment within a large search space; however, they may be retained if supported by additional evidence, such as consistent detection across replicates, appropriate modification patterns, manual *de novo* verification, or concordance with expected proteomic composition [1640, 1641].

Finally, the treatment of post-translational and diagenetic modifications is handled differently depending on the search strategy. In peptide identification workflows that search an explicit candidate-sequence space, algorithms distinguish between fixed modifications, which are assumed in the search model to be present on relevant residues with high consistency (e.g., carbamidomethylation of Cys introduced during alkylation), and variable modifications, which may or may not be present (e.g., oxidation, deamidation) [1642]. Variable modifications are essential for detecting diagenetic alteration, but each additional modification expands the candidate peptide space combinatorially [1642], thereby increasing computational cost and, critically, the likelihood of random matches between spectra and incorrect candidate sequences [1643]. For this reason, search strategies typically restrict variable modifications to improve the protein identification rate, unless there is strong *a priori* evidence for the modification to be common in the sample [1642, 1643]. However, diagenesis can produce both well characterised modifications (e.g., deamidation of Asn and Gln, oxidation of Met) and poorly characterised or heterogeneous mass shifts that may not be captured by predefined search parameters [1440, 1644, 1645]. Open [e.g., 1646–1649] or 'dependent peptide' [1650] search strategies address this by identifying systematic mass differences relative to confidently assigned peptides, although their interpretation remains challenging. In *de novo* sequencing, modifications are inferred from deviations between observed fragment-ion mass differences and canonical amino-acid masses [1606], but uncharacterised or overlapping mass shifts can make such assignments ambiguous, and may still require downstream interpretation or targeted re-searching [1651].

## 1.7 Research Aims & Thesis Overview

The foregoing sections situate the paradox of archaeological brain preservation (Section 1.1) within a molecular taphonomic framework. Decomposition at the molecular level comprises a set of competing, environment-sensitive reactions, and the analytical toolkit of palaeoproteomics provides a means of resolving their molecular products in ancient tissues. In the CNS, those reactions act on a substrate whose nature is chemically heterogeneous: the brain combines architectural diversity and a lipid-rich composition with regionally variable redox-active metal pools, and an inventory of modified and long-lived proteins that together generate distinct microenvironments with different susceptibilities to *post-mortem* change – a composition that, as the subsequent chapters demonstrate, primes it for a taphonomic trajectory unavailable to other organs. Understanding that trajectory requires integration of three complementary lines of evidence: the archaeological distribution of preserved brains, the molecular characterisation of the ancient proteins preserved therein, and the experimental determination of the processes that generate those palaeoproteomic profiles. The thesis is therefore organised as a progression from archaeological observation, to analytical framework, to experimentally resolved mechanism.

Chapter II addresses the first of these questions by asking whether archaeological brain preservation is genuinely rare, and what its large-scale distribution implies about the conditions under which it occurs. To do so, it compiles and analyses a global archive of more than 4,400 preserved human brains spanning the Holocene, drawing on more than 200 sources to document their frequency, geographic distribution, depositional settings, co-occurrence with other tissues, and preservational diversity. It then analyses this archive for large-scale temporal, geographic, and palaeoclimatic correlations, demonstrating that preserved brains are widespread and recurrent, and that a substantial proportion belong to an 'unknown' preservation type characterised by the persistence of nervous tissue in the absence of other soft tissues, most commonly in waterlogged, oxygen-poor environments. This finding establishes that brain preservation follows a distinct,

as-yet uncharacterised taphonomic trajectory, and identifies the need to determine the molecular mechanisms underpinning that trajectory as the central focus of the remainder of the thesis.

Chapter III addresses how that trajectory can be interrogated at the molecular level in archaeological soft tissue. In the absence of established palaeoproteomic workflows for non-mineralised internal organs, this chapter develops and evaluates an analytical and bioinformatic framework for deep palaeoproteomic recovery from preserved human brain tissue. Using archaeological human brain as the test substrate, it systematically compares extraction chemistries, clean-up strategies, and mass spectrometric acquisition modes, and assesses downstream identification workflows. The results show that urea-based solubilisation combined with high-resolution LC–MS/MS enables recovery of the largest and most compositionally diverse palaeoproteome yet reported from any archaeological material, with improved representation of hydrophobic, membrane-associated, and low-abundance intracellular proteins. This chapter therefore renders ancient brain tissue analytically tractable as a high-dimensional molecular dataset, and establishes the methodological basis required to observe, rather than infer, the products of *post-mortem* transformation.

Chapter IV then asks what molecular processes underpin the novel taphonomic trajectory identified in Chapter II, using (in part) the analytical framework established in Chapter III. This question is addressed experimentally by decaying whole mouse carcasses for six months under four burial regimes that vary in water and oxygen availability, and tracking time-resolved changes in the brain proteome using parallel DDA and DIA LC–MS/MS workflows. At the protein level, the chapter tests whether proteome composition diverges systematically between burial environments and through the PMI; at the peptide level, it models more than 1.26 million decay profiles to quantify persistence and loss, and relates those trajectories to sequence composition, structural context, domain architecture, and post-translational and diagenetic modification. The results demonstrate reproducible divergence in molecular fate between burial regimes, with waterlogged, hypoxic conditions favouring the selective persistence of peptides derived from structurally

ordered, redox-active, and membrane-associated regions. Modification patterns further indicate that these conditions promote radical-mediated oxidation followed by local termination and crosslinking, rather than chain-propagating fragmentation. This chapter therefore resolves the mechanistic component of the thesis, showing that selective brain preservation arises when environmental constraint and intrinsic tissue chemistry together channel *post-mortem* molecular change toward stabilisation rather than loss.

The final chapter (Chapter V) integrates these strands to develop a revised model of soft-tissue preservation. It argues that preserved brains are neither anomalous rarities nor lone survivors of arrested decomposition, but the outcome of selective molecular transformation governed by the interaction between tissue composition and burial environment. More broadly, it demonstrates that preservation is not the opposite of decay, but one of its chemically permissible outcomes under defined physicochemical constraints. In doing so, the thesis uses preservation of the CNS as a model system through which to reconsider the relationship between decomposition, molecular transformation, and long-term soft-tissue survival.

## 1.8 References


[1] J A Efremov. 'Taphonomy: new branch of palaeontology'. In: *Pan-American Geologist* 74 (2 1940), pp. 81–93.

[2] Gerhard C Cadée. 'The history of taphonomy'. In: *The processes of fossilization* 1 (1991). Ed. by Stephen Donovan, pp. 3–21.

[3] Ronald E Martin. 'Introduction: the science of taphonomy'. In: *Taphonomy*. Cambridge: Cambridge University Press, 28th Oct. 1999, pp. 1–26. DOI: 10.1017/cbo9780511612381.002.

[4] Anna K Behrensmeyer and Susan M Kidwell. 'Taphonomy's contributions to paleobiology'. In: *Paleobiology* 11 (1 1985), pp. 105–119. DOI: 10.1017/s009483730001143x.

[5] Derek E G Briggs. 'Molecular taphonomy of animal and plant cuticles: selective preservation and diagenesis'. In: *Philos. Trans. R. Soc. Lond. B Biol. Sci.* 354 (1379 29th Jan. 1999), pp. 7–17. DOI: 10.1098/rstb.1999.0356.

[6] Derek E G Briggs, Richard P Evershed and Matthew J Lockheart. 'The biomolecular paleontology of continental fossils'. In: *Paleobiology* 26 (S4 Jan. 2000), pp. 169–193. DOI: 10.1666/0094-8373(2000)26[169:tbpocf]2.0.co;2.

[7] Luis L Cabo, Dennis C Dirkmaat and Andrea M Zurek-ost. *Taphonomy and Biological Anthropology*. Ed. by Clark Spencer Larson. Wiley, 8th Mar. 2023, pp. 346–364. DOI: 10.1002/9781119828075.ch21.

[8] Andrea Baucon. 'Leonardo Da Vinci, the founding father of ichnology'. In: *Palaios* 25 (6 1st June 2010), pp. 361–367. DOI: 10.2110/palo.2009.p09-049r.

[9] Gordon Turner-Walker and Miranda Jans. 'Reconstructing taphonomic histories using histological analysis'. In: *Palaeogeogr. Palaeoclimatol. Palaeoecol.* 266 (3-4 Sept. 2008), pp. 227–235. DOI: 10.1016/j.palaeo.2008.03.024.

[10] A H Muller. 'Fossilization (Taphonomy)'. In: *Treatise on Invertebrate palontology, Pt. A, Introduction* (Dec. 1979). Ed. by Richard A Robison and Curt Teichert, A2–A78.

[11] R Lyman. 'What taphonomy is, what it isn't, and why taphonomists should care about the difference'. In: *Journal of taphonomy* 8 (2010), pp. 1–16.

[12] Carlton E Brett and Gordon C Baird. 'Comparative taphonomy; a key to paleoenvironmental interpretation based on fossil preservation'. In: *Palaios* 1 (3 1st June 1986), pp. 207–227. DOI: 10.2307/3514686.

[13] Ronald E Martin. 'Biostratinomy I: necrolysis, transport, and abrasion'. In: *Taphonomy*. Cambridge: Cambridge University Press, 28th Oct. 1999, pp. 27–109. DOI: 10.1017/cbo9780511612381.003.

[14] Ronald E Martin. 'Biostratinomy II: dissolution and early diagenesis'. In: *Taphonomy*. Cambridge: Cambridge University Press, 28th Oct. 1999, pp. 110–160. DOI: 10.1017/cbo9780511612381.004.

[15] Christopher R Noto. 'Hierarchical control of terrestrial vertebrate taphonomy over space and time: Discussion of mechanisms and implications for vertebrate paleobiology'. In: *Topics in Geobiology*. Dordrecht: Springer Netherlands, 2010, pp. 287–336. DOI: 10.1007/978-90-481-8643-3_8.

[16] Carlton E Brett and James R Thomka. 'Fossils and fossilisation'. In: *eLS* (2013). DOI: 10.1002/9780470015902.a0001621.pub2accidents.

[17] Charles P Egeland and Travis Rayne Pickering. 'Cruel traces: Bone surface modifications and their relevance to forensic science'. In: *WIRES Forensic Sci.* 3 (3 May 2021). DOI: 10.1002/wfs2.1400.

[18] James T Pokines and Christine Spiegel. 'Subaerial weathering and other terrestrial surface taphonomic processes'. In: *Manual of Forensic Taphonomy*. Boca Raton: CRC Press, 2nd Nov. 2021, pp. 403–442. DOI: 10.4324/9781003171492-11.

[19] Dominika Nociarová et al. 'Joint disassociation pattern from a taphonomical and anthropological point of view'. In: *Hist. Biol.* 37 (8 3rd Aug. 2025), pp. 1961–1967. DOI: 10.1080/08912963.2023.2230579.

[20] Carlton E Brett. 'Sequence stratigraphy, biostratigraphy, and taphonomy in shallow marine environments'. In: *Palaios* 10 (6 1st Dec. 1995), pp. 597–616. DOI: 10.2307/3515097.

[21] Ronald E Martin. 'Bioturbation'. In: *Taphonomy*. Cambridge: Cambridge University Press, 28th Oct. 1999, pp. 161–185. DOI: 10.1017/cbo9780511612381.005.

[22] Douglas H Ubelaker and Cassandra M DeGaglia. 'The impact of scavenging: perspective from casework in forensic anthropology'. In: *Forensic Sci. Res.* 5 (1 9th Feb. 2020), pp. 32–37. DOI: 10.1080/20961790.2019.1704473.

[23] Lara Indra et al. 'Uncovering forensic taphonomic agents: Animal scavenging in the European context'. In: *Biology (Basel)* 11 (4 15th Apr. 2022), p. 601. DOI: 10.3390/biology11040601.

[24] Shari L Forbes and David O Carter. 'Processes and mechanisms of death and decomposition of vertebrate carrion in terrestrial systems'. In: *Carrion Ecology, Evolution, and Their Applications*. 2nd Edition. Boca Raton: CRC Press, 4th June 2025, pp. 131–147. DOI: 10.1201/9781003610885-9.

[25] Heather R Jordan and Jeffery K Tomberlin. 'Abiotic and biotic factors regulating inter-kingdom engagement between insects and microbe activity on vertebrate remains'. In: *Insects* 8 (2 24th May 2017), E54. DOI: 10.3390/insects8020054.

[26] Allison R Mason, Lois S Taylor and Jennifer M DeBruyn. 'Microbial ecology of vertebrate decomposition in terrestrial ecosystems'. In: *FEMS Microbiol. Ecol.* 99 (2 24th Jan. 2023), fiad006. DOI: 10.1093/femsec/fiad006.

[27] B B Dent, S L Forbes and B H Stuart. 'Review of human decomposition processes in soil'. In: *Environ. Geol.* 45 (4 1st Feb. 2004), pp. 576–585. DOI: 10.1007/s00254-003-0913-z.

[28] Kara S Adams et al. 'Drying the mystery: a novel electronic sensor to quantify soft-tissue desiccation and natural mummification for forensic taphonomy'. In: *Sci. Rep.* 14 (1 7th Aug. 2024), p. 18294. DOI: 10.1038/s41598-024-69446-9.

[29] Christine Bailey et al. 'Assessing patterns of moisture content in decomposing, desiccated, and mummified tissue in western North Carolina'. In: *Forensic Sciences* 5 (4 1st Dec. 2025), p. 73. DOI: 10.3390/forensicsci5040073.

[30] James T Pokines et al. 'The effects of repeated wet-dry cycles as a component of bone weathering'. In: *J. Archaeol. Sci. Rep.* 17 (Feb. 2018), pp. 433–441. DOI: 10.1016/j.jasrep.2017.11.025.

[31] Sarah Stokes, Nicholas Márquez-Grant and Charlene Greenwood. 'Establishing a minimum PMI for bone sun bleaching in a UK environment with a controlled desert-simulated comparison'. In: *Int. J. Legal Med.* 134 (6 Nov. 2020), pp. 2297–2306. DOI: 10.1007/s00414-020-02385-y.

[32] W E D Evans. *The chemistry of death*. Springfield, Ill.: Thomas, 1963. xv, 101 p.

[33] Rhys Williams et al. 'Bone diagenesis and extremes of preservation in forensic science'. In: *Humans* 5 (1 24th Jan. 2025), p. 2. DOI: 10.3390/humans5010002.

[34] J D Schiffbauer et al. 'Thermally-induced structural and chemical alteration of organic-walled microfossils: an experimental approach to understanding fossil preservation in metasediments: Experimental thermal alteration of microfossils'. In: *Geobiology* 10 (5 1st Sept. 2012), pp. 402–423. DOI: 10.1111/j.1472-4669.2012.00332.x.

[35] David O Carter, David Yellowlees and Mark Tibbett. 'Moisture can be the dominant environmental parameter governing cadaver decomposition in soil'. In: *Forensic Sci. Int.* 200 (1-3 15th July 2010), pp. 60–66. DOI: 10.1016/j.forsciint.2010.03.031.

[36] Thomas Clements, Mark A Purnell and Sarah Gabbott. 'Experimental analysis of organ decay and pH gradients within a carcass and the implications for phosphatization of soft tissues'. In: *Palaeontology* 65 (4 July 2022). DOI: 10.1111/pala.12617.

[37] Nora Corthésy, Jonathan B Antcliffe and Farid Saleh. 'Taxon-specific redox conditions control fossilisation pathways'. In: *Nat. Commun.* 16 (1 29th Apr. 2025), p. 3993. DOI: 10.1038/s41467-025-59372-3.

[38] Elena Naimark et al. 'Decaying in different clays: implications for soft-tissue preservation'. In: *Palaeontology* 59 (4 July 2016), pp. 583–595. DOI: 10.1111/pala.12246.

[39] J L Bada, X S Wang and H Hamilton. 'Preservation of key biomolecules in the fossil record: current knowledge and future challenges'. In: *Philos. Trans. R. Soc. Lond. B Biol. Sci.* 354 (1379 29th Jan. 1999), 77–86, discussion 86–7. DOI: 10.1098/rstb.1999.0361.

[40] Colleen A Sullivan and Sarah W Keenan. 'Experimental dissolution of fossil bone under variable pH conditions'. In: *PLoS One* 17 (10 13th Oct. 2022), e0274084. DOI: 10.1371/journal.pone.0274084.

[41] E B Naimark et al. 'Complementary transformations of buried organic residues and the ambient sediment: Results of long-term taphonomic experiments'. In: *Paleontol. J.* 52 (2 5th Mar. 2018), pp. 109–122. DOI: 10.1134/s0031030118020053.

[42] Clive N Trueman. 'Chemical taphonomy of biomineralized tissues'. In: *Palaeontology* 56 (3 May 2013), pp. 475–486. DOI: 10.1111/pala.12041.

[43] Silvina Slagter et al. 'Controls on authigenic mineralization in experimental Ediacara-style preservation'. In: *Geobiology* 22 (4 1st July 2024), e12615. DOI: 10.1111/gbi.12615.

[44] Luke A Parry et al. 'Soft-bodied fossils are not simply rotten carcasses – toward a holistic understanding of exceptional fossil preservation: Exceptional fossil preservation is complex and involves the interplay of numerous biological and geological processes'. In: *Bioessays* 40 (1 1st Jan. 2018), p. 1700167. DOI: 10.1002/bies.201700167.

[45] Anna K Behrensmeyer, Susan M Kidwell and Robert A Gastaldo. 'Taphonomy and paleobiology'. In: *Paleobiology* 26 (S4 2000), pp. 103–147. DOI: 10.1017/s0094837300026907.

[46] Neal S Gupta and Derek E G Briggs. 'Taphonomy of animal organic skeletons through time'. In: *Topics in Geobiology*. Dordrecht: Springer Netherlands, 2010, pp. 199–221. DOI: 10.1007/978-90-481-8643-3_5.

[47] Derek E G Briggs. 'Experimental taphonomy'. In: *Palaios* 10 (6 1st Dec. 1995), pp. 539–550. DOI: 10.2307/3515093.

[48] Derek E G Briggs and Sean McMahon. 'The role of experiments in investigating the taphonomy of exceptional preservation'. In: *Palaeontology* 59 (1 Jan. 2016), pp. 1–11. DOI: 10.1111/pala.12219.

[49] Robert S Sansom. 'Experimental decay of soft tissues'. In: *Paleontol. Soc. Pap.* 20 (Oct. 2014), pp. 259–274. DOI: 10.1017/s1089332600002886.

[50] Evan T Saitta, Thomas G Kaye and Jakob Vinther. 'Sediment-encased maturation: a novel method for simulating diagenesis in organic fossil preservation'. In: *Palaeontology* 62 (1 Jan. 2019), pp. 135–150. DOI: 10.1111/pala.12386.

[51] B A Stankiewicz et al. 'Alternative origin of aliphatic polymer in kerogen'. In: *Geology* 28 (6 1st June 2000), p. 559. DOI: 10.1130/0091-7613(2000)28<559:aooapi>2.0.co;2.

[52] Neal S Gupta et al. 'The organic preservation of fossil arthropods: an experimental study'. In: *Proc. Biol. Sci.* 273 (1602 7th Nov. 2006), pp. 2777–2783. DOI: 10.1098/rspb.2006.3646.

[53] Neal S Gupta et al. 'Experimental evidence for the formation of geomacromolecules from plant leaf lipids'. In: *Org. Geochem.* 38 (1 Jan. 2007), pp. 28–36. DOI: 10.1016/j.orggeochem.2006.09.014.

[54] Neal S Gupta et al. 'Rapid incorporation of lipids into macromolecules during experimental decay of invertebrates: Initiation of geopolymer formation'. In: *Org. Geochem.* 40 (5 May 2009), pp. 589–594. DOI: 10.1016/j.orggeochem.2009.02.005.

[55] M M Rhead, G Eglinton and G H Draffan. 'Hydrocarbons produced by the thermal alteration of cholesterol under conditions simulating the maturation of sediments'. In: *Chem. Geol.* 8 (4 Dec. 1971), pp. 277–297. DOI: 10.1016/0009-2541(71)90022-2.

[56] H Mißbach et al. 'Testing the preservation of biomarkers during experimental maturation of an immature kerogen'. In: *Int. J. Astrobiology* 15 (3 July 2016), pp. 165–175. DOI: 10.1017/s1473550416000069.

[57] Evan T Saitta et al. 'Low fossilization potential of keratin protein revealed by experimental taphonomy'. In: *Palaeontology* 60 (4 July 2017), pp. 547–556. DOI: 10.1111/pala.12299.

[58] Arindam Roy et al. 'Sediment-encased pressure–temperature maturation experiments elucidate the impact of diagenesis on melanin-based fossil color and its paleobiological implications'. In: *Paleobiology* 49 (4 Nov. 2023), pp. 712–732. DOI: 10.1017/pab.2023.11.

[59] Jan-Peter Duda et al. 'Molecular fossils within bitumens and kerogens from the 1 Ga Lakhanda Lagerstätte (Siberia, Russia) and their significance for understanding early eukaryote evolution'. In: *Palaontol. Z.* 95 (4 Dec. 2021), pp. 577–592. DOI: 10.1007/s12542-021-00593-4.

[60] Kelly L Miles, Devin A Finaughty and Victoria E Gibbon. 'A review of experimental design in forensic taphonomy: moving towards forensic realism'. In: *Forensic Sci. Res.* 5 (4 13th Aug. 2020), pp. 249–259. DOI: 10.1080/20961790.2020.1792631.

[61] Mark A Purnell et al. 'Experimental analysis of soft-tissue fossilization: opening the black box'. In: *Palaeontology* 61 (3 May 2018), pp. 317–323. DOI: 10.1111/pala.12360.

[62] Adiël A Klompmaker, Roger W Portell and Michael G Frick. 'Comparative experimental taphonomy of eight marine arthropods indicates distinct differences in preservation potential'. In: *Palaeontology* 60 (6 Nov. 2017), pp. 773–794. DOI: 10.1111/pala.12314.

[63] Neil J Gostling, Xiping Dong and Philip C J Donoghue. 'Ontogeny and taphonomy: An experimental taphonomy study of the development of the brine shrimp *Artemia Salina*'. In: *Palaeontology* 52 (1 1st Jan. 2009), pp. 169–186. DOI: 10.1111/j.1475-4983.2008.00834.x.

[64] Robert S Sansom, Sarah E Gabbott and Mark A Purnell. 'Non-random decay of chordate characters causes bias in fossil interpretation'. In: *Nature* 463 (7282 11th Feb. 2010), pp. 797–800. DOI: 10.1038/nature08745.

[65] M S Micozzi. 'Experimental study of postmortem change under field conditions: effects of freezing, thawing, and mechanical injury'. In: *J. Forensic Sci.* 31 (3 July 1986), pp. 953–961. DOI: 10.1520/jfs11103j.

[66] David O Carter, D Yellowlees and Mark Tibbett. 'Temperature affects microbial decomposition of cadavers (Rattus rattus) in contrasting soils'. In: *Appl. Soil Ecol.* 40 (1 Sept. 2008), pp. 129–137. DOI: 10.1016/j.apsoil.2008.03.010.

[67] T Evans. 'Fluvial taphonomy'. In: *Manual of forensic taphonomy* (2021). DOI: 10.4324/9781003171492-06/fluvial-taphonomy-thomas-evans.

[68] Jonathan B Antcliffe et al. 'Rapid oxygen drawdown in decay experiments on marine ( *Palaemon varians* ) and freshwater ( *Neocaridina davidi* ) shrimps'. In: *R. Soc. Open Sci.* 13 (3 25th Mar. 2026), p. 251712. DOI: 10.1098/rsos.251712.

[69] Angi M Christensen and Sarah W Myers. 'Macroscopic observations of the effects of varying fresh water pH on bone: Effects of ph on bone'. In: *J. Forensic Sci.* 56 (2 1st Mar. 2011), pp. 475–479. DOI: 10.1111/j.1556-4029.2010.01646.x.

[70] Fabian Gäb et al. 'Experimental taphonomy of fish - role of elevated pressure, salinity and pH'. In: *Sci. Rep.* 10 (1 12th May 2020), p. 7839. DOI: 10.1038/s41598-020-64651-8.

[71] Lucy A Wilson and Nicholas J Butterfield. 'Sediment effects on the preservation of Burgess Shale–type compression fossils'. In: *Palaios* 29 (4 1st Apr. 2014), pp. 145–154. DOI: 10.2110/palo.2013.075.

[72] R W Mann, W M Bass and L Meadows. 'Time since death and decomposition of the human body: variables and observations in case and experimental field studies'. In: *J. Forensic Sci.* 35 (1 1st Jan. 1990), pp. 103–111. DOI: 10.1520/jfs12806j.

[73] Kathrin Janssen et al. 'The complex role of microbial metabolic activity in fossilization'. In: *Biol. Rev. Camb. Philos. Soc.* 97 (2 Apr. 2022), pp. 449–465. DOI: 10.1111/brv.12806.

[74] Robert S Sansom, Sarah E Gabbott and Mark A Purnell. 'Atlas of vertebrate decay: a visual and taphonomic guide to fossil interpretation'. In: *Palaeontology* 56 (3 May 2013), pp. 457–474. DOI: 10.1111/pala.12037.

[75] Yann Delannoy et al. 'Effects of the environment on bone mass: A human taphonomic study'. In: *Leg. Med. (Tokyo)* 20 (May 2016), pp. 61–67. DOI: 10.1016/j.legalmed.2016.04.006.

[76] Iris Sluis, Wilma Duijst and Tristan Krap. 'Bone histology for forensic anthropology: a technical review on the advances in microstructural analysis of taphonomically altered buried or subaerially exposed bone'. In: *Int. J. Legal Med.* 139 (6 10th Nov. 2025), pp. 2921–2938. DOI: 10.1007/s00414-025-03536-9.

[77] Noemi Procopio et al. 'Bone diagenesis in short timescales: Insights from an exploratory proteomic analysis'. In: *Biology (Basel)* 10 (6 23rd May 2021), p. 460. DOI: 10.3390/biology10060460.

[78] D A Finaughty et al. 'Next generation forensic taphonomy: Automation for experimental, field-based research'. In: *Forensic Sci. Int.* 345 (111616 1st Apr. 2023), p. 111616. DOI: 10.1016/j.forsciint.2023.111616.

[79] Laura A Benninger, David O Carter and Shari L Forbes. 'The biochemical alteration of soil beneath a decomposing carcass'. In: *Forensic Sci. Int.* 180 (2-3 18th Sept. 2008), pp. 70–75. DOI: 10.1016/j.forsciint.2008.07.001.

[80] Maria-Martina Quaggiotto et al. 'Dynamic soil nutrient and moisture changes under decomposing vertebrate carcasses'. In: *Biogeochemistry* 146 (1 16th Nov. 2019), pp. 71–82. DOI: 10.1007/s10533-019-00611-3.

[81] Emily N Junkins, Mark Speck and David O Carter. 'The microbiology, pH, and oxidation reduction potential of larval masses in decomposing carcasses on Oahu, Hawaii'. In: *J. Forensic Leg. Med.* 67 (1st Oct. 2019), pp. 37–48. DOI: 10.1016/j.jflm.2019.08.001.

[82] Maria E Mcnamara et al. 'Soft-tissue preservation in Miocene frogs from Libros, Spain: Insights into the genesis of decay microenvironments'. In: *Palaios* 24 (2 1st Feb. 2009), pp. 104–117. DOI: 10.2110/palo.2008.p08-017r.

[83] Robert S Sansom, Sarah E Gabbott and Mark A Purnell. 'Decay of vertebrate characters in hagfish and lamprey (Cyclostomata) and the implications for the vertebrate fossil record'. In: *Proc. Biol. Sci.* 278 (1709 22nd Apr. 2011), pp. 1150–1157. DOI: 10.1098/rspb.2010.1641.

[84] Duncan Je Murdock et al. 'Decay of velvet worms (Onychophora), and bias in the fossil record of lobopodians'. In: *BMC Evol. Biol.* 14 (1 29th Nov. 2014), p. 222. DOI: 10.1186/s12862-014-0222-z.

[85] Jason R Moore and David J Varricchio. 'Taphonomic pathways in vertebrate fossil assemblages illustrated by a bovine mass drowning event'. In: *Palaios* 33 (4 24th Apr. 2018), pp. 174–184. DOI: 10.2110/palo.2017.073.

[86] Derek E G Briggs and Roger E Summons. 'Ancient biomolecules: their origins, fossilization, and role in revealing the history of life: Prospects & Overviews'. In: *Bioessays* 36 (5 May 2014), pp. 482–490. DOI: 10.1002/bies.201400010.

[87] Kavita Matange et al. 'Biological polymers: Evolution, function, and significance'. In: *Acc. Chem. Res.* 58 (5 4th Mar. 2025), pp. 659–672. DOI: 10.1021/acs.accounts.4c00546.

[88] Morten E Allentoft et al. 'The half-life of DNA in bone: measuring decay kinetics in 158 dated fossils'. In: *Proc. Biol. Sci.* 279 (1748 7th Dec. 2012), pp. 4724–4733. DOI: 10.1098/rspb.2012.1745.

[89] Logan Kistler et al. 'A new model for ancient DNA decay based on paleogenomic meta-analysis'. In: *Nucleic Acids Res.* 45 (11 20th June 2017), pp. 6310–6320. DOI: 10.1093/nar/gkx361.

[90] M Buckley and C Wadsworth. 'Proteome degradation in ancient bone: Diagenesis and phylogenetic potential'. In: *Palaeogeogr. Palaeoclimatol. Palaeoecol.* 416 (C Dec. 2014), pp. 69–79. DOI: 10.1016/j.palaeo.2014.06.026.

[91] Caroline Wadsworth et al. 'Comparing ancient DNA survival and proteome content in 69 archaeological cattle tooth and bone samples from multiple European sites'. In: *J. Proteomics* 158 (C 31st Mar. 2017), pp. 1–8. DOI: 10.1016/j.jprot.2017.01.004.

[92] Raman Umamaheswaran and Suryendu Dutta. 'Preservation of proteins in the geosphere'. In: *Nat. Ecol. Evol.* 8 (5 May 2024), pp. 858–865. DOI: 10.1038/s41559-024-02366-z.

[93] Roger E Summons, Paula V Welander and David A Gold. 'Lipid biomarkers: molecular tools for illuminating the history of microbial life'. In: *Nat. Rev. Microbiol.* 20 (3 Mar. 2022), pp. 174–185. DOI: 10.1038/s41579-021-00636-2.

[94] Mike Pollard et al. 'Building lipid barriers: biosynthesis of cutin and suberin'. In: *Trends Plant Sci.* 13 (5 1st May 2008), pp. 236–246. DOI: 10.1016/j.tplants.2008.03.003.

[95] Guilhem Reyt et al. 'Two chemically distinct root lignin barriers control solute and water balance'. In: *Nat. Commun.* 12 (1 19th Apr. 2021), p. 2320. DOI: 10.1038/s41467-021-22550-0.

[96] Anzhou Xin and Klaus Herburger. 'Precursor biosynthesis regulation of lignin, suberin and cutin'. In: *Protoplasma* 258 (6 12th Nov. 2021), pp. 1171–1178. DOI: 10.1007/s00709-021-01676-4.

[97] Yuki Tobimatsu and Mathias Schuetz. 'Lignin polymerization: how do plants manage the chemistry so well?' In: *Curr. Opin. Biotechnol.* 56 (1st Apr. 2019), pp. 75–81. DOI: 10.1016/j.copbio.2018.10.001.

[98] Glenn Philippe et al. 'Cutin and suberin: assembly and origins of specialized lipidic cell wall scaffolds'. In: *Curr. Opin. Plant Biol.* 55 (1st June 2020), pp. 11–20. DOI: 10.1016/j.pbi.2020.01.008.

[99] Fred Beisson, Yonghua Li-Beisson and Mike Pollard. 'Solving the puzzles of cutin and suberin polymer biosynthesis'. In: *Curr. Opin. Plant Biol.* 15 (3 1st June 2012), pp. 329–337. DOI: 10.1016/j.pbi.2012.03.003.

[100] Eric A Fich, Nicholas A Segerson and Jocelyn K C Rose. 'The plant polyester cutin: Biosynthesis, structure, and biological roles'. In: *Annu. Rev. Plant Biol.* 67 (1 29th Apr. 2016), pp. 207–233. DOI: 10.1146/annurev-arplant-043015-111929.

[101] Elizabeth M Carrington et al. 'Biochemical changes across a carbon saturation gradient: Lignin, cutin, and suberin decomposition and stabilization in fractionated carbon pools'. In: *Soil Biol. Biochem.* 47 (1st Apr. 2012), pp. 179–190. DOI: 10.1016/j.soilbio.2011.12.024.

[102] Gerrit Angst et al. 'The fate of cutin and suberin of decaying leaves, needles and roots – Inferences from the initial decomposition of bound fatty acids'. In: *Org. Geochem.* 95 (1st May 2016), pp. 81–92. DOI: 10.1016/j.orggeochem.2016.02.006.

[103] B Artur Stankiewicz, Derek E G Briggs and Richard P Evershed. 'Chemical composition of Paleozoic and Mesozoic fossil invertebrate cuticles as revealed by pyrolysis−gas chromatography/mass spectrometry'. In: *Energy Fuels* 11 (3 1st May 1997), pp. 515–521. DOI: 10.1021/ef9601778.

[104] B A Stankiewicz et al. 'Molecular taphonomy of arthropod and plant cuticles from the Carboniferous of North America: implications for the origin of kerogen'. In: *J. Geol. Soc. London* 155 (3 May 1998), pp. 453–462. DOI: 10.1144/gsjgs.155.3.0453.

[105] Etienne Grienenberger and Teagen D Quilichini. 'The toughest material in the plant kingdom: An update on sporopollenin'. In: *Front. Plant Sci.* 12 (3rd Sept. 2021), p. 703864. DOI: 10.3389/fpls.2021.703864.

[106] Phillip E Jardine et al. 'Sporopollenin chemistry and its durability in the geological record: an integration of extant and fossil chemical data across the seed plants'. In: *Palaeontology* 64 (2 Mar. 2021), pp. 285–305. DOI: 10.1111/pala.12523.

[107] W T Fraser et al. 'Evolutionary stasis of sporopollenin biochemistry revealed by unaltered Pennsylvanian spores'. In: *New Phytol.* 196 (2 1st Oct. 2012), pp. 397–401. DOI: 10.1111/j.1469-8137.2012.04301.x.

[108] Lenize F Maia et al. 'The diversity of linear conjugated polyenes and colours in nature: Raman spectroscopy as a diagnostic tool'. In: *Chemphyschem* 22 (3 3rd Feb. 2021), pp. 231–249. DOI: 10.1002/cphc.202000818.

[109] Michael A van der Horst and Klaas J Hellingwerf. 'Photoreceptor proteins, "star actors of modern times": a review of the functional dynamics in the structure of representative members of six different photoreceptor families'. In: *Acc. Chem. Res.* 37 (1 Jan. 2004), pp. 13–20. DOI: 10.1021/ar020219d.

[110] Nikolay E Polyakov et al. 'The endless world of carotenoids-structural, chemical and biological aspects of some rare carotenoids'. In: *Int. J. Mol. Sci.* 24 (12 8th June 2023), p. 9885. DOI: 10.3390/ijms24129885.

[111] Vasilis Nikolaou et al. 'Porphyrins—valuable pigments of life'. In: *Front. Chem. Biol.* 2 (1346465 10th Jan. 2024), p. 1346465. DOI: 10.3389/fchbi.2023.1346465.

[112] Wen Song et al. 'Melanin: insights into structure, analysis, and biological activities for future development'. In: *J. Mater. Chem. B Mater. Biol. Med.* 11 (32 6th Sept. 2023), pp. 7528–7543. DOI: 10.1039/d3tb01132a.

[113] Daniel B Thomas et al. 'Seeking carotenoid pigments in amber-preserved fossil feathers'. In: *Sci. Rep.* 4 (1 9th June 2014), p. 5226. DOI: 10.1038/srep05226.

[114] Maria E McNamara et al. 'Reconstructing carotenoid-based and structural coloration in fossil skin'. In: *Curr. Biol.* 26 (8 25th Apr. 2016), pp. 1075–1082. DOI: 10.1016/j.cub.2016.02.038.

[115] N Gueneli et al. '1.1-billion-year-old porphyrins establish a marine ecosystem dominated by bacterial primary producers'. In: *Proc. Natl. Acad. Sci. U. S. A.* 115 (30 24th July 2018), E6978–E6986. DOI: 10.1073/pnas.1803866115.

[116] Mariam Tahoun et al. 'Chemistry of porphyrins in fossil plants and animals'. In: *RSC Adv.* 11 (13 10th Feb. 2021), pp. 7552–7563. DOI: 10.1039/d0ra10688g.

[117] K A Motovilov and A B Mostert. 'Melanin: Nature's 4th bioorganic polymer'. In: *Soft Matter* 20 (29 24th July 2024), pp. 5635–5651. DOI: 10.1039/d4sm00491d.

[118] Johan Lindgren et al. 'Interpreting melanin-based coloration through deep time: a critical review'. In: *Proc. Biol. Sci.* 282 (1813 22nd Aug. 2015), p. 20150614. DOI: 10.1098/rspb.2015.0614.

[119] Tiffany S Slater et al. 'Taphonomic experiments reveal authentic molecular signals for fossil melanins and verify preservation of phaeomelanin in fossils'. In: *Nat. Commun.* 14 (1 6th Oct. 2023), p. 5651. DOI: 10.1038/s41467-023-40570-w.

[120] Johan Lindgren et al. 'Molecular preservation of the pigment melanin in fossil melanosomes'. In: *Nat. Commun.* 3 (1 8th May 2012), p. 824. DOI: 10.1038/ncomms1819.

[121] Caitlin Colleary et al. 'Chemical, experimental, and morphological evidence for diagenetically altered melanin in exceptionally preserved fossils'. In: *Proc. Natl. Acad. Sci. U. S. A.* 112 (41 13th Oct. 2015), pp. 12592–12597. DOI: 10.1073/pnas.1509831112.

[122] Christopher S Rogers et al. 'Synchrotron X-ray absorption spectroscopy of melanosomes in vertebrates and cephalopods: implications for the affinity of Tullimonstrum'. In: *Proc. Biol. Sci.* 286 (1913 23rd Oct. 2019), p. 20191649. DOI: 10.1098/rspb.2019.1649.

[123] Keely Glass et al. 'Direct chemical evidence for eumelanin pigment from the Jurassic period'. In: *Proc. Natl. Acad. Sci. U. S. A.* 109 (26 26th June 2012), pp. 10218–10223. DOI: 10.1073/pnas.1118448109.

[124] Keely Glass et al. 'Impact of diagenesis and maturation on the survival of eumelanin in the fossil record'. In: *Org. Geochem.* 64 (C Nov. 2013), pp. 29–37. DOI: 10.1016/j.orggeochem.2013.09.002.

[125] Johan Lindgren et al. 'Skin pigmentation provides evidence of convergent melanism in extinct marine reptiles'. In: *Nature* 506 (7489 27th Feb. 2014), pp. 484–488. DOI: 10.1038/nature12899.

[126] Zixiao Yang et al. 'Cellular structure of dinosaur scales reveals retention of reptile-type skin during the evolutionary transition to feathers'. In: *Nat. Commun.* 15 (1 21st May 2024), p. 4063. DOI: 10.1038/s41467-024-48400-3.

[127] Daniel Falk et al. 'Evolutionary constraints on anuran melanin for 45 million years'. In: *iScience* 29 (1 16th Jan. 2026), p. 114220. DOI: 10.1016/j.isci.2025.114220.

[128] Valentina Rossi et al. 'Tissue-specific geometry and chemistry of modern and fossilized melanosomes reveal internal anatomy of extinct vertebrates'. In: *Proc. Natl. Acad. Sci. U. S. A.* 116 (36 3rd Sept. 2019), pp. 17880–17889. DOI: 10.1073/pnas.1820285116.

[129] Paul Meredith and Tadeusz Sarna. 'The physical and chemical properties of eumelanin'. In: *Pigment Cell Res.* 19 (6 1st Dec. 2006), pp. 572–594. DOI: 10.1111/j.1600-0749.2006.00345.x.

[130] Daniel J Van Hoomissen and Shubham Vyas. 'Impact of conjugation and hyperconjugation on the radical stability of allylic and benzylic systems: A theoretical study'. In: *J. Org. Chem.* 82 (11 2nd June 2017), pp. 5731–5742. DOI: 10.1021/acs.joc.7b00549.

[131] Tadeusz Sarna, Harold M Swartz and Andrzej Zadlo. 'Interaction of melanin with metal ions modulates their cytotoxic potential'. In: *Appl. Magn. Reson.* 53 (1 Jan. 2022), pp. 105–121. DOI: 10.1007/s00723-021-01386-3.

[132] Xianlin Han. 'Lipidomics for studying metabolism'. In: *Nat. Rev. Endocrinol.* 12 (11 Nov. 2016), pp. 668–679. DOI: 10.1038/nrendo.2016.98.

[133] Takeshi Harayama and Howard Riezman. 'Understanding the diversity of membrane lipid composition'. In: *Nat. Rev. Mol. Cell Biol.* 19 (5 7th May 2018), pp. 281–296. DOI: 10.1038/nrm.2017.138.

[134] Roger E Summons. 'The exceptional preservation of interesting and informative biomolecules'. In: *Paleontol. Soc. Pap.* 20 (Oct. 2014), pp. 217–236. DOI: 10.1017/s1089332600002862.

[135] Hai Lei et al. 'Ester bond: Chemically labile yet mechanically stable'. In: *ACS Nano* 17 (17 12th Sept. 2023), pp. 16870–16878. DOI: 10.1021/acsnano.3c03807.

[136] Clément Martin and François Verheggen. 'Odour profile of human corpses: A review'. In: *Forensic Chem.* 10 (1st Aug. 2018), pp. 27–36. DOI: 10.1016/j.forc.2018.07.002.

[137] Usman Ali et al. 'The functions of phospholipases and their hydrolysis products in plant growth, development and stress responses'. In: *Prog. Lipid Res.* 86 (101158 5th Apr. 2022), p. 101158. DOI: 10.1016/j.plipres.2022.101158.

[138] Derek A Pratt, Keri A Tallman and Ned A Porter. 'Free radical oxidation of polyunsaturated lipids: New mechanistic insights and the development of peroxyl radical clocks'. In: *Acc. Chem. Res.* 44 (6 21st June 2011), pp. 458–467. DOI: 10.1021/ar200024c.

[139] G Paquette, D B Kupranycz and Frvande Voort. 'The mechanisms of lipid autoxidation. I. Primary oxidation products'. In: *Can. Inst. Food Sci. Technol. J.* 18 (2 May 1985), pp. 112–118. DOI: 10.1016/s0315-5463(85)71767-1.

[140] G Hoppe et al. 'Oxidation products of cholesteryl linoleate are resistant to hydrolysis in macrophages, form complexes with proteins, and are present in human atherosclerotic lesions'. In: *J. Lipid Res.* 38 (7 1st July 1997), pp. 1347–1360. DOI: 10.1016/s0022-2275(20)37418-6.

[141] Martina Korber, Isabella Klein and Günther Daum. 'Steryl ester synthesis, storage and hydrolysis: A contribution to sterol homeostasis'. In: *Biochim. Biophys. Acta Mol. Cell Biol. Lipids* 1862 (12 1st Dec. 2017), pp. 1534–1545. DOI: 10.1016/j.bbalip.2017.09.002.

[142] Heinz Wilkes, René Jarling and Jan Schwarzbauer. 'Hydrocarbons and lipids: An introduction to structure, physicochemical properties, and natural occurrence'. In: *Hydrocarbons, Oils and Lipids: Diversity, Origin, Chemistry and Fate*. Cham: Springer International Publishing, 2020, pp. 1–47. DOI: 10.1007/978-3-319-54529-5_34-1.

[143] Helen L Whelton et al. 'A call for caution in the analysis of lipids and other small biomolecules from archaeological contexts'. In: *J. Archaeol. Sci.* 132 (105397 Aug. 2021), p. 105397. DOI: 10.1016/j.jas.2021.105397.

[144] Jochen J Brocks et al. 'Biomarker evidence for green and purple sulphur bacteria in a stratified Palaeoproterozoic sea'. In: *Nature* 437 (7060 6th Oct. 2005), pp. 866–870. DOI: 10.1038/nature04068.

[145] Ole G Mouritsen and Martin J Zuckermann. 'What's so special about cholesterol?' In: *Lipids* 39 (11 1st Nov. 2004), pp. 1101–1113. DOI: 10.1007/s11745-004-1336-x.

[146] W David Nes. 'Biosynthesis of cholesterol and other sterols'. In: *Chem. Rev.* 111 (10 12th Oct. 2011), pp. 6423–6451. DOI: 10.1021/cr200021m.

[147] A S Mackenzie et al. 'Chemical fossils: the geological fate of steroids'. In: *Science* 217 (4559 6th Aug. 1982), pp. 491–504. DOI: 10.1126/science.217.4559.491.

[148] Kelsey E Doiron et al. 'Discerning diagenetic pathways for discrete sterol precursors'. In: *Org. Geochem.* 201 (104935 Mar. 2025), p. 104935. DOI: 10.1016/j.orggeochem.2025.104935.

[149] T Brunoir et al. 'Common origin of sterol biosynthesis points to a feeding strategy shift in Neoproterozoic animals'. In: *Nat. Commun.* 14 (1 1st Dec. 2023), p. 7941. DOI: 10.1038/s41467-023-43545-z.

[150] Dane P Synnott et al. 'The diagenetic continuum of steroid hydrocarbon transformation from early diagenesis into the oil window'. In: *Geochim. Cosmochim. Acta* 342 (1st Feb. 2023), pp. 137–155. DOI: 10.1016/j.gca.2022.12.013.

[151] Leszek Marynowski et al. 'Occurrence and significance of mono-, di- and anhydrosaccharide biomolecules in Mesozoic and Cenozoic lignites and fossil wood'. In: *Org. Geochem.* 116 (Feb. 2018), pp. 13–22. DOI: 10.1016/j.orggeochem.2017.11.008.

[152] Carolyn R Bertozzi and David Rabuka. 'Structural basis of glycan diversity'. In: (2009).

[153] Nathan T Porter and Eric C Martens. 'The critical roles of polysaccharides in gut microbial ecology and physiology'. In: *Annu. Rev. Microbiol.* 71 (1 8th Sept. 2017), pp. 349–369. DOI: 10.1146/annurev-micro-102215-095316.

[154] Michael Diener et al. 'Primary, secondary, tertiary and Quaternary structure levels in linear polysaccharides: From random coil, to single helix to supramolecular assembly'. In: *Biomacromolecules* 20 (4 8th Apr. 2019), pp. 1731–1739. DOI: 10.1021/acs.biomac.9b00087.

[155] M Kacurakova et al. 'FT-IR study of plant cell wall model compounds: pectic polyasaccharides and hemicelluloses'. In: *Carbohydr. Polym.* 43 (2 1st Oct. 2000), pp. 195–203. DOI: 10.1016/s0144-8617(00)00151-x.

[156] Valdir Soldi. 'Stability and Degradation of Polysaccharides'. In: *Polysaccharides*. CRC Press, 30th Nov. 2004. DOI: 10.1201/9781420030822.ch14.

[157] Amanda G Henry. 'Formation and taphonomic processes affecting starch granules'. In: *Method and Theory in Paleoethnobotany*. University Press of Colorado, 2015, pp. 35–50. DOI: 10.5876/9781607323167.c003.

[158] Feng Liu et al. '280-m.y.-old fossil starch reveals early plant–animal mutualism'. In: *Geology* 46 (5 1st May 2018), pp. 423–426. DOI: 10.1130/g39929.1.

[159] Qiong Wu et al. 'High strength nanostructured films based on well-preserved -chitin nanofibrils'. In: *Nanoscale* 11 (22 6th June 2019), pp. 11001–11011. DOI: 10.1039/c9nr02870f.

[160] Majeti N V Ravi Kumar. 'A review of chitin and chitosan applications'. In: *React. Funct. Polym.* 46 (1 1st Nov. 2000), pp. 1–27. DOI: 10.1016/s1381-5148(00)00038-9.

[161] Daria N Poshina et al. 'Accessibility of chitin and chitosan in enzymatic hydrolysis: A review'. In: *Polym. Degrad. Stab.* 156 (1st Oct. 2018), pp. 269–278. DOI: 10.1016/j.polymdegradstab.2018.09.005.

[162] I C Gunsalus, B L Horecker and W A Wood. 'Pathways of carbohydrate metabolism in microorganisms'. In: *Bacteriol. Rev.* 19 (2 June 1955), pp. 79–128. DOI: 10.1128/br.19.2.79-128.1955.

[163] R M Aseeva, P A Sakharov and A M Sakharov. 'The physicochemical characteristics of oxidized polysaccharides'. In: *Russ. J. Phys. Chem. B* 3 (5 18th Oct. 2009), pp. 844–850. DOI: 10.1134/s1990793109050224.

[164] Corentin C Loron et al. 'Early fungi from the Proterozoic era in Arctic Canada'. In: *Nature* 570 (7760 June 2019), pp. 232–235. DOI: 10.1038/s41586-019-1217-0.

[165] H Ehrlich et al. 'Discovery of 505-million-year old chitin in the basal demosponge Vauxia gracilenta'. In: *Sci. Rep.* 3 (1 13th Dec. 2013), p. 3497. DOI: 10.1038/srep03497.

[166] G D Cody et al. 'Molecular signature of chitin-protein complex in Paleozoic arthropods'. In: *Geology* 39 (3 1st Mar. 2011), pp. 255–258. DOI: 10.1130/g31648.1.

[167] Elizabeth Bailey et al. 'Evidence for surviving chitin in Cambrian trilobites from the Carrara Formation, western north America'. In: *Palaios* 40 (12 1st Dec. 2025), pp. 379–387. DOI: 10.2110/palo.2024.025.

[168] Jianlin Song et al. 'Biodegradation of crystalline chitin: A review of recent advancement, challenges, and future study directions'. In: *J. Ocean Univ. China* 23 (5 10th Oct. 2024), pp. 1319–1328. DOI: 10.1007/s11802-024-5983-4.

[169] Mikhail V Tsurkan et al. 'Progress in chitin analytics'. In: *Carbohydr. Polym.* 252 (117204 15th Jan. 2021), p. 117204. DOI: 10.1016/j.carbpol.2020.117204.

[170] Anran Wei, Jimin Fu and Fenglin Guo. 'Mechanical properties of chitin polymorphs: A computational study'. In: *J. Mater. Sci.* 56 (20 12th July 2021), pp. 12048–12058. DOI: 10.1007/s10853-021-06086-8.

[171] T Suetake et al. 'Chitin-binding proteins in invertebrates and plants comprise a common chitin-binding structural motif'. In: *J. Biol. Chem.* 275 (24 16th June 2000), pp. 17929–17932. DOI: 10.1074/jbc.C000184200.

[172] Hermann Ehrlich. 'Chitin and collagen as universal and alternative templates in biomineralization'. In: *Int. Geol. Rev.* 52 (7-8 6th May 2010), pp. 661–699. DOI: 10.1080/00206811003679521.

[173] Neal S Gupta et al. 'Molecular structure of organic components in cephalopods: Evidence for oxidative cross linking in fossil marine invertebrates'. In: *Org. Geochem.* 39 (10 Oct. 2008), pp. 1405–1414. DOI: 10.1016/j.orggeochem.2008.06.008.

[174] Neal S Gupta and Roger E Summons. 'Fate of chitinous organisms in the geosphere'. In: *Topics in Geobiology*. Dordrecht: Springer Netherlands, 2011, pp. 133–151. DOI: 10.1007/978-90-481-9684-5_7.

[175] Engelbert Buxbaum. *Fundamentals of protein structure and function*. 2nd ed. Cham, Switzerland: Springer International Publishing, 30th Nov. 2015. 521 pp. DOI: 10.1007/978-3-319-19920-7.

[176] Rainer Bischoff and Hartmut Schlüter. 'Amino acids: chemistry, functionality and selected non-enzymatic post-translational modifications'. In: *J. Proteomics* 75 (8 18th Apr. 2012), pp. 2275–2296. DOI: 10.1016/j.jprot.2012.01.041.

[177] Kuladeep Das, Hemalatha Balaram and Kaustuv Sanyal. 'Amino acid chirality: Stereospecific conversion and physiological implications'. In: *ACS Omega* 9 (5 6th Feb. 2024), pp. 5084–5099. DOI: 10.1021/acsomega.3c08305.

[178] J L Reubsaet et al. 'Analytical techniques used to study the degradation of proteins and peptides: chemical instability'. In: *J. Pharm. Biomed. Anal.* 17 (6-7 1st Sept. 1998), pp. 955–978. DOI: 10.1016/s0731-7085(98)00063-6.

[179] Wenying Yan et al. 'The construction of an amino acid network for understanding protein structure and function'. In: *Amino Acids* 46 (6 13th June 2014), pp. 1419–1439. DOI: 10.1007/s00726-014-1710-6.

[180] J P Burnier et al. 'Gamma-carboxyglutamic acid'. In: *Mol. Cell. Biochem.* 39 (1 25th Sept. 1981), pp. 191–207. DOI: 10.1007/bf00232574.

[181] Heleen Meuzelaar, Jocelyne Vreede and Sander Woutersen. 'Influence of Glu/Arg, Asp/Arg, and Glu/Lys salt bridges on  -helical stability and folding kinetics'. In: *Biophys. J.* 110 (11 7th June 2016), pp. 2328–2341. DOI: 10.1016/j.bpj.2016.04.015.

[182] Eva Pluhařová et al. 'Peptide salt bridge stability: from gas phase via microhydration to bulk water simulations'. In: *J. Chem. Phys.* 137 (18 14th Nov. 2012), p. 185101. DOI: 10.1063/1.4765052.

[183] Richard J Sundberg and R Bruce Martin. 'Interactions of histidine and other imidazole derivatives with transition metal ions in chemical and biological systems'. In: *Chem. Rev.* 74 (4 1st Aug. 1974), pp. 471–517. DOI: 10.1021/cr60290a003.

[184] K Uchida. 'Histidine and lysine as targets of oxidative modification'. In: *Amino Acids* 25 (3-4 29th Dec. 2003), pp. 249–257. DOI: 10.1007/s00726-003-0015-y.

[185] M Rosário M Domingues et al. 'Identification of oxidation products and free radicals of tryptophan by mass spectrometry'. In: *J. Am. Soc. Mass Spectrom.* 14 (4 Apr. 2003), pp. 406–416. DOI: 10.1016/S1044-0305(03)00127-2.

[186] U Samanta, D Pal and P Chakrabarti. 'Environment of tryptophan side chains in proteins'. In: *Proteins* 38 (3 15th Feb. 2000), pp. 288–300. DOI: 10.1002/(sici)1097-0134(20000215)38:3<288::aid-prot5>3.0.co;2-7.

[187] Daniel J Mandell et al. 'Strengths of hydrogen bonds involving phosphorylated amino acid side chains'. In: *J. Am. Chem. Soc.* 129 (4 31st Jan. 2007), pp. 820–827. DOI: 10.1021/ja063019w.

[188] B X Yan and Y Q Sun. 'Glycine residues provide flexibility for enzyme active sites'. In: *J. Biol. Chem.* 272 (6 7th Feb. 1997), pp. 3190–3194. DOI: 10.1074/jbc.272.6.3190.

[189] P Y Chou and G D Fasman. 'Structural and functional role of leucine residues in proteins'. In: *J. Mol. Biol.* 74 (3 5th Mar. 1973), pp. 263–281. DOI: 10.1016/0022-2836(73)90372-0.

[190] Kalina Hristova and William C Wimley. 'A look at arginine in membranes'. In: *J. Membr. Biol.* 239 (1-2 Jan. 2011), pp. 49–56. DOI: 10.1007/s00232-010-9323-9.

[191] Marco A Saraiva, Carlos M Borges and M Helena Florêncio. 'Non-enzymatic model glycation reactions–a comprehensive study of the reactivity of a modified arginine with aldehydic and diketonic dicarbonyl compounds by electrospray mass spectrometry'. In: *J. Mass Spectrom.* 41 (6 1st June 2006), pp. 755–770. DOI: 10.1002/jms.1031.

[192] S C Li et al. 'Alpha-helical, but not beta-sheet, propensity of proline is determined by peptide environment'. In: *Proc. Natl. Acad. Sci. U. S. A.* 93 (13 25th June 1996), pp. 6676–6681. DOI: 10.1073/pnas.93.13.6676.

[193] J Jacob, H Duclohier and D S Cafiso. 'The role of proline and glycine in determining the backbone flexibility of a channel-forming peptide'. In: *Biophys. J.* 76 (3 1st Mar. 1999), pp. 1367–1376. DOI: 10.1016/S0006-3495(99)77298-X.

[194] Cyril Boulègue et al. 'Single proline residues can dictate the oxidative folding pathways of cysteine-rich peptides'. In: *J. Mol. Biol.* 358 (3 5th May 2006), pp. 846–856. DOI: 10.1016/j.jmb.2006.02.031.

[195] Bart Ghesquière and Kris Gevaert. 'Proteomics methods to study methionine oxidation: methionine sulfoxide proteomics'. In: *Mass Spectrom. Rev.* 33 (2 1st Mar. 2014), pp. 147–156. DOI: 10.1002/mas.21386.

[196] Jiska van der Reest et al. 'Proteome-wide analysis of cysteine oxidation reveals metabolic sensitivity to redox stress'. In: *Nat. Commun.* 9 (1 20th Apr. 2018), p. 1581. DOI: 10.1038/s41467-018-04003-3.

[197] Christian H Ahrens et al. 'A practical guide to small protein discovery and characterization using mass spectrometry'. In: *J. Bacteriol.* 204 (1 18th Jan. 2022), e0035321. DOI: 10.1128/JB.00353-21.

[198] David Bradley. 'The evolution of post-translational modifications'. In: *Curr. Opin. Genet. Dev.* 76 (101956 Oct. 2022), p. 101956. DOI: 10.1016/j.gde.2022.101956.

[199] Kelly N Chuh and Matthew R Pratt. 'Chemical methods for the proteome-wide identification of posttranslationally modified proteins'. In: *Curr. Opin. Chem. Biol.* 24 (1st Feb. 2015), pp. 27–37. DOI: 10.1016/j.cbpa.2014.10.020.

[200] Anne C Conibear. 'Deciphering protein post-translational modifications using chemical biology tools'. In: *Nat. Rev. Chem.* 4 (12 6th Dec. 2020), pp. 674–695. DOI: 10.1038/s41570-020-00223-8.

[201] Shahin Ramazi and Javad Zahiri. 'Posttranslational modifications in proteins: resources, tools and prediction methods'. In: *Database (Oxford)* 2021 (7th Apr. 2021), baab012. DOI: 10.1093/database/baab012.

[202] Christina Warinner, Kristine Korzow Richter and Matthew J Collins. 'Paleoproteomics'. In: *Chem. Rev.* 122 (16 24th Aug. 2022), pp. 13401–13446. DOI: 10.1021/acs.chemrev.1c00703.

[203] Bin Pan, Margaret S Ricci and Bernhardt L Trout. 'A molecular mechanism of hydrolysis of peptide bonds at neutral pH using a model compound'. In: *J. Phys. Chem. B* 115 (19 19th May 2011), pp. 5958–5970. DOI: 10.1021/jp1076802.

[204] Abhishek Singh et al. 'Site-selective peptide bond hydrolysis and ligation in water by short peptide-based assemblies'. In: *Proc. Natl. Acad. Sci. U. S. A.* 121 (31 30th July 2024), e2321396121. DOI: 10.1073/pnas.2321396121.

[205] V Erckes et al. 'Revealing deamidation and isoaspartate formation during peptide analysis, purification and storage by tandem mass spectrometry'. In: *RSC Med. Chem.* 17 (2 25th Feb. 2026), pp. 1144–1154. DOI: 10.1039/d5md01025j.

[206] Ethan J Walker et al. 'Protein folding stabilities are a major determinant of oxidation rates for buried methionine residues'. In: *J. Biol. Chem.* 298 (5 1st May 2022), p. 101872. DOI: 10.1016/j.jbc.2022.101872.

[207] Evan R Stair and Leslie M Hicks. 'Recent advances in mass spectrometry-based methods to investigate reversible cysteine oxidation'. In: *Curr. Opin. Chem. Biol.* 77 (102389 1st Dec. 2023), p. 102389. DOI: 10.1016/j.cbpa.2023.102389.

[208] Patrick Trouillas, Jacqueline Bergès and Chantal Houée-Lévin. 'Toward understanding the protein oxidation processes: • OH addition on tyrosine, phenylalanine, or methionine?: Protein Oxidation Processes: • OH Addition'. In: *Int. J. Quantum Chem.* 111 (6 1st May 2011), pp. 1143–1151. DOI: 10.1002/qua.22556.

[209] Luke Carroll et al. 'Formation and detection of oxidant-generated tryptophan dimers in peptides and proteins'. In: *Free Radic. Biol. Med.* 113 (1st Dec. 2017), pp. 132–142. DOI: 10.1016/j.freeradbiomed.2017.09.020.

[210] Christian Schöneich. 'Novel chemical degradation pathways of proteins mediated by tryptophan oxidation: tryptophan side chain fragmentation'. In: *J. Pharm. Pharmacol.* 70 (5 1st May 2018), pp. 655–665. DOI: 10.1111/jphp.12688.

[211] Mitsugu Akagawa. 'Protein carbonylation: molecular mechanisms, biological implications, and analytical approaches'. In: *Free Radic. Res.* 55 (4 Apr. 2021), pp. 307–320. DOI: 10.1080/10715762.2020.1851027.

[212] Lyndsey Prosser et al. 'Chemical carbonylation of arginine in peptides and proteins'. In: *J. Am. Chem. Soc.* 147 (12 26th Mar. 2025), pp. 10139–10150. DOI: 10.1021/jacs.4c14476.

[213] T Geiger and S Clarke. 'Deamidation, isomerization, and racemization at asparaginyl and aspartyl residues in peptides. Succinimide-linked reactions that contribute to protein degradation'. In: *J. Biol. Chem.* 262 (2 15th Jan. 1987), pp. 785–794. DOI: 10.1016/s0021-9258(19)75855-4.

[214] Aleksandra Twarda-Clapa et al. 'Advanced glycation end-products (AGEs): Formation, chemistry, classification, receptors, and diseases related to AGEs'. In: *Cells* 11 (8 12th Apr. 2022), p. 1312. DOI: 10.3390/cells11081312.

[215] T E Creighton. 'Disulphide bonds and protein stability'. In: *Bioessays* 8 (2 Feb. 1988), pp. 57–63. DOI: 10.1002/bies.950080204.

[216] W J Wedemeyer et al. 'Disulfide bonds and protein folding'. In: *Biochemistry* 39 (15 18th Apr. 2000), pp. 4207–4216. DOI: 10.1021/bi992922o.

[217] Timothy P Cleland, Elena R Schroeter and Caitlin Colleary. 'Diagenetiforms: A new term to explain protein changes as a result of diagenesis in paleoproteomics'. In: *J. Proteomics* 230 (103992 6th Jan. 2021), p. 103992. DOI: 10.1016/j.jprot.2020.103992.

[218] Ryan S Paterson et al. 'Phylogenetically informative proteins from an Early Miocene rhinocerotid'. In: *Nature* 643 (8072 9th July 2025), pp. 719–724. DOI: 10.1038/s41586-025-09231-4.

[219] Beatrice Demarchi et al. 'Protein sequences bound to mineral surfaces persist into deep time'. In: *Elife* 5 (27th Sept. 2016), e17092. DOI: 10.7554/eLife.17092.

[220] Mary Higby Schweitzer, Elena R Schroeter and Michael B Goshe. 'Protein molecular data from ancient (>1 million years old) fossil material: pitfalls, possibilities and grand challenges'. In: *Anal. Chem.* 86 (14 15th July 2014), pp. 6731–6740. DOI: 10.1021/ac500803w.

[221] Mary Higby Schweitzer et al. 'Paleoproteomics of Mesozoic dinosaurs and other Mesozoic fossils'. In: *Proteomics* 19 (16 Aug. 2019), e1800251. DOI: 10.1002/pmic.201800251.

[222] Pavel A Pevzner, Sangtae Kim and Julio Ng. 'Comment on "Protein sequences from mastodon and Tyrannosaurus rex revealed by mass spectrometry"'. In: *Science* 321 (5892 22nd Aug. 2008), 1040, author reply 1040. DOI: 10.1126/science.1155006.

[223] Mike Buckley et al. 'Comment on "Protein sequences from mastodon and Tyrannosaurus rex revealed by mass spectrometry"'. In: *Science* 319 (5859 4th Jan. 2008), 33, author reply 33. DOI: 10.1126/science.1147046.

[224] Elena R Schroeter, Timothy P Cleland and Mary H Schweitzer. 'Deep time paleoproteomics: Looking forward'. In: *J. Proteome Res.* 21 (1 7th Jan. 2022), pp. 9–19. DOI: 10.1021/acs.jproteome.1c00755.

[225] Steve Minchin and Julia Lodge. 'Understanding biochemistry: structure and function of nucleic acids'. In: *Essays Biochem.* 63 (4 16th Oct. 2019), pp. 433–456. DOI: 10.1042/EBC20180038.

[226] Andrew Travers and Georgi Muskhelishvili. 'DNA structure and function'. In: *FEBS J.* 282 (12 1st June 2015), pp. 2279–2295. DOI: 10.1111/febs.13307.

[227] Francis Yew Fu Tieng et al. 'A Hitchhiker's guide to RNA-RNA structure and interaction prediction tools'. In: *Brief. Bioinform.* 25 (1 22nd Nov. 2023), bbad421. DOI: 10.1093/bib/bbad421.

[228] Satu Mikkola, Tuomas Lönnberg and Harri Lönnberg. 'Phosphodiester models for cleavage of nucleic acids'. In: *Beilstein J. Org. Chem.* 14 (1 10th Apr. 2018), pp. 803–837. DOI: 10.3762/bjoc.14.68.

[229] Heidi Linjalahti and Satu Mikkola. 'Intra- and intermolecular interactions influence the reactivity of RNA oligonucleotides'. In: *Chem. Biodivers.* 4 (12 1st Dec. 2007), pp. 2938–2947. DOI: 10.1002/cbdv.200790243.

[230] Gottfried K Schroeder et al. 'The time required for water attack at the phosphorus atom of simple phosphodiesters and of DNA'. In: *Proc. Natl. Acad. Sci. U. S. A.* 103 (11 14th Mar. 2006), pp. 4052–4055. DOI: 10.1073/pnas.0510879103.

[231] Jesse Dabney, Matthias Meyer and Svante Pääbo. 'Ancient DNA damage'. In: *Cold Spring Harb. Perspect. Biol.* 5 (7 1st July 2013), a012567. DOI: 10.1101/cshperspect.a012567.

[232] Marc M Greenberg. 'Abasic and oxidized abasic site reactivity in DNA: enzyme inhibition, cross-linking, and nucleosome catalyzed reactions'. In: *Acc. Chem. Res.* 47 (2 18th Feb. 2014), pp. 646–655. DOI: 10.1021/ar400229d.

[233] Christopher S Nabel, Sara A Manning and Rahul M Kohli. 'The curious chemical biology of cytosine: deamination, methylation, and oxidation as modulators of genomic potential'. In: *ACS Chem. Biol.* 7 (1 20th Jan. 2012), pp. 20–30. DOI: 10.1021/cb2002895.

[234] S Pääbo. 'Ancient DNA: extraction, characterization, molecular cloning, and enzymatic amplification'. In: *Proc. Natl. Acad. Sci. U. S. A.* 86 (6 Mar. 1989), pp. 1939–1943. DOI: 10.1073/pnas.86.6.1939.

[235] Ulla Kaukinen et al. 'The reactivity of phosphodiester bonds within linear single-stranded oligoribonucleotides is strongly dependent on the base sequence'. In: *Nucleic Acids Res.* 30 (2 15th Jan. 2002), pp. 468–474. DOI: 10.1093/nar/30.2.468.

[236] Ran An et al. 'Non-enzymatic depurination of nucleic acids: factors and mechanisms'. In: *PLoS One* 9 (12 29th Dec. 2014), e115950. DOI: 10.1371/journal.pone.0115950.

[237] M Thomas P Gilbert et al. 'Characterization of genetic miscoding lesions caused by postmortem damage'. In: *Am. J. Hum. Genet.* 72 (1 1st Jan. 2003), pp. 48–61. DOI: 10.1086/345379.

[238] M Thomas P Gilbert et al. 'Recharacterization of ancient DNA miscoding lesions: insights in the era of sequencing-by-synthesis'. In: *Nucleic Acids Res.* 35 (1 2007), pp. 1–10. DOI: 10.1093/nar/gkl483.

[239] D A Kreutzer and J M Essigmann. 'Oxidized, deaminated cytosines are a source of C –> T transitions in vivo'. In: *Proc. Natl. Acad. Sci. U. S. A.* 95 (7 31st Mar. 1998), pp. 3578–3582. DOI: 10.1073/pnas.95.7.3578.

[240] Jonathan Houseley and David Tollervey. 'The many pathways of RNA degradation'. In: *Cell* 136 (4 20th Feb. 2009), pp. 763–776. DOI: 10.1016/j.cell.2009.01.019.

[241] Oliver Smith et al. 'Ancient RNA from Late Pleistocene permafrost and historical canids shows tissue-specific transcriptome survival'. In: *PLoS Biol.* 17 (7 July 2019), e3000166. DOI: 10.1371/journal.pbio.3000166.

[242] Bastian Fromm et al. 'Ancient microRNA profiles of 14,300-yr-old canid samples confirm taxonomic origin and provide glimpses into tissue-specific gene regulation from the Pleistocene'. In: *RNA* 27 (3 16th Feb. 2021), pp. 324–334. DOI: 10.1261/rna.078410.120.

[243] Daniel R Cuesta-Aguirre et al. 'A post-mortem molecular damage profile in the ancient human mitochondrial DNA'. In: *Mol. Ecol. Resour.* 25 (4 May 2025), e14061. DOI: 10.1111/1755-0998.14061.

[244] Paula F Campos et al. 'DNA in ancient bone - where is it located and how should we extract it?' In: *Ann. Anat.* 194 (1 20th Jan. 2012), pp. 7–16. DOI: 10.1016/j.aanat.2011.07.003.

[245] Robert N Grass et al. 'Robust chemical preservation of digital information on DNA in silica with error-correcting codes'. In: *Angew. Chem. Int. Ed Engl.* 54 (8 16th Feb. 2015), pp. 2552–2555. DOI: 10.1002/anie.201411378.

[246] Kurt H Kjær et al. 'A 2-million-year-old ecosystem in Greenland uncovered by environmental DNA'. In: *Nature* 612 (7939 Dec. 2022), pp. 283–291. DOI: 10.1038/s41586-022-05453-y.

[247] Emilio Mármol-Sánchez et al. 'Ancient RNA expression profiles from the extinct woolly mammoth'. In: *Cell* 189 (1 8th Jan. 2026), 52–69.e22. DOI: 10.1016/j.cell.2025.10.025.

[248] Sébastien Calvignac-Spencer and Carles Lalueza-Fox. 'A trunkload of ancient RNA'. In: *Cell* 189 (1 8th Jan. 2026), pp. 1–2. DOI: 10.1016/j.cell.2025.12.004.

[249] R S Morison. 'Death: process or event?' In: *Science* 173 (3998 20th Aug. 1971), pp. 694–698. DOI: 10.1126/science.173.3998.694.

[250] J L Bernat, C M Culver and B Gert. 'On the definition and criterion of death'. In: *Ann. Intern. Med.* 94 (3 Mar. 1981), pp. 389–394. DOI: 10.7326/0003-4819-94-3-389.

[251] Academy of Medical Royal Colleges. *A Code of Practice for the diagnosis and confirmation of death: 2025 update*. Academy of Medical Royal Colleges, 2025. 110 pp.

[252] D Gardiner et al. 'International perspective on the diagnosis of death'. In: *Br. J. Anaesth.* 108 (1 1st Jan. 2012), pp. i14–28. DOI: 10.1093/bja/aer397.

[253] E F Wijdicks. 'The diagnosis of brain death'. In: *N. Engl. J. Med.* 344 (16 19th Apr. 2001), pp. 1215–1221. DOI: 10.1056/NEJM200104193441606.

[254] Pierre Golstein and Guido Kroemer. 'Cell death by necrosis: towards a molecular definition'. In: *Trends Biochem. Sci.* 32 (1 1st Jan. 2007), pp. 37–43. DOI: 10.1016/j.tibs.2006.11.001.

[255] G Kroemer et al. 'Classification of cell death: recommendations of the Nomenclature Committee on Cell Death 2009'. In: *Cell Death Differ.* 16 (1 Jan. 2009), pp. 3–11. DOI: 10.1038/cdd.2008.150.

[256] C J Babapulle and N P Jayasundera. 'Cellular changes and time since death'. In: *Med. Sci. Law* 33 (3 July 1993), pp. 213–222. DOI: 10.1177/002580249303300306.

[257] Anurupa Choudhury and Anindita Mahanta. 'Estimation of time since death from morphological changes occurring in white blood cells after death'. In: *Cureus* 17 (8 11th Aug. 2025), e89773. DOI: 10.7759/cureus.89773.

[258] Pedro G Ferreira et al. 'The effects of death and post-mortem cold ischemia on human tissue transcriptomes'. In: *Nat. Commun.* 9 (1 13th Feb. 2018), p. 490. DOI: 10.1038/s41467-017-02772-x.

[259] Robert H Powers. 'The decomposition of human remains'. In: *Forensic Medicine of the Lower Extremity*. Totowa, NJ: Humana Press, 2005, pp. 3–15. DOI: 10.1385/1-59259-897-8:003.

[260] Robert C Janaway, Steven L Percival and Andrew S Wilson. 'Decomposition of human remains'. In: *Microbiology and Aging*. Totowa, NJ: Humana Press, 2009, pp. 313–334. DOI: 10.1007/978-1-59745-327-1_14.

[261] H Gill-King. 'Chemical and ultrastructural aspects of decomposition'. In: *Forensic Taphonomy*. CRC Press, 13th Dec. 1996, pp. 93–108. DOI: 10.1201/9781439821923.sec2.

[262] A Galloway et al. 'Decay rates of human remains in an arid environment'. In: *J. Forensic Sci.* 34 (3 May 1989), pp. 607–616. DOI: 10.1520/jfs12680j.

[263] A T Schäfer. 'Colour measurements of pallor mortis'. In: *Int. J. Legal Med.* 113 (2 2000), pp. 81–83. DOI: 10.1007/pl00007713.

[264] Khalil S Wardak and Stephen J Cina. 'Algor mortis: an erroneous measurement following postmortem refrigeration: Algor mortis'. In: *J. Forensic Sci.* 56 (5 1st Sept. 2011), pp. 1219–1221. DOI: 10.1111/j.1556-4029.2011.01811.x.

[265] Philip R Cohen, Ronald J Moss Jr and Joseph A Prahlow. 'Livor mortis and forensic dermatology: A review of death-related gravity-dependent lividity and postmortem hypostasis'. In: *Cureus* 17 (8 22nd Aug. 2025), e90760. DOI: 10.7759/cureus.90760.

[266] Shivpoojan Kori. 'Time since death from rigor mortis: Forensic prospective'. In: *J. Forensic Sci. Crim. Investig.* 9 (5 5th July 2018), pp. 1–10. DOI: 10.19080/jfsci.2018.09.555771.

[267] Madea Burkhard. 'Early postmortem changes'. In: *Encyclopedia of Forensic Sciences, Third Edition*. Elsevier, 2023, pp. 193–205. DOI: 10.1016/b978-0-12-823677-2.00011-8.

[268] Roger W Byard. 'Artefacts due to putrefactive gas production - an overview'. In: *Med. Sci. Law* 65 (1 Jan. 2025), pp. 65–70. DOI: 10.1177/00258024241275894.

[269] Gopi K Kolluru et al. 'Hydrogen sulfide chemical biology: pathophysiological roles and detection'. In: *Nitric Oxide* 35 (30th Nov. 2013), pp. 5–20. DOI: 10.1016/j.niox.2013.07.002.

[270] M Statheropoulos et al. 'Environmental aspects of VOCs evolved in the early stages of human decomposition'. In: *Sci. Total Environ.* 385 (1-3 15th Oct. 2007), pp. 221–227. DOI: 10.1016/j.scitotenv.2007.07.003.

[271] Jennifer M DeBruyn and Kathleen A Hauther. 'Postmortem succession of gut microbial communities in deceased human subjects'. In: *PeerJ* 5 (e3437 12th June 2017), e3437. DOI: 10.7717/peerj.3437.

[272] Valerie A Seitz et al. 'CaDAVEr: a metagenome-assembled genome catalog of microbial decomposers across vertebrate environments'. In: *Microbiol. Resour. Announc.* 14 (11 13th Nov. 2025), e0132324. DOI: 10.1128/mra.01323-24.

[273] M Lee Goff. 'Early post-mortem changes and stages of decomposition in exposed cadavers'. In: *Exp. Appl. Acarol.* 49 (1-2 Oct. 2009), pp. 21–36. DOI: 10.1007/s10493-009-9284-9.

[274] Timothy E Huntington, Leon G Higley and Frederick P Baxendale. 'Maggot development during morgue storage and its effect on estimating the post-mortem interval'. In: *J. Forensic Sci.* 52 (2 1st Mar. 2007), pp. 453–458. DOI: 10.1111/j.1556-4029.2007.00385.x.

[275] Noelia I Zanetti, Elena C Visciarelli and Nestor D Centeno. 'Associational patterns of scavenger beetles to decomposition stages'. In: *J. Forensic Sci.* 60 (4 July 2015), pp. 919–927. DOI: 10.1111/1556-4029.12781.

[276] Max Koppers, Nazmiye Özkan and Ginny G Farías. 'Complex interactions between membrane-bound organelles, biomolecular condensates and the cytoskeleton'. In: *Front. Cell Dev. Biol.* 8 (21st Dec. 2020), p. 618733. DOI: 10.3389/fcell.2020.618733.

[277] R Wayne Albers. *Phospholipid Bilayers*. Lippincott Raven, 1999.

[278] Liron Bar-Peled and Nora Kory. 'Principles and functions of metabolic compartmentalization'. In: *Nat. Metab.* 4 (10 20th Oct. 2022), pp. 1232–1244. DOI: 10.1038/s42255-022-00645-2.

[279] H Reynaldo López-Mirabal and Jakob R Winther. 'Redox characteristics of the eukaryotic cytosol'. In: *Biochim. Biophys. Acta* 1783 (4 1st Apr. 2008), pp. 629–640. DOI: 10.1016/j.bbamcr.2007.10.013.

[280] Tim Hohmann and Faramarz Dehghani. 'The cytoskeleton-A complex interacting meshwork'. In: *Cells* 8 (4 18th Apr. 2019), E362. DOI: 10.3390/cells8040362.

[281] Paola De Magistris and Wolfram Antonin. 'The dynamic nature of the nuclear envelope'. In: *Curr. Biol.* 28 (8 23rd Apr. 2018), R487–R497. DOI: 10.1016/j.cub.2018.01.073.

[282] Ljubava D Zorova et al. 'Mitochondrial membrane potential'. In: *Anal. Biochem.* 552 (1st July 2018), pp. 50–59. DOI: 10.1016/j.ab.2017.07.009.

[283] P Mitchell. 'Chemiosmotic coupling in oxidative and photosynthetic phosphorylation'. In: *Biol. Rev. Camb. Philos. Soc.* 41 (3 Aug. 1966), pp. 445–502. DOI: 10.1111/j.1469-185x.1966.tb01501.x.

[284] Seo-Hyun Kim, Young-Sin Cho and Yong-Keun Jung. 'Failure of lysosomal acidification and endomembrane network in neurodegeneration'. In: *Exp. Mol. Med.* 57 (11 18th Nov. 2025), pp. 2418–2428. DOI: 10.1038/s12276-025-01579-x.

[285] Quan Wang et al. 'Lysosomes' fallback strategies: more than just survival or death'. In: *Front. Cell Dev. Biol.* 13 (11th Mar. 2025), p. 1559504. DOI: 10.3389/fcell.2025.1559504.

[286] Rui Zhang, Marc A Vooijs and Tom Gh Keulers. 'Key mechanisms in lysosome stability, degradation and repair'. In: *Mol. Cell. Biol.* 45 (5 9th May 2025), pp. 212–224. DOI: 10.1080/10985549.2025.2494762.

[287] Hui Liu et al. 'Energy metabolism in health and diseases'. In: *Signal Transduct. Target. Ther.* 10 (1 18th Feb. 2025), p. 69. DOI: 10.1038/s41392-025-02141-x.

[288] Deirdre Nolfi-Donegan, Andrea Braganza and Sruti Shiva. 'Mitochondrial electron transport chain: Oxidative phosphorylation, oxidant production, and methods of measurement'. In: *Redox Biol.* 37 (101674 1st Oct. 2020), p. 101674. DOI: 10.1016/j.redox.2020.101674.

[289] Michael Jakob Voldsgaard Clausen and Hanne Poulsen. 'Sodium/potassium homeostasis in the cell'. In: *Met. Ions Life Sci.* Metal ions in life sciences 12 (2013), pp. 41–67. DOI: 10.1007/978-94-007-5561-1_3.

[290] M Yoshida, E Muneyuki and T Hisabori. 'ATP synthase–a marvellous rotary engine of the cell'. In: *Nat. Rev. Mol. Cell Biol.* 2 (9 Sept. 2001), pp. 669–677. DOI: 10.1038/35089509.

[291] Georgina K Cox and Todd E Gillis. 'Surviving anoxia: the maintenance of energy production and tissue integrity during anoxia and reoxygenation'. In: *J. Exp. Biol.* 223 (Pt 13 10th July 2020), jeb207613. DOI: 10.1242/jeb.207613.

[292] Hiroko P Indo et al. 'Evidence of ROS generation by mitochondria in cells with impaired electron transport chain and mitochondrial DNA damage'. In: *Mitochondrion* 7 (1-2 1st Feb. 2007), pp. 106–118. DOI: 10.1016/j.mito.2006.11.026.

[293] Margaret A Miller and James F Zachary. 'Mechanisms and morphology of cellular injury, adaptation, and death'. In: *Pathologic Basis of Veterinary Disease*. Elsevier, 17th Feb. 2017, 2–43.e19. DOI: 10.1016/b978-0-323-35775-3.00001-1.

[294] Meiqin Hu et al. 'Lysosomal solute and water transport'. In: *J. Cell Biol.* 221 (11 7th Nov. 2022), e202109133. DOI: 10.1083/jcb.202109133.

[295] Aakriti Jain and Roberto Zoncu. 'Organelle transporters and inter-organelle communication as drivers of metabolic regulation and cellular homeostasis'. In: *Mol. Metab.* 60 (101481 25th June 2022), p. 101481. DOI: 10.1016/j.molmet.2022.101481.

[296] Danny Liang et al. 'Cytotoxic edema: mechanisms of pathological cell swelling'. In: *Neurosurg. Focus* 22 (5 15th May 2007), E2. DOI: 10.3171/foc.2007.22.5.3.

[297] Marisa Brini and Ernesto Carafoli. 'The plasma membrane $Ca^{2+}$ ATPase and the plasma membrane sodium calcium exchanger cooperate in the regulation of cell calcium'. In: *Cold Spring Harb. Perspect. Biol.* 3 (2 1st Feb. 2011), a004168–a004168. DOI: 10.1101/cshperspect.a004168.

[298] Brittany A Potz, M Ruhul Abid and Frank W Sellke. 'Role of calpain in pathogenesis of human disease processes'. In: *J. Nat. Sci.* 2 (9 2016), e218.

[299] Rodrigo Portes Ureshino et al. 'The interplay between $Ca^{2+}$ signaling pathways and neurodegeneration'. In: *Int. J. Mol. Sci.* 20 (23 28th Nov. 2019), E6004. DOI: 10.3390/ijms20236004.

[300] Tingting Liu et al. 'Three-dimensional interactive network: Mitochondrial-metabolic-calcium homeostasis driving Alzheimer's disease'. In: *Genes Dis.* 13 (3 1st May 2026), p. 101846. DOI: 10.1016/j.gendis.2025.101846.

[301] Urška Repnik, Maruša Hafner Česen and Boris Turk. 'Lysosomal membrane permeabilization in cell death: concepts and challenges'. In: *Mitochondrion* 19 Pt A (Nov. 2014), pp. 49–57. DOI: 10.1016/j.mito.2014.06.006.

[302] Xiao Liu et al. 'Pathogen-induced lysosomal membrane permeabilization: A critical interface between host defense and cell death'. In: *Int. J. Mol. Sci.* 27 (3 3rd Feb. 2026). DOI: 10.3390/ijms27031515.

[303] Robert A Harris and Justin S Johnson. 'Glycolysis Overview'. In: *Reference Module in Biomedical Sciences*. Elsevier, 1st Jan. 2019. DOI: 10.1016/b978-0-12-801238-3.11342-x.

[304] Andrea E Donaldson and Iain L Lamont. 'Biochemistry changes that occur after death: potential markers for determining post-mortem interval'. In: *PLoS One* 8 (11 21st Nov. 2013), e82011. DOI: 10.1371/journal.pone.0082011.

[305] X W Guo and R D Cole. 'Chromatin aggregation changes substantially as pH varies within the physiological range'. In: *J. Biol. Chem.* 264 (20 15th July 1989), pp. 11653–11657. DOI: 10.1016/s0021-9258(18)80114-4.

[306] Julie Paxman et al. 'Age-dependent aggregation of ribosomal RNA-binding proteins links deterioration in chromatin stability with challenges to proteostasis'. In: *Elife* 11 (e75978 4th Oct. 2022), e75978. DOI: 10.7554/eLife.75978.

[307] Weijun Zhang et al. 'Role of lysosomal acidification dysfunction in mesenchymal stem cell senescence'. In: *Front. Cell Dev. Biol.* 10 (7th Feb. 2022), p. 817877. DOI: 10.3389/fcell.2022.817877.

[308] Mengdie Cao et al. 'Targeting lysosomes in human disease: from basic research to clinical applications'. In: *Signal Transduct. Target. Ther.* 6 (1 8th Nov. 2021), p. 379. DOI: 10.1038/s41392-021-00778-y.

[309] M S Jurkowitz-Alexander et al. 'Cell swelling, blebbing, and death are dependent on ATP depletion and independent of calcium during chemical hypoxia in a glial cell line (ROC-1)'. In: *J. Neurochem.* 59 (1 July 1992), pp. 344–352. DOI: 10.1111/j.1471-4159.1992.tb08910.x.

[310] Margaret M Krassner et al. 'Postmortem changes in brain cell structure: a review'. In: *Free Neuropathol.* 4 (Jan. 2023), p. 10. DOI: 10.17879/freeneuropathology-2023-4790.

[311] H Lee Sweeney and David W Hammers. 'Muscle contraction'. In: *Cold Spring Harb. Perspect. Biol.* 10 (2 1st Feb. 2018), a023200. DOI: 10.1101/cshperspect.a023200.

[312] E C Bate-Smith and J R Bendall. 'Rigor mortis and adenosine-triphosphate'. In: *J. Physiol.* 106 (2 2nd June 1947), pp. 177–185. DOI: 10.1113/jphysiol.1947.sp004202.

[313] P J Tarrant, J V McLoughlin and M G Harrington. 'Anaerobic glycosis in biopsy and post-mortem porcine longissimus dorsi muscle'. In: *Proc. R. Ir. Acad. B* 72 (5 1972), pp. 55–73.

[314] R Hamm. 'Postmortem breakdown of ATP and glycogen in ground muscle: A review'. In: *Meat Sci.* 1 (1 Jan. 1977), pp. 15–39. DOI: 10.1016/0309-1740(77)90029-8.

[315] Jiali Tang et al. 'Postmortem oxygen consumption by mitochondria and its effects on myoglobin form and stability'. In: *J. Agric. Food Chem.* 53 (4 23rd Feb. 2005), pp. 1223–1230. DOI: 10.1021/jf048646o.

[316] Weihao Zhu et al. 'New contributions to the relationship between sequential changes of ATP-related metabolites and post-mortem interval in rats'. In: *Leg. Med. (Tokyo)* 48 (101809 Feb. 2021), p. 101809. DOI: 10.1016/j.legalmed.2020.101809.

[317] Ivana Y Kuo and Barbara E Ehrlich. 'Signaling in muscle contraction'. In: *Cold Spring Harb. Perspect. Biol.* 7 (2 2nd Feb. 2015), a006023. DOI: 10.1101/cshperspect.a006023.

[318] Georgi Z Genchev, Tomoyoshi Kobayashi and Hui Lu. 'Calcium induced regulation of skeletal troponin–computational insights from molecular dynamics simulations'. In: *PLoS One* 8 (3 15th Mar. 2013), e58313. DOI: 10.1371/journal.pone.0058313.

[319] Amy E Rattenbury. 'Forensic taphonomy'. In: *Forensic Ecogenomics*. Elsevier, 2018, pp. 37–59. DOI: 10.1016/b978-0-12-809360-3.00002-3.

[320] Y Collan, E McDowell and B F Trump. 'Studies on the pathogenesis of ischemic cell injury. VI. Mitochondrial flocculent densities in autolysis: VI. Mitochondrial flocculent densities in autolysis'. In: *Virchows Arch. B Cell Pathol.* 35 (3 1981), pp. 189–199. DOI: 10.1007/bf02889159.

[321] Bart Wagner et al. *Ghadially's ultrastructural pathology of the cell and matrix*. 5th Edition. Boca Raton: CRC Press, 11th June 2025. 900 pp. DOI: 10.1201/9781003498551.

[322] Embriette R Hyde et al. 'The living dead: bacterial community structure of a cadaver at the onset and end of the bloat stage of decomposition'. In: *PLoS One* 8 (10 30th Oct. 2013), e77733. DOI: 10.1371/journal.pone.0077733.

[323] Ismail Can et al. 'Distinctive thanatomicrobiome signatures found in the blood and internal organs of humans'. In: *J. Microbiol. Methods* 106 (C Nov. 2014), pp. 1–7. DOI: 10.1016/j.mimet.2014.07.026.

[324] Z M Burcham et al. 'Fluorescently labeled bacteria provide insight on post-mortem microbial transmigration'. In: *Forensic Sci. Int.* 264 (July 2016), pp. 63–69. DOI: 10.1016/j.forsciint.2016.03.019.

[325] Ana Cláudia-Ferreira et al. 'The future is now: Unraveling the expanding potential of human (necro)microbiome in forensic investigations'. In: *Microorganisms* 11 (10 7th Oct. 2023), p. 2509. DOI: 10.3390/microorganisms11102509.

[326] Ruina Liu et al. 'Dissecting the microbial community structure of internal organs during the early postmortem period in a murine corpse model'. In: *BMC Microbiol.* 23 (1 10th Feb. 2023), p. 38. DOI: 10.1186/s12866-023-02786-0.

[327] Xin Huang et al. 'Microbial succession in human tissues postmortem: insights from 2bRAD-M sequencing'. In: *Microbiol. Spectr.* 14 (1 6th Jan. 2026), e0266624. DOI: 10.1128/spectrum.02666-24.

[328] Embriette R Hyde et al. 'Initial insights into bacterial succession during human decomposition'. In: *Int. J. Legal Med.* 129 (3 May 2015), pp. 661–671. DOI: 10.1007/s00414-014-1128-4.

[329] Sheng Hu et al. 'Multimodal approaches based on microbial data for accurate postmortem interval estimation'. In: *Microorganisms* 12 (11 30th Oct. 2024), p. 2193. DOI: 10.3390/microorganisms12112193.

[330] Michael A Mahowald et al. 'Characterizing a model human gut microbiota composed of members of its two dominant bacterial phyla'. In: *Proc. Natl. Acad. Sci. U. S. A.* 106 (14 7th Apr. 2009), pp. 5859–5864. DOI: 10.1073/pnas.0901529106.

[331] Fabian Rivera-Chávez, Christopher A Lopez and Andreas J Bäumler. 'Oxygen as a driver of gut dysbiosis'. In: *Free Radic. Biol. Med.* 105 (Apr. 2017), pp. 93–101. DOI: 10.1016/j.freeradbiomed.2016.09.022.

[332] Militza Carrero-Colón, Gene S Wickham and Ronald F Turco. 'Taxonomy, phylogeny, and physiology of fecal indicator bacteria'. In: *The Fecal Bacteria*. Washington, DC, USA: ASM Press, 9th Apr. 2014, pp. 23–38. DOI: 10.1128/9781555816865.ch2.

[333] Daniela Karasova et al. 'Host species adaptation of obligate gut anaerobes is dependent on their environmental survival'. In: *Microorganisms* 10 (6 25th May 2022), p. 1085. DOI: 10.3390/microorganisms10061085.

[334] Christian L Lauber et al. 'Vertebrate decomposition is accelerated by soil microbes'. In: *Appl. Environ. Microbiol.* 80 (16 Aug. 2014), pp. 4920–4929. DOI: 10.1128/AEM.00957-14.

[335] Jessica L Metcalf et al. 'Microbial community assembly and metabolic function during mammalian corpse decomposition'. In: *Science* 351 (6269 8th Jan. 2016), pp. 158–162. DOI: 10.1126/science.aad2646.

[336] Zachary M Burcham et al. 'Bacterial community succession, transmigration, and differential gene transcription in a controlled vertebrate decomposition model'. In: *Front. Microbiol.* 10 (18th Apr. 2019), p. 745. DOI: 10.3389/fmicb.2019.00745.

[337] Vassiliki A Boumba, Kallirroe S Ziavrou and Theodore Vougiouklakis. 'Biochemical pathways generating post-mortem volatile compounds co-detected during forensic ethanol analyses'. In: *Forensic Sci. Int.* 174 (2-3 30th Jan. 2008), pp. 133–151. DOI: 10.1016/j.forsciint.2007.03.018.

[338] Yoshihide Tokunou, Masanori Toyofuku and Nobuhiko Nomura. 'Physiological benefits of oxygen-terminating extracellular electron transfer'. In: *MBio* 13 (6 20th Dec. 2022), e0195722. DOI: 10.1128/mbio.01957-22.

[339] Fouad M F Elshaghabee et al. 'Ethanol production by selected intestinal microorganisms and lactic acid bacteria growing under different nutritional conditions'. In: *Front. Microbiol.* 7 (29th Jan. 2016), p. 47. DOI: 10.3389/fmicb.2016.00047.

[340] Caiping Sun et al. 'Propanol production through microbial fermentation of biomass'. In: *Bioresour. Bioprocess.* 12 (1 5th Nov. 2025), p. 127. DOI: 10.1186/s40643-025-00966-6.

[341] Kyoung-Min Choi et al. 'Postmortem proteomics to discover biomarkers for forensic PMI estimation'. In: *Int. J. Legal Med.* 133 (3 May 2019), pp. 899–908. DOI: 10.1007/s00414-019-02011-6.

[342] Angela Zissler et al. 'Postmortem protein degradation as a tool to estimate the PMI: A systematic review'. In: *Diagnostics (Basel)* 10 (12 26th Nov. 2020), E1014. DOI: 10.3390/diagnostics10121014.

[343] Angela Zissler et al. 'Influencing factors on postmortem protein degradation for PMI estimation: A systematic review'. In: *Diagnostics (Basel)* 11 (7 23rd June 2021), p. 1146. DOI: 10.3390/diagnostics11071146.

[344] Anjali Chhikara et al. 'Protein degradation patterns as biomarkers for post-mortem interval estimation: A comprehensive review of proteomic approaches in forensic science'. In: *J. Proteomics* 310 (105326 6th Jan. 2025), p. 105326. DOI: 10.1016/j.jprot.2024.105326.

[345] Weisheng Huang et al. 'The role of protein degradation in estimation postmortem interval and confirmation of cause of death in forensic pathology: A literature review'. In: *Int. J. Mol. Sci.* 25 (3 29th Jan. 2024), p. 1659. DOI: 10.3390/ijms25031659.

[346] Natalie E Diether and Benjamin P Willing. 'Microbial fermentation of dietary protein: An important factor in Diet Microbe Host interaction'. In: *Microorganisms* 7 (1 13th Jan. 2019), E19. DOI: 10.3390/microorganisms7010019.

[347] Kwon-young Choi. 'Nitrogen-neutral amino acids refinery: Deamination of amino acids for bio-alcohol and ammonia production'. In: *ChemBioEng Rev.* 8 (3 1st June 2021), pp. 213–226. DOI: 10.1002/cben.202000031.

[348] Anthony J Michael. 'Biosynthesis of polyamines and polyamine-containing molecules'. In: *Biochem. J.* 473 (15 1st Aug. 2016), pp. 2315–2329. DOI: 10.1042/BCJ20160185.

[349] Rachel M Wilson et al. 'Hydrogenation of organic matter as a terminal electron sink sustains high CO2:CH4 production ratios during anaerobic decomposition'. In: *Org. Geochem.* 112 (Oct. 2017), pp. 22–32. DOI: 10.1016/j.orggeochem.2017.06.011.

[350] Donald David Haines and Arpad Tosaki. 'Heme degradation in pathophysiology of and countermeasures to inflammation-associated disease'. In: *Int. J. Mol. Sci.* 21 (24 18th Dec. 2020), E9698. DOI: 10.3390/ijms21249698.

[351] Ruth Pietri, Elddie Román-Morales and Juan López-Garriga. 'Hydrogen sulfide and hemeproteins: knowledge and mysteries'. In: *Antioxid. Redox Signal.* 15 (2 15th July 2011), pp. 393–404. DOI: 10.1089/ars.2010.3698.

[352] K Fahmy, C H Gray and D C Nicholson. 'The reduction of bile pigments by faecal and intestinal bacteria'. In: *Biochim. Biophys. Acta* 264 (1 30th Mar. 1972), pp. 85–97. DOI: 10.1016/0304-4165(72)90119-5.

[353] Martha H Stipanuk. 'Metabolism of sulfur-containing amino acids: How the body copes with excess methionine, cysteine, and sulfide'. In: *J. Nutr.* 150 (Suppl 1 1st Oct. 2020), 2494S–2505S. DOI: 10.1093/jn/nxaa094.

[354] Shouta Nonoyama, Takayuki Shimizu and Shinji Masuda. 'The roles of hydrogen sulfide and reactive sulfur species in bacterial life within the human body'. In: *Nitric Oxide* 162 (18th June 2026), pp. 1–8. DOI: 10.1016/j.niox.2026.02.002.

[355] Anna Bilska-Wilkosz et al. 'The role of hemoproteins: Hemoglobin, myoglobin and neuroglobin in endogenous thiosulfate production processes'. In: *Int. J. Mol. Sci.* 18 (6 20th June 2017), E1315. DOI: 10.3390/ijms18061315.

[356] Fan Yang et al. 'Changes in microbial communities using pigs as a model for postmortem interval estimation'. In: *Microorganisms* 11 (11 20th Nov. 2023), p. 2811. DOI: 10.3390/microorganisms11112811.

[357] Kelly L Cobaugh, Sean M Schaeffer and Jennifer M DeBruyn. 'Functional and structural succession of soil microbial communities below decomposing human cadavers'. In: *PLoS One* 10 (6 12th June 2015), e0130201. DOI: 10.1371/journal.pone.0130201.

[358] Sheree J Finley et al. 'Microbial signatures of cadaver gravesoil during decomposition'. In: *Microb. Ecol.* 71 (3 Apr. 2016), pp. 524–529. DOI: 10.1007/s00248-015-0725-1.

[359] Torri B Thomas et al. 'Postmortem microbial communities in burial soil layers of skeletonized humans'. In: *J. Forensic Leg. Med.* 49 (July 2017), pp. 43–49. DOI: 10.1016/j.jflm.2017.05.009.

[360] Zachary M Burcham et al. 'A conserved interdomain microbial network underpins cadaver decomposition despite environmental variables'. In: *Nat. Microbiol.* 9 (3 Mar. 2024), pp. 595–613. DOI: 10.1038/s41564-023-01580-y.

[361] Alexandra L Emmons et al. 'Postmortem skeletal microbial community composition and function in buried human remains'. In: *mSystems* 7 (2 26th Apr. 2022), e0004122. DOI: 10.1128/msystems.00041-22.

[362] Donna B McIntyre et al. 'Microbial succession in decomposing carrion is driven by time, modulated by insects and microbial perturbation'. In: *Front. Microbiol.* 17 (4th May 2026), p. 1773208. DOI: 10.3389/fmicb.2026.1773208.

[363] Victoria Nieciecki et al. 'Insects shape the cadaver decomposition microbiome and postmortem interval estimation accuracy'. In: *mSystems* 11 (5 19th May 2026), e0068125. DOI: 10.1128/msystems.00681-25.

[364] Y T B Bambaradeniya, P A Magni and I R Dadour. 'Current status of five warm season Diptera species in estimating the Post-Mortem Interval'. In: *Ann. Entomol. Soc. Am.* 116 (1 17th Jan. 2023), pp. 19–50. DOI: 10.1093/aesa/saac023.

[365] Lipin Ren et al. 'A brief review of forensically important flesh flies (Diptera: Sarcophagidae)'. In: *Forensic Sci. Res.* 3 (1 22nd Mar. 2018), pp. 16–26. DOI: 10.1080/20961790.2018.1432099.

[366] Linda Brownlow et al. 'Case closed - Wrappings and encasement delays and reduces fly presence on body parts'. In: *Forensic Sci. Int.* 342 (111542 Jan. 2023), p. 111542. DOI: 10.1016/j.forsciint.2022.111542.

[367] Parul Sharma et al. 'A comparative study of decomposition and associated insects on pig carcasses buried at 40 and 80 cm depths'. In: *Sci. Rep.* 15 (1 14th Oct. 2025), p. 35802. DOI: 10.1038/s41598-025-19769-y.

[368] Nidya Alexandra Segura et al. 'Succession pattern of cadaverous entomofauna in a semi-rural area of Bogotá, Colombia'. In: *Forensic Sci. Int.* 187 (1-3 30th May 2009), pp. 66–72. DOI: 10.1016/j.forsciint.2009.02.018.

[369] Kirsty Griffiths, Matt N Krosch and Kirsty Wright. 'Variation in decomposition stages and carrion insect succession in a dry tropical climate and its effect on estimating postmortem interval'. In: *Forensic Sci. Res.* 5 (4 9th Apr. 2020), pp. 327–335. DOI: 10.1080/20961790.2020.1733830.

[370] Danisile Tembe and Samson Mukaratirwa. 'Insect succession and decomposition pattern on pig carrion during warm and cold seasons in KwaZulu-Natal province of South Africa'. In: *J. Med. Entomol.* 58 (6 9th Nov. 2021), pp. 2047–2057. DOI: 10.1093/jme/tjab099.

[371] Gengwang Hu et al. 'A preliminary study of body decomposition and arthropod succession in an arid area in Northwest China during summer'. In: *J. Med. Entomol.* 60 (2 6th Mar. 2023), pp. 306–315. DOI: 10.1093/jme/tjac174.

[372] Claudia Lange et al. 'Impact of intraspecific variation in insect microbiomes on host phenotype and evolution'. In: *ISME J.* 17 (11 2nd Nov. 2023), pp. 1798–1807. DOI: 10.1038/s41396-023-01500-2.

[373] Juanjuan Guo et al. 'Potential use of bacterial community succession for estimating post-mortem interval as revealed by high-throughput sequencing'. In: *Sci. Rep.* 6 (1 7th Apr. 2016), p. 24197. DOI: 10.1038/srep24197.

[374] Shantanu P Shukla et al. 'Microbiome-assisted carrion preservation aids larval development in a burying beetle'. In: *Proc. Natl. Acad. Sci. U. S. A.* 115 (44 30th Oct. 2018), pp. 11274–11279. DOI: 10.1073/pnas.1812808115.

[375] M J Swift. *Decomposition in terrestrial ecosystems*. Studies in ecology. Chichester, England: Wiley-Blackwell, 13th Nov. 1979. 400 pp.

[376] Jennifer M DeBruyn et al. 'Comparative decomposition of humans and pigs: Soil biogeochemistry, microbial activity and metabolomic profiles'. In: *Front. Microbiol.* 11 (2020), p. 608856. DOI: 10.3389/fmicb.2020.608856.

[377] Mary S Megyesi, Stephen P Nawrocki and Neal H Haskell. 'Using accumulated degree-days to estimate the postmortem interval from decomposed human remains'. In: *J. Forensic Sci.* 50 (3 6th May 2005), pp. 618–626. DOI: 10.1520/jfs2004017.

[378] Philip S Barton et al. 'Temperature dynamics in different body regions of decomposing vertebrate remains'. In: *Forensic Sci. Int.* 325 (110900 Aug. 2021), p. 110900. DOI: 10.1016/j.forsciint.2021.110900.

[379] Sarah W Keenan et al. 'Mortality hotspots: Nitrogen cycling in forest soils during vertebrate decomposition'. In: *Soil Biol. Biochem.* 121 (June 2018), pp. 165–176. DOI: 10.1016/j.soilbio.2018.03.005.

[380] Lois S Taylor et al. 'Transient hypoxia drives soil microbial community dynamics and biogeochemistry during human decomposition'. In: *FEMS Microbiol. Ecol.* 100 (10 14th Sept. 2024), fiae119. DOI: 10.1093/femsec/fiae119.

[381] Autumn Lennartz, Michelle D Hamilton and Russell Weaver. 'Moisture content in decomposing, desiccated, and mummified human tissue'. In: *Forensic Anthropol.* 3 (1 10th Feb. 2020), pp. 1–16. DOI: 10.5744/fa.2020.1001.

[382] Julius Strack and Martin J Smith. 'Predicted changes to the rate of human decomposition due to climate change during the 21st century'. In: *Forensic Sci. Int. Rep.* 7 (100321 July 2023), p. 100321. DOI: 10.1016/j.fsir.2023.100321.

[383] Tamsin C F Haslam and Mark Tibbett. 'Soils of contrasting pH affect the decomposition of buried mammalian (Ovis aries) skeletal muscle tissue'. In: *J. Forensic Sci.* 54 (4 July 2009), pp. 900–904. DOI: 10.1111/j.1556-4029.2009.01070.x.

[384] Janine Rietz et al. 'Temperature and pH dynamics during carcass decomposition and implications for disease management'. In: *Sci. Rep.* 15 (1 16th July 2025), p. 25795. DOI: 10.1038/s41598-025-07716-w.

[385] D W Hopkins, P E J Wiltshire and B D Turner. 'Microbial characteristics of soils from graves: an investigation at the interface of soil microbiology and forensic science'. In: *Appl. Soil Ecol.* 14 (3 June 2000), pp. 283–288. DOI: 10.1016/s0929-1393(00)00063-9.

[386] Ali Riza Tumer et al. 'Effects of different types of soil on decomposition: an experimental study'. In: *Leg. Med. (Tokyo)* 15 (3 1st May 2013), pp. 149–156. DOI: 10.1016/j.legalmed.2012.11.003.

[387] J P Fancher et al. 'An evaluation of soil chemistry in human cadaver decomposition islands: Potential for estimating postmortem interval (PMI)'. In: *Forensic Sci. Int.* 279 (Oct. 2017), pp. 130–139. DOI: 10.1016/j.forsciint.2017.08.002.

[388] Vivienne Heaton et al. 'Predicting the postmortem submersion interval for human remains recovered from U.K. waterways'. In: *J. Forensic Sci.* 55 (2 1st Mar. 2010), pp. 302–307. DOI: 10.1111/j.1556-4029.2009.01291.x.

[389] Glenys McGowan and Jonathan Prangnell. 'A method for calculating soil pressure overlying human burials'. In: *J. Archaeol. Sci.* 53 (Jan. 2015), pp. 12–18. DOI: 10.1016/j.jas.2014.09.016.

[390] Sarah Theresa Dorothea Ellingham, Pierre Perich and Morris Tidball-Binz. 'The fate of human remains in a maritime context and feasibility for forensic humanitarian action to assist in their recovery and identification'. In: *Forensic Sci. Int.* 279 (1st Oct. 2017), pp. 229–234. DOI: 10.1016/j.forsciint.2017.07.039.

[391] Megan A Hill and James T Pokines. 'Comparative analysis of fetal pig decomposition processes in burials of variable depths and wrapping'. In: *J. Forensic Sci.* 67 (6 1st Nov. 2022), pp. 2192–2202. DOI: 10.1111/1556-4029.15120.

[392] C-E A Winslow, A P Gagge and L P Herrington. 'The influence of air movement upon heat losses from the clothed human body'. In: *Am. J. Physiol.* 127 (3 30th Sept. 1939), pp. 505–518. DOI: 10.1152/ajplegacy.1939.127.3.505.

[393] Bahar S Razavi, Evgenia Blagodatskaya and Yakov Kuzyakov. 'Nonlinear temperature sensitivity of enzyme kinetics explains canceling effect-a case study on loamy haplic Luvisol'. In: *Front. Microbiol.* 6 (14th Oct. 2015), p. 1126. DOI: 10.3389/fmicb.2015.01126.

[394] Nina Lanzinger et al. 'Factors influencing the progression of post-mortem changes between scene and autopsy'. In: *Sci. Rep.* 16 (1 14th Jan. 2026), p. 1950. DOI: 10.1038/s41598-026-35786-x.

[395] Roy M Daniel and Michael J Danson. 'A new understanding of how temperature affects the catalytic activity of enzymes'. In: *Trends Biochem. Sci.* 35 (10 1st Oct. 2010), pp. 584–591. DOI: 10.1016/j.tibs.2010.05.001.

[396] Richard Wolfenden. 'Benchmark reaction rates, the stability of biological molecules in water, and the evolution of catalytic power in enzymes'. In: *Annu. Rev. Biochem.* 80 (1 7th July 2011), pp. 645–667. DOI: 10.1146/annurev-biochem-060409-093051.

[397] Hans Bisswanger. 'Enzyme assays'. In: *Perspect. Sci. (Neth)* 1 (1-6 1st May 2014), pp. 41–55. DOI: 10.1016/j.pisc.2014.02.005.

[398] Mark E Ritchie. 'Reaction and diffusion thermodynamics explain optimal temperatures of biochemical reactions'. In: *Sci. Rep.* 8 (1 23rd July 2018), p. 11105. DOI: 10.1038/s41598-018-28833-9.

[399] R M Daniel, M Dines and H H Petach. 'The denaturation and degradation of stable enzymes at high temperatures'. In: *Biochem. J.* 317 ( Pt 1) (1 1st July 1996), pp. 1–11. DOI: 10.1042/bj3170001.

[400] James R Lepock. 'How do cells respond to their thermal environment?' In: *Int. J. Hyperthermia* 21 (8 Dec. 2005), pp. 681–687. DOI: 10.1080/02656730500307298.

[401] Jã¼rgen Wiegel. 'Temperature spans for growth: Hypothesis and discussion'. In: *FEMS Microbiol. Lett.* 75 (2-3 1st June 1990), pp. 155–169. DOI: 10.1111/j.1574-6968.1990.tb04092.x.

[402] Xue Yan Sim et al. 'Unraveling the effect of redox potential on dark fermentative hydrogen production'. In: *Renew. Sustain. Energy Rev.* 187 (113755 1st Nov. 2023), p. 113755. DOI: 10.1016/j.rser.2023.113755.

[403] Manuel Joao Afecto Gonçalves, Cristina González-Fernández and Silvia Greses. 'Assessing the effect of temperature drop on a stable anaerobic fermentation for volatile fatty acids production'. In: *Bioengineered* 16 (1 3rd Dec. 2025), p. 2458369. DOI: 10.1080/21655979.2025.2458369.

[404] Eline M J Schotsmans et al. 'The impact of shallow burial on differential decomposition to the body: a temperate case study'. In: *Forensic Sci. Int.* 206 (1-3 20th Mar. 2011), e43–8. DOI: 10.1016/j.forsciint.2010.07.036.

[405] Stefan Pittner et al. 'The applicability of forensic time since death estimation methods for buried bodies in advanced decomposition stages'. In: *PLoS One* 15 (12 9th Dec. 2020), e0243395. DOI: 10.1371/journal.pone.0243395.

[406] Jonathan Prangnell and Glenys McGowan. 'Soil temperature calculation for burial site analysis'. In: *Forensic Sci. Int.* 191 (1-3 30th Oct. 2009), pp. 104–109. DOI: 10.1016/j.forsciint.2009.07.002.

[407] Artem Vitalievich Maikov, Jolandie Myburgh and Craig Adam Keyes. 'The effect of burial in containers filled with naturally occurring soil and mine tailings on decomposition: a porcine pilot study'. In: *Int. J. Legal Med.* 140 (3 20th May 2026), pp. 1763–1774. DOI: 10.1007/s00414-025-03715-8.

[408] Aidan P Johnson, Katarina M Mikac and James F Wallman. 'Thermogenesis in decomposing carcasses'. In: *Forensic Sci. Int.* 231 (1-3 10th Sept. 2013), pp. 271–277. DOI: 10.1016/j.forsciint.2013.05.031.

[409] Ai Hachiya et al. 'Necrophagous insects and internal temperature synergistically determine duration of the decomposition process for deer carcasses when vertebrate scavengers are excluded'. In: *Ecol. Evol.* 16 (4 Apr. 2026), e73476. DOI: 10.1002/ece3.73476.

[410] C O Gill and K G Newton. 'The ecology of bacterial spoilage of fresh meat at chill temperatures'. In: *Meat Sci.* 2 (3 1st July 1978), pp. 207–217. DOI: 10.1016/0309-1740(78)90006-2.

[411] Yujia Qiu et al. 'The effects of ventilation, humidity, and temperature on bacterial growth and bacterial genera distribution'. In: *Int. J. Environ. Res. Public Health* 19 (22 20th Nov. 2022), p. 15345. DOI: 10.3390/ijerph192215345.

[412] Helmut Sies, Ryan J Mailloux and Ursula Jakob. 'Fundamentals of redox regulation in biology'. In: *Nat. Rev. Mol. Cell Biol.* 25 (9 30th Sept. 2024), pp. 701–719. DOI: 10.1038/s41580-024-00730-2.

[413] Pankaj K Arora et al. 'OxDBase: a database of oxygenases involved in biodegradation'. In: *BMC Res. Notes* 2 (1 30th Apr. 2009), p. 67. DOI: 10.1186/1756-0500-2-67.

[414] Esteban Ortiz-Prado et al. 'Partial pressure of oxygen in the human body: a general review'. In: *Am. J. Blood Res.* 9 (1 15th Feb. 2019), pp. 1–14.

[415] S R Pezeshki and R D DeLaune. 'Soil oxidation–reduction in wetlands and its impact on plant functioning'. In: *Biology (Basel)* 1 (2 26th July 2012), pp. 196–221. DOI: 10.3390/biology1020196.

[416] Maximilian Barczok et al. 'Variability in soil redox response to seasonal flooding in a vernal pond'. In: *Front. Environ. Sci.* 11 (1114814 7th July 2023), p. 1114814. DOI: 10.3389/fenvs.2023.1114814.

[417] Tuomas J Mattila. 'Redox potential as a soil health indicator – how does it compare to microbial activity and soil structure?' In: *Plant Soil* 494 (1-2 Jan. 2024), pp. 617–625. DOI: 10.1007/s11104-023-06305-y.

[418] H Brix. 'Macrophyte-mediated oxygen transfer in wetlands: Transport mechanisms and rates'. In: *Constructed Wetlands for Water Quality Improvement*. 1st Edition. CRC Press, 23rd Sept. 2020, pp. 391–398. DOI: 10.1201/9781003069997-48.

[419] Michael G P McCabe, David J Maguire and Renaat Bourgain. 'The flux of oxygen within tissues'. In: *Adv. Exp. Med. Biol.* 540 (2003), pp. 291–295. DOI: 10.1007/978-1-4757-6125-2_41.

[420] Shivanjali Joshi-Barr et al. 'Exploiting oxidative microenvironments in the body as triggers for drug delivery systems'. In: *Antioxid. Redox Signal.* 21 (5 10th Aug. 2014), pp. 730–754. DOI: 10.1089/ars.2013.5754.

[421] He N Xu and Lin Z Li. 'Quantitative redox imaging biomarkers for studying tissue metabolic state and its heterogeneity'. In: *J. Innov. Opt. Health Sci.* 7 (2 Mar. 2014), p. 1430002. DOI: 10.1142/S179354581430002X.

[422] Emily M Lacroix et al. 'Effects of moisture and physical disturbance on pore-scale oxygen content and anaerobic metabolisms in upland soils'. In: *Sci. Total Environ.* 780 (146572 1st Aug. 2021), p. 146572. DOI: 10.1016/j.scitotenv.2021.146572.

[423] Emily M Lacroix et al. 'Consider the anoxic microsite: Acknowledging and appreciating spatiotemporal redox heterogeneity in soils and sediments'. In: *ACS Earth Space Chem.* 7 (9 21st Sept. 2023), pp. 1592–1609. DOI: 10.1021/acsearthspacechem.3c00032.

[424] G R Gibson, G T Macfarlane and J H Cummings. 'Occurrence of sulphate-reducing bacteria in human faeces and the relationship of dissimilatory sulphate reduction to methanogenesis in the large gut'. In: *J. Appl. Bacteriol.* 65 (2 Aug. 1988), pp. 103–111. DOI: 10.1111/j.1365-2672.1988.tb01498.x.

[425] G R Gibson, S Macfarlane and G T Macfarlane. 'Metabolic interactions involving sulphate-reducing and methanogenic bacteria in the human large intestine'. In: *FEMS Microbiol. Ecol.* 12 (2 1st June 1993), pp. 117–125. DOI: 10.1111/j.1574-6941.1993.tb00023.x.

[426] Aharon Oren. *Pers. comm.* 15th Sept. 2009.

[427] Antonin C André, Lorine Debande and Benoit S Marteyn. 'The selective advantage of facultative anaerobes relies on their unique ability to cope with changing oxygen levels during infection'. In: *Cell. Microbiol.* 23 (8 Aug. 2021), e13338. DOI: 10.1111/cmi.13338.

[428] Jianwei Chen et al. 'Impacts of chemical gradients on microbial community structure'. In: *ISME J.* 11 (4 Apr. 2017), pp. 920–931. DOI: 10.1038/ismej.2016.175.

[429] Huiyong Yin, Libin Xu and Ned A Porter. 'Free radical lipid peroxidation: mechanisms and analysis'. In: *Chem. Rev.* 111 (10 12th Oct. 2011), pp. 5944–5972. DOI: 10.1021/cr200084z.

[430] M Lourenço, E Ramos-Morales and R J Wallace. 'The role of microbes in rumen lipolysis and biohydrogenation and their manipulation'. In: *Animal* 4 (7 1st July 2010), pp. 1008–1023. DOI: 10.1017/S175173111000042X.

[431] Kun Shi et al. 'Manipulating the generation of reactive oxygen species through intermittent hypoxic stress for enhanced accumulation of arachidonic acid-rich lipids'. In: *Chem. Eng. Sci.* 186 (31st Aug. 2018), pp. 36–43. DOI: 10.1016/j.ces.2018.04.023.

[432] T L Bereuter et al. 'Post-mortem alterations of human lipids – part I: evaluation of adipocere formation and mummification by desiccation'. In: *Human Mummies*. Vienna: Springer Vienna, 1996, pp. 265–273. DOI: 10.1007/978-3-7091-6565-2_25.

[433] Ashraf G Madian and Fred E Regnier. 'Proteomic identification of carbonylated proteins and their oxidation sites'. In: *J. Proteome Res.* 9 (8 6th Aug. 2010), pp. 3766–3780. DOI: 10.1021/pr1002609.

[434] Elise Lévy et al. 'Causative links between protein aggregation and oxidative stress: A review'. In: *Int. J. Mol. Sci.* 20 (16 9th Aug. 2019), E3896. DOI: 10.3390/ijms20163896.

[435] Atef Mannaa and Franz-Georg Hanisch. 'Redox proteomes in human physiology and disease mechanisms'. In: *J. Proteome Res.* 19 (1 3rd Jan. 2020), pp. 1–17. DOI: 10.1021/acs.jproteome.9b00586.

[436] Celia Andrés Juan et al. 'The chemistry of reactive oxygen species (ROS) revisited: Outlining their role in biological macromolecules (DNA, lipids and proteins) and induced pathologies'. In: *Int. J. Mol. Sci.* 22 (9 28th Apr. 2021), p. 4642. DOI: 10.3390/ijms22094642.

[437] Richard Kehm et al. 'Protein oxidation - Formation mechanisms, detection and relevance as biomarkers in human diseases'. In: *Redox Biol.* 42 (101901 June 2021), p. 101901. DOI: 10.1016/j.redox.2021.101901.

[438] M J Mcinerney. 'Anaerobic hydrolysis and fermentation of fats and proteins'. In: *Biology of anaerobic microorganisms* (1988). Ed. by Alexander J B Zehnder, pp. 373–415.

[439] Zhe Deng et al. 'Anaerobic protein degradation: Effects of protein structural complexity, protein concentrations, carbohydrates, and volatile fatty acids'. In: *Bioresour. Technol. Rep.* 22 (101501 1st June 2023), p. 101501. DOI: 10.1016/j.biteb.2023.101501.

[440] Yizeng Li et al. 'The importance of water and hydraulic pressure in cell dynamics'. In: *J. Cell Sci.* 133 (20 21st Oct. 2020), jcs240341. DOI: 10.1242/jcs.240341.

[441] Maria A Perillo et al. 'The role of water in reactions catalysed by hydrolases under conditions of molecular crowding'. In: *Biophys. Rev.* 15 (4 9th Aug. 2023), pp. 639–660. DOI: 10.1007/s12551-023-01104-2.

[442] Daniel Whitaker and Matthew W Powner. 'On the aqueous origins of the condensation polymers of life'. In: *Nat. Rev. Chem.* 8 (11 27th Nov. 2024), pp. 817–832. DOI: 10.1038/s41570-024-00648-5.

[443] Margery Cortes-Clerget et al. 'Water as the reaction medium in organic chemistry: from our worst enemy to our best friend'. In: *Chem. Sci.* 12 (12 12th Feb. 2021), pp. 4237–4266. DOI: 10.1039/d0sc06000c.

[444] Zhouzhou Pan and Laurence Brassart. 'A reaction-diffusion framework for hydrolytic degradation of amorphous polymers based on a discrete chain scission model'. In: *Acta Biomater.* 167 (1st Sept. 2023), pp. 361–373. DOI: 10.1016/j.actbio.2023.06.021.

[445] Francesco Mallamace et al. 'Specific heat and transport functions of water'. In: *Int. J. Mol. Sci.* 21 (2 17th Jan. 2020), E622. DOI: 10.3390/ijms21020622.

[446] E Jéquier and F Constant. 'Water as an essential nutrient: the physiological basis of hydration'. In: *Eur. J. Clin. Nutr.* 64 (2 Feb. 2010), pp. 115–123. DOI: 10.1038/ejcn.2009.111.

[447] Sérgio F Sousa et al. 'Relationship between enzyme/substrate properties and enzyme efficiency in hydrolases'. In: *ACS Catal.* 5 (10 2nd Oct. 2015), pp. 5877–5887. DOI: 10.1021/acscatal.5b00923.

[448] Aoife C Fogarty and Damien Laage. 'Water dynamics in protein hydration shells: the molecular origins of the dynamical perturbation'. In: *J. Phys. Chem. B* 118 (28 17th July 2014), pp. 7715–7729. DOI: 10.1021/jp409805p.

[449] Damien Laage, Thomas Elsaesser and James T Hynes. 'Water dynamics in the hydration shells of biomolecules'. In: *Chem. Rev.* 117 (16 23rd Aug. 2017), pp. 10694–10725. DOI: 10.1021/acs.chemrev.6b00765.

[450] Ekta Shukla, Ameya D. Bendre and Sushama M. Gaikwad. 'Hydrolases: The most diverse class of enzymes'. In: *Hydrolases*. IntechOpen, 15th June 2022. DOI: 10.5772/intechopen.102350.

[451] Lisa Swann, Shari Forbes and Simon W Lewis. 'Observations of the temporal variation in chemical content of decomposition fluid: A preliminary study using pigs as a model system'. In: *Aust. J. Forensic Sci.* 42 (3 Sept. 2010), pp. 199–210. DOI: 10.1080/00450610903258102.

[452] Sarah W Keenan and Jennifer M DeBruyn. 'Changes to vertebrate tissue stable isotope ( 15N) composition during decomposition'. In: *Sci. Rep.* 9 (1 9th July 2019), p. 9929. DOI: 10.1038/s41598-019-46368-5.

[453] Ruili Wang et al. 'Decomposition kinetics and postmortem production of hydrogen sulfide and its metabolites'. In: *Forensic Sci. Int.* 340 (111426 1st Nov. 2022), p. 111426. DOI: 10.1016/j.forsciint.2022.111426.

[454] Jiawei Yang et al. 'Water volume influences antibiotic resistomes and microbiomes during fish corpse decomposition'. In: *Sci. Total Environ.* 789 (147977 1st Oct. 2021), p. 147977. DOI: 10.1016/j.scitotenv.2021.147977.

[455] Rui Zhou et al. 'Carcass decomposition influences the metabolic profiles and enriches noxious metabolites in different water types by widely targeted metabolomics'. In: *Chemosphere* 269 (129400 Apr. 2021), p. 129400. DOI: 10.1016/j.chemosphere.2020.129400.

[456] Hiroaki Sato et al. 'Determination of putrefactive amine and ammonia concentrations around decomposed corpses'. In: *J. Toxicol. Sci.* 50 (2 2025), pp. 75–81. DOI: 10.2131/jts.50.75.

[457] Suraj Melkani et al. 'Understanding the mechanisms of hydrolytic enzyme mediated organic matter decomposition under different land covers within a subtropical preserve'. In: *Front. Environ. Sci.* 13 (1564047 24th Apr. 2025), p. 1564047. DOI: 10.3389/fenvs.2025.1564047.

[458] Nicholas J Reichart et al. 'Impact of moisture on microbial decomposition phenotypes and enzyme dynamics'. In: *ISME J.* 19 (1 2nd Jan. 2025), wraf250. DOI: 10.1093/ismejo/wraf250.

[459] A-M Farnet et al. 'The importance of water availability in the reaction equilibrium of hydrolases in forest litters from a Mediterranean area: a study on lipases: The influence of water activity on enzymes in litters'. In: *Eur. J. Soil Sci.* 64 (5 Oct. 2013), pp. 661–666. DOI: 10.1111/ejss.12069.

[460] Drake Mboowa, Vinay Khatri and Jack N Saddler. 'The use of fluorescent protein-tagged carbohydrate-binding modules to evaluate the influence of drying on cellulose accessibility and enzymatic hydrolysis'. In: *RSC Adv.* 10 (45 15th July 2020), pp. 27152–27160. DOI: 10.1039/d0ra05333c.

[461] Wenxuan Mo and Bo Li. 'Initial characteristics of the dried poplar fiber as an accessibility indicator for its enzymatic digestibility in the whole hydrolysis process'. In: *Wood Sci. Technol.* 55 (5 Sept. 2021), pp. 1337–1357. DOI: 10.1007/s00226-021-01318-1.

[462] Yuanning Zhang et al. 'Hydrodynamics, diagenesis and hypoxia variably drive benthic oxygen flux in a river-reservoir system'. In: *Water Resour. Res.* 60 (1 Jan. 2024). DOI: 10.1029/2023wr035449.

[463] E S Bernhardt et al. 'The metabolic regimes of flowing waters: Metabolic regimes'. In: *Limnol. Oceanogr.* 63 (S1 Mar. 2018), S99–S118. DOI: 10.1002/lno.10726.

[464] D A Beard and J B Bassingthwaighte. 'Advection and diffusion of substances in biological tissues with complex vascular networks'. In: *Ann. Biomed. Eng.* 28 (3 Mar. 2000), pp. 253–268. DOI: 10.1114/1.273.

[465] Teamrat A Ghezzehei et al. 'On the role of soil water retention characteristic on aerobic microbial respiration'. In: *Biogeosciences* 16 (6 21st Mar. 2019), pp. 1187–1209. DOI: 10.5194/bg-16-1187-2019.

[466] Juan de la Cruz Jiménez and Ole Pedersen. 'Oxygen consumption and diffusional resistance both determine maximum root length'. In: *J. Exp. Bot.* (20th Jan. 2026), erag030. DOI: 10.1093/jxb/erag030.

[467] Ralf Conrad. 'Methane production in soil environments-anaerobic biogeochemistry and microbial life between flooding and desiccation'. In: *Microorganisms* 8 (6 11th June 2020), E881. DOI: 10.3390/microorganisms8060881.

[468] Meret Aeppli et al. 'Redox properties of solid phase electron acceptors affect anaerobic microbial respiration under oxygen-limited conditions in floodplain soils'. In: *Environ. Sci. Technol.* 56 (23 6th Dec. 2022), pp. 17462–17470. DOI: 10.1021/acs.est.2c05797.

[469] Ye Li et al. 'Oxygen availability regulates the quality of soil dissolved organic matter by mediating microbial metabolism and iron oxidation'. In: *Glob. Chang. Biol.* 28 (24 Dec. 2022), pp. 7410–7427. DOI: 10.1111/gcb.16445.

[470] Cam G Anderson et al. 'Seasonal controls on microbial depolymerization and oxidation of organic matter in floodplain soils'. In: *Environ. Sci. Technol.* (15th Sept. 2024). DOI: 10.1021/acs.est.4c05109.

[471] Ting Liu et al. 'Iron-driven fast decomposition of soil carbon under periodic Anoxia'. In: *Glob. Chang. Biol.* 31 (4 Apr. 2025), e70184. DOI: 10.1111/gcb.70184.

[472] Gregory A Cutter et al. 'Multiple oxidation state trace elements in suboxic waters off Peru: In situ redox processes and advective/diffusive horizontal transport'. In: *Mar. Chem.* 201 (Apr. 2018), pp. 77–89. DOI: 10.1016/j.marchem.2018.01.003.

[473] Chayan Lahiri and Gregg R Davidson. 'Heterogeneous oxygenation of wetland soils with increasing inundation: Redox potential, water depth, and preferential flow paths'. In: *Hydrol. Process.* 34 (6 15th Mar. 2020), pp. 1350–1358. DOI: 10.1002/hyp.13654.

[474] Ember M Morrissey et al. 'Salinity affects microbial activity and soil organic matter content in tidal wetlands'. In: *Glob. Chang. Biol.* 20 (4 Apr. 2014), pp. 1351–1362. DOI: 10.1111/gcb.12431.

[475] Jo A Werba et al. 'Effects of diversity and coalescence of species assemblages on ecosystem function at the margins of an environmental shift'. In: *PeerJ* 8 (e8608 9th Mar. 2020), e8608. DOI: 10.7717/peerj.8608.

[476] Lei Gao et al. 'Salinity-induced changes in diversity, stability, and functional profiles of microbial communities in different saline lakes in arid areas'. In: *Microb. Ecol.* 87 (1 1st Nov. 2024), p. 135. DOI: 10.1007/s00248-024-02442-8.

[477] Katherine Salazar-Alekseyeva, Gerhard J Herndl and Federico Baltar. 'Influence of salinity on the extracellular enzymatic activities of marine pelagic fungi'. In: *J. Fungi (Basel)* 10 (2 13th Feb. 2024), p. 152. DOI: 10.3390/jof10020152.

[478] Jonathon B Van Gray and Paul Ayayee. 'Examining the impacts of salt specificity on freshwater microbial community and functional potential following salinization'. In: *Environ. Microbiol.* 26 (5 May 2024), e16628. DOI: 10.1111/1462-2920.16628.

[479] Ashim Kumar Das et al. 'The impact of flooding on soil microbial communities and their functions: A review'. In: *Stresses* 5 (2 2nd May 2025), p. 30. DOI: 10.3390/stresses5020030.

[480] Chris L Dupont et al. 'Functional tradeoffs underpin salinity-driven divergence in microbial community composition'. In: *PLoS One* 9 (2 27th Feb. 2014), e89549. DOI: 10.1371/journal.pone.0089549.

[481] Chongxin Qian et al. 'Effects of salinity on anaerobic digestion: Performance, microbial physiology, and community dynamics'. In: *Bioresour. Technol.* 431 (132619 1st Sept. 2025), p. 132619. DOI: 10.1016/j.biortech.2025.132619.

[482] Lorena S Miranda et al. 'Adsorption–desorption behavior of heavy metals in aquatic environments: Influence of sediment, water and metal ionic properties'. In: *J. Hazard. Mater.* 421 (126743 5th Jan. 2022), p. 126743. DOI: 10.1016/j.jhazmat.2021.126743.

[483] Susan George et al. 'Dynamic modelling the effects of ionic strength and ion complexation on trace metal speciation during anaerobic digestion'. In: *J. Environ. Manage.* 343 (118144 1st Oct. 2023), p. 118144. DOI: 10.1016/j.jenvman.2023.118144.

[484] Rakesh Roshan Gantayat and Vetrimurugan Elumalai. 'Salinity-induced changes in heavy metal behavior and mobility in semi-arid coastal aquifers: A comprehensive review'. In: *Water (Basel)* 16 (7 5th Apr. 2024), p. 1052. DOI: 10.3390/w16071052.

[485] Connie A Rojas et al. 'Organic electron donors and terminal electron acceptors structure anaerobic microbial communities and interactions in a permanently stratified sulfidic lake'. In: *Front. Microbiol.* 12 (620424 23rd Apr. 2021), p. 620424. DOI: 10.3389/fmicb.2021.620424.

[486] Alina Mostovaya et al. 'Sulfate- and iron-dependent anaerobic methane oxidation occurring side-by-side in freshwater lake sediment'. In: *Limnol. Oceanogr.* 67 (1 Jan. 2022), pp. 231–246. DOI: 10.1002/lno.11988.

[487] Debarati Bhaduri et al. 'Interlinked chemical-biological processes in anoxic waterlogged soil – A review'. In: *Indian J. Agric. Sci.* 87 (12 14th Dec. 2017), pp. 1587–1599. DOI: 10.56093/ijas.v87i12.76483.

[488] K L Straub, M Benz and B Schink. 'Iron metabolism in anoxic environments at near neutral pH'. In: *FEMS Microbiol. Ecol.* 34 (3 Jan. 2001), pp. 181–186. DOI: 10.1111/j.1574-6941.2001.tb00768.x.

[489] Caroline M Plugge et al. 'Metabolic flexibility of sulfate-reducing bacteria'. In: *Front. Microbiol.* 2 (2nd May 2011), p. 81. DOI: 10.3389/fmicb.2011.00081.

[490] Roey Angel, Peter Claus and Ralf Conrad. 'Methanogenic archaea are globally ubiquitous in aerated soils and become active under wet anoxic conditions'. In: *ISME J.* 6 (4 Apr. 2012), pp. 847–862. DOI: 10.1038/ismej.2011.141.

[491] James L Caruso. 'Decomposition changes in bodies recovered from water'. In: *Acad. Forensic Pathol.* 6 (1 Mar. 2016), pp. 19–27. DOI: 10.23907/2016.003.

[492] Václav Kočí, Jaroslav Šesták and Robert Černý. 'Thermal inertia and evaluation of reaction kinetics: A critical review'. In: *Measurement (Lond.)* 198 (111354 July 2022), p. 111354. DOI: 10.1016/j.measurement.2022.111354.

[493] Juan G Rubalcaba et al. 'Oxygen limitation may affect the temperature and size dependence of metabolism in aquatic ectotherms'. In: *Proc. Natl. Acad. Sci. U. S. A.* 117 (50 15th Dec. 2020), pp. 31963–31968. DOI: 10.1073/pnas.2003292117.

[494] Jiwen Liu et al. 'Seasonal succession and temperature response pattern of a microbial community in the Yellow Sea Cold Water Mass'. In: *Appl. Environ. Microbiol.* 88 (17 13th Sept. 2022), e0116922. DOI: 10.1128/aem.01169-22.

[495] A Grunenwald et al. 'Novel contribution on the diagenetic physicochemical features of bone and teeth minerals, as substrates for ancient DNA typing'. In: *Anal. Bioanal. Chem.* 406 (19 July 2014), pp. 4691–4704. DOI: 10.1007/s00216-014-7863-z.

[496] H I Hollund et al. 'Are teeth better? Histological characterization of diagenesis in archaeological bone-tooth pairs and a discussion of the consequences for archaeometric sample selection and analyses'. In: *Int. J. Osteoarchaeol.* 25 (6 Nov. 2015), pp. 901–911. DOI: 10.1002/oa.2376.

[497] Christopher Kendall et al. 'Diagenesis of archaeological bone and tooth'. In: *Palaeogeogr. Palaeoclimatol. Palaeoecol.* 491 (Feb. 2018), pp. 21–37. DOI: 10.1016/j.palaeo.2017.11.041.

[498] Valentina Caruso et al. 'Bone diagenesis in archaeological and contemporary human remains: an investigation of bone 3D microstructure and minero-chemical assessment'. In: *Archaeol. Anthropol. Sci.* 12 (8 Aug. 2020). DOI: 10.1007/s12520-020-01090-6.

[499] Giulia Gallo et al. 'Characterization of structural changes in modern and archaeological burnt bone: Implications for differential preservation bias'. In: *PLoS One* 16 (7 28th July 2021), e0254529. DOI: 10.1371/journal.pone.0254529.

[500] L Gatti et al. 'Combining elemental and immunochemical analyses to characterize diagenetic alteration patterns in ancient skeletal remains'. In: *Sci. Rep.* 12 (1 24th Mar. 2022), p. 5112. DOI: 10.1038/s41598-022-08979-3.

[501] Cinzia Scaggion et al. 'An FTIR-based model for the diagenetic alteration of archaeological bones'. In: *J. Archaeol. Sci.* 161 (105900 Jan. 2024), p. 105900. DOI: 10.1016/j.jas.2023.105900.

[502] Yuping Li and Conrado Aparicio. 'Discerning the subfibrillar structure of mineralized collagen fibrils: a model for the ultrastructure of bone'. In: *PLoS One* 8 (9 23rd Sept. 2013), e76782. DOI: 10.1371/journal.pone.0076782.

[503] Arun K Nair et al. 'Molecular mechanics of mineralized collagen fibrils in bone'. In: *Nat. Commun.* 4 (1 2013), p. 1724. DOI: 10.1038/ncomms2720.

[504] Daniel J Buss et al. 'Hierarchical organization of bone in three dimensions: A twist of twists'. In: *J. Struct. Biol. X* 6 (100057 2022), p. 100057. DOI: 10.1016/j.yjsbx.2021.100057.

[505] Yan Liu, Dan Luo and Tie Wang. 'Hierarchical structures of bone and bioinspired bone tissue engineering'. In: *Small* 12 (34 Sept. 2016), pp. 4611–4632. DOI: 10.1002/smll.201600626.

[506] Natalie Reznikov et al. 'Fractal-like hierarchical organization of bone begins at the nanoscale'. In: *Science* 360 (6388 4th May 2018), eaao2189. DOI: 10.1126/science.aao2189.

[507] Noemi Procopio et al. 'Proteome variation with collagen yield in ancient bone'. In: *J. Proteome Res.* 20 (3 5th Mar. 2021), pp. 1754–1769. DOI: 10.1021/acs.jproteome.0c01014.

[508] Guillaume Falgayrac et al. 'Bone molecular modifications induced by diagenesis followed-up for 12 months'. In: *Biology (Basel)* 11 (10 21st Oct. 2022), p. 1542. DOI: 10.3390/biology11101542.

[509] M J Collins et al. 'The survival of organic matter in bone: a review'. In: *Archaeometry* 44 (3 Aug. 2002), pp. 383–394. DOI: 10.1111/1475-4754.t01-1-00071.

[510] Francesco Berna, Alan Matthews and Stephen Weiner. 'Solubilities of bone mineral from archaeological sites: the recrystallization window'. In: *J. Archaeol. Sci.* 31 (7 July 2004), pp. 867–882. DOI: 10.1016/j.jas.2003.12.003.

[511] Po-Yu Chen et al. 'Minerals form a continuum phase in mature cancellous bone'. In: *Calcif. Tissue Int.* 88 (5 May 2011), pp. 351–361. DOI: 10.1007/s00223-011-9462-8.

[512] Sarah W Keenan. 'Thermodynamic stabilities of apatite phases in a wetland system: Implications for bone diagenesis'. In: *Appl. Geochem.* 148 (105546 Jan. 2023), p. 105546. DOI: 10.1016/j.apgeochem.2022.105546.

[513] Qiang Li et al. 'Fossilization and low-grade metamorphism of Triassic marine reptiles from southwest China: A continuum of apatite transformation and fluorite precipitation'. In: *Chem. Geol.* 670 (122437 20th Dec. 2024), p. 122437. DOI: 10.1016/j.chemgeo.2024.122437.

[514] Sarah W Keenan et al. 'Evaluating the consequences of diagenesis and fossilization on bioapatite lattice structure and composition'. In: *Chem. Geol.* 413 (C Oct. 2015), pp. 18–27. DOI: 10.1016/j.chemgeo.2015.08.005.

[515] Sarah W Keenan and Annette Summers Engel. 'Early diagenesis and recrystallization of bone'. In: *Geochim. Cosmochim. Acta* 196 (C Jan. 2017), pp. 209–223. DOI: 10.1016/j.gca.2016.09.033.

[516] Anna G Kral et al. 'Rapid alteration of cortical bone in fresh- and seawater solutions visualized and quantified from the millimeter down to the atomic scale'. In: *Chem. Geol.* 609 (121060 20th Oct. 2022), p. 121060. DOI: 10.1016/j.chemgeo.2022.121060.

[517] Anna G Kral et al. 'Phosphate uptake is an essential process for rapid bone mineralization during early diagenesis – evidence from bone alteration experiments'. In: *Geochim. Cosmochim. Acta* 375 (June 2024), pp. 173–185. DOI: 10.1016/j.gca.2024.04.004.

[518] Oliver Wings. 'Authigenic minerals in fossil bones from the Mesozoic of England: poor correlation with depositional environments'. In: *Palaeogeogr. Palaeoclimatol. Palaeoecol.* 204 (1-2 Feb. 2004), pp. 15–32. DOI: 10.1016/s0031-0182(03)00709-0.

[519] Paul Ullmann, Kristyn Voegele and Kenneth Lacovara. 'Actualistic testing of the influence of groundwater chemistry on degradation of collagen I in bone'. In: *Minerals (Basel)* 13 (5 25th Apr. 2023), p. 596. DOI: 10.3390/min13050596.

[520] René-Paul Eustache et al. 'Medusa's gaze: Cell traces and fibrils but no collagen in permineralized Jurassic ichthyosaur bone'. In: *iScience* 28 (1 17th Jan. 2025), p. 111523. DOI: 10.1016/j.isci.2024.111523.

[521] Sarah W Keenan. 'From bone to fossil: A review of the diagenesis of bioapatite'. In: *Am. Mineral.* 101 (9 1st Sept. 2016), pp. 1943–1951. DOI: 10.2138/am-2016-5737.

[522] H Q Woodard and D R White. 'The composition of body tissues'. In: *Br. J. Radiol.* 59 (708 Dec. 1986), pp. 1209–1218. DOI: 10.1259/0007-1285-59-708-1209.

[523] Janusz Wiesław Błaszczyk. 'Biomolecular basis of life'. In: *Metabolites* 15 (6 16th June 2025), p. 404. DOI: 10.3390/metabo15060404.

[524] Thomas Clements and Sarah Gabbott. *Pers. comm.* 13th Apr. 2022.

[525] Landon A Anderson. 'A chemical framework for the preservation of fossil vertebrate cells and soft tissues'. In: *Earth Sci. Rev.* 240 (104367 18th May 2023), p. 104367. DOI: 10.1016/j.earscirev.2023.104367.

[526] Mara S Tapia, Stella M Alzamora and Jorge Chirife. 'Effects of water activity ($A_w$) on microbial stability: As a hurdle in food preservation'. In: *Water Activity in Foods*. Oxford, UK: Blackwell Publishing Ltd, 7th Apr. 2008, pp. 239–271. DOI: 10.1002/9780470376454.ch10.

[527] Osman Erkmen and T Faruk Bozoglu. 'Food preservation by reducing water activity'. In: *Food Microbiology: Principles into Practice*. Chichester, UK: John Wiley & Sons, Ltd, 22nd Apr. 2016, pp. 44–58. DOI: 10.1002/9781119237860.ch30.

[528] Andrew J Maneffa et al. 'Water activity in liquid food systems: A molecular scale interpretation'. In: *Food Chem.* 237 (15th Dec. 2017), pp. 1133–1138. DOI: 10.1016/j.foodchem.2017.06.046.

[529] Mario González-Jiménez et al. 'Lifting hofmeister's curse: Impact of cations on diffusion, hydrogen bonding, and clustering of water'. In: *J. Am. Chem. Soc.* 146 (1 10th Jan. 2024), pp. 368–376. DOI: 10.1021/jacs.3c09421.

[530] K Rezaei, E Jenab and F Temelli. 'Effects of water on enzyme performance with an emphasis on the reactions in supercritical fluids'. In: *Crit. Rev. Biotechnol.* 27 (4 Oct. 2007), pp. 183–195. DOI: 10.1080/07388550701775901.

[531] Naoto Tani et al. 'Postmortem water contents of major organs with regard to the cause of death'. In: *J. Forensic Leg. Med.* 65 (July 2019), pp. 48–54. DOI: 10.1016/j.jflm.2019.05.003.

[532] S Aturaliya and A Lukasewycz. 'Experimental forensic and bioanthropological aspects of soft tissue taphonomy: 1. Factors influencing postmortem tissue desiccation rate'. In: *J. Forensic Sci.* 44 (5 Sept. 1999), pp. 893–896. DOI: 10.1520/jfs12011j.

[533] Joseph L Watson et al. 'Macromolecular condensation buffers intracellular water potential'. In: *Nature* 623 (7988 Nov. 2023), pp. 842–852. DOI: 10.1038/s41586-023-06626-z.

[534] Valeria Conti Nibali and Martina Havenith. 'New insights into the role of water in biological function: studying solvated biomolecules using terahertz absorption spectroscopy in conjunction with molecular dynamics simulations'. In: *J. Am. Chem. Soc.* 136 (37 17th Sept. 2014), pp. 12800–12807. DOI: 10.1021/ja504441h.

[535] Saumyak Mukherjee and Lars V Schäfer. 'Spatially resolved hydration thermodynamics in biomolecular systems'. In: *J. Phys. Chem. B* 126 (20 26th May 2022), pp. 3619–3631. DOI: 10.1021/acs.jpcb.2c01088.

[536] Jayangika N Dahanayake and Katie R Mitchell-Koch. 'How does solvation layer mobility affect protein structural dynamics?' In: *Front. Mol. Biosci.* 5 (13th July 2018), p. 65. DOI: 10.3389/fmolb.2018.00065.

[537] Paulette Sofia Romero-Perez et al. 'When phased without water: Biophysics of cellular desiccation, from biomolecules to condensates'. In: *Chem. Rev.* 123 (14 26th July 2023), pp. 9010–9035. DOI: 10.1021/acs.chemrev.2c00659.

[538] Pedro H Lebre, Pieter De Maayer and Don A Cowan. 'Xerotolerant bacteria: surviving through a dry spell'. In: *Nat. Rev. Microbiol.* 15 (5 20th May 2017), pp. 285–296. DOI: 10.1038/nrmicro.2017.16.

[539] W D Grant. 'Life at low water activity'. In: *Philos. Trans. R. Soc. Lond. B Biol. Sci.* 359 (1448 29th Aug. 2004), 1249–66, discussion 1266–7. DOI: 10.1098/rstb.2004.1502.

[540] Aharon Oren. 'Microbial life at high salt concentrations: phylogenetic and metabolic diversity'. In: *Saline Systems* 4 (1 15th Apr. 2008), p. 2. DOI: 10.1186/1746-1448-4-2.

[541] Vincent Robert Guy Greffe and Jan Michiels. 'Desiccation-induced cell damage in bacteria and the relevance for inoculant production'. In: *Appl. Microbiol. Biotechnol.* 104 (9 13th May 2020), pp. 3757–3770. DOI: 10.1007/s00253-020-10501-6.

[542] Daniela Billi and Malcolm Potts. 'Life and death of dried prokaryotes'. In: *Res. Microbiol.* 153 (1 1st Jan. 2002), pp. 7–12. DOI: 10.1016/s0923-2508(01)01279-7.

[543] M Potts. 'Desiccation tolerance of prokaryotes'. In: *Microbiol. Rev.* 58 (4 Dec. 1994), pp. 755–805. DOI: 10.1128/mr.58.4.755-805.1994.

[544] Ana Belén Uceda et al. 'An overview on glycation: molecular mechanisms, impact on proteins, pathogenesis, and inhibition'. In: *Biophys. Rev.* 16 (2 Apr. 2024), pp. 189–218. DOI: 10.1007/s12551-024-01188-4.

[545] Miriam Saltmarch and Theodore P Labuza. 'Nonenzymatic browning via the Maillard reaction in foods'. In: *Diabetes* 31 (Supplement_3 1st June 1982), pp. 29–36. DOI: 10.2337/diab.31.3.s29.

[546] Moon B Yim et al. 'Protein glycation: Creation of catalytic sites for free radical generation'. In: *Ann. N. Y. Acad. Sci.* 928 (1 Apr. 2001), pp. 48–53. DOI: 10.1111/j.1749-6632.2001.tb05634.x.

[547] Tomasz Grzyb and Aleksandra Skłodowska. 'Introduction to bacterial anhydrobiosis: A general perspective and the mechanisms of desiccation-associated damage'. In: *Microorganisms* 10 (2 12th Feb. 2022), p. 432. DOI: 10.3390/microorganisms10020432.

[548] Wendell Q Sun and A Carl Leopold. 'Cytoplasmic vitrification and survival of anhydrobiotic organisms'. In: *Comp. Biochem. Physiol. A Comp. Physiol.* 117 (3 1st July 1997), pp. 327–333. DOI: 10.1016/s0300-9629(96)00271-x.

[549] Julia Buitink and Olivier Leprince. 'Glass formation in plant anhydrobiotes: survival in the dry state'. In: *Cryobiology* 48 (3 June 2004), pp. 215–228. DOI: 10.1016/j.cryobiol.2004.02.011.

[550] John F Ramirez et al. 'Water content, transition temperature and fragility influence protection and anhydrobiotic capacity'. In: *BBA Adv.* 5 (100115 24th Jan. 2024), p. 100115. DOI: 10.1016/j.bbadva.2024.100115.

[551] J H Crowe, J F Carpenter and L M Crowe. 'The role of vitrification in anhydrobiosis'. In: *Annu. Rev. Physiol.* 60 (1 1998), pp. 73–103. DOI: 10.1146/annurev.physiol.60.1.73.

[552] Yrjö Roos and Marcus Karel. 'Water and molecular weight effects on glass transitions in amorphous carbohydrates and carbohydrate solutions'. In: *J. Food Sci.* 56 (6 1st Nov. 1991), pp. 1676–1681. DOI: 10.1111/j.1365-2621.1991.tb08669.x.

[553] Adrien Lerbret and Frédéric Affouard. 'Molecular packing, hydrogen bonding, and fast dynamics in lysozyme/trehalose/glycerol and trehalose/glycerol glasses at low hydration'. In: *J. Phys. Chem. B* 121 (40 12th Oct. 2017), pp. 9437–9451. DOI: 10.1021/acs.jpcb.7b07082.

[554] Gil I Olgenblum, Liel Sapir and Daniel Harries. 'Properties of aqueous trehalose mixtures: Glass transition and hydrogen bonding'. In: *J. Chem. Theory Comput.* 16 (2 11th Feb. 2020), pp. 1249–1262. DOI: 10.1021/acs.jctc.9b01071.

[555] F A Hoekstra, E A Golovina and J Buitink. 'Mechanisms of plant desiccation tolerance'. In: *Trends Plant Sci.* 6 (9 Sept. 2001), pp. 431–438. DOI: 10.1016/s1360-1385(01)02052-0.

[556] Lois M Crowe. 'Lessons from nature: the role of sugars in anhydrobiosis'. In: *Comp. Biochem. Physiol. A Mol. Integr. Physiol.* 131 (3 1st Mar. 2002), pp. 505–513. DOI: 10.1016/s1095-6433(01)00503-7.

[557] Julia A Brom, Ruta G Petrikis and Gary J Pielak. 'How sugars protect dry protein structure'. In: *Biochemistry* 62 (5 7th Mar. 2023), pp. 1044–1052. DOI: 10.1021/acs.biochem.2c00692.

[558] Maarten A Mensink et al. 'How sugars protect proteins in the solid state and during drying (review): Mechanisms of stabilization in relation to stress conditions'. In: *Eur. J. Pharm. Biopharm.* 114 (May 2017), pp. 288–295. DOI: 10.1016/j.ejpb.2017.01.024.

[559] Johanna-Barbara Linse, Tobias M Fischbach and Jochen S Hub. 'How protein hydration depends on amino acid composition, peptide conformation, and force fields'. In: *Biophys. J.* 125 (1 6th Jan. 2026), pp. 255–269. DOI: 10.1016/j.bpj.2025.11.2683.

[560] Juliana Sakamoto Yoneda et al. 'Differential dehydration effects on globular proteins and intrinsically disordered proteins during film formation: Dehydration Effects on Protein Structures'. In: *Protein Sci.* 26 (4 Apr. 2017), pp. 718–726. DOI: 10.1002/pro.3118.

[561] F-X Gallat et al. 'Dynamical coupling of intrinsically disordered proteins and their hydration water: comparison with folded soluble and membrane proteins'. In: *Biophys. J.* 103 (1 3rd July 2012), pp. 129–136. DOI: 10.1016/j.bpj.2012.05.027.

[562] Thomas C Boothby et al. 'Tardigrades use intrinsically disordered proteins to survive desiccation'. In: *Mol. Cell* 65 (6 16th Mar. 2017), 975–984.e5. DOI: 10.1016/j.molcel.2017.02.018.

[563] Brett Janis, Clinton Belott and Michael A Menze. 'Role of intrinsic disorder in animal desiccation tolerance'. In: *Proteomics* 18 (21-22 Nov. 2018), e1800067. DOI: 10.1002/pmic.201800067.

[564] Shraddha Kc et al. 'Disordered proteins interact with the chemical environment to tune their protective function during drying'. In: *Elife* 13 (RP97231 19th Nov. 2024), RP97231. DOI: 10.7554/eLife.97231.

[565] Loyd V Allen Jr. 'Quality control: Water activity considerations for beyond-use dates'. In: *Int. J. Pharm. Compd.* 22 (4 July 2018), pp. 288–293.

[566] J Chirife and M P del Buera. 'Water activity, glass transition and microbial stability in concentrated/semimoist food systems'. In: *J. Food Sci.* 59 (5 1994), pp. 921–927. DOI: 10.1111/j.1365-2621.1994.tb08159.x.

[567] Micha Peleg. 'Models of the water activity effect on microbial growth rate and initiation'. In: *Appl. Microbiol. Biotechnol.* 106 (4 Feb. 2022), pp. 1375–1382. DOI: 10.1007/s00253-022-11792-7.

[568] Alberto Schiraldi. 'Microbial growth: Role of water activity and viscoelasticity of the cell compartments'. In: *Int. J. Mol. Sci.* 26 (17 1st Sept. 2025), p. 8508. DOI: 10.3390/ijms26178508.

[569] Martina Schweiger et al. 'Measurement of lipolysis'. In: *Methods Enzymol.* Methods in enzymology 538 (2014), pp. 171–193. DOI: 10.1016/B978-0-12-800280-3.00010-4.

[570] K Potthast, L Acker and R Hamm. 'Influence of water activity on the enzymatic changes in freeze-dehydrated muscle III. The breakdown of muscle lipids (author's transl): III. Abbau von Muskellipiden'. In: *Z. Lebensm. Unters. Forsch.* 165 (1 30th Sept. 1977), pp. 15–17. DOI: 10.1007/bf01461045.

[571] Alessia Gennaro et al. 'Understanding the dehydration stress in lipid vesicles by a combined quartz crystal microbalance and dielectric spectroscopy study'. In: *Phys. Status Solidi (A)* 217 (13 July 2020), p. 1900986. DOI: 10.1002/pssa.201900986.

[572] Sheeba Malik and Ananya Debnath. 'Dehydration induced dynamical heterogeneity and ordering mechanism of lipid bilayers'. In: *J. Chem. Phys.* 154 (17 7th May 2021), p. 174904. DOI: 10.1063/5.0044614.

[573] Christopher J Garvey et al. 'Phase separation in a ternary DPPC/DOPC/POPC system with reducing hydration'. In: *J. Colloid Interface Sci.* 638 (15th May 2023), pp. 719–732. DOI: 10.1016/j.jcis.2023.01.145.

[574] Madhurima Chattopadhyay et al. 'Hydration layer of only a few molecules controls lipid mobility in biomimetic membranes'. In: *J. Am. Chem. Soc.* 143 (36 15th Sept. 2021), pp. 14551–14562. DOI: 10.1021/jacs.1c04314.

[575] Hanna Orlikowska-Rzeznik et al. 'Dehydration of lipid membranes drives redistribution of cholesterol between lateral domains'. In: *J. Phys. Chem. Lett.* 15 (16 25th Apr. 2024), pp. 4515–4522. DOI: 10.1021/acs.jpclett.4c00332.

[576] Abhay Kumar and Snehasis Daschakraborty. 'What are the essential water molecules in regulating lipid membrane fluidity?' In: *J. Phys. Chem. B* 129 (24 19th June 2025), pp. 5998–6008. DOI: 10.1021/acs.jpcb.5c02234.

[577] Leann Barden and Eric A Decker. 'Lipid oxidation in low-moisture food: A review'. In: *Crit. Rev. Food Sci. Nutr.* 56 (15 17th Nov. 2016), pp. 2467–2482. DOI: 10.1080/10408398.2013.848833.

[578] J R Requena et al. 'Lipoxidation products as biomarkers of oxidative damage to proteins during lipid peroxidation reactions'. In: *Nephrol. Dial. Transplant* 11 Suppl 5 (supp5 1996), pp. 48–53. DOI: 10.1093/ndt/11.supp5.48.

[579] Elena Garre et al. 'Oxidative stress responses and lipid peroxidation damage are induced during dehydration in the production of dry active wine yeasts'. In: *Int. J. Food Microbiol.* 136 (3 1st Jan. 2010), pp. 295–303. DOI: 10.1016/j.ijfoodmicro.2009.10.018.

[580] Živko Jovanović et al. 'Characterization of oxidative and antioxidative events during dehydration and rehydration of resurrection plant Ramonda nathaliae'. In: *Plant Growth Regul.* 64 (3 July 2011), pp. 231–240. DOI: 10.1007/s10725-011-9563-4.

[581] Manoj Kumar et al. 'Desiccation induced oxidative stress and its biochemical responses in intertidal red alga Gracilaria corticata (Gracilariales, Rhodophyta)'. In: *Environ. Exp. Bot.* 72 (2 Sept. 2011), pp. 194–201. DOI: 10.1016/j.envexpbot.2011.03.007.

[582] Suruchi Parkhey, S C Naithani and S Keshavkant. 'ROS production and lipid catabolism in desiccating Shorea robusta seeds during aging'. In: *Plant Physiol. Biochem.* 57 (Aug. 2012), pp. 261–267. DOI: 10.1016/j.plaphy.2012.06.008.

[583] Qi Zhang et al. 'Formation mechanisms of reactive carbonyl species from fatty acids in dry-cured fish during storage in the presence of free radicals'. In: *Journal of Future Foods* 1 (2 Dec. 2021), pp. 203–210. DOI: 10.1016/j.jfutfo.2022.01.010.

[584] Julian Garrec et al. 'Lipid peroxidation in membranes: The peroxyl radical does not "float"'. In: *J. Phys. Chem. Lett.* 5 (10 15th May 2014), pp. 1653–1658. DOI: 10.1021/jz500502q.

[585] Jason Bosch et al. 'Microbial anhydrobiosis'. In: *Environ. Microbiol.* 23 (11 Nov. 2021), pp. 6377–6390. DOI: 10.1111/1462-2920.15699.

[586] Erhard Bremer and Reinhard Krämer. 'Responses of microorganisms to osmotic stress'. In: *Annu. Rev. Microbiol.* 73 (1 8th Sept. 2019), pp. 313–334. DOI: 10.1146/annurev-micro-020518-115504.

[587] J M Wood et al. 'Osmosensing and osmoregulatory compatible solute accumulation by bacteria'. In: *Comp. Biochem. Physiol. A Mol. Integr. Physiol.* 130 (3 Oct. 2001), pp. 437–460. DOI: 10.1016/s1095-6433(01)00442-1.

[588] Bert Poolman et al. 'How do membrane proteins sense water stress?: Osmosensing mechanisms'. In: *Mol. Microbiol.* 44 (4 May 2002), pp. 889–902. DOI: 10.1046/j.1365-2958.2002.02894.x.

[589] Maximino Manzanera. 'Dealing with water stress and microbial preservation'. In: *Environ. Microbiol.* 23 (7 July 2021), pp. 3351–3359. DOI: 10.1111/1462-2920.15096.

[590] J M Stark and M K Firestone. 'Mechanisms for soil moisture effects on activity of nitrifying bacteria'. In: *Appl. Environ. Microbiol.* 61 (1 Jan. 1995), pp. 218–221. DOI: 10.1128/aem.61.1.218-221.1995.

[591] Andrew Stevenson et al. 'Glycerol enhances fungal germination at the water-activity limit for life: Glycerol enhances germination at low water-activity'. In: *Environ. Microbiol.* 19 (3 Mar. 2017), pp. 947–967. DOI: 10.1111/1462-2920.13530.

[592] Jeffry S Nyman et al. 'The influence of water removal on the strength and toughness of cortical bone'. In: *J. Biomech.* 39 (5 2006), pp. 931–938. DOI: 10.1016/j.jbiomech.2005.01.012.

[593] Luca Bertinetti et al. 'Osmotically driven tensile stress in collagen-based mineralized tissues'. In: *J. Mech. Behav. Biomed. Mater.* 52 (Dec. 2015), pp. 14–21. DOI: 10.1016/j.jmbbm.2015.03.010.

[594] Richard G Haverkamp et al. 'Collagen dehydration'. In: *Int. J. Biol. Macromol.* 216 (1st Sept. 2022), pp. 140–147. DOI: 10.1016/j.ijbiomac.2022.06.180.

[595] Dhana Frerichs, Andrew Vidler and Christos Gatzidis. 'Computer graphics simulation of natural mummification by desiccation'. In: *Comput. Animat. Virtual Worlds* 31 (6 Nov. 2020). DOI: 10.1002/cav.1927.

[596] Konrad Spindler et al. *Human Mummies: A Global Survey of Their Status and the Techniques of Conservation*. Ed. by Konrad Spindler et al. 1996th ed. The Man in the Ice. Vienna, Austria: Springer, 17th May 1996. 296 pp.

[597] Céline Leccia, Véronique Alunni and Gérald Quatrehomme. 'Modern (forensic) mummies: A study of twenty cases'. In: *Forensic Sci. Int.* 288 (1st July 2018), 330.e1–330.e9. DOI: 10.1016/j.forsciint.2018.04.029.

[598] Ann-Sofie Ceciliason, Björn Käll and Håkan Sandler. 'Mummification in a forensic context: an observational study of taphonomic changes and the post-mortem interval in an indoor setting'. In: *Int. J. Legal Med.* 137 (4 July 2023), pp. 1077–1088. DOI: 10.1007/s00414-023-02986-3.

[599] Antonella Pedergnana et al. 'Mummified tissues'. In: *Encyclopedia of Archaeology (Second Edition)*. Elsevier, 1st Jan. 2024, pp. 941–948. DOI: 10.1016/b978-0-323-90799-6.00013-6.

[600] Donald B Anderson. 'Relative humidity or vapor pressure deficit'. In: *Ecology* 17 (2 1st Apr. 1936), pp. 277–282. DOI: 10.2307/1931468.

[601] Howell G M Edwards et al. 'Raman spectroscopy of natron: shedding light on ancient Egyptian mummification'. In: *Anal. Bioanal. Chem.* 388 (3 June 2007), pp. 683–689. DOI: 10.1007/s00216-007-1249-4.

[602] Arthur C Aufderheide. *The Scientific Study of Mummies*. Cambridge, England: Cambridge University Press, 13th Jan. 2011. 634 pp.

[603] Erich Brenner. 'Human body preservation - old and new techniques'. In: *J. Anat.* 224 (3 18th Mar. 2014), pp. 316–344. DOI: 10.1111/joa.12160.

[604] I Morimoto. 'Buddhist mummies in Japan'. In: *Kaibogaku Zasshi* 68 (4 1st Aug. 1993), pp. 381–398.

[605] Łukasz Szleszkowski et al. '"Salt mummification" - atypical method of embalming a corpse'. In: *Int. J. Legal Med.* 136 (6 24th Nov. 2022), pp. 1829–1840. DOI: 10.1007/s00414-022-02855-5.

[606] David E Pegg. 'Principles of cryopreservation'. In: *Methods Mol. Biol.* Methods in molecular biology (Clifton, N.J.) 1257 (2015), pp. 3–19. DOI: 10.1007/978-1-4939-2193-5_1.

[607] J O M Karlsson, E G Cravalho and M Toner. 'A model of diffusion-limited ice growth inside biological cells during freezing'. In: *J. Appl. Phys.* 75 (9 1st May 1994), pp. 4442–4455. DOI: 10.1063/1.355959.

[608] H D Goff. 'Measuring and interpreting the glass transition in frozen fods and model systems'. In: *Food Res. Int.* 27 (2 1st Jan. 1994), pp. 187–189. DOI: 10.1016/0963-9969(94)90160-0.

[609] Kathryn A Murray and Matthew I Gibson. 'Chemical approaches to cryopreservation'. In: *Nat. Rev. Chem.* 6 (8 18th July 2022), pp. 579–593. DOI: 10.1038/s41570-022-00407-4.

[610] Tae Hoon Jang et al. 'Cryopreservation and its clinical applications'. In: *Integr. Med. Res.* 6 (1 Mar. 2017), pp. 12–18. DOI: 10.1016/j.imr.2016.12.001.

[611] P Mazur. 'Freezing of living cells: mechanisms and implications'. In: *Am. J. Physiol.* 247 (3 Pt 1 Sept. 1984), pp. C125–42. DOI: 10.1152/ajpcell.1984.247.3.C125.

[612] Peter Kilbride et al. 'The transfer temperature from slow cooling to cryogenic storage is critical for optimal recovery of cryopreserved mammalian cells'. In: *PLoS One* 16 (11 16th Nov. 2021), e0259571. DOI: 10.1371/journal.pone.0259571.

[613] Fatemeh Amiri and James D Benson. 'A three-dimensional lattice-free agent-based model of intracellular ice formation and propagation and intercellular mechanics in liver tissues'. In: *R. Soc. Open Sci.* 11 (7 17th July 2024), p. 231337. DOI: 10.1098/rsos.231337.

[614] K Muldrew and L E McGann. 'Mechanisms of intracellular ice formation'. In: *Biophys. J.* 57 (3 Mar. 1990), pp. 525–532. DOI: 10.1016/S0006-3495(90)82568-6.

[615] Bumsoo Han and John C Bischof. 'Direct cell injury associated with eutectic crystallization during freezing'. In: *Cryobiology* 48 (1 Feb. 2004), pp. 8–21. DOI: 10.1016/j.cryobiol.2003.11.002.

[616] Geer Yang, Aili Zhang and Lisa X Xu. 'Intracellular ice formation and growth in MCF-7 cancer cells'. In: *Cryobiology* 63 (1 1st Aug. 2011), pp. 38–45. DOI: 10.1016/j.cryobiol.2011.04.007.

[617] Xiaoli Liu et al. 'Quantification of intracellular ice formation and recrystallization during freeze-thaw cycles and their relationship with the viability of pig iliac endothelium cells'. In: *Biopreserv. Biobank.* 14 (6 Dec. 2016), pp. 511–519. DOI: 10.1089/bio.2015.0111.

[618] James Wesley-Smith et al. 'Intracellular ice and cell survival in cryo-exposed embryonic axes of recalcitrant seeds of Acer saccharinum: an ultrastructural study of factors affecting cell and ice structures'. In: *Ann. Bot.* 113 (4 Mar. 2014), pp. 695–709. DOI: 10.1093/aob/mct284.

[619] Gregory M Fahy and Brian Wowk. 'Principles of ice-free cryopreservation by vitrification'. In: *Methods Mol. Biol.* Methods in molecular biology (Clifton, N.J.) 2180 (2021), pp. 27–97. DOI: 10.1007/978-1-0716-0783-1_2.

[620] Bakul S Bhatnagar, Robin H Bogner and Michael J Pikal. 'Protein stability during freezing: separation of stresses and mechanisms of protein stabilization'. In: *Pharm. Dev. Technol.* 12 (5 2007), pp. 505–523. DOI: 10.1080/10837450701481157.

[621] Enhong Cao et al. 'Effect of freezing and thawing rates on denaturation of proteins in aqueous solutions'. In: *Biotechnol. Bioeng.* 82 (6 20th June 2003), pp. 684–690. DOI: 10.1002/bit.10612.

[622] Ivonne Seifert and Wolfgang Friess. 'Freeze concentration during freezing: How does the maximally freeze concentrated solution influence protein stability?' In: *Int. J. Pharm.* 589 (119810 15th Nov. 2020), p. 119810. DOI: 10.1016/j.ijpharm.2020.119810.

[623] Iona P Garber Cohen, Pablo R Castello and F Luis González Flecha. 'Ice-induced partial unfolding and aggregation of an integral membrane protein'. In: *Biochim. Biophys. Acta* 1798 (11 Nov. 2010), pp. 2040–2047. DOI: 10.1016/j.bbamem.2010.07.035.

[624] Mónica Rosa, Christopher J Roberts and Miguel A Rodrigues. 'Connecting high-temperature and low-temperature protein stability and aggregation'. In: *PLoS One* 12 (5 4th May 2017), e0176748. DOI: 10.1371/journal.pone.0176748.

[625] Andrea Arsiccio et al. 'Heightened cold-denaturation of proteins at the ice-water interface'. In: *J. Am. Chem. Soc.* 142 (12 25th Mar. 2020), pp. 5722–5730. DOI: 10.1021/jacs.9b13454.

[626] Altug Ozcelikkale and Bumsoo Han. 'Thermal destabilization of collagen matrix hierarchical structure by freeze/thaw'. In: *PLoS One* 11 (1 14th Jan. 2016), e0146660. DOI: 10.1371/journal.pone.0146660.

[627] Alexander V Fonin et al. 'Intrinsically disordered proteins in crowded milieu: when chaos prevails within the cellular gumbo'. In: *Cell. Mol. Life Sci.* 75 (21 Nov. 2018), pp. 3907–3929. DOI: 10.1007/s00018-018-2894-9.

[628] S E Berkow et al. 'Lipases and lipids in human milk: effect of freeze-thawing and storage'. In: *Pediatr. Res.* 18 (12 Dec. 1984), pp. 1257–1262. DOI: 10.1203/00006450-198412000-00006.

[629] E Z Drobnis et al. 'Cold shock damage is due to lipid phase transitions in cell membranes: a demonstration using sperm as a model'. In: *J. Exp. Zool.* 265 (4 15th Mar. 1993), pp. 432–437. DOI: 10.1002/jez.1402650413.

[630] J Gautier et al. 'A low membrane lipid phase transition temperature is associated with a high cryotolerance of Lactobacillus delbrueckii subspecies bulgaricus CFL1'. In: *J. Dairy Sci.* 96 (9 1st Sept. 2013), pp. 5591–5602. DOI: 10.3168/jds.2013-6802.

[631] Woo Hyuk Jung et al. 'Freezing-driven ionic charge imbalance leads to pore formation and osmotic injury of lipid membranes'. In: *Comput. Biol. Med.* 189 (109960 1st May 2025), p. 109960. DOI: 10.1016/j.compbiomed.2025.109960.

[632] T Hullar and C Anastasio. 'Yields of hydrogen peroxide from the reaction of hydroxyl radical with organic compounds in solution and ice'. In: *Atmos. Chem. Phys.* 11 (14 22nd July 2011), pp. 7209–7222. DOI: 10.5194/acp-11-7209-2011.

[633] Junwei Song et al. 'Spontaneous production of H2O2 at the liquid-ice interface: A potential source of atmospheric oxidants'. In: *Environ. Sci. Technol.* 58 (51 24th Dec. 2024), pp. 22691–22699. DOI: 10.1021/acs.est.4c07546.

[634] Jianyong Wu et al. 'The overlooked driver of microplastic chemical oxidation in cold soils: Reactive oxygen species generation mediated by freeze-thaw cycles'. In: *Environ. Sci. Technol.* 59 (46 25th Nov. 2025), pp. 24987–24996. DOI: 10.1021/acs.est.5c07624.

[635] Ayla Soyer et al. 'Effects of freezing temperature and duration of frozen storage on lipid and protein oxidation in chicken meat'. In: *Food Chem.* 120 (4 15th June 2010), pp. 1025–1030. DOI: 10.1016/j.foodchem.2009.11.042.

[636] Nima Hematyar et al. 'Relationship between lipid and protein oxidation in fish'. In: *Aquac. Res.* 50 (5 May 2019), pp. 1393–1403. DOI: 10.1111/are.14012.

[637] Yulong Bao et al. 'Freezing of meat and aquatic food: Underlying mechanisms and implications on protein oxidation'. In: *Compr. Rev. Food Sci. Food Saf.* 20 (6 Nov. 2021), pp. 5548–5569. DOI: 10.1111/1541-4337.12841.

[638] Sam Al-Dalali, Cong Li and Baocai Xu. 'Effect of frozen storage on the lipid oxidation, protein oxidation, and flavor profile of marinated raw beef meat'. In: *Food Chem.* 376 (131881 15th May 2022), p. 131881. DOI: 10.1016/j.foodchem.2021.131881.

[639] Xingge Wu et al. 'Effect of freeze–thaw cycles on the oxidation of protein and fat and its relationship with the formation of heterocyclic aromatic amines and advanced glycation end products in raw meat'. In: *Molecules* 26 (5 26th Feb. 2021), p. 1264. DOI: 10.3390/molecules26051264.

[640] P Buford Price and Todd Sowers. 'Temperature dependence of metabolic rates for microbial growth, maintenance, and survival'. In: *Proc. Natl. Acad. Sci. U. S. A.* 101 (13 30th Mar. 2004), pp. 4631–4636. DOI: 10.1073/pnas.0400522101.

[641] Jackie Goordial. 'Cryomicrobial ecology: Still much to learn about life left out in the cold'. In: *mSystems* 6 (5 26th Oct. 2021), e0085221. DOI: 10.1128/mSystems.00852-21.

[642] Lavinia Iancu, Andrea Bonicelli and Noemi Procopio. 'Decomposition in an extreme cold environment and associated microbiome-prediction model implications for the postmortem interval estimation'. In: *Front. Microbiol.* 15 (13th May 2024), p. 1392716. DOI: 10.3389/fmicb.2024.1392716.

[643] James A Bradley et al. 'Active and dormant microorganisms on glacier surfaces'. In: *Geobiology* 21 (2 Mar. 2023), pp. 244–261. DOI: 10.1111/gbi.12535.

[644] Mark D McDonald et al. 'What is microbial dormancy?' In: *Trends Microbiol.* 32 (2 Feb. 2024), pp. 142–150. DOI: 10.1016/j.tim.2023.08.006.

[645] Rachel Mackelprang et al. 'Microbial survival strategies in ancient permafrost: insights from metagenomics'. In: *ISME J.* 11 (10 11th Oct. 2017), pp. 2305–2318. DOI: 10.1038/ismej.2017.93.

[646] E M Rivkina et al. 'Metabolic activity of permafrost bacteria below the freezing point'. In: *Appl. Environ. Microbiol.* 66 (8 Aug. 2000), pp. 3230–3233. DOI: 10.1128/AEM.66.8.3230-3233.2000.

[647] Nicolai S Panikov and Maria V Sizova. 'Growth kinetics of microorganisms isolated from Alaskan soil and permafrost in solid media frozen down to â 35Â°C: Growth kinetics in frozen media'. In: *FEMS Microbiol. Ecol.* 59 (2 1st Feb. 2007), pp. 500–512. DOI: 10.1111/j.1574-6941.2006.00210.x.

[648] Ezekiel K Bore et al. 'Microbial metabolism in soil at subzero temperatures: Adaptation mechanisms revealed by position-specific 13C labeling'. In: *Front. Microbiol.* 8 (29th May 2017), p. 946. DOI: 10.3389/fmicb.2017.00946.

[649] Corien Bakermans and Mark Skidmore. 'Microbial respiration in ice at subzero temperatures (–4°C to –33°C): Microbial respiration in ice at –4°C to –33°C'. In: *Environ. Microbiol. Rep.* 3 (6 Dec. 2011), pp. 774–782. DOI: 10.1111/j.1758-2229.2011.00298.x.

[650] Haena Park et al. 'Effects of freezing rate on structural changes in L-lactate dehydrogenase during the freezing process'. In: *Sci. Rep.* 11 (1 1st July 2021), p. 13643. DOI: 10.1038/s41598-021-93127-6.

[651] P Prentø. 'The effects of freezing, storage, and thawing on cell compartment integrity and ultrastructure'. In: *Histochem. Cell Biol.* 108 (6 Dec. 1997), pp. 543–547. DOI: 10.1007/s004180050195.

[652] Yuemei Zhang and Per Ertbjerg. 'Effects of frozen-then-chilled storage on proteolytic enzyme activity and water-holding capacity of pork loin'. In: *Meat Sci.* 145 (Nov. 2018), pp. 375–382. DOI: 10.1016/j.meatsci.2018.07.017.

[653] Daniel B Hewins et al. 'Measuring the effect of freezing on hydrolytic and oxidative extracellular enzyme activities associated with plant litter decomposition'. In: *Pedobiologia (Jena)* 59 (5-6 Nov. 2016), pp. 253–256. DOI: 10.1016/j.pedobi.2016.09.002.

[654] Maki Miura et al. 'Freeze–thaw and dry–wet events reduce microbial extracellular enzyme activity, but not organic matter turnover in an agricultural grassland soil'. In: *Appl. Soil Ecol.* 144 (Dec. 2019), pp. 196–199. DOI: 10.1016/j.apsoil.2019.08.002.

[655] Michael R Zimmerman and Arthur C Aufderheide. 'The frozen family of utqiagvik: The autopsy findings'. In: *Arctic Anthropol.* 21 (1 1984), pp. 53–64.

[656] D N Notman et al. 'Arctic paleoradiology: portable radiographic examination of two frozen sailors from the Franklin expedition (1845-1848)'. In: *AJR Am. J. Roentgenol.* 149 (2 Aug. 1987), pp. 347–350. DOI: 10.2214/ajr.149.2.347.

[657] M W Hess et al. 'Histological investigations on the Tyrolean Ice Man'. In: *Am. J. Phys. Anthropol.* 106 (4 1st Aug. 1998), pp. 521–532. DOI: 10.1002/(SICI)1096-8644(199808)106:4<521::AID-AJPA7>3.0.CO;2-L.

[658] Carlos H Previgliano et al. 'Radiologic evaluation of the Llullaillaco mummies'. In: *AJR Am. J. Roentgenol.* 181 (6 Dec. 2003), pp. 1473–1479. DOI: 10.2214/ajr.181.6.1811473.

[659] Christina Papageorgopoulou, Karl Link and Frank J Rühli. 'Histology of a woolly mammoth (Mammuthus primigenius) preserved in permafrost, Yamal peninsula, northwest Siberia: Histology of a woolly mammoth'. In: *Anat. Rec. (Hoboken)* 298 (6 June 2015), pp. 1059–1071. DOI: 10.1002/ar.23148.

[660] Anastasia Kharlamova et al. 'Preserved brain of the Woolly mammoth (Mammuthus primigenius (Blumenbach 1799)) from the Yakutian permafrost'. In: *Quat. Int.* 406 (June 2016), pp. 86–93. DOI: 10.1016/j.quaint.2014.09.073.

[661] N V Serdyuk et al. 'New data on the internal organs of a frozen Yukagir bison mummy (Bison priscus Bojanus, 1827), Yakutia, Russia'. In: *Dokl. Biol. Sci.* 467 (1 Mar. 2016), pp. 89–92. DOI: 10.1134/S0012496616020125.

[662] Shunji Hattori et al. 'Preservation of collagen in the soft tissues of frozen mammoths'. In: *PLoS One* 16 (10 29th Oct. 2021), e0258699. DOI: 10.1371/journal.pone.0258699.

[663] Seraphin H Unterberger et al. 'Morphological and tissue characterization with 3D reconstruction of a 350-year-old Austrian Ardea purpurea glacier mummy'. In: *Biology (Basel)* 12 (1 11th Jan. 2023), p. 114. DOI: 10.3390/biology12010114.

[664] Athanasios Makristathis et al. 'Fatty acid composition and preservation of the Tyrolean Iceman and other mummies'. In: *J. Lipid Res.* 43 (12 Dec. 2002), pp. 2056–2061. DOI: 10.1194/jlr.m100424-jlr200.

[665] Frank Maixner et al. 'Paleoproteomic study of the Iceman's brain tissue'. In: *Cell. Mol. Life Sci.* 70 (19 Oct. 2013), pp. 3709–3722. DOI: 10.1007/s00018-013-1360-y.

[666] Darima Garmaeva et al. 'Histological stability of the Malolyakhovsky mammoth tissues to permafrost conditions'. In: *Biol. Commun.* 68 (4 31st Dec. 2023), pp. 291–296. DOI: 10.21638/spbu03.2023.408.

[667] Xia Li et al. 'New insights into the mechanism of freeze-induced damage based on ice crystal morphology and exudate proteomics'. In: *Food Res. Int.* 161 (111757 Nov. 2022), p. 111757. DOI: 10.1016/j.foodres.2022.111757.

[668] Gabriela Calábková et al. 'Microbial degradation of Pleistocene permafrost-sealed fossil mammal remains'. In: *Quat. Res.* 111 (Jan. 2023), pp. 84–106. DOI: 10.1017/qua.2022.28.

[669] Terence J Painter. 'Lindow man, Tollund man and other peat-bog bodies: The preservative and antimicrobial action of Sphagnan, a reactive glycuronoglycan with tanning and sequestering properties'. In: *Carbohydr. Polym.* 15 (2 Jan. 1991), pp. 123–142. DOI: 10.1016/0144-8617(91)90028-b.

[670] Niels Lynnerup. 'Bog bodies'. In: *Anat. Rec. (Hoboken)* 298 (6 June 2015), pp. 1007–1012. DOI: 10.1002/ar.23138.

[671] Gwendolyn T Pipes and Joseph B Yavitt. 'Biochemical components of *Sphagnum* and persistence in peat soil'. In: *Can. J. Soil Sci.* 102 (3 1st Sept. 2022), pp. 785–795. DOI: 10.1139/cjss-2021-0137.

[672] Lauren Bryan et al. 'Sphagnan in Sphagnum-dominated peatlands: bioavailability and effects on organic matter stabilization'. In: *Biogeochemistry* 167 (5 10th Apr. 2024), pp. 665–680. DOI: 10.1007/s10533-024-01134-2.

[673] C Zaccone et al. 'Diagenetic trends in the phenolic constituents of Sphagnum-dominated peat and its corresponding humic acid fraction'. In: *Org. Geochem.* 39 (7 July 2008), pp. 830–838. DOI: 10.1016/j.orggeochem.2008.04.018.

[674] Tomáš Hájek et al. 'Cell-wall polysaccharides play an important role in decay resistance of Sphagnum and actively depressed decomposition in vitro'. In: *Biogeochemistry* 103 (1-3 Apr. 2011), pp. 45–57. DOI: 10.1007/s10533-010-9444-3.

[675] Fereidoon Shahidi and Chandrika Sewwandi Dissanayaka. 'Phenolic-protein interactions: insight from in-silico analyses – a review'. In: *Food Prod. Process. Nutr.* 5 (1 3rd Jan. 2023). DOI: 10.1186/s43014-022-00121-0.

[676] Behzad Masoumi et al. 'A review of protein-phenolic acid interaction: reaction mechanisms and applications'. In: *Crit. Rev. Food Sci. Nutr.* 64 (11 2024), pp. 3539–3555. DOI: 10.1080/10408398.2022.2132376.

[677] Mana Yoshimura et al. 'Protein-tannins binding mode in hydrolyzable tannins-induced protein aggregation'. In: *Food Chem.* 493 (Pt 1 30th Nov. 2025), p. 145672. DOI: 10.1016/j.foodchem.2025.145672.

[678] T J McIntosh et al. 'Polyphenols increase adhesion between lipid bilayers by forming interbilayer bridges'. In: *Basic Life Sci.* 66 (1999), pp. 451–470. DOI: 10.1007/978-1-4615-4139-4_24.

[679] Aleksandra Ukalska-Jaruga et al. 'Characterization of soil organic matter individual fractions (fulvic acids, humic acids, and humins) by spectroscopic and electrochemical techniques in agricultural soils'. In: *Agronomy (Basel)* 11 (6 26th May 2021), p. 1067. DOI: 10.3390/agronomy11061067.

[680] A G Zavarzina et al. 'Humic substances: Hypotheses and reality (a review)'. In: *Eurasian Soil Sci.* 54 (12 Dec. 2021), pp. 1826–1854. DOI: 10.1134/s1064229321120164.

[681] Di Wu et al. 'Preparation and molecular structural characterization of fulvic acid extracted from different types of peat'. In: *Molecules* 28 (19 23rd Sept. 2023), p. 6780. DOI: 10.3390/molecules28196780.

[682] J T A Verhoeven and W M Liefveld. 'The ecological significance of organochemical compounds in*Sphagnum*'. In: *Acta Bot. Neerl.* 46 (2 1st June 1997), pp. 117–130. DOI: 10.1111/plb.1997.46.2.117.

[683] Samo Lešnik, Marko Jukić and Urban Bren. 'Unveiling polyphenol-protein interactions: a comprehensive computational analysis'. In: *J. Cheminform.* 17 (1 10th Apr. 2025), p. 50. DOI: 10.1186/s13321-025-00997-3.

[684] N J Baxter et al. 'Multiple interactions between polyphenols and a salivary proline-rich protein repeat result in complexation and precipitation'. In: *Biochemistry* 36 (18 6th May 1997), pp. 5566–5577. DOI: 10.1021/bi9700328.

[685] Agnieszka Kosińska et al. 'Interactions between tannins and proteins isolated from broad bean seeds (Vicia faba Major) yield soluble and non-soluble complexes'. In: *Eur. Food Res. Technol.* 233 (2 Aug. 2011), pp. 213–222. DOI: 10.1007/s00217-011-1506-9.

[686] Marica T Engström, Valtteri Virtanen and Juha-Pekka Salminen. 'Influence of the hydrolyzable tannin structure on the characteristics of insoluble hydrolyzable tannin-protein complexes'. In: *J. Agric. Food Chem.* 70 (41 19th Oct. 2022), pp. 13036–13048. DOI: 10.1021/acs.jafc.2c01765.

[687] Martine Morzel, Francis Canon and Sylvain Guyot. 'Interactions between salivary proteins and dietary polyphenols: Potential consequences on gastrointestinal digestive events'. In: *J. Agric. Food Chem.* 70 (21 1st June 2022), pp. 6317–6327. DOI: 10.1021/acs.jafc.2c01183.

[688] B A Stankiewicz et al. 'Assessment of bog-body tissue preservation by pyrolysis-gas chromatography/mass spectrometry'. In: *Rapid Commun. Mass Spectrom.* 11 (17 1997), pp. 1884–1890. DOI: 10.1002/(SICI)1097-0231(199711)11:17<1884::AID-RCM62>3.0.CO;2-5.

[689] Cody L Hoop et al. 'Revealing accessibility of cryptic protein binding sites within the functional collagen fibril'. In: *Biomolecules* 7 (4 1st Nov. 2017), E76. DOI: 10.3390/biom7040076.

[690] Jie Zhu et al. 'Cryptic binding sites become accessible through surface reconstruction of the type I collagen fibril'. In: *Sci. Rep.* 8 (1 9th Nov. 2018), p. 16646. DOI: 10.1038/s41598-018-34616-z.

[691] H R Tang, A D Covington and R A Hancock. 'Structure-activity relationships in the hydrophobic interactions of polyphenols with cellulose and collagen'. In: *Biopolymers* 70 (3 Oct. 2003), pp. 403–413. DOI: 10.1002/bip.10499.

[692] Leping Wu et al. 'Mechanism and effects of polyphenol derivatives for modifying collagen'. In: *ACS Biomater. Sci. Eng.* 5 (9 9th Sept. 2019), pp. 4272–4284. DOI: 10.1021/acsbiomaterials.9b00593.

[693] Carolina Añazco et al. 'Exploring the interplay between polyphenols and lysyl oxidase enzymes for maintaining extracellular matrix homeostasis'. In: *Int. J. Mol. Sci.* 24 (13 1st July 2023), p. 10985. DOI: 10.3390/ijms241310985.

[694] Yang Wang et al. 'Effects of covalent or noncovalent binding of different polyphenols to acid-soluble collagen on protein structure, functionality, and digestibility'. In: *J. Agric. Food Chem.* 71 (48 6th Dec. 2023), pp. 19020–19032. DOI: 10.1021/acs.jafc.3c06510.

[695] Xuemei Yang et al. 'Solubility characteristics of soil humic substances as a function of pH: mechanisms and biogeochemical perspectives'. In: *Biogeosciences* 22 (7 9th Apr. 2025), pp. 1745–1765. DOI: 10.5194/bg-22-1745-2025.

[696] Rebecca Sutton and Garrison Sposito. 'Molecular structure in soil humic substances: the new view'. In: *Environ. Sci. Technol.* 39 (23 1st Dec. 2005), pp. 9009–9015. DOI: 10.1021/es050778q.

[697] Ruggero Angelico et al. 'Humic substances: From supramolecular aggregation to fractal conformation – is there time for a new paradigm?' In: *Appl. Sci. (Basel)* 13 (4 9th Feb. 2023), p. 2236. DOI: 10.3390/app13042236.

[698] Michael H B Hayes and Maria Roulia. 'Relevance of organic matter compositions, structures and associations to soil aggregates and to sustainable productivity'. In: *Agronomy (Basel)* 15 (9 13th Sept. 2025), p. 2182. DOI: 10.3390/agronomy15092182.

[699] Elena A Vialykh et al. 'Emergent functional behaviour of humic substances perceived as complex labile aggregates of small organic molecules and oligomers'. In: *Environ. Chem.* 16 (7 1st Nov. 2019), pp. 505–516. DOI: 10.1071/en19095.

[700] Mathias Gotsmy et al. 'Exploring the structure and dynamics of proteins in soil organic matter'. In: *Proteins* 89 (8 5th Mar. 2021), pp. 925–936. DOI: 10.1002/prot.26070.

[701] Jeanne E Tomaszewski, René P Schwarzenbach and Michael Sander. 'Protein encapsulation by humic substances'. In: *Environ. Sci. Technol.* 45 (14 15th July 2011), pp. 6003–6010. DOI: 10.1021/es200663h.

[702] D C Olk et al. 'Using humic fractions to understand natural organic matter processes in soil and water: Selected studies and applications'. In: *J. Environ. Qual.* 48 (6 Nov. 2019), pp. 1633–1643. DOI: 10.2134/jeq2019.03.0100.

[703] Kimberly L Jones and Charles R O'Melia. 'Protein and humic acid adsorption onto hydrophilic membrane surfaces: effects of pH and ionic strength'. In: *J. Memb. Sci.* 165 (1 Jan. 2000), pp. 31–46. DOI: 10.1016/s0376-7388(99)00218-5.

[704] Eirini S Papadaki et al. 'Assessment of humic and fulvic acid sorbing potential for heavy metals in water'. In: *Foundations* 3 (4 7th Dec. 2023), pp. 788–804. DOI: 10.3390/foundations3040044.

[705] Maria Luisa Astolfi et al. 'Sphagnum moss and peat comparative study: Metal release, binding properties and antioxidant activity'. In: *PLoS One* 19 (8 19th Aug. 2024), e0307210. DOI: 10.1371/journal.pone.0307210.

[706] T J Painter. 'Carbohydrate polymers in food preservation: an integrated view of the Maillard reaction with special reference to discoveries of preserved foods in Sphagnum …' In: *Carbohydr. Polym.* (1998).

[707] Leina El Hosry et al. 'Maillard reaction: Mechanism, influencing parameters, advantages, disadvantages, and food industrial applications: A review'. In: *Foods* 14 (11 26th May 2025), p. 1881. DOI: 10.3390/foods14111881.

[708] Susie J Meade, Antonia G Miller and Juliet A Gerrard. 'The role of dicarbonyl compounds in non-enzymatic crosslinking: a structure-activity study'. In: *Bioorg. Med. Chem.* 11 (6 20th Mar. 2003), pp. 853–862. DOI: 10.1016/s0968-0896(02)00564-3.

[709] Nicolas Walpen et al. 'Electron-donating phenolic and electron-accepting quinone moieties in peat dissolved organic matter: Quantities and redox transformations in the context of peat biogeochemistry'. In: *Environ. Sci. Technol.* 52 (9 1st May 2018), pp. 5236–5245. DOI: 10.1021/acs.est.8b00594.

[710] Yuting Li et al. 'Quantifying the efficiency of o-benzoquinones reaction with amino acids and related nucleophiles by cyclic voltammetry'. In: *Food Chem.* 317 (126454 1st July 2020), p. 126454. DOI: 10.1016/j.foodchem.2020.126454.

[711] Shosuke Ito, Manickam Sugumaran and Kazumasa Wakamatsu. 'Chemical reactivities of ortho-Quinones produced in living organisms: Fate of quinonoid products formed by tyrosinase and phenoloxidase action on phenols and catechols'. In: *Int. J. Mol. Sci.* 21 (17 24th Aug. 2020), E6080. DOI: 10.3390/ijms21176080.

[712] Helena Kieserling et al. 'Protein–phenolic interactions and reactions: Discrepancies, challenges, and opportunities'. In: *Compr. Rev. Food Sci. Food Saf.* 23 (5 1st Sept. 2024), e70015. DOI: 10.1111/1541-4337.70015.

[713] A Pind, C Freeman and M A Lock. 'Enzymic degradation of phenolic materials in peatlands — measurement of phenol oxidase activity'. In: *Plant Soil* 159 (2 Feb. 1994), pp. 227–231. DOI: 10.1007/bf00009285.

[714] Felix Panis and Annette Rompel. 'Biochemical investigations of five recombinantly expressed tyrosinases reveal two novel mechanisms impacting carbon storage in wetland ecosystems'. In: *Environ. Sci. Technol.* 57 (37 19th Sept. 2023), pp. 13863–13873. DOI: 10.1021/acs.est.3c02910.

[715] Gordon Turner-Walker and Elizabeth E Peacock. 'Preliminary results of bone diagenesis in Scandinavian bogs'. In: *Palaeogeogr. Palaeoclimatol. Palaeoecol.* 266 (3-4 Sept. 2008), pp. 151–159. DOI: 10.1016/j.palaeo.2008.03.027.

[716] Jan M Pestka et al. 'Skeletal analysis and comparison of bog bodies from Northern European peat bogs'. In: *Sci. Nat.* 97 (4 Apr. 2010), pp. 393–402. DOI: 10.1007/s00114-010-0653-3.

[717] R P Evershed and R C Connolly. 'Lipid preservation in Lindow man'. In: *Sci. Nat.* 75 (3 1st Mar. 1988), pp. 143–145. DOI: 10.1007/bf00405306.

[718] Arndt F Schilling et al. 'Brief communication: Two and three-dimensional analysis of bone mass and microstructure in a bog body from the Iron Age'. In: *Am. J. Phys. Anthropol.* 135 (4 Apr. 2008), pp. 479–483. DOI: 10.1002/ajpa.20751.

[719] Robert C Janaway et al. 'Taphonomic change to the buried body and associated materials in an upland peat environment: experiments using pig carcasses as human body analogues'. In: *Mummies in a New Millenium*. Ed. by N Lynnerup, C Andreasen and J Berglund. Nuuk, Greenland: Greenland National Museum, Archives and Danish Polar Center, 2003, pp. 56–59.

[720] Graeme T Swindles et al. 'Climate and water-table levels regulate peat accumulation rates across Europe'. In: *PLoS One* 20 (7 23rd July 2025), e0327422. DOI: 10.1371/journal.pone.0327422.

[721] Roy van Beek et al. 'Bogs, bones and bodies: the deposition of human remains in northern European mires (9000 BC–AD 1900)'. In: *Antiquity* 97 (391 Feb. 2023), pp. 120–140. DOI: 10.15184/aqy.2022.163.

[722] J van der Plicht et al. 'Dating bog bodies by means of 14C-AMS'. In: *J. Archaeol. Sci.* 31 (4 Apr. 2004), pp. 471–491. DOI: 10.1016/j.jas.2003.09.012.

[723] Nina H Nielsen et al. 'Diet and radiocarbon dating of Tollund Man: New analyses of an Iron Age bog body from Denmark'. In: *Radiocarbon* 60 (5 Oct. 2018), pp. 1533–1545. DOI: 10.1017/rdc.2018.127.

[724] Bjarne Henning Nielsen, Tina Christensen and Karin Margarita Frei. 'New insights from forgotten bog bodies: The potential of bog skeletons for investigating the phenomenon of deposition of human remains in bogs during prehistory'. In: *J. Archaeol. Sci.* 120 (105166 Aug. 2020), p. 105166. DOI: 10.1016/j.jas.2020.105166.

[725] Jonathan E Nichols and Dorothy M Peteet. 'Rapid expansion of northern peatlands and doubled estimate of carbon storage'. In: *Nat. Geosci.* 12 (11 Nov. 2019), pp. 917–921. DOI: 10.1038/s41561-019-0454-z.

[726] Douglas H Ubelaker and Kristina M Zarenko. 'Adipocere: what is known after over two centuries of research'. In: *Forensic Sci. Int.* 208 (1-3 20th May 2011), pp. 167–172. DOI: 10.1016/j.forsciint.2010.11.024.

[727] Shari L Forbes et al. 'A preliminary investigation of the stages of adipocere formation'. In: *J. Forensic Sci.* 49 (3 May 2004), pp. 566–574. DOI: 10.1520/jfs2002230.

[728] Stephanie J Notter et al. 'Solid-phase extraction in combination with GC/MS for the quantification of free fatty acids in adipocere'. In: *Eur. J. Lipid Sci. Technol.* 110 (1 Jan. 2008), pp. 73–80. DOI: 10.1002/ejlt.200700159.

[729] Stephanie J Notter et al. 'The initial changes of fat deposits during the decomposition of human and pig remains'. In: *J. Forensic Sci.* 54 (1 1st Jan. 2009), pp. 195–201. DOI: 10.1111/j.1556-4029.2008.00911.x.

[730] Chang Liu et al. 'Free fatty acids composition in adipocere of the Kwäday Dän Ts'ìnchí ancient remains found in a glacier: Free fatty acids composition in adipocere'. In: *J. Forensic Sci.* 55 (4 July 2010), pp. 1039–1043. DOI: 10.1111/j.1556-4029.2010.01373.x.

[731] T Takatori et al. 'The mechanism of experimental adipocere formation: substrate specificity on microbial production of hydroxy and oxo fatty acids'. In: *Forensic Sci. Int.* 35 (4 1st Dec. 1987), pp. 277–281. DOI: 10.1016/0379-0738(87)90099-5.

[732] T Takatori. 'Investigations on the mechanism of adipocere formation and its relation to other biochemical reactions'. In: *Forensic Sci. Int.* 80 (1-2 28th June 1996), pp. 49–61. DOI: 10.1016/0379-0738(96)01927-5.

[733] Karl-Erich Jaeger et al. 'Bacterial lipases'. In: *FEMS Microbiol. Rev.* 15 (1 Sept. 1994), pp. 29–63. DOI: 10.1111/j.1574-6976.1994.tb00121.x.

[734] Heinz-Christian Fründ and Dirk Schoenen. 'Quantification of adipocere degradation with and without access to oxygen and to the living soil'. In: *Forensic Sci. Int.* 188 (1-3 1st July 2009), pp. 18–22. DOI: 10.1016/j.forsciint.2009.03.005.

[735] Dirk Schoenen and Hanne Schoenen. 'Adipocere formation – the result of insufficient microbial degradation'. In: *Forensic Sci. Int.* 226 (1-3 10th Mar. 2013), 301.e1–6. DOI: 10.1016/j.forsciint.2013.01.023.

[736] T Takatori. 'The mechanism of human adipocere formation'. In: *Leg. Med. (Tokyo)* 3 (4 1st Dec. 2001), pp. 193–204. DOI: 10.1016/s1344-6223(01)00036-0.

[737] Veronica Schiaffi, Frédéric Barras and Emmanuelle Bouveret. 'Matching the beta-oxidation gene repertoire with the wide diversity of fatty acids'. In: *Curr. Opin. Microbiol.* 77 (102402 Feb. 2024), p. 102402. DOI: 10.1016/j.mib.2023.102402.

[738] Veronica Schiaffi et al. 'The essential role of 2,4-dienoyl-CoA reductase for the degradation of complex fatty acid mixtures'. In: *MBio* 16 (12 10th Dec. 2025), e0220325. DOI: 10.1128/mbio.02203-25.

[739] Diana Z Sousa et al. 'Microbial communities involved in anaerobic degradation of unsaturated or saturated long-chain fatty acids'. In: *Appl. Environ. Microbiol.* 73 (4 Feb. 2007), pp. 1054–1064. DOI: 10.1128/AEM.01723-06.

[740] H Gotouda et al. 'The mechanism of experimental adipocere formation: hydration and dehydrogenation in microbial synthesis of hydroxy and oxo fatty acids'. In: *Forensic Sci. Int.* 37 (4 June 1988), pp. 249–257. DOI: 10.1016/0379-0738(88)90233-2.

[741] F Yan et al. 'Preliminary quantitative investigation of postmortem adipocere formation'. In: *J. Forensic Sci.* 46 (3 1st May 2001), pp. 609–614. DOI: 10.1520/jfs15012j.

[742] Hideyuki Nushida et al. 'Adipocere formation via hydrogenation of linoleic acid in a victim kept under dry concealment'. In: *Forensic Sci. Int.* 175 (2-3 5th Mar. 2008), pp. 160–165. DOI: 10.1016/j.forsciint.2007.06.008.

[743] Joohyun Kang, Byung Hee Kim and Yohan Yoon. 'Meat spoilage by bacteria: Influencing factors, volatile compounds, and organoleptic alterations'. In: *Food Sci. Anim. Resour.* 46 (1 3rd Mar. 2026), p. 42. DOI: 10.1007/s44463-025-00025-w.

[744] Randolph J Moses. 'Experimental adipocere formation: implications for adipocere formation on buried bone: Adipocere formation on buried bone'. In: *J. Forensic Sci.* 57 (3 May 2012), pp. 589–595. DOI: 10.1111/j.1556-4029.2011.02032.x.

[745] Roy G Bossert. 'The metallic soaps'. In: *J. Chem. Educ.* 27 (1 1st Jan. 1950), p. 10. DOI: 10.1021/ed027p10.

[746] Shari L Forbes, Boyd B Dent and Barbara H Stuart. 'The effect of soil type on adipocere formation'. In: *Forensic Sci. Int.* 154 (1 10th Nov. 2005), pp. 35–43. DOI: 10.1016/j.forsciint.2004.09.108.

[747] Shari L Forbes, Barbara H Stuart and Boyd B Dent. 'The effect of the burial environment on adipocere formation'. In: *Forensic Sci. Int.* 154 (1 10th Nov. 2005), pp. 24–34. DOI: 10.1016/j.forsciint.2004.09.107.

[748] Shari L Forbes, Barbara H Stuart and Boyd B Dent. 'The effect of the method of burial on adipocere formation'. In: *Forensic Sci. Int.* 154 (1 10th Nov. 2005), pp. 44–52. DOI: 10.1016/j.forsciint.2004.09.109.

[749] Thomas L Bereuter, Werner Mikenda and Christian Reiter. 'Iceman's mummification – implications from infrared spectroscopical and histological studies'. In: *Chem. Eur. J.* 3 (7 July 1997), pp. 1032–1038. DOI: 10.1002/chem.19970030708.

[750] S Fiedler et al. 'Adipocere withstands 1600 years of fluctuating groundwater levels in soil'. In: *J. Archaeol. Sci.* 36 (7 July 2009), pp. 1328–1333. DOI: 10.1016/j.jas.2009.01.017.

[751] T Takatori and A Yamaoka. 'The mechanism of adipocere formation 1. Identification and chemical properties of hydroxy fatty acids in adipocere'. In: *Forensic Sci.* 9 (1 Jan. 1977), pp. 63–73. DOI: 10.1016/0300-9432(77)90068-1.

[752] R P Evershed. 'Chemical composition of a bog body adipocere'. In: *Archaeometry* 34 (2 Aug. 1992), pp. 253–265. DOI: 10.1111/j.1475-4754.1992.tb00496.x.

[753] T Takatori et al. 'Microbial production of hydroxy and oxo fatty acids by several microorganisms as a model of adipocere formation'. In: *Forensic Sci. Int.* 32 (1 Aug. 1986), pp. 5–11. DOI: 10.1016/0379-0738(86)90152-0.

[754] S Fiedler et al. 'The chemistry of death–Adipocere degradation in modern graveyards'. In: *Forensic Sci. Int.* 257 (1st Dec. 2015), pp. 320–328. DOI: 10.1016/j.forsciint.2015.09.010.

[755] S Pfeiffer, S Milne and R M Stevenson. 'The natural decomposition of adipocere'. In: *J. Forensic Sci.* 43 (2 Mar. 1998), pp. 368–370. DOI: 10.1520/jfs16147j.

[756] G E Cotton, A C Aufderheide and V G Goldschmidt. 'Preservation of human tissue immersed for five years in fresh water of known temperature'. In: *J. Forensic Sci.* 32 (4 July 1987), pp. 1125–1130. DOI: 10.1520/jfs12427j.

[757] J Adachi et al. 'Epicoprostanol found in adipocere from five human autopsies'. In: *Lipids* 32 (11 Nov. 1997), pp. 1155–1160. DOI: 10.1007/s11745-997-0148-3.

[758] B X Mayer, C Reiter and T L Bereuter. 'Investigation of the triacylglycerol composition of iceman's mummified tissue by high-temperature gas chromatography'. In: *J. Chromatogr. B Biomed. Sci. Appl.* 692 (1 25th Apr. 1997), pp. 1–6. DOI: 10.1016/s0378-4347(96)00501-4.

[759] Roger W Byard. 'Adipocere-the fat of graveyards'. In: *Am. J. Forensic Med. Pathol.* 37 (3 Sept. 2016), pp. 208–210. DOI: 10.1097/PAF.0000000000000251.

[760] Adis Salihbegović et al. 'Histological observations on adipocere in human remains buried for 21 years at the Tomašica grave-site in Bosnia and Herzegovina'. In: *Bosn. J. Basic Med. Sci.* 18 (3 1st Aug. 2018), pp. 234–239. DOI: 10.17305/bjbms.2018.3343.

[761] Anish Zacharia et al. 'Distinct infrastructure of lipid networks in visceral and subcutaneous adipose tissues in overweight humans'. In: *Am. J. Clin. Nutr.* 112 (4 1st Oct. 2020), pp. 979–990. DOI: 10.1093/ajcn/nqaa195.

[762] C Y Henderson et al. 'Adipocere inside nineteenth century femora: The effect of grave conditions: Adipocere inside nineteenth century femora'. In: *Int. J. Osteoarchaeol.* 25 (6 7th Nov. 2015), pp. 960–967. DOI: 10.1002/oa.2350.

[763] P F Mellen, M A Lowry and M S Micozzi. 'Experimental observations on adipocere formation'. In: *J. Forensic Sci.* 38 (1 Jan. 1993), pp. 91–93. DOI: 10.1520/jfs13379j.

[764] Tyler G O'Brien and Amy C Kuehner. 'Waxing grave about adipocere: soft tissue change in an aquatic context'. In: *J. Forensic Sci.* 52 (2 Mar. 2007), pp. 294–301. DOI: 10.1111/j.1556-4029.2006.00362.x.

[765] G Eglinton and G A Logan. 'Molecular preservation'. In: *Philos. Trans. R. Soc. Lond. B Biol. Sci.* 333 (1268 30th Sept. 1991), 315–27, discussion 327–8. DOI: 10.1098/rstb.1991.0081.

[766] Julien Alleon et al. 'Organic molecular heterogeneities can withstand diagenesis'. In: *Sci. Rep.* 7 (1 4th May 2017), p. 1508. DOI: 10.1038/s41598-017-01612-8.

[767] Mary H Schweitzer et al. 'A role for iron and oxygen chemistry in preserving soft tissues, cells and molecules from deep time'. In: *Proc. Biol. Sci.* 281 (1775 22nd Jan. 2014), p. 20132741. DOI: 10.1098/rspb.2013.2741.

[768] Jasmina Wiemann et al. 'Fossilization transforms vertebrate hard tissue proteins into N-heterocyclic polymers'. In: *Nat. Commun.* 9 (1 9th Nov. 2018), p. 4741. DOI: 10.1038/s41467-018-07013-3.

[769] W T Roubal and A L Tappel. 'Polymerization of proteins induced by free-radical lipid peroxidation'. In: *Arch. Biochem. Biophys.* 113 (1 Jan. 1966), pp. 150–155. DOI: 10.1016/0003-9861(66)90168-8.

[770] Michael J Davies. 'Protein oxidation and peroxidation'. In: *Biochem. J.* 473 (7 1st Apr. 2016), pp. 805–825. DOI: 10.1042/BJ20151227.

[771] Eduardo Fuentes-Lemus et al. 'Oxidative crosslinking of peptides and proteins: Mechanisms of formation, detection, characterization and quantification'. In: *Molecules* 27 (1 21st Dec. 2021), p. 15. DOI: 10.3390/molecules27010015.

[772] H W Gardner. 'Oxygen radical chemistry of polyunsaturated fatty acids'. In: *Free Radic. Biol. Med.* 7 (1 1989), pp. 65–86. DOI: 10.1016/0891-5849(89)90102-0.

[773] Ismael Tejero et al. 'Theoretical modeling of hydroxyl-radical-induced lipid peroxidation reactions'. In: *J. Phys. Chem. B* 111 (20 24th May 2007), pp. 5684–5693. DOI: 10.1021/jp0650782.

[774] Amin Reyhani et al. 'Fenton-chemistry-mediated radical polymerization'. In: *Macromol. Rapid Commun.* 40 (18 Sept. 2019), e1900220. DOI: 10.1002/marc.201900220.

[775] Zhongwei Zhao. 'Hydroxyl radical generations form the physiologically relevant Fenton-like reactions'. In: *Free Radic. Biol. Med.* 208 (1st Nov. 2023), pp. 510–515. DOI: 10.1016/j.freeradbiomed.2023.09.013.

[776] Chi Zhang et al. 'The degradation pathways of contaminants by reactive oxygen species generated in the Fenton/Fenton-like systems'. In: *Chin. Chem. Lett.* 35 (10 Oct. 2024), p. 109579. DOI: 10.1016/j.cclet.2024.109579.

[777] B A Wagner, G R Buettner and C P Burns. 'Free radical-mediated lipid peroxidation in cells: oxidizability is a function of cell lipid bis-allylic hydrogen content'. In: *Biochemistry* 33 (15 19th Apr. 1994), pp. 4449–4453. DOI: 10.1021/bi00181a003.

[778] Z X Chen, Y Li and F Huang. 'Persistent and stable organic radicals: Design, synthesis, and applications'. In: *Chem* 7 (2 11th Feb. 2021), pp. 288–332. DOI: 10.1016/j.chempr.2020.09.024.

[779] Leesa M Smith, Heather M Aitken and Michelle L Coote. 'The fate of the peroxyl radical in autoxidation: How does polymer degradation really occur?' In: *Acc. Chem. Res.* 51 (9 18th Sept. 2018), pp. 2006–2013. DOI: 10.1021/acs.accounts.8b00250.

[780] Xu Li et al. 'Kinetic models to understand the coexistence of formation and decomposition of hydroperoxide during lipid oxidation'. In: *Food Res. Int.* 136 (109314 Oct. 2020), p. 109314. DOI: 10.1016/j.foodres.2020.109314.

[781] Vassiliki G Kontogianni and Ioannis P Gerothanassis. 'Analytical and structural tools of lipid hydroperoxides: Present state and future perspectives'. In: *Molecules* 27 (7 25th Mar. 2022), p. 2139. DOI: 10.3390/molecules27072139.

[782] Karen M Schaich. 'Thinking outside the classical chain reaction box of lipid oxidation'. In: *Lipid Technol.* 24 (3 Mar. 2012), pp. 55–58. DOI: 10.1002/lite.201200170.

[783] Camille Banoun et al. 'Intermolecular C-O bond formation with alkoxyl radicals: Photoredox-catalyzed -alkoxylation of carbonyl compounds'. In: *Org. Lett.* 23 (22 19th Nov. 2021), pp. 8926–8930. DOI: 10.1021/acs.orglett.1c03444.

[784] Masahiro Murakami and Naoki Ishida. ' -Scission of Alkoxy Radicals in Synthetic Transformations'. In: *Chem. Lett.* 46 (12 5th Dec. 2017), pp. 1692–1700. DOI: 10.1246/cl.170834.

[785] Bebiana C Sousa, Andrew R Pitt and Corinne M Spickett. 'Chemistry and analysis of HNE and other prominent carbonyl-containing lipid oxidation compounds'. In: *Free Radic. Biol. Med.* 111 (Oct. 2017), pp. 294–308. DOI: 10.1016/j.freeradbiomed.2017.02.003.

[786] Antonio Ayala, Mario F Muñoz and Sandro Argüelles. 'Lipid peroxidation: production, metabolism, and signaling mechanisms of malondialdehyde and 4-hydroxy-2-nonenal'. In: *Oxid. Med. Cell. Longev.* 2014 (8th May 2014), p. 360438. DOI: 10.1155/2014/360438.

[787] Luca Valgimigli. 'Lipid peroxidation and antioxidant protection'. In: *Biomolecules* 13 (9 24th Aug. 2023), p. 1291. DOI: 10.3390/biom13091291.

[788] Yixiao Huang et al. 'Interrelationship of lipid aldehydes (MDA, 4-HNE, and 4-ONE) mediated protein oxidation in muscle foods'. In: *Crit. Rev. Food Sci. Nutr.* 64 (32 Nov. 2024), pp. 11809–11825. DOI: 10.1080/10408398.2023.2245029.

[789] A B Doktorov, N N Lukzen and J B Pedersen. 'Analysis of lipid peroxidation kinetics. 1. Role of recombination of alkyl and peroxyl radicals'. In: *J. Phys. Chem. B* 112 (37 18th Sept. 2008), pp. 11854–11861. DOI: 10.1021/jp709921m.

[790] Ned A Porter. 'A perspective on free radical autoxidation: the physical organic chemistry of polyunsaturated fatty acid and sterol peroxidation'. In: *J. Org. Chem.* 78 (8 19th Apr. 2013), pp. 3511–3524. DOI: 10.1021/jo4001433.

[791] E R Stadtman and R L Levine. 'Free radical-mediated oxidation of free amino acids and amino acid residues in proteins'. In: *Amino Acids* 25 (3-4 Dec. 2003), pp. 207–218. DOI: 10.1007/s00726-003-0011-2.

[792] M J Davies, S Fu and R T Dean. 'Protein hydroperoxides can give rise to reactive free radicals'. In: *Biochem. J.* 305 ( Pt 2) (2 15th Jan. 1995), pp. 643–649. DOI: 10.1042/bj3050643.

[793] E R Stadtman and B S Berlett. 'Fenton chemistry revisited: amino acid oxidation'. In: *Basic Life Sci.* 49 (1988), pp. 131–136. DOI: 10.1007/978-1-4684-5568-7_18.

[794] Fobang Liu et al. 'Release of free amino acids upon oxidation of peptides and proteins by hydroxyl radicals'. In: *Anal. Bioanal. Chem.* 409 (9 Mar. 2017), pp. 2411–2420. DOI: 10.1007/s00216-017-0188-y.

[795] B N Nukuna, M B Goshe and V E Anderson. 'Sites of hydroxyl radical reaction with amino acids identified by (2)H NMR detection of induced (1)H/(2)H exchange'. In: *J. Am. Chem. Soc.* 123 (6 14th Feb. 2001), pp. 1208–1214. DOI: 10.1021/ja003342d.

[796] Jon Uranga, Jon I Mujika and Jon M Matxain. '$\bullet$OH oxidation toward S- and OH-containing amino acids'. In: *J. Phys. Chem. B* 119 (50 17th Dec. 2015), pp. 15430–15442. DOI: 10.1021/acs.jpcb.5b09825.

[797] Xiaoran Roger Liu et al. 'Hydroxyl-radical reaction pathways for the fast photochemical oxidation of proteins platform as revealed by 18O isotopic labeling'. In: *Anal. Chem.* 91 (14 16th July 2019), pp. 9238–9245. DOI: 10.1021/acs.analchem.9b02134.

[798] Chryssostomos Chatgilialoglu et al. 'Assessment of hydroxyl radical reactivity in sulfur-containing amino acid models under acidic pH'. In: *Int. J. Mol. Sci.* 26 (15 25th July 2025), p. 7203. DOI: 10.3390/ijms26157203.

[799] E R Stadtman. 'Oxidation of free amino acids and amino acid residues in proteins by radiolysis and by metal-catalyzed reactions'. In: *Annu. Rev. Biochem.* 62 (1 1993), pp. 797–821. DOI: 10.1146/annurev.bi.62.070193.004053.

[800] J I Mujika, J Uranga and J M Matxain. 'Computational study on the attack of $\cdot$OH radicals on aromatic amino acids'. In: *Chem. Eur. J.* 19 (21 17th May 2013), pp. 6862–6873. DOI: 10.1002/chem.201203862.

[801] J G Kiselar et al. 'Hydroxyl radical probe of protein surfaces using synchrotron X-ray radiolysis and mass spectrometry'. In: *Int. J. Radiat. Biol.* 78 (2 Feb. 2002), pp. 101–114. DOI: 10.1080/09553000110094805.

[802] Guozhong Xu and Mark R Chance. 'Radiolytic modification of sulfur-containing amino acid residues in model peptides: fundamental studies for protein footprinting'. In: *Anal. Chem.* 77 (8 15th Apr. 2005), pp. 2437–2449. DOI: 10.1021/ac0484629.

[803] Dorairajan Balasubramanian and Ritu Kanwar. 'Molecular pathology of dityrosine cross-links in proteins: structural and functional analysis of four proteins'. In: *Mol. Cell. Biochem.* 234-235 (1-2 May 2002), pp. 27–38. DOI: 10.1023/a:1015927907418.

[804] Juan David Figueroa et al. 'Formation and characterization of crosslinks, including Tyr-Trp species, on one electron oxidation of free Tyr and Trp residues by carbonate radical anion'. In: *RSC Adv.* 10 (43 3rd July 2020), pp. 25786–25800. DOI: 10.1039/d0ra04051g.

[805] C L Hawkins and M J Davies. 'Generation and propagation of radical reactions on proteins'. In: *Biochim. Biophys. Acta* 1504 (2-3 2nd Apr. 2001), pp. 196–219. DOI: 10.1016/s0005-2728(00)00252-8.

[806] J Neuzil, J M Gebicki and R Stocker. 'Radical-induced chain oxidation of proteins and its inhibition by chain-breaking antioxidants'. In: *Biochem. J.* 293 ( Pt 3) (3 1st Aug. 1993), pp. 601–606. DOI: 10.1042/bj2930601.

[807] J R Requena et al. 'Quantification of malondialdehyde and 4-hydroxynonenal adducts to lysine residues in native and oxidized human low-density lipoprotein'. In: *Biochem. J.* 322 ( Pt 1) (1 15th Feb. 1997), pp. 317–325. DOI: 10.1042/bj3220317.

[808] A Negre-Salvayre et al. 'Advanced lipid peroxidation end products in oxidative damage to proteins. Potential role in diseases and therapeutic prospects for the inhibitors'. In: *Br. J. Pharmacol.* 153 (1 Jan. 2008), pp. 6–20. DOI: 10.1038/sj.bjp.0707395.

[809] Navin Rauniyar and Laszlo Prokai. 'Detection and identification of 4-hydroxy-2-nonenal Schiff-base adducts along with products of Michael addition using data-dependent neutral loss-driven MS3 acquisition: method evaluation through an in vitro study on cytochrome c oxidase modifications'. In: *Proteomics* 9 (22 Nov. 2009), pp. 5188–5193. DOI: 10.1002/pmic.200900116.

[810] Lidija Milkovic et al. 'The 4-hydroxynonenal-protein adducts and their biological relevance: Are some proteins preferred targets?' In: *Antioxidants (Basel)* 12 (4 1st Apr. 2023), p. 856. DOI: 10.3390/antiox12040856.

[811] H Esterbauer, R J Schaur and H Zollner. 'Chemistry and biochemistry of 4-hydroxynonenal, malonaldehyde and related aldehydes'. In: *Free Radic. Biol. Med.* 11 (1 1st Jan. 1991), pp. 81–128. DOI: 10.1016/0891-5849(91)90192-6.

[812] Lawrence M Sayre et al. 'Protein adducts generated from products of lipid oxidation: focus on HNE and one'. In: *Drug Metab. Rev.* 38 (4 2006), pp. 651–675. DOI: 10.1080/03602530600959508.

[813] Xiaochun Zhu et al. 'Mass spectrometric evidence for the existence of distinct modifications of different proteins by 2(E),4(E)-decadienal'. In: *Chem. Res. Toxicol.* 23 (3 15th Mar. 2010), pp. 467–473. DOI: 10.1021/tx900379a.

[814] Catarina B Afonso et al. 'A mass spectrometry approach for the identification and localization of small aldehyde modifications of proteins'. In: *Arch. Biochem. Biophys.* 646 (15th May 2018), pp. 38–45. DOI: 10.1016/j.abb.2018.03.026.

[815] Paul A Grimsrud et al. 'Oxidative stress and covalent modification of protein with bioactive aldehydes'. In: *J. Biol. Chem.* 283 (32 8th Aug. 2008), pp. 21837–21841. DOI: 10.1074/jbc.R700019200.

[816] Corinne M Spickett and Andrew R Pitt. 'Modification of proteins by reactive lipid oxidation products and biochemical effects of lipoxidation'. In: *Essays Biochem.* 64 (1 17th Feb. 2020), pp. 19–31. DOI: 10.1042/EBC20190058.

[817] Tomas Bolumar, Leif H Skibsted and Vibeke Orlien. 'Kinetics of the formation of radicals in meat during high pressure processing'. In: *Food Chem.* 134 (4 15th Oct. 2012), pp. 2114–2120. DOI: 10.1016/j.foodchem.2012.04.013.

[818] Yechuan Huang, Wen Zhang and Shuangli Xiong. 'Modeling the effect of thermal combined with high-pressure treatment on intramuscular lipid oxidation in pork'. In: *J. Food Process Eng.* 42 (6 Oct. 2019). DOI: 10.1111/jfpe.13240.

[819] Anja Rakotondramavo et al. 'Monitoring oxidation during the storage of pressure-treated cooked ham and impact on technological attributes'. In: *Heliyon* 5 (8 Aug. 2019), e02285. DOI: 10.1016/j.heliyon.2019.e02285.

[820] Francisco J Hidalgo and Rosario Zamora. 'Amino acid degradations produced by lipid oxidation products'. In: *Crit. Rev. Food Sci. Nutr.* 56 (8 10th June 2016), pp. 1242–1252. DOI: 10.1080/10408398.2012.761173.

[821] Richard M LoPachin et al. 'Molecular mechanisms of 4-hydroxy-2-nonenal and acrolein toxicity: nucleophilic targets and adduct formation'. In: *Chem. Res. Toxicol.* 22 (9 Sept. 2009), pp. 1499–1508. DOI: 10.1021/tx900147g.

[822] S R Thorpe and J W Baynes. 'Maillard reaction products in tissue proteins: new products and new perspectives'. In: *Amino Acids* 25 (3-4 Dec. 2003), pp. 275–281. DOI: 10.1007/s00726-003-0017-9.

[823] G Vistoli et al. 'Advanced glycoxidation and lipoxidation end products (AGEs and ALEs): an overview of their mechanisms of formation'. In: *Free Radic. Res.* 47 Suppl 1 (sup1 Aug. 2013), pp. 3–27. DOI: 10.3109/10715762.2013.815348.

[824] Nurbubu T Moldogazieva et al. 'Oxidative stress and advanced lipoxidation and glycation end products (ALEs and AGEs) in aging and age-related diseases'. In: *Oxid. Med. Cell. Longev.* 2019 (14th Aug. 2019), p. 3085756. DOI: 10.1155/2019/3085756.

[825] V A Yaylayan and A Huyghues-Despointes. 'Chemistry of Amadori rearrangement products: analysis, synthesis, kinetics, reactions, and spectroscopic properties'. In: *Crit. Rev. Food Sci. Nutr.* 34 (4 1994), pp. 321–369. DOI: 10.1080/10408399409527667.

[826] S-J Cho et al. 'The road to advanced glycation end products: A mechanistic perspective'. In: *Curr. Med. Chem.* 14 (15 1st June 2007), pp. 1653–1671. DOI: 10.2174/092986707780830989.

[827] Christian Sibbersen and Mogens Johannsen. 'Dicarbonyl derived post-translational modifications: chemistry bridging biology and aging-related disease'. In: *Essays Biochem.* 64 (1 17th Feb. 2020), pp. 97–110. DOI: 10.1042/EBC20190057.

[828] Jingmin Zeng and Michael J Davies. 'Evidence for the formation of adducts and S-(carboxymethyl)cysteine on reaction of alpha-dicarbonyl compounds with thiol groups on amino acids, peptides, and proteins'. In: *Chem. Res. Toxicol.* 18 (8 Aug. 2005), pp. 1232–1241. DOI: 10.1021/tx050074u.

[829] Sudipta Panja et al. 'Proximal cysteine residues in proteins promote N -carboxyalkylation of lysine residues by  -dicarbonyl compounds'. In: *J. Biol. Chem.* 301 (4 Apr. 2025), p. 108377. DOI: 10.1016/j.jbc.2025.108377.

[830] M O Lederer and R G Klaiber. 'Cross-linking of proteins by Maillard processes: characterization and detection of lysine-arginine cross-links derived from glyoxal and methylglyoxal'. In: *Bioorg. Med. Chem.* 7 (11 Nov. 1999), pp. 2499–2507. DOI: 10.1016/s0968-0896(99)00212-6.

[831] Rasoul Nasiri et al. 'Cross-linking mechanisms of arginine and lysine with alpha,beta-dicarbonyl compounds in aqueous solution'. In: *J. Phys. Chem. A* 115 (46 24th Nov. 2011), pp. 13542–13555. DOI: 10.1021/jp205558d.

[832] Vicky De Groof et al. 'Medium chain carboxylic acids from complex organic feedstocks by mixed culture fermentation'. In: *Molecules* 24 (3 22nd Jan. 2019), E398. DOI: 10.3390/molecules24030398.

[833] Grégoire B L Henry et al. 'A specific H2/CO2 consumption molar ratio of 3 as a signature for the chain elongation of carboxylates from brewer's spent grain acidogenesis'. In: *Front. Bioeng. Biotechnol.* 11 (1st June 2023), p. 1165197. DOI: 10.3389/fbioe.2023.1165197.

[834] Yuandong Cui et al. 'Mechanistic insights and catalyst design for the selective hydrogenolysis of cellulose to C2-C3 alcohols'. In: *Chem. Sci.* 17 (7 18th Feb. 2026), pp. 3449–3479. DOI: 10.1039/d5sc09595f.

[835] Kameh Tajvidi, Peter J C Hausoul and Regina Palkovits. 'Hydrogenolysis of cellulose over Cu-based catalysts-analysis of the reaction network'. In: *ChemSusChem* 7 (5 May 2014), pp. 1311–1317. DOI: 10.1002/cssc.201300978.

[836] Elizabeth M Boatman et al. 'Mechanisms of soft tissue and protein preservation in Tyrannosaurus rex'. In: *Sci. Rep.* 9 (1 30th Oct. 2019), p. 15678. DOI: 10.1038/s41598-019-51680-1.

[837] Frederico A C Azevedo et al. 'Equal numbers of neuronal and nonneuronal cells make the human brain an isometrically scaled-up primate brain'. In: *J. Comp. Neurol.* 513 (5 10th Apr. 2009), pp. 532–541. DOI: 10.1002/cne.21974.

[838] Suzana Herculano-Houzel. 'The human brain in numbers: a linearly scaled-up primate brain'. In: *Front. Hum. Neurosci.* 3 (9th Nov. 2009), p. 31. DOI: 10.3389/neuro.09.031.2009.

[839] Alain Goriely. 'Eighty-six billion and counting: do we know the number of neurons in the human brain?' In: *Brain* 148 (3 6th Mar. 2025), pp. 689–691. DOI: 10.1093/brain/awae390.

[840] Y Tang et al. 'Total regional and global number of synapses in the human brain neocortex'. In: *Synapse* 41 (3 1st Sept. 2001), pp. 258–273. DOI: 10.1002/syn.1083.

[841] Wieslaw L Nowinski. 'On human nanoscale synaptome: Morphology modeling and storage estimation'. In: *PLoS One* 19 (9 25th Sept. 2024), e0310156. DOI: 10.1371/journal.pone.0310156.

[842] Laura Sancho, Minerva Contreras and Nicola J Allen. 'Glia as sculptors of synaptic plasticity'. In: *Neurosci. Res.* 167 (June 2021), pp. 17–29. DOI: 10.1016/j.neures.2020.11.005.

[843] Wookbong Kwon, Michael R Williamson and Benjamin Deneen. 'A functional perspective on astrocyte heterogeneity'. In: *Trends Neurosci.* 48 (9 Sept. 2025), pp. 691–705. DOI: 10.1016/j.tins.2025.06.009.

[844] Antonio Pinto-Duarte et al. 'Conservation of glial density and cell-type ratios within a brain region across mammals'. In: *PNAS Nexus* 4 (11 16th Nov. 2025), pgaf314. DOI: 10.1093/pnasnexus/pgaf314.

[845] Dasiel O Borroto-Escuela et al. 'Understanding electrical and chemical transmission in the brain'. In: *Front. Cell. Neurosci.* 18 (26th June 2024), p. 1398862. DOI: 10.3389/fncel.2024.1398862.

[846] Marco Terenzio, Giampietro Schiavo and Mike Fainzilber. 'Compartmentalized signaling in neurons: From cell biology to neuroscience'. In: *Neuron* 96 (3 1st Nov. 2017), pp. 667–679. DOI: 10.1016/j.neuron.2017.10.015.

[847] Patrick C Nahirney and Marie-Eve Tremblay. 'Brain ultrastructure: Putting the pieces together'. In: *Front. Cell Dev. Biol.* 9 (18th Feb. 2021), p. 629503. DOI: 10.3389/fcell.2021.629503.

[848] Kimberly Siletti et al. 'Transcriptomic diversity of cell types across the adult human brain'. In: *Science* 382 (6667 13th Oct. 2023), eadd7046. DOI: 10.1126/science.add7046.

[849] Xinyue Chen et al. 'A brain cell atlas integrating single-cell transcriptomes across human brain regions'. In: *Nat. Med.* 30 (9 Sept. 2024), pp. 2679–2691. DOI: 10.1038/s41591-024-03150-z.

[850] Jonah Langlieb et al. 'The molecular cytoarchitecture of the adult mouse brain'. In: *Nature* 624 (7991 Dec. 2023), pp. 333–342. DOI: 10.1038/s41586-023-06818-7.

[851] Zizhen Yao et al. 'A high-resolution transcriptomic and spatial atlas of cell types in the whole mouse brain'. In: *Nature* 624 (7991 Dec. 2023), pp. 317–332. DOI: 10.1038/s41586-023-06812-z.

[852] Meng Zhang et al. 'Molecularly defined and spatially resolved cell atlas of the whole mouse brain'. In: *Nature* 624 (7991 Dec. 2023), pp. 343–354. DOI: 10.1038/s41586-023-06808-9.

[853] Diego Szczupak et al. 'The relevance of heterotopic callosal fibers to interhemispheric connectivity of the mammalian brain'. In: *Cereb. Cortex* 33 (8 4th Apr. 2023), pp. 4752–4760. DOI: 10.1093/cercor/bhac377.

[854] Paolo Barbaresi et al. 'Intrinsic organization of the corpus callosum'. In: *Front. Physiol.* 15 (1st July 2024), p. 1393000. DOI: 10.3389/fphys.2024.1393000.

[855] Evelina Fedorenko, John Duncan and Nancy Kanwisher. 'Broad domain generality in focal regions of frontal and parietal cortex'. In: *Proc. Natl. Acad. Sci. U. S. A.* 110 (41 8th Oct. 2013), pp. 16616–16621. DOI: 10.1073/pnas.1315235110.

[856] Larry W Swanson, Joel D Hahn and Olaf Sporns. 'Organizing principles for the cerebral cortex network of commissural and association connections'. In: *Proc. Natl. Acad. Sci. U. S. A.* 114 (45 7th Nov. 2017), E9692–E9701. DOI: 10.1073/pnas.1712928114.

[857] Elena Borra and Giuseppe Luppino. 'Large-scale temporo-parieto-frontal networks for motor and cognitive motor functions in the primate brain'. In: *Cortex* 118 (Sept. 2019), pp. 19–37. DOI: 10.1016/j.cortex.2018.09.024.

[858] James M Shine et al. 'The impact of the human thalamus on brain-wide information processing'. In: *Nat. Rev. Neurosci.* 24 (7 26th July 2023), pp. 416–430. DOI: 10.1038/s41583-023-00701-0.

[859] S Murray Sherman and W Martin Usrey. 'Transthalamic pathways for cortical function'. In: *J. Neurosci.* 44 (35 28th Aug. 2024), e0909242024. DOI: 10.1523/JNEUROSCI.0909-24.2024.

[860] Teresa Guillamón-Vivancos et al. 'Sensory modality-specific wiring of thalamocortical circuits'. In: *Nat. Rev. Neurosci.* 26 (10 30th Oct. 2025), pp. 623–641. DOI: 10.1038/s41583-025-00945-y.

[861] Ebtesam A Al-Suhaimi and Firdos Alam Khan. 'The pituitary gland: Functional relationship with the hypothalamus, structure, and physiology'. In: *Emerging Concepts in Endocrine Structure and Functions*. Singapore: Springer Nature Singapore, 2022, pp. 73–131. DOI: 10.1007/978-981-16-9016-7_4.

[862] Harmony Fong, Jing Zheng and Deborah Kurrasch. 'The structural and functional complexity of the integrative hypothalamus'. In: *Science* 382 (6669 27th Oct. 2023), pp. 388–394. DOI: 10.1126/science.adh8488.

[863] Mansi Goel et al. 'Integrative functions of the hypothalamus: Linking cognition, emotion and physiology for well-being and adaptability'. In: *Ann. Neurosci.* 32 (2 Apr. 2025), pp. 128–142. DOI: 10.1177/09727531241255492.

[864] Ebtesam A Al-Suhaimi and Firdos Alam Khan. 'Adrenal glands, pineal gland, and the circadian rhythm: Structure and physiology'. In: *Emerging Concepts in Endocrine Structure and Functions*. Singapore: Springer Nature Singapore, 2022, pp. 201–245. DOI: 10.1007/978-981-16-9016-7_7.

[865] Silvia Arber and Rui M Costa. 'Networking brainstem and basal ganglia circuits for movement'. In: *Nat. Rev. Neurosci.* 23 (6 14th June 2022), pp. 342–360. DOI: 10.1038/s41583-022-00581-w.

[866] Vincent Coulombe et al. 'A topographic atlas of the human brainstem in the ponto-mesencephalic junction plane'. In: *Front. Neuroanat.* 15 (13th Aug. 2021), p. 627656. DOI: 10.3389/fnana.2021.627656.

[867] Lynne Barker. 'How to build a brainstem'. In: *How to Build a Human Brain*. Cham: Springer International Publishing, 2024, pp. 41–75. DOI: 10.1007/978-3-031-55297-7_2.

[868] Xue Liu et al. 'The superior colliculus: Cell types, connectivity, and behavior'. In: *Neurosci. Bull.* 38 (12 Dec. 2022), pp. 1519–1540. DOI: 10.1007/s12264-022-00858-1.

[869] Brian R Noga and Patrick J Whelan. 'The mesencephalic locomotor region: Beyond locomotor control'. In: *Front. Neural Circuits* 16 (9th May 2022), p. 884785. DOI: 10.3389/fncir.2022.884785.

[870] Claudius F Kratochwil, Upasana Maheshwari and Filippo M Rijli. 'The long journey of pontine nuclei neurons: From rhombic lip to Cortico-ponto-cerebellar circuitry'. In: *Front. Neural Circuits* 11 (17th May 2017), p. 33. DOI: 10.3389/fncir.2017.00033.

[871] Haleh Karbasforoushan, Runfeng Tian and James Baker. 'There is a topographic organization in human cortico-pontine connectivity'. In: *Brain Commun.* 4 (2 22nd Feb. 2022), fcac047. DOI: 10.1093/braincomms/fcac047.

[872] K Michael Spyer and Alexander V Gourine. 'Chemosensory pathways in the brainstem controlling cardiorespiratory activity'. In: *Philos. Trans. R. Soc. Lond. B Biol. Sci.* 364 (1529 12th Sept. 2009), pp. 2603–2610. DOI: 10.1098/rstb.2009.0082.

[873] Daniel B Zoccal et al. 'The nucleus of the solitary tract and the coordination of respiratory and sympathetic activities'. In: *Front. Physiol.* 5 (25th June 2014), p. 238. DOI: 10.3389/fphys.2014.00238.

[874] Megan R Carey. 'The cerebellum'. In: *Curr. Biol.* 34 (1 8th Jan. 2024), R7–R11. DOI: 10.1016/j.cub.2023.11.048.

[875] Lynne Barker. 'How to build a cerebellum'. In: *How to Build a Human Brain*. Cham: Springer International Publishing, 2024, pp. 77–109. DOI: 10.1007/978-3-031-55297-7_3.

[876] Mitsunori Matsumae et al. 'Research into the physiology of cerebrospinal fluid reaches a new horizon: Intimate exchange between cerebrospinal fluid and interstitial fluid may contribute to maintenance of homeostasis in the central nervous system'. In: *Neurol. Med. Chir. (Tokyo)* 56 (7 15th July 2016), pp. 416–441. DOI: 10.2176/nmc.ra.2016-0020.

[877] Hayrettin Tumani, André Huss and Franziska Bachhuber. 'The cerebrospinal fluid and barriers - anatomic and physiologic considerations'. In: *Handb. Clin. Neurol.* 146 (2017), pp. 21–32. DOI: 10.1016/B978-0-12-804279-3.00002-2.

[878] Natalia Czarniak et al. 'Cerebrospinal fluid-basic concepts review'. In: *Biomedicines* 11 (5 17th May 2023), p. 1461. DOI: 10.3390/biomedicines11051461.

[879] Christer Betsholtz et al. 'Advances and controversies in meningeal biology'. In: *Nat. Neurosci.* 27 (11 Nov. 2024), pp. 2056–2072. DOI: 10.1038/s41593-024-01701-8.

[880] Gideon Idumah, Erkki Somersalo and Daniela Calvetti. 'A spatially distributed model of brain metabolism highlights the role of diffusion in brain energy metabolism'. In: *J. Theor. Biol.* 572 (111567 7th Sept. 2023), p. 111567. DOI: 10.1016/j.jtbi.2023.111567.

[881] Alexandre Poulain, Jørgen Riseth and Vegard Vinje. 'Multi-compartmental model of glymphatic clearance of solutes in brain tissue'. In: *PLoS One* 18 (3 7th Mar. 2023), e0280501. DOI: 10.1371/journal.pone.0280501.

[882] Gesa Carstens et al. 'Metabolite transport across central nervous system barriers'. In: *J. Cereb. Blood Flow Metab.* 44 (7 July 2024), pp. 1063–1077. DOI: 10.1177/0271678X241241908.

[883] Tetsuya Takano et al. 'Neuronal polarization'. In: *Development* 142 (12 15th June 2015), pp. 2088–2093. DOI: 10.1242/dev.114454.

[884] Shaul Yogev and Kang Shen. 'Establishing Neuronal Polarity with environmental and intrinsic mechanisms'. In: *Neuron* 96 (3 1st Nov. 2017), pp. 638–650. DOI: 10.1016/j.neuron.2017.10.021.

[885] Moritz Stingl, Andreas Draguhn and Martin Both. 'A dendrite is a dendrite is a dendrite? Dendritic signal integration beyond the "antenna" model'. In: *Pflugers Arch.* 477 (1 Jan. 2025), pp. 9–16. DOI: 10.1007/s00424-024-03004-0.

[886] Le Gao et al. 'Single-neuron analysis of dendrites and axons reveals the network organization in mouse prefrontal cortex'. In: *Nat. Neurosci.* 26 (6 June 2023), pp. 1111–1126. DOI: 10.1038/s41593-023-01339-y.

[887] G J Kress and S Mennerick. 'Action potential initiation and propagation: upstream influences on neurotransmission'. In: *Neuroscience* 158 (1 12th Jan. 2009), pp. 211–222. DOI: 10.1016/j.neuroscience.2008.03.021.

[888] Christopher S von Bartheld, Jami Bahney and Suzana Herculano-Houzel. 'The search for true numbers of neurons and glial cells in the human brain: A review of 150 years of cell counting: Quantifying neurons and glia in human brain'. In: *J. Comp. Neurol.* 524 (18 15th Dec. 2016), pp. 3865–3895. DOI: 10.1002/cne.24040.

[889] Andrea Ortega et al. 'ASTROGLIA: Molecular mechanisms, functional roles, and neurophysiological implications in the central nervous system'. In: *Life (Basel)* 15 (10 24th Sept. 2025), p. 1505. DOI: 10.3390/life15101505.

[890] Ciaran Murphy-Royal et al. 'Astroglial glutamate transporters in the brain: Regulating neurotransmitter homeostasis and synaptic transmission: Astroglial glutamate uptake'. In: *J. Neurosci. Res.* 95 (11 Nov. 2017), pp. 2140–2151. DOI: 10.1002/jnr.24029.

[891] Elidie Beard et al. 'Astrocytes as key regulators of brain energy metabolism: New therapeutic perspectives'. In: *Front. Physiol.* 12 (2021), p. 825816. DOI: 10.3389/fphys.2021.825816.

[892] Christine Stadelmann et al. 'Myelin in the central nervous system: Structure, function, and pathology'. In: *Physiol. Rev.* 99 (3 1st July 2019), pp. 1381–1431. DOI: 10.1152/physrev.00031.2018.

[893] Mikael Simons, Erin M Gibson and Klaus-Armin Nave. 'Oligodendrocytes: Myelination, plasticity, and axonal support'. In: *Cold Spring Harb. Perspect. Biol.* 16 (10 1st Oct. 2024), a041359. DOI: 10.1101/cshperspect.a041359.

[894] Ukpong B Eyo and Long-Jun Wu. 'Microglia: Lifelong patrolling immune cells of the brain'. In: *Prog. Neurobiol.* 179 (101614 Aug. 2019), p. 101614. DOI: 10.1016/j.pneurobio.2019.04.003.

[895] Sarah J Pfau et al. 'Characteristics of blood-brain barrier heterogeneity between brain regions revealed by profiling vascular and perivascular cells'. In: *Nat. Neurosci.* 27 (10 Oct. 2024), pp. 1892–1903. DOI: 10.1038/s41593-024-01743-y.

[896] Yuqing Xiang, Qiuxiang Gu and Dong Liu. 'Brain endothelial cells in blood-brain barrier regulation and neurological therapy'. In: *Int. J. Mol. Sci.* 26 (12 18th June 2025), p. 5843. DOI: 10.3390/ijms26125843.

[897] Antonio J Jiménez et al. 'Structure and function of the ependymal barrier and diseases associated with ependyma disruption'. In: *Tissue Barriers* 2 (1 19th Mar. 2014), e28426. DOI: 10.4161/tisb.28426.

[898] Adam MacDonald et al. 'Single cell transcriptomics of ependymal cells across age, region and species reveals cilia-related and metal ion regulatory roles as major conserved ependymal cell functions'. In: *Front. Cell. Neurosci.* 15 (15th July 2021), p. 703951. DOI: 10.3389/fncel.2021.703951.

[899] Giuliana Mannino et al. 'Adult stem cell niches for tissue homeostasis'. In: *J. Cell. Physiol.* 237 (1 Jan. 2022), pp. 239–257. DOI: 10.1002/jcp.30562.

[900] Isidora Banjac, Martti Maimets and Kim B Jensen. 'Maintenance of high-turnover tissues during and beyond homeostasis'. In: *Cell Stem Cell* 30 (4 6th Apr. 2023), pp. 348–361. DOI: 10.1016/j.stem.2023.03.008.

[901] Andreas Bergmann and Hermann Steller. 'Apoptosis, stem cells, and tissue regeneration'. In: *Sci. Signal.* 3 (145 26th Oct. 2010), re8. DOI: 10.1126/scisignal.3145re8.

[902] Siiri E Iismaa et al. 'Comparative regenerative mechanisms across different mammalian tissues'. In: *NPJ Regen. Med.* 3 (1 23rd Feb. 2018), p. 6. DOI: 10.1038/s41536-018-0044-5.

[903] Jeffrey W Brown, Charles J Cho and Jason C Mills. 'Paligenosis: Cellular remodeling during tissue repair'. In: *Annu. Rev. Physiol.* 84 (1 10th Feb. 2022), pp. 461–483. DOI: 10.1146/annurev-physiol-061121-035954.

[904] Daniel Moreno-Blas, Teresa Adell and Cristina González-Estévez. 'Autophagy in tissue repair and regeneration'. In: *Cells* 14 (4 14th Feb. 2025), p. 282. DOI: 10.3390/cells14040282.

[905] José M Frade and María C Ovejero-Benito. 'Neuronal cell cycle: the neuron itself and its circumstances'. In: *Cell Cycle* 14 (5 2015), pp. 712–720. DOI: 10.1080/15384101.2015.1004937.

[906] Karl Herrup and Yan Yang. 'Cell cycle regulation in the postmitotic neuron: oxymoron or new biology?' In: *Nat. Rev. Neurosci.* 8 (5 May 2007), pp. 368–378. DOI: 10.1038/nrn2124.

[907] Laura J A Hardwick et al. 'Cell cycle regulation of proliferation versus differentiation in the central nervous system'. In: *Cell Tissue Res.* 359 (1 Jan. 2015), pp. 187–200. DOI: 10.1007/s00441-014-1895-8.

[908] Honorine Destain, Manasa Prahlad and Paschalis Kratsios. 'Maintenance of neuronal identity in C. elegans and beyond: Lessons from transcription and chromatin factors'. In: *Semin. Cell Dev. Biol.* 154 (Pt A 15th Feb. 2024), pp. 35–47. DOI: 10.1016/j.semcdb.2023.07.001.

[909] A J Kole, R P Annis and M Deshmukh. 'Mature neurons: equipped for survival'. In: *Cell Death Dis.* 4 (6 27th June 2013), e689. DOI: 10.1038/cddis.2013.220.

[910] Inge Seim, Siming Ma and Vadim N Gladyshev. 'Gene expression signatures of human cell and tissue longevity'. In: *NPJ Aging Mech. Dis.* 2 (1 7th July 2016), p. 16014. DOI: 10.1038/npjamd.2016.14.

[911] Rafael Arrojo E Drigo et al. 'Age mosaicism across multiple scales in adult tissues'. In: *Cell Metab.* 30 (2 6th Aug. 2019), 343–351.e3. DOI: 10.1016/j.cmet.2019.05.010.

[912] Eric Sah et al. 'The cellular senescence stress response in post-mitotic brain cells: Cell survival at the expense of tissue degeneration'. In: *Life (Basel)* 11 (3 11th Mar. 2021), p. 229. DOI: 10.3390/life11030229.

[913] Janeth Alva-Medina et al. 'Continued stabilization of the nuclear higher-order structure of post-mitotic neurons in vivo'. In: *PLoS One* 6 (6 23rd June 2011), e21360. DOI: 10.1371/journal.pone.0021360.

[914] Armando Aranda-Anzaldo. 'The post-mitotic state in neurons correlates with a stable nuclear higher-order structure'. In: *Commun. Integr. Biol.* 5 (2 1st Mar. 2012), pp. 134–139. DOI: 10.4161/cib.18761.

[915] Yusuke Kageyama et al. 'Mitochondrial division ensures the survival of postmitotic neurons by suppressing oxidative damage'. In: *J. Cell Biol.* 197 (4 14th May 2012), pp. 535–551. DOI: 10.1083/jcb.201110034.

[916] Emilie Hollville, Selena E Romero and Mohanish Deshmukh. 'Apoptotic cell death regulation in neurons'. In: *FEBS J.* 286 (17 Sept. 2019), pp. 3276–3298. DOI: 10.1111/febs.14970.

[917] Dylan A Reid et al. 'Incorporation of a nucleoside analog maps genome repair sites in postmitotic human neurons'. In: *Science* 372 (6537 2nd Apr. 2021), pp. 91–94. DOI: 10.1126/science.abb9032.

[918] Kirsty L Spalding et al. 'Dynamics of hippocampal neurogenesis in adult humans'. In: *Cell* 153 (6 6th June 2013), pp. 1219–1227. DOI: 10.1016/j.cell.2013.05.002.

[919] Maura Boldrini et al. 'Human Hippocampal Neurogenesis Persists throughout Aging'. In: *Cell Stem Cell* 22 (4 5th Apr. 2018), 589–599.e5. DOI: 10.1016/j.stem.2018.03.015.

[920] Matthew K Tobin et al. 'Human hippocampal neurogenesis persists in aged adults and Alzheimer's disease patients'. In: *Cell Stem Cell* 24 (6 6th June 2019), 974–982.e3. DOI: 10.1016/j.stem.2019.05.003.

[921] F Doetsch et al. 'Subventricular zone astrocytes are neural stem cells in the adult mammalian brain'. In: *Cell* 97 (6 11th June 1999), pp. 703–716. DOI: 10.1016/s0092-8674(00)80783-7.

[922] Daniel A Lim and Arturo Alvarez-Buylla. 'The adult ventricular-subventricular zone (V-SVZ) and olfactory bulb (OB) neurogenesis'. In: *Cold Spring Harb. Perspect. Biol.* 8 (5 2nd May 2016), a018820. DOI: 10.1101/cshperspect.a018820.

[923] Arantxa Cebrian-Silla et al. 'Single-cell analysis of the ventricular-subventricular zone reveals signatures of dorsal and ventral adult neurogenesis'. In: *Elife* 10 (e67436 14th July 2021), e67436. DOI: 10.7554/eLife.67436.

[924] Alvaro Duque, Jon I Arellano and Pasko Rakic. 'An assessment of the existence of adult neurogenesis in humans and value of its rodent models for neuropsychiatric diseases'. In: *Mol. Psychiatry* 27 (1 Jan. 2022), pp. 377–382. DOI: 10.1038/s41380-021-01314-8.

[925] Kang Shen and Peter Scheiffele. 'Genetics and cell biology of building specific synaptic connectivity'. In: *Annu. Rev. Neurosci.* 33 (1 21st July 2010), pp. 473–507. DOI: 10.1146/annurev.neuro.051508.135302.

[926] Shaul Yogev and Kang Shen. 'Cellular and molecular mechanisms of synaptic specificity'. In: *Annu. Rev. Cell Dev. Biol.* 30 (1 15th Aug. 2014), pp. 417–437. DOI: 10.1146/annurev-cellbio-100913-012953.

[927] Miao Cao, Hao Huang and Yong He. 'Developmental connectomics from infancy through early childhood'. In: *Trends Neurosci.* 40 (8 Aug. 2017), pp. 494–506. DOI: 10.1016/j.tins.2017.06.003.

[928] Rodrigo Suárez et al. 'Cortical activity emerges in region-specific patterns during early brain development'. In: *Proc. Natl. Acad. Sci. U. S. A.* 120 (22 30th May 2023), e2208654120. DOI: 10.1073/pnas.2208654120.

[929] Travis E Faust, Georgia Gunner and Dorothy P Schafer. 'Mechanisms governing activity-dependent synaptic pruning in the developing mammalian CNS'. In: *Nat. Rev. Neurosci.* 22 (11 20th Nov. 2021), pp. 657–673. DOI: 10.1038/s41583-021-00507-y.

[930] Elena W Adlaf et al. 'Adult-born neurons modify excitatory synaptic transmission to existing neurons'. In: *Elife* 6 (30th Jan. 2017), e19886. DOI: 10.7554/eLife.19886.

[931] Sofia Grade and Magdalena Götz. 'Neuronal replacement therapy: previous achievements and challenges ahead'. In: *NPJ Regen. Med.* 2 (1 23rd Oct. 2017), p. 29. DOI: 10.1038/s41536-017-0033-0.

[932] Kurt A Sailor, Alejandro F Schinder and Pierre-Marie Lledo. 'Adult neurogenesis beyond the niche: its potential for driving brain plasticity'. In: *Curr. Opin. Neurobiol.* 42 (Feb. 2017), pp. 111–117. DOI: 10.1016/j.conb.2016.12.001.

[933] Conrad Kiyoshi and Andrea Tedeschi. 'Axon growth and synaptic function: A balancing act for axonal regeneration and neuronal circuit formation in CNS trauma and disease'. In: *Dev. Neurobiol.* 80 (7-8 1st July 2020), pp. 277–301. DOI: 10.1002/dneu.22780.

[934] Gabriel N Aughey. 'Maintenance of neuronal fate and transcriptional identity'. In: *Biol. Open* 12 (6 15th June 2023), bio059953. DOI: 10.1242/bio.059953.

[935] Erin N Lottes and Daniel N Cox. 'Homeostatic roles of the proteostasis network in dendrites'. In: *Front. Cell. Neurosci.* 14 (14th Aug. 2020), p. 264. DOI: 10.3389/fncel.2020.00264.

[936] Linhao Ruan et al. 'Mitochondria-associated proteostasis'. In: *Annu. Rev. Biophys.* 49 (1 6th May 2020), pp. 41–67. DOI: 10.1146/annurev-biophys-121219-081604.

[937] Elena I Rugarli and Thomas Langer. 'Mitochondrial quality control: a matter of life and death for neurons: Mitochondrial quality control and neurodegeneration'. In: *EMBO J.* 31 (6 21st Mar. 2012), pp. 1336–1349. DOI: 10.1038/emboj.2012.38.

[938] Thomas Misgeld and Thomas L Schwarz. 'Mitostasis in neurons: Maintaining mitochondria in an extended cellular architecture'. In: *Neuron* 96 (3 1st Nov. 2017), pp. 651–666. DOI: 10.1016/j.neuron.2017.09.055.

[939] Yifei Zheng et al. 'Mitochondria at the crossroads: Quality control mechanisms in neuronal senescence and neurodegeneration'. In: *Neurobiol. Dis.* 208 (106862 May 2025), p. 106862. DOI: 10.1016/j.nbd.2025.106862.

[940] Oliwia Koszła and Przemysław Sołek. 'Misfolding and aggregation in neurodegenerative diseases: protein quality control machinery as potential therapeutic clearance pathways'. In: *Cell Commun. Signal.* 22 (1 30th Aug. 2024), p. 421. DOI: 10.1186/s12964-024-01791-8.

[941] Joel Theophilus Johnson, Fila Winifred Awosiminiala and Christian Kosisochukwu Anumudu. 'Exploring protein misfolding and aggregate pathology in neurodegenerative diseases: From molecular mechanisms to clinical interventions'. In: *Appl. Sci. (Basel)* 15 (18 22nd Sept. 2025), p. 10285. DOI: 10.3390/app151810285.

[942] Annika Höhn, Antonella Tramutola and Roberta Cascella. 'Proteostasis failure in neurodegenerative diseases: Focus on oxidative stress'. In: *Oxid. Med. Cell. Longev.* 2020 (27th Mar. 2020), p. 5497046. DOI: 10.1155/2020/5497046.

[943] Annwyne Houldsworth. 'Role of oxidative stress in neurodegenerative disorders: a review of reactive oxygen species and prevention by antioxidants'. In: *Brain Commun.* 6 (1 2nd Jan. 2024), fcad356. DOI: 10.1093/braincomms/fcad356.

[944] Carmen Martínez-Cué and Noemí Rueda. 'Cellular senescence in neurodegenerative diseases'. In: *Front. Cell. Neurosci.* 14 (11th Feb. 2020), p. 16. DOI: 10.3389/fncel.2020.00016.

[945] Shirel Argueti-Ostrovsky et al. 'All roads lead to Rome: Different molecular players converge to common toxic pathways in neurodegeneration'. In: *Cells* 10 (9 16th Sept. 2021), p. 2438. DOI: 10.3390/cells10092438.

[946] Hikaru Fukutomi et al. 'Neurite imaging reveals microstructural variations in human cerebral cortical gray matter'. In: *Neuroimage* 182 (15th Nov. 2018), pp. 488–499. DOI: 10.1016/j.neuroimage.2018.02.017.

[947] Erhan Genç et al. 'Diffusion markers of dendritic density and arborization in gray matter predict differences in intelligence'. In: *Nat. Commun.* 9 (1 15th May 2018), p. 1905. DOI: 10.1038/s41467-018-04268-8.

[948] Paula Sanchez-Molina et al. 'From mouse to human: Comparative analysis between grey and white matter by synchrotron-Fourier transformed infrared microspectroscopy'. In: *Biomolecules* 10 (8 24th July 2020), E1099. DOI: 10.3390/biom10081099.

[949] J S O'Brien and E L Sampson. 'Lipid composition of the normal human brain: gray matter, white matter, and myelin'. In: *J. Lipid Res.* 6 (4 1st Oct. 1965), pp. 537–544. DOI: 10.1016/s0022-2275(20)39619-x.

[950] R Douglas Fields. 'White matter in learning, cognition and psychiatric disorders'. In: *Trends Neurosci.* 31 (7 July 2008), pp. 361–370. DOI: 10.1016/j.tins.2008.04.001.

[951] Marina Zavolskova et al. 'Lipid composition diversity of the human brain white matter tracts'. In: *J. Neurochem.* 169 (3 Mar. 2025), e70042. DOI: 10.1111/jnc.70042.

[952] Yannick Poitelon, Ashley M Kopec and Sophie Belin. 'Myelin fat facts: An overview of lipids and fatty acid metabolism'. In: *Cells* 9 (4 27th Mar. 2020), E812. DOI: 10.3390/cells9040812.

[953] Laura Montani. 'Lipids in regulating oligodendrocyte structure and function'. In: *Semin. Cell Dev. Biol.* 112 (Apr. 2021), pp. 114–122. DOI: 10.1016/j.semcdb.2020.07.016.

[954] Alexander Kister and Ilya Kister. 'Overview of myelin, major myelin lipids, and myelin-associated proteins'. In: *Front. Chem.* 10 (2022), p. 1041961. DOI: 10.3389/fchem.2022.1041961.

[955] Olaf Jahn, Stefan Tenzer and Hauke B Werner. 'Myelin proteomics: molecular anatomy of an insulating sheath'. In: *Mol. Neurobiol.* 40 (1 Aug. 2009), pp. 55–72. DOI: 10.1007/s12035-009-8071-2.

[956] Alessandra Donato et al. 'Neuronal sub-compartmentalization: a strategy to optimize neuronal function: Neuronal sub-compartments'. In: *Biol. Rev. Camb. Philos. Soc.* 94 (3 June 2019), pp. 1023–1037. DOI: 10.1111/brv.12487.

[957] Mutsuo Nuriya and Masato Yasui. 'Endfeet serve as diffusion-limited subcellular compartments in astrocytes'. In: *J. Neurosci.* 33 (8 20th Feb. 2013), pp. 3692–3698. DOI: 10.1523/JNEUROSCI.3050-12.2013.

[958] Shannon N Rhoads et al. 'Neurons and astrocytes have distinct organelle signatures and responses to stress'. In: *Cell Rep.* 44 (9 23rd Sept. 2025), p. 116280. DOI: 10.1016/j.celrep.2025.116280.

[959] Zacharie Taoufiq et al. 'Hidden proteome of synaptic vesicles in the mammalian brain'. In: *Proc. Natl. Acad. Sci. U. S. A.* 117 (52 29th Dec. 2020), pp. 33586–33596. DOI: 10.1073/pnas.2011870117.

[960] Marc van Oostrum et al. 'The proteomic landscape of synaptic diversity across brain regions and cell types'. In: *Cell* 186 (24 22nd Nov. 2023), 5411–5427.e23. DOI: 10.1016/j.cell.2023.09.028.

[961] Rita Reig-Viader et al. 'Synaptic proteome diversity is shaped by the levels of glutamate receptors and their regulatory proteins'. In: *Nat. Commun.* 16 (1 25th Nov. 2025), p. 10487. DOI: 10.1038/s41467-025-65490-9.

[962] Ke Xu, Guisheng Zhong and Xiaowei Zhuang. 'Actin, spectrin, and associated proteins form a periodic cytoskeletal structure in axons'. In: *Science* 339 (6118 25th Jan. 2013), pp. 452–456. DOI: 10.1126/science.1232251.

[963] Steven L Jones, Farida Korobova and Tatyana Svitkina. 'Axon initial segment cytoskeleton comprises a multiprotein submembranous coat containing sparse actin filaments'. In: *J. Cell Biol.* 205 (1 14th Apr. 2014), pp. 67–81. DOI: 10.1083/jcb.201401045.

[964] Chuansheng Zhang and Matthew N Rasband. 'Cytoskeletal control of axon domain assembly and function'. In: *Curr. Opin. Neurobiol.* 39 (Aug. 2016), pp. 116–121. DOI: 10.1016/j.conb.2016.05.001.

[965] Andrew D Nelson and Paul M Jenkins. 'Axonal membranes and their domains: Assembly and function of the axon initial segment and node of Ranvier'. In: *Front. Cell. Neurosci.* 11 (9th May 2017), p. 136. DOI: 10.3389/fncel.2017.00136.

[966] Antoine G Godin et al. 'Single-nanotube tracking reveals the nanoscale organization of the extracellular space in the live brain'. In: *Nat. Nanotechnol.* 12 (3 Mar. 2017), pp. 238–243. DOI: 10.1038/nnano.2016.248.

[967] Carson Ingo et al. 'Studying neurons and glia non-invasively via anomalous subdiffusion of intracellular metabolites'. In: *Brain Struct. Funct.* 223 (8 Nov. 2018), pp. 3841–3854. DOI: 10.1007/s00429-018-1719-9.

[968] Henrik Lundell et al. 'Compartmental diffusion and microstructural properties of human brain gray and white matter studied with double diffusion encoding magnetic resonance spectroscopy of metabolites and water'. In: *Neuroimage* 234 (117981 1st July 2021), p. 117981. DOI: 10.1016/j.neuroimage.2021.117981.

[969] Nikos K Karamanos et al. 'A guide to the composition and functions of the extracellular matrix'. In: *FEBS J.* 288 (24 Dec. 2021), pp. 6850–6912. DOI: 10.1111/febs.15776.

[970] James Melrose, Anthony J Hayes and Gregory Bix. 'The CNS/PNS extracellular matrix provides instructive guidance cues to neural cells and neuroregulatory proteins in neural development and repair'. In: *Int. J. Mol. Sci.* 22 (11 25th May 2021), p. 5583. DOI: 10.3390/ijms22115583.

[971] James Melrose. 'Hyaluronan hydrates and compartmentalises the CNS/PNS extracellular matrix and provides niche environments conducive to the optimisation of neuronal activity'. In: *J. Neurochem.* 166 (4 Aug. 2023), pp. 637–653. DOI: 10.1111/jnc.15915.

[972] Shinji Miyata and Hiroshi Kitagawa. 'Formation and remodeling of the brain extracellular matrix in neural plasticity: Roles of chondroitin sulfate and hyaluronan'. In: *Biochim. Biophys. Acta Gen. Subj.* 1861 (10 1st Oct. 2017), pp. 2420–2434. DOI: 10.1016/j.bbagen.2017.06.010.

[973] Xin Yang. 'Chondroitin sulfate proteoglycans: key modulators of neuronal plasticity, long-term memory, neurodegenerative, and psychiatric disorders'. In: *Rev. Neurosci.* 31 (5 28th July 2020), pp. 555–568. DOI: 10.1515/revneuro-2019-0117.

[974] Charles Nicholson and Sabina Hrabětová. 'Brain extracellular space: The final frontier of neuroscience'. In: *Biophys. J.* 113 (10 21st Nov. 2017), pp. 2133–2142. DOI: 10.1016/j.bpj.2017.06.052.

[975] Alexander Dityatev, Melitta Schachner and Peter Sonderegger. 'The dual role of the extracellular matrix in synaptic plasticity and homeostasis'. In: *Nat. Rev. Neurosci.* 11 (11 Nov. 2010), pp. 735–746. DOI: 10.1038/nrn2898.

[976] Sabina Hrabetova et al. 'Unveiling the extracellular space of the brain: From super-resolved microstructure to in vivo function'. In: *J. Neurosci.* 38 (44 31st Oct. 2018), pp. 9355–9363. DOI: 10.1523/JNEUROSCI.1664-18.2018.

[977] Jan Tønnesen, Sabina Hrabětová and Federico N Soria. 'Local diffusion in the extracellular space of the brain'. In: *Neurobiol. Dis.* 177 (105981 Feb. 2023), p. 105981. DOI: 10.1016/j.nbd.2022.105981.

[978] Marco Franchi et al. 'Extracellular matrix biomechanical roles and adaptation in health and disease'. In: *FEBS J.* 291 (3 Feb. 2024), pp. 430–440. DOI: 10.1111/febs.16938.

[979] Shofiul Azam et al. 'The ageing brain: Molecular and cellular basis of neurodegeneration'. In: *Front. Cell Dev. Biol.* 9 (13th Aug. 2021), p. 683459. DOI: 10.3389/fcell.2021.683459.

[980] Mitzi M Gonzales et al. 'Biological aging processes underlying cognitive decline and neurodegenerative disease'. In: *J. Clin. Invest.* 132 (10 16th May 2022), e158453. DOI: 10.1172/JCI158453.

[981] Jiseon Lee and Hee-Jin Kim. 'Normal aging induces changes in the brain and neurodegeneration progress: Review of the structural, biochemical, metabolic, cellular, and molecular changes'. In: *Front. Aging Neurosci.* 14 (30th June 2022), p. 931536. DOI: 10.3389/fnagi.2022.931536.

[982] Nitesh Sanghai and Geoffrey K Tranmer. 'Biochemical and molecular pathways in neurodegenerative diseases: An integrated view'. In: *Cells* 12 (18 20th Sept. 2023), p. 2318. DOI: 10.3390/cells12182318.

[983] Polu Picheswara Rao and Shubham Mishra. 'Genetic convergence in brain aging and neurodegeneration: from cellular mechanisms to therapeutic targets'. In: *J. Neurogenet.* 39 (4 Dec. 2025), pp. 140–159. DOI: 10.1080/01677063.2025.2571127.

[984] Martina F Callaghan et al. 'Widespread age-related differences in the human brain microstructure revealed by quantitative magnetic resonance imaging'. In: *Neurobiol. Aging* 35 (8 Aug. 2014), pp. 1862–1872. DOI: 10.1016/j.neurobiolaging.2014.02.008.

[985] Yana Blinkouskaya et al. 'Brain aging mechanisms with mechanical manifestations'. In: *Mech. Ageing Dev.* 200 (111575 Dec. 2021), p. 111575. DOI: 10.1016/j.mad.2021.111575.

[986] Virenkumar A Pandya and Rickie Patani. 'Region-specific vulnerability in neurodegeneration: lessons from normal ageing'. In: *Ageing Res. Rev.* 67 (101311 1st May 2021), p. 101311. DOI: 10.1016/j.arr.2021.101311.

[987] Mark P Mattson and Thiruma V Arumugam. 'Hallmarks of brain aging: Adaptive and pathological modification by metabolic states'. In: *Cell Metab.* 27 (6 5th June 2018), pp. 1176–1199. DOI: 10.1016/j.cmet.2018.05.011.

[988] T Teissier, E Boulanger and V Deramecourt. 'Normal ageing of the brain: Histological and biological aspects'. In: *Rev. Neurol. (Paris)* 176 (9 1st Nov. 2020), pp. 649–660. DOI: 10.1016/j.neurol.2020.03.017.

[989] Filipa Gaspar-Silva, Diogo Trigo and Joana Magalhaes. 'Ageing in the brain: mechanisms and rejuvenating strategies'. In: *Cell. Mol. Life Sci.* 80 (7 24th June 2023), p. 190. DOI: 10.1007/s00018-023-04832-6.

[990] Kathleen Grabert et al. 'Microglial brain region-dependent diversity and selective regional sensitivities to aging'. In: *Nat. Neurosci.* 19 (3 Mar. 2016), pp. 504–516. DOI: 10.1038/nn.4222.

[991] Yarlagadda Anusha-Kiran et al. 'Regional heterogeneity in mitochondrial function underlies region specific vulnerability in human brain ageing: Implications for neurodegeneration'. In: *Free Radic. Biol. Med.* 193 (Pt 1 20th Nov. 2022), pp. 34–57. DOI: 10.1016/j.freeradbiomed.2022.09.027.

[992] William E Allen et al. 'Molecular and spatial signatures of mouse brain aging at single-cell resolution'. In: *Cell* 186 (1 5th Jan. 2023), 194–208.e18. DOI: 10.1016/j.cell.2022.12.010.

[993] Oliver Hahn et al. 'Atlas of the aging mouse brain reveals white matter as vulnerable foci'. In: *Cell* 186 (19 14th Sept. 2023), 4117–4133.e22. DOI: 10.1016/j.cell.2023.07.027.

[994] Yanxi Chen et al. 'Regional- and cell type-specific changes of the human brain during aging'. In: *Hum. Brain* 2 (3 10th Jan. 2024). DOI: 10.37819/hb.3.1780.

[995] Kelly Jin et al. 'Brain-wide cell-type-specific transcriptomic signatures of healthy ageing in mice'. In: *Nature* 638 (8049 Feb. 2025), pp. 182–196. DOI: 10.1038/s41586-024-08350-8.

[996] Shu-Min Chou et al. 'Neuronal senescence in the aged brain'. In: *Aging Dis.* 14 (5 1st Oct. 2023), pp. 1618–1632. DOI: 10.14336/AD.2023.0214.

[997] Ivan Dikic. 'Proteasomal and autophagic degradation systems'. In: *Annu. Rev. Biochem.* 86 (1 20th June 2017), pp. 193–224. DOI: 10.1146/annurev-biochem-061516-044908.

[998] Christian Pohl and Ivan Dikic. 'Cellular quality control by the ubiquitin-proteasome system and autophagy'. In: *Science* 366 (6467 15th Nov. 2019), pp. 818–822. DOI: 10.1126/science.aax3769.

[999] Aaron Ciechanover and Yong Tae Kwon. 'Protein quality control by molecular chaperones in neurodegeneration'. In: *Front. Neurosci.* 11 (6th Apr. 2017), p. 185. DOI: 10.3389/fnins.2017.00185.

[1000] Sharon A Tooze and Giampietro Schiavo. 'Liaisons dangereuses: autophagy, neuronal survival and neurodegeneration'. In: *Curr. Opin. Neurobiol.* 18 (5 1st Oct. 2008), pp. 504–515. DOI: 10.1016/j.conb.2008.09.015.

[1001] Laurie D Cohen et al. 'Metabolic turnover of synaptic proteins: kinetics, interdependencies and implications for synaptic maintenance'. In: *PLoS One* 8 (5 2nd May 2013), e63191. DOI: 10.1371/journal.pone.0063191.

[1002] Stefano L Giandomenico, Beatriz Alvarez-Castelao and Erin M Schuman. 'Proteostatic regulation in neuronal compartments'. In: *Trends Neurosci.* 45 (1 Jan. 2022), pp. 41–52. DOI: 10.1016/j.tins.2021.08.002.

[1003] Célia Alecki et al. 'Localized molecular chaperone synthesis maintains neuronal dendrite proteostasis'. In: *Nat. Commun.* 15 (1 30th Dec. 2024), p. 10796. DOI: 10.1038/s41467-024-55055-7.

[1004] Andrea K H Stavoe and Erika L F Holzbaur. 'Autophagy in neurons'. In: *Annu. Rev. Cell Dev. Biol.* 35 (1 6th Oct. 2019), pp. 477–500. DOI: 10.1146/annurev-cellbio-100818-125242.

[1005] Mathieu Bourdenx et al. 'Chaperone-mediated autophagy prevents collapse of the neuronal metastable proteome'. In: *Cell* 184 (10 13th May 2021), 2696–2714.e25. DOI: 10.1016/j.cell.2021.03.048.

[1006] Claudio Hetz. 'Adapting the proteostasis capacity to sustain brain healthspan'. In: *Cell* 184 (6 18th Mar. 2021), pp. 1545–1560. DOI: 10.1016/j.cell.2021.02.007.

[1007] Marijn Kuijpers. 'Keeping synapses in shape: degradation pathways in the healthy and aging brain'. In: *Neuronal Signal.* 6 (2 15th June 2022), NS20210063. DOI: 10.1042/NS20210063.

[1008] Mark S Hipp, Prasad Kasturi and F Ulrich Hartl. 'The proteostasis network and its decline in ageing'. In: *Nat. Rev. Mol. Cell Biol.* 20 (7 July 2019), pp. 421–435. DOI: 10.1038/s41580-019-0101-y.

[1009] Mark S Hipp and F Ulrich Hartl. 'Interplay of proteostasis capacity and protein aggregation: Implications for cellular function and disease'. In: *J. Mol. Biol.* 436 (14 15th July 2024), p. 168615. DOI: 10.1016/j.jmb.2024.168615.

[1010] David Vilchez, Isabel Saez and Andrew Dillin. 'The role of protein clearance mechanisms in organismal ageing and age-related diseases'. In: *Nat. Commun.* 5 (1 8th Dec. 2014), p. 5659. DOI: 10.1038/ncomms6659.

[1011] Ewa Sikora et al. 'Cellular senescence in brain aging'. In: *Front. Aging Neurosci.* 13 (25th Feb. 2021), p. 646924. DOI: 10.3389/fnagi.2021.646924.

[1012] Nalini R Rao, Arun Upadhyay and Jeffrey N Savas. 'Derailed protein turnover in the aging mammalian brain'. In: *Mol. Syst. Biol.* 20 (2 Feb. 2024), pp. 120–139. DOI: 10.1038/s44320-023-00009-2.

[1013] Ian H Guldner et al. 'Ageing promotes microglial accumulation of slow-degrading synaptic proteins'. In: *Nature* 650 (8103 Feb. 2026), pp. 930–941. DOI: 10.1038/s41586-025-09987-9.

[1014] Paolo d'Errico and Melanie Meyer-Luehmann. 'Mechanisms of pathogenic tau and A protein spreading in Alzheimer's disease'. In: *Front. Aging Neurosci.* 12 (27th Aug. 2020), p. 265. DOI: 10.3389/fnagi.2020.00265.

[1015] Bruna Bellaver et al. 'Astrocyte reactivity influences amyloid- effects on tau pathology in preclinical Alzheimer's disease'. In: *Nat. Med.* 29 (7 29th July 2023), pp. 1775–1781. DOI: 10.1038/s41591-023-02380-x.

[1016] Altaf A Abdulkhaliq et al. 'Amyloid- and Tau in Alzheimer's disease: pathogenesis, mechanisms, and interplay'. In: *Cell Death Dis.* 17 (1 9th Jan. 2026), p. 21. DOI: 10.1038/s41419-025-08186-8.

[1017] Ariadna Recasens and Benjamin Dehay. 'Alpha-synuclein spreading in Parkinsonâ€™s disease'. In: *Front. Neuroanat.* 8 (18th Dec. 2014), p. 159. DOI: 10.3389/fnana.2014.00159.

[1018] George K Tofaris. 'Initiation and progression of -synuclein pathology in Parkinson's disease'. In: *Cell. Mol. Life Sci.* 79 (4 26th Mar. 2022), p. 210. DOI: 10.1007/s00018-022-04240-2.

[1019] Emma L Scotter, Han-Jou Chen and Christopher E Shaw. 'TDP-43 proteinopathy and ALS: Insights into disease mechanisms and therapeutic targets'. In: *Neurotherapeutics* 12 (2 Apr. 2015), pp. 352–363. DOI: 10.1007/s13311-015-0338-x.

[1020] Diana Arseni et al. 'Structure of pathological TDP-43 filaments from ALS with FTLD'. In: *Nature* 601 (7891 Jan. 2022), pp. 139–143. DOI: 10.1038/s41586-021-04199-3.

[1021] Enza Maria Verde et al. 'Molecular mechanisms of protein aggregation in ALS-FTD: Focus on TDP-43 and cellular protective responses'. In: *Cells* 14 (10 8th May 2025), p. 680. DOI: 10.3390/cells14100680.

[1022] D A.T. Nijholt et al. 'Removing protein aggregates: The role of proteolysis in neurodegeneration'. In: *Curr. Med. Chem.* 18 (16 1st June 2011), pp. 2459–2476. DOI: 10.2174/092986711795843236.

[1023] Alberim Kurtishi et al. 'Cellular proteostasis in neurodegeneration'. In: *Mol. Neurobiol.* 56 (5 May 2019), pp. 3676–3689. DOI: 10.1007/s12035-018-1334-z.

[1024] Mamta Rai et al. 'Contribution of proteases to the hallmarks of aging and to age-related neurodegeneration'. In: *Aging Cell* 21 (5 1st May 2022), e13603. DOI: 10.1111/acel.13603.

[1025] Larissa-Nele Schaffert and Wayne G Carter. 'Do post-translational modifications influence protein aggregation in neurodegenerative diseases: A systematic review'. In: *Brain Sci.* 10 (4 11th Apr. 2020), E232. DOI: 10.3390/brainsci10040232.

[1026] Wei Li et al. 'Abnormal protein post-translational modifications induces aggregation and abnormal deposition of protein, mediating neurodegenerative diseases'. In: *Cell Biosci.* 14 (1 12th Feb. 2024), p. 22. DOI: 10.1186/s13578-023-01189-y.

[1027] Silvia Bolognin, Luigi Messori and Paolo Zatta. 'Metal ion physiopathology in neurodegenerative disorders'. In: *Neuromolecular Med.* 11 (4 28th Nov. 2009), pp. 223–238. DOI: 10.1007/s12017-009-8102-1.

[1028] Leilei Chen et al. 'Homeostasis and metabolism of iron and other metal ions in neurodegenerative diseases'. In: *Signal Transduct. Target. Ther.* 10 (1 3rd Feb. 2025), p. 31. DOI: 10.1038/s41392-024-02071-0.

[1029] Shrabani Das et al. 'Heavy metal-induced disruption of the autophagy-lysosomal pathway: implications for aging and neurodegenerative disorders'. In: *Biometals* 38 (2 17th Apr. 2025), pp. 371–417. DOI: 10.1007/s10534-025-00665-x.

[1030] Kathleen A Burke, Elizabeth A Yates and Justin Legleiter. 'Biophysical insights into how surfaces, including lipid membranes, modulate protein aggregation related to neurodegeneration'. In: *Front. Neurol.* 4 (1st Mar. 2013), p. 17. DOI: 10.3389/fneur.2013.00017.

[1031] Maria Andreasen, Nikolai Lorenzen and Daniel Otzen. 'Interactions between misfolded protein oligomers and membranes: A central topic in neurodegenerative diseases?' In: *Biochim. Biophys. Acta* 1848 (9 1st Sept. 2015), pp. 1897–1907. DOI: 10.1016/j.bbamem.2015.01.018.

[1032] Amulya Nidhi Shrivastava et al. 'Physico-pathologic mechanisms involved in neurodegeneration: Misfolded protein-plasma membrane interactions'. In: *Neuron* 95 (1 5th July 2017), pp. 33–50. DOI: 10.1016/j.neuron.2017.05.026.

[1033] Tim Baldensperger, Miriam Preissler and Christian F W Becker. 'Non-enzymatic posttranslational protein modifications in protein aggregation and neurodegenerative diseases'. In: *RSC Chem. Biol.* 6 (2 5th Feb. 2025), pp. 129–149. DOI: 10.1039/d4cb00221k.

[1034] D G Knorre, N V Kudryashova and T S Godovikova. 'Chemical and functional aspects of posttranslational modification of proteins'. In: *Acta Naturae* 1 (3 Oct. 2009), pp. 29–51. DOI: 10.32607/20758251-2009-1-3-29-51.

[1035] Robert Harmel and Dorothea Fiedler. 'Features and regulation of non-enzymatic post-translational modifications'. In: *Nat. Chem. Biol.* 14 (3 14th Feb. 2018), pp. 244–252. DOI: 10.1038/nchembio.2575.

[1036] Erin Q Jennings, Kristofer S Fritz and James J Galligan. 'Biochemical genesis of enzymatic and non-enzymatic post-translational modifications'. In: *Mol. Aspects Med.* 86 (101053 Aug. 2022), p. 101053. DOI: 10.1016/j.mam.2021.101053.

[1037] John C Price et al. 'Analysis of proteome dynamics in the mouse brain'. In: *Proc. Natl. Acad. Sci. U. S. A.* 107 (32 10th Aug. 2010), pp. 14508–14513. DOI: 10.1073/pnas.1006551107.

[1038] Eugenio F Fornasiero et al. 'Precisely measured protein lifetimes in the mouse brain reveal differences across tissues and subcellular fractions'. In: *Nat. Commun.* 9 (1 12th Oct. 2018), p. 4230. DOI: 10.1038/s41467-018-06519-0.

[1039] Wenxue Li et al. 'Turnover atlas of proteome and phosphoproteome across mouse tissues and brain regions'. In: *Cell* 188 (8 17th Apr. 2025), 2267–2287.e21. DOI: 10.1016/j.cell.2025.02.021.

[1040] Verena Kluever et al. 'Protein lifetimes in aged brains reveal a proteostatic adaptation linking physiological aging to neurodegeneration'. In: *Sci. Adv.* 8 (20 20th May 2022), eabn4437. DOI: 10.1126/sciadv.abn4437.

[1041] Brandon H Toyama et al. 'Identification of long-lived proteins reveals exceptional stability of essential cellular structures'. In: *Cell* 154 (5 29th Aug. 2013), pp. 971–982. DOI: 10.1016/j.cell.2013.07.037.

[1042] Seok Heo et al. 'Identification of long-lived synaptic proteins by proteomic analysis of synaptosome protein turnover'. In: *Proc. Natl. Acad. Sci. U. S. A.* 115 (16 17th Apr. 2018), E3827–E3836. DOI: 10.1073/pnas.1720956115.

[1043] Xiaosong Liu et al. 'Long-lived proteins and DNA as candidate predictive biomarkers for tissue associated diseases'. In: *iScience* 27 (4 19th Apr. 2024), p. 109642. DOI: 10.1016/j.isci.2024.109642.

[1044] Lindsay A Osso and Ethan G Hughes. 'Dynamics of mature myelin'. In: *Nat. Neurosci.* 27 (8 Aug. 2024), pp. 1449–1461. DOI: 10.1038/s41593-024-01642-2.

[1045] K C DesJardins and P Morell. 'Phosphate groups modifying myelin basic proteins are metabolically labile; methyl groups are stable'. In: *J. Cell Biol.* 97 (2 Aug. 1983), pp. 438–446. DOI: 10.1083/jcb.97.2.438.

[1046] Bettina Sarg, Klaus Faserl and Herbert H Lindner. 'Identification of novel site-specific alterations in the modification level of myelin basic protein isolated from mouse brain at different ages using capillary electrophoresis-mass spectrometry'. In: *Proteomics* 17 (19 1st Oct. 2017), p. 1700269. DOI: 10.1002/pmic.201700269.

[1047] Sunil S Adav. 'Advances in the study of protein deamidation: Unveiling its influence on aging, disease progression, forensics and therapeutic efficacy'. In: *Proteomes* 13 (2 5th June 2025), p. 24. DOI: 10.3390/proteomes13020024.

[1048] Dylan L Riggs et al. 'Analysis of glutamine deamidation: Products, pathways, and kinetics'. In: *Anal. Chem.* 91 (20 15th Oct. 2019), pp. 13032–13038. DOI: 10.1021/acs.analchem.9b03127.

[1049] Hongqian Yang and Roman A Zubarev. 'Mass spectrometric analysis of asparagine deamidation and aspartate isomerization in polypeptides: General'. In: *Electrophoresis* 31 (11 June 2010), pp. 1764–1772. DOI: 10.1002/elps.201000027.

[1050] Sunil S Adav et al. 'Dementia-linked amyloidosis is associated with brain protein deamidation as revealed by proteomic profiling of human brain tissues'. In: *Mol. Brain* 9 (1 19th Feb. 2016), p. 20. DOI: 10.1186/s13041-016-0200-z.

[1051] Sunil S Adav and Siu Kwan Sze. 'Insight of brain degenerative protein modifications in the pathology of neurodegeneration and dementia by proteomic profiling'. In: *Mol. Brain* 9 (1 3rd Nov. 2016), p. 92. DOI: 10.1186/s13041-016-0272-9.

[1052] Alan Zanardi and Massimo Alessio. 'Ceruloplasmin deamidation in neurodegeneration: From loss to gain of function'. In: *Int. J. Mol. Sci.* 22 (2 11th Jan. 2021), E663. DOI: 10.3390/ijms22020663.

[1053] Jijing Wang et al. 'Deamidation-related blood biomarkers show promise for early diagnostics of neurodegeneration'. In: *Biomark. Res.* 10 (1 27th Dec. 2022), p. 91. DOI: 10.1186/s40364-022-00435-8.

[1054] Davis Joseph. 'The Unified Theory of Neurodegeneration Pathogenesis based on axon deamidation'. In: *Int. J. Mol. Sci.* 26 (9 27th Apr. 2025), p. 4143. DOI: 10.3390/ijms26094143.

[1055] S Clarke. 'Propensity for spontaneous succinimide formation from aspartyl and asparaginyl residues in cellular proteins'. In: *Int. J. Pept. Protein Res.* 30 (6 Dec. 1987), pp. 808–821. DOI: 10.1111/j.1399-3011.1987.tb03390.x.

[1056] Ohgi Takahashi, Ryota Kirikoshi and Noriyoshi Manabe. 'Racemization of the succinimide intermediate formed in proteins and peptides: A computational study of the mechanism catalyzed by dihydrogen phosphate ion'. In: *Int. J. Mol. Sci.* 17 (10 10th Oct. 2016), E1698. DOI: 10.3390/ijms17101698.

[1057] G I Szendrei et al. 'Aspartate-bond isomerization affects the major conformations of synthetic peptides'. In: *Eur. J. Biochem.* 226 (3 15th Dec. 1994), pp. 917–924. DOI: 10.1111/j.1432-1033.1994.t01-1-00917.x.

[1058] András Láng et al. 'Off-pathway 3D-structure provides protection against spontaneous Asn/Asp isomerization: shielding proteins Achilles heel'. In: *Q. Rev. Biophys.* 53 (e2 31st Jan. 2020), e2. DOI: 10.1017/S003358351900009X.

[1059] Stefanie Ritz-Timme and Matthew J Collins. 'Racemization of aspartic acid in human proteins'. In: *Ageing Res. Rev.* 1 (1 Feb. 2002), pp. 43–59. DOI: 10.1016/s0047-6374(01)00363-3.

[1060] Victor V Dyakin, Thomas M Wisniewski and Abel Lajtha. 'Racemization in post-translational modifications relevance to protein aging, aggregation and neurodegeneration: Tip of the iceberg'. In: *Symmetry (Basel)* 13 (3 Mar. 2021), p. 455. DOI: 10.3390/sym13030455.

[1061] Flaviyan Jerome Irudayanathan et al. 'Deciphering deamidation and isomerization in therapeutic proteins: Effect of neighboring residue'. In: *MAbs* 14 (1 Jan. 2022), p. 2143006. DOI: 10.1080/19420862.2022.2143006.

[1062] T Shimizu et al. 'Isoaspartate formation and neurodegeneration in Alzheimer's disease'. In: *Arch. Biochem. Biophys.* 381 (2 15th Sept. 2000), pp. 225–234. DOI: 10.1006/abbi.2000.1955.

[1063] Richard R Desrosiers and Irvens Fanélus. 'Damaged proteins bearing L-isoaspartyl residues and aging: a dynamic equilibrium between generation of isomerized forms and repair by PIMT'. In: *Curr. Aging Sci.* 4 (1 1st Feb. 2011), pp. 8–18. DOI: 10.2174/1874609811104010008.

[1064] Noriko Fujii et al. 'D-amino acid residues in proteins related to aging and age-related diseases and a new analysis of the isomers in proteins'. In: *D-Amino Acids*. Tokyo: Springer Japan, 2016, pp. 241–254. DOI: 10.1007/978-4-431-56077-7_15.

[1065] Victor V Dyakin, Thomas M Wisniewski and Abel Lajtha. 'Chiral interface of amyloid beta (A ): Relevance to protein aging, aggregation and neurodegeneration'. In: *Symmetry (Basel)* 12 (4 7th Apr. 2020), p. 585. DOI: 10.3390/sym12040585.

[1066] Thomas A Shoff et al. 'Determination of trends underlying aspartic acid isomerization in intact proteins reveals unusually rapid isomerization of tau'. In: *ACS Chem. Neurosci.* 16 (4 19th Feb. 2025), pp. 673–686. DOI: 10.1021/acschemneuro.4c00721.

[1067] Evan E Hubbard et al. 'Spontaneous isomerization of tau is most prevalent in Alzheimer's disease'. In: *NeuroMarkers* 3 (2 1st June 2026), p. 100152. DOI: 10.1016/j.neumar.2025.100152.

[1068] T Kimura et al. 'Accumulation of advanced glycation end products of the Maillard reaction with age in human hippocampal neurons'. In: *Neurosci. Lett.* 208 (1 12th Apr. 1996), pp. 53–56. DOI: 10.1016/0304-3940(96)12537-4.

[1069] Utkarsh Reddy Addi et al. 'Age-related neuronal damage by advanced glycation end products through altered proteostasis'. In: *Chem. Biol. Interact.* 355 (109840 1st Mar. 2022), p. 109840. DOI: 10.1016/j.cbi.2022.109840.

[1070] Katarzyna Zgutka et al. 'A role for advanced glycation end products in molecular ageing'. In: *Int. J. Mol. Sci.* 24 (12 8th June 2023), p. 9881. DOI: 10.3390/ijms24129881.

[1071] Hans-Joachim Lüth et al. 'Age- and stage-dependent accumulation of advanced glycation end products in intracellular deposits in normal and Alzheimer's disease brains'. In: *Cereb. Cortex* 15 (2 Feb. 2005), pp. 211–220. DOI: 10.1093/cercor/bhh123.

[1072] Masayoshi Takeuchi and Sho-Ichi Yamagishi. 'Possible involvement of advanced glycation end-products (AGEs) in the pathogenesis of Alzheimer's disease'. In: *Curr. Pharm. Des.* 14 (10 2008), pp. 973–978. DOI: 10.2174/138161208784139693.

[1073] Velandai Srikanth et al. 'Advanced glycation endproducts and their receptor RAGE in Alzheimer's disease'. In: *Neurobiol. Aging* 32 (5 May 2011), pp. 763–777. DOI: 10.1016/j.neurobiolaging.2009.04.016.

[1074] Annabelle Chambers et al. 'Advanced glycation end product formation in human cerebral cortex increases with Alzheimer-type neuropathologic changes but is not independently associated with dementia in a population-derived aging brain cohort'. In: *J. Neuropathol. Exp. Neurol.* 79 (9 1st Sept. 2020), pp. 950–958. DOI: 10.1093/jnen/nlaa064.

[1075] Dhivya Kothandan et al. 'Advanced glycation end products-induced Alzheimer's disease and its novel therapeutic approaches: A comprehensive review'. In: *Cureus* 16 (5 30th May 2024), e61373. DOI: 10.7759/cureus.61373.

[1076] Jianling Xie et al. 'Cellular signalling of the receptor for advanced glycation end products (RAGE)'. In: *Cell. Signal.* 25 (11 1st Nov. 2013), pp. 2185–2197. DOI: 10.1016/j.cellsig.2013.06.013.

[1077] Chieh-Yu Shen et al. 'The development of Maillard reaction, and advanced glycation end product (AGE)-receptor for AGE (RAGE) signaling inhibitors as novel therapeutic strategies for patients with AGE-related diseases'. In: *Molecules* 25 (23 27th Nov. 2020), E5591. DOI: 10.3390/molecules25235591.

[1078] Qing Yue et al. 'Receptor for advanced glycation end products (RAGE): A pivotal hub in immune diseases'. In: *Molecules* 27 (15 2nd Aug. 2022), p. 4922. DOI: 10.3390/molecules27154922.

[1079] S D Yan et al. 'Enhanced cellular oxidant stress by the interaction of advanced glycation end products with their receptors/binding proteins'. In: *J. Biol. Chem.* 269 (13 1st Apr. 1994), pp. 9889–9897. DOI: 10.1016/s0021-9258(17)36966-1.

[1080] M P Wautier et al. 'Activation of NADPH oxidase by AGE links oxidant stress to altered gene expression via RAGE'. In: *Am. J. Physiol. Endocrinol. Metab.* 280 (5 1st May 2001), E685–94. DOI: 10.1152/ajpendo.2001.280.5.E685.

[1081] Agnila Chakraborty, Saad Ahmed Sami and Kay Kay Shain Marma. 'A comprehensive review on RAGE-facilitated pathological pathways connecting Alzheimer's disease, diabetes mellitus, and cardiovascular diseases'. In: *Egypt. J. Intern. Med.* 33 (1 Dec. 2021). DOI: 10.1186/s43162-021-00081-w.

[1082] Wen Li et al. 'Roles of the receptor for advanced glycation end products and its ligands in the pathogenesis of Alzheimer's disease'. In: *Int. J. Mol. Sci.* 26 (1 5th Jan. 2025), p. 403. DOI: 10.3390/ijms26010403.

[1083] Kazuya Toriumi et al. 'Role of glyoxalase 1 in methylglyoxal detoxification-the broad player of psychiatric disorders'. In: *Redox Biol.* 49 (102222 Feb. 2022), p. 102222. DOI: 10.1016/j.redox.2021.102222.

[1084] Björn Kuhla et al. 'Age- and stage-dependent glyoxalase I expression and its activity in normal and Alzheimer's disease brains'. In: *Neurobiol. Aging* 28 (1 Jan. 2007), pp. 29–41. DOI: 10.1016/j.neurobiolaging.2005.11.007.

[1085] Gemma Aragonès et al. 'The glyoxalase system in age-related diseases: Nutritional intervention as anti-ageing strategy'. In: *Cells* 10 (8 22nd July 2021), p. 1852. DOI: 10.3390/cells10081852.

[1086] Jyotiska Chaudhuri et al. 'The role of advanced glycation end products in aging and metabolic diseases: Bridging association and causality'. In: *Cell Metab.* 28 (3 4th Sept. 2018), pp. 337–352. DOI: 10.1016/j.cmet.2018.08.014.

[1087] Vanesa Cepas et al. 'Redox signaling and advanced glycation endproducts (AGEs) in diet-related diseases'. In: *Antioxidants (Basel)* 9 (2 6th Feb. 2020), E142. DOI: 10.3390/antiox9020142.

[1088] Wiramon Rungratanawanich et al. 'Advanced glycation end products (AGEs) and other adducts in aging-related diseases and alcohol-mediated tissue injury'. In: *Exp. Mol. Med.* 53 (2 10th Feb. 2021), pp. 168–188. DOI: 10.1038/s12276-021-00561-7.

[1089] Maxime Fournet, Frédéric Bonté and Alexis Desmoulière. 'Glycation damage: A possible hub for major pathophysiological disorders and aging'. In: *Aging Dis.* 9 (5 1st Oct. 2018), pp. 880–900. DOI: 10.14336/AD.2017.1121.

[1090] Paul A C Cloos and Stephan Christgau. 'Non-enzymatic covalent modifications of proteins: mechanisms, physiological consequences and clinical applications'. In: *Matrix Biol.* 21 (1 Jan. 2002), pp. 39–52. DOI: 10.1016/s0945-053x(01)00188-3.

[1091] Gabriella Leo et al. 'Deamidation at asparagine and glutamine as a major modification upon deterioration/aging of proteinaceous binders in mural paintings'. In: *Anal. Chem.* 83 (6 15th Mar. 2011), pp. 2056–2064. DOI: 10.1021/ac1027275.

[1092] Nienke L van Doorn et al. 'Site-specific deamidation of glutamine: a new marker of bone collagen deterioration: Site-specific deamidation of glutamine'. In: *Rapid Commun. Mass Spectrom.* 26 (19 15th Oct. 2012), pp. 2319–2327. DOI: 10.1002/rcm.6351.

[1093] Julie Wilson, Nienke L van Doorn and Matthew J Collins. 'Assessing the extent of bone degradation using glutamine deamidation in collagen'. In: *Anal. Chem.* 84 (21 6th Nov. 2012), pp. 9041–9048. DOI: 10.1021/ac301333t.

[1094] Caroline Solazzo et al. 'Modeling deamidation in sheep -keratin peptides and application to archeological wool textiles'. In: *Anal. Chem.* 86 (1 7th Jan. 2014), pp. 567–575. DOI: 10.1021/ac4026362.

[1095] Frido Welker et al. 'Variations in glutamine deamidation for a Châtelperronian bone assemblage as measured by peptide mass fingerprinting of collagen'. In: *Sci. Technol. Archaeol. Res.* 3 (1 Jan. 2017), pp. 15–27. DOI: 10.1080/20548923.2016.1258825.

[1096] Abigail Ramsøe et al. 'DeamiDATE 1.0: Site-specific deamidation as a tool to assess authenticity of members of ancient proteomes'. In: *J. Archaeol. Sci.* 115 (105080 Mar. 2020), p. 105080. DOI: 10.1016/j.jas.2020.105080.

[1097] Samantha Brown et al. 'Examining collagen preservation through glutamine deamidation at Denisova Cave'. In: *J. Archaeol. Sci.* 133 (105454 Sept. 2021), p. 105454. DOI: 10.1016/j.jas.2021.105454.

[1098] Abigail Ramsøe et al. 'Assessing the degradation of ancient milk proteins through site-specific deamidation patterns'. In: *Sci. Rep.* 11 (1 8th Apr. 2021), p. 7795. DOI: 10.1038/s41598-021-87125-x.

[1099] Manasij Pal Chowdhury and Michael Buckley. 'Trends in deamidation across archaeological bones, ceramics and dental calculus'. In: *Methods* 200 (1st Apr. 2022), pp. 67–79. DOI: 10.1016/j.ymeth.2021.08.004.

[1100] J L Bada and P M Helfman. 'Amino acid racemization dating of fossil bones'. In: *World Archaeol.* 7 (2 Oct. 1975), pp. 160–173. DOI: 10.1080/00438243.1975.9979630.

[1101] G Lubec and B Lubec. 'Racemization rates of amino acids for dating ancient samples'. In: *Amino Acids* 4 (1-2 Feb. 1993), pp. 1–3. DOI: 10.1007/BF00805796.

[1102] B J Johnson and G H Miller. 'Archaeological applications of amino acid racemization'. In: *Archaeometry* 39 (2 1st Aug. 1997), pp. 265–287. DOI: 10.1111/j.1475-4754.1997.tb00806.x.

[1103] M J Collins, E R Waite and A C van Duin. 'Predicting protein decomposition: the case of aspartic-acid racemization kinetics'. In: *Philos. Trans. R. Soc. Lond. B Biol. Sci.* 354 (1379 29th Jan. 1999), pp. 51–64. DOI: 10.1098/rstb.1999.0359.

[1104] Mehdi Moini, Christopher M Rollman and Christine A M France. 'Dating human bone: is racemization dating species-specific?' In: *Anal. Chem.* 85 (23 3rd Dec. 2013), pp. 11211–11215. DOI: 10.1021/ac402917z.

[1105] Ardith D Bravenec, Karen D Ward and Timothy J Ward. 'Amino acid racemization and its relation to geochronology and archaeometry'. In: *J. Sep. Sci.* 41 (6 20th Feb. 2018), pp. 1489–1506. DOI: 10.1002/jssc.201701506.

[1106] Marc R Dickinson, Adrian M Lister and Kirsty E H Penkman. 'A new method for enamel amino acid racemization dating: A closed system approach'. In: *Quat. Geochronol.* 50 (Mar. 2019), pp. 29–46. DOI: 10.1016/j.quageo.2018.11.005.

[1107] Catherine A Cobb and Marsha P Cole. 'Oxidative and nitrative stress in neurodegeneration'. In: *Neurobiol. Dis.* 84 (1st Dec. 2015), pp. 4–21. DOI: 10.1016/j.nbd.2015.04.020.

[1108] Anju Singh et al. 'Oxidative stress: A key modulator in neurodegenerative diseases'. In: *Molecules* 24 (8 22nd Apr. 2019), E1583. DOI: 10.3390/molecules24081583.

[1109] Dimitris Korovesis, Teresa Rubio-Tomás and Nektarios Tavernarakis. 'Oxidative stress in age-related neurodegenerative diseases: An overview of recent tools and findings'. In: *Antioxidants (Basel)* 12 (1 5th Jan. 2023), p. 131. DOI: 10.3390/antiox12010131.

[1110] Alessandra Altomare et al. 'Lipid peroxidation derived reactive carbonyl species in free and conjugated forms as an index of lipid peroxidation: limits and perspectives'. In: *Redox Biol.* 42 (101899 June 2021), p. 101899. DOI: 10.1016/j.redox.2021.101899.

[1111] James Nathan Cobley, Maria Luisa Fiorello and Damian Miles Bailey. '13 reasons why the brain is susceptible to oxidative stress'. In: *Redox Biol.* 15 (May 2018), pp. 490–503. DOI: 10.1016/j.redox.2018.01.008.

[1112] Gaewyn Ellison, Ashley L Hollings and Mark J Hackett. 'A review of the "metallome" within neurons and glia, as revealed by elemental mapping of brain tissue'. In: *BBA Adv.* 2 (100038 1st Jan. 2022), p. 100038. DOI: 10.1016/j.bbadva.2021.100038.

[1113] Peter Schönfeld and Georg Reiser. 'Brain energy metabolism spurns fatty acids as fuel due to their inherent mitotoxicity and potential capacity to unleash neurodegeneration'. In: *Neurochem. Int.* 109 (Oct. 2017), pp. 68–77. DOI: 10.1016/j.neuint.2017.03.018.

[1114] Daniela-Marilena Trofin et al. 'Oxidative stress in brain function'. In: *Antioxidants (Basel)* 14 (3 28th Feb. 2025), p. 297. DOI: 10.3390/antiox14030297.

[1115] Mariona Jové et al. 'Lipid adaptations against oxidative challenge in the healthy adult human brain'. In: *Antioxidants (Basel)* 12 (1 12th Jan. 2023), p. 177. DOI: 10.3390/antiox12010177.

[1116] Giovanna Cenini, Ana Lloret and Roberta Cascella. 'Oxidative stress in neurodegenerative diseases: From a mitochondrial Point of View'. In: *Oxid. Med. Cell. Longev.* 2019 (9th May 2019), p. 2105607. DOI: 10.1155/2019/2105607.

[1117] C Venkateshappa et al. 'Elevated oxidative stress and decreased antioxidant function in the human hippocampus and frontal cortex with increasing age: implications for neurodegeneration in Alzheimer's disease'. In: *Neurochem. Res.* 37 (8 Aug. 2012), pp. 1601–1614. DOI: 10.1007/s11064-012-0755-8.

[1118] Mototada Shichiri. 'The role of lipid peroxidation in neurological disorders'. In: *J. Clin. Biochem. Nutr.* 54 (3 May 2014), pp. 151–160. DOI: 10.3164/jcbn.14-10.

[1119] Orjona V Taso et al. 'Lipid peroxidation products and their role in neurodegenerative diseases'. In: *Ann. Res. Hosp.* 3 (0 16th Jan. 2019), pp. 2–2. DOI: 10.21037/arh.2018.12.02.

[1120] Kieran Allowitz et al. 'Oxidative stress-mediated lipid peroxidation-derived lipid aldehydes in the pathophysiology of neurodegenerative diseases'. In: *Curr. Neuropharmacol.* 23 (6 2025), pp. 671–685. DOI: 10.2174/011570159X342720241014164650.

[1121] Sharon C W Ng et al. 'Free radical chain reactions and polyunsaturated fatty acids in brain lipids'. In: *ACS Omega* 7 (29 26th July 2022), pp. 25337–25345. DOI: 10.1021/acsomega.2c02285.

[1122] Stefania Pizzimenti et al. 'Interaction of aldehydes derived from lipid peroxidation and membrane proteins'. In: *Front. Physiol.* 4 (4th Sept. 2013), p. 242. DOI: 10.3389/fphys.2013.00242.

[1123] Neven Zarkovic et al. 'Pathophysiological relevance of aldehydic protein modifications'. In: *J. Proteomics* 92 (30th Oct. 2013), pp. 239–247. DOI: 10.1016/j.jprot.2013.02.004.

[1124] Giuseppina Barrera et al. 'Lipid peroxidation-derived aldehydes, 4-hydroxynonenal and malondialdehyde in aging-related disorders'. In: *Antioxidants (Basel)* 7 (8 30th July 2018), E102. DOI: 10.3390/antiox7080102.

[1125] Anna Martínez et al. 'Protein targets of oxidative damage in human neurodegenerative diseases with abnormal protein aggregates'. In: *Brain Pathol.* 20 (2 1st Mar. 2010), pp. 281–297. DOI: 10.1111/j.1750-3639.2009.00326.x.

[1126] Mayelín Domínguez et al. 'Redox proteomic profiling of neuroketal-adducted proteins in human brain: Regional vulnerability at middle age increases in the elderly'. In: *Free Radic. Biol. Med.* 95 (1st June 2016), pp. 1–15. DOI: 10.1016/j.freeradbiomed.2016.02.034.

[1127] Pamela J Urrutia and Daniel A Bórquez. 'Expanded bioinformatic analysis of Oximouse dataset reveals key putative processes involved in brain aging and cognitive decline'. In: *Free Radic. Biol. Med.* 207 (Oct. 2023), pp. 200–211. DOI: 10.1016/j.freeradbiomed.2023.07.018.

[1128] M Perluigi et al. 'Redox proteomics in aging rat brain: involvement of mitochondrial reduced glutathione status and mitochondrial protein oxidation in the aging process'. In: *J. Neurosci. Res.* 88 (16 Dec. 2010), pp. 3498–3507. DOI: 10.1002/jnr.22500.

[1129] Elizabeth A Pollina et al. 'A NPAS4-NuA4 complex couples synaptic activity to DNA repair'. In: *Nature* 614 (7949 15th Feb. 2023), pp. 732–741. DOI: 10.1038/s41586-023-05711-7.

[1130] Irina Vazquez-Villasenor et al. 'Persistent DNA damage alters the neuronal transcriptome suggesting cell cycle dysregulation and altered mitochondrial function'. In: *Eur. J. Neurosci.* 54 (9 Nov. 2021), pp. 6987–7005. DOI: 10.1111/ejn.15466.

[1131] Michael A Lodato and Jennifer S Ziegenfuss. 'The two faces of DNA oxidation in genomic and functional mosaicism during aging in human neurons'. In: *Front. Aging* 3 (12th Oct. 2022), p. 991460. DOI: 10.3389/fragi.2022.991460.

[1132] Lee J Martin. 'DNA damage and repair: relevance to mechanisms of neurodegeneration: Relevance to mechanisms of neurodegeneration'. In: *J. Neuropathol. Exp. Neurol.* 67 (5 May 2008), pp. 377–387. DOI: 10.1097/NEN.0b013e31816ff780.

[1133] Hei-Man Chow and Karl Herrup. 'Genomic integrity and the ageing brain'. In: *Nat. Rev. Neurosci.* 16 (11 14th Nov. 2015), pp. 672–684. DOI: 10.1038/nrn4020.

[1134] Ram Madabhushi et al. 'Activity-induced DNA breaks govern the expression of neuronal early-response genes'. In: *Cell* 161 (7 18th June 2015), pp. 1592–1605. DOI: 10.1016/j.cell.2015.05.032.

[1135] Agnese Cristini et al. 'Dual processing of R-loops and topoisomerase I induces transcription-dependent DNA double-strand breaks'. In: *Cell Rep.* 28 (12 17th Sept. 2019), 3167–3181.e6. DOI: 10.1016/j.celrep.2019.08.041.

[1136] Ilse Delint-Ramirez et al. 'Calcineurin dephosphorylates topoisomerase II and regulates the formation of neuronal-activity-induced DNA breaks'. In: *Mol. Cell* 82 (20 20th Oct. 2022), 3794–3809.e8. DOI: 10.1016/j.molcel.2022.09.012.

[1137] Morgan Crewe and Ram Madabhushi. 'Topoisomerase-mediated DNA damage in neurological disorders'. In: *Front. Aging Neurosci.* 13 (25th Nov. 2021), p. 751742. DOI: 10.3389/fnagi.2021.751742.

[1138] Keith W Caldecott. 'DNA single-strand break repair and human genetic disease'. In: *Trends Cell Biol.* 32 (9 Sept. 2022), pp. 733–745. DOI: 10.1016/j.tcb.2022.04.010.

[1139] Guogang Xu et al. 'Base excision repair, aging and health span'. In: *Mech. Ageing Dev.* 129 (7-8 1st July 2008), pp. 366–382. DOI: 10.1016/j.mad.2008.03.001.

[1140] Giovana S Leandro, Peter Sykora and Vilhelm A Bohr. 'The impact of base excision DNA repair in age-related neurodegenerative diseases'. In: *Mutat. Res.* 776 (1st June 2015), pp. 31–39. DOI: 10.1016/j.mrfmmm.2014.12.011.

[1141] Dennis Kjølhede Jeppesen, Vilhelm A Bohr and Tinna Stevnsner. 'DNA repair deficiency in neurodegeneration'. In: *Prog. Neurobiol.* 94 (2 1st July 2011), pp. 166–200. DOI: 10.1016/j.pneurobio.2011.04.013.

[1142] Keith W Caldecott, Michael E Ward and André Nussenzweig. 'The threat of programmed DNA damage to neuronal genome integrity and plasticity'. In: *Nat. Genet.* 54 (2 Feb. 2022), pp. 115–120. DOI: 10.1038/s41588-021-01001-y.

[1143] Z Li et al. 'Impaired DNA double-strand break repair contributes to the age-associated rise of genomic instability in humans'. In: *Cell Death Differ.* 23 (11 1st Nov. 2016), pp. 1765–1777. DOI: 10.1038/cdd.2016.65.

[1144] Gwyneth Welch and Li-Huei Tsai. 'Mechanisms of DNA damage-mediated neurotoxicity in neurodegenerative disease'. In: *EMBO Rep.* 23 (6 7th June 2022), e54217. DOI: 10.15252/embr.202154217.

[1145] Francis Rodier et al. 'Persistent DNA damage signalling triggers senescence-associated inflammatory cytokine secretion'. In: *Nat. Cell Biol.* 11 (8 Aug. 2009), pp. 973–979. DOI: 10.1038/ncb1909.

[1146] Jianghao Qian et al. 'Alteration in the chromatin landscape during the DNA damage response: Continuous rotation of the gear driving cellular senescence and aging'. In: *DNA Repair (Amst.)* 131 (103572 1st Nov. 2023), p. 103572. DOI: 10.1016/j.dnarep.2023.103572.

[1147] Zeming Wu, Jing Qu and Guang-Hui Liu. 'Roles of chromatin and genome instability in cellular senescence and their relevance to ageing and related diseases'. In: *Nat. Rev. Mol. Cell Biol.* 25 (12 3rd Dec. 2024), pp. 979–1000. DOI: 10.1038/s41580-024-00775-3.

[1148] Peter J McKinnon. 'Maintaining genome stability in the nervous system'. In: *Nat. Neurosci.* 16 (11 Nov. 2013), pp. 1523–1529. DOI: 10.1038/nn.3537.

[1149] Dai Ihara, Nur Rasyiqin Rasli and Yu Katsuyama. 'How do neurons live long and healthy? The mechanism of neuronal genome integrity'. In: *Front. Neurosci.* 19 (19th Mar. 2025), p. 1552790. DOI: 10.3389/fnins.2025.1552790.

[1150] Ru-Zhou Zhao et al. 'Mitochondrial electron transport chain, ROS generation and uncoupling (Review)'. In: *Int. J. Mol. Med.* 44 (1 1st July 2019), pp. 3–15. DOI: 10.3892/ijmm.2019.4188.

[1151] Pablo Hernansanz-Agustín and José Antonio Enríquez. 'Generation of reactive oxygen species by mitochondria'. In: *Antioxidants (Basel)* 10 (3 9th Mar. 2021), p. 415. DOI: 10.3390/antiox10030415.

[1152] Paweł Kowalczyk et al. 'Mitochondrial oxidative stress-A causative factor and therapeutic target in many diseases'. In: *Int. J. Mol. Sci.* 22 (24 13th Dec. 2021), p. 13384. DOI: 10.3390/ijms222413384.

[1153] Andrew Nguyen et al. 'Mechanisms of mitochondrial oxidative stress in brain injury: From pathophysiology to therapeutics'. In: *Oxygen (Basel)* 3 (2 7th June 2023), pp. 163–178. DOI: 10.3390/oxygen3020012.

[1154] Dimitry A Chistiakov et al. 'Mitochondrial aging and age-related dysfunction of mitochondria'. In: *Biomed Res. Int.* 2014 (1 10th Apr. 2014), p. 238463. DOI: 10.1155/2014/238463.

[1155] P Mecocci et al. 'Oxidative damage to mitochondrial DNA shows marked age-dependent increases in human brain'. In: *Ann. Neurol.* 34 (4 1st Oct. 1993), pp. 609–616. DOI: 10.1002/ana.410340416.

[1156] Nadee Nissanka and Carlos T Moraes. 'Mitochondrial DNA damage and reactive oxygen species in neurodegenerative disease'. In: *FEBS Lett.* 592 (5 1st Mar. 2018), pp. 728–742. DOI: 10.1002/1873-3468.12956.

[1157] Guo Chen, Guido Kroemer and Oliver Kepp. 'Mitophagy: An emerging role in aging and age-associated diseases'. In: *Front. Cell Dev. Biol.* 8 (26th Mar. 2020), p. 200. DOI: 10.3389/fcell.2020.00200.

[1158] Indumathi Somasundaram et al. 'Mitochondrial dysfunction and its association with age-related disorders'. In: *Front. Physiol.* 15 (2nd July 2024), p. 1384966. DOI: 10.3389/fphys.2024.1384966.

[1159] Mei-Yao Lin and Zu-Hang Sheng. 'Regulation of mitochondrial transport in neurons'. In: *Exp. Cell Res.* 334 (1 15th May 2015), pp. 35–44. DOI: 10.1016/j.yexcr.2015.01.004.

[1160] Zu-Hang Sheng. 'The interplay of axonal energy homeostasis and mitochondrial trafficking and anchoring'. In: *Trends Cell Biol.* 27 (6 1st June 2017), pp. 403–416. DOI: 10.1016/j.tcb.2017.01.005.

[1161] Amrita Mandal and Catherine M Drerup. 'Axonal transport and mitochondrial function in neurons'. In: *Front. Cell. Neurosci.* 13 (9th Aug. 2019), p. 373. DOI: 10.3389/fncel.2019.00373.

[1162] Hasnaa A Elfawy and Biswadeep Das. 'Crosstalk between mitochondrial dysfunction, oxidative stress, and age related neurodegenerative disease: Etiologies and therapeutic strategies'. In: *Life Sci.* 218 (1st Feb. 2019), pp. 165–184. DOI: 10.1016/j.lfs.2018.12.029.

[1163] Plamena R Angelova, Noemi Esteras and Andrey Y Abramov. 'Mitochondria and lipid peroxidation in the mechanism of neurodegeneration: Finding ways for prevention'. In: *Med. Res. Rev.* 41 (2 1st Mar. 2021), pp. 770–784. DOI: 10.1002/med.21712.

[1164] Patrycja Michalska and Rafael León. 'When it comes to an end: Oxidative stress crosstalk with protein aggregation and neuroinflammation induce neurodegeneration'. In: *Antioxidants (Basel)* 9 (8 12th Aug. 2020), E740. DOI: 10.3390/antiox9080740.

[1165] Dominic S A Simpson and Peter L Oliver. 'ROS generation in microglia: Understanding oxidative stress and inflammation in neurodegenerative disease'. In: *Antioxidants (Basel)* 9 (8 13th Aug. 2020), E743. DOI: 10.3390/antiox9080743.

[1166] Jun Ding et al. 'A metabolome atlas of the aging mouse brain'. In: *Nat. Commun.* 12 (1 15th Oct. 2021), p. 6021. DOI: 10.1038/s41467-021-26310-y.

[1167] Mauricio G Martín and Carlos G Dotti. 'Plasma membrane and brain dysfunction of the old: Do we age from our membranes?' In: *Front. Cell Dev. Biol.* 10 (6th Oct. 2022), p. 1031007. DOI: 10.3389/fcell.2022.1031007.

[1168] Emily L Que, Dylan W Domaille and Christopher J Chang. 'Metals in neurobiology: probing their chemistry and biology with molecular imaging'. In: *Chem. Rev.* 108 (5 May 2008), pp. 1517–1549. DOI: 10.1021/cr078203u.

[1169] Henryk Kozlowski et al. 'Copper, iron, and zinc ions homeostasis and their role in neurodegenerative disorders (metal uptake, transport, distribution and regulation)'. In: *Coord. Chem. Rev.* 253 (21-22 1st Nov. 2009), pp. 2665–2685. DOI: 10.1016/j.ccr.2009.05.011.

[1170] Carla Garza-Lombó et al. 'Neurotoxicity linked to dysfunctional metal ion homeostasis and xenobiotic metal exposure: Redox signaling and oxidative stress'. In: *Antioxid. Redox Signal.* 28 (18 20th June 2018), pp. 1669–1703. DOI: 10.1089/ars.2017.7272.

[1171] Helena Ohrvik and Dennis J Thiele. 'How copper traverses cellular membranes through the mammalian copper transporter 1, Ctr1: Mammalian copper uptake and mobilization by Ctr1'. In: *Ann. N. Y. Acad. Sci.* 1314 (1 May 2014), pp. 32–41. DOI: 10.1111/nyas.12371.

[1172] Tina Skjørringe et al. 'Divalent metal transporter 1 (DMT1) in the brain: implications for a role in iron transport at the blood-brain barrier, and neuronal and glial pathology'. In: *Front. Mol. Neurosci.* 8 (8th June 2015), p. 19. DOI: 10.3389/fnmol.2015.00019.

[1173] Qian Guo et al. 'Transferrin receptors'. In: *Exp. Mol. Med.* 57 (4 Apr. 2025), pp. 724–732. DOI: 10.1038/s12276-025-01436-x.

[1174] Joseph R Prohaska. 'Role of copper transporters in copper homeostasis'. In: *Am. J. Clin. Nutr.* 88 (3 Sept. 2008), 826S–9S. DOI: 10.1093/ajcn/88.3.826S.

[1175] Jonathon Telianidis et al. 'Role of the P-Type ATPases, ATP7A and ATP7B in brain copper homeostasis'. In: *Front. Aging Neurosci.* 5 (23rd Aug. 2013), p. 44. DOI: 10.3389/fnagi.2013.00044.

[1176] Ji Chen et al. 'The molecular mechanisms of copper metabolism and its roles in human diseases'. In: *Pflugers Arch.* 472 (10 Oct. 2020), pp. 1415–1429. DOI: 10.1007/s00424-020-02412-2.

[1177] Yumei An et al. 'The role of copper homeostasis in brain disease'. In: *Int. J. Mol. Sci.* 23 (22 10th Nov. 2022), p. 13850. DOI: 10.3390/ijms232213850.

[1178] Chiara A De Benedictis et al. 'Expression analysis of zinc transporters in nervous tissue cells reveals neuronal and synaptic localization of ZIP4'. In: *Int. J. Mol. Sci.* 22 (9 26th Apr. 2021), p. 4511. DOI: 10.3390/ijms22094511.

[1179] Stephanie L Baringer, Ian A Simpson and James R Connor. 'Brain iron acquisition: An overview of homeostatic regulation and disease dysregulation'. In: *J. Neurochem.* 165 (5 1st June 2023), pp. 625–642. DOI: 10.1111/jnc.15819.

[1180] Soheila Sabouri, Marzieh Rostamirad and Robert E Dempski. 'Unlocking the brain's zinc code: implications for cognitive function and disease'. In: *Front. Biophys.* 2 (11th June 2024), p. 1406868. DOI: 10.3389/frbis.2024.1406868.

[1181] Azhaar Ashraf et al. 'Regional distributions of iron, copper and zinc and their relationships with Glia in a normal aging mouse model'. In: *Front. Aging Neurosci.* 11 (19th Dec. 2019), p. 351. DOI: 10.3389/fnagi.2019.00351.

[1182] Omamuyovwi M Ijomone et al. 'The aging brain: impact of heavy metal neurotoxicity'. In: *Crit. Rev. Toxicol.* 50 (9 19th Oct. 2020), pp. 801–814. DOI: 10.1080/10408444.2020.1838441.

[1183] Aleksandra Górska et al. 'Distribution of iron, copper, zinc and cadmium in Glia, their influence on glial cells and relationship with neurodegenerative diseases'. In: *Brain Sci.* 13 (6 5th June 2023), p. 911. DOI: 10.3390/brainsci13060911.

[1184] Dominic Hare et al. 'A delicate balance: Iron metabolism and diseases of the brain'. In: *Front. Aging Neurosci.* 5 (18th July 2013), p. 34. DOI: 10.3389/fnagi.2013.00034.

[1185] Yijia Liu et al. 'Dual-state emission $Fe^{2+}$-activation probe capable of high-contrast brain imaging reveals an age-dependent accumulation of $Fe^{2+}$ in the brain'. In: *Anal. Chem.* 97 (48 9th Dec. 2025), pp. 26668–26676. DOI: 10.1021/acs.analchem.5c05215.

[1186] Takahiko Imai et al. 'Intracellular $Fe^{2+}$ accumulation in endothelial cells and pericytes induces blood-brain barrier dysfunction in secondary brain injury after brain hemorrhage'. In: *Sci. Rep.* 9 (1 17th Apr. 2019), p. 6228. DOI: 10.1038/s41598-019-42370-z.

[1187] Yuting Wu et al. 'Simultaneous $Fe^{2+}/Fe^{3+}$ imaging shows $Fe^{3+}$ over $Fe^{2+}$ enrichment in Alzheimer's disease mouse brain'. In: *Sci. Adv.* 9 (16 21st Apr. 2023), eade7622. DOI: 10.1126/sciadv.ade7622.

[1188] Romana Burgetova et al. 'Age-related magnetic susceptibility changes in deep grey matter and cerebral cortex of normal young and middle-aged adults depicted by whole brain analysis'. In: *Quant. Imaging Med. Surg.* 11 (9 Sept. 2021), pp. 3906–3919. DOI: 10.21037/qims-21-87.

[1189] Jing Li et al. 'Iron deposition characteristics of deep gray matter in elderly individuals in the community revealed by quantitative susceptibility mapping and multiple factor analysis'. In: *Front. Aging Neurosci.* 13 (14th Apr. 2021), p. 611891. DOI: 10.3389/fnagi.2021.611891.

[1190] Gaiying Li et al. 'Age-dependent changes in brain iron deposition and volume in deep gray matter nuclei using quantitative susceptibility mapping'. In: *Neuroimage* 269 (119923 1st Apr. 2023), p. 119923. DOI: 10.1016/j.neuroimage.2023.119923.

[1191] Julio Acosta-Cabronero et al. 'In vivo MRI mapping of brain iron deposition across the adult lifespan'. In: *J. Neurosci.* 36 (2 13th Jan. 2016), pp. 364–374. DOI: 10.1523/JNEUROSCI.1907-15.2016.

[1192] Petr Dusek et al. 'Cerebral iron deposition in neurodegeneration'. In: *Biomolecules* 12 (5 17th May 2022), p. 714. DOI: 10.3390/biom12050714.

[1193] David J Madden and Jenna L Merenstein. 'Quantitative susceptibility mapping of brain iron in healthy aging and cognition'. In: *Neuroimage* 282 (120401 15th Nov. 2023), p. 120401. DOI: 10.1016/j.neuroimage.2023.120401.

[1194] Luigi Zecca et al. 'The role of iron and copper molecules in the neuronal vulnerability of locus coeruleus and substantia nigra during aging'. In: *Proc. Natl. Acad. Sci. U. S. A.* 101 (26 29th June 2004), pp. 9843–9848. DOI: 10.1073/pnas.0403495101.

[1195] F A Zucca et al. 'Neuromelanin and iron in human locus coeruleus and substantia nigra during aging: consequences for neuronal vulnerability'. In: *J. Neural Transm. (Vienna)* 113 (6 June 2006), pp. 757–767. DOI: 10.1007/s00702-006-0453-2.

[1196] Yufan Chen et al. 'Regional age-related changes of neuromelanin and iron in the substantia nigra based on neuromelanin accumulation and iron deposition'. In: *Eur. Radiol.* 33 (5 May 2023), pp. 3704–3714. DOI: 10.1007/s00330-023-09411-8.

[1197] Qiqi Chen et al. 'Iron deposition in Parkinson's disease by quantitative susceptibility mapping'. In: *BMC Neurosci.* 20 (1 22nd May 2019), p. 23. DOI: 10.1186/s12868-019-0505-9.

[1198] I Friedrich et al. 'Cell specific quantitative iron mapping on brain slices by immuno-μPIXE in healthy elderly and Parkinson's disease'. In: *Acta Neuropathol. Commun.* 9 (1 22nd Mar. 2021), p. 47. DOI: 10.1186/s40478-021-01145-2.

[1199] Asuncion Carmona et al. 'Metal dyshomeostasis in the substantia nigra of patients with Parkinson's disease or multiple sclerosis'. In: *J. Neurochem.* 168 (2 Feb. 2024), pp. 128–141. DOI: 10.1111/jnc.16040.

[1200] Marian Valko et al. 'Redox- and non-redox-metal-induced formation of free radicals and their role in human disease'. In: *Arch. Toxicol.* 90 (1 Jan. 2016), pp. 1–37. DOI: 10.1007/s00204-015-1579-5.

[1201] Hoi-Shan Wong et al. 'Production of superoxide and hydrogen peroxide from specific mitochondrial sites under different bioenergetic conditions'. In: *J. Biol. Chem.* 292 (41 13th Oct. 2017), pp. 16804–16809. DOI: 10.1074/jbc.R117.789271.

[1202] Quynh V Duong et al. 'Identifying site-specific superoxide and hydrogen peroxide production rates from the mitochondrial electron transport system using a computational strategy'. In: *Function (Oxf.)* 2 (6 20th Sept. 2021), zqab050. DOI: 10.1093/function/zqab050.

[1203] Klaudia Jomova et al. 'The role of redox-active iron, copper, manganese, and redox-inactive zinc in toxicity, oxidative stress, and human diseases'. In: *EXCLI J.* 24 (25th July 2025), pp. 880–954. DOI: 10.17179/excli2025-8449.

[1204] Juan Du and Janusz M Gebicki. 'Proteins are major initial cell targets of hydroxyl free radicals'. In: *Int. J. Biochem. Cell Biol.* 36 (11 Nov. 2004), pp. 2334–2343. DOI: 10.1016/j.biocel.2004.05.012.

[1205] Roberto Morelli et al. 'Fenton-dependent damage to carbohydrates: free radical scavenging activity of some simple sugars'. In: *J. Agric. Food Chem.* 51 (25 3rd Dec. 2003), pp. 7418–7425. DOI: 10.1021/jf030172q.

[1206] Barry Halliwell et al. 'Hydroxyl radical is a significant player in oxidative DNA damage in vivo'. In: *Chem. Soc. Rev.* 50 (15 7th Aug. 2021), pp. 8355–8360. DOI: 10.1039/d1cs00044f.

[1207] Peter W Halcrow et al. 'Role of endolysosome function in iron metabolism and brain carcinogenesis'. In: *Semin. Cancer Biol.* 76 (Nov. 2021), pp. 74–85. DOI: 10.1016/j.semcancer.2021.06.013.

[1208] Guofen Gao et al. 'Brain iron metabolism, redox balance and neurological diseases'. In: *Antioxidants (Basel)* 12 (6 16th June 2023), p. 1289. DOI: 10.3390/antiox12061289.

[1209] Jaewang Lee and Dong-Hoon Hyun. 'The interplay between intracellular iron homeostasis and neuroinflammation in neurodegenerative diseases'. In: *Antioxidants (Basel)* 12 (4 12th Apr. 2023), p. 918. DOI: 10.3390/antiox12040918.

[1210] Marcin Kruszewski. 'Labile iron pool: the main determinant of cellular response to oxidative stress'. In: *Mutat. Res.* 531 (1-2 29th Oct. 2003), pp. 81–92. DOI: 10.1016/j.mrfmmm.2003.08.004.

[1211] Alexandra Barbouti et al. 'Implication of dietary iron-chelating bioactive compounds in molecular mechanisms of oxidative stress-induced cell ageing'. In: *Antioxidants (Basel)* 10 (3 21st Mar. 2021), p. 491. DOI: 10.3390/antiox10030491.

[1212] Scott J Dixon et al. 'Ferroptosis: an iron-dependent form of nonapoptotic cell death'. In: *Cell* 149 (5 25th May 2012), pp. 1060–1072. DOI: 10.1016/j.cell.2012.03.042.

[1213] Matilde Maiorino, Marcus Conrad and Fulvio Ursini. 'GPx4, lipid peroxidation, and cell death: Discoveries, rediscoveries, and open issues'. In: *Antioxid. Redox Signal.* 29 (1 1st July 2018), pp. 61–74. DOI: 10.1089/ars.2017.7115.

[1214] Fulvio Ursini and Matilde Maiorino. 'Lipid peroxidation and ferroptosis: The role of GSH and GPx4'. In: *Free Radic. Biol. Med.* 152 (20th May 2020), pp. 175–185. DOI: 10.1016/j.freeradbiomed.2020.02.027.

[1215] Xin Chen et al. 'Ferroptosis: machinery and regulation'. In: *Autophagy* 17 (9 Sept. 2021), pp. 2054–2081. DOI: 10.1080/15548627.2020.1810918.

[1216] Luc Rochette et al. 'Lipid peroxidation and iron metabolism: Two corner stones in the homeostasis control of ferroptosis'. In: *Int. J. Mol. Sci.* 24 (1 27th Dec. 2022), p. 449. DOI: 10.3390/ijms24010449.

[1217] Yiyan Sun et al. 'Mechanisms of ferroptosis and emerging links to the pathology of neurodegenerative diseases'. In: *Front. Aging Neurosci.* 14 (28th June 2022), p. 904152. DOI: 10.3389/fnagi.2022.904152.

[1218] Inês Costa et al. 'Molecular mechanisms of ferroptosis and their involvement in brain diseases'. In: *Pharmacol. Ther.* 244 (108373 1st Apr. 2023), p. 108373. DOI: 10.1016/j.pharmthera.2023.108373.

[1219] Yuichiro J Suzuki, Marina Carini and D Allan Butterfield. 'Protein carbonylation'. In: *Antioxid. Redox Signal.* 12 (3 Mar. 2010), pp. 323–325. DOI: 10.1089/ars.2009.2887.

[1220] Ravi Chand Bollineni, Ralf Hoffmann and Maria Fedorova. 'Proteome-wide profiling of carbonylated proteins and carbonylation sites in HeLa cells under mild oxidative stress conditions'. In: *Free Radic. Biol. Med.* 68 (Mar. 2014), pp. 186–195. DOI: 10.1016/j.freeradbiomed.2013.11.030.

[1221] Shun-Long Weng et al. 'Investigation and identification of protein carbonylation sites based on position-specific amino acid composition and physicochemical features'. In: *BMC Bioinformatics* 18 (Suppl 3 14th Mar. 2017), p. 66. DOI: 10.1186/s12859-017-1472-8.

[1222] Mario Estévez, Silvia Díaz-Velasco and Remigio Martínez. 'Protein carbonylation in food and nutrition: a concise update'. In: *Amino Acids* 54 (4 Apr. 2022), pp. 559–573. DOI: 10.1007/s00726-021-03085-6.

[1223] Mario Estévez et al. 'Malondialdehyde interferes with the formation and detection of primary carbonyls in oxidized proteins'. In: *Redox Biol.* 26 (101277 Sept. 2019), p. 101277. DOI: 10.1016/j.redox.2019.101277.

[1224] Thomas Nyström. 'Role of oxidative carbonylation in protein quality control and senescence'. In: *EMBO J.* 24 (7 6th Apr. 2005), pp. 1311–1317. DOI: 10.1038/sj.emboj.7600599.

[1225] Drazen Petrov and Bojan Zagrovic. 'Microscopic analysis of protein oxidative damage: effect of carbonylation on structure, dynamics, and aggregability of villin headpiece'. In: *J. Am. Chem. Soc.* 133 (18 11th May 2011), pp. 7016–7024. DOI: 10.1021/ja110577e.

[1226] Maya Tanase et al. 'Role of carbonyl modifications on aging-associated protein aggregation'. In: *Sci. Rep.* 6 (1 18th Jan. 2016), p. 19311. DOI: 10.1038/srep19311.

[1227] Jiyeon Han. 'Copper trafficking systems in cells: insights into coordination chemistry and toxicity'. In: *Dalton Trans.* 52 (42 31st Oct. 2023), pp. 15277–15296. DOI: 10.1039/d3dt02166a.

[1228] T D Rae et al. 'Undetectable intracellular free copper: the requirement of a copper chaperone for superoxide dismutase'. In: *Science* 284 (5415 30th Apr. 1999), pp. 805–808. DOI: 10.1126/science.284.5415.805.

[1229] M Thomas Morgan et al. 'Ratiometric two-photon microscopy reveals attomolar copper buffering in normal and Menkes mutant cells'. In: *Proc. Natl. Acad. Sci. U. S. A.* 116 (25 18th June 2019), pp. 12167–12172. DOI: 10.1073/pnas.1900172116.

[1230] Julianna Kardos et al. 'Copper signalling: causes and consequences'. In: *Cell Commun. Signal.* 16 (1 22nd Oct. 2018), p. 71. DOI: 10.1186/s12964-018-0277-3.

[1231] Yuanyuan Wang et al. 'Copper homeostasis and neurodegenerative diseases'. In: *Neural Regen. Res.* 20 (11 1st Nov. 2025), pp. 3124–3143. DOI: 10.4103/NRR.NRR-D-24-00642.

[1232] May T Maung et al. 'The molecular and cellular basis of copper dysregulation and its relationship with human pathologies'. In: *FASEB J.* 35 (9 1st Sept. 2021), e21810. DOI: 10.1096/fj.202100273RR.

[1233] Md Selim Hossain et al. 'Altered copper transport in oxidative stress-dependent brain endothelial barrier dysfunction associated with Alzheimer's disease'. In: *Vascul. Pharmacol.* 157 (107433 1st Dec. 2024), p. 107433. DOI: 10.1016/j.vph.2024.107433.

[1234] Sumin Lee et al. 'Activity-based sensing with a metal-directed acyl imidazole strategy reveals cell type-dependent pools of labile brain copper'. In: *J. Am. Chem. Soc.* 142 (35 2nd Sept. 2020), pp. 14993–15003. DOI: 10.1021/jacs.0c05727.

[1235] Peter Tsvetkov et al. 'Copper induces cell death by targeting lipoylated TCA cycle proteins'. In: *Science* 375 (6586 18th Mar. 2022), pp. 1254–1261. DOI: 10.1126/science.abf0529.

[1236] Su-Ran Li, Lin-Lin Bu and Lulu Cai. 'Cuproptosis: lipoylated TCA cycle proteins-mediated novel cell death pathway'. In: *Signal Transduct. Target. Ther.* 7 (1 13th May 2022), p. 158. DOI: 10.1038/s41392-022-01014-x.

[1237] Zhipeng Zhu et al. 'Copper homeostasis and cuproptosis in central nervous system diseases'. In: *Cell Death Dis.* 15 (11 21st Nov. 2024), p. 850. DOI: 10.1038/s41419-024-07206-3.

[1238] Wolfgang Maret. 'The redox biology of redox-inert zinc ions'. In: *Free Radic. Biol. Med.* 134 (Apr. 2019), pp. 311–326. DOI: 10.1016/j.freeradbiomed.2019.01.006.

[1239] Sung Ryul Lee. 'Critical role of zinc as either an antioxidant or a prooxidant in cellular systems'. In: *Oxid. Med. Cell. Longev.* 2018 (1 20th Mar. 2018). Ed. by Glenda Gobe, p. 9156285. DOI: 10.1155/2018/9156285.

[1240] Laura J Blakemore and Paul Q Trombley. 'Zinc as a neuromodulator in the central nervous system with a focus on the olfactory bulb'. In: *Front. Cell. Neurosci.* 11 (21st Sept. 2017), p. 297. DOI: 10.3389/fncel.2017.00297.

[1241] Chen Zhang et al. 'Neuronal signalling of zinc: from detection and modulation to function'. In: *Open Biol.* 12 (9 7th Sept. 2022), p. 220188. DOI: 10.1098/rsob.220188.

[1242] Y Li et al. 'Rapid translocation of $Zn^{2+}$ from presynaptic terminals into postsynaptic hippocampal neurons after physiological stimulation'. In: *J. Neurophysiol.* 86 (5 Nov. 2001), pp. 2597–2604. DOI: 10.1152/jn.2001.86.5.2597.

[1243] Trevor G Smart, Alastair M Hosie and Paul S Miller. 'Zn2+ ions: modulators of excitatory and inhibitory synaptic activity'. In: *Neuroscientist* 10 (5 Oct. 2004), pp. 432–442. DOI: 10.1177/1073858404263463.

[1244] Angela Maria Vergnano et al. 'Zinc dynamics and action at excitatory synapses'. In: *Neuron* 82 (5 4th June 2014), pp. 1101–1114. DOI: 10.1016/j.neuron.2014.04.034.

[1245] R H Olesen et al. 'Obesity and age-related alterations in the gene expression of zinc-transporter proteins in the human brain'. In: *Transl. Psychiatry* 6 (6 14th June 2016), e838. DOI: 10.1038/tp.2016.83.

[1246] Sara M Hancock et al. 'Zinc transporter-3 knockout mice demonstrate age-dependent alterations in the metalloproteome'. In: *Int. J. Mol. Sci.* 21 (3 28th Jan. 2020), E839. DOI: 10.3390/ijms21030839.

[1247] Travis J A Craddock et al. 'The zinc dyshomeostasis hypothesis of Alzheimer's disease'. In: *PLoS One* 7 (3 23rd Mar. 2012), e33552. DOI: 10.1371/journal.pone.0033552.

[1248] Meghan C McCord and Elias Aizenman. 'The role of intracellular zinc release in aging, oxidative stress, and Alzheimerâ€™s disease'. In: *Front. Aging Neurosci.* 6 (17th Apr. 2014), p. 77. DOI: 10.3389/fnagi.2014.00077.

[1249] Joana S Cristóvão, Renata Santos and Cláudio M Gomes. 'Metals and neuronal metal binding proteins implicated in Alzheimer's disease'. In: *Oxid. Med. Cell. Longev.* 2016 (1 10th Jan. 2016). Ed. by Felipe Dal Pizzol, p. 9812178. DOI: 10.1155/2016/9812178.

[1250] Zhuoya Xie, Hongrong Wu and Jianfeng Zhao. 'Multifunctional roles of zinc in Alzheimer's disease'. In: *Neurotoxicology* 80 (Sept. 2020), pp. 112–123. DOI: 10.1016/j.neuro.2020.07.003.

[1251] Carlo Bertoni-Freddari et al. 'Brain aging: The zinc connection'. In: *Exp. Gerontol.* 43 (5 May 2008), pp. 389–393. DOI: 10.1016/j.exger.2007.11.001.

[1252] Stuart D Portbury and Paul A Adlard. 'Zinc signal in brain diseases'. In: *Int. J. Mol. Sci.* 18 (12 23rd Nov. 2017), E2506. DOI: 10.3390/ijms18122506.

[1253] Ruize Sun et al. 'Zinc in cognitive impairment and aging'. In: *Biomolecules* 12 (7 18th July 2022), p. 1000. DOI: 10.3390/biom12071000.

[1254] C J Frederickson et al. 'Importance of zinc in the central nervous system: the zinc-containing neuron'. In: *J. Nutr.* 130 (5S Suppl May 2000), 1471S–83S. DOI: 10.1093/jn/130.5.1471S.

[1255] Rebecca F Krall, Thanos Tzounopoulos and Elias Aizenman. 'The function and regulation of zinc in the brain'. In: *Neuroscience* 457 (1st Mar. 2021), pp. 235–258. DOI: 10.1016/j.neuroscience.2021.01.010.

[1256] Emil C Toescu and Martin Vreugdenhil. 'Calcium and normal brain ageing'. In: *Cell Calcium* 47 (2 Feb. 2010), pp. 158–164. DOI: 10.1016/j.ceca.2009.11.013.

[1257] Marisa Brini et al. 'Neuronal calcium signaling: function and dysfunction'. In: *Cell. Mol. Life Sci.* 71 (15 Aug. 2014), pp. 2787–2814. DOI: 10.1007/s00018-013-1550-7.

[1258] Marc Gleichmann and Mark P Mattson. 'Neuronal calcium homeostasis and dysregulation'. In: *Antioxid. Redox Signal.* 14 (7 1st Apr. 2011), pp. 1261–1273. DOI: 10.1089/ars.2010.3386.

[1259] Elisa Mitiko Kawamoto, Carmen Vivar and Simonetta Camandola. 'Physiology and pathology of calcium signaling in the brain'. In: *Front. Pharmacol.* 3 (13th Apr. 2012), p. 61. DOI: 10.3389/fphar.2012.00061.

[1260] Caterina Peggion et al. 'Plasma membrane calcium ATPases and cerebellar pathology: what's the role in the ataxia?' In: *Biol. Direct* 20 (1 6th Nov. 2025), p. 109. DOI: 10.1186/s13062-025-00702-2.

[1261] Hyunsu Jung et al. 'Dysfunction of mitochondrial $Ca^{2+}$ regulatory machineries in brain aging and neurodegenerative diseases'. In: *Front. Cell Dev. Biol.* 8 (18th Dec. 2020), p. 599792. DOI: 10.3389/fcell.2020.599792.

[1262] Gerard Griffioen. 'Calcium dyshomeostasis drives pathophysiology and neuronal demise in age-related neurodegenerative diseases'. In: *Int. J. Mol. Sci.* 24 (17 26th Aug. 2023), p. 13243. DOI: 10.3390/ijms241713243.

[1263] D Murchison and W H Griffith. 'Increased calcium buffering in basal forebrain neurons during aging'. In: *J. Neurophysiol.* 80 (1 July 1998), pp. 350–364. DOI: 10.1152/jn.1998.80.1.350.

[1264] David Murchison and William H Griffith. 'Calcium buffering systems and calcium signaling in aged rat basal forebrain neurons'. In: *Aging Cell* 6 (3 June 2007), pp. 297–305. DOI: 10.1111/j.1474-9726.2007.00293.x.

[1265] Robert L Campbell and Peter L Davies. 'Structure-function relationships in calpains'. In: *Biochem. J.* 447 (3 1st Nov. 2012), pp. 335–351. DOI: 10.1042/BJ20120921.

[1266] Si-Ying Cheng et al. 'Regulatory role of calpain in neuronal death'. In: *Neural Regen. Res.* 13 (3 Mar. 2018), pp. 556–562. DOI: 10.4103/1673-5374.228762.

[1267] Angelo O Rosa and Stanley I Rapoport. 'Intracellular- and extracellular-derived $Ca^{2+}$ influence phospholipase A(2)-mediated fatty acid release from brain phospholipids'. In: *Biochim. Biophys. Acta* 1791 (8 Aug. 2009), pp. 697–705. DOI: 10.1016/j.bbalip.2009.03.009.

[1268] Cristelle Hugo et al. 'Development of calcium-dependent phospholipase A2 inhibitors to target cellular senescence and oxidative stress in neurodegenerative diseases'. In: *Antioxid. Redox Signal.* 41 (16-18 10th Dec. 2024), pp. 1100–1116. DOI: 10.1089/ars.2024.0794.

[1269] Yong-Wang Li et al. 'The significance of calcium ions in cerebral ischemia-reperfusion injury: mechanisms and intervention strategies'. In: *Front. Mol. Biosci.* 12 (12th May 2025), p. 1585758. DOI: 10.3389/fmolb.2025.1585758.

[1270] A Cristina Rego and Catarina R Oliveira. 'Mitochondrial dysfunction and reactive oxygen species in excitotoxicity and apoptosis: implications for the pathogenesis of neurodegenerative diseases'. In: *Neurochem. Res.* 28 (10 Oct. 2003), pp. 1563–1574. DOI: 10.1023/a:1025682611389.

[1271] Paul S Brookes et al. 'Calcium, ATP, and ROS: a mitochondrial love–hate triangle'. In: *Am. J. Physiol. Cell Physiol.* 287 (4 Oct. 2004), pp. C817–33. DOI: 10.1152/ajpcell.00139.2004.

[1272] Cristina Camello-Almaraz et al. 'Mitochondrial reactive oxygen species and $Ca^{2+}$ signaling'. In: *Am. J. Physiol. Cell Physiol.* 291 (5 Nov. 2006), pp. C1082–8. DOI: 10.1152/ajpcell.00217.2006.

[1273] Hagai Rottenberg and Jan B Hoek. 'The path from mitochondrial ROS to aging runs through the mitochondrial permeability transition pore'. In: *Aging Cell* 16 (5 Oct. 2017), pp. 943–955. DOI: 10.1111/acel.12650.

[1274] John J Lemasters et al. 'Role of mitochondrial inner membrane permeabilization in necrotic cell death, apoptosis, and autophagy'. In: *Antioxid. Redox Signal.* 4 (5 Oct. 2002), pp. 769–781. DOI: 10.1089/152308602760598918.

[1275] Rita M L La Rovere et al. 'Intracellular $Ca^{2+}$ signaling and $Ca^{2+}$ microdomains in the control of cell survival, apoptosis and autophagy'. In: *Cell Calcium* 60 (2 1st Aug. 2016), pp. 74–87. DOI: 10.1016/j.ceca.2016.04.005.

[1276] E Suryana et al. 'Empirically derived formulae for calculation of age- and region-related levels of iron, copper and zinc in the adult C57BL/6 mouse brain'. In: *Neurobiol. Aging* 136 (Apr. 2024), pp. 34–43. DOI: 10.1016/j.neurobiolaging.2024.01.003.

[1277] Somayra S A Mamsa et al. 'Correlative analysis of metallomic gene expression and metal ion content within the mouse hippocampus'. In: *Metallomics* 17 (4 28th Mar. 2025), mfaf009. DOI: 10.1093/mtomcs/mfaf009.

[1278] Aaron Atkinson and Dennis R Winge. 'Metal acquisition and availability in the mitochondria'. In: *Chem. Rev.* 109 (10 12th Oct. 2009), pp. 4708–4721. DOI: 10.1021/cr900006y.

[1279] Bogdan Florin Gh Popescu and Helen Nichol. 'Mapping brain metals to evaluate therapies for neurodegenerative disease: Mapping brain metals to evaluate therapies for neurodegenerative disease'. In: *CNS Neurosci. Ther.* 17 (4 Aug. 2011), pp. 256–268. DOI: 10.1111/j.1755-5949.2010.00149.x.

[1280] Wei Zheng and Andrew D Monnot. 'Regulation of brain iron and copper homeostasis by brain barrier systems: implication in neurodegenerative diseases'. In: *Pharmacol. Ther.* 133 (2 1st Feb. 2012), pp. 177–188. DOI: 10.1016/j.pharmthera.2011.10.006.

[1281] Kevin J Barnham and Ashley I Bush. 'Biological metals and metal-targeting compounds in major neurodegenerative diseases'. In: *Chem. Soc. Rev.* 43 (19 7th Oct. 2014), pp. 6727–6749. DOI: 10.1039/c4cs00138a.

[1282] Miao-Miao Lin et al. 'Mitochondrial-derived damage-associated molecular patterns amplify neuroinflammation in neurodegenerative diseases'. In: *Acta Pharmacol. Sin.* 43 (10 Oct. 2022), pp. 2439–2447. DOI: 10.1038/s41401-022-00879-6.

[1283] Noah A H Brooks, Ishvin Riar and Andis Klegeris. 'Mitochondrial damage-associated molecular patterns: Neuroimmunomodulators in central nervous system pathophysiology'. In: *Neural Regen. Res.* 21 (4 1st Apr. 2026), pp. 1322–1338. DOI: 10.4103/NRR.NRR-D-24-01459.

[1284] Cláudia M Deus et al. 'Mitochondrial damage-associated molecular patterns content in extracellular vesicles promotes early inflammation in neurodegenerative disorders'. In: *Cells* 11 (15 1st Aug. 2022), p. 2364. DOI: 10.3390/cells11152364.

[1285] Amanda Sierra et al. 'Microglia derived from aging mice exhibit an altered inflammatory profile'. In: *Glia* 55 (4 Mar. 2007), pp. 412–424. DOI: 10.1002/glia.20468.

[1286] Rommy von Bernhardi, Laura Eugenín-von Bernhardi and Jaime Eugenín. 'Microglial cell dysregulation in brain aging and neurodegeneration'. In: *Front. Aging Neurosci.* 7 (20th July 2015), p. 124. DOI: 10.3389/fnagi.2015.00124.

[1287] Alyssa L Thomas et al. 'Naturally-aged microglia exhibit phagocytic dysfunction accompanied by gene expression changes reflective of underlying neurologic disease'. In: *Sci. Rep.* 12 (1 14th Nov. 2022), p. 19471. DOI: 10.1038/s41598-022-21920-y.

[1288] Edward C Koellhoffer, Louise D McCullough and Rodney M Ritzel. 'Old maids: Aging and its impact on microglia function'. In: *Int. J. Mol. Sci.* 18 (4 5th Apr. 2017), E769. DOI: 10.3390/ijms18040769.

[1289] Shaimaa Mahmoud et al. 'Astrocytes maintain glutamate homeostasis in the CNS by controlling the balance between glutamate uptake and release'. In: *Cells* 8 (2 20th Feb. 2019), E184. DOI: 10.3390/cells8020184.

[1290] Alison C Todd and Giles E Hardingham. 'The regulation of astrocytic glutamate transporters in health and neurodegenerative diseases'. In: *Int. J. Mol. Sci.* 21 (24 17th Dec. 2020), E9607. DOI: 10.3390/ijms21249607.

[1291] Jens V Andersen and Arne Schousboe. 'Milestone Review: Metabolic dynamics of glutamate and GABA mediated neurotransmission - The essential roles of astrocytes'. In: *J. Neurochem.* 166 (2 July 2023), pp. 109–137. DOI: 10.1111/jnc.15811.

[1292] Stefan Passlick et al. 'Disruption of glutamate transport and homeostasis by acute metabolic stress'. In: *Front. Cell. Neurosci.* 15 (2nd Feb. 2021), p. 637784. DOI: 10.3389/fncel.2021.637784.

[1293] Angeles Almeida, Daniel Jimenez-Blasco and Juan P Bolaños. 'Cross-talk between energy and redox metabolism in astrocyte-neuron functional cooperation'. In: *Essays Biochem.* 67 (1 3rd Mar. 2023), pp. 17–26. DOI: 10.1042/EBC20220075.

[1294] Xenia Abadin et al. 'Neuroinflammation in age-related neurodegenerative diseases: Role of mitochondrial oxidative stress'. In: *Antioxidants (Basel)* 13 (12 22nd Nov. 2024), p. 1440. DOI: 10.3390/antiox13121440.

[1295] Alhamdu Adamu et al. 'The role of neuroinflammation in neurodegenerative diseases: current understanding and future therapeutic targets'. In: *Front. Aging Neurosci.* 16 (12th Apr. 2024), p. 1347987. DOI: 10.3389/fnagi.2024.1347987.

[1296] Huan Liu et al. 'Aging of cerebral white matter'. In: *Ageing Res. Rev.* 34 (1st Mar. 2017), pp. 64–76. DOI: 10.1016/j.arr.2016.11.006.

[1297] Janos Groh and Mikael Simons. 'White matter aging and its impact on brain function'. In: *Neuron* 113 (1 8th Jan. 2025), pp. 127–139. DOI: 10.1016/j.neuron.2024.10.019.

[1298] Shima Safaiyan et al. 'Age-related myelin degradation burdens the clearance function of microglia during aging'. In: *Nat. Neurosci.* 19 (8 Aug. 2016), pp. 995–998. DOI: 10.1038/nn.4325.

[1299] Marie-Theres Weil et al. 'Loss of myelin basic protein function triggers myelin breakdown in models of demyelinating diseases'. In: *Cell Rep.* 16 (2 12th July 2016), pp. 314–322. DOI: 10.1016/j.celrep.2016.06.008.

[1300] Agata Matejuk et al. 'Altered lipid metabolism in CNS demyelination and remyelination are key elements driving progressive MS'. In: *Int. J. Mol. Sci.* 26 (17 27th Aug. 2025), p. 8314. DOI: 10.3390/ijms26178314.

[1301] K J Smith, R Kapoor and P A Felts. 'Demyelination: the role of reactive oxygen and nitrogen species'. In: *Brain Pathol.* 9 (1 Jan. 1999), pp. 69–92. DOI: 10.1111/j.1750-3639.1999.tb00212.x.

[1302] G W Konat and R C Wiggins. 'Effect of reactive oxygen species on myelin membrane proteins'. In: *J. Neurochem.* 45 (4 Oct. 1985), pp. 1113–1118. DOI: 10.1111/j.1471-4159.1985.tb05530.x.

[1303] Mahavir Singh, Aniruddh Kapoor and Aruni Bhatnagar. 'Oxidative and reductive metabolism of lipid-peroxidation derived carbonyls'. In: *Chem. Biol. Interact.* 234 (5th June 2015), pp. 261–273. DOI: 10.1016/j.cbi.2014.12.028.

[1304] J Alberto Ortega et al. 'Exploring the properties and potential of the neural extracellular matrix for next-generation regenerative therapies'. In: *Wiley Interdiscip. Rev. Nanomed. Nanobiotechnol.* 16 (3 1st May 2024), e1962. DOI: 10.1002/wnan.1962.

[1305] Chuang Ge and Maral Tajerian. 'The extracellular matrix as a dynamic regulator of brain function and plasticity'. In: *Neurobiol. Dis.* 223 (107374 1st June 2026), p. 107374. DOI: 10.1016/j.nbd.2026.107374.

[1306] P Lorenzo Bozzelli et al. 'Proteolytic remodeling of perineuronal nets: Effects on synaptic plasticity and neuronal population dynamics'. In: *Neural Plast.* 2018 (4th Feb. 2018), p. 5735789. DOI: 10.1155/2018/5735789.

[1307] Bhanu P Tewari et al. 'A glial perspective on the extracellular matrix and perineuronal net remodeling in the central nervous system'. In: *Front. Cell. Neurosci.* 16 (20th Oct. 2022), p. 1022754. DOI: 10.3389/fncel.2022.1022754.

[1308] Michael McKenna et al. 'Multiple particle tracking detects changes in brain extracellular matrix and predicts neurodevelopmental age'. In: *ACS Nano* 15 (5 25th May 2021), pp. 8559–8573. DOI: 10.1021/acsnano.1c00394.

[1309] Matthias Hebisch et al. 'The impact of the cellular environment and aging on modeling Alzheimer's disease in 3D cell culture models'. In: *Adv. Sci. (Weinh.)* 10 (8 Mar. 2023), e2205037. DOI: 10.1002/advs.202205037.

[1310] Marsha C Lampi and Cynthia A Reinhart-King. 'Targeting extracellular matrix stiffness to attenuate disease: From molecular mechanisms to clinical trials'. In: *Sci. Transl. Med.* 10 (422 3rd Jan. 2018), eaao0475. DOI: 10.1126/scitranslmed.aao0475.

[1311] Hannah C Bennett et al. 'Aging drives cerebrovascular network remodeling and functional changes in the mouse brain'. In: *Nat. Commun.* 15 (1 30th July 2024), p. 6398. DOI: 10.1038/s41467-024-50559-8.

[1312] Mina Elahy et al. 'Blood-brain barrier dysfunction developed during normal aging is associated with inflammation and loss of tight junctions but not with leukocyte recruitment'. In: *Immun. Ageing* 12 (1 7th Mar. 2015), p. 2. DOI: 10.1186/s12979-015-0029-9.

[1313] J Duncombe et al. 'Ageing causes prominent neurovascular dysfunction associated with loss of astrocytic contacts and gliosis'. In: *Neuropathol. Appl. Neurobiol.* 43 (6 Oct. 2017), pp. 477–491. DOI: 10.1111/nan.12375.

[1314] Eduardo Frías-Anaya et al. 'Age-related ultrastructural neurovascular changes in the female mouse cortex and hippocampus'. In: *Neurobiol. Aging* 101 (May 2021), pp. 273–284. DOI: 10.1016/j.neurobiolaging.2020.12.008.

[1315] Patrick C Nahirney, Patrick Reeson and Craig E Brown. 'Ultrastructural analysis of blood-brain barrier breakdown in the peri-infarct zone in young adult and aged mice'. In: *J. Cereb. Blood Flow Metab.* 36 (2 Feb. 2016), pp. 413–425. DOI: 10.1177/0271678X15608396.

[1316] Andrew C Yang et al. 'Physiological blood-brain transport is impaired with age by a shift in transcytosis'. In: *Nature* 583 (7816 1st July 2020), pp. 425–430. DOI: 10.1038/s41586-020-2453-z.

[1317] Yibin Zhao et al. 'Factors influencing the blood-brain barrier permeability'. In: *Brain Res.* 1788 (147937 1st Aug. 2022), p. 147937. DOI: 10.1016/j.brainres.2022.147937.

[1318] Stephen B Hladky and Margery A Barrand. 'Elimination of substances from the brain parenchyma: efflux via perivascular pathways and via the blood-brain barrier'. In: *Fluids Barriers CNS* 15 (1 19th Oct. 2018), p. 30. DOI: 10.1186/s12987-018-0113-6.

[1319] Damir Janigro et al. 'Peripheral blood and salivary biomarkers of blood-brain barrier permeability and neuronal damage: Clinical and applied concepts'. In: *Front. Neurol.* 11 (2020), p. 577312. DOI: 10.3389/fneur.2020.577312.

[1320] Ke Song et al. 'Oxidative stress-mediated blood-brain barrier (BBB) disruption in neurological diseases'. In: *Oxid. Med. Cell. Longev.* 2020 (1 3rd July 2020), pp. 1–27. DOI: 10.1155/2020/4356386.

[1321] Margarita Shuvalova et al. 'The role of reactive oxygen species in the regulation of the blood-brain barrier'. In: *Tissue Barriers* 13 (2 2025), p. 2361202. DOI: 10.1080/21688370.2024.2361202.

[1322] Stephen B Hladky and Margery A Barrand. 'Fluid and ion transfer across the blood-brain and blood-cerebrospinal fluid barriers; a comparative account of mechanisms and roles'. In: *Fluids Barriers CNS* 13 (1 31st Oct. 2016), p. 19. DOI: 10.1186/s12987-016-0040-3.

[1323] Vismitha Rajeev et al. 'Pathophysiology of blood brain barrier dysfunction during chronic cerebral hypoperfusion in vascular cognitive impairment'. In: *Theranostics* 12 (4 16th Jan. 2022), pp. 1639–1658. DOI: 10.7150/thno.68304.

[1324] Angela D Levy, Howard Theodore Harcke and Craig T Mallak. 'Postmortem imaging: MDCT features of postmortem change and decomposition: MDCT features of postmortem change and decomposition'. In: *Am. J. Forensic Med. Pathol.* 31 (1 Mar. 2010), pp. 12–17. DOI: 10.1097/PAF.0b013e3181c65e1a.

[1325] Haruki Fukuda et al. 'Postmortem computed tomography-based evaluation of brain decomposition: Correlation with postmortem interval and cause-of-death determinability'. In: *Leg. Med. (Tokyo)* 78 (102710 1st Oct. 2025), p. 102710. DOI: 10.1016/j.legalmed.2025.102710.

[1326] Francesca Parisi et al. 'Morphological and immunohistochemical changes in progressive postmortem autolysis of the Murine brain'. In: *Animals (Basel)* 14 (24 20th Dec. 2024), p. 3676. DOI: 10.3390/ani14243676.

[1327] Macy Garrood et al. 'Preservation of cellular structure via immersion fixation in brain banking'. In: *Free Neuropathol.* 6 (4th Jan. 2025), p. 4. DOI: 10.17879/freeneuropathology-2025-6104.

[1328] Klaus Weber et al. 'Onset and progression of postmortem histological changes in the central nervous system of RccHan™: WIST rats'. In: *Front. Vet. Sci.* 11 (21st May 2024), p. 1378609. DOI: 10.3389/fvets.2024.1378609.

[1329] Robert H Garman. 'Histology of the central nervous system'. In: *Toxicol. Pathol.* 39 (1 Jan. 2011), pp. 22–35. DOI: 10.1177/0192623310389621.

[1330] Audrey D Lafrenaye and J Marc Simard. 'Bursting at the seams: Molecular mechanisms mediating astrocyte swelling'. In: *Int. J. Mol. Sci.* 20 (2 15th Jan. 2019), E330. DOI: 10.3390/ijms20020330.

[1331] Michel J A M van Putten et al. 'Dysregulation of astrocyte ion homeostasis and its relevance for stroke-induced brain damage'. In: *Int. J. Mol. Sci.* 22 (11 26th May 2021), p. 5679. DOI: 10.3390/ijms22115679.

[1332] Stephen B Hladky and Margery A Barrand. 'Alterations in brain fluid physiology during the early stages of development of ischaemic oedema'. In: *Fluids Barriers CNS* 21 (1 10th June 2024), p. 51. DOI: 10.1186/s12987-024-00534-8.

[1333] R Lindenberg. 'Morphotropic and morphostatic necrobiosis; investigations on nerve cells of the brain'. In: *Am. J. Pathol.* 32 (6 Nov. 1956), pp. 1147–1177.

[1334] H Shibayama and J Kitoh. 'The postmortem changes of pyramidal neurons in the hippocampus of rats'. In: *Folia Psychiatr. Neurol. Jpn.* 30 (1 1st Mar. 1976), pp. 73–91. DOI: 10.1111/j.1440-1819.1976.tb00113.x.

[1335] Jiro Suzuki. 'Histological study'. In: *Treatment of Cerebral Infarction*. Vienna: Springer Vienna, 1987, pp. 23–53. DOI: 10.1007/978-3-7091-8861-3_3.

[1336] T Badonic et al. 'Ultrastructural changes of neurons in dependence on the death cause in human brain'. In: *Funct. Dev. Morphol.* 2 (4 1992), pp. 231–234.

[1337] Rachel R Howie et al. 'Determination of postmortem interval in mice'. In: *J. Am. Assoc. Lab. Anim. Sci.* 63 (4 1st July 2024), pp. 428–436. DOI: 10.30802/AALAS-JAALAS-23-000107.

[1338] P H Gibson and B E Tomlinson. 'Vacuolation in the human cerebral cortex and its relationship to the interval between death and autopsy and to synapse numbers: an electron microscopic study'. In: *Neuropathol. Appl. Neurobiol.* 5 (1 Jan. 1979), pp. 1–7. DOI: 10.1111/j.1365-2990.1979.tb00608.x.

[1339] Andrey V Shubin et al. 'Cytoplasmic vacuolization in cell death and survival'. In: *Oncotarget* 7 (34 23rd Aug. 2016), pp. 55863–55889. DOI: 10.18632/oncotarget.10150.

[1340] J Weickenmeier et al. 'Brain stiffens post mortem'. In: *J. Mech. Behav. Biomed. Mater.* 84 (Aug. 2018), pp. 88–98. DOI: 10.1016/j.jmbbm.2018.04.009.

[1341] Nina Reiter, Friedrich Paulsen and Silvia Budday. 'Mechanisms of mechanical load transfer through brain tissue'. In: *Sci. Rep.* 13 (1 29th May 2023), p. 8703. DOI: 10.1038/s41598-023-35768-3.

[1342] Ulf Karlsson and Robert L Schultz. 'Fixation of the central nervous system for electron microscopy by aldehyde perfusion'. In: *J. Ultrastruct. Res.* 14 (1-2 1st Jan. 1966), pp. 47–63. DOI: 10.1016/s0022-5320(66)80034-5.

[1343] A Routtenberg and S Tarrant. 'Synaptic morphology and cytoplasmic densities: rapid post-mortem effects'. In: *Tissue Cell* 6 (4 1st Jan. 1974), pp. 777–788. DOI: 10.1016/0040-8166(74)90015-9.

[1344] R C Roberts et al. 'Synaptic organization of the human striatum: a postmortem ultrastructural study'. In: *J. Comp. Neurol.* 374 (4 28th Oct. 1996), pp. 523–534. DOI: 10.1002/(SICI)1096-9861(19961028)374:4<523::AID-CNE4>3.0.CO;2-3.

[1345] Jung-Hwa Tao-Cheng et al. 'Structural changes at synapses after delayed perfusion fixation in different regions of the mouse brain'. In: *J. Comp. Neurol.* 501 (5 10th Apr. 2007), pp. 731–740. DOI: 10.1002/cne.21276.

[1346] D K von Lubitz and N H Diemer. 'Cerebral ischemia in the rat: ultrastructural and morphometric analysis of synapses in stratum radiatum of the hippocampal CA-1 region'. In: *Acta Neuropathol.* 61 (1 1983), pp. 52–60. DOI: 10.1007/bf00688386.

[1347] T L Petit and J C LeBoutillier. 'Quantifying synaptic number and structure: effects of stain and post-mortem delay'. In: *Brain Res.* 517 (1-2 28th May 1990), pp. 269–275. DOI: 10.1016/0006-8993(90)91037-h.

[1348] Tatiana Kovalenko et al. 'Ischemia-induced modifications in hippocampal CA1 stratum radiatum excitatory synapses'. In: *Hippocampus* 16 (10 2006), pp. 814–825. DOI: 10.1002/hipo.20211.

[1349] Alexander G Nikonenko et al. 'Structural features of ischemic damage in the hippocampus'. In: *Anat. Rec. (Hoboken)* 292 (12 1st Dec. 2009), pp. 1914–1921. DOI: 10.1002/ar.20969.

[1350] Sorin Hostiuc et al. 'Usefulness of ultrastructure studies for the estimation of the postmortem interval. A systematic review'. In: *Rom. J. Morphol. Embryol.* 58 (2 2017), pp. 377–384.

[1351] Zvonimir Vrselja et al. 'Restoration of brain circulation and cellular functions hours post-mortem'. In: *Nature* 568 (7752 Apr. 2019), pp. 336–343. DOI: 10.1038/s41586-019-1099-1.

[1352] Jill R Glausier, Anisha Konanur and David A Lewis. 'Factors affecting ultrastructural quality in the prefrontal cortex of the postmortem human brain'. In: *J. Histochem. Cytochem.* 67 (3 Mar. 2019), pp. 185–202. DOI: 10.1369/0022155418819481.

[1353] X Liu and A Brun. 'Synaptophysin immunoreactivity is stable 36 h postmortem'. In: *Dementia* 6 (4 July 1995), pp. 211–217. DOI: 10.1159/000106949.

[1354] Pietro Scaduto et al. 'Preservation of global synaptic excitatory to inhibitory ratio during long postmortem intervals'. In: *Sci. Rep.* 10 (1 25th May 2020), p. 8626. DOI: 10.1038/s41598-020-65377-3.

[1355] S Rees. 'A quantitative electron microscopic study of the ageing human cerebral cortex'. In: *Acta Neuropathol.* 36 (4 21st Dec. 1976), pp. 347–362. DOI: 10.1007/bf00699640.

[1356] R S Williams, R J Ferrante and V S Caviness Jr. 'The Golgi rapid method in clinical neuropathology: the morphologic consequences of suboptimal fixation'. In: *J. Neuropathol. Exp. Neurol.* 37 (1 1st Jan. 1978), pp. 13–33. DOI: 10.1097/00005072-197801000-00002.

[1357] Karin Boekhoorn, Marian Joels and Paul J Lucassen. 'Increased proliferation reflects glial and vascular-associated changes, but not neurogenesis in the presenile Alzheimer hippocampus'. In: *Neurobiol. Dis.* 24 (1 1st Oct. 2006), pp. 1–14. DOI: 10.1016/j.nbd.2006.04.017.

[1358] Pierre Lavenex et al. 'Postmortem changes in the neuroanatomical characteristics of the primate brain: hippocampal formation'. In: *J. Comp. Neurol.* 512 (1 1st Jan. 2009), pp. 27–51. DOI: 10.1002/cne.21906.

[1359] Kinga Tóth et al. 'Loss and reorganization of calretinin-containing interneurons in the epileptic human hippocampus'. In: *Brain* 133 (9 24th Sept. 2010), pp. 2763–2777. DOI: 10.1093/brain/awq149.

[1360] Carolina Gonzalez-Riano et al. 'Metabolomics and neuroanatomical evaluation of post-mortem changes in the hippocampus'. In: *Brain Struct. Funct.* 222 (6 Aug. 2017), pp. 2831–2853. DOI: 10.1007/s00429-017-1375-5.

[1361] S J Buell. 'Golgi-Cox and rapid golgi methods as applied to autopsied human brain tissue: widely disparate results: Widely disparate results'. In: *J. Neuropathol. Exp. Neurol.* 41 (5 1st Sept. 1982), pp. 500–507. DOI: 10.1097/00005072-198209000-00003.

[1362] B Jacobs and A B Scheibel. 'A quantitative dendritic analysis of Wernicke's area in humans. I. Lifespan changes'. In: *J. Comp. Neurol.* 327 (1 1st Jan. 1993), pp. 83–96. DOI: 10.1002/cne.903270107.

[1363] F M Benes, M S Todtenkopf and P Kostoulakos. 'GluR5,6,7 subunit immunoreactivity on apical pyramidal cell dendrites in hippocampus of schizophrenics and manic depressives'. In: *Hippocampus* 11 (5 1st Oct. 2001), pp. 482–491. DOI: 10.1002/hipo.1065.

[1364] L Y Yeung, M S M Wai and D T Yew. 'Silver impregnation of the prefrontal cortices in the brains with long postmortem delay'. In: *Int. J. Neurosci.* 120 (4 8th Apr. 2010), pp. 314–317. DOI: 10.3109/00207450903243507.

[1365] Benjamin D Boros et al. 'Dendritic spines provide cognitive resilience against Alzheimer's disease: Synaptic Resilience in AD'. In: *Ann. Neurol.* 82 (4 1st Oct. 2017), pp. 602–614. DOI: 10.1002/ana.25049.

[1366] Sujan C Das et al. 'DiI-mediated analysis of presynaptic and postsynaptic structures in human postmortem brain tissue'. In: *J. Comp. Neurol.* 527 (18 15th Dec. 2019), pp. 3087–3098. DOI: 10.1002/cne.24722.

[1367] Macy Garrood et al. 'Evaluating ultrastructural preservation quality in banked brain tissue'. In: *Free Neuropathol.* 6 (25th June 2025), p. 13. DOI: 10.17879/freeneuropathology-2025-6763.

[1368] L J Garey et al. 'Reduced dendritic spine density on cerebral cortical pyramidal neurons in schizophrenia'. In: *J. Neurol. Neurosurg. Psychiatry* 65 (4 1st Oct. 1998), pp. 446–453. DOI: 10.1136/jnnp.65.4.446.

[1369] L Pantoni, J H Garcia and J A Gutierrez. 'Cerebral white matter is highly vulnerable to ischemia'. In: *Stroke* 27 (9 Sept. 1996), 1641–6, discussion 1647. DOI: 10.1161/01.str.27.9.1641.

[1370] Jeison Monroy-Gómez et al. 'Effect of postmortem degradation on the preservation of viral particles and rabies antigens in mice brains. Light and electron microscopic study'. In: *Viruses* 12 (9 26th Aug. 2020), E938. DOI: 10.3390/v12090938.

[1371] K A Ansari et al. 'Qualitative and quantitative studies on human myelin basic protein in situ with respect to time interval between death and autopsy'. In: *J. Neuropathol. Exp. Neurol.* 35 (2 Mar. 1976), pp. 180–190. DOI: 10.1097/00005072-197603000-00005.

[1372] Mariella Sele et al. 'Optimization of ultrastructural preservation of human brain for transmission electron microscopy after long post-mortem intervals'. In: *Acta Neuropathol. Commun.* 7 (1 3rd Sept. 2019), p. 144. DOI: 10.1186/s40478-019-0794-3.

[1373] Aschwin de Wolf et al. 'Ultrastructural characterization of prolonged normothermic and cold cerebral ischemia in the adult rat'. In: *Rejuvenation Res.* 23 (3 June 2020), pp. 193–206. DOI: 10.1089/rej.2019.2225.

[1374] D E Haines and T W Jenkins. 'Studies on the epithalamus. I. Morphology of post-mortem degeneration: the habenular nucleus in dog'. In: *J. Comp. Neurol.* 132 (3 1st Mar. 1968), pp. 405–417. DOI: 10.1002/cne.901320304.

[1375] Xiao-Bo Liu and Cynthia M Schumann. 'Optimization of electron microscopy for human brains with long-term fixation and fixed-frozen sections'. In: *Acta Neuropathol. Commun.* 2 (1 11th Apr. 2014), p. 42. DOI: 10.1186/2051-5960-2-42.

[1376] Ilyess Zemmoura et al. 'How Klingler's dissection permits exploration of brain structural connectivity? An electron microscopy study of human white matter'. In: *Brain Struct. Funct.* 221 (5 June 2016), pp. 2477–2486. DOI: 10.1007/s00429-015-1050-7.

[1377] Anastasia Yendiki et al. 'Post mortem mapping of connectional anatomy for the validation of diffusion MRI'. In: *Neuroimage* 256 (119146 1st Aug. 2022), p. 119146. DOI: 10.1016/j.neuroimage.2022.119146.

[1378] J E C Bywater, P Glees and H Hauffe. 'The variability of neuron structure caused by the type of fixation or by the autolytic changes'. In: *1962*. De Gruyter, 31st Dec. 1962, pp. 147–161. DOI: 10.1515/9783112519806-003.

[1379] F Ikuta, A Hirano and H M Zimmerman. 'An experimental study of post-mortem alterations in the granular layer of the cerebellar cortex'. In: *J. Neuropathol. Exp. Neurol.* 22 (4 1st Oct. 1963), pp. 581–593. DOI: 10.1097/00005072-196310000-00002.

[1380] R Albrechtsen. 'Naphthylamidase used as a lysosome marker in the study of acute selective necrosis of the internal granular layer of cerebellum'. In: *Acta Pathol. Microbiol. Scand. A* 85 (6 1st Nov. 1977), pp. 875–888. DOI: 10.1111/j.1699-0463.1977.tb03904.x.

[1381] J W Finnie, P C Blumbergs and J Manavis. 'Temporal sequence of autolysis in the cerebellar cortex of the mouse'. In: *J. Comp. Pathol.* 154 (4 1st May 2016), pp. 323–328. DOI: 10.1016/j.jcpa.2016.03.005.

[1382] R L Friede and W H Van Houten. 'Relations between postmortem alterations and glycolytic metabolism in the brain'. In: *Exp. Neurol.* 4 (3 1st Sept. 1961), pp. 197–204. DOI: 10.1016/0014-4886(61)90041-3.

[1383] Apeksha N Agarwal, Andrea R Gilbert and Daniel D Mais. 'Correlation of cerebellar granular layer autolysis with ante-mortem systemic acid-base status'. In: *Cell Tissue Bank.* 22 (3 Sept. 2021), pp. 505–509. DOI: 10.1007/s10561-021-09900-4.

[1384] Daniel R Rissi, Ricardo E Mendes and Claudio S L Barros. 'The artifact of cerebellar granule cell layer conglutination in veterinary medicine: a brief historical perspective and review'. In: *J. Vet. Diagn. Invest.* 36 (6 Nov. 2024), pp. 933–936. DOI: 10.1177/10406387241270024.

[1385] James Mackintosh MacKenzie. 'Examining the decomposed brain'. In: *Am. J. Forensic Med. Pathol.* 35 (4 Dec. 2014), pp. 265–270. DOI: 10.1097/PAF.0000000000000111.

[1386] Enrico Cappellini, Matthew J Collins and M Thomas P Gilbert. 'Biochemistry. Unlocking ancient protein palimpsests'. In: *Science* 343 (6177 21st Mar. 2014), pp. 1320–1322. DOI: 10.1126/science.1249274.

[1387] Enrico Cappellini et al. 'Ancient biomolecules and evolutionary inference'. In: *Annu. Rev. Biochem.* 87 (1 20th June 2018), pp. 1029–1060. DOI: 10.1146/annurev-biochem-062917-012002.

[1388] Jessica Hendy. 'Ancient protein analysis in archaeology'. In: *Sci. Adv.* 7 (3 Jan. 2021), eabb9314. DOI: 10.1126/sciadv.abb9314.

[1389] Michael Buckley. 'Paleoproteomics: An introduction to the analysis of ancient proteins by soft ionisation mass spectrometry'. In: *Population Genomics*. Cham: Springer International Publishing, 2018, pp. 31–52. DOI: 10.1007/13836_2018_50.

[1390] Michael Buckley et al. 'Species identification by analysis of bone collagen using matrix-assisted laser desorption/ionisation time-of-flight mass spectrometry: Species identification of bone collagen using MALDI-TOF-MS'. In: *Rapid Commun. Mass Spectrom.* 23 (23 Dec. 2009), pp. 3843–3854. DOI: 10.1002/rcm.4316.

[1391] Patrick Leopold Rüther et al. 'SPIN enables high throughput species identification of archaeological bone by proteomics'. In: *Nat. Commun.* 13 (1 5th May 2022), p. 2458. DOI: 10.1038/s41467-022-30097-x.

[1392] Ian Engels et al. 'Classification of collagens via peptide ambiguation, in a paleoproteomic LC-MS/MS-based taxonomic pipeline'. In: *J. Proteome Res.* 24 (4 4th Apr. 2025), pp. 1907–1925. DOI: 10.1021/acs.jproteome.4c00962.

[1393] Katelyn Elizabeth Mason et al. 'Protein-based forensic identification using genetically variant peptides in human bone'. In: *Forensic Sci. Int.* 288 (1st July 2018), pp. 89–96. DOI: 10.1016/j.forsciint.2018.04.016.

[1394] Trevor Borja et al. 'Proteomic genotyping of fingermark donors with genetically variant peptides'. In: *Forensic Sci. Int. Genet.* 42 (Sept. 2019), pp. 21–30. DOI: 10.1016/j.fsigen.2019.05.005.

[1395] Fanny Chu et al. 'Human identification using genetically variant peptides in biological forensic evidence'. In: *ACS Symposium Series*. ACS Symposium Series. American Chemical Society. Washington, DC: American Chemical Society, 1st Jan. 2019, pp. 107–123. DOI: 10.1021/bk-2019-1339.ch007.

[1396] Nicolas Andre Stewart et al. 'Sex determination of human remains from peptides in tooth enamel'. In: *Proc. Natl. Acad. Sci. U. S. A.* 114 (52 26th Dec. 2017), pp. 13649–13654. DOI: 10.1073/pnas.1714926115.

[1397] Julia A Gamble et al. 'Advancing sex estimation from amelogenin: Applications to archaeological, deciduous, and fragmentary dental enamel'. In: *J. Archaeol. Sci. Rep.* 54 (104430 Apr. 2024), p. 104430. DOI: 10.1016/j.jasrep.2024.104430.

[1398] Meaghan Mackie et al. 'Preservation of the metaproteome: variability of protein preservation in ancient dental calculus'. In: *Sci. Technol. Archaeol. Res.* 3 (1 11th Aug. 2017), pp. 74–86. DOI: 10.1080/20548923.2017.1361629.

[1399] Caitlin Colleary et al. 'Molecular preservation in mammoth bone and variation based on burial environment'. In: *Sci. Rep.* 11 (1 29th Jan. 2021), p. 2662. DOI: 10.1038/s41598-021-81849-6.

[1400] Ragnheiður Diljá Ásmundsdóttir et al. 'Early Holocene preservation differences between cortical and trabecular bone proteomes'. In: *J. Archaeol. Sci. Rep.* 57 (104643 1st Sept. 2024), p. 104643. DOI: 10.1016/j.jasrep.2024.104643.

[1401] Miranda Evans et al. 'The impact of cooking and burial on proteins: a characterisation of experimental foodcrusts and ceramics'. In: *R. Soc. Open Sci.* 11 (9 Sept. 2024), p. 240610. DOI: 10.1098/rsos.240610.

[1402] Biancamaria Bonucci et al. 'Ancient microbial DNA and proteins preserve in concretions covering human remains'. In: *iScience* 28 (8 15th Aug. 2025), p. 113182. DOI: 10.1016/j.isci.2025.113182.

[1403] Qitao Hu et al. 'Comparing protein stability in modern and ancient sabkha environments: Implications for molecular remnants on ancient Mars'. In: *Int. J. Mol. Sci.* 26 (13 21st June 2025), p. 5978. DOI: 10.3390/ijms26135978.

[1404] Lucrezia Gatti et al. 'Deep-time preservation of amino acids in mammalian fossil tooth enamel'. In: *Commun. Biol.* 9 (1 18th Feb. 2026), p. 381. DOI: 10.1038/s42003-026-09716-6.

[1405] Paul V Ullmann et al. 'Taphonomic and diagenetic pathways to protein preservation, part I: The case of Tyrannosaurus rex specimen MOR 1125'. In: *Biology (Basel)* 10 (11 17th Nov. 2021), p. 1193. DOI: 10.3390/biology10111193.

[1406] Paul V Ullmann, Richard D Ash and John B Scannella. 'Taphonomic and diagenetic pathways to protein preservation, part II: The case of Brachylophosaurus canadensis specimen MOR 2598'. In: *Biology (Basel)* 11 (8 5th Aug. 2022), p. 1177. DOI: 10.3390/biology11081177.

[1407] Lijie Tang et al. 'Comparative proteomic analysis of residual proteins in waterlogged ancient leather'. In: *J. Proteomics* 322 (105537 6th Jan. 2026), p. 105537. DOI: 10.1016/j.jprot.2025.105537.

[1408] Louise Le Meillour et al. 'Identification of degraded bone and tooth splinters from arid environments using palaeoproteomics'. In: *Palaeogeogr. Palaeoclimatol. Palaeoecol.* 511 (Dec. 2018), pp. 472–482. DOI: 10.1016/j.palaeo.2018.09.013.

[1409] Brian Thomas and Stephen Taylor. 'Proteomes of the past: the pursuit of proteins in paleontology'. In: *Expert Rev. Proteomics* 16 (11-12 Nov. 2019), pp. 881–895. DOI: 10.1080/14789450.2019.1700114.

[1410] Andrea Bonicelli et al. 'Insights into the differential preservation of bone proteomes in inhumed and entombed cadavers from Italian forensic caseworks'. In: *J. Proteome Res.* 21 (5 6th May 2022), pp. 1285–1298. DOI: 10.1021/acs.jproteome.1c00904.

[1411] Carli Peters et al. 'Bone collagen from subtropical Australia is preserved for more than 50,000 years'. In: *Commun. Earth Environ.* 4 (1 25th Nov. 2023). DOI: 10.1038/s43247-023-01114-8.

[1412] Alicia R Ventresca Miller et al. 'Permafrost preservation reveals proteomic evidence for yak milk consumption in the 13th century'. In: *Commun. Biol.* 6 (1 31st Mar. 2023), p. 351. DOI: 10.1038/s42003-023-04723-3.

[1413] Caroline Wadsworth and Mike Buckley. 'Proteome degradation in fossils: investigating the longevity of protein survival in ancient bone: Proteome degradation in fossils'. In: *Rapid Commun. Mass Spectrom.* 28 (6 30th Mar. 2014), pp. 605–615. DOI: 10.1002/rcm.6821.

[1414] Alexandra Morton-Hayward et al. 'Deep palaeoproteomic profiling of archaeological human brains'. In: *PLoS One* 20 (5 28th May 2025), e0324246. DOI: 10.1371/journal.pone.0324246.

[1415] Lindsay D Rogers and Christopher M Overall. 'Proteolytic post-translational modification of proteins: proteomic tools and methodology'. In: *Mol. Cell. Proteomics* 12 (12 25th Dec. 2013), pp. 3532–3542. DOI: 10.1074/mcp.M113.031310.

[1416] Noemi Procopio et al. 'Forensic proteomics for the evaluation of the post-mortem decay in bones'. In: *J. Proteomics* 177 (15th Apr. 2018), pp. 21–30. DOI: 10.1016/j.jprot.2018.01.016.

[1417] Marat D Kazanov et al. 'Structural determinants of limited proteolysis'. In: *J. Proteome Res.* 10 (8 5th Aug. 2011), pp. 3642–3651. DOI: 10.1021/pr200271w.

[1418] Marcin J Suskiewicz et al. 'Context-dependent resistance to proteolysis of intrinsically disordered proteins'. In: *Protein Sci.* 20 (8 1st Aug. 2011), pp. 1285–1297. DOI: 10.1002/pro.657.

[1419] Joseph A Marsh. 'Buried and accessible surface area control intrinsic protein flexibility'. In: *J. Mol. Biol.* 425 (17 9th Sept. 2013), pp. 3250–3263. DOI: 10.1016/j.jmb.2013.06.019.

[1420] Csaba Magyar et al. 'Origin of increased solvent accessibility of peptide bonds in mutual Synergetic Folding proteins'. In: *Int. J. Mol. Sci.* 22 (24 14th Dec. 2021), p. 13404. DOI: 10.3390/ijms222413404.

[1421] Linqi Cheng et al. 'Advancing protein therapeutics through proximity-induced chemistry'. In: *Cell Chem. Biol.* 31 (3 21st Mar. 2024), pp. 428–445. DOI: 10.1016/j.chembiol.2023.09.004.

[1422] Shen Luo and Rodney L Levine. 'Methionine in proteins defends against oxidative stress'. In: *FASEB J.* 23 (2 Feb. 2009), pp. 464–472. DOI: 10.1096/fj.08-118414.

[1423] Jared A Delmar et al. 'Machine learning prediction of methionine and tryptophan photooxidation susceptibility'. In: *Mol. Ther. Methods Clin. Dev.* 21 (11th June 2021), pp. 466–477. DOI: 10.1016/j.omtm.2021.03.023.

[1424] H T Wright. 'Sequence and structure determinants of the nonenzymatic deamidation of asparagine and glutamine residues in proteins'. In: *Protein Eng.* 4 (3 1st Feb. 1991), pp. 283–294. DOI: 10.1093/protein/4.3.283.

[1425] Vera Timm et al. 'Identification and characterization of oxidation and deamidation sites in monoclonal rat/mouse hybrid antibodies'. In: *J. Chromatogr. B Analyt. Technol. Biomed. Life Sci.* 878 (9-10 15th Mar. 2010), pp. 777–784. DOI: 10.1016/j.jchromb.2010.01.036.

[1426] Amanda L Pace et al. 'Asparagine deamidation dependence on buffer type, pH, and temperature'. In: *J. Pharm. Sci.* 102 (6 1st June 2013), pp. 1712–1723. DOI: 10.1002/jps.23529.

[1427] Dylan L Riggs, Sonia V Gomez and Ryan R Julian. 'Sequence and solution effects on the prevalence of d-isomers produced by deamidation'. In: *ACS Chem. Biol.* 12 (11 17th Nov. 2017), pp. 2875–2882. DOI: 10.1021/acschembio.7b00686.

[1428] Luigi Grassi and Chiara Cabrele. 'Susceptibility of protein therapeutics to spontaneous chemical modifications by oxidation, cyclization, and elimination reactions'. In: *Amino Acids* 51 (10-12 Nov. 2019), pp. 1409–1431. DOI: 10.1007/s00726-019-02787-2.

[1429] Ji Min Lee et al. 'Control of protein stability by post-translational modifications'. In: *Nat. Commun.* 14 (1 13th Jan. 2023), p. 201. DOI: 10.1038/s41467-023-35795-8.

[1430] M Pal Chowdhury et al. 'Collagen deamidation in archaeological bone as an assessment for relative decay rates'. In: *Archaeometry* 61 (6 1st Dec. 2019), pp. 1382–1398. DOI: 10.1111/arcm.12492.

[1431] Emmajay Sutherland, Tim S Veth and Nicholas M Riley. 'Revisiting the effect of trypsin digestion buffers on artificial deamidation'. In: *J. Am. Soc. Mass Spectrom.* 36 (3 5th Mar. 2025), pp. 457–462. DOI: 10.1021/jasms.4c00389.

[1432] Elena R Schroeter and Timothy P Cleland. 'Glutamine deamidation: an indicator of antiquity, or preservational quality?: Glutamine deamidation: indicator of antiquity?' In: *Rapid Commun. Mass Spectrom.* 30 (2 30th Jan. 2016), pp. 251–255. DOI: 10.1002/rcm.7445.

[1433] Manasij Pal Chowdhury et al. 'Novel deep eutectic solvent-based protein extraction method for pottery residues and archeological implications'. In: *J. Proteome Res.* 21 (11 4th Nov. 2022), pp. 2619–2634. DOI: 10.1021/acs.jproteome.2c00340.

[1434] Dorothea Mylopotamitaki et al. 'Comparing extraction method efficiency for high-throughput palaeoproteomic bone species identification'. In: *Sci. Rep.* 13 (1 26th Oct. 2023), p. 18345. DOI: 10.1038/s41598-023-44885-y.

[1435] Therese Dau, Giulia Bartolomucci and Juri Rappsilber. 'Proteomics using protease alternatives to trypsin benefits from sequential digestion with trypsin'. In: *Anal. Chem.* 92 (14 21st July 2020), pp. 9523–9527. DOI: 10.1021/acs.analchem.0c00478.

[1436] Liam T Lanigan et al. 'Multi-protease analysis of Pleistocene bone proteomes'. In: *J. Proteomics* 228 (103889 30th Sept. 2020), p. 103889. DOI: 10.1016/j.jprot.2020.103889.

[1437] Zandra Fagernäs et al. 'Digging deeper into ancient skeletal proteomes through consecutive digestion with multiple proteases'. In: *J. Proteomics* 298 (105143 30th Apr. 2024), p. 105143. DOI: 10.1016/j.jprot.2024.105143.

[1438] Timothy P Cleland and Elena R Schroeter. 'A comparison of common mass spectrometry approaches for paleoproteomics'. In: *J. Proteome Res.* 17 (3 2nd Mar. 2018), pp. 936–945. DOI: 10.1021/acs.jproteome.7b00703.

[1439] Naim Abdul-Khalek et al. 'Insight on physicochemical properties governing peptide MS1 response in HPLC-ESI-MS/MS: A deep learning approach'. In: *Comput. Struct. Biotechnol. J.* 21 (22nd July 2023), pp. 3715–3727. DOI: 10.1016/j.csbj.2023.07.027.

[1440] Yun Chiang, Frido Welker and Matthew James Collins. 'Spectra without stories: reporting 94% dark and unidentified ancient proteomes'. In: *Open Res. Eur.* 4 (15th Apr. 2024), p. 71. DOI: 10.12688/openreseurope.17225.1.

[1441] Ismael Rodriguez Palomo et al. 'Benchmarking the identification of a single degraded protein to explore optimal search strategies for ancient proteins'. In: *Peer Community J.* 4 (e107 21st Nov. 2024). DOI: 10.24072/pcjournal.491.

[1442] Enrico Cappellini et al. 'Proteomic analysis of a pleistocene mammoth femur reveals more than one hundred ancient bone proteins'. In: *J. Proteome Res.* 11 (2 3rd Feb. 2012), pp. 917–926. DOI: 10.1021/pr200721u.

[1443] Frido Welker et al. 'Ancient proteins resolve the evolutionary history of Darwin's South American ungulates'. In: *Nature* 522 (7554 4th June 2015), pp. 81–84. DOI: 10.1038/nature14249.

[1444] Frido Welker et al. 'Palaeoproteomic evidence identifies archaic hominins associated with the Châtelperronian at the Grotte du Renne'. In: *Proc. Natl. Acad. Sci. U. S. A.* 113 (40 4th Oct. 2016), pp. 11162–11167. DOI: 10.1073/pnas.1605834113.

[1445] Frido Welker et al. 'Middle Pleistocene protein sequences from the rhinoceros genus Stephanorhinus and the phylogeny of extant and extinct Middle/Late Pleistocene Rhinocerotidae'. In: *PeerJ* 5 (e3033 14th Mar. 2017), e3033. DOI: 10.7717/peerj.3033.

[1446] Enrico Cappellini et al. 'Early Pleistocene enamel proteome from Dmanisi resolves Stephanorhinus phylogeny'. In: *Nature* 574 (7776 Oct. 2019), pp. 103–107. DOI: 10.1038/s41586-019-1555-y.

[1447] Fahu Chen et al. 'A late Middle Pleistocene Denisovan mandible from the Tibetan Plateau'. In: *Nature* 569 (7756 May 2019), pp. 409–412. DOI: 10.1038/s41586-019-1139-x.

[1448] Ivo R Horn et al. 'Palaeoproteomics of bird bones for taxonomic classification'. In: *Zool. J. Linn. Soc.* 186 (3 25th June 2019), pp. 650–665. DOI: 10.1093/zoolinnean/zlz012.

[1449] Samantha Presslee et al. 'Palaeoproteomics resolves sloth relationships'. In: *Nat. Ecol. Evol.* 3 (7 July 2019), pp. 1121–1130. DOI: 10.1038/s41559-019-0909-z.

[1450] Frido Welker et al. 'Enamel proteome shows that Gigantopithecus was an early diverging pongine'. In: *Nature* 576 (7786 Dec. 2019), pp. 262–265. DOI: 10.1038/s41586-019-1728-8.

[1451] Jeana L Drake, Julian P Whitelegge and David K Jacobs. 'First sequencing of ancient coral skeletal proteins'. In: *Sci. Rep.* 10 (1 10th Nov. 2020), p. 19407. DOI: 10.1038/s41598-020-75846-4.

[1452] Beatrice Demarchi et al. 'Ancient proteins resolve controversy over the identity of Genyornis eggshell'. In: *Proc. Natl. Acad. Sci. U. S. A.* 119 (43 25th Oct. 2022), e2109326119. DOI: 10.1073/pnas.2109326119.

[1453] Fabrice Bray et al. 'Extinct species identification from late middle Pleistocene and earlier Upper Pleistocene bone fragments and tools not recognizable from their osteomorphological study by an enhanced proteomics protocol'. In: *Archaeometry* 65 (1 1st Feb. 2023), pp. 196–212. DOI: 10.1111/arcm.12800.

[1454] Daniel R Green et al. 'Eighteen million years of diverse enamel proteomes from the East African Rift'. In: *Nature* 643 (8072 9th July 2025), pp. 712–718. DOI: 10.1038/s41586-025-09040-9.

[1455] Takumi Tsutaya et al. 'Palaeoproteomic identification of breast milk protein residues from the archaeological skeletal remains of a neonatal dog'. In: *Sci. Rep.* 9 (1 6th Sept. 2019), p. 12841. DOI: 10.1038/s41598-019-49183-0.

[1456] Carine Froment et al. 'Analysis of 5000 year-old human teeth using optimized large-scale and targeted proteomics approaches for detection of sex-specific peptides'. In: *J. Proteomics* 211 (103548 16th Jan. 2020), p. 103548. DOI: 10.1016/j.jprot.2019.103548.

[1457] Anne-Marie Bacon et al. 'A multi-proxy approach to exploring Homo sapiens' arrival, environments and adaptations in Southeast Asia'. In: *Sci. Rep.* 11 (1 26th Oct. 2021), p. 21080. DOI: 10.1038/s41598-021-99931-4.

[1458] Sarah Fiddyment et al. 'Girding the loins? Direct evidence of the use of a medieval English parchment birthing girdle from biomolecular analysis'. In: *R. Soc. Open Sci.* 8 (3 10th Mar. 2021), p. 202055. DOI: 10.1098/rsos.202055.

[1459] Anthony Gasparini et al. 'Biological sex VS. Archaeological Gender: Enamel peptide analysis of the horsemen of the Early Middle age necropolises of Campochiaro (Molise, Italy)'. In: *J. Archaeol. Sci. Rep.* 41 (103337 1st Feb. 2022), p. 103337. DOI: 10.1016/j.jasrep.2021.103337.

[1460] Barry Shaw et al. 'Antibody-based sex determination of human skeletal remains'. In: *iScience* 26 (11 17th Nov. 2023), p. 108191. DOI: 10.1016/j.isci.2023.108191.

[1461] K N White et al. 'Enhancing mummy 'palaeobiographies' through the use of multidisciplinary techniques and approaches'. In: *J. Archaeol. Sci. Rep.* 47 (103784 1st Feb. 2023), p. 103784. DOI: 10.1016/j.jasrep.2022.103784.

[1462] Claire Koenig et al. 'Automated high-throughput biological sex identification from archeological human dental enamel using targeted proteomics'. In: *J. Proteome Res.* 23 (11 1st Nov. 2024), pp. 5107–5121. DOI: 10.1021/acs.jproteome.4c00557.

[1463] Luise Ørsted Brandt et al. 'Species identification of archaeological skin objects from Danish bogs: comparison between mass spectrometry-based peptide sequencing and microscopy-based methods'. In: *PLoS One* 9 (9 26th Sept. 2014), e106875. DOI: 10.1371/journal.pone.0106875.

[1464] Rikai Sawafuji et al. 'Proteomic profiling of archaeological human bone'. In: *R. Soc. Open Sci.* 4 (6 June 2017), p. 161004. DOI: 10.1098/rsos.161004.

[1465] Nina Sophia Mahlke et al. 'Molecular clocks in ancient proteins: Do they reflect the age at death even after millennia?' In: *Int. J. Legal Med.* 135 (4 17th July 2021), pp. 1225–1233. DOI: 10.1007/s00414-021-02522-1.

[1466] Agnes Bona et al. 'Mass spectrometric identification of ancient proteins as potential molecular biomarkers for a 2000-year-old osteogenic sarcoma'. In: *PLoS One* 9 (1 27th Jan. 2014), e87215. DOI: 10.1371/journal.pone.0087215.

[1467] Christina Warinner et al. 'Pathogens and host immunity in the ancient human oral cavity'. In: *Nat. Genet.* 46 (4 Apr. 2014), pp. 336–344. DOI: 10.1038/ng.2906.

[1468] Jessica Hendy et al. 'The challenge of identifying tuberculosis proteins in archaeological tissues'. In: *J. Archaeol. Sci.* 66 (C Feb. 2016), pp. 146–153. DOI: 10.1016/j.jas.2016.01.003.

[1469] Jana Jones et al. 'Identification of proteins from 4200-year-old skin and muscle tissue biopsies from ancient Egyptian mummies of the first intermediate period shows evidence of acute inflammation and severe immune response'. In: *Philos. Trans. A Math. Phys. Eng. Sci.* 374 (2079 28th Oct. 2016), p. 20150373. DOI: 10.1098/rsta.2015.0373.

[1470] Cristina Pérez-Martínez et al. 'Usefulness of protein analysis for detecting pathologies in bone remains'. In: *Forensic Sci. Int.* 258 (Jan. 2016), pp. 68–73. DOI: 10.1016/j.forsciint.2015.11.009.

[1471] Rosa R Jersie-Christensen et al. 'Quantitative metaproteomics of medieval dental calculus reveals individual oral health status'. In: *Nat. Commun.* 9 (1 20th Nov. 2018), p. 4744. DOI: 10.1038/s41467-018-07148-3.

[1472] Anna K Fotakis et al. 'Multi-omic detection of Mycobacterium leprae in archaeological human dental calculus'. In: *Philos. Trans. R. Soc. Lond. B Biol. Sci.* 375 (1812 23rd Nov. 2020), p. 20190584. DOI: 10.1098/rstb.2019.0584.

[1473] Francesco Fontani et al. 'Bioarchaeological and paleogenomic profiling of the unusual Neolithic burial from Grotta di Pietra Sant'Angelo (Calabria, Italy)'. In: *Sci. Rep.* 13 (1 24th July 2023), p. 11978. DOI: 10.1038/s41598-023-39250-y.

[1474] Yoko Uchida-Fukuhara et al. 'Palaeoproteomic investigation of an ancient human skeleton with abnormal deposition of dental calculus'. In: *Sci. Rep.* 14 (1 11th Mar. 2024), p. 5938. DOI: 10.1038/s41598-024-55779-y.

[1475] Shevan Wilkin et al. 'Sequential trypsin and ProAlanase digestions unearth immunological protein biomarkers shrouded by skeletal collagen'. In: *iScience* 27 (5 17th May 2024), p. 109663. DOI: 10.1016/j.isci.2024.109663.

[1476] Giulia Riccomi et al. 'Palaeoproteomic characterization of archaeological dental calculus reveals precarious periodontal health in pre-Roman Italy (7th-4th century BCE)'. In: *J. Proteomics* 320 (105503 15th Sept. 2025), p. 105503. DOI: 10.1016/j.jprot.2025.105503.

[1477] Mathias Uhlén et al. 'Proteomics. Tissue-based map of the human proteome'. In: *Science* 347 (6220 23rd Jan. 2015), p. 1260419. DOI: 10.1126/science.1260419.

[1478] Lihua Jiang et al. 'A quantitative proteome map of the human body'. In: *Cell* 183 (1 1st Oct. 2020), 269–283.e19. DOI: 10.1016/j.cell.2020.08.036.

[1479] Tomer Shlomi et al. 'Network-based prediction of human tissue-specific metabolism'. In: *Nat. Biotechnol.* 26 (9 17th Sept. 2008), pp. 1003–1010. DOI: 10.1038/nbt.1487.

[1480] Bingsen Zhang and Frank C Schroeder. 'Mechanisms of metabolism-coupled protein modifications'. In: *Nat. Chem. Biol.* 21 (6 June 2025), pp. 819–830. DOI: 10.1038/s41589-024-01805-z.

[1481] C Diskin, T A J Ryan and L A J O'Neill. 'Modification of proteins by metabolites in immunity'. In: *Immunity* 54 (1 12th Jan. 2021), pp. 19–31. DOI: 10.1016/j.immuni.2020.09.014.

[1482] Steven B Wells et al. 'Multimodal profiling reveals tissue-directed signatures of human immune cells altered with age'. In: *Nat. Immunol.* 26 (9 Sept. 2025), pp. 1612–1625. DOI: 10.1038/s41590-025-02241-4.

[1483] Vaishnavi Ravikumar, Carsten Jers and Ivan Mijakovic. 'Elucidating host-pathogen interactions based on post-translational modifications using proteomics approaches'. In: *Front. Microbiol.* 6 (20th Nov. 2015), p. 1313. DOI: 10.3389/fmicb.2015.01312.

[1484] Lirit Duchovni, Genrieta Shmunis and Lior Lobel. 'Posttranslational modifications: an emerging functional layer of diet-host-microbe interactions'. In: *MBio* 15 (10 16th Oct. 2024), e0238724. DOI: 10.1128/mbio.02387-24.

[1485] Rubén Dario Díaz Martín et al. 'Proteomics as a new tool in forensic sciences'. In: *Span. J. Leg. Med.* 45 (3 July 2019), pp. 114–122. DOI: 10.1016/j.remle.2019.08.001.

[1486] Georgia Ntasi et al. 'Molecular signatures written in bone proteins of 79 AD victims from Herculaneum and Pompeii'. In: *Sci. Rep.* 12 (1 27th May 2022), p. 8401. DOI: 10.1038/s41598-022-12042-6.

[1487] Muhammad Kaleem, Arooj Munawar and Afshan Maqbool. 'Revealing the role of proteins in the field of forensic investigations'. In: *Forensic Insights and Health Sciences Bulletin* 2 (1 30th Apr. 2024), pp. 29–39. DOI: 10.56770/fi2024215.

[1488] Jessica Hendy et al. 'A guide to ancient protein studies'. In: *Nat. Ecol. Evol.* 2 (5 May 2018), pp. 791–799. DOI: 10.1038/s41559-018-0510-x.

[1489] P Boomathi Pandeswari and Varatharajan Sabareesh. 'Middle-down approach: a choice to sequence and characterize proteins/proteomes by mass spectrometry'. In: *RSC Adv.* 9 (1 19th Dec. 2018), pp. 313–344. DOI: 10.1039/c8ra07200k.

[1490] Jack L Bennett et al. 'Uncovering hidden protein modifications with native top-down mass spectrometry'. In: *Nat. Methods* 22 (10 Oct. 2025), pp. 2127–2137. DOI: 10.1038/s41592-025-02846-5.

[1491] Timothy K Toby, Luca Fornelli and Neil L Kelleher. 'Progress in top-down proteomics and the analysis of proteoforms'. In: *Annu. Rev. Anal. Chem. (Palo Alto Calif.)* 9 (1 12th June 2016), pp. 499–519. DOI: 10.1146/annurev-anchem-071015-041550.

[1492] Yuming Jiang et al. 'Comprehensive overview of bottom-up proteomics using mass spectrometry'. In: *ACS Meas. Sci. Au* 4 (4 21st Aug. 2024), pp. 338–417. DOI: 10.1021/acsmeasuresciau.3c00068.

[1493] Michael Buckley et al. 'A fossil protein chimera; difficulties in discriminating dinosaur peptide sequences from modern cross-contamination'. In: *Proc. Biol. Sci.* 284 (1855 31st May 2017), p. 20170544. DOI: 10.1098/rspb.2017.0544.

[1494] Alexandra L Morton-Hayward et al. 'A conscious rethink: Why is brain tissue commonly preserved in the archaeological record? Commentary on: Petrone P, Pucci P, Niola M, et al. Heat-induced brain vitrification from the Vesuvius eruption in C.E. 79. N Engl J Med 2020;382:383-4. DOI: 10.1056/NEJMc1909867'. In: *Sci. Technol. Archaeol. Res.* 6 (1 1st Jan. 2020), pp. 87–95. DOI: 10.1080/20548923.2020.1815398.

[1495] Jaroslav Pavelka et al. 'Challenge to molecular archaeology—Sediments contaminated by allochthonous animal proteins'. In: *J. Liq. Chromatogr. Relat. Technol.* 43 (19-20 13th Dec. 2020), pp. 863–874. DOI: 10.1080/10826076.2020.1838925.

[1496] Jean-Philippe Antignac et al. 'The ion suppression phenomenon in liquid chromatography–mass spectrometry and its consequences in the field of residue analysis'. In: *Anal. Chim. Acta* 529 (1-2 Jan. 2005), pp. 129–136. DOI: 10.1016/j.aca.2004.08.055.

[1497] Kelly Hodge et al. 'Cleaning up the masses: exclusion lists to reduce contamination with HPLC-MS/MS'. In: *J. Proteomics* 88 (2nd Aug. 2013), pp. 92–103. DOI: 10.1016/j.jprot.2013.02.023.

[1498] Haidy Metwally, Robert G McAllister and Lars Konermann. 'Exploring the mechanism of salt-induced signal suppression in protein electrospray mass spectrometry using experiments and molecular dynamics simulations'. In: *Anal. Chem.* 87 (4 17th Feb. 2015), pp. 2434–2442. DOI: 10.1021/ac5044016.

[1499] Evan Saitta et al. 'Non-avian dinosaur eggshell calcite contains ancient, endogenous amino acids'. In: *bioRxiv* (3rd June 2020). DOI: 10.1101/2020.06.02.129999.

[1500] Ioannis Kontopoulos et al. 'Screening archaeological bone for palaeogenetic and palaeoproteomic studies'. In: *PLoS One* 15 (6 25th June 2020), e0235146. DOI: 10.1371/journal.pone.0235146.

[1501] Samantha Presslee et al. 'Assessment of different screening methods for selecting palaeontological bone samples for peptide sequencing'. In: *J. Proteomics* 230 (103986 6th Jan. 2021), p. 103986. DOI: 10.1016/j.jprot.2020.103986.

[1502] Jakob Hansen et al. 'A comparative study of commercially available, minimally invasive, sampling methods on Early Neolithic humeri analysed via palaeoproteomics'. In: *J. Archaeol. Sci.* 167 (106002 July 2024), p. 106002. DOI: 10.1016/j.jas.2024.106002.

[1503] M Di Matteo et al. 'Portable ER-FTIR as a non-destructive method to pre-screen collagen for ZooMS analysis in archaeology'. In: *J. Cult. Herit.* 78 (Mar. 2026), pp. 55–66. DOI: 10.1016/j.culher.2026.01.009.

[1504] Beatrice Demarchi et al. 'Never boring: Non-invasive palaeoproteomics of mummified human skin'. In: *J. Archaeol. Sci.* 119 (105145 July 2020), p. 105145. DOI: 10.1016/j.jas.2020.105145.

[1505] Virginie Sinet-Mathiot et al. 'The effect of eraser sampling for proteomic analysis on Palaeolithic bone surface microtopography'. In: *Sci. Rep.* 11 (1 8th Dec. 2021), p. 23611. DOI: 10.1038/s41598-021-02823-w.

[1506] Dylan H Multari et al. 'Development of a novel minimally invasive sampling and analysis technique using skin sampling tape strips for bioarchaeological proteomics'. In: *J. Archaeol. Sci.* 139 (105548 1st Mar. 2022), p. 105548. DOI: 10.1016/j.jas.2022.105548.

[1507] Isabelle Fabrizi et al. 'Low-invasive sampling method for taxonomic for the identification of archaeological and paleontological bones by proteomics of their collagens'. In: *bioRxiv* (20th Oct. 2023). DOI: 10.1101/2023.10.18.562897.

[1508] Albína Hulda Pálsdóttir et al. 'Not a limitless resource: ethics and guidelines for destructive sampling of archaeofaunal remains'. In: *R. Soc. Open Sci.* 6 (10 2nd Oct. 2019), p. 191059. DOI: 10.1098/rsos.191059.

[1509] L G van der Sluis et al. 'Identification and tentative removal of collagen glue in Palaeolithic worked bone objects: implications for ZooMS and radiocarbon dating'. In: *Sci. Rep.* 13 (1 13th Dec. 2023), p. 22119. DOI: 10.1038/s41598-023-49242-7.

[1510] Zandra Fagernäs et al. 'New methods on the block: Taxonomic identification of archaeological bones in resin-embedded sediments through paleoproteomics'. In: *PNAS Nexus* 4 (10 14th Oct. 2025), pgaf289. DOI: 10.1093/pnasnexus/pgaf289.

[1511] Carley A Crann and Tara Grant. 'Radiocarbon age of consolidants and adhesives used in archaeological conservation'. In: *J. Archaeol. Sci. Rep.* 24 (1st Apr. 2019), pp. 1059–1063. DOI: 10.1016/j.jasrep.2019.03.023.

[1512] Ellery Frahm et al. 'Every contact leaves a trace: Documenting contamination in lithic residue studies at the Middle Palaeolithic sites of Lusakert Cave 1 (Armenia) and Crvena Stijena (Montenegro)'. In: *PLoS One* 17 (4 7th Apr. 2022), e0266362. DOI: 10.1371/journal.pone.0266362.

[1513] Kristine Korzow Richter et al. 'A primer for ZooMS applications in archaeology'. In: *Proc. Natl. Acad. Sci. U. S. A.* 119 (20 17th May 2022), e2109323119. DOI: 10.1073/pnas.2109323119.

[1514] Anne Marie Høier Eriksen et al. 'Releasing the microbes from old bones: the effect of different DNA extraction protocols on microbial community profiling'. In: *Sci. Technol. Archaeol. Res.* 6 (1 1st Jan. 2020), pp. 1–15. DOI: 10.1080/20548923.2020.1738115.

[1515] Anne Marie Høier Eriksen et al. 'Exploring DNA degradation in situ and in museum storage through genomics and metagenomics'. In: *Commun. Biol.* 8 (1 10th Feb. 2025), p. 210. DOI: 10.1038/s42003-025-07616-9.

[1516] Georgia Ntasi et al. 'Proteomic characterization of collagen-based animal glues for restoration'. In: *J. Proteome Res.* 21 (9 2nd Sept. 2022), pp. 2173–2184. DOI: 10.1021/acs.jproteome.2c00232.

[1517] Rocio Prisby et al. 'Wheat-based glues in conservation and cultural heritage: (dis)solving the proteome of flour and starch pastes and their adhering properties'. In: *J. Proteome Res.* 23 (5 3rd May 2024), pp. 1649–1665. DOI: 10.1021/acs.jproteome.3c00804.

[1518] Matthew J Rardin. 'Rapid assessment of contaminants and interferences in mass spectrometry data using Skyline'. In: *J. Am. Soc. Mass Spectrom.* 29 (6 17th June 2018), pp. 1327–1330. DOI: 10.1007/s13361-018-1940-z.

[1519] Laura S Weyrich et al. 'Laboratory contamination over time during low-biomass sample analysis'. In: *Mol. Ecol. Resour.* 19 (4 1st July 2019), pp. 982–996. DOI: 10.1111/1755-0998.13011.

[1520] Francesco Romano, Samanta Milani and Cesare M Joppolo. 'Airborne particle and microbiological human emission rate investigation for cleanroom clothing combinations'. In: *Build. Environ.* 180 (106967 Aug. 2020), p. 106967. DOI: 10.1016/j.buildenv.2020.106967.

[1521] Andreas F Widmer and Reno Frei. 'Decontamination, disinfection, and sterilization'. In: *Manual of Clinical Microbiology, 10th Edition*. American Society of Microbiology, 1st Jan. 2011, pp. 143–173. DOI: 10.1128/9781555816728.ch11.

[1522] Mariana Vassal et al. 'Combination of UVC light with antimicrobial agents for enhanced disinfection of surfaces and liquids'. In: *J. Environ. Chem. Eng.* 11 (3 June 2023), p. 109639. DOI: 10.1016/j.jece.2023.109639.

[1523] Shib Sankar Basak and Asok Adak. 'Physicochemical methods for disinfection of contaminated surfaces - a way to control infectious diseases'. In: *J. Environ. Health Sci. Eng.* 22 (1 June 2024), pp. 53–64. DOI: 10.1007/s40201-024-00893-2.

[1524] Tim Sandle and Madhu Raju Saghee. 'Some considerations for the implementation of disposable technology and single-use systems in biopharmaceuticals'. In: *J. Commer. Biotechnol.* 17 (4 2nd Nov. 2011), pp. 319–329. DOI: 10.1057/jcb.2011.21.

[1525] Teresa Martínez-Sena et al. 'Monitoring of system conditioning after blank injections in untargeted UPLC-MS metabolomic analysis'. In: *Sci. Rep.* 9 (1 8th July 2019), p. 9822. DOI: 10.1038/s41598-019-46371-w.

[1526] David L Tabb et al. 'Repeatability and reproducibility in proteomic identifications by liquid chromatography-tandem mass spectrometry'. In: *J. Proteome Res.* 9 (2 5th Feb. 2010), pp. 761–776. DOI: 10.1021/pr9006365.

[1527] J P Simpson et al. 'The effects of demineralisation and sampling point variability on the measurement of glutamine deamidation in type I collagen extracted from bone'. In: *J. Archaeol. Sci.* 69 (C May 2016), pp. 29–38. DOI: 10.1016/j.jas.2016.02.002.

[1528] Siyuan Pang et al. 'Comparison of different protocols for demineralization of cortical bone'. In: *Sci. Rep.* 11 (1 29th Mar. 2021), p. 7012. DOI: 10.1038/s41598-021-86257-4.

[1529] J Cody Craig et al. 'A quality analysis of bony specimens for optimal ethylenediaminetetraacetic acid (EDTA) decalcification'. In: *Int. J. Surg. Pathol.* 30 (8 Dec. 2022), pp. 853–860. DOI: 10.1177/10668969221088877.

[1530] Karren S Palmer et al. 'Comparing the use of magnetic beads with ultrafiltration for ancient dental calculus proteomics'. In: *J. Proteome Res.* 20 (3 5th Mar. 2021), pp. 1689–1704. DOI: 10.1021/acs.jproteome.0c00862.

[1531] Noemi Procopio and Michael Buckley. 'Minimizing laboratory-induced decay in bone proteomics'. In: *J. Proteome Res.* 16 (2 3rd Feb. 2017), pp. 447–458. DOI: 10.1021/acs.jproteome.6b00564.

[1532] Caitlin Colleary, Nicole C Little and Timothy P Cleland. 'Microwave-assisted acid hydrolysis for whole-bone proteomics and paleoproteomics'. In: *Rapid Commun. Mass Spectrom.* 34 (2 30th Jan. 2020), e8568. DOI: 10.1002/rcm.8568.

[1533] Luise Ørsted Brandt et al. 'Palaeoproteomics identifies beaver fur in Danish high-status Viking Age burials - direct evidence of fur trade'. In: *PLoS One* 17 (7 27th July 2022), e0270040. DOI: 10.1371/journal.pone.0270040.

[1534] Caroline Solazzo and Tracy Niepold. 'A simplified sample preparation for hair and skin proteins towards the application of archaeological fur and leather'. In: *J. Proteomics* 274 (104821 15th Mar. 2023), p. 104821. DOI: 10.1016/j.jprot.2023.104821.

[1535] Jannie Amsgaard Ebsen et al. 'Identifying archaeological leather – discussing the potential of grain pattern analysis and zooarchaeology by mass spectrometry (ZooMS) through a case study involving medieval shoe parts from Denmark'. In: *J. Cult. Herit.* 39 (Sept. 2019), pp. 21–31. DOI: 10.1016/j.culher.2019.04.008.

[1536] Luise Ørsted Brandt et al. 'Human and animal skin identified by palaeoproteomics in Scythian leather objects from Ukraine'. In: *PLoS One* 18 (12 13th Dec. 2023), e0294129. DOI: 10.1371/journal.pone.0294129.

[1537] Katerina Danko et al. 'Detergent-assisted protein digestion-on the way to avoid the key bottleneck of shotgun bottom-up proteomics'. In: *Int. J. Mol. Sci.* 23 (22 11th Nov. 2022), p. 13903. DOI: 10.3390/ijms232213903.

[1538] Suttipong Suttapitugsakul et al. 'Evaluation and optimization of reduction and alkylation methods to maximize peptide identification with MS-based proteomics'. In: *Mol. Biosyst.* 13 (12 21st Nov. 2017), pp. 2574–2582. DOI: 10.1039/c7mb00393e.

[1539] Elien Vandermarliere, Michael Mueller and Lennart Martens. 'Getting intimate with trypsin, the leading protease in proteomics'. In: *Mass Spectrom. Rev.* 32 (6 Nov. 2013), pp. 453–465. DOI: 10.1002/mas.21376.

[1540] Jesse Rodriguez et al. 'Does trypsin cut before proline?' In: *J. Proteome Res.* 7 (1 Jan. 2008), pp. 300–305. DOI: 10.1021/pr0705035.

[1541] M Shahid Mansuri et al. 'Optimal conditions for carrying out trypsin digestions on complex proteomes: From bulk samples to single cells'. In: *J. Proteomics* 297 (105109 15th Apr. 2024), p. 105109. DOI: 10.1016/j.jprot.2024.105109.

[1542] Louise Le Meillour et al. 'Increasing sustainability in palaeoproteomics by optimizing digestion times for large-scale archaeological bone analyses'. In: *iScience* 27 (4 19th Apr. 2024), p. 109432. DOI: 10.1016/j.isci.2024.109432.

[1543] Timothy P Cleland et al. 'SPEED-E: A modified version of the sample preparation by Easy extraction and Digestion(-free) protocol for enamel-based sex estimation in archaeological remains'. In: *J. Archaeol. Sci.* 168 (106006 Aug. 2024), p. 106006. DOI: 10.1016/j.jas.2024.106006.

[1544] Alberto J Taurozzi et al. 'Deep-time phylogenetic inference by paleoproteomic analysis of dental enamel'. In: *Nat. Protoc.* 19 (7 26th July 2024), pp. 2085–2116. DOI: 10.1038/s41596-024-00975-3.

[1545] Juri Rappsilber, Yasushi Ishihama and Matthias Mann. 'Stop and go extraction tips for matrix-assisted laser desorption/ionization, nanoelectrospray, and LC/MS sample pretreatment in proteomics'. In: *Anal. Chem.* 75 (3 1st Feb. 2003), pp. 663–670. DOI: 10.1021/ac026117i.

[1546] Yasushi Ishihama, Juri Rappsilber and Matthias Mann. 'Modular stop and go extraction tips with stacked disks for parallel and multidimensional Peptide fractionation in proteomics'. In: *J. Proteome Res.* 5 (4 Apr. 2006), pp. 988–994. DOI: 10.1021/pr050385q.

[1547] Wendong Chen et al. 'Simple and integrated spintip-based technology applied for deep proteome profiling'. In: *Anal. Chem.* 88 (9 3rd May 2016), pp. 4864–4871. DOI: 10.1021/acs.analchem.6b00631.

[1548] Yu-Ching Liu, Yu-Ting Huang and Chao-Jung Chen. 'Development of a high-pH reversed-phase well plate for peptide fractionation and deep proteome analysis of cells and exosomes'. In: *Anal. Bioanal. Chem.* 414 (7 31st Mar. 2022), pp. 2513–2522. DOI: 10.1007/s00216-022-03892-0.

[1549] Christopher S Hughes et al. 'Single-pot, solid-phase-enhanced sample preparation for proteomics experiments'. In: *Nat. Protoc.* 14 (1 Jan. 2019), pp. 68–85. DOI: 10.1038/s41596-018-0082-x.

[1550] Harvey E Johnston et al. 'Solvent precipitation SP3 (SP4) enhances recovery for proteomics sample preparation without magnetic beads'. In: *Anal. Chem.* 94 (29 26th July 2022), pp. 10320–10328. DOI: 10.1021/acs.analchem.1c04200.

[1551] Albena Mihailova, Elsa Lundanes and Tyge Greibrokk. 'Determination and removal of impurities in 2-D LC-MS of peptides'. In: *J. Sep. Sci.* 29 (4 Mar. 2006), pp. 576–581. DOI: 10.1002/jssc.200500496.

[1552] Linhui Zhai et al. 'Systematic research on the pretreatment of peptides for quantitative proteomics using a C microcolumn'. In: *Proteomics* 13 (15 Aug. 2013), pp. 2229–2237. DOI: 10.1002/pmic.201200591.

[1553] Kosuke Ogata and Yasushi Ishihama. 'CoolTip: Low-temperature solid-phase extraction microcolumn for capturing hydrophilic peptides and phosphopeptides'. In: *Mol. Cell. Proteomics* 20 (100170 3rd Nov. 2021), p. 100170. DOI: 10.1016/j.mcpro.2021.100170.

[1554] Mark E Jennings 2nd et al. 'Total retention liquid chromatography-mass spectrometry to achieve maximum protein sequence coverage'. In: *Anal. Chem.* 93 (12 30th Mar. 2021), pp. 5054–5060. DOI: 10.1021/acs.analchem.0c04292.

[1555] Anca-Narcisa Neagu et al. 'Applications of tandem Mass Spectrometry (MS/MS) in protein analysis for biomedical research'. In: *Molecules* 27 (8 8th Apr. 2022), p. 2411. DOI: 10.3390/molecules27082411.

[1556] Bruno Domon and Ruedi Aebersold. 'Mass spectrometry and protein analysis'. In: *Science* 312 (5771 14th Apr. 2006), pp. 212–217. DOI: 10.1126/science.1124619.

[1557] Ludovic C Gillet et al. 'Targeted data extraction of the MS/MS spectra generated by data-independent acquisition: a new concept for consistent and accurate proteome analysis'. In: *Mol. Cell. Proteomics* 11 (6 June 2012), O111.016717. DOI: 10.1074/mcp.O111.016717.

[1558] Matthew J Rardin et al. 'MS1 peptide ion intensity chromatograms in MS2 (SWATH) data independent acquisitions. Improving post acquisition analysis of proteomic experiments'. In: *Mol. Cell. Proteomics* 14 (9 Sept. 2015), pp. 2405–2419. DOI: 10.1074/mcp.O115.048181.

[1559] Akhilesh Kumar Kuril. 'Navigating mass spectrometry: A comprehensive guide to basic concepts and techniques'. In: *SSRN Electron. J.* (8th Feb. 2024). DOI: 10.2139/ssrn.4879107.

[1560] Mahmud Hossain. 'The mass spectrometer and its components'. In: *Selected Reaction Monitoring Mass Spectrometry (SRM-MS) in Proteomics*. Cham: Springer International Publishing, 2020, pp. 17–52. DOI: 10.1007/978-3-030-53433-2_2.

[1561] Juraj Lenčo et al. 'Reversed-phase liquid chromatography of peptides for bottom-up proteomics: A tutorial'. In: *J. Proteome Res.* 21 (12 2nd Dec. 2022), pp. 2846–2892. DOI: 10.1021/acs.jproteome.2c00407.

[1562] Nobuo Tanaka et al. 'Stationary phase effects in reversed-phase liquid chromatography'. In: *J. Chromatogr. A* 656 (1-2 17th Dec. 1993), pp. 265–287. DOI: 10.1016/0021-9673(93)80805-i.

[1563] Jake L Rafferty, J Ilja Siepmann and Mark R Schure. 'Mobile phase effects in reversed-phase liquid chromatography: a comparison of acetonitrile/water and methanol/water solvents as studied by molecular simulation'. In: *J. Chromatogr. A* 1218 (16 22nd Apr. 2011), pp. 2203–2213. DOI: 10.1016/j.chroma.2011.02.012.

[1564] Andreas Steinhoff, Alexandra Höltzel and Ulrich Tallarek. 'Mobile-phase contributions to analyte retention and selectivity in reversed-phase liquid chromatography: 1. General effects'. In: *J. Phys. Chem. B* 129 (25 26th June 2025), pp. 6385–6400. DOI: 10.1021/acs.jpcb.5c01695.

[1565] Pablo M Scrosati and Lars Konermann. 'Atomistic details of peptide reversed-phase liquid chromatography from molecular dynamics simulations'. In: *Anal. Chem.* 95 (7 21st Feb. 2023), pp. 3892–3900. DOI: 10.1021/acs.analchem.2c05667.

[1566] Gurpur Rakesh D Prabhu et al. 'Mass spectrometry using electrospray ionization'. In: *Nat. Rev. Methods Primers* 3 (1 23rd Mar. 2023), p. 23. DOI: 10.1038/s43586-023-00203-4.

[1567] Elnaz Aliyari and Lars Konermann. 'Formation of gaseous peptide ions from electrospray droplets: Competition between the ion evaporation mechanism and charged residue mechanism'. In: *Anal. Chem.* 94 (21 31st May 2022), pp. 7713–7721. DOI: 10.1021/acs.analchem.2c01355.

[1568] J A Loo et al. 'Multiply charged negative ions by electrospray ionization of polypeptides and proteins'. In: *Anal. Chem.* 64 (1 1st Jan. 1992), pp. 81–88. DOI: 10.1021/ac00025a015.

[1569] A T Iavarone, J C Jurchen and E R Williams. 'Supercharged protein and peptide ions formed by electrospray ionization'. In: *Anal. Chem.* 73 (7 1st Apr. 2001), pp. 1455–1460. DOI: 10.1021/ac001251t.

[1570] Lars Konermann et al. 'Unraveling the mechanism of electrospray ionization'. In: *Anal. Chem.* 85 (1 2nd Jan. 2013), pp. 2–9. DOI: 10.1021/ac302789c.

[1571] Xin Ma. 'Recent advances in mass spectrometry-based structural elucidation techniques'. In: *Molecules* 27 (19 30th Sept. 2022), p. 6466. DOI: 10.3390/molecules27196466.

[1572] Deyber Arley Vargas Medina et al. 'The overshadowed role of electron ionization-mass spectrometry in analytical biotechnology'. In: *Curr. Opin. Biotechnol.* 82 (102965 1st Aug. 2023), p. 102965. DOI: 10.1016/j.copbio.2023.102965.

[1573] Graeme C McAlister et al. 'Analysis of the acidic proteome with negative electron-transfer dissociation mass spectrometry'. In: *Anal. Chem.* 84 (6 20th Mar. 2012), pp. 2875–2882. DOI: 10.1021/ac203430u.

[1574] Marija Nišavić et al. 'High-efficiency microflow and nanoflow negative electrospray ionization of peptides induced by gas-phase proton transfer reactions'. In: *Anal. Chem.* 89 (9 2nd May 2017), pp. 4847–4854. DOI: 10.1021/acs.analchem.6b04466.

[1575] Pelayo A Penanes et al. 'Potential of negative-ion-mode proteomics: An MS1-only approach'. In: *J. Proteome Res.* 22 (8 4th Aug. 2023), pp. 2734–2742. DOI: 10.1021/acs.jproteome.3c00307.

[1576] Anthony M Haag. 'Mass analyzers and mass spectrometers'. In: *Adv. Exp. Med. Biol.* 919 (2016), pp. 157–169. DOI: 10.1007/978-3-319-41448-5_7.

[1577] Sabitha Vadakedath et al. 'The principle, types, and applications of mass spectrometry: A comprehensive review'. In: *Biomed. Biotechnol.* 7 (1 22nd Oct. 2022), pp. 6–22. DOI: 10.12691/bb-7-1-2.

[1578] Ting Huang et al. 'Combining precursor and fragment information for improved detection of differential abundance in data independent acquisition'. In: *Mol. Cell. Proteomics* 19 (2 Feb. 2020), pp. 421–430. DOI: 10.1074/mcp.RA119.001705.

[1579] Klemens Fröhlich et al. 'Data-independent acquisition: A milestone and prospect in clinical mass spectrometry-based proteomics'. In: *Mol. Cell. Proteomics* 23 (8 1st Aug. 2024), p. 100800. DOI: 10.1016/j.mcpro.2024.100800.

[1580] Reta Birhanu Kitata, Jhih-Ci Yang and Yu-Ju Chen. 'Advances in data-independent acquisition mass spectrometry towards comprehensive digital proteome landscape'. In: *Mass Spectrom. Rev.* 42 (6 Nov. 2023), pp. 2324–2348. DOI: 10.1002/mas.21781.

[1581] Aivett Bilbao et al. 'Processing strategies and software solutions for data-independent acquisition in mass spectrometry'. In: *Proteomics* 15 (5-6 Mar. 2015), pp. 964–980. DOI: 10.1002/pmic.201400323.

[1582] Christopher M Rose et al. 'Neutron encoded labeling for peptide identification'. In: *Anal. Chem.* 85 (10 21st May 2013), pp. 5129–5137. DOI: 10.1021/ac400476w.

[1583] Ágnes Révész et al. 'Collision energies: Optimization strategies for bottom-up proteomics'. In: *Mass Spectrom. Rev.* 42 (4 1st July 2023), pp. 1261–1299. DOI: 10.1002/mas.21763.

[1584] Leann M Mikesh et al. 'The utility of ETD mass spectrometry in proteomic analysis'. In: *Biochim. Biophys. Acta* 1764 (12 1st Dec. 2006), pp. 1811–1822. DOI: 10.1016/j.bbapap.2006.10.003.

[1585] Paul J Boersema, Shabaz Mohammed and Albert J R Heck. 'Phosphopeptide fragmentation and analysis by mass spectrometry'. In: *J. Mass Spectrom.* 44 (6 June 2009), pp. 861–878. DOI: 10.1002/jms.1599.

[1586] Clement M Potel, Simone Lemeer and Albert J R Heck. 'Phosphopeptide fragmentation and site localization by mass spectrometry: An update'. In: *Anal. Chem.* 91 (1 2nd Jan. 2019), pp. 126–141. DOI: 10.1021/acs.analchem.8b04746.

[1587] Yufeng Shen et al. 'Effectiveness of CID, HCD, and ETD with FT MS/MS for degradomic-peptidomic analysis: comparison of peptide identification methods'. In: *J. Proteome Res.* 10 (9 2nd Sept. 2011), pp. 3929–3943. DOI: 10.1021/pr200052c.

[1588] Chengjian Tu et al. 'Performance investigation of proteomic identification by HCD/CID fragmentations in combination with high/low-resolution detectors on a tribrid, high-field Orbitrap instrument'. In: *PLoS One* 11 (7 29th July 2016), e0160160. DOI: 10.1371/journal.pone.0160160.

[1589] R J Chalkley et al. 'Statistical analysis of Peptide electron transfer dissociation fragmentation mass spectrometry'. In: *Anal. Chem.* 82 (2 15th Jan. 2010), pp. 579–584. DOI: 10.1021/ac9018582.

[1590] Katalin F Medzihradszky and Robert J Chalkley. 'Lessons in de novo peptide sequencing by tandem mass spectrometry'. In: *Mass Spectrom. Rev.* 34 (1 Jan. 2015), pp. 43–63. DOI: 10.1002/mas.21406.

[1591] Ruedi Aebersold and Matthias Mann. 'Mass spectrometry-based proteomics'. In: *Nature* 422 (6928 13th Mar. 2003), pp. 198–207. DOI: 10.1038/nature01511.

[1592] Jinhong Shi and Fang-Xiang Wu. 'Protein inference by assembling peptides identified from tandem mass spectra'. In: *Curr. Bioinform.* 4 (3 1st Sept. 2009), pp. 226–233. DOI: 10.2174/157489309789071048.

[1593] Prajita Pandey. 'A systematic approach to selecting the right tool for mass spectrometry data analysis in protein and peptide bioanalysis'. In: *J. Mass Spectrom.* 61 (2 1st Feb. 2026), e70025. DOI: 10.1002/jms.70025.

[1594] Alexey I Nesvizhskii. 'Protein identification by tandem mass spectrometry and sequence database searching'. In: *Methods Mol. Biol.* 367 (2007), pp. 87–119. DOI: 10.1385/1-59745-275-0:87.

[1595] Pavel Sinitcyn, Jan Daniel Rudolph and Jürgen Cox. 'Computational methods for understanding mass spectrometry–based shotgun proteomics data'. In: *Annu. Rev. Biomed. Data Sci.* 1 (1 20th July 2018), pp. 207–234. DOI: 10.1146/annurev-biodatasci-080917-013516.

[1596] Fangfei Zhang et al. 'Data-independent acquisition mass spectrometry-based proteomics and software tools: A glimpse in 2020'. In: *Proteomics* 20 (17-18 Sept. 2020), e1900276. DOI: 10.1002/pmic.201900276.

[1597] Zainab Noor et al. 'Mass spectrometry-based protein identification in proteomics-a review'. In: *Brief. Bioinform.* 22 (2 22nd Mar. 2021), pp. 1620–1638. DOI: 10.1093/bib/bbz163.

[1598] Rune Matthiesen. 'Algorithms for database-dependent search of MS/MS data'. In: *Methods Mol. Biol.* 1007 (2013), pp. 119–138. DOI: 10.1007/978-1-62703-392-3_5.

[1599] Kenneth Verheggen et al. 'Anatomy and evolution of database search engines-a central component of mass spectrometry based proteomic workflows'. In: *Mass Spectrom. Rev.* 39 (3 May 2020), pp. 292–306. DOI: 10.1002/mas.21543.

[1600] Lindsay K Pino et al. 'Acquiring and analyzing data independent acquisition proteomics experiments without spectrum libraries'. In: *Mol. Cell. Proteomics* 19 (7 July 2020), pp. 1088–1103. DOI: 10.1074/mcp.P119.001913.

[1601] Katalin Barkovits et al. 'Reproducibility, specificity and accuracy of relative quantification using spectral library-based data-independent acquisition'. In: *Mol. Cell. Proteomics* 19 (1 1st Jan. 2020), pp. 181–197. DOI: 10.1074/mcp.RA119.001714.

[1602] Brian C Searle et al. 'Generating high quality libraries for DIA MS with empirically corrected peptide predictions'. In: *Nat. Commun.* 11 (1 25th Mar. 2020), p. 1548. DOI: 10.1038/s41467-020-15346-1.

[1603] Lilian R Heil et al. 'Building spectral libraries from narrow-window data-independent acquisition mass spectrometry data'. In: *J. Proteome Res.* 21 (6 3rd June 2022), pp. 1382–1391. DOI: 10.1021/acs.jproteome.1c00895.

[1604] Bo Wen et al. 'Deep learning in proteomics'. In: *Proteomics* 20 (21-22 1st Nov. 2020), e1900335. DOI: 10.1002/pmic.201900335.

[1605] Jesse G Meyer. 'Deep learning neural network tools for proteomics'. In: *Cell Rep. Methods* 1 (2 21st June 2021), p. 100003. DOI: 10.1016/j.crmeth.2021.100003.

[1606] Wout Bittremieux et al. 'Deep learning methods for DE Novo peptide sequencing'. In: *Mass Spectrom. Rev.* 45 (3 1st May 2026), pp. 507–526. DOI: 10.1002/mas.21919.

[1607] Lidong He, Chad R Weisbrod and Alan G Marshall. 'Protein de novo sequencing by top-down and middle-down MS/MS: Limitations imposed by mass measurement accuracy and gaps in sequence coverage'. In: *Int. J. Mass Spectrom.* 427 (1st Apr. 2018), pp. 107–113. DOI: 10.1016/j.ijms.2017.11.012.

[1608] Kevin McDonnell, Enda Howley and Florence Abram. 'The impact of noise and missing fragmentation cleavages on de novo peptide identification algorithms'. In: *Comput. Struct. Biotechnol. J.* 20 (19th Mar. 2022), pp. 1402–1412. DOI: 10.1016/j.csbj.2022.03.008.

[1609] Thilo Muth and Bernhard Y Renard. 'Evaluating de novo sequencing in proteomics: already an accurate alternative to database-driven peptide identification?' In: *Brief. Bioinform.* 19 (5 28th Sept. 2018), pp. 954–970. DOI: 10.1093/bib/bbx033.

[1610] Tim Van Den Bossche et al. 'Metaproteomics beyond databases: Addressing the challenges and potentials of DE Novo sequencing'. In: *Proteomics* 25 (17-18 1st Sept. 2025), pp. 51–61. DOI: 10.1002/pmic.202400321.

[1611] Korrawe Karunratanakul et al. 'Uncovering thousands of new peptides with sequence-mask-search hybrid DE Novo peptide sequencing framework'. In: *Mol. Cell. Proteomics* 18 (12 Dec. 2019), pp. 2478–2491. DOI: 10.1074/mcp.TIR119.001656.

[1612] Shiva Ebrahimi and Xuan Guo. 'Transformer-based de novo peptide sequencing for data-independent acquisition mass spectrometry'. In: *Proc. IEEE Int. Symp. Bioinformatics Bioeng.* 2023 (Dec. 2023), pp. 28–35. DOI: 10.1109/bibe60311.2023.00013.

[1613] Ronghui Lou and Wenqing Shui. 'Acquisition and analysis of DIA-based proteomic data: A comprehensive survey in 2023'. In: *Mol. Cell. Proteomics* 23 (2 1st Feb. 2024), p. 100712. DOI: 10.1016/j.mcpro.2024.100712.

[1614] Chih-Chiang Tsou et al. 'DIA-Umpire: comprehensive computational framework for data-independent acquisition proteomics'. In: *Nat. Methods* 12 (3 Mar. 2015), 258–64, 7 p following 264. DOI: 10.1038/nmeth.3255.

[1615] Ngoc Hieu Tran et al. 'Deep learning enables de novo peptide sequencing from data-independent-acquisition mass spectrometry'. In: *Nat. Methods* 16 (1 Jan. 2019), pp. 63–66. DOI: 10.1038/s41592-018-0260-3.

[1616] Mostafa Kalhor et al. 'Rescoring peptide spectrum matches: Boosting proteomics performance by integrating peptide property predictors into peptide identification'. In: *Mol. Cell. Proteomics* 23 (7 1st July 2024), p. 100798. DOI: 10.1016/j.mcpro.2024.100798.

[1617] Sven Degroeve and Lennart Martens. 'MS2PIP: a tool for MS/MS peak intensity prediction'. In: *Bioinformatics* 29 (24 15th Dec. 2013), pp. 3199–3203. DOI: 10.1093/bioinformatics/btt544.

[1618] Siegfried Gessulat et al. 'Prosit: proteome-wide prediction of peptide tandem mass spectra by deep learning'. In: *Nat. Methods* 16 (6 27th June 2019), pp. 509–518. DOI: 10.1038/s41592-019-0426-7.

[1619] Mostafa Kalhor et al. 'Prosit-XL: enhanced cross-linked peptide identification by fragment intensity prediction to study protein interactions and structures'. In: *Nat. Commun.* 16 (1 1st July 2025), p. 5429. DOI: 10.1038/s41467-025-61203-4.

[1620] Brian A Risk, Nathan J Edwards and Morgan C Giddings. 'A peptide-spectrum scoring system based on ion alignment, intensity, and pair probabilities'. In: *J. Proteome Res.* 12 (9 6th Sept. 2013), pp. 4240–4247. DOI: 10.1021/pr400286p.

[1621] Jürgen Cox et al. 'Andromeda: a peptide search engine integrated into the MaxQuant environment'. In: *J. Proteome Res.* 10 (4 1st Apr. 2011), pp. 1794–1805. DOI: 10.1021/pr101065j.

[1622] David L Tabb, Christopher G Fernando and Matthew C Chambers. 'MyriMatch: highly accurate tandem mass spectral peptide identification by multivariate hypergeometric analysis'. In: *J. Proteome Res.* 6 (2 18th Feb. 2007), pp. 654–661. DOI: 10.1021/pr0604054.

[1623] Varun Ananth et al. 'A learned score function improves the power of mass spectrometry database search'. In: *Bioinformatics* 40 (Suppl 1 28th June 2024), pp. i410–i417. DOI: 10.1093/bioinformatics/btae218.

[1624] Yonghan Yu and Ming Li. 'Towards highly sensitive deep learning-based end-to-end database search for tandem mass spectrometry'. In: *Nat. Mach. Intell.* 7 (1 6th Jan. 2025), pp. 85–95. DOI: 10.1038/s42256-024-00960-1.

[1625] Joshua E Elias and Steven P Gygi. 'Target-decoy search strategy for increased confidence in large-scale protein identifications by mass spectrometry'. In: *Nat. Methods* 4 (3 Mar. 2007), pp. 207–214. DOI: 10.1038/nmeth1019.

[1626] Mikhail M Savitski et al. 'A scalable approach for protein false discovery rate estimation in large proteomic data sets'. In: *Mol. Cell. Proteomics* 14 (9 Sept. 2015), pp. 2394–2404. DOI: 10.1074/mcp.M114.046995.

[1627] Guanghui Wang et al. 'Decoy methods for assessing false positives and false discovery rates in shotgun proteomics'. In: *Anal. Chem.* 81 (1 1st Jan. 2009), pp. 146–159. DOI: 10.1021/ac801664q.

[1628] Sangjeong Lee, Heejin Park and Hyunwoo Kim. 'Comparison of false-discovery rates of various decoy databases'. In: *Proteome Sci.* 19 (1 18th Sept. 2021), p. 11. DOI: 10.1186/s12953-021-00179-7.

[1629] Suruchi Aggarwal et al. 'False discovery rate: the Achilles' heel of proteogenomics'. In: *Brief. Bioinform.* 23 (5 20th Sept. 2022), bbac163. DOI: 10.1093/bib/bbac163.

[1630] Yang Xie, Wei Pan and Arkady B Khodursky. 'A note on using permutation-based false discovery rate estimates to compare different analysis methods for microarray data'. In: *Bioinformatics* 21 (23 1st Dec. 2005), pp. 4280–4288. DOI: 10.1093/bioinformatics/bti685.

[1631] Robert J Chalkley. 'When target-decoy false discovery rate estimations are inaccurate and how to spot instances'. In: *J. Proteome Res.* 12 (2 1st Feb. 2013), pp. 1062–1064. DOI: 10.1021/pr301063v.

[1632] Andy Lin et al. 'Improving peptide-level mass spectrometry analysis via double competition'. In: *J. Proteome Res.* 21 (10 7th Oct. 2022), pp. 2412–2420. DOI: 10.1021/acs.jproteome.2c00282.

[1633] Xinpei Yi, Fuzhou Gong and Yan Fu. 'Transfer posterior error probability estimation for peptide identification'. In: *BMC Bioinformatics* 21 (1 4th May 2020), p. 173. DOI: 10.1186/s12859-020-3485-y.

[1634] Lukas Käll et al. 'Posterior error probabilities and false discovery rates: two sides of the same coin'. In: *J. Proteome Res.* 7 (1 Jan. 2008), pp. 40–44. DOI: 10.1021/pr700739d.

[1635] Thomas Burger. 'Gentle introduction to the statistical foundations of false discovery rate in quantitative proteomics'. In: *J. Proteome Res.* 17 (1 5th Jan. 2018), pp. 12–22. DOI: 10.1021/acs.jproteome.7b00170.

[1636] Zhibin Ning et al. 'Peptide-centric approaches provide an alternative perspective to re-examine quantitative proteomic data'. In: *Anal. Chem.* 88 (4 16th Feb. 2016), pp. 1973–1978. DOI: 10.1021/acs.analchem.5b04148.

[1637] Alexey I Nesvizhskii et al. 'A statistical model for identifying proteins by tandem mass spectrometry'. In: *Anal. Chem.* 75 (17 1st Sept. 2003), pp. 4646–4658. DOI: 10.1021/ac0341261.

[1638] Alexey I Nesvizhskii and Ruedi Aebersold. 'Interpretation of shotgun proteomic data: the protein inference problem: The protein inference problem'. In: *Mol. Cell. Proteomics* 4 (10 1st Oct. 2005), pp. 1419–1440. DOI: 10.1074/mcp.R500012-MCP200.

[1639] Yupeng Zhao and Yen-Han Lin. 'Whole-cell protein identification using the concept of unique peptides'. In: *Genomics Proteomics Bioinformatics* 8 (1 Mar. 2010), pp. 33–41. DOI: 10.1016/S1672-0229(10)60004-6.

[1640] Roger Higdon and Eugene Kolker. 'A predictive model for identifying proteins by a single peptide match'. In: *Bioinformatics* 23 (3 1st Feb. 2007), pp. 277–280. DOI: 10.1093/bioinformatics/btl595.

[1641] Nitin Gupta and Pavel A Pevzner. 'False discovery rates of protein identifications: a strike against the two-peptide rule'. In: *J. Proteome Res.* 8 (9 Sept. 2009), pp. 4173–4181. DOI: 10.1021/pr9004794.

[1642] Fanni Bugyi et al. 'Influence of post-translational modifications on protein identification in database searches'. In: *ACS Omega* 6 (11 23rd Mar. 2021), pp. 7469–7477. DOI: 10.1021/acsomega.0c05997.

[1643] J Svozil and K Baerenfaller. 'A cautionary tale on the inclusion of variable posttranslational modifications in database-dependent searches of mass spectrometry data'. In: *Methods Enzymol.* Methods in enzymology 586 (10th Jan. 2017), pp. 433–452. DOI: 10.1016/bs.mie.2016.11.007.

[1644] Timothy P Cleland, Elena R Schroeter and Mary H Schweitzer. 'Biologically and diagenetically derived peptide modifications in moa collagens'. In: *Proc. Biol. Sci.* 282 (1808 7th June 2015), p. 20150015. DOI: 10.1098/rspb.2015.0015.

[1645] Miranda Evans. 'The Demodifier: A tool for screening modification-induced alternate peptide taxonomy in palaeoproteomics'. In: *PLoS One* 21 (1 12th Jan. 2026), e0339465. DOI: 10.1371/journal.pone.0339465.

[1646] Andy T Kong et al. 'MSFragger: ultrafast and comprehensive peptide identification in mass spectrometry-based proteomics'. In: *Nat. Methods* 14 (5 May 2017), pp. 513–520. DOI: 10.1038/nmeth.4256.

[1647] Zhiwu An et al. 'PTMiner: Localization and quality control of protein modifications detected in an open search and its application to comprehensive post-translational modification characterization in human proteome'. In: *Mol. Cell. Proteomics* 18 (2 Feb. 2019), pp. 391–405. DOI: 10.1074/mcp.RA118.000812.

[1648] Dmitry M Avtonomov, Andy Kong and Alexey I Nesvizhskii. 'DeltaMass: Automated detection and visualization of mass shifts in proteomic Open-search results'. In: *J. Proteome Res.* 18 (2 1st Feb. 2019), pp. 715–720. DOI: 10.1021/acs.jproteome.8b00728.

[1649] Daniel J Geiszler et al. 'PTM-Shepherd: analysis and summarization of post-translational and chemical modifications from open search results'. In: *Mol. Cell. Proteomics* 20 (100018 1st Dec. 2020), p. 100018. DOI: 10.1074/mcp.TIR120.002216.

[1650] Jürgen Cox and Matthias Mann. 'MaxQuant enables high peptide identification rates, individualized p.p.b.-range mass accuracies and proteome-wide protein quantification'. In: *Nat. Biotechnol.* 26 (12 Dec. 2008), pp. 1367–1372. DOI: 10.1038/nbt.1511.

[1651] Sam van Puyenbroeck et al. 'Limitations of *de novo* sequencing in resolving sequence ambiguity'. In: *bioRxiv* (23rd Aug. 2025), p. 2025.08.19.671052. DOI: 10.1101/2025.08.19.671052.

# 2

# Human Brains Preserve in Diverse Environments for at least 12,000 Years

Morton-Hayward, A.L., Anderson, R.P., Saupe, E.E., Larson G., & Cosmidis J.G.
*Human Brains Preserve in Diverse Environments for at least 12,000 Years.*
**Proc. Biol. Sci. 2024**, *291*(2019): 20232606.
doi.org/10.1098/rspb.2023.2606

## 2.1 Author Contributions

**Table 2.1** | Summary of individual contributions to this chapter, described using the Contributor Roles Taxonomy (CRediT) system [1].

| Author | Contribution |
|---|---|
| *Morton-Hayward, A.L.* | Study conception; Methodology; Computation; Formal analysis; Investigation: data/evidence collection; Resources; Data curation; Manuscript preparation: writing the initial draft; Manuscript preparation: critical review, commentary and revision; Manuscript preparation: visualisation/data presentation; Project administration; Funding acquisition. |
| *Anderson, R.P.* | Manuscript preparation: critical review, commentary and revision. |
| *Saupe, E.E.* | Computation; Resources; Manuscript preparation: critical review, commentary and revision; Supervision. |
| *Larson, G.* | Manuscript preparation: critical review, commentary and revision; Supervision. |
| *Cosmidis, J.G.* | Manuscript preparation: critical review, commentary and revision. |

## 2.2 Abstract

The brain is thought to be amongst the first human organs to decompose after death. The discovery of brains preserved in the archaeological record is therefore regarded

as unusual. Although mechanisms such as dehydration, freezing, saponification, and tanning are known to allow for the preservation of the brain on short timescales in association with other soft tissues ($\lesssim 4,000$ years), discoveries of older brains, especially in the absence of other soft tissues, are rare. Here, we collated an archive of $> 4,400$ human brains preserved in the archaeological record across $\sim 12,000$ years, $> 1,300$ of which constitute the only soft tissue preserved amongst otherwise skeletonised remains. We found that brains of this type persist on timescales exceeding those preserved by other means, which suggests an unknown mechanism may be responsible for preservation particular to the central nervous system. The untapped archive of preserved ancient brains represents an opportunity for bioarchaeological studies of human evolution, health, and disease.

## 2.3 Background

Since the mid-17$^{\text{th}}$ C., more than 4,400 human brains have been unearthed from the last 12,000 years of the archaeological record, over 1,300 of which are preserved amongst otherwise skeletonised remains. Despite this volume of finds, the perception remains that preserved brains represent 'unique' or 'extremely rare' discoveries [2]. Human soft tissues are understood to persist through time by well characterised mechanisms of preservation such as dehydration, freezing, and tanning, brought about by anthropogenic (i.e., the result of deliberate human intervention) or naturally occurring factors. Thus, it is not surprising that the brain endures alongside other internal organs where there is extensive soft-tissue preservation. Brains are found in the desiccated remains of desert burials [3], the frozen corpses of mountain passes [4], and the tanned bog bodies of low-lying wetlands [5]. However, the preservation of brains in the absence of other soft tissues – for example, amongst ancient human bones dredged from a swampy pond [6] – is unexpected, poorly reported, and represents an untapped source of bioarchaeological information.

Despite the prospective palaeobiological applications, no comprehensive or systematic effort has been made to collectively investigate preserved brains for factors that might explain why this organ persists when other soft tissues do

**Box 2.1 | *Early reports of brains in the absence of other soft tissues***

Almost three hundred years ago the lone preservation of the brain was discussed in some detail by the 18th-C. physician Thouret (AD 1749–1810), who reported brains exhumed from the putrid, overfull cemetery at Église des Saints-Innocents, Paris, France [8]. Having found the same phenomenon at different sites [9], and noting fellow academics who had shared these observations [10], he described the preserved nervous tissues in disparate conditions of deterioration. Some brains were 'soft, pulpy and pliable', others 'firmer, more solid', shrunken to varying degrees and discoloured, but nonetheless possessing visible surface convolutions with identifiable sulci and gyri [9]. The curious, persistent material ('*indestructibles*' [9]) of which they were composed so intrigued Thouret's colleague, Fourcroy (AD 1755–1809), that he embarked on a lifetime's study of the human brain and so birthed the modern discipline of neurochemistry [11–13].

> *I have observed that even where all other viscera had entirely decomposed, the brain still remained almost in its entirety... This of all the viscera was the organ one would least expect to find preserved long after death... [yet] by such a singular prerogative among all other parts of the body, the brain enjoys the ability of preserving itself long-term, in the midst of destruction, and even in the depths of the earth.* [9]

A century prior, however, Père Théophile Raynaud (AD 1587–1663) described dozens of brains preserved amongst otherwise skeletonised remains, and his *De Incorruptione Cadaverum* (1651) appears to be the earliest extant published report on the phenomenon [14]. For instance, a 'perfectly intact and sound' brain, freed from the split skull thirteen years after burial 'while the rest of the body had turned to ashes', so shocked Francisco Vallés (AD 1524–1592), the pre-eminent physician of Renaissance Spain, that he denied such a thing could have happened without a miracle [14]. Relatedly, Raynaud describes the disinterred remains of Saint Hedwig of Silesia (AD 1174–1243), who had died some four hundred years prior: 'when the bones of the sacred body were lifted up, after the flesh had been consumed... [the brain of this] most holy woman... [was believed to have been] miraculously preserved by divine power' [14]. However, the author also notes the persistence of the brain 'after many years... [in the bodies] of those who had escaped from harlotry' in a cemetery in Avignon, France. In fact, the French theologian recognised that – saint or sinner – the brain had the potential to preserve long after death 'uncorrupted, and free from decay' [14].

not. At the dawn of the 20th C., anatomist and Egyptologist Elliot Smith (AD 1871–1937) derided the 'scanty literature' on preserved brains, arguing that 'almost every archaeologist who has excavated... is aware of the fact that the brain is preserved in the crania of a very large proportion' of human remains disinterred [7] (Box 2.1). To test the long-held hypothesis that human brain preservation is a rare phenomenon, we compiled an archive of preserved human brains in the archaeological record. We statistically analysed this body of data to establish their prevalence, persistence, and the diversity of preservation types; described the nature of differentially preserved nervous tissues; and quantified their global and temporal distribution. We then discuss the value of leveraging preserved human brains for studies of palaeopathology and archaeogenetics.

## 2.4 Results

We identified a total of 4,405 preserved human brains from 213 unique sources, which were reported from every world region except Antarctica (Figure 2.1a; Appendix A.2). These brains are universally described as discoloured and shrunken (i.e., reduced in volume compared to the brains of living humans), albeit with reported variations in their degree of discolouration and shrinkage. For example, more than 500 brains from a Pre-dynastic cemetery in Upper Egypt ($\sim 6,150$ years Before Present [y BP]) were 'as much as two-thirds of the original length of the brain, or they may have shrunk to less than half the length' [7]. We identified five types of brain preservation (Figure 2.2), of which dehydration, freezing, saponification, and tanning are well characterised modes of soft-tissue preservation in human remains [15]. However, there may be overlap between preservation mechanisms, given the complexity of decomposition as a system of interrelated biogeochemical processes [16], and the subjective nature of reporting in some cases. For example, brains exposed to a combination of low temperatures, low humidity, and circulating air currents (e.g., those found at high altitude) might be more accurately described as 'freeze-dried' than 'frozen' or 'dehydrated'.

We have also designated a fifth mechanism, which does not appear to have been codified in the literature on brain preservation, as 'unknown'. Almost one-third of reported brains (30.1%, $n = 1,328$) exhibit this fifth mode of preservation. A variety of depositional contexts are described; including tombs [17], burial mounds [18], shipwrecks [19], wooden [2] and lead [20] coffins, shallow [19] and mass [21] graves, fragmentary remains [22] and severed heads [23]. Although the presence of clay and iron are commonly noted in the sedimentary matrix (30.0%, $n = 20/69$ sites), their abundance is not quantified. Brains of this unknown type almost exclusively (98.5%, $n = 1,308/1,328$) constitute the only soft tissue preserved amongst otherwise skeletonised remains, which suggests there may be a preservation mechanism particular to the CNS.

The frequency of preserved human brains (Figure 2.1b) through the Holocene Epoch (the last $\sim$ 12,000 y BP) reveals a general trend of decreasing frequency

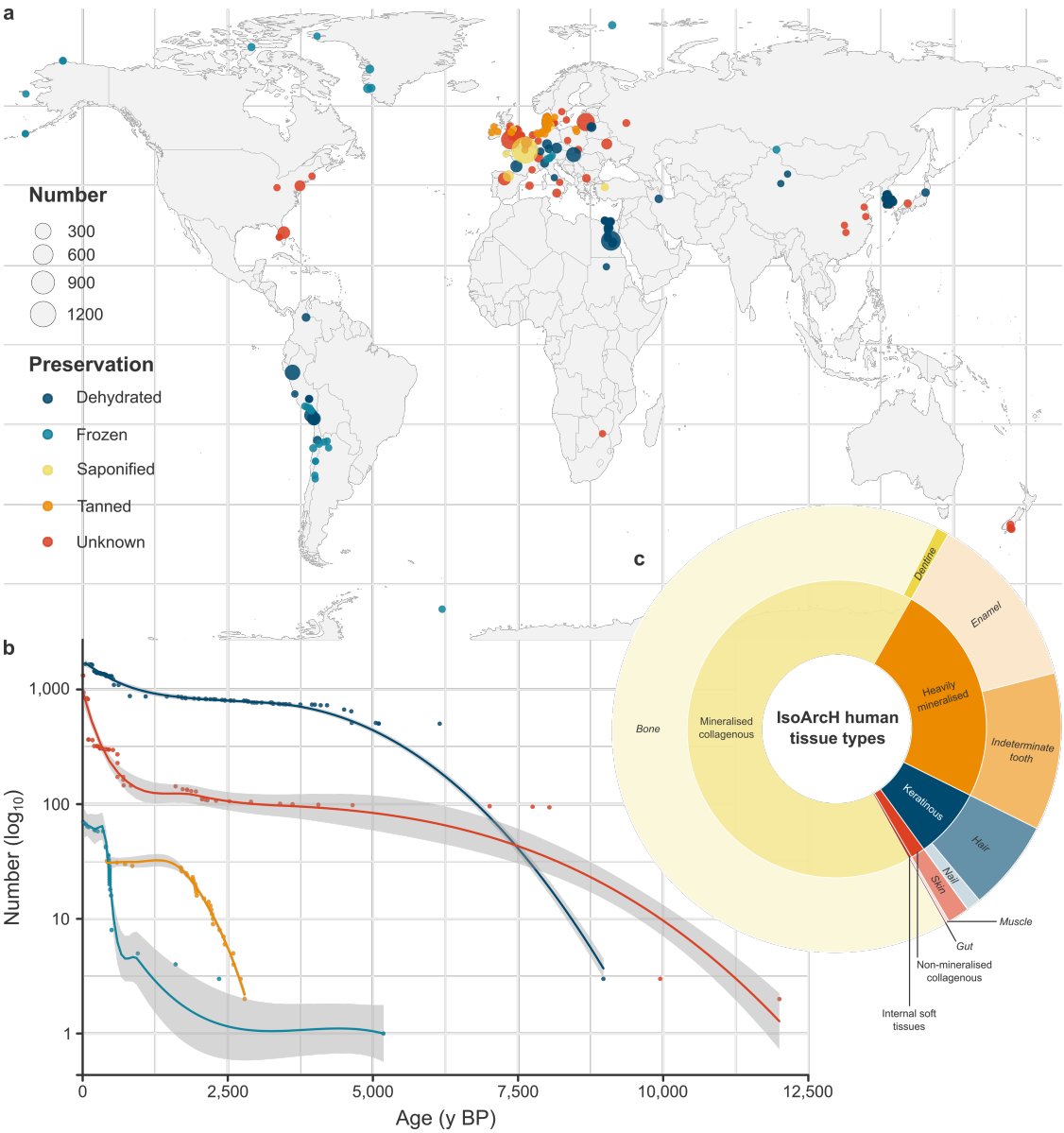



**Figure 2.1 | Distribution and frequency of preserved human brains by type, compared with soft tissues in the IsoArcH repository. (a)** Global distribution of preserved human brains by type: dehydrated (37.8%, $n = 1,667$), frozen (1.6%, $n = 70$), saponified (29.7%, $n = 1,308$), tanned (0.7%, $n = 32$), and unknown (30.1%, $n = 1,328$). Circles represent archaeological sites, and their diameter reflects the sample size of brains at each site. **(b)** Number of preserved human brains through time by type (note the log-scale $y$-axis). Locally estimated scatterplot smoothing (LOESS) shows conditional means with 95% confidence intervals (CIs). The saponified type is not shown, given insufficient data points ($n = 7$) for LOESS regression. **(c)** 10 types of human remains ($n = 13,407$) in the IsoArcH repository [24]. Mineralised collagenous (i.e., bone [$n = 8,762$] and dentine [$n = 125$]) tissues represent the bulk of the database at 66.3% of total samples ($n = 8,887/13,407$), followed by heavily-mineralised (i.e., tooth of indeterminate subtype [$n = 1,720$] and enamel [$n = 1,527$]) and keratinous (i.e., hair [$n = 879$], nail [$n = 138$] and beard [$n = 4$]) tissues at 24.2% ($n = 3,247/13,407$) and 7.6% ($n = 1,021/13,407$), respectively. Non-mineralised collagenous (i.e., skin [$n = 209$]) and internal soft tissues (i.e., muscle [$n = 34$] and gut [$n = 9$]) together comprise a small fraction of the database at 1.9% ($n = 252/13,407$).

with increasing archaeological age (i.e., PMI). The numbers of frozen and tanned brains decrease more rapidly after $\sim$ 500 and 1,500 y BP, respectively, while the number of dehydrated brains declines more slowly over a longer period, $\sim$ 4,000 y BP. Saponified brains ($n = 1,308$) are reported from just seven archaeological sites, comprising too few data points to meaningfully plot a distribution. By contrast, brains of the unknown preservation type are known to persist beyond 12,000 y BP [e.g., 25] (Supplementary Data S1).

To evaluate the abundance of preserved human brains relative to other bioarchaeological remains, we compared their occurrence with that of preserved human soft tissues reported in searchable databases. Internal soft tissues (representing muscle and gut only) comprise just 0.3% ($n = 43/13,407$) of human bioarchaeological samples in the IsoArcH repository [24] (Figure 2.1c), which documents more than 400 archaeological sites across Europe and the Middle East from the Mesolithic ($\sim$ 9,000 y BP) to the 20$^{\text{th}}$ C. AD. By contrast, the number of preserved brains identified in the literature during the same time period is markedly higher ($n = 3,862$), and far exceeds the number of heavily mineralised tissues represented in the repository (e.g., teeth [$n = 1,720$], which have a high preservation potential given their inorganic mineral content and number of anatomical elements). Other archaeological databases (e.g., ARIADNE, ADS) contained no records of soft tissues. Similarly, only a minority of sources that describe the preservation of nervous tissues (6.5%, $n = 18/277$) report the frequency with which these were recovered (i.e., the number of brains preserved as a measure of individuals excavated): although the average is approximately one in three (35.7%), there is considerable variation (2.5–100.0%).

Using Kruskal–Wallis rank sum tests with *post hoc* Dunn pairwise comparisons (Holm-adjusted), we identified statistically significant differences in terms of archaeological age ($\chi^2[4] = 24.86$, $p = 5.42 \times 10^{-5}$), elevation (i.e., height above sea level; $\chi^2[4] = 41.12$, $p = 2.50 \times 10^{-8}$), latitude ($\chi^2[4] = 86.32$, $p = 7.96 \times 10^{-18}$), maximum temperature ($\chi^2[4] = 84.50$, $p = 1.95 \times 10^{-17}$), and mean precipitation ($\chi^2[4] = 14.34$, $p = 6.30 \times 10^{-3}$) among all types of preservation (Figures 2.3 and 2.4).

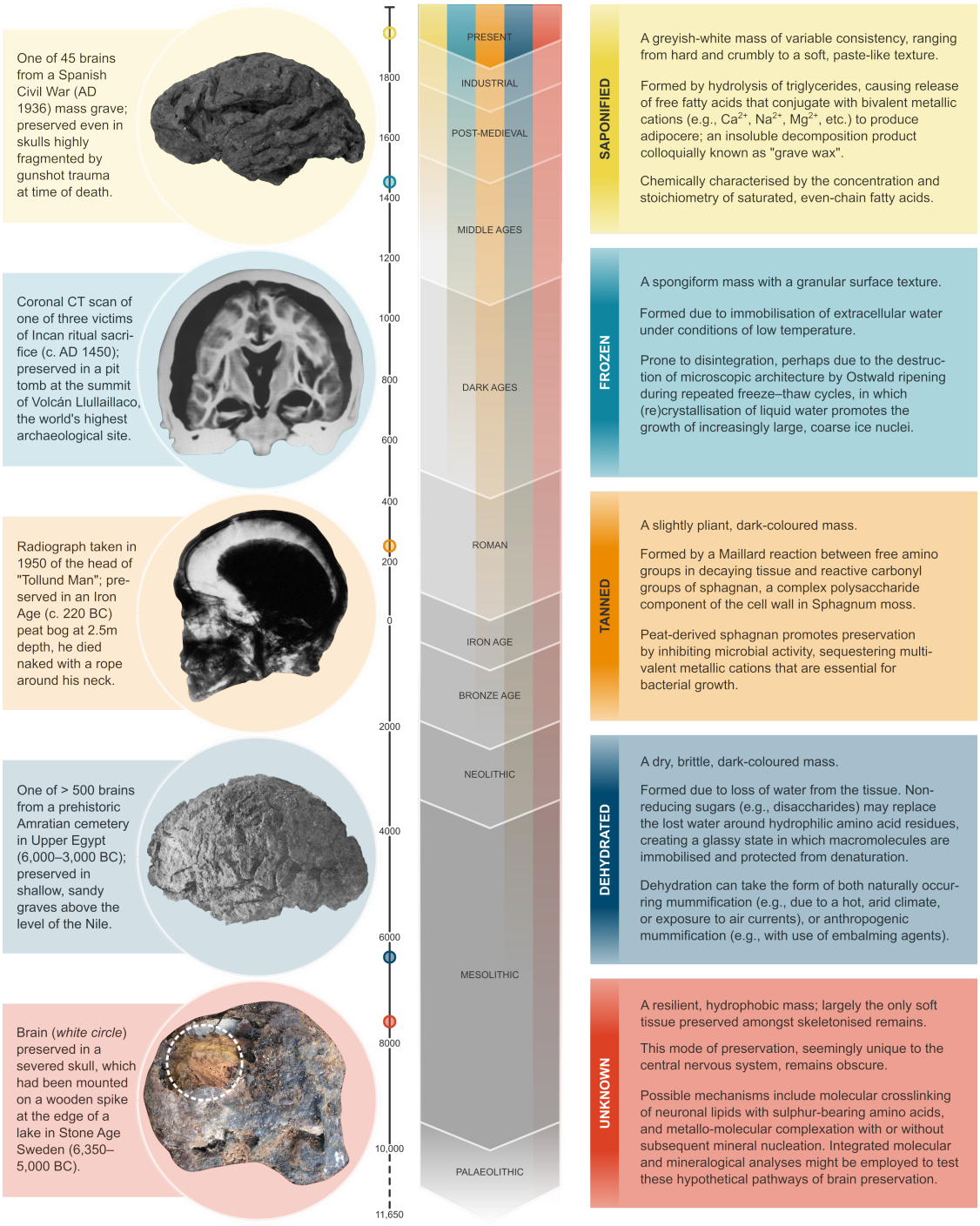



**Figure 2.2 | Five mechanisms of brain preservation.** Morphological and biochemical features of brains preserved by each mechanism, and illustrative cases. Images adapted from source material for saponified [26], frozen [27], tanned [28], dehydrated [7], and unknown [29] brains.

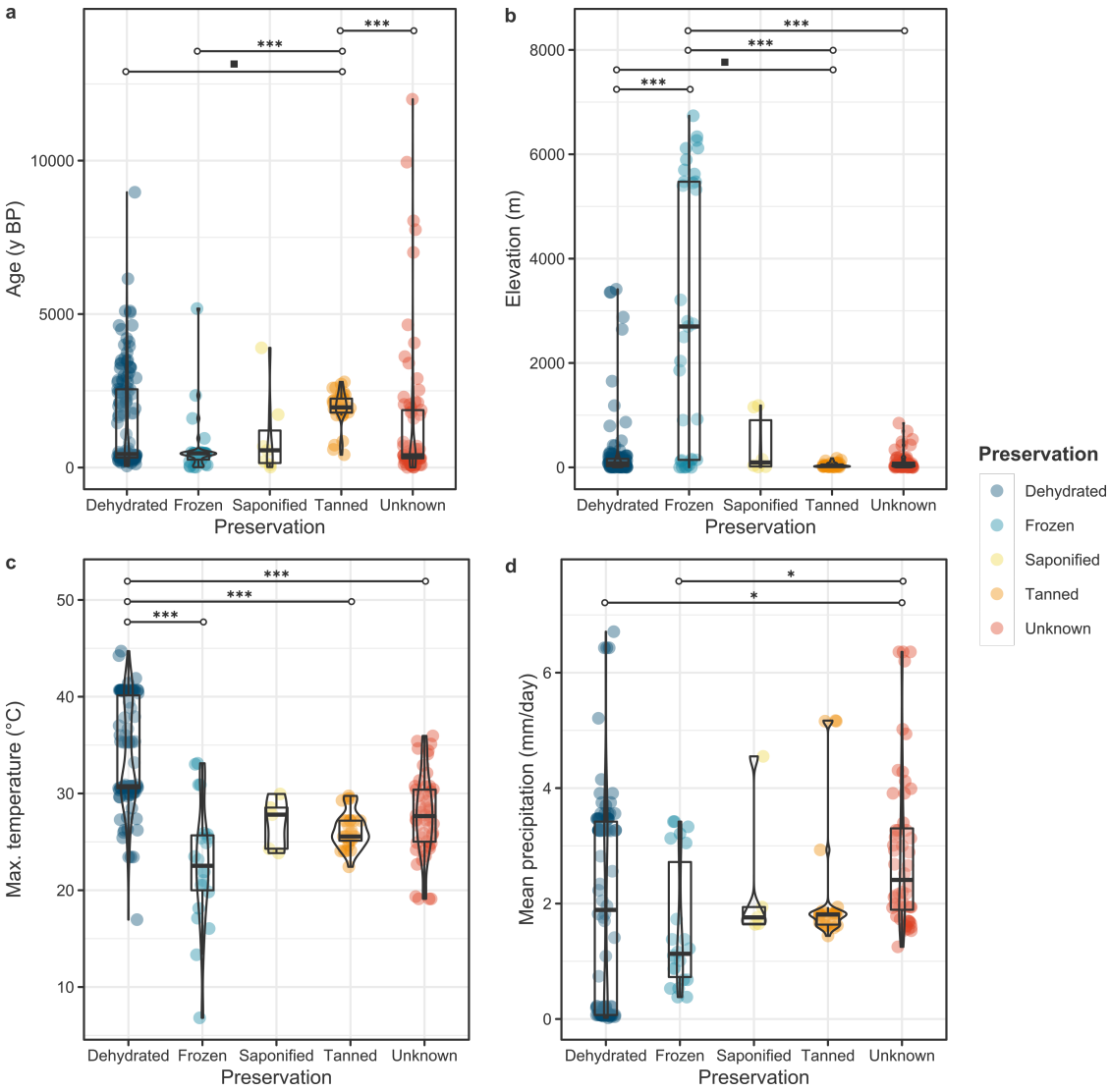



**Figure 2.3 | Relationships between depositional context and preservation type.** Results of Kruskal–Wallis rank sum and *post hoc* Dunn tests with Holm adjustment for multiple comparisons at 95% CI, for preservation type with respect to **(a)** archaeological age, **(b)** elevation, and the **(c)** maximum monthly temperature and **(d)** mean annual precipitation experienced from the time of death to time of excavation. Circles represent archaeological sites. Only statistically significant comparisons are shown, and indicated by the following significance codes: $***$ = $p$-value $< .0001$; $**$ = $p$-value $\leq .001$; $*$ = $p$-value $\leq .01$. Results for latitude shown in Figure 2.4a. Approximately one-quarter of terrestrial sites (26.4%, $n = 73/276$) fell on grid cells with no climatic data and were excluded from the analysis (Appendix A.3).

Dehydrated brains constitute the largest proportion of the dataset (37.8%, $n = 1,667/4{,}405$), with several large assemblages of naturally mummified remains represented, including the aforementioned prehistoric site in Upper Egypt, containing more than 500 individuals 'in every one of which the brain was preserved' [7]. Over their taphonomic history, dehydrated brains experienced the highest maximum monthly temperature (mean [standard error of the mean, SEM] = 33.52 [0.48] °C), whereas frozen brains experienced the lowest (22.68 [1.11] °C). Frozen brains are associated with the highest average elevation (2,920 [449] m) and, over their taphonomic history, the lowest daily precipitation (1.57 [0.19] mm/d): for example, victims of Incan ritual sacrifice at the cold, dry summit of Andean volcanoes [27]. Tanned brains are found at the lowest average elevation (44 [7] m) and the highest average latitudes (54.71 [0.26] °), comprising mainly Iron Age bog bodies from northern Europe (71.9%, $n = 23/32$). Saponified brains cluster at mid-latitudes (48.01 [2.34] °), but a range of depositional contexts are identified, including the waterlogged coffin of an infant interred at the confluence of the Rivers Odet, Steir, and Jet in 13$^{\text{th}}$ C. France ($\sim$ 688 y BP) [30], and rapid burial in a fire disaster following an earthquake during the Bronze Age ($\sim$ 3,900 y BP) in Western Anatolia, Turkey [31]. The vast majority (91.7%, $n = 1,200/1{,}308$) of saponified brains, however, are reported from a single site: burials dating to the Middle Ages, disinterred from Paris' largest cemetery prior to the French Revolution [9]. The contribution of this site to both the saponified type and the total dataset (27.2%, $n = 1,200/4{,}405$) is substantial, and highlights the impact of reporting bias in the literature. Excepting this single context, saponified brains represent a small proportion of the archive (3.4%, $n = 108/3{,}205$).

Preservation types tend to correlate with a single present-day Köppen climate classification. Dehydrated brains are found principally in hot deserts (BWh; 42.6%, $n = 58/136$ sites), where high solar angles and nearly constant high-pressure systems create intense sunshine with little precipitation, producing some of the highest warm-month mean temperatures on Earth (generally 29–35 °C) [32, 33]. Similarly, approximately one-fifth of dehydrated brains (22.1%, $n = 30/136$ sites) are

found in humid continental climates (Dwa), featuring hot summers and dry winters with warm-month mean temperatures exceeding 22 °C and winter precipitation less than 10% that of the wettest summer month [32, 33]. By contrast, frozen brains are largely confined to polar tundras (ET; 72.7%, $n = 24/33$ sites), typified by monthly mean temperatures below 10 °C [33]. In these regions, low vapour pressure of atmospheric water results in little precipitation; however, evapotranspiration is equally low, allowing waterlogging of terrain.

Tanned brains are reported exclusively from oceanic climates (Cfb; 100.0%, $n = 32/32$ sites), which also host the most saponified brains (71.4%, $n = 5/7$ sites) and those of the unknown type (47.8%, $n = 33/69$ sites) (Figure 2.4b and c). These climates are relatively mild year-round (generally 10–22 °C), with no significant difference in precipitation between seasons [33]. A further one-third of brains of the unknown type are found in humid subtropical climates, which feature hot summers when precipitation peaks and storms reach the level of monsoons: 17.4% are found in regions that experience fully humid winters (Cfa; $n = 12/69$ sites), during which daily thundershowers remain common, while 14.5% experience dry winters (Cwa; $n = 10/69$ sites) [32, 33]. Accordingly, brains of the unknown type are associated with the highest daily precipitation over their taphonomic history (2.88 [0.17] mm/d).

## 2.5 Discussion

### 2.5.1 Geographic, palaeoclimatic, and temporal trends in brain preservation

The archaeological record preserves ancient human brains across timescales. Although these ancient brains are found worldwide, trends in their prevalence and persistence with palaeoclimate point to underlying environmental biases toward different types of preservation in space and time.

Saponified brains, however, are reported from too few sites to meaningfully probe these trends. Moreover, nervous tissues represent an unlikely substrate for preservation *via* saponification, which involves the formation of adipocere through

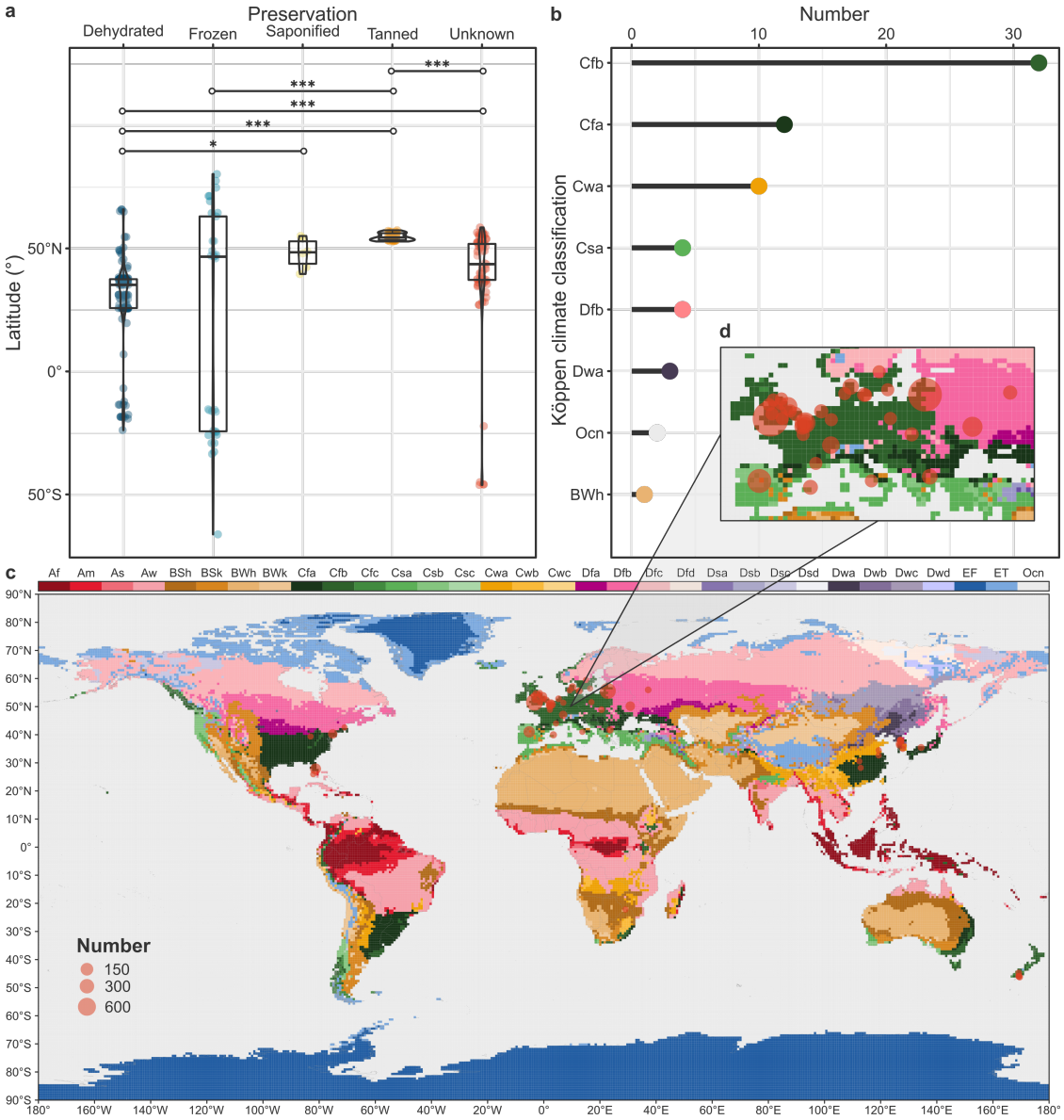



**Figure 2.4 | Relationships between geographic location and unknown preservation type. (a)** Results of Kruskal–Wallis rank sum and *post hoc* Dunn test with Holm adjustment for multiple comparisons at 95% CI, for all preservation types with respect to latitude. Only statistically significant comparisons are shown, and indicated by the following significance codes: $*** = p\text{-value} < .0001$; $** = p\text{-value} \leq .001$; $* = p\text{-value} \leq .01$. **(b)** Number of Köppen climate classifications based on data for the period AD 1986–2010 for archaeological sites yielding brains of the unknown preservation type. **(c)** World map of Köppen–Geiger climate data for the period AD 1986–2010 at 5′ resolution [32, 34], illustrating locations of archaeological sites yielding brains of the unknown preservation type. Circles represent archaeological sites, and their diameter reflects the sample size of brains at each site. **(d)** Distribution of brains of the unknown preservation type in Europe, where the majority (60.0%, $n = 40/69$) have been excavated from locations principally experiencing an oceanic climate (Cfb; 72.5%, $n = 29/40$).

**Box 2.2 | *Saponification, or the formation of adipocere***

Several studies of archaeological nervous tissues [26, 30, 31, 38] have posited the brain's transformation to adipocere, a greyish-white decomposition product colloquially known as 'grave wax' [39], as a mechanism of its preservation (Section 1.4.4). This notion has remained largely unchallenged [but see 23]; despite not only the biochemical incompatibility of nervous tissue with saponification [37], but also the regularity with which it has been recovered from depositional contexts not chemically conducive to this process [40], and the frequency with which it has been found in otherwise skeletonised remains (i.e., in the absence of preservation of other soft tissues by conversion to adipocere) [26, 30, 31, 38].

Evidence for adipocere formation in preserved brains is limited. It has been suggested that 45 brains from a Spanish Civil War (AD 1936) mass grave [26] are preserved in this way due to the presence of saturated fatty acids that may be indicative of adipocere [41]. Such compounds, however, are also present in fresh brain tissue [37] and it is unclear whether any of the fatty acids identified are abundant, nor which species are dominant. Oleic, linoleic and ricinoleic acids have also been reported in brains preserved at this site [42]: the former two are unsaturated fatty acids which may or may not be present as minor constituents of adipocere (and in high concentrations would be counter-indicative [43]), and the latter possesses a melting point too low to contribute to adipocere formation [44]. While a quantitative lipid profile uniquely characteristic of adipocere formation (i.e., saponification of triglycerides) has not been conclusively confirmed in preserved brains [45], other saponifiable lipids abundant in nervous tissue (e.g., glycerophospho- or sphingo-lipids) [37] could participate in similar reactions *post-mortem*. The possibility of a comparable mechanism involving brain-specific lipids should not be discounted.

the hydrolysis of triglycerides [35]. Adipocere forms readily from adipose tissue (the body's fatty, subcutaneous connective tissue), given it is composed almost entirely ($> 98\%$) of triglycerides [36]. Although a lipid-rich organ, the brain contains less than 1% triglycerides [37]. This mechanism of preservation may be misidentified in brains reported as saponified (Box 2.2).

It is perhaps not surprising to find that dehydrated brains are largely excavated from hot deserts, frozen brains from polar tundras, and tanned brains from temperate regions where bogs are widely distributed. That tanned brains and brains of the unknown type are largely confined to regions which, in AD 2000 (i.e., at the point of excavation, given a median date of source publication), experienced an oceanic climate may prove an artefact of excavation bias toward Europe. However, brains of the unknown type are also found in humid subtropical climates, similarly characterised by regular rainfall [46], in regions as disparate as North America, Asia, and Oceania. Unlike tanned brains, they are not confined to peat bogs and, most intriguing, are the only soft tissue remaining.

The features of the unknown preservation type appear to be reflective of a genuinely disparate mode of soft-tissue preservation operating in diverse environments. Apart from similar climates, few unifying factors can be identified that

characterise the depositional contexts in which preserved brains of the unknown type are found. That sites yielding brains of the unknown type are distinguished by the highest daily precipitation of all preservation modes runs contrary to the general taphonomic understanding that heavy rainfall increases the rate of decay [47]; although specifically subaerial decomposition (i.e., exposed soft tissues) may be slowed due to the suppression of insect activity [48], and the impact of precipitation alone may be difficult to disentangle from other environmental variables [49]. The anecdotal presence of clay and iron in sediments with brains of the unknown type might imply the importance of what is dissolved in the gravesoil by the action of rainfall [50]; however the effect of gravesoil chemistry and matric potential (i.e., water content) [51] on decay retardation, and particularly their broader associations with geography and palaeoclimate, remains little investigated.

Although there is a general trend of decreasing frequency of preserved brains with increasing archaeological age (Figure 2.1b), differences in the rate of loss suggest differences in the persistence of preservation types. All mechanisms of brain preservation identified involve loss of water from the tissue, except for saponification (which involves its consumption). However, the sharp decline in the number of frozen brains after $\sim 500$ y BP, for example, compared with the more steady decrease in the number of dehydrated brains over $\sim 4{,}000$ y BP, might suggest that removing extracellular water is more stable than immobilising it. Further, these trends suggest that ephemeral preservation of the brain on $\lesssim 4{,}000$ y timescales may occur where decomposition is arrested impermanently by transitory environmental conditions (e.g., temperature extremes facilitating dehydration or freezing) [52]: when the environmental conditions arresting these processes change (e.g., climate warming), decomposition proceeds and the tissues are lost. Meanwhile, brains of the unknown type persist for millennia in numbers that are orders of magnitude higher than what is observed for other preservation types.

### 2.5.2 Mechanisms of brain preservation on geological timescales

It is unclear what accounts for the unknown mechanism of preservation, in which the human brain persists on longer geological timescales ($\gtrsim$ 12,000 y; *vs.* the maximum age of dehydrated: 8,970 y, frozen: 5,180 y, saponified: 3,900 y, and tanned: 2,790 y), after other organs have perished. The skull might afford the brain protection from exogenous agents of degradation (e.g., [in]vertebrate scavenging, humidity/aridity, soil pH, etc.), akin to bone marrow shielded within the medullary cavity, the decomposition of which is inhibited where cortical integrity is maintained [53]. However, preserved brains have been discovered in skulls fragmented by both *peri-mortem* trauma [54] and taphonomic damage [55]. The persistence of the brain in this unknown type of preservation, irrespective of any protective action of the skull and in varied depositional settings, suggests some intrinsic quality associated with nervous tissue itself that permits long-term preservation.

Molecular crosslinking is a viable possibility for the unknown preservation mechanism. During soft-tissue fossilisation, proteins, lipids, and sugars converge in composition through lipidation and glycation to form chemically stable, polymerised macromolecules [56]. This process involves crosslinking between amino-acid residues and RCS formed in early diagenesis [57], the period after the death and burial of an organism (Figure 2.5a). Thiol-bearing residues crosslink selectively in the presence of lipid-derived RCS and with adjacent hydrophobic residues [57]. With reactive, sulfur-containing side chains, thiol-bearing residues tend to be sequestered in the core of transmembrane proteins, which are tightly bonded to membrane lipids and feature a high proportion of hydrophobic residues (Figure 2.5b) [58]. The brain, which has the highest tissue-enriched expression of transmembrane proteins of any tissue [59], represents an ideal mixture of sulfurous, lipid-rich precursor reagents for this hypothesised pathway to fossilisation.

The formation of inorganic phases, such as *via* metal complexation followed by mineral nucleation, that replicate or chemically stabilise nervous tissues, represents another possibility for the unknown preservation mechanism. Iron, the most

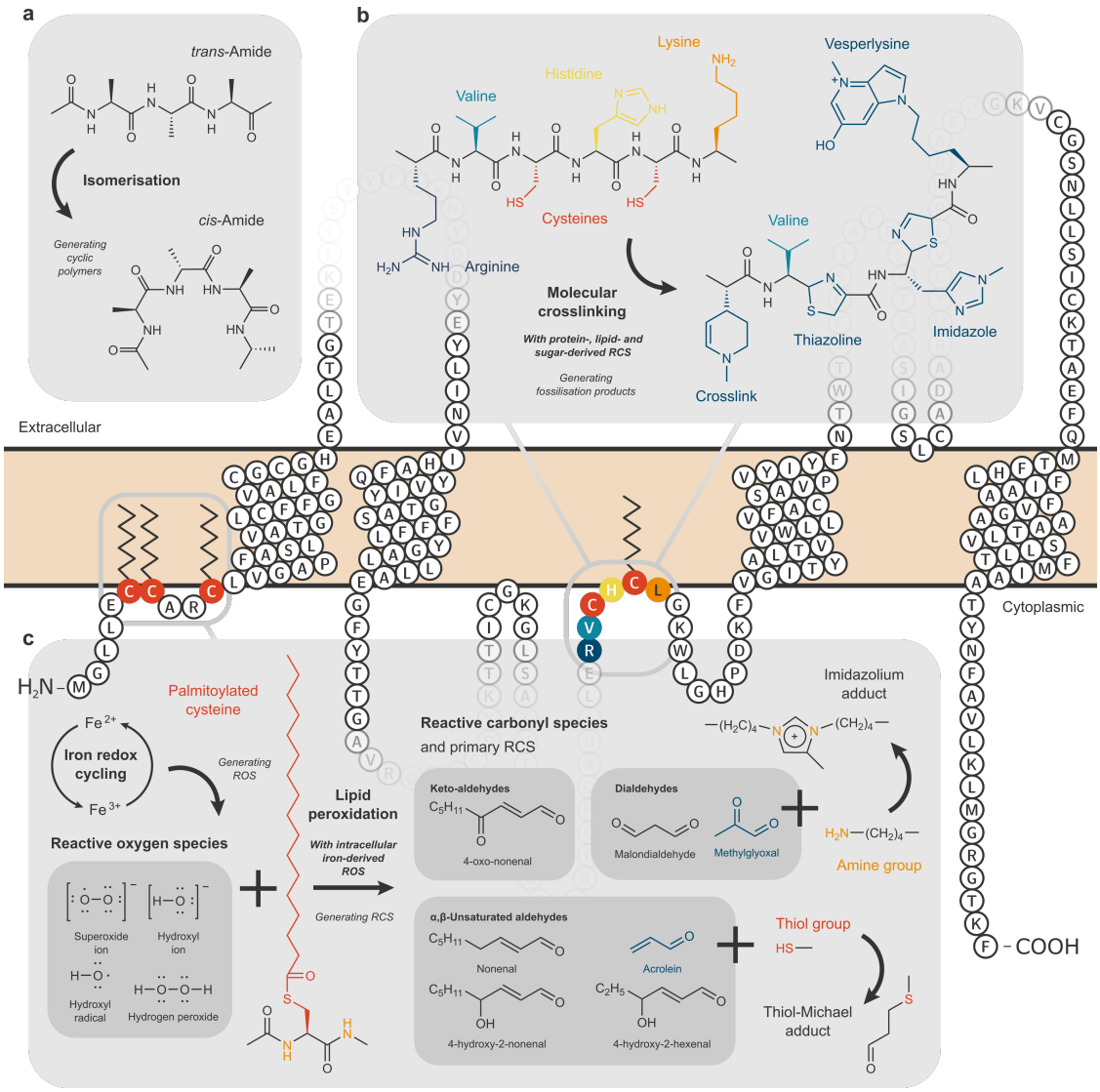



**Figure 2.5 | Chemical processes of molecular crosslinking and metal complexation potentially underpinning the unknown preservation mechanism.** Proteoform of human PLP1, the major transmembrane protein of the CNS [60], illustrating (*top to bottom*) the extracellular, transmembrane, and cytoplasmic spaces; created with Protter (v.1.0) [61]. **(a)** Covalent crosslinks formed during normal physiological processes within and between polypeptides are crucial for determining protein structure and function. However, unintentional crosslinking (e.g., *via* lipidation and glycation) converts intact peptide bonds (trans-amides) to cis-amides, as N-, O- and S-heterocyclic polymers are produced by isomerisation about the C–N bond. This cyclisation results in a more stable molecule that might persist through time [57]. **(b)** Early crosslinking preferentially involves highly reactive amino-acid residues. Arg (R), Cys (C), His (H) and Lys (L) form characteristic fossilisation products *via* crosslinking with adjacent residues (particularly hydrophobic sites; e.g. Val [V]) or RCS [57]; a process that may be catalysed by transition metals such as iron. **(c)** Intracellular iron redox cycling generates ROS that induce lipid peroxidation [62], which in turn yields RCS that become available for molecular crosslinking. Brain transmembrane proteins such as PLP1 feature multiple lipid-bonded, sulfurous amino acids (e.g., palmitoylated Cys) [60], whose fragmented N- and S-containing functional groups react with primary RCS (e.g., methylglyoxal and acrolein) to form adducts [63]. These products then undergo condensation to form resistant, high-molecular-weight polymers that are stable on geological timescales [64].

abundant transition metal in living organisms [65], is especially abundant in the brain where it accumulates with ageing [66]. Its presence in association with preserved brains has been confirmed through histological analysis [21], and conjectured on the basis of macroscopic observations: for example, yellow to black surface colours of 25 brains from a medieval cemetery ($\sim$ 520 y BP; AD 1316–1539) in Hull [19]. The diversity of colours might suggest iron species in a variety of oxidation and coordination states; for instance, ferric (Fe[III]) oxides tend to be red-orange (hematite and ferrihydrite) or yellow (goethite), while ferrous (Fe[II]) sulfides (like pyrite) and ferrous-ferric oxides (like magnetite) are black [67].

In addition to forming inorganic phases, metals may enhance the potential for organic crosslinking, providing overlap between these possible preservation mechanisms. For instance, fossil melanic pigments from skin, eyes, ink, and feathers dating to at least the Late Jurassic ($<$ 195 Ma) have been accredited to the crosslinked nature of the melanin molecule *in vivo* [64]. Alongside crosslinked peptide–lipid components, melanin comprises several polymers with negatively charged carboxyl, hydroxyl and amine groups that bind metallic cations to form stable complexes [68]. Heavier metals such as Fe(III) and Cu(II) bind most strongly and accumulate over time [69], and elevated concentrations have been reported in diagenetically-altered and fossil melanosomes [70].

Melanin is found in multiple brain regions as neuromelanin: a darkly pigmented, insoluble substance whose concentration increases with age. Neuromelanin is well known for its affinity for iron, which it chelates and accumulates in various oxidation states [71]. The capacity of neuromelanin to sequester toxic metal ions renders neuromelanin protective in a range of NDDs [68], but might also represent a means of stabilising labile biomolecules in the brain on geological timescales. Relatedly, diagenetic incorporation of sulfur in functionalised lipids (i.e., natural vulcanisation) promotes the *in situ* polymerisation of melanin [72]; this potentially rapid process (taking place within hundreds of years of deposition [73]) generates kerogens, recalcitrant macromolecules composed of long-chain hydrocarbons crosslinked

by (poly-)sulfide bridges [74]. The sulfurous, lipid-rich brain may be especially susceptible to such a pathway to fossilisation.

In contrast with diagenesis, one means of accumulating metallo-molecular complexes in the brain during life is disturbance of neuronal iron homeostasis [75]. While vital for healthy brain function, excess concentrations and certain oxidation states of iron may be toxic, which generate harmful free radicals [75]. Under normal physiological conditions, neuronal iron is stored as the redox-inactive mineral ferrihydrite (ferric oxide) within the iron storage protein ferritin. However, when iron–protein binding is disrupted *post-mortem*, ferrihydrite reduces to form a redox-active ferrous mineral phase, which may be subsequently oxidised to form magnetite (ferrous-ferric oxide) [62]. This redox cycling represents a 'significant and sustained source' of ROS that might continue to be generated *post-mortem* [62]. ROS induce lipid peroxidation, which generates reactive aldehydes that can crosslink with thiol-bearing amino-acid residues to form supramolecular adducts [76] (Figure 2.5c). Moreover, the generation of nanocrystalline iron oxides dramatically accelerates the nucleation reaction of protein aggregates, which act as sites for further crosslinking [77]. The deep-time stabilisation of proteins *via* iron-catalysed free radical reactions [56, 78, 79] has been argued previously to preserve endogenous amino-acid residues from fossil soft tissues. Copper is another transition metal abundant in the brain and, with similarly variable valency to iron, might also participate in redox cycling of this type to complex with organics [80]. In fact, copper was first implicated in the preservation of ancient North American brain tissue over a century ago [18].

The interplay of crosslinking and complexation has been extensively investigated in the brain *in vivo* given its central role in brain ageing and neurodegenerative disorders [75]. For instance, clinical studies have probed neuronal protein retention as a function of temperature in the short ($< 96$ h) PMI [e.g., 81]. Little is known, however, about diagenetic crosslinking of neuronal proteins on longer timescales. Mass spectrometric strategies for characterising the nature and modification of protein–lipid [82], melanic [83] and metallo-molecular complexes [84] are well established and provide a means to evaluate the crosslinked nature of preserved

brains. In addition, non-destructive spectroscopic methods are well suited for rapid, *in situ* characterisation of molecular fingerprints [85] and their diagenetic alteration [57] in fossil organic matter, and constitute a valuable corroborative approach for precious, ancient samples. Finally, a range of largely X-ray based methods might be employed to refine the identity [86], oxidation state [87] and tissue distribution [88] of metals and minerals intimately associated with preserved nervous tissues.

### 2.5.3 Palaeobiological applications of preserved brains

The record of preserved nervous systems is not confined to ancient human brains. In AD 1888, palaeontologist E. T. Newton (AD 1840–1930) described a preserved brain within a new species of pterosaur from the Upper Lias of the North Yorkshire coast, England (175–183 Ma) [89]. Numerous non-human brains have been identified in the archaeological and fossil records since. Amongst the youngest preserved brains are those of dozens of Antarctic fauna (e.g., seals [90] and penguins [91]) exposed in the polar desert, spanning $\sim$ 100–3,270 y BP. At the other end of the planet, Pleistocene mammals, including mammoth [92] and bison [93], entombed in permafrost in the Russian Arctic, have remained frozen over many millennia, up to $\sim$ 45,000 y BP.

Amongst the oldest preserved nervous systems are those of early animals dating from the Cambrian Explosion, more than 500 Ma [94] (Box 2.3). By illuminating how nervous tissues first evolved, these ancient preserved tissues are proving useful in understanding where fossils are placed on the tree of life [95], and in reconciling fossil morphology with predictions from developmental biology [96]. Evolutionary insights like these are now possible precisely because of the morphological disparity of metazoan nervous systems, which are highly heterogeneous in their ultrastructure and function [97]. At the molecular level, however, their biochemical composition is relatively conserved [98, 99], and neurochemical maps suggest homologies between the vertebrate and invertebrate nervous system ground plan [100]. This shared cellular foundation raises the possibility that the preservational mechanisms hypothesised above might operate in a range of taxa across the animal kingdom throughout the Phanerozoic.

**Box 2.3 | *Non-human brains persist over half a billion years of Earth history***

The record of non-human nervous tissues stretches over vast geological timescales, as far as the base of the Phanerozoic Eon (541 Ma) [94]. These ancient CNS derive mainly from fossil sites of exceptional soft-tissue preservation in North America and China: for example, 84 CNS of the stem-arthropod *Stanleycaris hirpex* [95] and 20 CNS of the annelid worm *Canadia spinosa* [101] are preserved in the Burgess Shale of British Columbia, Canada (509–504.5 Ma). With few exceptions (e.g., five insects in amber from the Middle Oligocene [25–30 Ma; 102], or 64 tadpoles from the Late Miocene [11.6–5.3 Ma; 103]) the palaeontological archive of non-human CNS is dominated by those preserved in marine environments, reflecting the fossil record in general.

In these oceanic burial contexts, a range of different preservation types have been identified. Phosphatisation, for instance, preserves exquisite (even cellular [104]) detail, and has been associated with persistence of the CNS in 14 fireworms from the Late Cretaceous (100.5–93.9 Ma) [105] and two giant bristletails from the Middle Triassic (240 Ma) [106]. Relatively high concentrations of iron have been noted in some fossil nervous tissues preserved by carbon compression [107, 108], and a role for biogenic iron in CNS fossilisation has been proposed [109]; but little work has been done to investigate the part played by tissue chemistry in stabilisation of non-biomineralising tissues. Experimental taphonomy will be crucial to future work in this area.

Soft tissues are generally a richer source of biomolecular information than hard tissues *in vivo* [110], yet only a handful of preserved animal [111] and human [4, 23, 112–114] brains have been sampled for proteins, lipids and ancient deoxyribonucleic acid (aDNA). Amongst the human brains studied, the 'Heslington' brain ($\sim$ 2,500 y; Yorkshire, UK) has yielded 783 proteins, the largest palaeoproteome retrieved from any archaeological material investigated to-date [114]. For comparison, $\sim$ 100 proteins have been recovered from Iron Age dental calculus [115], and 15 from an Early Neolithic bone finger ring [116]. Preserved human brains, then, may constitute an exceptionally rich reservoir of ancient biomolecules, and their ubiquity in the geological record represents an untapped source of palaeobiological data. Below we outline specific areas of future research.

#### 2.5.3.1 Palaeopathology

Preserved nervous tissues could advance our understanding of the pathogenesis of neurological disease, particularly in ancient humans. Whereas methods for the study of brain ageing and NDDs in archaeological contexts remain limited, clinical neuroscience relies on the precise quantitation of a host of protein biomarkers for neurodegenerative processes, whose relative expressions are known to indicate disease progression [117]. Given the richness of human brain palaeoproteomes

[4, 114], it is possible that potential outliers in terms of protein expression and modification might be investigated as indicators of ancient NDDs. Similarly, the composition and distribution of diverse human brain lipids have been profiled for a variety of modern metabolic disorders [118]; particularly those involving disturbances in lipid homeostasis, such as diabetes and obesity. Preserved brain lipids may also provide insight into the nutritional status (i.e., the richness or poorness of one's diet) of ancient humans.

#### 2.5.3.2 Archaeogenetics

aDNA recovered from preserved human brains might answer questions about our genetic history that the phylogeography of modern populations cannot address [119]. Over 30 years ago, the first attempts were made at retrieval and sequencing of aDNA from $\sim$ 8,000 y BP preserved human brain tissue [120]. Since then, two studies of preserved human brains have yielded promising results: Oh *et al.* [17] sampled aDNA from preserved brain and the associated bone, while Graw *et al.* [121] additionally sampled the associated teeth. The former reported markedly higher yields of less fragmented aDNA from the brain, while the latter recovered aDNA exclusively from the brain. In fact, genomic profiling studies [e.g., 122] of *post-mortem* soft tissues suggest that the human brain yields the highest number of analytes and quality and quantity of DNA amongst organs sampled, even many decades *post-mortem*.

A further opportunity is the isolation of ancient chromatin (a complex of DNA and proteins forming chromosomes) from preserved nervous tissues, which might enable investigation of epigenetic patterns of aDNA methylation [123]. These heritable changes in gene expression are phylogenetically informative molecular targets that elucidate evolutionary trajectories [124] and ecological adaptations [125] at the population level, as well as permitting the study of phenotype (e.g., age-at-death [126] and morphological characters [127]) of ancient individuals. Finally, where retrieval of aDNA may be hampered by the limited preservation of intact molecules in older time intervals of the Quaternary Period (2.58 Ma to Present) [but see 128, 129], preserved brains permit the investigation of human evolution by

other means. For instance, the retention of anatomical landmarks and recognisable sulci and gyri suggests that the diagenetic shrinkage of preserved brains may be isotropic: if the microarchitecture of a coherent neural network is as well preserved as the proteome and external topography [114], investigations of internal structure might provide insights into brain plasticity in ancestral humans.

## 2.6 Conclusions

The discovery of over 4,400 preserved human brains, with more than 1,300 as old as 12,000 y and preserved in the absence of other soft tissues, suggests that nervous tissues persist in an abundance that has been overlooked in the archaeological literature. Our analyses reveal statistically significant differences in the geographic, palaeoclimatic, and temporal distribution of human brains preserved throughout the Holocene by ephemeral conditions that arrest their decay. Molecular crosslinking and metal complexation (with or without subsequent mineral precipitation) represent feasible, testable mechanisms by which labile nervous tissues might preserve brains on even longer, geological timescales.

The archive compiled here represents the first step toward a comprehensive, systematic investigation of ancient brains beyond $\sim$ 12,000 y BP, and is essential to maximising the molecular and morphological information they yield as the most metabolically active organ in the body, and amongst the most commonly preserved soft tissues. Ancient brains may provide new and unique palaeobiological insights, helping us to better understand the history of major neurological disorders, ancient cognition and behaviour, and the evolution of nervous tissues and their functions.

## 2.7 Methods

For detailed methodology, see Appendix A.3. We searched for literature reporting preservation of brain tissues in the archaeological record (Figure A.1 and Table A.1) for common features of tissue appearance and depositional environment. We identified five types of brain preservation (Table A.2) and calculated their frequency

(i.e., number of brains preserved as a measure of individuals excavated; Table A.3). We georeferenced each site using Google Earth Pro (v.7.3.6.9345), and assessed environmental conditions at each using estimates of palaeoclimate [130–132], before assigning Köppen climate classifications [32]. We computed summary statistics for archaeological age, elevation, latitude, maximum monthly temperature, and mean annual precipitation for each brain, grouping by preservation type (Table A.4). These variables were tested for normality and homogeneity of variance (Table A.5) using R (v.4.3.2) [133], and Kruskal–Wallis rank sum tests with *post hoc* Dunn pairwise comparisons (Holm-adjusted) (Tables A.6–A.10) were performed to probe significant differences between preservation types with respect to depositional context.

## 2.8 Acknowledgements

We thank Sonia O'Connor and Terry O'Connor for their invaluable support, and Matthew Collins for discussions at the outset. We are indebted to many conservators – particularly Trish Biers, Sharon Clough, Nandy Dolman, Per Thorling Hadsund, Fredrik Hallgren, Bart Lambert, Kimberlee Moran, and April Pijpelink – for their ongoing collaboration. AMH was supported by the Natural Environment Research Council (NE/S007474/1) and the Anglo-Danish Society. RPA was supported by All Souls College and the Royal Society (URF/R1/221220 and RF/ERE/221057). EES was supported by a Leverhulme Prize and the Natural Environment Research Council (NE/V011405/1).

## 2.9 References

[1] Liz Allen et al. 'Publishing: Credit where credit is due'. In: *Nature* 508 (7496 17th Apr. 2014), pp. 312–313. DOI: 10.1038/508312a.

[2] E P Chudá et al. 'A unique case of human naturally mummified cerebellum from Slovakia found in two skulls in St. Martin cathedral (Spisska Kapitula, Eastern Slovakia)'. In: *Ceská Antropologie* 60 (1 2010), pp. 16–19.

[3] Peter C Gerszten and A Julio Martínez. 'The neuropathology of south American mummies'. In: *Neurosurgery* 36 (4 Apr. 1995), pp. 756–761. DOI: 10.1097/00006123-199504000-00017.

[4] Frank Maixner et al. 'Paleoproteomic study of the Iceman's brain tissue'. In: *Cell. Mol. Life Sci.* 70 (19 Oct. 2013), pp. 3709–3722. DOI: 10.1007/s00018-013-1360-y.

[5] Don Brothwell, David Liversage and Birthe Gottlieb. 'Radiographic and forensic aspects of the female huldremose body'. In: *J. Dan. Archaeol.* 9 (1 Jan. 1990), pp. 157–178. DOI: 10.1080/0108464x.1990.10590041.

[6] G H Doran et al. 'Anatomical, cellular and molecular analysis of 8,000-yr-old human brain tissue from the Windover archaeological site'. In: *Nature* 323 (6091 1986), pp. 803–806. DOI: 10.1038/323803a0.

[7] G E Smith. 'On the natural preservation of the brain in the ancient Egyptians'. In: *J. Anat. Physiol.* 36 (Pt 4 July 1902), pp. 375–384.1.

[8] M Thouret. 'Rapport sur les Exhumations du Cimetière et de l'Église des Saints Innocens'. In: *Histoire de la Société Royale de Médecine avec les Mémoires de Médecine et de Physique Médicale*. Paris, France: Théophile Barrois le Jeune, 1790, pp. 238–271.

[9] M Thouret. 'Mémoire. Sur la nature de la substance du cerveau, et sur la propriété qu'il paroît avoir de se conserver long-tems après toutes les autres parties, dans les corps qui se décomposent au sein de la terre'. In: *Journal Phys.* 38 (1791), pp. 329–340.

[10] Donald B Tower. *Brain Chemistry and the French Connection, 1791–1841: An Account of the Chemical Analyses of the Human Brain by Thouret (1791), Fourcroy (1793), Vauquelin (1811), Couerbe (1834), and Frémy (1841)*. New York, USA: Raven, 1994.

[11] A Fourcroy. 'Mémoires sur les différents états des cadavres trouvés dans les fouilles de Cimetière des Innocens en 1786 et 1787'. In: *Ann. Chim.* 5 (1790), pp. 154–185.

[12] M Fourcroy. 'Deuxième mémoire. Sur les matières animales trouvées dans la Cimetière des Innocens à Paris, pendant les fouilles qu'on a faites en 1786 et 1787. Examen chimique de la matière grasse des cadavers contenus dans les fosses communes'. In: *Ann. Chim. (Paris)* 8 (1791), pp. 17–73.

[13] T L Sourkes. 'The origins of neurochemistry: the chemical study of the brain in France at the end of the eighteenth century'. In: *J. Hist. Med. Allied Sci.* 47 (3 July 1992), pp. 322–339. DOI: 10.1093/jhmas/47.3.322.

[14] Théophile Raynaud. *De incorruptione cadaverum, occasione demortui fœminei corporis post aliquot secula incorrupti, nuper refossi carpentoracti*. Aberdeen, Scotland: Edward Raban, 1651. 360 pp.

[15] E M J Schotsmans, N Márquez-Grant and S L Forbes. *Taphonomy of human remains: Forensic analysis of the dead and the depositional environment*. Ed. by Eline M J Schotsmans, Nicholas Marquez-Grant and Shari L Forbes. 1st ed. Nashville, TN: John Wiley & Sons, 31st Mar. 2017. 542 pp. DOI: 10.1002/9781118953358.

[16] Luke A Parry et al. 'Soft-bodied fossils are not simply rotten carcasses – toward a holistic understanding of exceptional fossil preservation: Exceptional fossil preservation is complex and involves the interplay of numerous biological and geological processes'. In: *Bioessays* 40 (1 1st Jan. 2018), p. 1700167. DOI: 10.1002/bies.201700167.

[17] Chang Seok Oh et al. 'Amplification of DNA remnants in mummified human brains from medieval Joseon tombs of Korea'. In: *Anthropol. Anz.* 70 (1 2013), pp. 57–81. DOI: 10.1127/0003-5548/2012/0225.

[18] F W Putnam. *22nd Report of the Trustees of the Peabody Museum of American Archaeology and Ethnology*. 2. Harvard University, 1888.

[19] Sonia O'Connor. 'Brain pseudomorphs: grey matter, grey sediments, and grey literature'. In: *Bones and the Man: Studies in Honour of Don Brothwell*. Ed. by Keith M Dobney and Terry O'Connor. Barnsley, England: Oxbow Books, 23rd July 2002, pp. 41–50.

[20] Thomas Joseph Pettigrew. 'Chap. XVIII - On Modern Embalmings'. In: *A History of Egyptian Mummies*. Ed. by Thomas Joseph Pettigrew. Cambridge, UK: Cambridge University Press, 1834, pp. 251–260.

[21] S Radanov et al. 'A unique case of naturally occurring mummification of human brain tissue'. In: *Int. J. Legal Med.* 105 (3 1992), pp. 173–175. DOI: 10.1007/bf01625172.

[22] Joseph Barnard Davis. *Thesaurus Craniorum: Catalogue of the Skulls of the Various Races of Man*. Vol. 2. London: The Subscribers, 1867. 374 pp.

[23] Sonia O'Connor et al. 'Exceptional preservation of a prehistoric human brain from Heslington, Yorkshire, UK'. In: *J. Archaeol. Sci.* 38 (7 1st July 2011), pp. 1641–1654. DOI: 10.1016/j.jas.2011.02.030.

[24] Kevin Salesse et al. 'IsoArcH.eu: An open-access and collaborative isotope database for bioarchaeological samples from the Graeco-Roman world and its margins'. In: *J. Archaeol. Sci. Rep.* 19 (June 2018), pp. 1050–1055. DOI: 10.1016/j.jasrep.2017.07.030.

[25] P Walter. 'Fossilized human brains found'. In: *Palacio* 27 (13-18 1929), pp. 203–204.

[26] Fernando Serrulla et al. 'Preserved brains from the Spanish Civil War mass grave (1936) at La Pedraja1, Burgos, Spain'. In: *Sci. Justice* 56 (6 Dec. 2016), pp. 453–463. DOI: 10.1016/j.scijus.2016.08.001.

[27] Carlos H Previgliano et al. 'Radiologic evaluation of the Llullaillaco mummies'. In: *AJR Am. J. Roentgenol.* 181 (6 Dec. 2003), pp. 1473–1479. DOI: 10.2214/ajr.181.6.1811473.

[28] Christian Fischer. 'Bog bodies of Denmark and northwestern Europe'. In: *Mummies, Disease and Ancient Cultures*. Ed. by Thomas Aidan Cockburn, Eve Cockburn and Theodore A Reyman. Cambridge: Cambridge University Press, 30th Apr. 1998, pp. 237–262. DOI: 10.1017/cbo9781139878340.015.

[29] Hallgren F, Berggren K, Arnberg A, Hartzell L, Larsson B. *Kanaljorden, Motala. Rituella våtmarksdepositioner och boplatslämningar från äldre stenålder, yngre stenålder och järnålder.* Stiftelsen Kulturmiljövård Rapport, 2021.

[30] Christina Papageorgopoulou et al. 'Preservation of cell structures in a medieval infant brain: a paleohistological, paleogenetic, radiological and physico-chemical study'. In: *Neuroimage* 50 (3 15th Apr. 2010), pp. 893–901. DOI: 10.1016/j.neuroimage.2010.01.029.

[31] M A Altinoz et al. 'Human brains found in a fire-affected 4000-years old Bronze Age tumulus layer rich in soil alkalines and boron in Kutahya, Western Anatolia'. In: *Homo* 65 (1 Feb. 2014), pp. 33–50. DOI: 10.1016/j.jchb.2013.08.005.

[32] Markus Kottek et al. 'World Map of the Köppen-Geiger climate classification updated'. In: *Meteorol. Z.* 15 (3 10th July 2006), pp. 259–263. DOI: 10.1127/0941-2948/2006/0130.

[33] M C Peel, B L Finlayson and T A McMahon. 'Updated world map of the Köppen-Geiger climate classification'. In: *Hydrol. Earth Syst. Sci.* 11 (5 11th Oct. 2007), pp. 1633–1644. DOI: 10.5194/hess-11-1633-2007.

[34] Franz Rubel et al. 'The climate of the European Alps: Shift of very high resolution Köppen-Geiger climate zones 1800–2100'. In: *Meteorol. Z.* 26 (2 25th Apr. 2017), pp. 115–125. DOI: 10.1127/metz/2016/0816.

[35] Shari L Forbes et al. 'A preliminary investigation of the stages of adipocere formation'. In: *J. Forensic Sci.* 49 (3 May 2004), pp. 566–574. DOI: 10.1520/jfs2002230.

[36] M J Dawkins and J F Stevens. 'Fatty acid composition of triglycerides from adipose tissue'. In: *Nature* 209 (5028 12th Mar. 1966), pp. 1145–1146. DOI: 10.1038/2091145a0.

[37] J S O'Brien and E L Sampson. 'Lipid composition of the normal human brain: gray matter, white matter, and myelin'. In: *J. Lipid Res.* 6 (4 1st Oct. 1965), pp. 537–544. DOI: 10.1016/s0022-2275(20)39619-x.

[38] Izabella Tkocz, Peter Bytzer and Franz Bierring. 'Preserved brains in medieval skulls'. In: *Am. J. Phys. Anthropol.* 51 (2 Aug. 1979), pp. 197–202. DOI: 10.1002/ajpa.1330510206.

[39] Paola A Magni, Jessica Lawn and Edda E Guareschi. 'A practical review of adipocere: Key findings, case studies and operational considerations from crime scene to autopsy'. In: *J. Forensic Leg. Med.* 78 (102109 Feb. 2021), p. 102109. DOI: 10.1016/j.jflm.2020.102109.

[40] R C Turner, M Rhodes and J P Wild. 'The Roman body found on grewelthorpe moor in 1850: A reappraisal'. In: *Britannia* 22 (1991 1991), p. 191. DOI: 10.2307/526639.

[41] Manuel Algarra, José E Rodríguez-Borges and Joaquim C G Esteves da Silva. 'LC-MS identification of derivatized free fatty acids from adipocere in soil samples: Liquid Chromatography'. In: *J. Sep. Sci.* 33 (2 Feb. 2010), pp. 143–154. DOI: 10.1002/jssc.200900614.

[42] Francisco Etxeberria and Fernando Serrulla. 'El caso de los cerebros de la Pedraja: Ciencias forenses y memoria histórica en España'. In: *Mètode Rev. difus. investig.* (10 8th Jan. 2020), pp. 109–117. DOI: 10.7203/metode.10.13295.

[43] Stephanie J Notter et al. 'Solid-phase extraction in combination with GC/MS for the quantification of free fatty acids in adipocere'. In: *Eur. J. Lipid Sci. Technol.* 110 (1 Jan. 2008), pp. 73–80. DOI: 10.1002/ejlt.200700159.

[44] Takehiko Takatori et al. 'Identification of 10-hydroxy-12-octadecenoic acid in adipocere'. In: *Forensic Sci. Int.* 23 (2-3 Nov. 1983), pp. 117–122. DOI: 10.1016/0379-0738(83)90140-8.

[45] Andrina Lerchi et al. 'Implementation of adipocere fingerprinting in archaeology by applying a forensic approach'. In: *Trends Analyt. Chem.* 157 (116801 Dec. 2022), p. 116801. DOI: 10.1016/j.trac.2022.116801.

[46] Deliang Chen and Hans Weiteng Chen. 'Using the Köppen classification to quantify climate variation and change: An example for 1901–2010'. In: *Environ. Dev.* 6 (Apr. 2013), pp. 69–79. DOI: 10.1016/j.envdev.2013.03.007.

[47] Karin Kõrgesaar et al. 'Taphonomic model of decomposition'. In: *Leg. Med. (Tokyo)* 56 (102031 May 2022), p. 102031. DOI: 10.1016/j.legalmed.2022.102031.

[48] Sameera A Gunawardena et al. 'Retrospective analysis of factors affecting rate of skeletonization within a tropical climate'. In: *Sci. Justice* 63 (5 Sept. 2023), pp. 638–650. DOI: 10.1016/j.scijus.2023.08.001.

[49] Iris Sluis, Wilma Duijst and Tristan Krap. 'Subaerial decomposition of small-sized remains in The Netherlands: Important findings regarding the PMI of a four-year taphonomic study'. In: *Biology (Basel)* 12 (9 24th Aug. 2023), p. 1164. DOI: 10.3390/biology12091164.

[50] David O Carter, David Yellowlees and Mark Tibbett. 'Moisture can be the dominant environmental parameter governing cadaver decomposition in soil'. In: *Forensic Sci. Int.* 200 (1-3 15th July 2010), pp. 60–66. DOI: 10.1016/j.forsciint.2010.03.031.

[51] Clément Martin et al. 'Forensic taphonomy: Characterization of the gravesoil chemistry using a multivariate approach combining chemical and volatile analyses'. In: *Forensic Sci. Int.* 318 (110569 Jan. 2021), p. 110569. DOI: 10.1016/j.forsciint.2020.110569.

[52] Derek E G Briggs. 'The role of decay and mineralization in the preservation of soft-bodied fossils'. In: *Annu. Rev. Earth Planet. Sci.* 31 (1 May 2003), pp. 275–301. DOI: 10.1146/annurev.earth.31.100901.144746.

[53] Noemi Procopio et al. 'Bone diagenesis in short timescales: Insights from an exploratory proteomic analysis'. In: *Biology (Basel)* 10 (6 23rd May 2021), p. 460. DOI: 10.3390/biology10060460.

[54] Sara Gummesson, Fredrik Hallgren and Anna Kjellström. 'Keep your head high: skulls on stakes and cranial trauma in Mesolithic Sweden'. In: *Antiquity* 92 (361 Feb. 2018), pp. 74–90. DOI: 10.15184/aqy.2017.210.

[55] Gemma Prats-Muñoz et al. 'A paleoneurohistological study of 3,000-year-old mummified brain tissue from the mediterranean bronze age'. In: *Pathobiology* 79 (5 21st June 2012), pp. 239–246. DOI: 10.1159/000334353.

[56] Jasmina Wiemann et al. 'Fossilization transforms vertebrate hard tissue proteins into N-heterocyclic polymers'. In: *Nat. Commun.* 9 (1 9th Nov. 2018), p. 4741. DOI: 10.1038/s41467-018-07013-3.

[57] Jasmina Wiemann, Jason M Crawford and Derek E G Briggs. 'Phylogenetic and physiological signals in metazoan fossil biomolecules'. In: *Sci. Adv.* 6 (28 July 2020), eaba6883. DOI: 10.1126/sciadv.aba6883.

[58] Evgeni Grazhdankin, Michal Stepniewski and Henri Xhaard. 'Modeling membrane proteins: The importance of cysteine amino-acids'. In: *J. Struct. Biol.* 209 (1 1st Jan. 2020), p. 107400. DOI: 10.1016/j.jsb.2019.10.002.

[59] Mathias Uhlén et al. 'Proteomics. Tissue-based map of the human proteome'. In: *Science* 347 (6220 23rd Jan. 2015), p. 1260419. DOI: 10.1126/science.1260419.

[60] T Weimbs and W Stoffel. 'Proteolipid protein (PLP) of CNS myelin: positions of free, disulfide-bonded, and fatty acid thioester-linked cysteine residues and implications for the membrane topology of PLP'. In: *Biochemistry* 31 (49 15th Dec. 1992), pp. 12289–12296. DOI: 10.1021/bi00164a002.

[61] Ulrich Omasits et al. 'Protter: interactive protein feature visualization and integration with experimental proteomic data'. In: *Bioinformatics* 30 (6 15th Mar. 2014), pp. 884–886. DOI: 10.1093/bioinformatics/btt607.

[62] James Everett et al. 'Evidence of redox-active iron formation following aggregation of ferrihydrite and the Alzheimer's disease peptide -amyloid'. In: *Inorg. Chem.* 53 (6 17th Mar. 2014), pp. 2803–2809. DOI: 10.1021/ic402406g.

[63] G Vistoli et al. 'Advanced glycoxidation and lipoxidation end products (AGEs and ALEs): an overview of their mechanisms of formation'. In: *Free Radic. Res.* 47 Suppl 1 (sup1 Aug. 2013), pp. 3–27. DOI: 10.3109/10715762.2013.815348.

[64] Derek E G Briggs and Roger E Summons. 'Ancient biomolecules: their origins, fossilization, and role in revealing the history of life: Prospects & Overviews'. In: *Bioessays* 36 (5 May 2014), pp. 482–490. DOI: 10.1002/bies.201400010.

[65] Arif Tasleem Jan et al. 'Heavy metals and human health: Mechanistic insight into toxicity and counter defense system of antioxidants'. In: *Int. J. Mol. Sci.* 16 (12 10th Dec. 2015), pp. 29592–29630. DOI: 10.3390/ijms161226183.

[66] Animesh Alexander Raha et al. 'Interplay of ferritin accumulation and ferroportin loss in ageing brain: Implication for protein aggregation in Down syndrome dementia, Alzheimer's, and Parkinson's diseases'. In: *Int. J. Mol. Sci.* 23 (3 19th Jan. 2022), p. 1060. DOI: 10.3390/ijms23031060.

[67] A C Scheinost and U Schwertmann. 'Color identification of iron oxides and hydroxysulfates: Use and limitations'. In: *Soil Sci. Soc. Am. J.* 63 (5 Sept. 1999), pp. 1463–1471. DOI: 10.2136/sssaj1999.6351463x.

[68] Tadeusz Sarna, Harold M Swartz and Andrzej Zadlo. 'Interaction of melanin with metal ions modulates their cytotoxic potential'. In: *Appl. Magn. Reson.* 53 (1 Jan. 2022), pp. 105–121. DOI: 10.1007/s00723-021-01386-3.

[69] Frederik Lermyte et al. 'Emerging approaches to investigate the influence of transition metals in the proteinopathies'. In: *Cells* 8 (10 10th Oct. 2019), E1231. DOI: 10.3390/cells8101231.

[70] Valentina Rossi, Samuel M Webb and Maria McNamara. 'Maturation experiments reveal bias in the chemistry of fossil melanosomes'. In: *Geology* 49 (7 1st July 2021), pp. 784–788. DOI: 10.1130/g48696.1.

[71] Alexandra Moreno-García et al. 'The neuromelanin paradox and its dual role in oxidative stress and neurodegeneration'. In: *Antioxidants (Basel)* 10 (1 16th Jan. 2021), p. 124. DOI: 10.3390/antiox10010124.

[72] Maria E McNamara et al. 'Fossilization of melanosomes via sulfurization'. In: *Palaeontology* 59 (3 May 2016), pp. 337–350. DOI: 10.1111/pala.12238.

[73] Jaap S Sinninghe Damsté et al. 'Rapid sulfurisation of highly branched isoprenoid (HBI) alkenes in sulfidic Holocene sediments from Ellis Fjord, Antarctica'. In: *Org. Geochem.* 38 (1 Jan. 2007), pp. 128–139. DOI: 10.1016/j.orggeochem.2006.08.003.

[74] E W Tegelaar et al. 'A reappraisal of kerogen formation'. In: *Geochim. Cosmochim. Acta* 53 (11 1st Nov. 1989), pp. 3103–3106. DOI: 10.1016/0016-7037(89)90191-9.

[75] Marco T Núñez et al. 'Iron toxicity in neurodegeneration'. In: *Biometals* 25 (4 Aug. 2012), pp. 761–776. DOI: 10.1007/s10534-012-9523-0.

[76] Halyna Semchyshyn. 'Is carbonyl/AGE/RAGE stress a hallmark of the brain aging?' In: *Pflugers Arch.* 473 (5 May 2021), pp. 723–734. DOI: 10.1007/s00424-021-02529-y.

[77] Zahra Yarjanli et al. 'Iron oxide nanoparticles may damage to the neural tissue through iron accumulation, oxidative stress, and protein aggregation'. In: *BMC Neurosci.* 18 (1 26th June 2017), p. 51. DOI: 10.1186/s12868-017-0369-9.

[78] Mary H Schweitzer et al. 'A role for iron and oxygen chemistry in preserving soft tissues, cells and molecules from deep time'. In: *Proc. Biol. Sci.* 281 (1775 22nd Jan. 2014), p. 20132741. DOI: 10.1098/rspb.2013.2741.

[79] Landon A Anderson. 'A chemical framework for the preservation of fossil vertebrate cells and soft tissues'. In: *Earth Sci. Rev.* 240 (104367 18th May 2023), p. 104367. DOI: 10.1016/j.earscirev.2023.104367.

[80] Foozhan Tahmasebinia and Saeed Emadi. 'Effect of metal chelators on the aggregation of beta-amyloid peptides in the presence of copper and iron'. In: *Biometals* 30 (2 Apr. 2017), pp. 285–293. DOI: 10.1007/s10534-017-0005-2.

[81] Jeffrey A Blair et al. 'Individual case analysis of postmortem interval time on brain tissue preservation'. In: *PLoS One* 11 (3 16th Mar. 2016), e0151615. DOI: 10.1371/journal.pone.0151615.

[82] João Nunes et al. 'Mass spectrometry-based methodologies for targeted and untargeted identification of protein covalent adducts (adductomics): Current status and challenges'. In: *High Throughput* 8 (2 23rd Apr. 2019), E9. DOI: 10.3390/ht8020009.

[83] Ioana-Ecaterina Pralea et al. 'From extraction to advanced analytical methods: The challenges of melanin analysis'. In: *Int. J. Mol. Sci.* 20 (16 13th Aug. 2019), E3943. DOI: 10.3390/ijms20163943.

[84] Allegra T Aron et al. 'Native mass spectrometry-based metabolomics identifies metal-binding compounds'. In: *Nat. Chem.* 14 (1 Jan. 2022), pp. 100–109. DOI: 10.1038/s41557-021-00803-1.

[85] C C Loron et al. 'Molecular fingerprints resolve affinities of Rhynie chert organic fossils'. In: *Nat. Commun.* 14 (1 13th Mar. 2023), p. 1387. DOI: 10.1038/s41467-023-37047-1.

[86] Pierre Gueriau et al. 'Trace elemental imaging of rare earth elements discriminates tissues at microscale in flat fossils'. In: *PLoS One* 9 (1 29th Jan. 2014), e86946. DOI: 10.1371/journal.pone.0086946.

[87] R A Wogelius et al. 'Trace metals as biomarkers for eumelanin pigment in the fossil record'. In: *Science* 333 (6049 16th Sept. 2011), pp. 1622–1626. DOI: 10.1126/science.1205748.

[88] Pierre Gueriau et al. 'Visualizing mineralization processes and fossil anatomy using synchronous synchrotron X-ray fluorescence and X-ray diffraction mapping'. In: *J. R. Soc. Interface* 17 (169 Aug. 2020), p. 20200216. DOI: 10.1098/rsif.2020.0216.

[89] Edwin Tulley Newton. 'XIX. On the skull, brain, and auditory organ a new species of pterosaurian ( *Scaphognathus purdoni* ), from the upper lias near whitby, Yorkshire'. In: *Philos. Trans. R. Soc. Lond.* 179 (179 31st Dec. 1888), pp. 503–537. DOI: 10.1098/rstb.1888.0019.

[90] T L Pewe, N R Rivard and G A Llano. 'Mummified seal carcasses in the McMurdo Sound Region, Antarctica'. In: *Science* 130 (3377 18th Sept. 1959), p. 716. DOI: 10.1126/science.130.3377.716.

[91] Yuesong Gao et al. 'Last millennium Adélie penguin mortality and colony abandonment events on Long Peninsula, East Antarctica'. In: *J. Geophys. Res. Biogeosci.* 123 (9 Sept. 2018), pp. 2878–2889. DOI: 10.1029/2018jg004550.

[92] Anastasia Kharlamova et al. 'Preserved brain of the Woolly mammoth (Mammuthus primigenius (Blumenbach 1799)) from the Yakutian permafrost'. In: *Quat. Int.* 406 (June 2016), pp. 86–93. DOI: 10.1016/j.quaint.2014.09.073.

[93] N V Serdyuk et al. 'New data on the internal organs of a frozen Yukagir bison mummy (Bison priscus Bojanus, 1827), Yakutia, Russia'. In: *Dokl. Biol. Sci.* 467 (1 Mar. 2016), pp. 89–92. DOI: 10.1134/S0012496616020125.

[94] Gregory D Edgecombe, Xiaoya Ma and Nicholas J Strausfeld. 'Unlocking the early fossil record of the arthropod central nervous system'. In: *Philos. Trans. R. Soc. Lond. B Biol. Sci.* 370 (1684 19th Dec. 2015), p. 20150038. DOI: 10.1098/rstb.2015.0038.

[95] Joseph Moysiuk and Jean-Bernard Caron. 'A three-eyed radiodont with fossilized neuroanatomy informs the origin of the arthropod head and segmentation'. In: *Curr. Biol.* 32 (15 8th Aug. 2022), 3302–3316.e2. DOI: 10.1016/j.cub.2022.06.027.

[96] Joanna M Wolfe and Javier Ortega-Hernández. 'Evolution: Oh, my Cambrian nerves'. In: *Curr. Biol.* 31 (19 11th Oct. 2021), R1132–R1135. DOI: 10.1016/j.cub.2021.08.065.

[97] Benjamin Liebeskind et al. 'Evolution of animal neural systems'. In: *bioRxiv* (14th Mar. 2017). DOI: 10.1101/116715.

[98] D Sandeman. 'Homology and convergence in vertebrate and invertebrate nervous systems'. In: *Sci. Nat.* 86 (8 1st Aug. 1999), pp. 378–387. DOI: 10.1007/s001140050637.

[99] E M Leise. 'Modular construction of nervous systems: a basic principle of design for invertebrates and vertebrates'. In: *Brain Res. Brain Res. Rev.* 15 (1 Jan. 1990), pp. 1–23. DOI: 10.1016/0165-0173(90)90009-d.

[100] Simona Candiani et al. 'A neurochemical map of the developing amphioxus nervous system'. In: *BMC Neurosci.* 13 (1 7th June 2012), p. 59. DOI: 10.1186/1471-2202-13-59.

[101] Luke Parry and Jean-Bernard Caron. 'Canadia spinosa and the early evolution of the annelid nervous system'. In: *Sci. Adv.* 5 (9 Sept. 2019), eaax5858. DOI: 10.1126/sciadv.aax5858.

[102] D Grimaldi et al. 'Electron microscopic studies of mummified tissues in amber fossils'. In: *Am. Mus. Novit.* 3097 (3097 May 1994), p. 31.

[103] Maria E McNamara et al. 'Exceptionally preserved tadpoles from the Miocene of Libros, Spain: ecomorphological reconstruction and the impact of ontogeny upon taphonomy'. In: *Lethaia* 43 (3 Sept. 2010), pp. 290–306. DOI: 10.1111/j.1502-3931.2009.00192.x.

[104] D E Briggs and A J Kear. 'Fossilization of soft tissue in the laboratory'. In: *Science* 259 (5100 5th Mar. 1993), pp. 1439–1442. DOI: 10.1126/science.259.5100.1439.

[105] Luke A Parry et al. 'A new fireworm (Amphinomidae) from the Cretaceous of Lebanon identified from three-dimensionally preserved myoanatomy'. In: *BMC Evol. Biol.* 15 (1 17th Nov. 2015), p. 256. DOI: 10.1186/s12862-015-0541-8.

[106] Matteo Montagna et al. 'Central nervous system and muscular bundles preserved in a 240 million year old giant bristletail (Archaeognatha: Machilidae)'. In: *Sci. Rep.* 7 (1 7th Apr. 2017), p. 46016. DOI: 10.1038/srep46016.

[107] Xiaoya Ma et al. 'Complex brain and optic lobes in an early Cambrian arthropod'. In: *Nature* 490 (7419 11th Oct. 2012), pp. 258–261. DOI: 10.1038/nature11495.

[108] Tian Lan et al. 'Leanchoiliidae reveals the ancestral organization of the stem euarthropod brain'. In: *Curr. Biol.* 31 (19 11th Oct. 2021), 4397–4404.e2. DOI: 10.1016/j.cub.2021.07.048.

[109] Farid Saleh et al. 'Biogenic iron preserves structures during fossilization: A hypothesis: Iron from decaying tissues may stabilize their morphology in the fossil record: Iron from decaying tissues may stabilize their morphology in the fossil record'. In: *Bioessays* 42 (6 June 2020), e1900243. DOI: 10.1002/bies.201900243.

[110] Dongxue Wang et al. 'A deep proteome and transcriptome abundance atlas of 29 healthy human tissues'. In: *Mol. Syst. Biol.* 15 (2 18th Feb. 2019), e8503. DOI: 10.15252/msb.20188503.

[111] E M Kreps et al. 'Brain lipids in fossilized mammoths, mammuthus primigenius'. In: *Comp. Biochem. Physiol. B* 68 (1 Jan. 1981), pp. 135–140. DOI: 10.1016/0305-0491(81)90192-9.

[112] M J Kim et al. 'Human mummified brain from a medieval tomb with lime-soil mixture barrier of the Joseon Dynasty, Korea: Mummified Brain from Medieval Tomb in Korea'. In: *Int. J. Osteoarchaeol.* 18 (6 Nov. 2008), pp. 614–623. DOI: 10.1002/oa.962.

[113] Pierpaolo Petrone et al. 'Heat-Induced Brain Vitrification from the Vesuvius Eruption in c.e. 79'. In: *N. Engl. J. Med.* 382 (4 23rd Jan. 2020), pp. 383–384. DOI: 10.1056/NEJMc1909867.

[114] Axel Petzold et al. 'Protein aggregate formation permits millennium-old brain preservation'. In: *J. R. Soc. Interface* 17 (162 Jan. 2020), p. 20190775. DOI: 10.1098/rsif.2019.0775.

[115] Jessica Hendy et al. 'Proteomic evidence of dietary sources in ancient dental calculus'. In: *Proc. Biol. Sci.* 285 (1883 18th July 2018), p. 20180977. DOI: 10.1098/rspb.2018.0977.

[116] Theis Zetner Trolle Jensen et al. 'The biomolecular characterization of a finger ring contextually dated to the emergence of the Early Neolithic from Syltholm, Denmark'. In: *R. Soc. Open Sci.* 7 (1 Jan. 2020), p. 191172. DOI: 10.1098/rsos.191172.

[117] Artur Schumacher-Schuh et al. 'Advances in proteomic and metabolomic profiling of neurodegenerative diseases'. In: *Front. Neurol.* 12 (2021), p. 792227. DOI: 10.3389/fneur.2021.792227.

[118] Ying-Yong Zhao, Xian-Long Cheng and Rui-Chao Lin. 'Lipidomics applications for discovering biomarkers of diseases in clinical chemistry'. In: *Int. Rev. Cell Mol. Biol.* International review of cell and molecular biology 313 (2014), pp. 1–26. DOI: 10.1016/B978-0-12-800177-6.00001-3.

[119] Luca Ermini et al. 'Complete mitochondrial genome sequence of the Tyrolean Iceman'. In: *Curr. Biol.* 18 (21 11th Nov. 2008), pp. 1687–1693. DOI: 10.1016/j.cub.2008.09.028.

[120] S Pääbo, J A Gifford and A C Wilson. 'Mitochondrial DNA sequences from a 7000-year old brain'. In: *Nucleic Acids Res.* 16 (20 25th Oct. 1988), pp. 9775–9787. DOI: 10.1093/nar/16.20.9775.

[121] M Graw, H J Weisser and S Lutz. 'DNA typing of human remains found in damp environments'. In: *Forensic Sci. Int.* 113 (1-3 11th Sept. 2000), pp. 91–95. DOI: 10.1016/s0379-0738(00)00221-8.

[122] Shashank Pooniya et al. 'Quality and quantity of extracted deoxyribonucleic Acid (DNA) from preserved soft tissues of putrefied unidentifiable human corpse'. In: *J. Lab. Physicians* 6 (1 Jan. 2014), pp. 31–35. DOI: 10.4103/0974-2727.129088.

[123] David Gokhman, Eran Meshorer and Liran Carmel. 'Epigenetics: It's getting old. Past meets future in paleoepigenetics'. In: *Trends Ecol. Evol.* 31 (4 Apr. 2016), pp. 290–300. DOI: 10.1016/j.tree.2016.01.010.

[124] Laura Niiranen et al. 'Epigenomic modifications in modern and ancient genomes'. In: *Genes (Basel)* 13 (2 20th Jan. 2022), p. 178. DOI: 10.3390/genes13020178.

[125] Yichen Liu, Laura S Weyrich and Bastien Llamas. 'More arrows in the ancient DNA quiver: Use of paleoepigenomes and paleomicrobiomes to investigate animal adaptation to environment'. In: *Mol. Biol. Evol.* 37 (2 1st Feb. 2020), pp. 307–319. DOI: 10.1093/molbev/msz231.

[126] Jakob Skou Pedersen et al. 'Genome-wide nucleosome map and cytosine methylation levels of an ancient human genome'. In: *Genome Res.* 24 (3 Mar. 2014), pp. 454–466. DOI: 10.1101/gr.163592.113.

[127] David Gokhman et al. 'Differential DNA methylation of vocal and facial anatomy genes in modern humans'. In: *Nat. Commun.* 11 (1 4th Mar. 2020), p. 1189. DOI: 10.1038/s41467-020-15020-6.

[128] Tom van der Valk et al. 'Million-year-old DNA sheds light on the genomic history of mammoths'. In: *Nature* 591 (7849 Mar. 2021), pp. 265–269. DOI: 10.1038/s41586-021-03224-9.

[129] Kurt H Kjær et al. 'A 2-million-year-old ecosystem in Greenland uncovered by environmental DNA'. In: *Nature* 612 (7939 Dec. 2022), pp. 283–291. DOI: 10.1038/s41586-022-05453-y.

[130] Taraka Davies-Barnard et al. 'Quantifying the influence of the terrestrial biosphere on glacial-interglacial climate dynamics'. In: *Clim. Past Discuss.* (10th Feb. 2017), pp. 1–22. DOI: 10.5194/cp-2017-12.

[131] Joy S Singarayer, Paul J Valdes and William H G Roberts. 'Ocean dominated expansion and contraction of the late Quaternary tropical rainbelt'. In: *Sci. Rep.* 7 (1 24th Aug. 2017), p. 9382. DOI: 10.1038/s41598-017-09816-8.

[132] Erin E Saupe et al. 'Spatio-temporal climate change contributes to latitudinal diversity gradients'. In: *Nat. Ecol. Evol.* 3 (10 Oct. 2019), pp. 1419–1429. DOI: 10.1038/s41559-019-0962-7.

[133] R Core Team. *R: A language and environment for statistical computing*. Vienna, Austria: R Foundation for Statistical Computing, 2023.

# 3

# Deep Palaeoproteomic Profiling of Archaeological Human Brains

Morton-Hayward, A.L., Flannery, S., Vendrell, I., & Fischer, R. (2025).
*Deep Palaeoproteomic Profiling of Archaeological Human Brains.*
**PLoS One 2025**, *20*(5): e0324246.
doi.org/10.1371/journal.pone.0324246

## 3.1 Author Contributions

**Table 3.1** | Summary of individual contributions to this chapter, described using the CRediT system [1].

| Author | Contribution |
|---|---|
| *Morton-Hayward, A.L.* | Study conception; Methodology; Computation; Formal analysis; Investigation: performed the experiments; Investigation: data/evidence collection; Resources; Data curation; Manuscript preparation: writing the initial draft; Manuscript preparation: critical review, commentary and revision; Manuscript preparation: visualisation/data presentation; Project administration; Funding acquisition. |
| *Flannery, S.* | Methodology; Investigation: performed the experiments; Investigation: data/evidence collection; Resources; Data curation; Manuscript preparation: critical review, commentary and revision. |
| *Vendrell, I.* | Methodology; Investigation: data/evidence collection; Resources; Data curation; Manuscript preparation: critical review, commentary and revision. |
| *Fischer, R.* | Methodology; Resources; Manuscript preparation: critical review, commentary and revision; Supervision; Funding acquisition. |

## 3.2 Abstract

Palaeoproteomics leverages the persistence, diversity, and biological import of ancient proteins to explore the past, and answer fundamental questions about phylogeny, environment, diet, and disease. These insights are largely gleaned from hard tissues like bone and teeth, as well established protocols exist for extracting ancient proteins from mineralised tissues. No such method, however, exists for the soft tissues, which are underexplored in palaeoproteomics given permission for destructive analysis routinely depends on a proven methodology. Considering less than one-tenth of all human proteins are expressed in bone, compared to three-quarters in the internal organs, the amount of biological information presently inaccessible is substantial. We address this omission with an optimised LC–FAIMS–MS/MS workflow yielding the largest, most diverse palaeoproteome yet described. Using archaeological human brains, we test ten protocols with varied chemistries and find that urea lysis effectively disrupts preserved membrane regions to expose low-abundant, intracellular analytes. Further, we show that ion mobility spectrometry improves unique protein identification by as much as 40%, and represents a means of 'cleaning' dirty archaeological samples. Our methodology will be useful for improving protein recovery from a range of ancient tissues and depositional environments.

## 3.3 Introduction

Proteins are long-lived biomolecules able to persist for millions of years in the archaeological record [2–4]. Their longevity derives in part from their structure, comprising long chains of 20 standard amino acids (each of which possesses a chemically distinct side chain) folded into complex secondary, tertiary, and quaternary structures, which are compounded by an array of possible PTMs. This compact architecture packs the same amount of sequence information as DNA into approximately one-sixth the number of atoms and, with fewer chemical bonds, degrades more slowly than the double helix that encodes it [5]. Ancient protein sequences thus trace the same phylogenetic relationships as DNA, with the additional

advantage that preservation of *in vivo* PTMs yields physiological information on the lived experience of long-dead lineages [6]. That is, where DNA provides the potential, proteins provide the record. Their persistence and biochemical diversity make proteins an ideal vehicle for navigating the recent and deep past [7], and the challenge of palaeoproteomics is to retrieve, identify, and make sense of their remnants as they transition from the biosphere to the lithosphere [5].

To be detected and analysed, proteins must first be extracted. Sample preparation remains the major bottleneck in any bottom-up proteomics workflow given the complexity of biological samples and the multi-stage processes associated with it [8–10], which typically include cell lysis, protein denaturation, disulfide bond reduction, sulfhydryl group alkylation, and digestion of proteins into peptides for efficient separation by LC and detection by MS. This complexity is only exacerbated in an archaeological context, where the action of time has further depleted and degraded the ancient proteome [11]. Nonetheless, ancient proteomes have been retrieved from hard tissues like bone and teeth in diverse taxa [5], and a handful of studies have investigated the efficiency of different methods for extracting ancient proteins from these remains [12–14]. However, archaeological soft tissues remain underexplored as repositories of ancient proteins: those few to-date have been restricted largely to hair [15] and skin [16–18], and no method optimisation has been conducted beyond extraction from keratinised and collagenous tissues. Ancient hair, skin and bone proteomes largely comprise keratins and collagens, and less than 9% of all human proteins are expressed in bone ($n = 1,730/20{,}162$) [19]. By contrast, 76% are expressed in the brain ($n = 15,331/20{,}162$) [20], and the ancient brain proteome is thus an order of magnitude more diverse, reflective of its functional complexity [21]. The same is likely true of other internal organs preserved in the archaeological record, such as the intestines (75%) [22, 23], stomach (72%) [24, 25], kidneys (71%) [26, 27], lungs (71%) [28, 29] and heart (68%) [30, 31].

More than 4,400 human brains have been excavated from an array of environments worldwide, some up to 12,000 years old [32]; just two, however, have been probed by LC–MS/MS [21, 33]. Soft tissues of the internal organs (and particularly

the brain) comprise substantially greater proportions of lipid-linked membrane proteins than hard tissues [20]. Anchored in the lipid bilayer environment, membrane proteins comprise one or more $\alpha$-helical domains [34] whose hydrophobic nature can cause aggregation in aqueous solutions [35], which makes sample preparation challenging. Membrane proteins are often extracted and kept soluble with strong denaturants (e.g., urea) or ionic detergents (e.g., SDS) which, when maintained above their critical micelle concentration, effectively disrupt the lipid bilayer [36]. While such agents may facilitate extraction, they can inhibit proteolysis and interfere with separation by LC and detection by MS, hampering protein recovery [10, 37]. As such, a range of sample clean-up methods exist at both the protein- and peptide-level (i.e., conducted before or after proteolysis) that aim to remove reagents that would otherwise negatively impact downstream analyses [38]. However, additional steps cause sample losses, which it is crucial to minimise in cases where low starting material availability must be a consideration [39], such as with archaeological tissues. Moreover, choices made at each stage of the proteomics workflow affect the composition of the recovered proteome: for example, reagents can selectively enrich or deplete functional classes of proteins and cellular components, depending on the underlying chemistry [40–42].

We test 10 protocols for ancient protein recovery from brain tissues using a bottom-up LC–MS/MS approach, comparing the effectiveness of a range of extraction buffers and clean-up strategies (Figure 3.1). The former include urea, SDS and sodium laurate (SL); while the latter include the in-StageTip method (iST) [43], solid-phase extraction (SPE), suspension trapping (S-Trap) [44], filter-aided sample preparation (FASP) [45], single-pot solid-phase-enhanced sample preparation (SP3) [46], and in-gel purification with SDS–polyacrylamide gel electrophoresis (SDS–PAGE). We assess the use of a high-field asymmetric-waveform ion mobility spectrometry (FAIMS) source at different compensation voltages (CVs) to reduce chemical noise and improve detection of low-abundant proteins. Finally, the range of laboratory-based options available to the protein chemist is paralleled by the array of analytical software available to the bioinformatician: we test protein identification

and relative quantification with DIA-NN [47], FragPipe [48], MaxQuant [49] and PEAKS® Studio (Bioinformatics Solutions, Inc.). We assess the efficacy, efficiency (i.e., performance relative to ease of use), and suitability of all options for broad application in palaeoproteomics, comparing protocols on the basis of numbers of identified precursors, peptides and proteins, intensity-based absolute quantification (iBAQ), protein scoring, hydropathy and isoelectric point (pI), levels of reagent-based contamination, and functional and cellular enrichment biases.

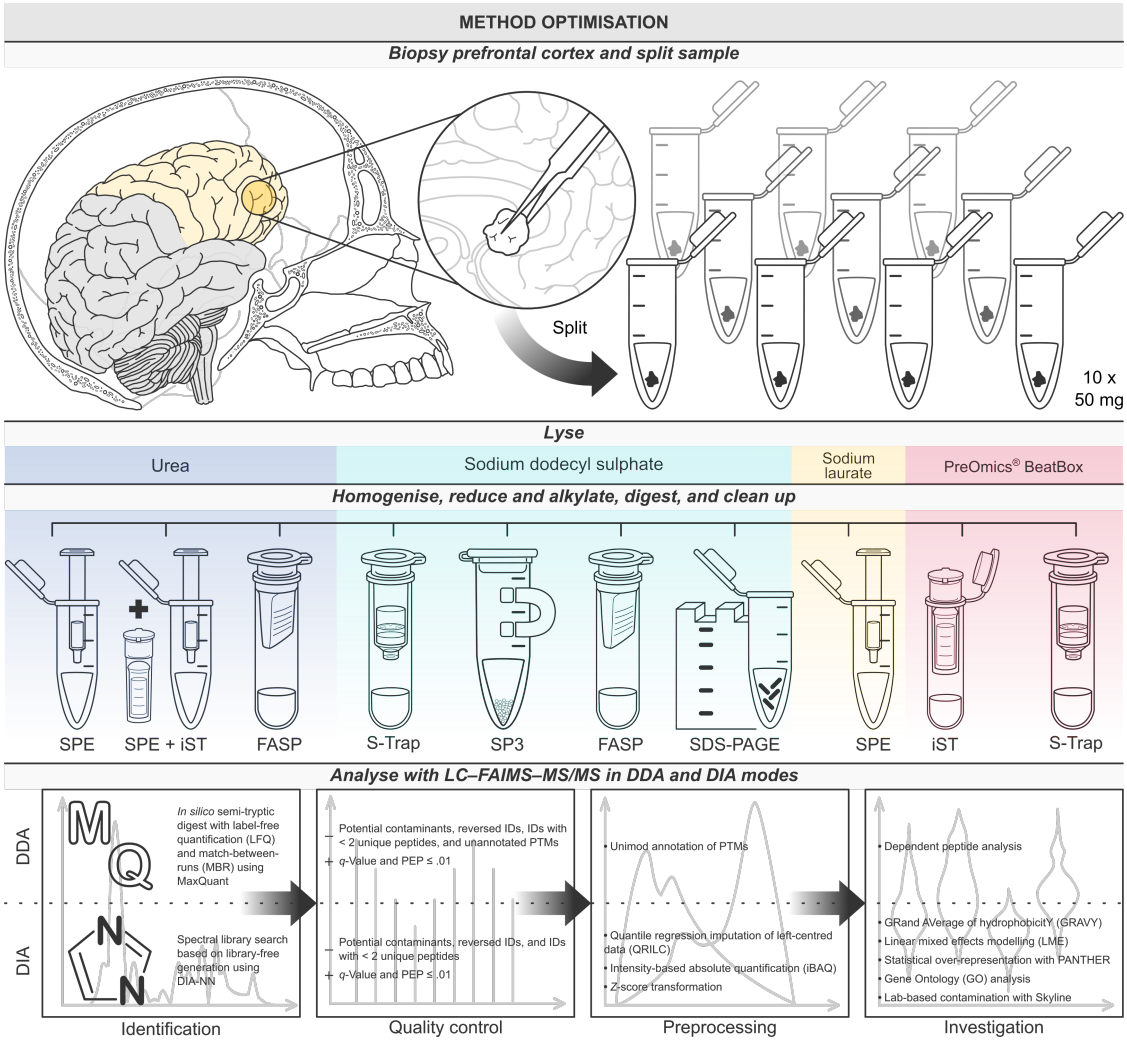



**Figure 3.1 | Overview of the study design.** A single cortical biopsy was taken from the anterior right frontal lobe and separated into 10 samples of 50 mg, which were lysed with four different extraction methods (urea, SDS, SL, and PreOmics® BeatBox) before homogenisation by bead-beating. After reduction, alkylation, and digestion with trypsin, samples were processed with one of seven clean-up methods either in-solution (iST, SPE, SPE + iST), in-gel (SDS–PAGE), on-filter (FASP, S-Trap) or on-bead (SP3). Samples were analysed by LC–FAIMS–MS/MS in DDA and DIA modes and, based on preliminary testing with a range of software (Table B.11), the final DDA dataset was processed in MaxQuant (v.2.6.1.0) [49], and the DIA dataset in DIA-NN (v.1.9) [47].

## 3.4 Materials & Methods

### 3.4.1 Archaeological brain material

Approximately 4,500 individuals were excavated from the site of the former Blackberry Hill Hospital in the Fishponds area of Bristol, UK (2018–2022, Cotswold Archaeology), one in 10 of which evidenced preserved brain tissues ($n = 456$). Originally built as Stapleton Prison (1779–1814) to house prisoners of war from Britain's conflicts with France, Spain, the Netherlands and the USA throughout the late 18$^{\text{th}}$ C., the site became a hospital during Bristol's 1832 cholera outbreak, and was converted to the Stapleton Workhouse shortly thereafter (1837–1890). In the 20$^{\text{th}}$ C., it evolved into Manor Park Hospital, later Blackberry Hill Hospital, before its closure in 2007.

Immediately post-excavation, brains were refrigerated at 4 °C in airtight containers, without washing or preservative treatment, and acquisitioned by the Duckworth Laboratory (University of Cambridge). One brain (SK 17999) was selected for investigation based on the exceptional quality of its preservation, possessing identifiable cerebral hemispheres with intact sulci and gyri that facilitated confident and reproducible sampling. A single cortical biopsy was taken from the anterior right frontal lobe, which was separated into 10 samples of 50 mg; these were stored at −80 °C prior to analysis. Permission for destructive sampling was sought and obtained from the Duckworth Laboratory, and ethical approval from the Central University Research Ethics Committee at the University of Oxford (R80617/RE001). All necessary permits were obtained for the described study, which complied with all relevant regulations.

### 3.4.2 In-solution

#### 3.4.2.1 PreOmics® BeatBox iST

The sample was processed according to the iST Sample Preparation Kit protocol (v.4.0; PreOmics®) [50] (Section B.2.1.1 and Table B.1). A 50 mg aliquot of brain was lysed with 50 mg glass beads in 100 µL of LYSE, using BeatBox sonication

for 10 cycles of 30 s. Proteins were further denatured at 95 °C and 1,000 rpm for 10 min in an Eppendorf ThermoMixer® C (Thermo Fisher Scientific). Digestion was performed with 50 µL DIGEST at 37 °C and 500 rpm for 3 h. The sample was acidified with 100 µL STOP then clarified at 20 °C and 500 rpm for 1 min, followed by centrifugation at 20 °C and 16,000 rcf for 1 min. Peptides were purified using the PreOmics® iST method as described in the iST Sample Preparation Kit protocol (v.4.0; PreOmics®) [50]. Eluted peptides were dried by vacuum centrifugation for storage at −20 °C, then reconstituted in 50 µL LC-LOAD at 20 °C and 500 rpm for 5 min prior to LC–MS analysis.

#### 3.4.2.2 Urea with SPE (and iST)

A 50 mg aliquot of brain was lysed in 8 M urea, 100 mM triethylammonium bicarbonate (TEAB) pH 8.5, using a Precellys® 24 Touch homogeniser (Bertin Technologies) for three cycles of 30 s at 5,500 rpm (Sections B.2.1.2 and B.2.1.3; Tables B.2 and B.3). The sample was placed on ice between cycles to reduce heating. Proteins were further denatured at 20 °C and 1,000 rpm for 30 min in an Eppendorf ThermoMixer® C (Thermo Fisher Scientific). Cys reduction and alkylation were performed at 20 °C and 1,000 rpm for 30 min with 10 mM tris(2-carboxyethyl)phosphine (TCEP) and 50 mM iodoacetamide (IAA), respectively. The urea concentration was diluted to 1.5 M with 50 mM TEAB pH 8.5. Digestion was performed with 1 µg trypsin (MS-grade, Promega) overnight at 37 °C and 1,250 rpm. The sample was acidified with TFA to 1% then clarified by centrifugation at 20 °C and 22,000 rcf for 10 min. Peptides were diluted 10-fold in 0.1% trifluoroacetic acid (TFA), 2% acetonitrile (ACN) then purified by SPE (SOLA™ SPE, Thermo Fisher Scientific). The sample was split: subsample A underwent no further clean-up, and eluted peptides were dried by vacuum centrifugation for storage at −20 °C, then reconstituted in 0.1% formic acid (FA), 3% ACN prior to LC–MS analysis. Subsample B was subjected to the PreOmics® iST method [50], and eluted peptides dried by vacuum centrifugation for storage at −20 °C, then reconstituted in 50 µL LC–LOAD at 20 °C and 500 rpm for 5 min prior to LC–MS analysis.

#### 3.4.2.3 Sodium laurate with SPE

A 50 mg aliquot of brain was lysed in 1% SL, 100 mM TEAB pH 8.5, using a Precellys® 24 Touch homogeniser (Bertin Technologies) for three cycles of 30 s at 5,500 rpm (Section B.2.1.4 and Table B.4). The sample was placed on ice between cycles to reduce heating. Proteins were further denatured in an ultrasonic bath at 4 °C for 10 min. Cys reduction and alkylation were performed at 20 °C without shaking for 30 min with 10 mM TCEP and 20 mM IAA, respectively. Digestion was performed with 1 µg trypsin (MS-grade, Promega) at 37 °C and 1,000 rpm for 3 h. The sample was acidified with TFA to 1% then clarified by centrifugation at 20 °C and 22,000 rcf for 5 min. To remove SL, a volume of ethyl acetate equal to the volume of supernatant was added and the sample centrifuged at 20 °C and 15,000 rcf for 10 min, before removal of the lower phase and repetition of this step. Peptides were diluted 10-fold in 0.1% TFA, 2% ACN then purified by SPE (SOLA™ SPE, Thermo Fisher Scientific). Eluted peptides were dried by vacuum centrifugation for storage at −20 °C, then reconstituted in 0.1% FA, 3% ACN prior to LC–MS analysis.

### 3.4.3 In-gel

#### 3.4.3.1 SDS–PAGE

A 50 mg aliquot of brain was lysed in 5% SDS, 100 mM TEAB pH 8.5, using a Precellys® 24 Touch homogeniser (Bertin Technologies) for three cycles of 30 s at 5,500 rpm (Section B.2.2.1 and Table B.5). The sample was placed on ice between cycles to reduce heating. NuPAGE™ LDS (4×) sample buffer (Invitrogen™, Thermo Fisher Scientific) was added with 200 mM dithiothreitol (DTT) to a final concentration of 50 mM, before incubating at 20 °C and 2,000 rpm for 1 h. The sample was loaded into six lanes of a 1 mm NuPAGE™ Bis-Tris gel, mounted in a Mini Gel Tank and loaded with NuPAGE™ MES SDS (20×) running buffer (all Invitrogen™, Thermo Fisher Scientific). The gel was run at 120 V for 10 min before removal and staining with InstantBlue™ dye (Sigma–Aldrich). Each gel lane was excised into approximately 1 $mm^2$ cubes and combined, before submersion in 5% acetic acid at 20 °C and 1,000 rpm overnight in an Eppendorf ThermoMixer® C

(Thermo Fisher Scientific). Cys reduction was performed with 10 mM DTT at 20 °C without shaking for 30 min, followed by alkylation with 50 mM IAA at 20 °C without shaking for 30 min. The gel pieces were dehydrated with ACN at 20 °C and rehydrated with 100 mM ammonium bicarbonate at 20 °C prior to digestion, which was performed with 1 µg trypsin (MS-grade, Promega) in 50 mM ambic overnight at 37 °C without shaking. Peptides were eluted with 5% FA, 50–85% ACN, dried by vacuum centrifugation for storage at −20 °C, then reconstituted in 0.1% FA, 3% ACN prior to LC–MS analysis.

### 3.4.4 On-filter

#### 3.4.4.1 PreOmics® BeatBox with S-Trap™ micro

A 50 mg aliquot of brain was lysed in 5% SDS reducing buffer, 10 mM TCEP and 100 mM TEAB pH 8.5, using BeatBox sonication (PreOmics®) for 10 cycles of 30 s (Section B.2.3.1 and Table B.6). Cys alkylation was performed with 20 mM IAA at 20 °C without shaking for 30 min. The sample was acidified with phosphoric acid to 1.2% concentration, and loaded onto an S-Trap™ micro (Protifi, Biosys Technologies, Inc.). Digestion was performed on-filter in 50 mM TEAB pH 8.5 with 1 µg trypsin (MS-grade, Promega) overnight at 37 °C without shaking. The sample was eluted sequentially with 50 mM TEAB pH 8.5, 0.2% FA, then 0.2% FA, 50% ACN. Eluted peptides were dried by vacuum centrifugation for storage at −20 °C, then reconstituted in 0.1% FA, 3% ACN prior to LC–MS analysis.

#### 3.4.4.2 SDS with S-Trap™ micro

A 50 mg aliquot of brain was lysed in 5% SDS reducing buffer, 10 mM TCEP and 100 mM TEAB pH 8.5, using a Precellys® 24 Touch homogeniser (Bertin Technologies) for three cycles of 30 s at 5,500 rpm (Section B.2.3.2 and Table B.7). The sample was placed on ice between cycles to reduce heating. Cys alkylation was performed with 20 mM IAA at 20 °C without shaking for 30 min. The sample was acidified with phosphoric acid to 1.2% concentration, and loaded onto an

S-Trap™ micro (Protifi, Biosys Technologies, Inc.). Digestion was performed on-filter in 50 mM TEAB pH 8.5 with 1 µg trypsin (MS-grade, Promega) overnight at 37 °C without shaking. The sample was eluted sequentially with 50 mM TEAB pH 8.5, 0.2% FA, then 0.2% FA, 50% ACN. Eluted peptides were dried by vacuum centrifugation for storage at −20 °C, then reconstituted in 0.1% FA, 3% ACN prior to LC–MS analysis.

#### 3.4.4.3 Urea with FASP

A 50 mg aliquot of brain was lysed in 8 M urea, 100 mM TEAB pH 8.5, using a Precellys® 24 Touch homogeniser (Bertin Technologies) for three cycles of 30 s at 5,500 rpm (Section B.2.3.3 and Table B.8). The sample was placed on ice between cycles to reduce heating. The sample was filtered with a Sartorius Vivacon™ 500 30 kDa molecular-weight cut-off (MWCO) filter (Thermo Fisher Scientific), centrifuged at 20 °C and 14,300 rcf for 10 min. Cys reduction and alkylation were performed with 10 mM TCEP and 50 mM IAA respectively, on-filter in 8 M urea, 100 mM TEAB pH 8.5 at 20 °C without shaking for 30 min. The filter was washed three times with 50 mM TEAB pH 8.5, and digestion performed with 1 µg trypsin (MS-grade, Promega) overnight at 37 °C without shaking. Peptides were eluted with dilution in 0.1% TFA and three cycles of centrifugation at 20 °C and 14,300 rcf for 10 min. Eluted peptides were dried by vacuum centrifugation for storage at −20 °C, then reconstituted in 0.1% FA, 3% ACN prior to LC–MS analysis.

#### 3.4.4.4 SDS with FASP

A 50 mg aliquot of brain was lysed in 5% SDS, 100 mM TEAB pH 8.5, using a Precellys® 24 Touch homogeniser (Bertin Technologies) for three cycles of 30 s at 5,500 rpm (Section B.2.3.4 and Table B.9). The sample was placed on ice between cycles to reduce heating. The sample was filtered with a Sartorius Vivacon™ 500 30 kDa MWCO filter (Thermo Fisher Scientific), centrifuged at 20 °C and 14,300 rcf for 10 min. Cys reduction and alkylation were performed with 10 mM TCEP and 50 mM IAA respectively, on-filter in 8 M urea, 100 mM TEAB pH 8.5 at 20 °C without shaking for 30 min. The filter was washed three times with 50 mM TEAB

pH 8.5, and digestion performed with 1 µg trypsin (MS-grade, Promega) overnight at 37 °C without shaking. Peptides were eluted with dilution in 0.1% TFA and three cycles of centrifugation at 20 °C and 14,300 rcf for 10 min. Eluted peptides were dried by vacuum centrifugation for storage at −20 °C, then reconstituted in 0.1% FA, 3% ACN prior to LC–MS analysis.

### 3.4.5 On-bead

#### 3.4.5.1 SP3

A 50 mg aliquot of brain was lysed in 0.5% SDS using a Precellys® 24 Touch homogeniser (Bertin Technologies) for three cycles of 30 s at 5,500 rpm (Section B.2.4.1 and Table B.10). The sample was placed on ice between cycles to reduce heating. Cys reduction was performed with 5 mM DTT at 20 °C without shaking for 30 min, followed by alkylation with 20 mM IAA at 20 °C without shaking for 30 min. The sample was combined with 3 µL of SP3 beads (1:1 hydrophobic:hydrophilic) and ACN added to a final concentration of 70%, before mixing at 20 °C and 1,000 rpm for 18 min. The sample was placed on a magnetic rack and the beads allowed to settle for 2 min, before being washed three times with 100% ACN. Beads were resuspended in 50 mM TEAB pH 8.5 and digestion performed with 1 µg trypsin (MS-grade, Promega) overnight at 37 °C and 1,000 rpm. The sample was acidified with TFA to 1% and eluted peptides were dried by vacuum centrifugation for storage at −20 °C, then reconstituted in 0.1% FA, 3% ACN prior to LC–MS analysis.

### 3.4.6 Data acquisition

LC–FAIMS–MS/MS was performed on a Vanquish Neo UHPLC coupled to an Orbitrap™ Ascend Tribrid™ mass spectrometer equipped with a FAIMS Pro Duo interface (all Thermo Fisher Scientific). This system was benchmarked against a Hela cell lysate to ensure optimal performance. The Vanquish Neo was operated in 'Trap and Elute' mode, using a PepMap™ Neo Trap Cartridge (5 mm × 300 µm) and EASY-Spray™ PepMap™ Neo UHPLC Column (50 cm × 75 µm, 1,500 bar; both Thermo Fisher Scientific). Tryptic peptides were trapped and separated with a

60 min linear gradient; from 2% to 18% buffer B (0.1% FA in ACN) in buffer A (0.1% FA in $H_2O$) over 40 min, from 18% to 35% B over 20 min, and from 35% to 99% B over 15 min at 300 nL/min flow rate.

In DDA mode, MS1 spectra were acquired in the Orbitrap™ at 120K resolution between 38–1500 $m/z$, with an automatic gain control (AGC) target of $4 \times 10^5$ ions, a maximum injection time of 251 ms, radio frequency (RF) lens array at 30%, and advanced peak determination toggled on. Precursor ions were fragmented using high energy collisional dissociation with 30% normalised collision energy (NCE). MS2 spectra were acquired in the ion trap with rapid scan mode, a quad isolation window of 1.2 $m/z$, an AGC target of $5 \times 10^3$ ions, and a maximum injection time of 50 ms. The FAIMS Pro Duo was operated at standard resolution with a carrier gas flow rate of 3.8 L/min and cycling through two CVs (−40 V and −55 V), with 1 s/CV. In DIA mode, MS1 spectra were acquired in the Orbitrap™ at 45K resolution between 350–1650 $m/z$, with an AGC target of $5 \times 10^5$ ions, a maximum injection time of 91 ms, and RF lens array at 30%. MS2 spectra were acquired using the tMSn scan function at 30K resolution over 40 scan windows (with variable isolation width) covering the full 350–1650 $m/z$ range, with an AGC target of $4 \times 10^6$ ions, an automatic maximum injection time, and 30% NCE. The FAIMS source was operated at standard resolution with a carrier gas flow rate of 3.8 L/min, and CV of −45 V.

### 3.4.7 Data analysis

Eight searches of all LC–FAIMS–MS/MS raw data files acquired in DDA ($n = 10$) and DIA mode ($n = 10$) were conducted using a range of software packages for protein identification and quantification (Table B.11). In all cases, data were searched against the human brain proteome with semi-specific tryptic digestion and up to three missed cleavages allowed [51], with the following modifications: carbamidomethylation of Cys (fixed), N-terminal acetylation (variable), oxidation of Met and Pro (variable), and deamidation of Asn, Gln and Arg (variable). The human brain proteome was retrieved by downloading all protein-coding genes detected in the human brain ($n = 15,331$) from the Human Protein Atlas (v.23.0,

accessed 15.02.2024) [20], and converting Ensembl identifiers to UniProt accession numbers using the UniProt ID mapping tool (v.2024.01) [52]. Having removed duplicates, the remaining proteins ($n = 15,049$) were downloaded as a FASTA file.

A search of DDA data based on *in silico* FASTA digest with LFQ and match-between-runs (MBR) in MaxQuant (v.2.4.3.0) [49] yielded the fewest unique proteins identified at 1% FDR but the most information in terms of protein modification, and all further analyses of DDA data were performed on this dataset using the R programming language (v.2024.04.2) [53]. Global peptide and protein lists were removed of potential contaminants, reversed identifications, and identifications with $< 2$ unique peptides, then filtered for $q$-value and PEP $\leq .01$. Modified specific and dependent peptide lists were removed of unannotated modifications and those corresponding to $< 2$ unique peptides, then filtered for $q$-value and PEP $\leq .05$.

Spectral library search of DIA data based on library-free generation with DIA-NN (v.1.9) [47] yielded the most confident identifications at 1% FDR (mean global $Q$-value: $2.7 \times 10^{-3}$), and all further analyses of DIA data were conducted on this dataset. DIA data were preprocessed using the R package `DIAgui` (v.1.4.2) [54], which implements the `iq` package (v.1.9.12) [55] for calculating proteome-wide LFQ by delayed normalisation and maximal peptide ratio extraction (*aka.* MaxLFQ) [56], and the `imputeLCMD` package for left-centred missing data imputation [57]. Precursors were filtered using the following parameters: precursor $q$-value $\leq .01$, protein group $q$-value $\leq .01$, and protein and gene-group $q$-values $\leq 1$. Peptides and protein groups were filtered with the same parameters. iBAQ was performed on protein groups [58]: data were $\log_2$-transformed to normalise the data range, and missing data imputed using quantile regression imputation of left-censored data (QRILC) [59]. A $z$-score transformation on samples was subsequently performed to enable comparison of proteomic profiles across protocols: this approach standardises the data for each protocol by giving each sample a mean of 0 and a standard deviation (SD) of 1 across all proteins [60].

GRand AVerage of hydropathY (GRAVY) scores were calculated using the Kyte–Doolittle hydrophobicity scale [61], and the average pI using Isoelectric Point

Calculator (IPC) 2.0 [62]. Both measures were calculated at the protein-level for the subset of proteins identified in all protocols ($n = 98$), and at the peptide-level for peptides corresponding to these proteins recovered by each protocol. This 'common proteome' allowed for a comparison in terms of the relative hydropathy of recovered peptides corresponding to these proteins against a shared pool. Statistical testing was performed to probe significant differences between methods: the data failed a Shapiro–Wilk test for normality ($W[10] = .984$, $p = 2.5 \times 10^{-2}$) and Levene's test for homogeneity of variance ($F[10] = 6.93$, $p = 7.6 \times 10^{-11}$). Given the data is not independent (all protocols having been conducted on the same biopsy), and given the inequality of proteome size across protocols, a linear mixed-effects model with Satterthwaite *t*-tests ($n = 10$) and *post hoc* pairwise comparison using Bonferroni correction at 95% CI was developed for both GRAVY and pI scores, using the R packages `lme4` (v.1.1.35.5) [63] and `emmeans` (v.1.10.3) [64]. It should be noted that any statistically significant differences must be treated with caution given that, due to the irreplaceable nature of archaeological material, we were unable to perform replicate extractions (Section 3.5.3).

Over- and under-representation (i.e., the difference between the number of observed *vs.* expected proteins) was investigated at the protein class level using a Fisher's exact test and Bonferroni correction with the Protein ANalysis THrough Evolutionary Relationships (PANTHER) classification system (v.19.0) [65]. Gene Ontology (GO) functional enrichment analysis was also performed in PANTHER using a Fisher's exact test and Bonferroni correction, to investigate enrichment in cellular components [66]. Finally, levels of common laboratory contamination were assessed using Skyline (v.24.1) [67] to extract features from raw LC–FAIMS–MS/MS data corresponding to potential targets in the Molecular Contaminant List [68], and extracted ion chromatograms processed using the `HowDirty` R package (v.0.2.1) [69].

## 3.5 Results

### 3.5.1 Benchmarking protocol performance with ion mobility spectrometry

While the number of unique proteins varied with the search strategy used (Figure B.1a), employing a FAIMS source increased protein detection by an average of 39.0% for DIA and 26.4% for DDA regardless of the search strategy, with a CV of −45 V yielding the most identifications (510 *vs.* −40 V: 487; Figure B.1b). Total numbers of proteotypic precursors, peptides and proteins recovered with each protocol in DIA are summarised in the Supplementary (Table B.13), and the total numbers of unique proteins and overlap in proteomic profiles illustrated in Figure 3.2. The best-performing protocols in terms of protein recovery were the PreOmics® BeatBox iST ($n = 1,205$) followed by urea with FASP ($n = 1,157$), which also yielded the highest numbers of proteins recovered exclusively by one method ($n = 111$ and 59 respectively). To the best of our knowledge, these represent the largest and most diverse palaeoproteomes identified in any archaeological material investigated to-date. SP3 yielded the fewest total proteins ($n = 104$), with less than a third as many identifications as SL with SPE ($n = 339$). Given the overall effectiveness of urea-based methods, we latterly tested SP3 following urea extraction, but this did not improve protein recovery appreciably ($n = 139$). While more than half of identifications (53.7%, $n = 797/1{,}483$) were common to the best-performing methods, less than one-quarter (23.0%, $n = 121/525$) were shared by the worst-performing. Statistical over-representation testing for protein class of this common subset (Table B.13) indicated statistically significant enrichment by almost 30-fold of tubulins (fold enrichment [FE]: 26.68, $p = .03$) and intermediate filaments (24.19, $p = .003$). GO functional enrichment analysis suggested that the majority of protocols (80.0%, $n = 8/10$) enriched first and foremost for cytoskeletal fibres such as these (Supplementary Data S1); however, urea-based protocols enriched principally for the mitochondrial ATP synthase complex (e.g., with SPE: 7.11, $p = .008$; with FASP: 6.58, $p = .01$).

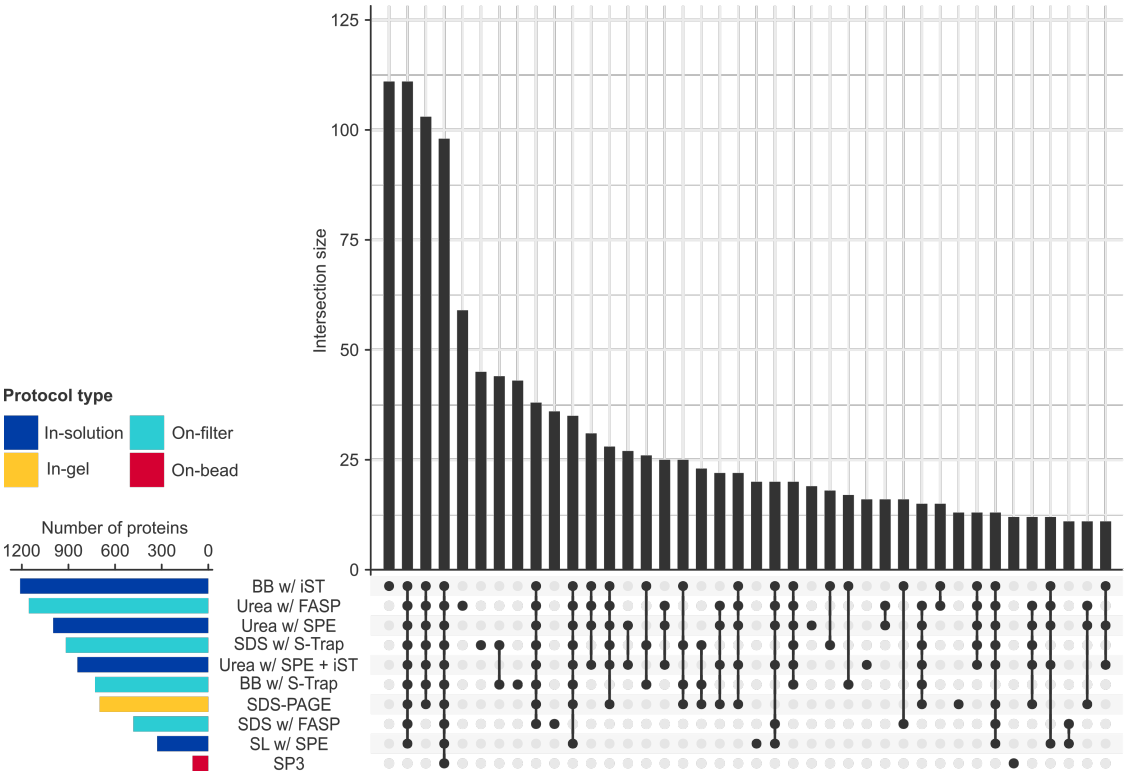



**Figure 3.2 | Total numbers of proteins retrieved with each protocol.** Upset plot of the number of unique proteins at 1% FDR and $q$-value $\leq .01$ recovered by each protocol (*bottom left*), and the number (*top*) and nature (*bottom right*) of intersections in the data.

Unsupervised hierarchical clustering of iBAQ by protocol (Figure 3.3a) illustrated the range of protein recovery; particularly, the extent of missing data with SP3, for which 94.5% ($n = 1,973/1,087$) of proteins had a $z$-score $< 0$ (i.e., below average for the dataset), compared with the highest intensities yielded by urea with FASP, for which almost the same proportion (93.2%, $n = 1,945/2,087$) had a $z$-score $> 0$ (i.e., above average for the dataset). Correlation analysis with hierarchical clustering (Figure 3.3b) revealed only positive correlations (i.e., $\rho > 0$) between protocols, suggesting the identification and quantification of overlapping proteomic data, albeit with varying degrees of similarity. While direct reproducibility assessments were not performed, the observed correlations suggested that protocols sharing an extraction buffer or clean-up method yield comparable iBAQ intensities, preserving protein relative abundance proportions. For instance, the strongest correlations were observed between urea extraction on-filter and in-solution (FASP with SPE:$\rho = .796$, $p < .001$; FASP with SPE + iST: $\rho = .778$, $p < .001$), followed

by clean-up with S-Trap, regardless of extraction buffer ($\rho = 0.744$, $p < .001$). In contrast, weak correlation between divergent protocols (e.g., SL with SPE *vs.* BeatBox with S-Trap: $\rho = .037$, $p < .005$) suggested disparities in quantification, potentially due to differences in protein denaturation, solubility, digestion, or purification. Multidimensional scaling (Figure 3.3c) corroborated these trends with the emergence of two clusters. The first pertains largely to what might be considered 'high-performance' protocols ($\gtrsim 1,000$ protein identifications, exceeding the upper quartile for the dataset [$n = 984$ proteins]), which share either urea extraction or iST clean-up; while the second pertains largely to 'mid-performance' protocols (500–1,000 identifications, encompassing the median for the dataset [$n = 790$]), which share SDS extraction. 'Low-performance' protocols ($\lesssim 500$ identifications, below the lower quartile for the dataset [$n = 530$]) appear as outliers in Cartesian space.

Average missed tryptic cleavages and MS1/MS2 signal ratios may be tentatively used as gauges of digestion and fragmentation efficiency respectively (Figure 3.4a and b). On-filter clean-up methods with S-Trap evidenced among the lowest average missed cleavages (e.g., with SDS: 0.12) but the highest MS1/MS2 signal ratios (with SDS: 1.57), which suggest that, while proteolysis was relatively complete, fragmentation was not. The reverse pattern was observed for on-filter clean-up methods with FASP, which featured among the highest missed cleavages (e.g., with SDS: 0.18) and the lowest MS1/MS2 signal ratios (with SDS: 1.15). Mean sequence coverage across all protocols was relatively low ($< 5\%$; Figure 3.4c), as expected for ancient proteins. The highest median coverage was obtained by extraction using urea (with FASP: 4.20%; with SPE + iST: 4.05%). BeatBox with S-Trap, although a mid-performance protocol in terms of protein recovery ($n = 735$ identifications), yielded the lowest median (0.00%) and mean (2.22%) coverage, alongside SP3 (median: 0.00%; mean: 2.27%).

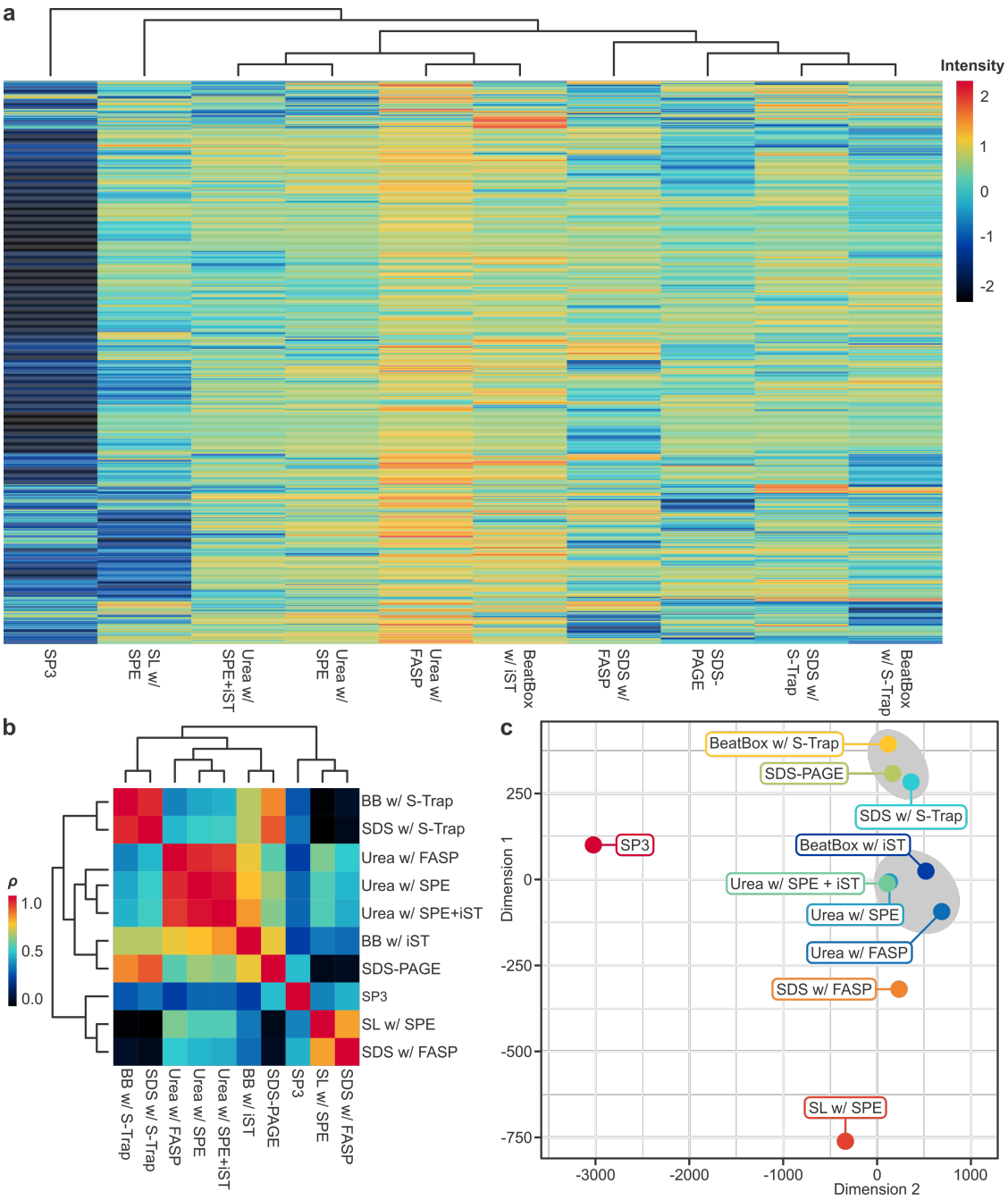



**Figure 3.3 | Unsupervised data clustering and multivariate ordination analyses. (a)** Heat map with hierarchically clustered dendrograms of iBAQ by protocol. iBAQ data were $\log_2$-transformed and missing data imputed using QRILC, before a $z$-score transformation on samples was applied. Each row represents a recovered protein ($n = 2,087$) clustered by Manhattan distance with complete linkage (dendrograms not shown), and each column a protocol clustered by Euclidean distance. **(b)** Pearson's correlation coefficient ($\rho$) matrix with hierarchically clustered dendrograms of iBAQ by protocol. As a normalised measure of covariance, $\rho$ has a value between –1 (perfect negative correlation) and 1 (perfect positive correlation); however, note the restricted range illustrated (0.0–1.0), reflecting the fact that only positive correlations exist between protocols in our dataset. **(c)** Metric multidimensional scaling plot with Manhattan distance of iBAQ data by protocol. The distance between data points in two-dimensional Cartesian space correlates with the dissimilarity between those points. Grey circles delineate clusters.

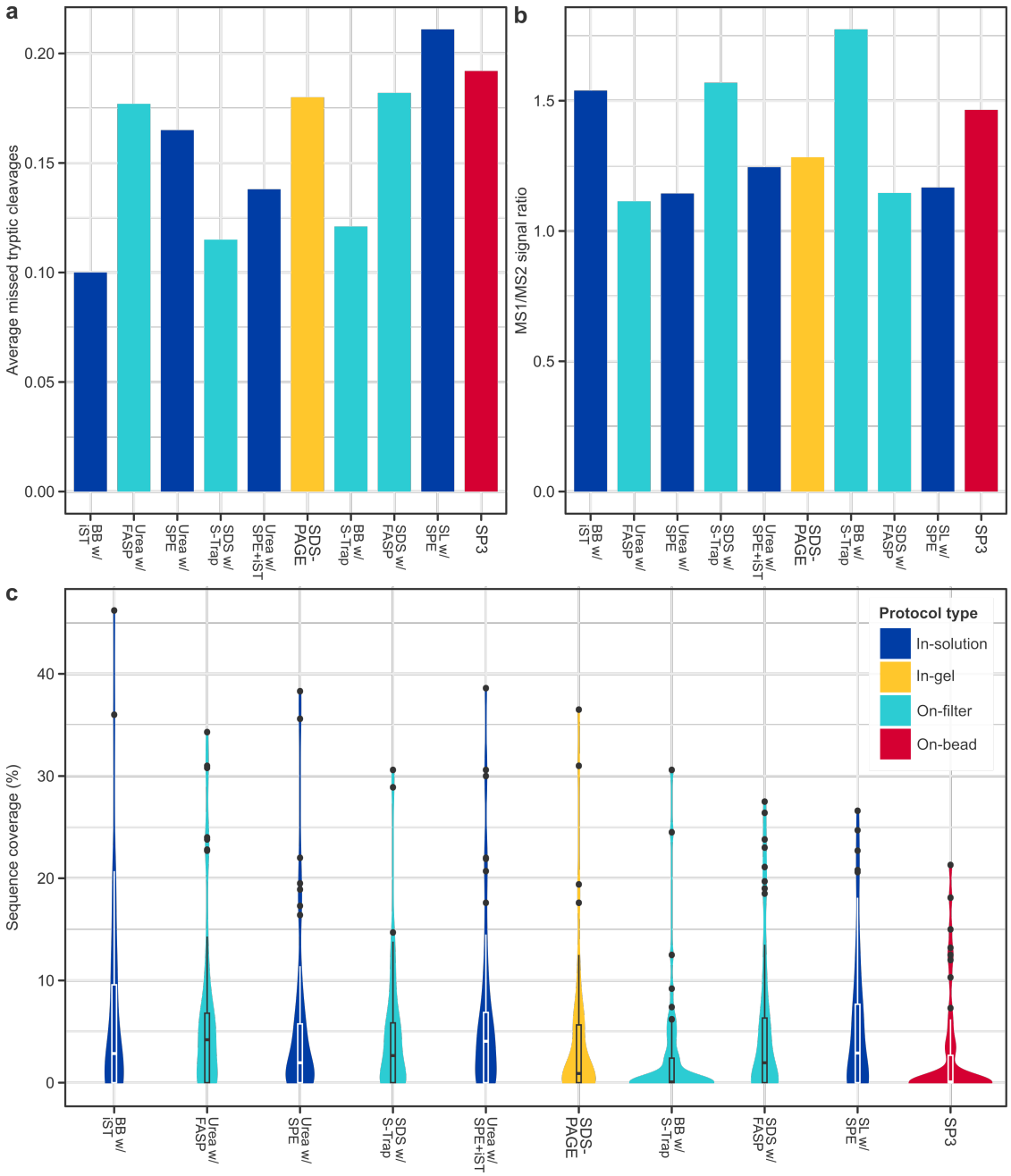



**Figure 3.4 | Measures of extraction efficiency.** Bar charts of the **(a)** average missed tryptic cleavages and **(b)** MS1/MS2 signal ratios by protocol, gauges of digestion and fragmentation, respectively. **(c)** Violin plots of the range of sequence coverage of unique proteins identified at 1% FDR and $q$-value $\leq .01$, retrieved by each protocol. Boxplots indicate the median and upper and lower quartiles, and black dots represent statistical outliers. Colours are consistent across panels, and in each panel protocols are ordered by (*left to right*) highest to lowest total proteins.

### 3.5.2 Identifying biases in modification, hydropathy, isoelectric point, and contamination

During diagenesis (the period after death and burial), ancient proteins are progressively degraded by hydrolysis and modified by deamidation (so-called, 'diagenetic PTMs'). DDA data was analysed to assess the extent of tryptic *vs.* non-tryptic peptide identification (i.e., the extent of diagenetic peptide bond cleavage), and the nature and extent of protein modification. Approximately two-thirds of the dataset comprised tryptic peptides, being cleaved C-terminal to either Lys (33.4%, $n = 194/580$) or Arg (32.8%, $n = 190/580$); of the remaining non-tryptic third, the most common cleavage sites were C-terminal to aliphatic Leu (5.2%, $n = 30/580$) and aromatic Phe (4.5%, $n = 26/580$). More than half of all non-tryptic peptides (53.6%, $n = 105/196$) corresponded to myelin proteolipid protein (Figure B.2), with the myelin protein class more than 40-fold enriched (FE: 43.85, $p = 7.7 \times 10^{-3}$). SDS with S-Trap and urea with FASP yielded the highest numbers of non-tryptic peptides ($n = 73$ and 67 respectively), while BeatBox with iST yielded the fewest ($n = 29$) after SP3 ($n = 21$), despite being the best-performing protocol in terms of protein recovery.

The nature and extent of deamidation – a common diagenetic PTM to ancient proteins, but also potentially induced during sample preparation – was assessed for both endogenous and contaminant peptides (Figure 3.5). In contrast to mid- and high-performance protocols, low-performance protocols evidenced greater proportions of deamidated contaminants than endogenous peptides (e.g., SP3: 42.4% *vs.* 15.5%). On average, approximately half of deamidated sites in endogenous peptides affected Asn (51.4%), approximately one-third Gln (30.2%), and approximately one-fifth Arg (18.3%). Functional enrichment analysis suggested that deamidation of Arg disproportionately affected cellular components associated with the myelin sheath (strength: 2.0; $p = 4.5 \times 10^{-6}$). In addition to PTMs explicitly searched for, a dependent peptide search identified $> 200$ annotated modifications to $\geq 2$ peptides (Figure 3.6 and table B.14), of which the most frequent were loss of water ($n = 14$), acetaldehyde adduct formation ($n = 11$), and metal-catalysed oxidation ($n = 8$).

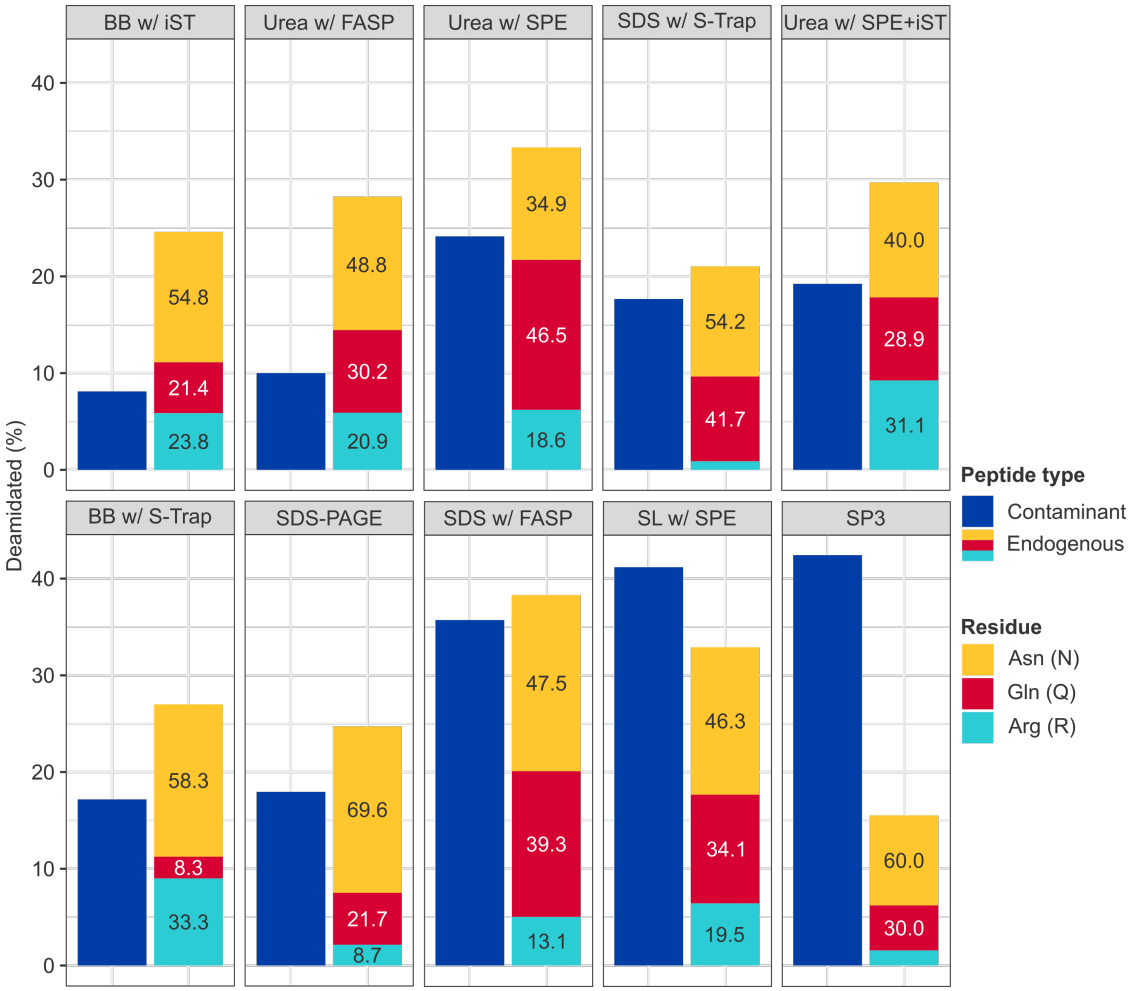



**Figure 3.5 | Nature and extent of deamidation.** Percentage of deamidated contaminant (*left*) and endogenous (*right*) peptides at 1% FDR and $q$-value $\leq .05$ by protocol (*left to right*, highest to lowest total proteins). Endogenous peptides are coloured by the affected amino acid, with numbers indicating the percentage each type of deamidation represents of the total.

Statistical testing revealed significant differences in peptide hydropathy between protocols (Figures 3.7 and 3.8). GRAVY scores were calculated for the entire brain proteome ($n = 15,049$; mean [SD]: –0.382 [0.392]) and for all peptides retrieved across the experiment. While only 13.0% of the total brain proteome is hydrophobic, an average of 39.6% [0.06] of recovered peptides were hydrophobic, suggesting a preferential preservation of hydrophobic domains. In contrast, peptides corresponding to proteins identified by all protocols exhibited lower-than-expected mean hydropathy values, indicating that more hydrophilic domains were preferentially retrieved (Table B.15). However, only the low-performance protocol, SDS with FASP, showed a statistically significant deviation (–0.600 [0.863], $p = 8.1 \times 10^{-3}$;

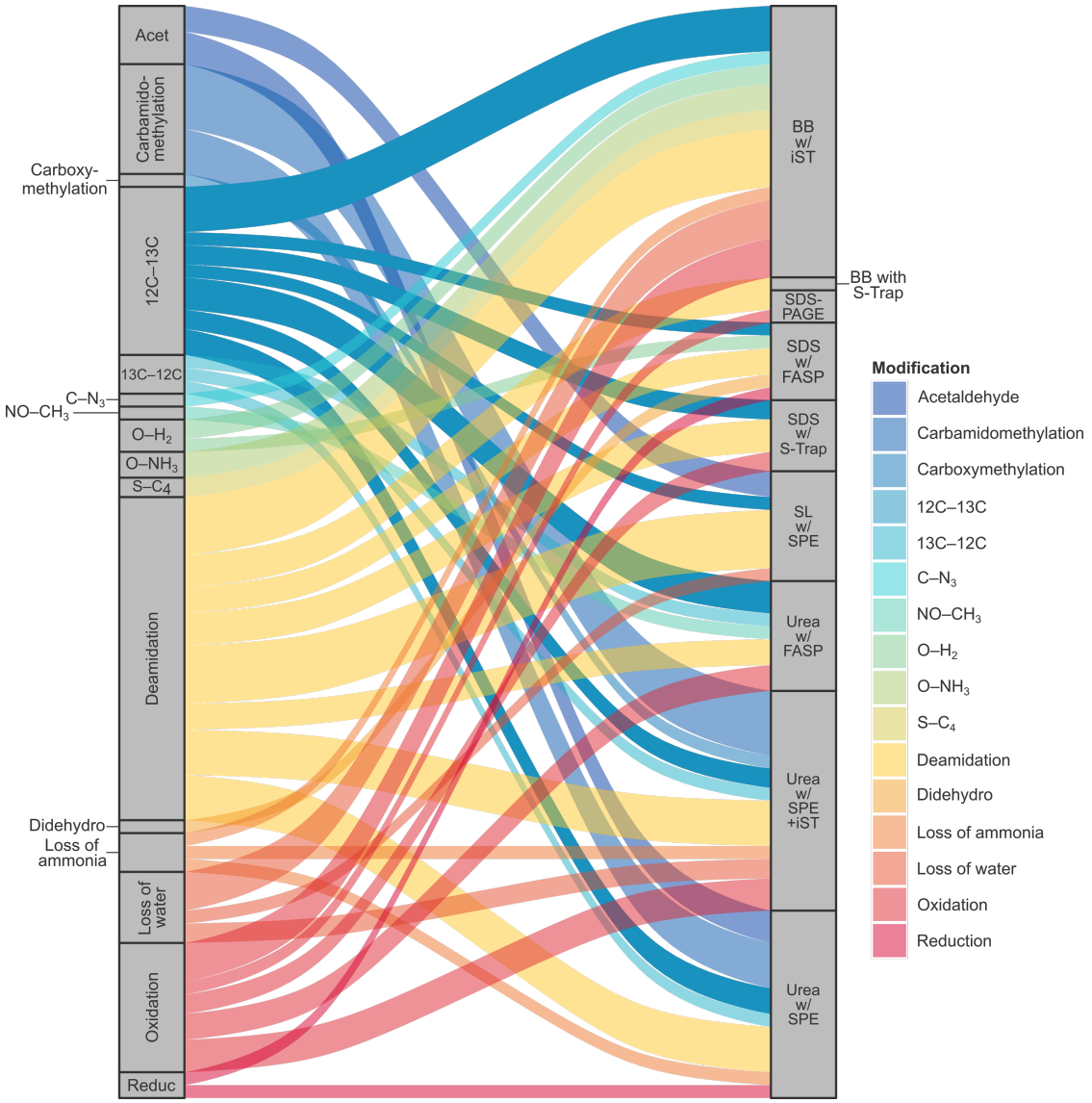



**Figure 3.6 | Discovery of covalent modifications.** Alluvial diagram of modifications (*left*) to ≥ 2 unique peptides per protocol (*right*), identified by dependent peptide search. SP3 is not shown, since no identifications met the ≥ 2 unique peptides threshold.

Table B.16), and 90% ($n = 9/10$) of significant pairwise comparisons involved SDS with FASP, suggesting it was an outlier in this regard. Meanwhile, urea-based in-solution methods exhibited the most positive estimated effect ($E$) on GRAVY scores, indicating that they extracted relatively more hydrophobic peptides than other reagents or clean-up strategies (e.g., urea with SPE + iST *vs.* SL: $E = 0.196$, $p = 3.4 \times 10^{-2}$).

Analogous statistical testing of the average pI revealed that, like hydropathy, pI of retrieved peptides was lower than expected for the common pool (Figures 3.9

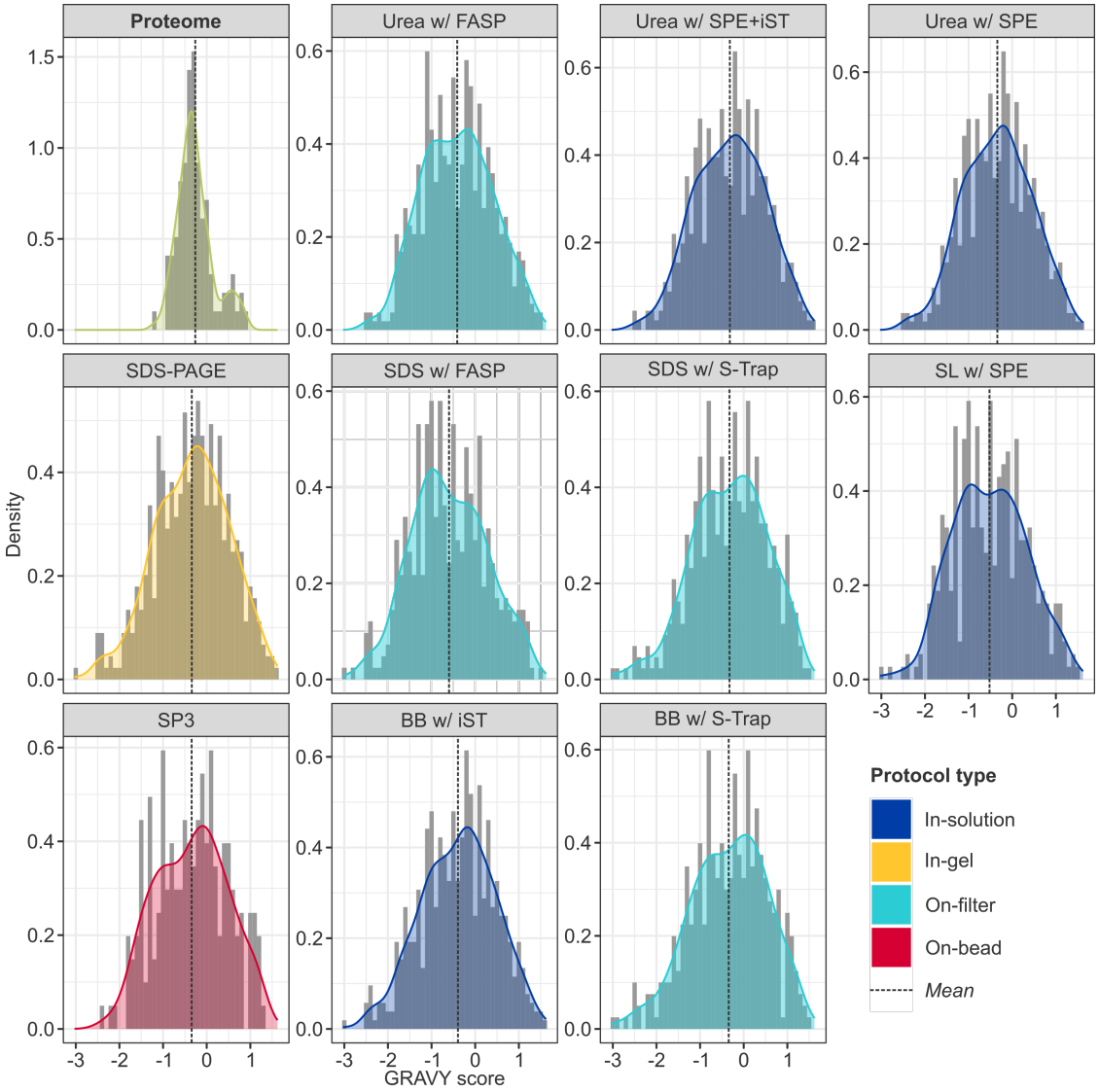



**Figure 3.7 | Distribution of GRAVY scores by protocol.** Distribution of GRAVY scores calculated at the protein-level for proteins retrieved in all protocols (the 'common proteome', *green*), and at the peptide-level for proteins recovered by each protocol, with smoothed density curves. Given the variability in sample sizes, data has been normalised to reflect relative frequency rather than absolute counts (note the differing *y*-axes) and facilitate visual pairwise comparison of extraction buffers (broadly, horizontal rows; e.g., urea, *top*) and clean-up strategies (broadly, vertical columns; e.g., SPE, *right*). Dashed lines reflect the mean GRAVY score: a higher score indicates more hydrophobic peptides, and a lower score more hydrophilic peptides.

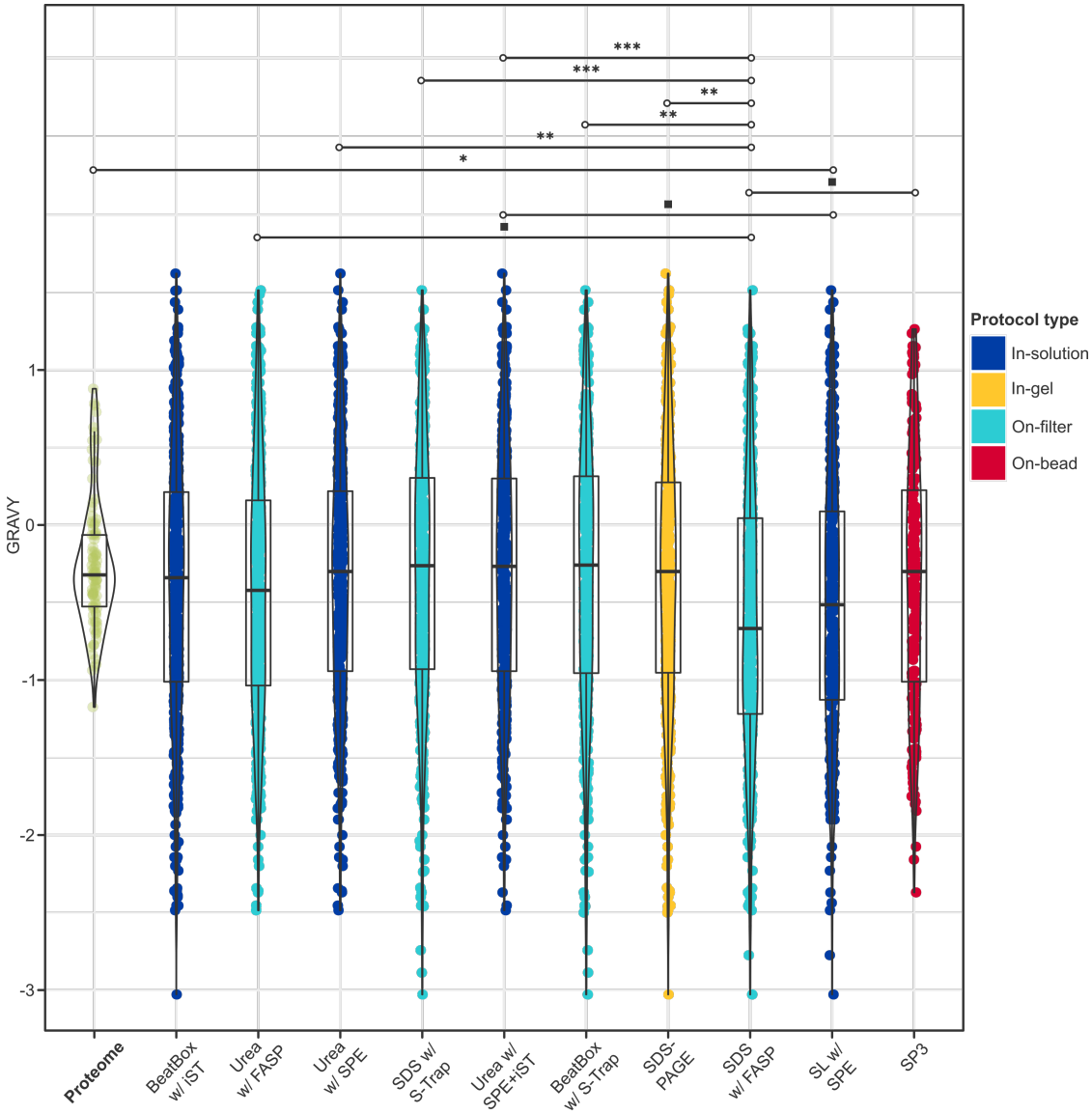



**Figure 3.8 | Hydropathic profiles retrieved with each protocol.** Results of a linear mixed effects model with Satterthwaite $t$-tests ($n_{obs}$= 4,383) and *post hoc* pairwise comparisons ($n$ = 55) with Bonferroni correction at 95% CI with respect to GRAVY score, calculated at the protein-level for proteins retrieved in all protocols (the 'common proteome', *green*), and at the peptide-level for proteins recovered by each protocol (*left to right*, highest to lowest total proteins). A higher GRAVY score indicates more hydrophobic peptides, and a lower score more hydrophilic peptides. Only statistically significant comparisons are shown (for all other comparisons, see Table B.16), and indicated by the following significance codes: $***$ = $p$-value < .0001; $**$ = $p$-value ≤ .001; $*$ = $p$-value ≤ .01; ■ = $p$-value ≤ .05.

and 3.10), suggesting that more acidic peptides were preferentially retrieved. This relationship was statistically significant for all in-solution protocols (e.g., urea with SPE + iST: $p = 3.0 \times 10^{-4}$), and for on-filter methods with FASP (e.g., urea with FASP: $p = 8.1 \times 10^{-3}$; Tables B.17 and B.18). Although the common proteome exhibited the expected bimodal distribution in pI for a eukaryotic proteome [70], a shift toward lower values was apparent: while the major peak associated with cytoplasmic proteins occurred as expected at $\sim 5.0$, the major peak corresponding to integral membrane proteins was shifted from $\sim 8.5$ to $\sim 7.5$ [71]. By contrast, all protocols evidenced a distinct trimodal distribution, with major peaks at $\sim 4.5$ and 6.5, and a minor peak at $\sim$ 9.0, in descending order of density (with the exception of BeatBox with S-Trap, whose peak at $\sim 6.5$ marginally exceeded that at $\sim 4.5$; 0.266 *vs.* 0.248). Corresponding to nuclear proteins [72], this minor peak evidenced the greatest density in urea-based protocols (e.g., urea with SPE: 0.080), corroborating the observation of GO functional enrichment for the mitochondrial compartment with this lysis buffer.

Common laboratory contaminants identified with associated risk levels are illustrated in Figure 3.11a. Global risk level was 'very low' (1) in nine of ten protocols, and 'low' (2) in BeatBox with S-Trap. Kit-based protocols (i.e., those involving BeatBox and/or iST technology) evidenced a higher abundance of more diverse contaminants, particularly anionic surfactants such as Triton, Tween, and IGEPAL-630/NP40. Polyethylene glycol (PEG) was the most abundant contaminant detected at risk level $\geq 4$ (i.e., 'high' or 'very high') in all samples, posing the greatest risk in the SDS with FASP and urea with SPE + iST protocols. However, no patterns could be discerned in terms of the abundance of PEG contamination and the use of particular extraction buffers or clean-up methods (Figure 3.11b); nor with the frequency of heating, vortexing, shaking, centrifugation, sonication, or homogenisation steps.

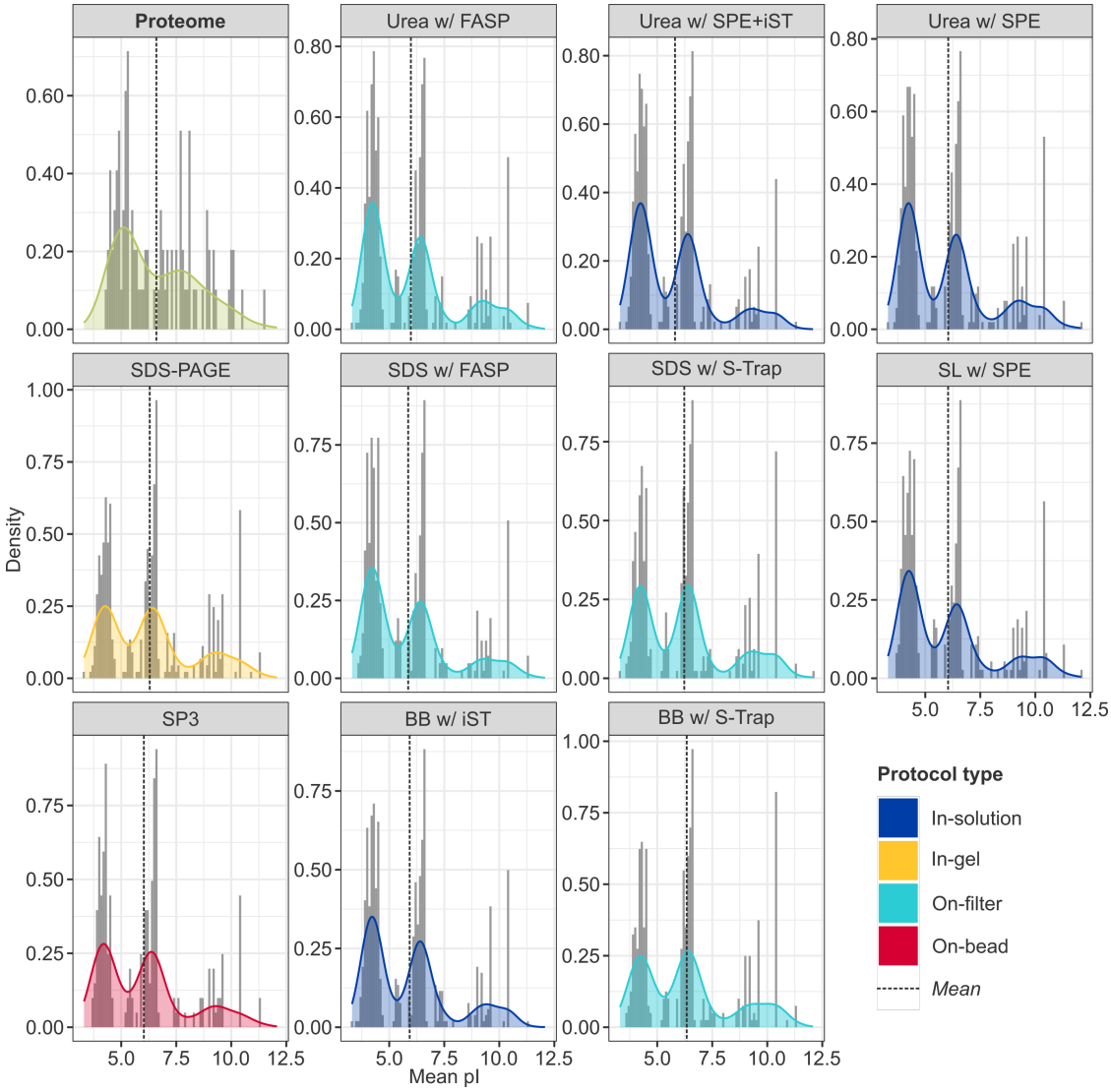



**Figure 3.9 | Distribution of isoelectric point by protocol.** Distribution of mean pI calculated at the protein-level for proteins retrieved in all protocols (the 'common proteome', *green*), and at the peptide-level for proteins recovered by each protocol, with smoothed density curves. Given the variability in sample sizes, data has been normalised to reflect relative frequency rather than absolute counts (note the differing *y*-axes) and facilitate visual pairwise comparison of extraction buffers (broadly, horizontal rows; e.g., urea, *top*) and clean-up strategies (broadly, vertical columns; e.g., SPE, *right*). Dashed lines reflect the mean pI: a higher value indicates more basic peptides, and a lower value more acidic peptides.

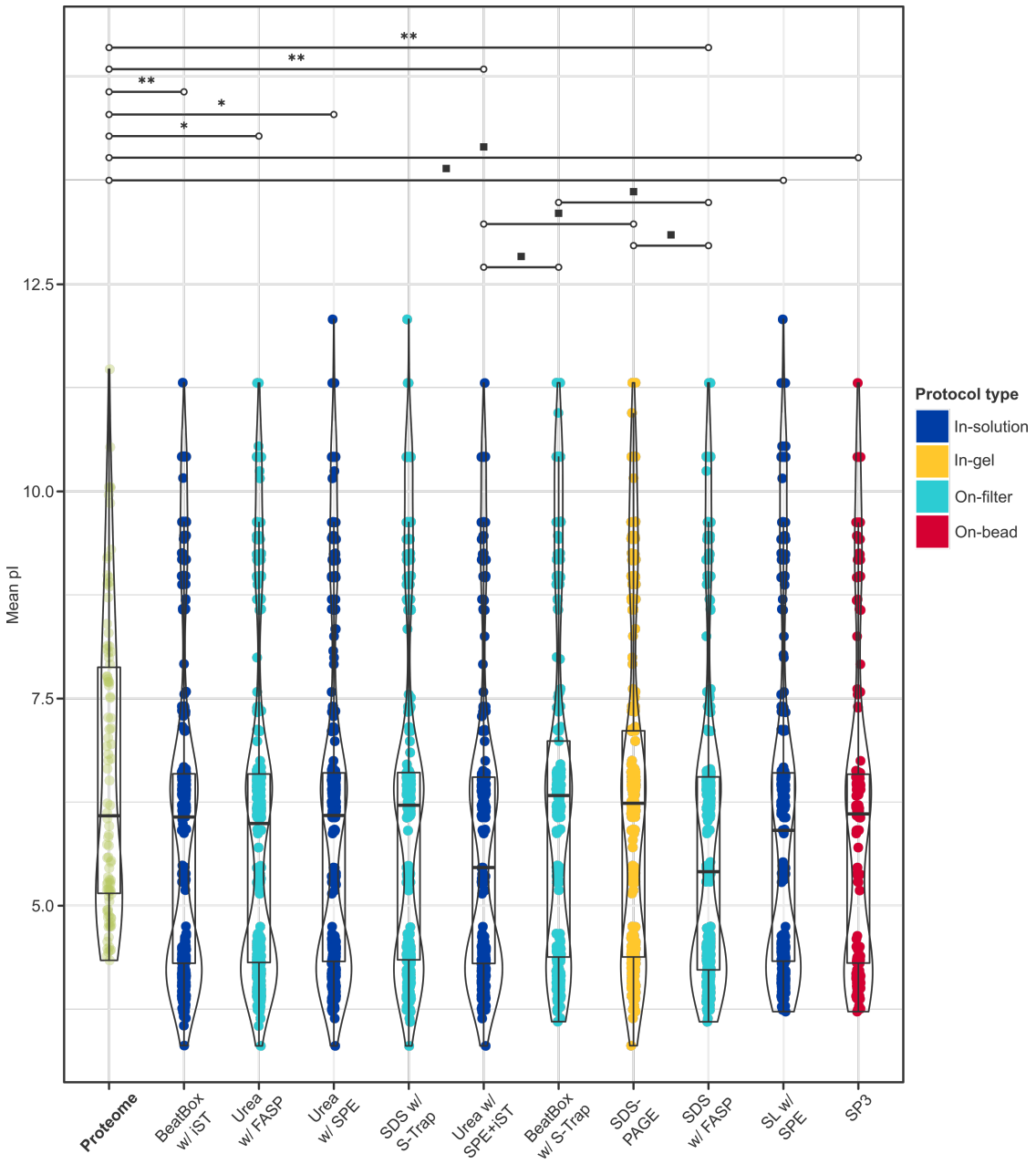



**Figure 3.10 | Isoelectric profiles retrieved with each protocol.** Results of a linear mixed effects model with Satterthwaite $t$-tests ($n_{obs}$= 4,383) and *post hoc* pairwise comparisons ($n$ = 55) with Bonferroni correction at 95% CI with respect to mean pI, calculated at the protein-level for proteins retrieved in all protocols (the 'common proteome', *green*), and at the peptide-level for proteins recovered by each protocol (*left to right*, highest to lowest total proteins). A higher mean pI indicates more basic peptides, and a lower mean pI more acidic peptides. Only statistically significant comparisons are shown (for all other comparisons, see Table B.18), and indicated by the following significance codes: $***$ = $p$-value < .0001; $**$ = $p$-value $\leq$ .001; $*$ = $p$-value $\leq$ .01; ■ = $p$-value $\leq$ .05.

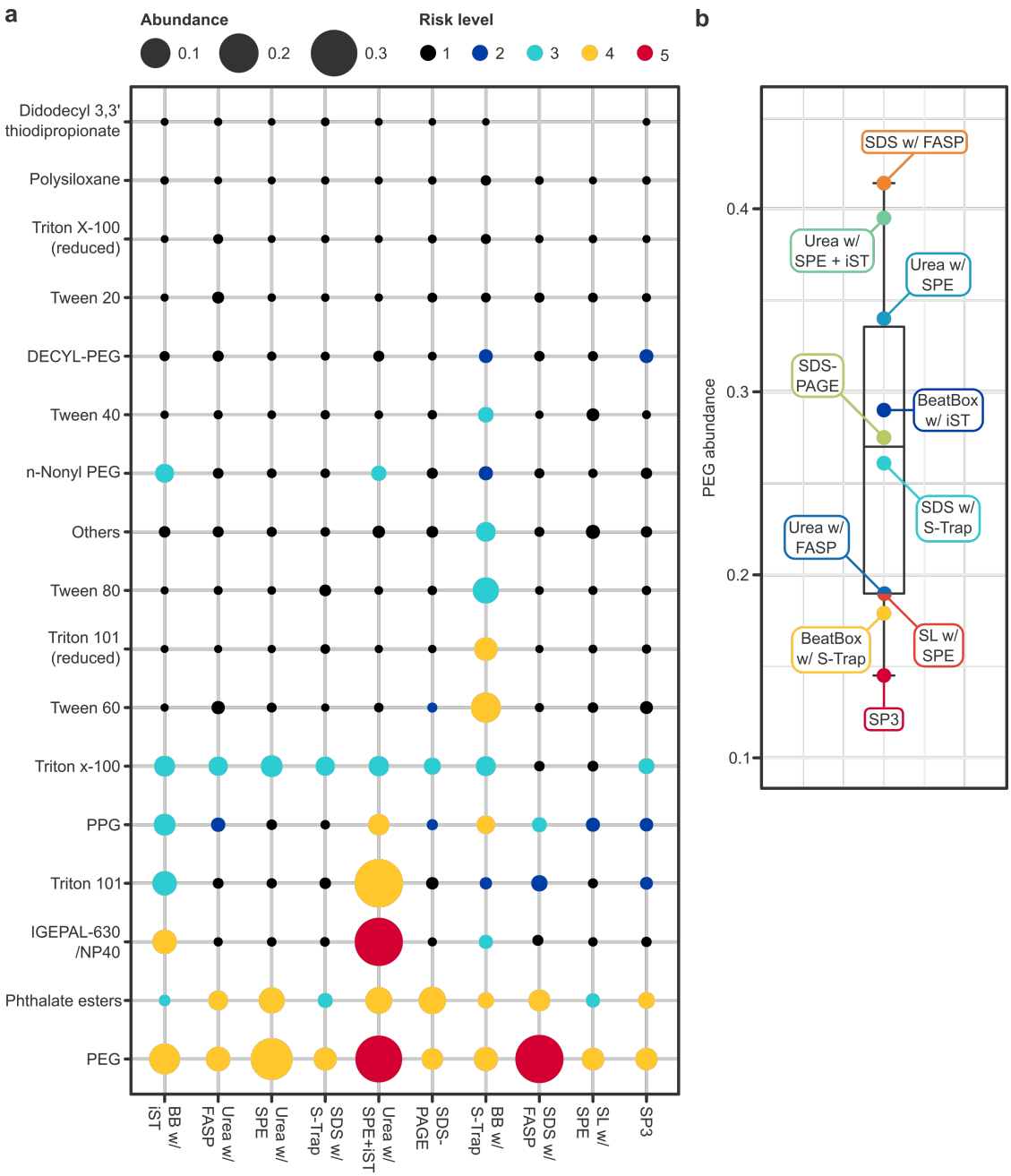



**Figure 3.11 | Abundance of common laboratory contaminants.** **(a)** Dotplot of contaminants ($y$-axis) identified by protocol ($x$-axis; *left to right*, highest to lowest total proteins). Point size indicates total abundance and point colour indicates risk level, which are designated very high (5), high (4), medium (3), low (2) and very low (1). **(b)** Boxplot of PEG abundance by protocol.

### 3.5.3 Limitations

Our study was conducted on 10 equal-sized subsamples from a single brain biopsy. Given the destructive nature of the analysis and irreplaceable nature of the material, we elected not to perform replicate extractions: this decision is in line with ethical considerations regarding the treatment of human remains in archaeology, which stipulate a reduced program of sampling for proof-of-concept studies where the feasibility and/or applicability of a method may be questionable [73, 74]. Our approach minimised biological variability and provided the internal consistency necessary to ensure that we could effectively compare the efficacy and efficiency of the tested protocols; however, we were unable to assess technical variability. Building on this proof-of-concept study, further work should incorporate both biological and technical replicates to test the generalisability of our findings to a broader population and context.

## 3.6 Discussion

Only a fraction of the *in vivo* proteome is expected to persist in the archaeological record, and those proteins that survive diagenesis to be extracted, analysed and identified are generally mineralised, highly abundant, and/or possess particular structural features [75]. In this work, we address the absence of a sensitive and specific protocol in palaeoproteomics for non-mineralised tissues. We assessed the efficacy, efficiency and suitability of extraction buffers and clean-up strategies with varied chemistries using archaeological human brain, and describe an optimised LC–FAIMS–MS/MS workflow yielding the largest, most diverse palaeoproteome recovered from any archaeological or fossil material to-date. Further, although 50 mg starting material was employed for extraction, just 5% was injected into the LC–MS platform; demonstrating that even smaller amounts of tissue could be sufficient for deep palaeoproteomic analysis.

We found that urea-based methods (both in-solution and on-filter) proved the most effective and efficient overall, evidencing low contamination and high numbers

of protein identifications with relatively high intensities and sequence coverage. In addition, our results suggested that urea-based methods facilitated the recovery of a broader range of peptides, thereby providing greater access to the full diversity of the palaeoproteome: specifically, a greater proportion of non-tryptic and hydrophobic peptides corresponding to membrane proteins, which are more abundant in soft than hard tissues [20]. A chaotropic agent, urea denatures proteins by disrupting non-covalent interactions (such as hydrogen bonds and van der Waals forces), decreasing the net hydrophobic effect of hydrophobic regions and forcing unfolded proteins into solution. This same action destabilises lipid bilayers (compromising membrane integrity and liberating intracellular components) and protein aggregates, which accumulate in aged organs like the brain [76], heart [77], and kidneys [78], and which have previously been identified in preserved soft tissues [79]. Indeed, with the exception of SDS–PAGE, urea-based methods were the only to enrich primarily for recovery of the intracellular mitochondrial ATP synthase complex, a critical component of energy production in soft tissues [80], which possess metabolic rates many times that of mineralised tissues [81]. While further work will be required to confirm its suitability for a wider range of samples (Section 3.5.3), urea lysis is likely to be more effective for archaeological soft tissues than those used conventionally in palaeoproteomics for mineralised tissues, such as weak acids or chelating agents [13].

Across the experiment, we identified preferential preservation of hydrophobic proteins, but retrieval of relatively acidic (low-pI) peptides. Protein extraction is strongly influenced by hydropathic and isoelectric behaviour, both of which govern solubility [82]; it is likely that molecular decomposition follows similar principles. During soft-tissue decay, the breakdown of proteins and other biomolecules generates acidic byproducts – such as lactic acid, fatty acids, and negatively charged amino acids like Asp and Glu – which lower the pH of the surrounding tissue [83]. Under these conditions, hydrophobic proteins, being largely insoluble, are more likely to persist than their hydrophilic counterparts, as their tendency to precipitate and aggregate dominates in all but the most alkaline environments [84]. Consequently, hydrophobic components are notoriously challenging to solubilise and extract [85, 86].

While this alone may explain the observed bias toward more soluble, low-pI peptides in our dataset, our pI analyses suggest an additional influence. Proteome-wide distribution studies of pI [70, 71, 87] reveal an 'acidic shoulder' (pI $\sim$ 4.75) adjacent to the major acidic peak, which is attributed to an over-representation of low-pI cytoplasmic and extracellular proteins [70]. Cytoskeletal proteins, in particular, are extremely acid-biased, with a clear low-pI shift and trimodal distribution, in contrast to the bimodal distribution observed in cytoplasmic proteins from the same subcellular compartment [70]. This difference is thought to arise from the polymeric nature of cytoskeletal proteins, which precludes true solubility [70] (although progressive changes in solubility have been noted *post-mortem* [88, 89]). In our dataset, which features an over-representation of cytoskeletal proteins, the major peak aligns with this acidic shoulder, suggesting that these recalcitrant fibres contribute to both the preservation and retrieval biases observed.

In step with current best practices in palaeoproteomics [5, 7], our study employed stringent search parameters – such as requiring $> 2$ unique peptides for an identification – to ensure the authenticity of ancient proteins. This stipulation works well for archaeological tissues like bone, skin and hair, where contamination with modern collagens and keratins (which it is essential to minimise but difficult to eliminate [7]) risks misclassifying exogenous peptides as ancient [90]. However, it is likely that for archaeological internal organs, where the risk of a false-positive of this nature is much lower, this stringency leads to more false negatives: that is, discarding genuine identifications that may be better authenticated by other means (e.g., use of post-processing classifiers).

Beyond the risk of false negatives, a greater concern is that genuine identifications may be missed altogether if (semi-)tryptic peptides from digested proteins compete with highly degraded, non-tryptic peptides or contaminants for fragmentation and ionisation. In this respect, the sensitivity of the MS system employed is crucial: the Orbitrap™ Ascend features a number of improvements to the Tribrid™ architecture (including a second ion-routing multipole, which permits parallel ion injection) that together increase the scan speed and sensitivity of the instrument, producing a

greater number of higher-quality tandem mass spectra [91]. However, this enhanced sensitivity could also elevate chemical noise, particularly if smaller and/or degraded molecules – such as lipids, metabolites, or other non-peptide contaminants – are transmitted more efficiently into the mass spectrometer.

To address these challenges, we found that LC–FAIMS–MS/MS improves unique protein identification by up to 40%, and represents an effective means of 'cleaning' dirty archaeological samples, regardless of the extraction buffer or clean-up strategy used upstream. By filtering out singly charged ions associated with chemical noise, FAIMS both improved the signal-to-noise ratio in complex samples and enabled the detection of low-abundant analytes that would otherwise have been masked, overlapping in mass-to-charge with interfering ions. Moreover, we demonstrate that FAIMS is a highly tuneable technique: because CVs can be optimised to select for ions with specific mobility characteristics, it is likely to be broadly useful for improving protein recovery not only from a range of ancient tissues, but even from a range of depositional environments. Given $> 90\%$ of fragment ion spectra from ancient samples fail to be assigned [92], further work in optimising collision energies – or indeed, precursory separation by LC – is expected to help tackle this problem for palaeoproteomics, particularly if coupled with FAIMS.

In sum, this study aimed to identify a suitable method for extracting ancient proteins from soft tissues, maximising the amount of biological information recoverable, and laying the groundwork for future research. As this method generates increasingly large datasets, optimising their management and analysis presents a new and exciting challenge for palaeoproteomics.

## 3.7 Acknowledgements

We are grateful to Sharon Clough and Trish Biers for access to samples. We thank members of the Discovery Proteomics Facility, and the Kessler and Fischer groups at the Target Discovery Institute for useful discussions and support. AMH was supported by the Natural Environment Research Council (NE/S007474/1).

## 3.8 References


[1] Liz Allen et al. 'Publishing: Credit where credit is due'. In: *Nature* 508 (7496 17th Apr. 2014), pp. 312–313. DOI: 10.1038/508312a.

[2] Beatrice Demarchi et al. 'Protein sequences bound to mineral surfaces persist into deep time'. In: *Elife* 5 (27th Sept. 2016), e17092. DOI: 10.7554/eLife.17092.

[3] Suryendu Dutta et al. 'Chemical evidence of preserved collagen in 54-million-year-old fish vertebrae'. In: *Palaeontology* 63 (2 Mar. 2020), pp. 195–202. DOI: 10.1111/pala.12469.

[4] Tyede H Schmidt-Schultz, Mike Reich and Michael Schultz. 'Exceptionally preserved extracellular bone matrix proteins from the late Neogene proboscidean Anancus (Mammalia: Proboscidea)'. In: *Palaontol. Z.* 95 (4 Dec. 2021), pp. 757–765. DOI: 10.1007/s12542-021-00566-7.

[5] Christina Warinner, Kristine Korzow Richter and Matthew J Collins. 'Paleoproteomics'. In: *Chem. Rev.* 122 (16 24th Aug. 2022), pp. 13401–13446. DOI: 10.1021/acs.chemrev.1c00703.

[6] Frido Welker. 'Palaeoproteomics for human evolution studies'. In: *Quat. Sci. Rev.* 190 (June 2018), pp. 137–147. DOI: 10.1016/j.quascirev.2018.04.033.

[7] Jessica Hendy et al. 'A guide to ancient protein studies'. In: *Nat. Ecol. Evol.* 2 (5 May 2018), pp. 791–799. DOI: 10.1038/s41559-018-0510-x.

[8] Leigh A Weston, Kerry M Bauer and Amanda B Hummon. 'Comparison of bottom-up proteomic approaches for LC-MS analysis of complex proteomes'. In: *Anal. Methods* 5 (18 21st Sept. 2013), p. 4615. DOI: 10.1039/C3AY40853A.

[9] Ileana R León et al. 'Quantitative assessment of in-solution digestion efficiency identifies optimal protocols for unbiased protein analysis'. In: *Mol. Cell. Proteomics* 12 (10 1st Oct. 2013), pp. 2992–3005. DOI: 10.1074/mcp.M112.025585.

[10] Zora Brough, Zhiyu Zhao and Franck Duong van Hoa. 'From bottom-up to cell surface proteomics: detergents or no detergents, that is the question'. In: *Biochem. Soc. Trans.* 52 (3 26th June 2024), pp. 1253–1263. DOI: 10.1042/BST20231020.

[11] Raman Umamaheswaran and Suryendu Dutta. 'Preservation of proteins in the geosphere'. In: *Nat. Ecol. Evol.* 8 (5 May 2024), pp. 858–865. DOI: 10.1038/s41559-024-02366-z.

[12] Liam T Lanigan et al. 'Multi-protease analysis of Pleistocene bone proteomes'. In: *J. Proteomics* 228 (103889 30th Sept. 2020), p. 103889. DOI: 10.1016/j.jprot.2020.103889.

[13] Dorothea Mylopotamitaki et al. 'Comparing extraction method efficiency for high-throughput palaeoproteomic bone species identification'. In: *Sci. Rep.* 13 (1 26th Oct. 2023), p. 18345. DOI: 10.1038/s41598-023-44885-y.

[14] Shevan Wilkin et al. 'Sequential trypsin and ProAlanase digestions unearth immunological protein biomarkers shrouded by skeletal collagen'. In: *iScience* 27 (5 17th May 2024), p. 109663. DOI: 10.1016/j.isci.2024.109663.

[15] Luise Ørsted Brandt et al. 'Palaeoproteomics identifies beaver fur in Danish high-status Viking Age burials - direct evidence of fur trade'. In: *PLoS One* 17 (7 27th July 2022), e0270040. DOI: 10.1371/journal.pone.0270040.

[16] Jannie Amsgaard Ebsen et al. 'Identifying archaeological leather – discussing the potential of grain pattern analysis and zooarchaeology by mass spectrometry (ZooMS) through a case study involving medieval shoe parts from Denmark'. In: *J. Cult. Herit.* 39 (Sept. 2019), pp. 21–31. DOI: 10.1016/j.culher.2019.04.008.

[17] Beatrice Demarchi et al. 'Never boring: Non-invasive palaeoproteomics of mummified human skin'. In: *J. Archaeol. Sci.* 119 (105145 July 2020), p. 105145. DOI: 10.1016/j.jas.2020.105145.

[18] Luise Ørsted Brandt et al. 'Human and animal skin identified by palaeoproteomics in Scythian leather objects from Ukraine'. In: *PLoS One* 18 (12 13th Dec. 2023), e0294129. DOI: 10.1371/journal.pone.0294129.

[19] Tobias Fretwurst et al. 'Proteomic profiling of human bone from different anatomical sites - A pilot study'. In: *Proteomics Clin. Appl.* 16 (5 1st Sept. 2022), e2100049. DOI: 10.1002/prca.202100049.

[20] Mathias Uhlén et al. 'Proteomics. Tissue-based map of the human proteome'. In: *Science* 347 (6220 23rd Jan. 2015), p. 1260419. DOI: 10.1126/science.1260419.

[21] Axel Petzold et al. 'Protein aggregate formation permits millennium-old brain preservation'. In: *J. R. Soc. Interface* 17 (162 Jan. 2020), p. 20190775. DOI: 10.1098/rsif.2019.0775.

[22] Lena M Öhrström et al. 'Radiological findings in an ancient Iranian salt mummy (Chehrābād ca. 410-350 BC)'. In: *Skeletal Radiol.* 44 (6 June 2015), pp. 811–821. DOI: 10.1007/s00256-015-2103-y.

[23] Dan Chen et al. 'Autopsy and forensic study on a rare human corpse preserved over two thousand years: The Mawangdui ancient cadaver'. In: *Biopreserv. Biobank.* 17 (2 Apr. 2019), pp. 105–112. DOI: 10.1089/bio.2019.0001.

[24] Raffaella Bianucci et al. 'Forensic analysis reveals acute decompensation of chronic heart failure in a 3500-year-old Egyptian dignitary'. In: *J. Forensic Sci.* 61 (5 Sept. 2016), pp. 1378–1381. DOI: 10.1111/1556-4029.13138.

[25] Stephanie Panzer et al. 'Evidence of neurofibromatosis type 1 in a multi-morbid Inca child mummy: A paleoradiological investigation using computed tomography'. In: *PLoS One* 12 (4 12th Apr. 2017), e0175000. DOI: 10.1371/journal.pone.0175000.

[26] Stephanie Panzer, Albert R Zink and Dario Piombino-Mascali. 'Scenes from the past: Radiologic evidence of anthropogenic mummification in the Capuchin catacombs of Palermo, Sicily'. In: *Radiographics* 30 (4 July 2010), pp. 1123–1132. DOI: 10.1148/rg.304095174.

[27] Tiina Väre et al. 'Computed tomography of mummified human remains in old Finnish churches, a case study: the mummified remains of a 17th-century vicar revisited'. In: *Postmediev. Archaeol.* 50 (2 3rd May 2016), pp. 368–379. DOI: 10.1080/00794236.2016.1151280.

[28] M J Kim et al. 'Medieval mummy from yangju'. In: *Archaeol. Ethnol. Anthr. Eurasia* 28 (1 Dec. 2006), pp. 122–129. DOI: 10.1134/s156301100604013x.

[29] Sangyeub Lee et al. 'Paleopathological analysis on bronchial washing fluid from a mummy: The "General Hak-Bong" mummy, Korea'. In: *Basic Appl. Pathol.* 1 (4 Dec. 2008), pp. 164–167. DOI: 10.1111/j.1755-9294.2008.00039.x.

[30] Stephanie Panzer et al. 'Reconstructing the life of an unknown (ca. 500 years-old South American Inca) mummy–multidisciplinary study of a Peruvian Inca mummy suggests severe Chagas disease and ritual homicide'. In: *PLoS One* 9 (2 26th Feb. 2014), e89528. DOI: 10.1371/journal.pone.0089528.

[31] Dario Piombino-Mascali et al. 'Atherosclerosis in mummified human remains from Vilnius, Lithuania (18th-19th centuries AD): a computed tomographic investigation: Atherosclerosis in Lithuanian Mummies'. In: *Am. J. Hum. Biol.* 26 (5 Sept. 2014), pp. 676–681. DOI: 10.1002/ajhb.22578.

[32] Alexandra L Morton-Hayward et al. 'Human brains preserve in diverse environments for at least 12 000 years'. In: *Proc. Biol. Sci.* 291 (2019 27th Mar. 2024), p. 20232606. DOI: 10.1098/rspb.2023.2606.

[33] Frank Maixner et al. 'Paleoproteomic study of the Iceman's brain tissue'. In: *Cell. Mol. Life Sci.* 70 (19 Oct. 2013), pp. 3709–3722. DOI: 10.1007/s00018-013-1360-y.

[34] O Vit and J Petrak. 'Integral membrane proteins in proteomics. How to break open the black box?' In: *J. Proteomics* 153 (5th Feb. 2017), pp. 8–20. DOI: 10.1016/j.jprot.2016.08.006.

[35] Dajana Vuckovic et al. 'Membrane proteomics by high performance liquid chromatography-tandem mass spectrometry: Analytical approaches and challenges'. In: *Proteomics* 13 (3-4 Feb. 2013), pp. 404–423. DOI: 10.1002/pmic.201200340.

[36] R M Garavito and S Ferguson-Miller. 'Detergents as tools in membrane biochemistry'. In: *J. Biol. Chem.* 276 (35 31st Aug. 2001), pp. 32403–32406. DOI: 10.1074/jbc.R100031200.

[37] Xi Zhang. 'Detergents: Friends not foes for high-performance membrane proteomics toward precision medicine'. In: *Proteomics* 17 (3-4 1st Feb. 2017), p. 1600209. DOI: 10.1002/pmic.201600209.

[38] Martial Rey et al. 'Effective removal of nonionic detergents in protein mass spectrometry, hydrogen/deuterium exchange, and proteomics'. In: *Anal. Chem.* 82 (12 15th June 2010), pp. 5107–5116. DOI: 10.1021/ac100171m.

[39] Peter Feist and Amanda B Hummon. 'Proteomic challenges: sample preparation techniques for microgram-quantity protein analysis from biological samples'. In: *Int. J. Mol. Sci.* 16 (2 5th Feb. 2015), pp. 3537–3563. DOI: 10.3390/ijms16023537.

[40] Mao Peng et al. 'Protease bias in absolute protein quantitation'. In: *Nat. Methods* 9 (6 30th May 2012), pp. 524–525. DOI: 10.1038/nmeth.2031.

[41] Timo Glatter, Erik Ahrné and Alexander Schmidt. 'Comparison of different sample preparation protocols reveals lysis buffer-specific extraction biases in gram-negative bacteria and human cells'. In: *J. Proteome Res.* 14 (11 6th Nov. 2015), pp. 4472–4485. DOI: 10.1021/acs.jproteome.5b00654.

[42] Frank Klont et al. 'Assessment of sample preparation bias in mass spectrometry-based proteomics'. In: *Anal. Chem.* 90 (8 17th Apr. 2018), pp. 5405–5413. DOI: 10.1021/acs.analchem.8b00600.

[43] Nils A Kulak et al. 'Minimal, encapsulated proteomic-sample processing applied to copy-number estimation in eukaryotic cells'. In: *Nat. Methods* 11 (3 Mar. 2014), pp. 319–324. DOI: 10.1038/nmeth.2834.

[44] Alexandre Zougman, Peter J Selby and Rosamonde E Banks. 'Suspension trapping (STrap) sample preparation method for bottom-up proteomics analysis'. In: *Proteomics* 14 (9 May 2014), pp. 1006–1000. DOI: 10.1002/pmic.201300553.

[45] Jacek R Wiśniewski et al. 'Universal sample preparation method for proteome analysis'. In: *Nat. Methods* 6 (5 May 2009), pp. 359–362. DOI: 10.1038/nmeth.1322.

[46] Christopher S Hughes et al. 'Single-pot, solid-phase-enhanced sample preparation for proteomics experiments'. In: *Nat. Protoc.* 14 (1 Jan. 2019), pp. 68–85. DOI: 10.1038/s41596-018-0082-x.

[47] Vadim Demichev et al. 'DIA-NN: neural networks and interference correction enable deep proteome coverage in high throughput'. In: *Nat. Methods* 17 (1 Jan. 2020), pp. 41–44. DOI: 10.1038/s41592-019-0638-x.

[48] Fengchao Yu et al. 'Analysis of DIA proteomics data using MSFragger-DIA and FragPipe computational platform'. In: *Nat. Commun.* 14 (1 12th July 2023), p. 4154. DOI: 10.1038/s41467-023-39869-5.

[49] Stefka Tyanova, Tikira Temu and Juergen Cox. 'The MaxQuant computational platform for mass spectrometry-based shotgun proteomics'. In: *Nat. Protoc.* 11 (12 Dec. 2016), pp. 2301–2319. DOI: 10.1038/nprot.2016.136.

[50] PreOmics. *iST Sample Preparation Kit 8x*. Version 4.0. 2025.

[51] Siri Hildonen, Trine Grønhaug Halvorsen and Léon Reubsaet. 'Why less is more when generating tryptic peptides in bottom-up proteomics'. In: *Proteomics* 14 (17-18 1st Sept. 2014), pp. 2031–2041. DOI: 10.1002/pmic.201300479.

[52] UniProt Consortium. 'UniProt: The universal protein knowledgebase in 2023'. In: *Nucleic Acids Res.* 51 (D1 6th Jan. 2023), pp. D523–D531. DOI: 10.1093/nar/gkac1052.

[53] R Core Team. *R: A language and environment for statistical computing*. Vienna, Austria: R Foundation for Statistical Computing, 2024.

[54] Marc-Antoine Gerault, Luc Camoin and Samuel Granjeaud. 'DIAgui: a Shiny application to process the output from DIA-NN'. In: *Bioinform. Adv.* 4 (1 13th Jan. 2024), vbae001. DOI: 10.1093/bioadv/vbae001.

[55] Thang V Pham, Alex A Henneman and Connie R Jimenez. 'iq: an R package to estimate relative protein abundances from ion quantification in DIA-MS-based proteomics'. In: *Bioinformatics* 36 (8 15th Apr. 2020), pp. 2611–2613. DOI: 10.1093/bioinformatics/btz961.

[56] Jürgen Cox et al. 'Accurate proteome-wide label-free quantification by delayed normalization and maximal peptide ratio extraction, termed MaxLFQ'. In: *Mol. Cell. Proteomics* 13 (9 Sept. 2014), pp. 2513–2526. DOI: 10.1074/mcp.M113.031591.

[57] Mingyi Liu and Ashok Dongre. 'Proper imputation of missing values in proteomics datasets for differential expression analysis'. In: *Brief. Bioinform.* 22 (3 20th May 2021), bbaa112. DOI: 10.1093/bib/bbaa112.

[58] Björn Schwanhäusser et al. 'Global quantification of mammalian gene expression control'. In: *Nature* 473 (7347 19th May 2011), pp. 337–342. DOI: 10.1038/nature10098.

[59] Cosmin Lazar et al. 'Accounting for the multiple natures of missing values in label-free quantitative proteomics data sets to compare imputation strategies'. In: *J. Proteome Res.* 15 (4 1st Apr. 2016), pp. 1116–1125. DOI: 10.1021/acs.jproteome.5b00981.

[60] Luis B Carvalho et al. 'Normalization methods in mass spectrometry-based analytical proteomics: A case study based on renal cell carcinoma datasets'. In: *Talanta* 266 (Pt 1 1st Jan. 2024), p. 124953. DOI: 10.1016/j.talanta.2023.124953.

[61] J Kyte and R F Doolittle. 'A simple method for displaying the hydropathic character of a protein'. In: *J. Mol. Biol.* 157 (1 5th May 1982), pp. 105–132. DOI: 10.1016/0022-2836(82)90515-0.

[62] Lukasz Pawel Kozlowski. 'IPC 2.0: prediction of isoelectric point and pKa dissociation constants'. In: *Nucleic Acids Res.* 49 (W1 2nd July 2021), W285–W292. DOI: 10.1093/nar/gkab295.

[63] Douglas Bates et al. 'Fitting linear mixed-effects models Usinglme4'. In: *J. Stat. Softw.* 67 (1 7th Oct. 2015), pp. 1–48. DOI: 10.18637/jss.v067.i01.

[64] Russell V Lenth. *Pers. comm.* 2024.

[65] Paul D Thomas et al. 'PANTHER: Making genome-scale phylogenetics accessible to all'. In: *Protein Sci.* 31 (1 Jan. 2022), pp. 8–22. DOI: 10.1002/pro.4218.

[66] M Ashburner et al. 'Gene ontology: tool for the unification of biology. The Gene Ontology Consortium'. In: *Nat. Genet.* 25 (1 May 2000), pp. 25–29. DOI: 10.1038/75556.

[67] Brendan MacLean et al. 'Skyline: an open source document editor for creating and analyzing targeted proteomics experiments'. In: *Bioinformatics* 26 (7 1st Apr. 2010), pp. 966–968. DOI: 10.1093/bioinformatics/btq054.

[68] Matthew J Rardin. 'Rapid assessment of contaminants and interferences in mass spectrometry data using Skyline'. In: *J. Am. Soc. Mass Spectrom.* 29 (6 17th June 2018), pp. 1327–1330. DOI: 10.1007/s13361-018-1940-z.

[69] David Gomez-Zepeda et al. 'HowDirty: An R package to evaluate molecular contaminants in LC-MS experiments'. In: *Proteomics* 24 (8 7th Apr. 2024), e2300134. DOI: 10.1002/pmic.202300134.

[70] Atsushi Kurotani et al. 'Localization-specific distributions of protein pI in human proteome are governed by local pH and membrane charge'. In: *BMC Mol. Cell Biol.* 20 (1 20th Aug. 2019), p. 36. DOI: 10.1186/s12860-019-0221-4.

[71] Alexander A Tokmakov, Atsushi Kurotani and Ken-Ichi Sato. 'Protein pI and intracellular localization'. In: *Front. Mol. Biosci.* 8 (29th Nov. 2021), p. 775736. DOI: 10.3389/fmolb.2021.775736.

[72] Russell Schwartz, Claire S Ting and Jonathan King. 'Whole proteome pI values correlate with subcellular localizations of proteins for organisms within the three domains of life'. In: *Genome Res.* 11 (5 1st May 2001), pp. 703–709. DOI: 10.1101/gr.158701.

[73] Simon Mays et al. 'Science and the Dead A guideline for the destructive sampling of archaeological human remains for scientifi c analysis'. In: (1st Jan. 2013).

[74] Kirsty Squires, Thomas Booth and Charlotte A Roberts. 'The ethics of sampling human skeletal remains for destructive analyses'. In: *Ethical Approaches to Human Remains*. Cham: Springer International Publishing, 2019, pp. 265–297. DOI: 10.1007/978-3-030-32926-6_12.

[75] Caroline Wadsworth and Mike Buckley. 'Proteome degradation in fossils: investigating the longevity of protein survival in ancient bone: Proteome degradation in fossils'. In: *Rapid Commun. Mass Spectrom.* 28 (6 30th Mar. 2014), pp. 605–615. DOI: 10.1002/rcm.6821.

[76] Itamar Harel et al. 'Identification of protein aggregates in the aging vertebrate brain with prion-like and phase-separation properties'. In: *Cell Rep.* 43 (6 25th June 2024), p. 112787. DOI: 10.1016/j.celrep.2023.112787.

[77] Rajeshwary Ghosh et al. 'Protein and mitochondria quality control mechanisms and cardiac aging'. In: *Cells* 9 (4 10th Apr. 2020), E933. DOI: 10.3390/cells9040933.

[78] Takeshi Yamamoto and Yoshitaka Isaka. 'Pathological mechanisms of kidney disease in ageing'. In: *Nat. Rev. Nephrol.* 20 (9 18th Sept. 2024), pp. 603–615. DOI: 10.1038/s41581-024-00868-4.

[79] Jasmina Wiemann et al. 'Fossilization transforms vertebrate hard tissue proteins into N-heterocyclic polymers'. In: *Nat. Commun.* 9 (1 9th Nov. 2018), p. 4741. DOI: 10.1038/s41467-018-07013-3.

[80] Kelsey L McLaughlin et al. 'Novel approach to quantify mitochondrial content and intrinsic bioenergetic efficiency across organs'. In: *Sci. Rep.* 10 (1 19th Oct. 2020), p. 17599. DOI: 10.1038/s41598-020-74718-1.

[81] Zimian Wang et al. 'Specific metabolic rates of major organs and tissues across adulthood: evaluation by mechanistic model of resting energy expenditure'. In: *Am. J. Clin. Nutr.* 92 (6 Dec. 2010), pp. 1369–1377. DOI: 10.3945/ajcn.2010.29885.

[82] T Arakawa and S N Timasheff. 'Theory of protein solubility'. In: *Methods Enzymol.* Methods in enzymology 114 (1st Jan. 1985), pp. 49–77. DOI: 10.1016/0076-6879(85)14005-x.

[83] Robert H Powers. 'The decomposition of human remains'. In: *Forensic Medicine of the Lower Extremity*. Totowa, NJ: Humana Press, 2005, pp. 3–15. DOI: 10.1385/1-59259-897-8:003.

[84] K A Dill. 'Dominant forces in protein folding'. In: *Biochemistry* 29 (31 7th Aug. 1990), pp. 7133–7155. DOI: 10.1021/bi00483a001.

[85] Andreas O Helbig, Albert J R Heck and Monique Slijper. 'Exploring the membrane proteome–challenges and analytical strategies'. In: *J. Proteomics* 73 (5 10th Mar. 2010), pp. 868–878. DOI: 10.1016/j.jprot.2010.01.005.

[86] Lutz A Eichacker et al. 'Hiding behind hydrophobicity. Transmembrane segments in mass spectrometry'. In: *J. Biol. Chem.* 279 (49 3rd Dec. 2004), pp. 50915–50922. DOI: 10.1074/jbc.M405875200.

[87] Songfeng Wu et al. 'Multi-modality of pI distribution in whole proteome'. In: *Proteomics* 6 (2 Jan. 2006), pp. 449–455. DOI: 10.1002/pmic.200500221.

[88] Zeinab ElHajj et al. 'Effects of postmortem delays on protein composition and oxidation'. In: *Brain Res. Bull.* 121 (Mar. 2016), pp. 98–104. DOI: 10.1016/j.brainresbull.2016.01.005.

[89] Margaret M Krassner et al. 'Postmortem changes in brain cell structure: a review'. In: *Free Neuropathol.* 4 (Jan. 2023), p. 10. DOI: 10.17879/freeneuropathology-2023-4790.

[90] Abigail Ramsøe et al. 'Assessing the degradation of ancient milk proteins through site-specific deamidation patterns'. In: *Sci. Rep.* 11 (1 8th Apr. 2021), p. 7795. DOI: 10.1038/s41598-021-87125-x.

[91] Yuchen He et al. 'Evaluation of the Orbitrap Ascend Tribrid mass spectrometer for shotgun proteomics'. In: *Anal. Chem.* 95 (28 18th July 2023), pp. 10655–10663. DOI: 10.1021/acs.analchem.3c01155.

[92] Yun Chiang, Frido Welker and Matthew James Collins. 'Spectra without stories: reporting 94% dark and unidentified ancient proteomes'. In: *Open Res. Eur.* 4 (15th Apr. 2024), p. 71. DOI: 10.12688/openreseurope.17225.1.

# 4

# Molecular Solution to the Paradox of Ancient Brain Preservation

Morton-Hayward, A.L., Flannery, S., Berry, P., Vendrell, I.,
Johansen, A., Hansen, M., & Fischer, R.
*Molecular Solution to the Paradox of Ancient Brain Preservation.*
**J. Proteome Res. 2026**, *25*(7): 6c00200.
doi.org/10.1021/acs.jproteome.6c00200

## 4.1 Author Contributions

**Table 4.1** | Summary of individual contributions to this chapter, described using the CRediT system [1].

| Author | Contribution |
|---|---|
| *Morton-Hayward, A.L.* | Study conception; Methodology; Computation; Formal analysis; Investigation: performed the experiments; Investigation: data/evidence collection; Resources; Data curation; Manuscript preparation: writing the initial draft; Manuscript preparation: critical review, commentary and revision; Manuscript preparation: visualisation/data presentation; Project administration; Funding acquisition. |
| *Flannery, S.* | Methodology; Investigation: performed the experiments; Investigation: data/evidence collection; Resources; Data curation; Manuscript preparation: critical review, commentary and revision. |
| *Berry, P.* | Methodology; Investigation: performed the experiments; Investigation: data/evidence collection; Resources; Data curation; Manuscript preparation: critical review, commentary and revision. |
| *Vendrell, I.* | Methodology; Investigation: data/evidence collection; Resources; Data curation; Manuscript preparation: critical review, commentary and revision. |
| *Johansen, A.* | Resources; Manuscript preparation: critical review, commentary and revision. |
| *Hansen, M.* | Resources; Manuscript preparation: critical review, commentary and revision. |
| *Fischer, R.* | Methodology; Resources; Manuscript preparation: critical review, commentary and revision; Supervision; Funding acquisition. |

## 4.2 Abstract

Brains decompose rapidly after death yet frequently survive in the archaeological record, including $> 1,300$ cases of waterlogged, oxygen-poor graves in which the brain is the only preserved soft tissue amongst otherwise skeletonised remains. To address this paradox we decayed mouse carcasses for six months in four burial regimes varying in water and oxygen availability, characterised the brain proteome by high-resolution LC–MS/MS using parallel DDA and DIA workflows at six PMIs, and modelled $> 1.26$ million peptide-specific decay trajectories to identify decay-prone and -resistant sequences. Oxygen availability exerted the main control on molecular fate: oxic burials produced widespread protein loss, whereas wet, hypoxic conditions favoured retention of a distinctive subset of decay-resistant peptides. These surviving sequences were structurally ordered, enriched in redox-active residues and in regions that bind metals and lipids, and bore modification patterns consistent with radical-mediated oxidative crosslinking rather than fragmentation. By linking intrinsic tissue chemistry and environmental context, our results move brain preservation from anomaly to expectation: resolving why brains outlast other soft tissues in waterlogged, oxygen-poor burials, and revealing that the molecular signatures of *post-mortem* peptide persistence closely mirror those of pathological protein stabilisation in brain ageing and neurodegeneration.

## 4.3 Introduction

More than 4,400 human brains have been recovered from burial sites spanning the last 12,000 years [2], and some of the oldest animal fossils preserve nervous tissue long after muscles and viscera have disappeared [e.g., 3–6]; yet the brain is among the first organs to break down after death [7]. This contradiction between the brain's persistence over millennia and its biochemical lability *post-mortem* suggests that the CNS follows a taphonomic trajectory – a pathway by which biological tissues are altered, degraded, or preserved from the moment of death to

their eventual recovery – that is both organ-specific, and mechanistically distinct from those stabilising other soft tissues.

In many cases, brain preservation fits familiar taphonomic trajectories. Dehydration, freezing, tanning, and saponification can stabilise multiple organs simultaneously, and preserved brains are often recovered alongside other soft tissues under these regimes [2]. However, nearly one-third of archaeological human brains ($> 1,300$) belong to an 'unknown' preservation type: a resilient, shrunken mass that occurs as the sole surviving soft tissue within otherwise skeletonised remains, most commonly in waterlogged, low-oxygen environments [2]. On the basis of their burial context and molecular composition, it has been proposed that these brains follow an organ-specific taphonomic trajectory governed by extensive molecular crosslinking [8, 9] catalysed by metals such as iron and copper [2], conceptually consistent with iron-mediated oxidative [10–12] and glycoxidative/lipoxidative [13] pathways implicated in deep-time fossilisation of other soft tissues [14]. This hypothesis remains conjectural, given we lack a time-resolved picture of how the brain decomposes in different burial environments.

Although archaeological brain preservation unfolds over centuries to millennia, the taphonomic trajectory that enables such survival is expected to be established much earlier. The early PMI – on the order of days to months – is critical for determining long-term molecular fate [15], because it is during this period that a range of biogeochemical factors [16] interact either to permit continued degradation, or to divert tissues onto stabilising pathways [17–20]. Once labile components are lost and diffusion-limited chemistries become established, subsequent molecular change is expected to proceed slowly and conservatively [15]. Thus, identifying the molecular mechanisms that operate during early decay is essential for understanding why certain tissues persist on archaeological and, occasionally, palaeontological timescales.

The existence of organ-specific taphonomic trajectories [21–25] also bears on how *post-mortem* molecular profiles are interpreted more broadly. Preserved

brains constitute the richest known reservoirs of ancient proteins [26], and *post-mortem* brain tissue is routinely examined in forensic [27] and neuropathological contexts [28]; yet, across these settings, late-stage proteomic profiles are increasingly treated as informative rather than incidental. It is often assumed that, after the initial decomposition phase of autolysis (i.e., digestion of a tissue by its own enzymes), recovered proteins and their associated modifications primarily reflect *ante-mortem* biology rather than *post-mortem* chemistry [29]. The prevalence of selectively preserved brains in waterlogged, oxygen-poor environments challenges this assumption, suggesting instead that burial conditions can actively redirect molecular fate, and thereby shape the composition of the surviving proteome.

To test this possibility, we tracked time-resolved changes in the brain proteome of mice following burial under environmental conditions differing in water and oxygen availability (Figure 4.1). Using high-resolution LC–MS/MS with parallel DDA and DIA workflows, we quantified peptide and protein abundance across a six-month PMI, and modelled $>$ 1.26 million peptide-specific decay profiles. We show that brain preservation in waterlogged, low-oxygen settings reflects the selective survival of peptides with shared sequence, structural, domain, and modification features, rather than uniform retention of the proteome. Identifying these features provides a basis for predicting which regions and types of proteins are likely to persist after death in different burial environments, and highlights mechanistic parallels with peptide architectures associated with pathological protein stabilisation in life.

## 4.4 Methods

### 4.4.1 Experimental taphonomy

A comprehensive description of all experimental and analytical procedures is provided in the Supplementary Methods (Appendix C.4). All experimental procedures complied with the Danish Animal Experimentation Inspectorate (2020-15-0201-00432), and ethical approval was obtained from the Central University Research Ethics Committee at the University of Oxford (R80617/RE001). In brief, male, specific pathogen-free mice ($n$ = 72; C57BL/6JRj, Janvier Laboratories)

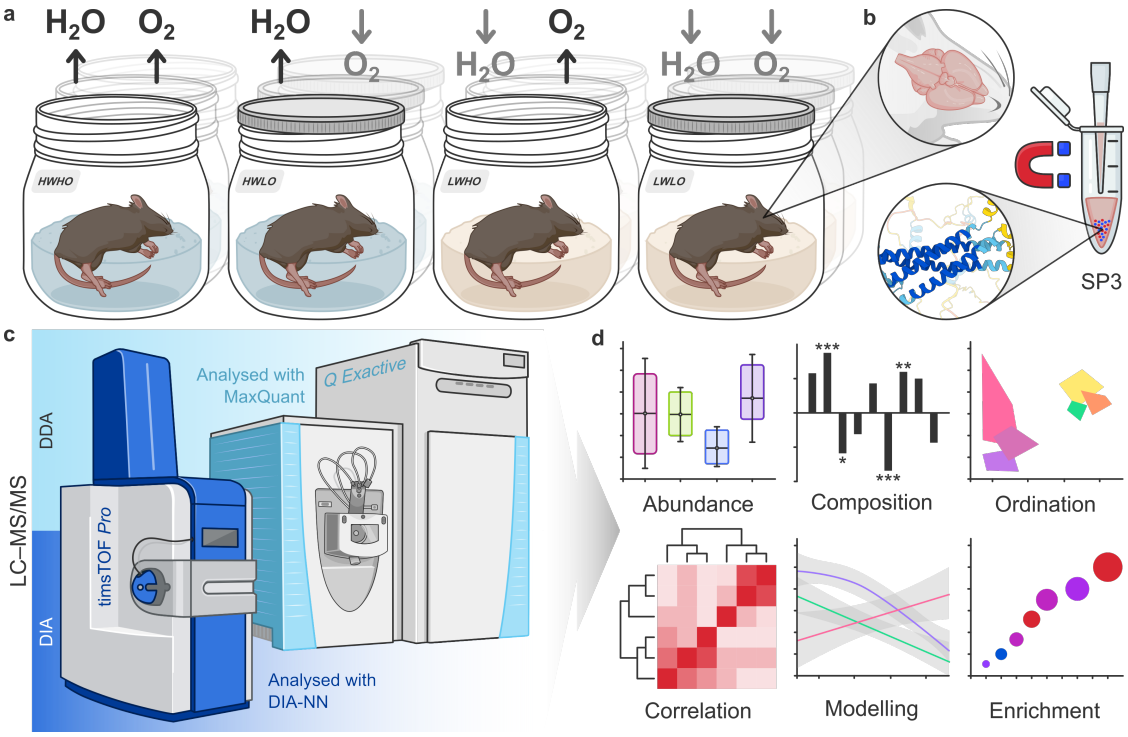



**Figure 4.1 | Overview of experimental and analytical workflow. (a)** Experimental design. Whole mouse carcasses ($n = 72$) were buried individually in sterilised glass jars filled with sterilised quartz sand and ultra-pure water under four burial regimes differing in water and oxygen availability: wet–oxic (HWHO), wet–hypoxic (HWLO), dry–oxic (LWHO), and dry–hypoxic (LWLO). Upward arrows indicate greater water and/or oxygen availability, and downward arrows indicate restricted availability. Carcasses were sampled at six time points (24 hours, 72 hours, one week, six weeks, three months, and six months), with three biological replicates per condition–time combination. **(b)** Brains were dissected, briefly homogenised, and proteins extracted using SP3-based digestion. (3D protein structure illustrated with AlphaFold [30].) **(c)** Parallel LC–MS/MS acquisition strategies were employed [31]: DDA ($n = 72$) on a Q Exactive™ Plus Hybrid Quadrupole-Orbitrap™ mass spectrometer (Thermo Fisher Scientific) to maximise peptide and PTM identification, and DIA ($n = 72$) on a TimsTOF Pro mass spectrometer (Bruker) for quantitative proteome-wide profiling. DDA data were analysed with MaxQuant (v.2.4.3.0) [32] and DIA data with DIA-NN (v.2.0) [33]. **(d)** Downstream analytical framework applied to identify biochemical, compositional, structural, functional, and post-translational correlates of peptide and protein preservation, including multivariate ordination of scaled protein abundances, correlation and clustering analyses, modelling of peptide-specific decay profiles across burial conditions and PMIs, and differential abundance and functional enrichment analyses.

were reared and sacrificed under identical conditions for the purposes of other scientific research [34], and were donated to our study. Immediately after death, whole carcasses were flash-frozen in liquid $N_2$ and stored at −80 °C. Immediately prior to the decay experiment, carcasses were thawed to room temperature. All equipment underwent dry heat sterilisation at 160 °C overnight prior to use. Carcasses were buried individually in 500 mL glass Kilner jars containing 500 g of sterile quartz sand (210–297 µm granularity; Sigma–Aldrich), and four burial environments established by factorial variation of waterlogging and oxygenation:

wet–oxic (HWHO), wet–hypoxic (HWLO), dry–oxic (LWHO), dry–hypoxic (LWLO). Wet and dry conditions were emulated by adding 180 mL and 90 mL ultrapure Milli-Q® $H_2O$ (Sigma–Aldrich), respectively; oxic and hypoxic conditions (i.e., with and without atmospheric exchange and oxygen replenishment) were emulated by leaving jars open, or sealing them with an airtight silicon gasket. In wet conditions, water loss was periodically assessed by mass and corrected by replacement to maintain target moisture. All jars were placed together in a fume hood with controlled temperature (20 °C), ambient laboratory lighting, and air circulation. Three biological replicates were decayed per condition at each of six time points (24 hours, 72 hours, one week, six weeks, three months, and six months; $n = 12$ mice per time point). At each time point, brains were dissected, homogenised, subdivided into five aliquots of approximately 80 mg, flash-frozen in liquid $N_2$, and stored at −80 °C prior to proteomic analysis.

### 4.4.2 Proteomics

For DDA ($n = 72$), tissue was lysed in 100 mM ammonium bicarbonate with 2% SDS (both Sigma–Aldrich), homogenised using a Precellys® 24 Touch homogeniser (Bertin Technologies), and protein concentration estimated by bicinchoninic assay (BCA; Table C.24). For DIA ($n = 72$), an analogous workflow was used with Pierce® RIPA lysis (Thermo Fisher Scientific) and adjusted protein input (Table C.25). Proteins were reduced, alkylated, and processed by SP3 bead-assisted tryptic digestion [35] prior to analysis by LC–MS/MS.

### 4.4.3 Data analysis

DDA and DIA raw files ($n = 144$) were searched against a curated *Mus musculus* brain reference proteome ($n = 6,252$ proteins) [36] using semi-specific tryptic digestion, the fixed modification of carbamidomethylation of Cys, and the following variable PTMs: oxidation of Met and Pro; deamidation of Asn, Gln, and Arg; and protein N-terminal acetylation. DDA data were searched in MaxQuant (v.2.4.3.0) [32] using LFQ–MBR and dependent peptide search. DIA data were searched in

DIA-NN (v.2.0) [33] using a library-free workflow, and processed in `DIAgui` (v.1.4.2) [37] to perform MaxLFQ [38] and missing-value imputation by QRILC [39, 40]. To reduce the dependence of raw LFQ intensities on protein size, protein-level analyses were conducted on $\log_2$-transformed iBAQ values, whereas peptide-level analyses were performed on peptide intensities.

Global patterns in proteome composition were explored using principal component analysis (PCA) and uniform manifold approximation and projection (UMAP) of scaled $\log_2$ iBAQ values, revealing clear separation between 'early' ($< 6$ weeks) and 'late' ($\geq 6$ weeks) PMIs. Differential protein abundance between early and late PMI was assessed on a per-condition basis with empirical-Bayes-moderated linear modelling, which stabilises variance estimates across proteins and improves statistical power in high-dimensional proteomic datasets with limited replicate numbers. Significantly differentially abundant proteins were then grouped by $k$-means clustering according to whether they decreased or became relatively enriched throughout the PMI; these groups were then subjected to GO enrichment analysis to identify the biological processes, molecular functions, and cellular components associated with each. Peptide preservation was quantified by modelling $\log_2$-intensity as a function of PMI to obtain peptide-specific decay slopes, and data-driven thresholds on these slopes used to classify peptides as labile (decay-prone), putative (intermediate), and recalcitrant (decay-resistant). Biochemical, compositional, structural, functional, and post-translational correlates of preservation were then investigated by comparing known biochemical determinants of protein degradation rates [41] – including hydropathy, net charge, isoelectric point, sequence coverage, peptide length, amino-acid composition, predicted secondary structure, intrinsic disorder, functional features, and modification frequencies – between preservation classes using appropriate regression and enrichment frameworks with multiple-testing correction.

## 4.5 Results

A comprehensive description of all findings is provided in the Supplementary Results (Appendix C.2).

### 4.5.1 Divergent taphonomic trajectories under oxic and hypoxic burial

To quantify how burial environment shapes decomposition of the brain proteome, we measured total protein concentration and protein identifications through time across four environments varying in water and oxygen availability, and summarised compositional change with multivariate ordination. The mean number of identified proteins decreased as decomposition progressed (Supplementary Data S1; Table C.1), although a small, non-significant increase in mean protein concentration was observed at 72 hours relative to 24 hours, potentially reflective of early autolytic accumulation effects (Figure C.1). Protein recovery was strongly environment-dependent, with the lowest mean recoveries in wet–oxic samples and the highest in dry–hypoxic samples (Figure C.2a). Although most unique proteins (i.e., distinct protein groups; 69.6%) were identified at every time point (Figure C.3b), and almost all unique proteins were identified in every condition (93.8%; Figure C.2b), significant differences emerged between early ($<$ 6 weeks) and late ($\geq$ 6 weeks) PMIs, and in comparisons involving wet–oxic burial (Tables C.2 and C.3). Temporal profiles indicated an apparent 'pseudo-enrichment' of proteins under hypoxia (Figure 4.2a), with mean identifications at six months higher than at three months; whereas oxic conditions evidenced continued decline, including an order-of-magnitude reduction in wet–oxic samples by six months.

To visualise these taphonomic trajectories, we ordinated samples by proteomic composition using PCA and UMAP. PCA separated early from late PMIs along the first principal component (Figure 4.2b), which explained 73.7% of the total variance, and showed tight clustering of early time points but greater dispersion among later time points. UMAP recapitulated this temporal ordering and, at late PMI, highlighted oxygenation as a major axis of divergence (Figure 4.2c):

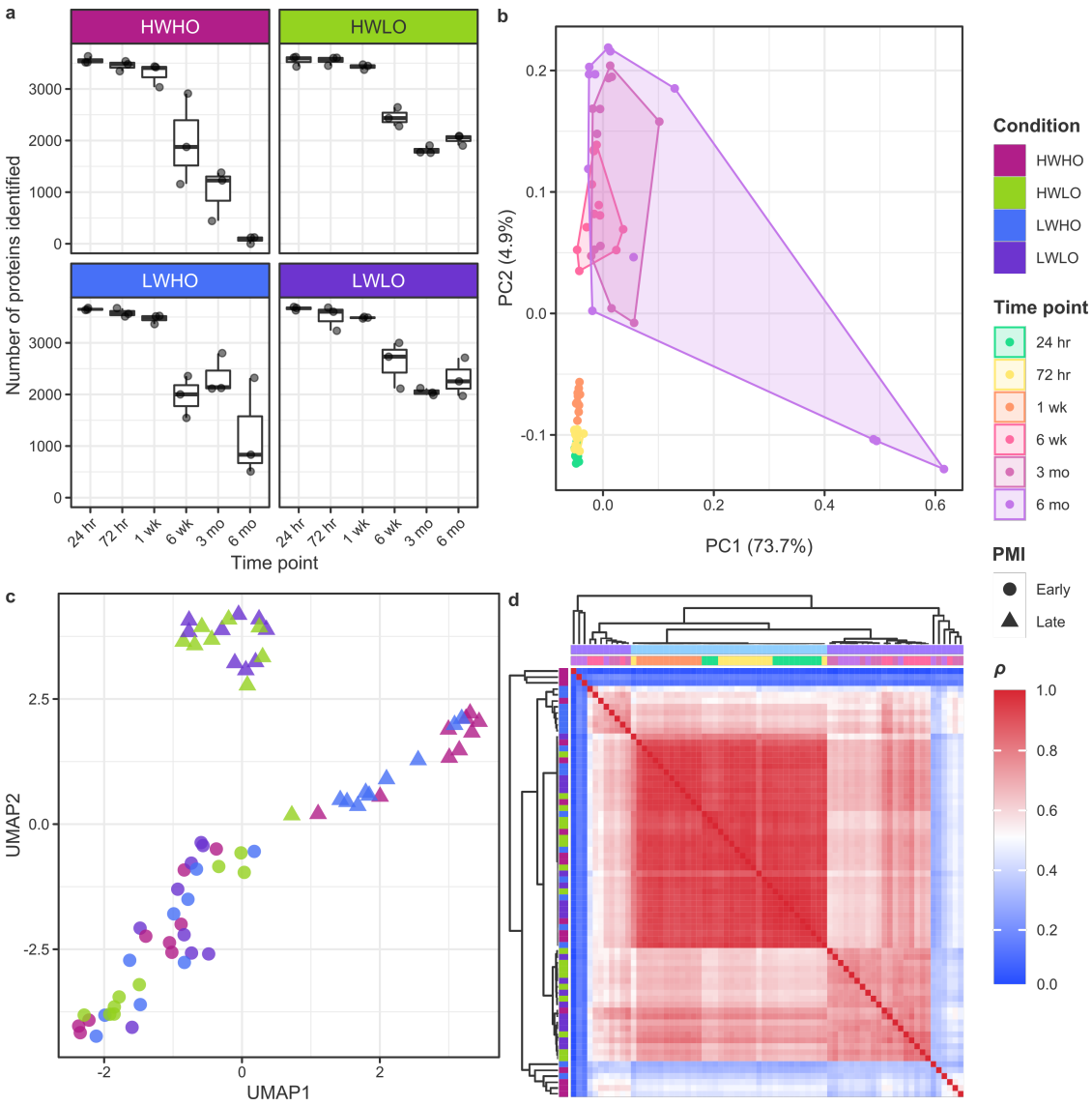



**Figure 4.2 | Divergent taphonomic trajectories under oxic and hypoxic burial.** **(a)** Jittered box plots of the number of proteins identified at 1% FDR and $q$-value $\leq .01$ recovered at each time point, in each burial condition. **(b)** PCA plot of normalised, batch effect-corrected abundance data (standardised and mean-centred) for all samples ($n = 72$; Section C.4.3.2). Each point represents the principal component (PC) score of a unique protein ($n = 3,910$), with colours reflecting the time point at which that protein was in its highest mean condition. Together, PCs 1 and 2 explain 78.6% of the variation in the dataset. **(c)** UMAP plot of normalised, batch effect-corrected abundance data (standardised and scaled) for all samples ($n = 72$; Section C.4.3.2). Each point represents a sample, with colours reflecting the burial condition, and shapes the associated PMI. **(d)** Pearson's correlation coefficient ($\rho$) matrix with hierarchically clustered dendrograms of unique proteins ($n = 3,910$; Section C.4.3.2). As a normalised measure of covariance, $\rho$ has a value between –1 (perfect negative correlation) and 1 (perfect positive correlation); however, note the restricted range illustrated (0.0–1.0), reflecting the fact that only positive correlations were observed between proteomic profiles.

oxic samples extended the early-PMI trajectory, whereas hypoxic samples formed a distinct late-PMI cluster. Correlation analysis with hierarchical clustering supported this separation (Figure 4.2d), with stronger within-group similarity among late hypoxic samples and greater variability among late oxic samples. Together, these analyses indicate that oxygen availability is a dominant factor shaping late-stage proteomic composition, consistent with divergent taphonomic trajectories under oxic *vs.* hypoxic burial.

### 4.5.2 *Post-mortem* shifts in brain proteome composition

We next asked how the functional composition of the brain proteome changes along different taphonomic trajectories. Using linear modelling with $k$-means and hierarchical clustering of protein abundance through time, we defined two major groups: proteins generally more abundant at early PMI across environments ($n = 1,886$), and proteins relatively more abundant at late PMI in hypoxic conditions ($n = 1,112$; Figures C.4–C.8).

GO enrichment of these clusters revealed clear *post-mortem* shifts in biological processes, molecular functions and cellular components (Figures C.9–C.11). Proteins peaking in abundance at early PMI were characterised by mRNA- and translation-related processes (e.g., peptide biosynthesis, ribonucleoprotein complex biogenesis), with molecular functions reflecting (m)RNA binding, GTPase regulator activity, and structural constituents of the ribosome. Cellular component annotations were dominated by ribonucleoprotein assemblies, nuclear bodies, and chromosomal regions. By contrast, proteins peaking at late PMI were associated with energy and nucleotide metabolism (e.g., aerobic respiration, ATP metabolic process) and redox chemistry, with molecular functions dominated by oxidoreductase (including peroxidase) activities, cytoskeletal protein binding, and chaperone or receptor binding. Cellular component terms localised to membrane protein complexes – particularly mitochondrial and organelle inner membranes – as well as neuronal structures such as synapses, axons, and myelin, and to supramolecular fibres.

Together, these results indicate a *post-mortem* progression from a relatively life-like, regulatory- and translation-focused intracellular proteome, to an enzyme-rich, membrane-associated proteome characterising late-stage taphonomic trajectories.

### 4.5.3 Peptide-specific decay profiles in different environments

To resolve taphonomic trajectories at the peptide level, we fit more than 1.26 million peptide-specific decay profiles across environments and time points, and grouped peptides into labile, putative, and recalcitrant preservation classes based on data-driven thresholds applied to peptide-specific decay slopes (Supplementary Data S2). No peptides from wet–oxic samples met the quality criteria (all exhibited SEs $> 90^{\text{th}}$ percentile and/or detection frequencies $< 90^{\text{th}}$ percentile; Section C.4.3.3) and were therefore excluded from peptide-level decay profiling; however, their low abundance and high variability at late PMI were themselves inconsistent with stability. Across the remaining conditions, labile peptides decayed rapidly, losing five $\log_2$ units of intensity over the PMI (Figure 4.3a), whereas putatively preserved peptides exhibited a shallower decline, with loss of two $\log_2$ units. By contrast, recalcitrant peptides evidenced little net loss overall and, in wet–hypoxic and dry–oxic conditions, increased in relative intensity with PMI. In dry–hypoxic conditions, recalcitrant peptides showed a modest early-to-mid PMI decrease, followed by a rebound to levels exceeding those at 24 hours. In wet–hypoxic samples, labile peptides exhibited an initial phase of relative stability not evident in other environments, followed by accelerated loss after an estimated breakpoint around the first week *post-mortem*, although the timing approximated by segmented regression was uncertain. Thus, although the overall stability hierarchy (labile $\ll$ putative $\ll$ recalcitrant) was conserved, peptide decay profiles were modulated by burial environment.

To quantify recalcitrance probabilistically, we fitted logistic regression models to peptide decay behaviour and assessed classification performance with bootstrap resampling and precision–recall analysis (Figure C.12). Calibration and discrimination metrics – including calibration intercept and slope, Brier scores, Spiegelhalter's

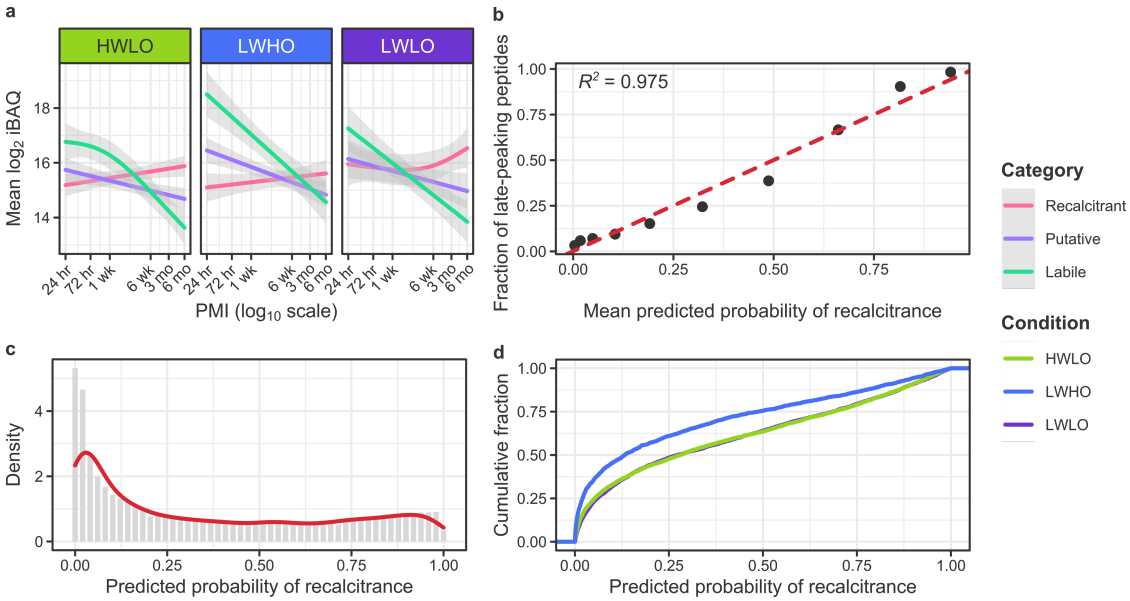



**Figure 4.3 | Peptide-specific decay profiles in different environments.** No peptides detected in the wet–oxic condition met quality criteria, and were excluded from analyses. **(a)** Generalised additive model fits of mean $\log_2$ iBAQ *vs.* PMI ($\log_{10}$ scale) for recalcitrant, putative and labile peptides in each condition ($n = 277,469$ peptide–condition–time observations; 16,128 unique peptides; Section C.4.3.3). Solid lines represent the estimated smooth functions, and shaded ribbons denote 95% CIs. **(b)** Scatter plot of the observed fraction of late-peaking peptides *vs.* the mean predicted probability of recalcitrance, binned by prediction quantiles. Each point represents one bin of peptides sorted by their predicted recalcitrant score; the red dashed line is the ideal 1:1 calibration. The close alignment of points and high coefficient of determination ($R^2 = 0.975$) indicate that the model's probability estimates accurately reflect the true likelihood of late-peaking behaviour (Section C.4.3.3). **(c)** Distribution of predicted probabilities of recalcitrance. Grey bars show the density-scaled histogram of model-predicted scores ($n = 50$ bins), while the red curve is a smoothed kernel density estimate (Section C.4.3.3). **(d)** Empirical cumulative distribution of predicted probabilities of recalcitrance, stratified by burial condition. Each curve shows the fraction of peptides with a predicted probability $\leq x$ (Section C.4.3.3).

$Z$-statistics, and ROC analysis (Section C.4.3.3) – indicated excellent model performance (Figure C.13), with predicted probabilities closely matching observed recalcitrance frequencies (Figure 4.3b). The predicted probability distribution was strongly right-skewed (Figure 4.3c): half of all peptides (50.1%) had low recalcitrance probability ($P < 0.25$), whereas a high-probability tail ($P > 0.75$) contained nearly one-fifth (19.6%) of peptides with strong preservation potential. Peptides from hypoxic conditions were enriched in this high-probability subset relative to oxic conditions (Figure 4.3d). Together, these models suggest that low-oxygen environments are associated with a larger fraction of peptides exhibiting decay profiles consistent with persistence and relative enrichment as more labile material is lost.

### 4.5.4 Environmental controls on recalcitrant peptide classes

We then asked how recalcitrant peptides are distributed across environments, and from which protein classes they derive. Wet–hypoxic conditions yielded both the largest pool ($n = 2,647$) and the highest proportion (37.4%) of recalcitrant peptides (Figure 4.4a), and hypoxic samples showed greater overlap in recalcitrant peptides with one another than was observed for peptides identified exclusively under oxic conditions. Over-representation analysis indicated that the protein classes corresponding to recalcitrant peptides differed across water- and oxygen-availability regimes (Figure 4.4b): hypoxic conditions yielded four times as many enriched classes as oxic conditions, with particularly strong enrichment of peroxidases, calcium-binding proteins, and metalloproteases (Tables C.4–C.6). Despite most proteins being detected under all conditions (Figure C.2b), only a small subset of peptides ($n = 414$) was recalcitrant in every environment; this shared set was enriched in oxidoreductases, proteases, and other metabolite interconversion enzymes. These enrichments suggest that recalcitrance is associated with preferential retention of peptides from proteins linked to redox chemistry, proteolysis, and metal or calcium binding.

### 4.5.5 Physicochemical, sequence, and structural predictors of peptide recalcitrance

We first investigated whether simple physicochemical properties could explain peptide recalcitrance. Hydropathy evidenced small, context-dependent differences under hypoxia, but overall effect sizes were negligible, and net charge and isoelectric point did not distinguish preservation categories (Figure C.14; Tables C.7–C.9). Peptide-recovery metrics were similarly weak discriminators: mean peptide length and protein sequence coverage differed only modestly between preservation types and, although contrasts were strongest in wet–oxic conditions when analyses were stratified by environment, effect sizes remained small (Figure C.15; Tables C.10–C.12). Overall, averaged physicochemical properties and recovery metrics explain little of the variance in peptide persistence across burial environments.

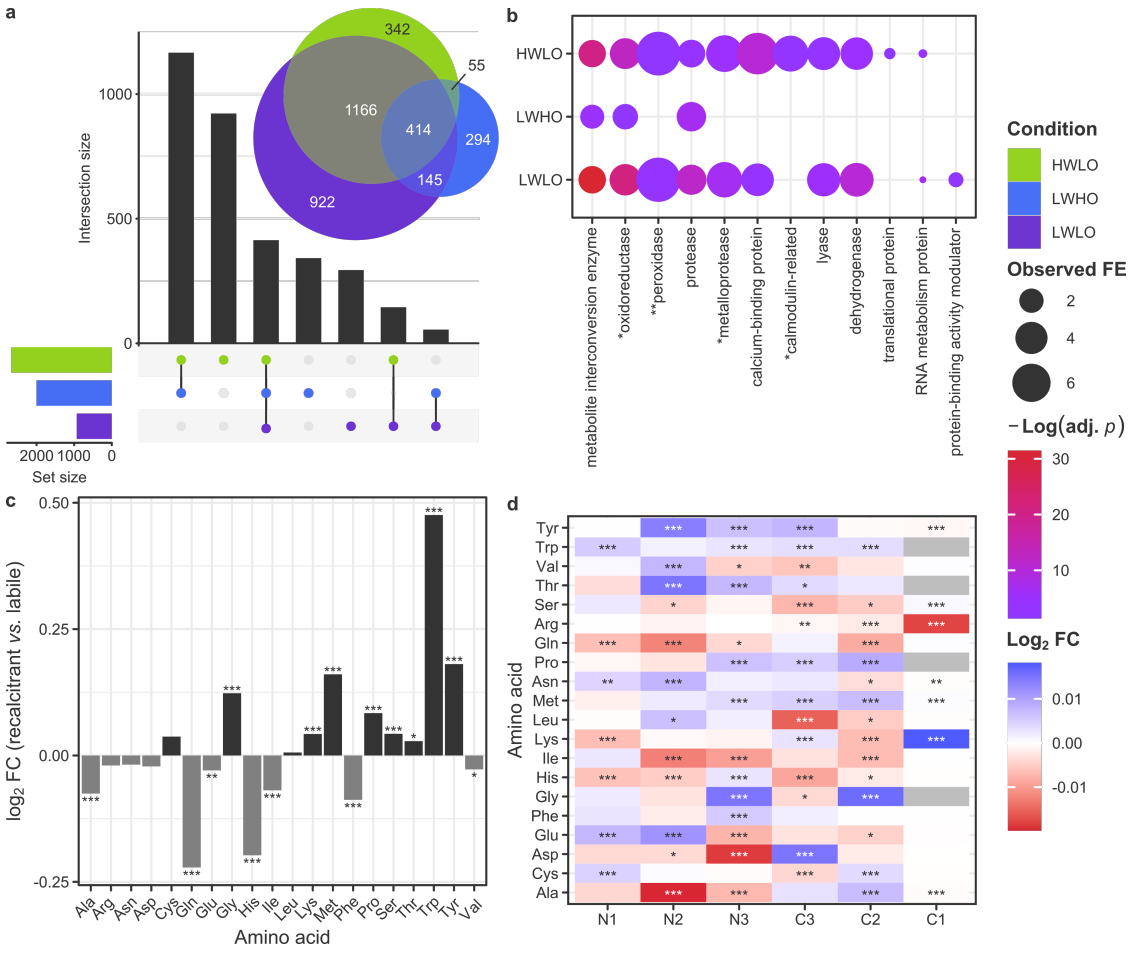



**Figure 4.4 | Protein features associated with recalcitrance.** No peptides detected in the wet–oxic condition met quality criteria, and were excluded from analyses. **(a)** Upset plot of the number of unique recalcitrant peptides in each experimental condition ($n = 3,338$). Horizontal bars indicate the total peptides per individual condition, connected dots denote the condition(s) contributing to each intersection, and vertical bars indicate intersection sizes. Inset is a scaled Euler diagram illustrating overlap in recalcitrant peptides across conditions: circle areas are proportional to the total peptides per individual condition, and numbers in overlapping regions indicate peptides shared between conditions. **(b)** Over-representation of protein classes among recalcitrant peptides: each point represents a protein class corresponding to recalcitrant peptides across experimental conditions ($n = 3,338$; Section C.4.3.4). Point size represents the degree of fold enrichment (FE; i.e., observed *vs.* expected numbers of proteins), where values $< 1$ indicate under-representation. Point colour denotes the $-\log_{10}$ of the adjusted $p$-value. Protein subclasses are indicated with an asterisk ($*$) to the right of parent classes, reflecting hierarchical relationships. Only statistically significant results are shown. **(c)** Bar chart of mean $\log_2$-fold change ($\log_2$FC; recalcitrant *vs.* labile) in amino-acid frequency across peptides ($n = 77,508$; Section C.4.3.5). Values $> 0$ indicate enrichment of a residue in recalcitrant peptides (*dark grey*), values $< 0$ indicate depletion of a residue (*light grey*), and values $= 0$ indicate no difference in representation between recalcitrant and labile classes. **(d)** Heat map showing positional amino-acid enrichment at peptide termini (N1–N3, C1–C3) between recalcitrant and labile peptides ($n = 77,508$). $\text{Log}_2$-FC (recalcitrant *vs.* labile) was estimated by linear modelling of one-hot encoded terminal residues (Section C.4.3.5), and adjusted significance indicated by the following codes: $*** = p$-value $< .0001$; $** = p$-value $\leq .001$; $* = p$-value $\leq .05$.

Sequence and predicted structural metrics, however, showed strong separation between preservation categories. Recalcitrant peptides were enriched in redox-active aromatic and sulfur-containing residues (Trp, Tyr, and Met), as well as Gly and Pro, and were depleted in residues intrinsically susceptible to hydrolysis, destructive oxidation, or fragmentation, particularly Gln and His (Figure 4.4c). Positional analyses further revealed small but reproducible biases near peptide termini (Figure 4.4d), indicating that decay resistance depends not only on overall amino-acid composition but also on the positional distribution of residues within peptides. These compositional and positional patterns are compatible with selective survival of structurally constrained peptides enriched in residues capable of stabilising or terminating local radicals.

Recalcitrant peptides were more likely to be $\beta$-sheet-dominant (50.2% *vs.* 40.8%) and less likely to be $\alpha$-helix-dominant (48.3% *vs.* 57.8%) than labile peptides, with coil-dominant peptides rare in both categories ($< 1.5\%$). Logistic regression confirmed a strong negative association between $\alpha$-helical content and recalcitrance, alongside positive associations with $\beta$-sheet content and higher predicted structural confidence (Tables C.13–C.16). Recalcitrant peptides also exhibited lower predicted intrinsic disorder than labile and putative peptides, particularly under hypoxic conditions (Tables C.17–C.19). These results suggest that decay resistance is better predicted by local structure and residue chemistry than by averaged physicochemical properties, and show that recalcitrant peptides are biased toward $\beta$-sheet-rich, structurally ordered sequences enriched in redox-active residues. Several of these intrinsic sequence and structural features are also characteristic of peptides that become selectively stabilised in neurodegenerative proteinopathies [42, 43], pointing to a potential parallel at the level of molecular architecture between peptide recalcitrance and pathological protein stabilisation.

### 4.5.6 Protein features and modifications associated with recalcitrance

We next investigated how peptide recalcitrance relates to protein features by annotating recovered peptides with UniProt-derived information on protein topology, domains, regions, and PTMs. Because UniProt annotations are hierarchical, we first assessed feature bias across higher annotation levels, which revealed widespread but weak associations with preservation category (Tables C.20 and C.21); these effects largely reflect aggregation across many heterogeneous features, and are not individually informative. We therefore focused on descriptor-level annotations, where a restricted subset of features exhibited large and robust associations with recalcitrance ($n = 18$; Supplementary Data S3). At this level, extracellular domains were three-fold enriched in recalcitrant peptides, whereas cytoplasmic and mitochondrial domains were three-fold enriched in labile peptides. Calcium-dependent phospholipid-binding domains evidenced the strongest domain-level biases, being approximately four- to 16-fold more common in recalcitrant than labile peptides.

Finally, we examined how PTMs differed between early and late PMI among different burial environments (Figure C.16). In wet–oxic conditions, which demonstrated the most extensive molecular loss, late-PMI peptides exhibited up to five-fold increased odds of oxidative and alkylative modifications, alongside reduced sodium and calcium adduction. In hypoxic conditions, late-PMI peptides evidenced approximately two-fold increased odds of di-oxidation events – particularly on Trp and Met – and of Trp-to-kynurenine conversion specifically under wet–hypoxic burial. Taken together, the enrichment of calcium-dependent phospholipid-binding domains and distinct oxidative modification profiles under hypoxia indicate that peptide recalcitrance is associated with specific protein domains and redox-related PTMs, rather than reflecting non-specific resistance to decay. Given redox- and metal-mediated chemical processes involving aromatic residues are also implicated in molecular

change during neurodegeneration [44], these results raise the possibility that *post-mortem* peptide persistence and *in vivo* neurodegenerative change may be shaped by overlapping reaction chemistries operating in very different biological contexts.

## 4.6 Discussion

Brains are among the most decay-prone organs after death, yet are disproportionately preserved as the sole surviving soft tissue in waterlogged, oxygen-poor burial environments [2]. Previous work on a single archaeological brain has struggled to identify a unifying preservation mechanism, being based principally on protein-level abundance [8] or on a small number of abundant proteins [45]. By fitting more than 1.26 million peptide-level decay profiles across multiple experimental conditions and PMIs, our results show that this paradox reflects a distinct taphonomic trajectory – that is, a discrete *post-mortem* pathway of molecular transformation – to which nervous tissue is uniquely predisposed in wet–hypoxic conditions. This trajectory emerges consistently across the experiment and is defined by convergent sequence, structural, domain, and modification signatures that are most parsimoniously explained by radical-mediated oxidative crosslinking within membrane-associated microenvironments.

A key implication of our time-resolved, peptide-specific decay profiling approach is that chemical regimes associated with molecular preservation are established early in decomposition, on the order of weeks *post-mortem*. The brain proteome initially follows a broadly similar trajectory across burial conditions, characterised by early autolytic and hydrolytic fragmentation; with advancing PMI, however, oxygen availability becomes the dominant determinant of molecular fate. Oxic conditions are associated with accelerating protein loss, whereas hypoxic conditions evidence greater proteomic retention, tighter clustering in ordination space, and the selective persistence of a subset of recalcitrant peptides. This divergence is accompanied by condition-dependent patterns of oxidative modification, consistent with an early-established, oxidative crosslinking pathway that subsequently constrains longer-term molecular preservation. Studies of deep-time fossilisation have similarly proposed

that oxidative crosslinking in the immediate PMI may stabilise soft tissues before complete degradation occurs [10, 11]; our results suggest that such stabilisation need not outpace decay as a separate, antithetical process but rather that preservation can emerge from decay itself when oxidative chemistry proceeds under diffusion-limited, oxygen-restricted conditions.

Crucially, water and oxygen availability together appear to influence whether oxidation proceeds as a chain-propagating process that progressively accumulates damage, or as a self-limiting sequence of local initiation–termination events (Section C.3.1; Table C.22). When oxygen is readily available in an aqueous environment, oxygen-dependent radical propagation is more readily maintained [46], increasing the likelihood of chain-amplified oxidative fragmentation and widespread molecular loss. When oxygen is restricted, however, radical propagation is less likely to be sustained and oxidation more likely to be self-limiting [46], with termination occurring at the site of radical generation by quenching (e.g., with Met) or covalent coupling with nearby reactive groups (e.g., Trp, Tyr) [47]. The selective preservation of brain tissue in waterlogged, oxygen-poor burials may therefore reflect a chemically constrained regime in which hydration facilitates radical chemistry, while hypoxia prevents its escalation into wholesale destruction.

Within this regime, preservation is not predicted by physicochemical properties (such as hydropathy and charge) but rather by compositional, structural, and domain biases (Section C.3.2). Recalcitrant peptides are enriched in large aromatic amino acids (Trp, Tyr) and sulfur-containing Met, and depleted in polar amides (Gln), imidazole-containing His, and small aliphatic residues (Ala, Val, Ile, Leu). These biases are consistent across environments but most pronounced under hypoxia. The chemical significance of this pattern is that Trp and Tyr readily form stabilised radical intermediates and oxidation products capable of participating in covalent crosslinking [48], while Met can buffer oxidative flux and modulate local radical availability [49] (Table C.23). In contrast, Gln and His are disposed toward deamidation [50] and metal-catalysed self-oxidation [51] respectively, which promote fragmentation and solubilisation. Importantly, modification data

independently support this interpretation: oxic conditions are dominated at late PMI by more extensive oxidative and alkylative damage, whereas hypoxic conditions feature increased Trp-to-kynurenine conversion and di-oxidation events, particularly localised to aromatic residues.

In wet–hypoxic conditions, recalcitrant peptides are enriched in $\beta$-sheet structure, depleted in $\alpha$-helical structure, and exhibit higher predicted structural confidence and lower intrinsic disorder. Whereas $\alpha$-helices are generally more flexible and solvent-exposed [52], $\beta$-sheets are densely hydrogen-bonded, closely packed, and relatively resistant to enzymatic and hydrolytic attack [53]; and their enrichment among recalcitrant peptides is consistent with the durability of fibrillar and amyloid-like protein architectures in both biological [54, 55] and archaeological [56, 57] contexts. Notably, accumulation of $\beta$-sheet-rich, structurally ordered protein assemblies is also a defining feature of aggregates that accrue during normal ageing and in NDDs [58], reflecting the intrinsic stability and degradation resistance of these conformations.

Finally, recalcitrant peptides are depleted in cytoplasmic and mitochondrial domains and strongly enriched – by up to sixteen-fold – in calcium-dependent phospholipid-binding C2 domains. C2 domains mediate $Ca^{2+}$-regulated binding of proteins to anionic phospholipids on membrane surfaces [59], and their enrichment indicates that peptide persistence is disproportionately associated with proteins stabilised at membranes, rather than within freely soluble intracellular compartments. Loss of ionic homeostasis and rising intracellular $Ca^{2+}$ during *post-mortem* decay [7] would be expected to further promote sustained membrane association of such proteins. Membrane-adjacent microenvironments are structurally constrained, concentrating redox-active substrates and catalysts (such as lipids and metals) while restricting diffusion and oxygen availability relative to the cytosol. In this context, radical oxidation is less likely to proceed *via* chain propagation, which requires continuous access to molecular oxygen [60], and more likely to locally terminate *via* crosslinking. Such crosslinking would be expected to reduce molecular mobility and

solubility, sterically hinder enzymatic and hydrolytic attack, and promote formation of insoluble aggregates resistant to degradation [61].

A further factor likely reinforcing this taphonomic trajectory is the brain's unusually large and heterogeneous reservoir of redox-active iron [62]. Nervous tissue contains high iron concentrations relative to most other soft tissues, distributed across multiple pools such as heme proteins, ferritin-bound stores, and iron-rich compartments associated with mitochondria, myelin, and oligodendrocytes [63]. In life, these pools are tightly regulated to support oxidative metabolism while limiting collateral damage [64]. After death, however, progressive membrane failure and loss of regulatory control are expected to alter iron speciation and availability, increasing the likelihood of local metal-catalysed radical generation. Importantly, such chemistry need not produce uniform oxidative destruction: when redox reactions involving iron occur within membrane-adjacent or diffusion-limited microenvironments, they may favour the formation of short-lived aromatic radicals that terminate by covalent crosslinking rather than by chain-propagating oxidation (Table C.22). The enrichment of peroxidases – which often involve heme iron or metal cofactors [65] – among recalcitrant peptides is compatible with localised, metal-associated redox chemistry, in which iron-containing cofactors may contribute to peroxide-driven radical formation without sustaining chain-propagating oxidation.

The brain is particularly predisposed to follow this trajectory. In life, it is among the most oxidatively stressed organs: it consumes a disproportionate share of oxygen, is rich in redox-active metals, and relies heavily on antioxidant and repair systems to maintain protein integrity [66]. Additionally, the brain combines extreme membrane density [67], an abundance of structurally stable, long-lived proteins that accumulate heterogeneous oxidative modifications during life [68], and anatomical sequestration within the cranial vault. Together, these features establish a *post-mortem* environment characterised by pre-existing chemical and structural heterogeneity, limited molecular mobility, and restricted oxygen exchange; conditions that favour local, diffusion-limited radical reactions and termination by crosslinking rather than runaway, chain-propagating oxidation. Notably, the

molecular features that define this *post-mortem* pathway closely parallel those that stabilise aggregation-prone protein assemblies in NDDs: enrichment of $\beta$-sheet and structurally ordered fragments [69], redox-active residue modifications [70], and oxidative crosslinks [71] are hallmarks of pathological protein aggregation *in vivo*. While the biological contexts differ fundamentally, these parallels indicate that common chemical processes govern protein persistence across clinical and geological timescales.

## 4.7 Conclusions

This study provides a molecular explanation for the long-standing paradox of selective brain preservation by demonstrating that waterlogged, oxygen-poor conditions divert the brain proteome onto a distinct taphonomic trajectory, characterised by radical-mediated oxidative crosslinking in membrane-associated microenvironments. We show that water and oxygen availability together determine whether *post-mortem* oxidation proceeds as a chain-propagating process that drives widespread proteomic loss, or as a diffusion-limited sequence of local radical reactions that favours persistence of a defined subset of peptides. The brain's unique confluence of biochemical, structural, and anatomical features restricts molecular diffusion and oxygen availability, concentrating radical chemistry at membrane-adjacent compartments where termination by crosslinking is favoured. As a result, peptide recalcitrance is not idiosyncratic but probabilistic, and can be predicted from environmental conditions. The resulting molecular signatures – ordered $\beta$-sheet structure and aromatic residue modifications consistent with local radical termination – mirror those observed in pathological protein stabilisation during brain ageing and neurodegeneration, underscoring how constrained oxidative chemistry can generate stability across disparate biological and temporal contexts. More broadly, this study shows that decay is not the opposite of preservation but, under specific chemical constraints, one of its mechanisms: the same oxidative reactions that drive molecular destruction can also generate molecular stability.

## 4.8 Limitations

Two aspects of our experimental design warrant explicit consideration. First, carcasses were flash-frozen in liquid $N_2$ and stored at $-80\,^{\circ}C$ prior to burial, a step without a natural precedent. Although such handling is routine in proteomics and likely exerted limited influence on the proteomic profile relative to larger environmental effects [72–75], freezing inevitably alters cellular architecture and protein conformation to some degree. However, given all carcasses underwent identical handling and storage procedures, any freeze–thaw effects were systematic across conditions, preserving the validity of cross-condition comparisons. The principal implication is thus one of ecological realism, rather than experimental comparability.

Second, oxygen availability was operationally manipulated through atmospheric access, but dissolved oxygen and redox conditions were not directly monitored during decay. Recent experimental taphonomy studies [76, 77] demonstrate that decaying carcasses can rapidly consume dissolved oxygen from their immediate surroundings, including in systems open to atmospheric diffusion, reaching hypoxic or anoxic conditions within hours to days. It is therefore possible that all conditions became effectively oxygen-depleted at the carcass–matrix interface within the first two time points (24 and 72 hours), regardless of bulk oxygen availability. Accordingly, our oxic treatments should be understood as operational contrasts in atmospheric exchange and oxygen replenishment, rather than as continuously oxygenated systems throughout the PMI.

Importantly, this does not undermine – and may in fact reinforce – the wet–hypoxic taphonomic trajectory we describe. Our mechanistic model holds that preservation depends not on a simple binary distinction between oxic and anoxic conditions, but on whether oxidative radical chemistry is permitted but constrained. If rapid, carcass-driven oxygen drawdown early in the PMI was common to all wet conditions, as these recent studies suggest [76, 77], the divergence observed between wet–oxic and wet–hypoxic burial would then reflect differences in the rate and extent of oxygen depletion, with slower or less complete drawdown in open systems permitting a longer interval of sustained chain-propagating oxidation sufficient to

drive greater molecular fragmentation and loss. Further work integrating real-time redox monitoring with proteomic profiling at the carcass–matrix interface will refine the temporal and spatial dynamics of this transition.

## 4.9 Supporting Information

The following supporting information (Box 4.1) is available online: `doi.org/10.1021/acs.jproteome.6c00200`.

**Box 4.1 | *Supporting Information***

Supplementary Results; Supplementary Discussion; Supplementary Methods; **Table S1.** Proteins recovered by experimental condition and time point; **Fig S1.** Protein concentration during decomposition; **Fig S2.** Proteomic profiles by burial environment; **Fig S3.** Proteomic profiles by time point; **Table S2.** Protein abundance at different time points; **Table S3.** Protein abundance in different burial environments; **Fig S4.** Complex heatmap of scaled protein iBAQ data with integrated linear modelling, $k$-means and hierarchical clustering of proteins globally; **Fig S5.** Complex heatmap of scaled protein iBAQ data with integrated linear modelling, $k$-means and hierarchical clustering of proteins in wet–oxic conditions; **Fig S6.** Complex heatmap of scaled protein iBAQ data with integrated linear modelling, $k$-means and hierarchical clustering of proteins in wet–hypoxic conditions; **Fig S7.** Complex heatmap of scaled protein iBAQ data with integrated linear modelling, $k$-means and hierarchical clustering of proteins in dry–oxic conditions; **Fig S8.** Complex heatmap of scaled protein iBAQ data with integrated linear modelling, $k$-means and hierarchical clustering of proteins in dry–hypoxic conditions; **Fig S9.** Biological process enrichment of proteins at early and late PMI; **Fig S10.** Molecular function enrichment of proteins at early and late PMI; **Fig S11.** Cellular component enrichment of proteins at early and late PMI; **Fig S12.** Precision–recall for early- and late-peaking peptide classifiers across conditions; **Fig S13.** Calibration and discrimination of the peptide-level recalcitrance classifier; **Table S4.** Over-representation test results for PANTHER protein class corresponding to recalcitrant peptides identified in wet–hypoxic conditions; **Table S5.** Over-representation test results for PANTHER protein class corresponding to recalcitrant peptides identified in dry–oxic conditions; **Table S6.** Over-representation test results for PANTHER protein class corresponding to recalcitrant peptides identified in dry–hypoxic conditions; **Fig S14.** Hydropathy by burial environment; **Table S7.** Hydropathy by preservation category; **Table S8.** Net charge by preservation category; **Table S9.** Isoelectric point by preservation category; **Fig S15.** Sequence coverage distributions by preservation category within burial environments; **Table S10.** Mean peptide length and sequence coverage by preservation category; **Table S11.** Mean peptide length by preservation category; **Table S12.** Sequence coverage by preservation category; **Table S13.** Secondary structure by preservation category; **Table S14.** Weighted $\alpha$-helix fraction by preservation category and burial environment; **Table S15.** Weighted $\beta$-sheet fraction by preservation category and burial environment; **Table S16.** Predicted secondary structure model confidence by preservation category; **Table S17.** Intrinsic disorder by preservation category; **Table S18.** Mean IUPred score by preservation category and burial environment; **Table S19.** Fraction disordered by preservation category and burial environment; **Table S20.** UniProt feature section by preservation category; **Table S21.** UniProt feature type by preservation category; **Fig S16.** Odds of modification at late *vs.* early PMI by burial environment; **Table S22.** Dominant radical oxidation pathways under contrasting hydration and oxygen regimes; **Table S23.** Reactivity and preservation potential of key amino-acid residues; **Table S24.** Sample mass and protein concentration for the DDA dataset; **Table S25.** Sample mass and protein concentration for the DIA dataset; **Fig S17.** Determination of optimal number of clusters for hierarchical clustering analysis of iBAQ data.

## 4.10 Data Availability

The LC–MS/MS data have been deposited to the ProteomeXchange Consortium *via* the PRIDE [78] partner repository with the dataset identifier, PXD074190.

## 4.11 Acknowledgements

We thank Sandra Breum Andersen and Sigri Kløve for donation of mouse carcasses, and Greger Larson and Erin Saupe for helpful discussions. The authors acknowledge use of the Centre for Proteome Research Shared Research Facility (CPR SRF) provided by Liverpool Shared Research Facilities, Faculty of Health and Life Sciences, University of Liverpool. AMH was supported by the Natural Environment Research Council (NE/S007474/1), and the NERC Environmental Omics Facility (NEOF1502).

## 4.12 References

[1] Liz Allen et al. 'Publishing: Credit where credit is due'. In: *Nature* 508 (7496 17th Apr. 2014), pp. 312–313. DOI: 10.1038/508312a.

[2] Alexandra L Morton-Hayward et al. 'Human brains preserve in diverse environments for at least 12 000 years'. In: *Proc. Biol. Sci.* 291 (2019 27th Mar. 2024), p. 20232606. DOI: 10.1098/rspb.2023.2606.

[3] Gregory D Edgecombe, Xiaoya Ma and Nicholas J Strausfeld. 'Unlocking the early fossil record of the arthropod central nervous system'. In: *Philos. Trans. R. Soc. Lond. B Biol. Sci.* 370 (1684 19th Dec. 2015), p. 20150038. DOI: 10.1098/rstb.2015.0038.

[4] Nicholas J Strausfeld, Xiaoya Ma and Gregory D Edgecombe. 'Fossils and the evolution of the arthropod brain'. In: *Curr. Biol.* 26 (20 24th Oct. 2016), R989–R1000. DOI: 10.1016/j.cub.2016.09.012.

[5] Farid Saleh et al. 'Biogenic iron preserves structures during fossilization: A hypothesis: Iron from decaying tissues may stabilize their morphology in the fossil record: Iron from decaying tissues may stabilize their morphology in the fossil record'. In: *Bioessays* 42 (6 June 2020), e1900243. DOI: 10.1002/bies.201900243.

[6] Joanna M Wolfe and Javier Ortega-Hernández. 'Evolution: Oh, my Cambrian nerves'. In: *Curr. Biol.* 31 (19 11th Oct. 2021), R1132–R1135. DOI: 10.1016/j.cub.2021.08.065.

[7] H Gill-King. 'Chemical and ultrastructural aspects of decomposition'. In: *Forensic Taphonomy.* CRC Press, 13th Dec. 1996, pp. 93–108. DOI: 10.1201/9781439821923.sec2.

[8] Axel Petzold et al. 'Protein aggregate formation permits millennium-old brain preservation'. In: *J. R. Soc. Interface* 17 (162 Jan. 2020), p. 20190775. DOI: 10.1098/rsif.2019.0775.

[9] Emma J Thimbleby et al. 'High performance mass spectrometry reveals possible kerogen substructures in persistent ancient human brain'. In: *J. Archaeol. Sci.* 161 (105898 Jan. 2024), p. 105898. DOI: 10.1016/j.jas.2023.105898.

[10] Mary H Schweitzer et al. 'A role for iron and oxygen chemistry in preserving soft tissues, cells and molecules from deep time'. In: *Proc. Biol. Sci.* 281 (1775 22nd Jan. 2014), p. 20132741. DOI: 10.1098/rspb.2013.2741.

[11] Elizabeth M Boatman et al. 'Mechanisms of soft tissue and protein preservation in Tyrannosaurus rex'. In: *Sci. Rep.* 9 (1 30th Oct. 2019), p. 15678. DOI: 10.1038/s41598-019-51680-1.

[12] Paul V Ullmann, Richard D Ash and John B Scannella. 'Taphonomic and diagenetic pathways to protein preservation, part II: The case of Brachylophosaurus canadensis specimen MOR 2598'. In: *Biology (Basel)* 11 (8 5th Aug. 2022), p. 1177. DOI: 10.3390/biology11081177.

[13] Jasmina Wiemann et al. 'Fossilization transforms vertebrate hard tissue proteins into N-heterocyclic polymers'. In: *Nat. Commun.* 9 (1 9th Nov. 2018), p. 4741. DOI: 10.1038/s41467-018-07013-3.

[14] Landon A Anderson. 'A chemical framework for the preservation of fossil vertebrate cells and soft tissues'. In: *Earth Sci. Rev.* 240 (104367 18th May 2023), p. 104367. DOI: 10.1016/j.earscirev.2023.104367.

[15] Derek E G Briggs. 'Experimental taphonomy'. In: *Palaios* 10 (6 1st Dec. 1995), pp. 539–550. DOI: 10.2307/3515093.

[16] Luke A Parry et al. 'Soft-bodied fossils are not simply rotten carcasses – toward a holistic understanding of exceptional fossil preservation: Exceptional fossil preservation is complex and involves the interplay of numerous biological and geological processes'. In: *Bioessays* 40 (1 1st Jan. 2018), p. 1700167. DOI: 10.1002/bies.201700167.

[17] Robert S Sansom. 'Experimental decay of soft tissues'. In: *Paleontol. Soc. Pap.* 20 (Oct. 2014), pp. 259–274. DOI: 10.1017/s1089332600002886.

[18] Derek E G Briggs and Sean McMahon. 'The role of experiments in investigating the taphonomy of exceptional preservation'. In: *Palaeontology* 59 (1 Jan. 2016), pp. 1–11. DOI: 10.1111/pala.12219.

[19] Mark A Purnell et al. 'Experimental analysis of soft-tissue fossilization: opening the black box'. In: *Palaeontology* 61 (3 May 2018), pp. 317–323. DOI: 10.1111/pala.12360.

[20] Thomas Clements and Sarah Gabbott. *Pers. comm.* 13th Apr. 2022.

[21] Robert S Sansom, Sarah E Gabbott and Mark A Purnell. 'Non-random decay of chordate characters causes bias in fossil interpretation'. In: *Nature* 463 (7282 11th Feb. 2010), pp. 797–800. DOI: 10.1038/nature08745.

[22] Robert S Sansom, Sarah E Gabbott and Mark A Purnell. 'Decay of vertebrate characters in hagfish and lamprey (Cyclostomata) and the implications for the vertebrate fossil record'. In: *Proc. Biol. Sci.* 278 (1709 22nd Apr. 2011), pp. 1150–1157. DOI: 10.1098/rspb.2010.1641.

[23] Duncan Je Murdock et al. 'Decay of velvet worms (Onychophora), and bias in the fossil record of lobopodians'. In: *BMC Evol. Biol.* 14 (1 29th Nov. 2014), p. 222. DOI: 10.1186/s12862-014-0222-z.

[24] Robert S Sansom. 'Preservation and phylogeny of Cambrian ecdysozoans tested by experimental decay of Priapulus'. In: *Sci. Rep.* 6 (1 6th Sept. 2016), p. 32817. DOI: 10.1038/srep32817.

[25] Thomas Clements, Mark A Purnell and Sarah Gabbott. 'Experimental analysis of organ decay and pH gradients within a carcass and the implications for phosphatization of soft tissues'. In: *Palaeontology* 65 (4 July 2022). DOI: 10.1111/pala.12617.

[26] Alexandra Morton-Hayward et al. 'Deep palaeoproteomic profiling of archaeological human brains'. In: *PLoS One* 20 (5 28th May 2025), e0324246. DOI: 10.1371/journal.pone.0324246.

[27] James Mackintosh MacKenzie. 'Examining the decomposed brain'. In: *Am. J. Forensic Med. Pathol.* 35 (4 Dec. 2014), pp. 265–270. DOI: 10.1097/PAF.0000000000000111.

[28] Matthew R Hynd et al. 'Biochemical and molecular studies using human autopsy brain tissue: Human autopsy studies'. In: *J. Neurochem.* 85 (3 May 2003), pp. 543–562. DOI: 10.1046/j.1471-4159.2003.01747.x.

[29] Margaret M Krassner et al. 'Postmortem changes in brain cell structure: a review'. In: *Free Neuropathol.* 4 (Jan. 2023), p. 10. DOI: 10.17879/freeneuropathology-2023-4790.

[30] John Jumper et al. 'Highly accurate protein structure prediction with AlphaFold'. In: *Nature* 596 (7873 Aug. 2021), pp. 583–589. DOI: 10.1038/s41586-021-03819-2.

[31] Xun Zou et al. 'In-depth analysis of data characteristics and comparative evaluation of dda and dia accuracy in label-free quantitative proteomics of biological samples'. In: *Clin. Proteomics* 23 (1 11th Dec. 2025), p. 2. DOI: 10.1186/s12014-025-09572-2.

[32] Stefka Tyanova, Tikira Temu and Juergen Cox. 'The MaxQuant computational platform for mass spectrometry-based shotgun proteomics'. In: *Nat. Protoc.* 11 (12 Dec. 2016), pp. 2301–2319. DOI: 10.1038/nprot.2016.136.

[33] Vadim Demichev et al. 'DIA-NN: neural networks and interference correction enable deep proteome coverage in high throughput'. In: *Nat. Methods* 17 (1 Jan. 2020), pp. 41–44. DOI: 10.1038/s41592-019-0638-x.

[34] Sigri Kløve et al. 'Early-life *Helicobacter pylori* infection worsens metabolic state in mice receiving a high-fat diet'. In: *bioRxiv* biorxiv;2025.04.27.650497v1 (30th Apr. 2025). DOI: 10.1101/2025.04.27.650497.

[35] Christopher S Hughes et al. 'Single-pot, solid-phase-enhanced sample preparation for proteomics experiments'. In: *Nat. Protoc.* 14 (1 Jan. 2019), pp. 68–85. DOI: 10.1038/s41596-018-0082-x.

[36] Artemis G Korovesi et al. 'Normal mouse brain proteome II: Analysis of brain regions by high-resolution mass spectrometry'. In: *Cancer Genomics Proteomics* 17 (6 Nov. 2020), pp. 757–767. DOI: 10.21873/cgp.20230.

[37] Marc-Antoine Gerault, Luc Camoin and Samuel Granjeaud. 'DIAgui: a Shiny application to process the output from DIA-NN'. In: *Bioinform. Adv.* 4 (1 13th Jan. 2024), vbae001. DOI: 10.1093/bioadv/vbae001.

[38] Jürgen Cox et al. 'Accurate proteome-wide label-free quantification by delayed normalization and maximal peptide ratio extraction, termed MaxLFQ'. In: *Mol. Cell. Proteomics* 13 (9 Sept. 2014), pp. 2513–2526. DOI: 10.1074/mcp.M113.031591.

[39] Cosmin Lazar et al. 'Accounting for the multiple natures of missing values in label-free quantitative proteomics data sets to compare imputation strategies'. In: *J. Proteome Res.* 15 (4 1st Apr. 2016), pp. 1116–1125. DOI: 10.1021/acs.jproteome.5b00981.

[40] Mingyi Liu and Ashok Dongre. 'Proper imputation of missing values in proteomics datasets for differential expression analysis'. In: *Brief. Bioinform.* 22 (3 20th May 2021), bbaa112. DOI: 10.1093/bib/bbaa112.

[41] Miguel Correa Marrero and Inigo Barrio-Hernandez. 'Toward understanding the biochemical determinants of protein degradation rates'. In: *ACS Omega* 6 (8 2nd Mar. 2021), pp. 5091–5100. DOI: 10.1021/acsomega.0c05318.

[42] Martin von Bergen et al. 'Tau aggregation is driven by a transition from random coil to beta sheet structure'. In: *Biochim. Biophys. Acta* 1739 (2-3 3rd Jan. 2005), pp. 158–166. DOI: 10.1016/j.bbadis.2004.09.010.

[43] Deborah J Tew et al. 'Stabilization of neurotoxic soluble beta-sheet-rich conformations of the Alzheimer's disease amyloid-beta peptide'. In: *Biophys. J.* 94 (7 1st Apr. 2008), pp. 2752–2766. DOI: 10.1529/biophysj.107.119909.

[44] Irene Villalón-García et al. 'Vicious cycle of lipid peroxidation and iron accumulation in neurodegeneration'. In: *Neural Regen. Res.* 18 (6 June 2023), pp. 1196–1202. DOI: 10.4103/1673-5374.358614.

[45] Aaron S Mohammed and Vladimir N Uversky. 'Intrinsic disorder as a natural preservative: High levels of intrinsic disorder in proteins found in the 2600-year-old human brain'. In: *Biology (Basel)* 11 (12 25th Nov. 2022), p. 1704. DOI: 10.3390/biology11121704.

[46] Clemens von Sonntag and Heinz-Peter Schuchmann. 'The elucidation of peroxyl radical reactions in aqueous solution with the help of radiation-chemical methods'. In: *Angew. Chem., Int. Ed. Engl.* 30 (10 Oct. 1991), pp. 1229–1253. DOI: 10.1002/anie.199112291.

[47] Michael J Davies. 'Protein oxidation and peroxidation'. In: *Biochem. J.* 473 (7 1st Apr. 2016), pp. 805–825. DOI: 10.1042/BJ20151227.

[48] Eduardo Fuentes-Lemus et al. 'Oxidative crosslinking of peptides and proteins: Mechanisms of formation, detection, characterization and quantification'. In: *Molecules* 27 (1 21st Dec. 2021), p. 15. DOI: 10.3390/molecules27010015.

[49] Geumsoo Kim, Stephen J Weiss and Rodney L Levine. 'Methionine oxidation and reduction in proteins'. In: *Biochim. Biophys. Acta* 1840 (2 Feb. 2014), pp. 901–905. DOI: 10.1016/j.bbagen.2013.04.038.

[50] Xiaojuan Li, Cheng Lin and Peter B O'Connor. 'Glutamine deamidation: differentiation of glutamic acid and gamma-glutamic acid in peptides by electron capture dissociation'. In: *Anal. Chem.* 82 (9 1st May 2010), pp. 3606–3615. DOI: 10.1021/ac9028467.

[51] Can Wang et al. 'Fenton-like reaction of the iron(II)-histidine complex generates hydroxyl radicals: implications for oxidative stress and Alzheimer's disease'. In: *Chem. Commun. (Camb.)* 57 (92 19th Nov. 2021), pp. 12293–12296. DOI: 10.1039/d1cc05000a.

[52] Eldon G Emberly et al. 'Flexibility of alpha-helices: results of a statistical analysis of database protein structures'. In: *J. Mol. Biol.* 327 (1 14th Mar. 2003), pp. 229–237. DOI: 10.1016/s0022-2836(03)00097-4.

[53] James S Nowick. 'Exploring beta-sheet structure and interactions with chemical model systems'. In: *Acc. Chem. Res.* 41 (10 18th Oct. 2008), pp. 1319–1330. DOI: 10.1021/ar800064f.

[54] David Eisenberg and Mathias Jucker. 'The amyloid state of proteins in human diseases'. In: *Cell* 148 (6 16th Mar. 2012), pp. 1188–1203. DOI: 10.1016/j.cell.2012.02.022.

[55] Brandon H Toyama and Martin W Hetzer. 'Protein homeostasis: live long, won't prosper'. In: *Nat. Rev. Mol. Cell Biol.* 14 (1 Jan. 2013), pp. 55–61. DOI: 10.1038/nrm3496.

[56] Marek Janko et al. 'Nanostructure and mechanics of mummified type I collagen from the 5300-year-old Tyrolean Iceman'. In: *Proc. Biol. Sci.* 277 (1692 7th Aug. 2010), pp. 2301–2309. DOI: 10.1098/rspb.2010.0377.

[57] Hermann Ehrlich et al. 'Discovery of mammalian collagens I and III within ancient poriferan biopolymer spongin'. In: *Nat. Commun.* 16 (1 13th Mar. 2025), p. 2515. DOI: 10.1038/s41467-025-57460-y.

[58] Sylvain E Lesné et al. 'Brain amyloid- oligomers in ageing and Alzheimer's disease'. In: *Brain* 136 (Pt 5 9th May 2013), pp. 1383–1398. DOI: 10.1093/brain/awt062.

[59] A K Hinderliter et al. 'Membrane domain formation by calcium-dependent, lipid-binding proteins: insights from the C2 motif'. In: *Biochim. Biophys. Acta* 1448 (2 10th Dec. 1998), pp. 227–235. DOI: 10.1016/s0167-4889(98)00146-3.

[60] Eugene Pliss et al. 'Kinetic analysis of the reactivity of peroxyl radicals in chain oxidation of unsaturated compounds'. In: *React. Kinet. Mech. Catal.* 137 (1 16th Nov. 2023), pp. 53–76. DOI: 10.1007/s11144-023-02524-7.

[61] Tobias Jung, Annika Höhn and Tilman Grune. 'The proteasome and the degradation of oxidized proteins: Part II - protein oxidation and proteasomal degradation'. In: *Redox Biol.* 2 (1st Jan. 2014), pp. 99–104. DOI: 10.1016/j.redox.2013.12.008.

[62] Jeff H Duyn and John Schenck. 'Contributions to magnetic susceptibility of brain tissue: Magnetic Susceptibility of Brain Tissue'. In: *NMR Biomed.* 30 (4 1st Apr. 2017), e3546. DOI: 10.1002/nbm.3546.

[63] Qiqi Gao et al. 'Role of iron in brain development, aging, and neurodegenerative diseases'. In: *Ann. Med.* 57 (1 Dec. 2025), p. 2472871. DOI: 10.1080/07853890.2025.2472871.

[64] Haining Long et al. 'Iron homeostasis imbalance and ferroptosis in brain diseases'. In: *MedComm* 4 (4 1st Aug. 2023), e298. DOI: 10.1002/mco2.298.

[65] Kathryn D Bewley et al. 'Multi-heme proteins: nature's electronic multi-purpose tool'. In: *Biochim. Biophys. Acta* 1827 (8-9 1st Aug. 2013), pp. 938–948. DOI: 10.1016/j.bbabio.2013.03.010.

[66] Klaudia Jomova et al. 'Metals, oxidative stress and neurodegenerative disorders'. In: *Mol. Cell. Biochem.* 345 (1-2 22nd Dec. 2010), pp. 91–104. DOI: 10.1007/s11010-010-0563-x.

[67] Mauricio G Martín and Carlos G Dotti. 'Plasma membrane and brain dysfunction of the old: Do we age from our membranes?' In: *Front. Cell Dev. Biol.* 10 (6th Oct. 2022), p. 1031007. DOI: 10.3389/fcell.2022.1031007.

[68] Eugenio F Fornasiero et al. 'Precisely measured protein lifetimes in the mouse brain reveal differences across tissues and subcellular fractions'. In: *Nat. Commun.* 9 (1 12th Oct. 2018), p. 4230. DOI: 10.1038/s41467-018-06519-0.

[69] Sjors H W Scheres, Benjamin Ryskeldi-Falcon and Michel Goedert. 'Molecular pathology of neurodegenerative diseases by cryo-EM of amyloids'. In: *Nature* 621 (7980 27th Sept. 2023), pp. 701–710. DOI: 10.1038/s41586-023-06437-2.

[70] Paula Cadenas-Garrido et al. 'Using redox proteomics to gain new insights into neurodegenerative disease and protein modification'. In: *Antioxidants (Basel)* 13 (1 20th Jan. 2024), p. 127. DOI: 10.3390/antiox13010127.

[71] Stefanie Grimm et al. 'Protein oxidative modifications in the ageing brain: consequence for the onset of neurodegenerative disease'. In: *Free Radic. Res.* 45 (1 Jan. 2011), pp. 73–88. DOI: 10.3109/10715762.2010.512040.

[72] Lisa J Zimmerman et al. 'Global stability of plasma proteomes for mass spectrometry-based analyses'. In: *Mol. Cell. Proteomics* 11 (6 1st June 2012), p. M111.014340. DOI: 10.1074/mcp.M111.014340.

[73] H Auer et al. 'The effects of frozen tissue storage conditions on the integrity of RNA and protein'. In: *Biotech. Histochem.* 89 (7 Oct. 2014), pp. 518–528. DOI: 10.3109/10520295.2014.904927.

[74] Maryam Shabihkhani et al. 'The procurement, storage, and quality assurance of frozen blood and tissue biospecimens in pathology, biorepository, and biobank settings'. In: *Clin. Biochem.* 47 (4-5 Mar. 2014), pp. 258–266. DOI: 10.1016/j.clinbiochem.2014.01.002.

[75] Janine Geissenberger et al. 'Effect of temporary freezing on postmortem protein degradation patterns'. In: *Int. J. Legal Med.* 137 (6 Nov. 2023), pp. 1803–1814. DOI: 10.1007/s00414-023-03024-y.

[76] Nora Corthésy, Jonathan B Antcliffe and Farid Saleh. 'Taxon-specific redox conditions control fossilisation pathways'. In: *Nat. Commun.* 16 (1 29th Apr. 2025), p. 3993. DOI: 10.1038/s41467-025-59372-3.

[77] Jonathan B Antcliffe et al. 'Rapid oxygen drawdown in decay experiments on marine ( *Palaemon varians* ) and freshwater ( *Neocaridina davidi* ) shrimps'. In: *R. Soc. Open Sci.* 13 (3 25th Mar. 2026), p. 251712. DOI: 10.1098/rsos.251712.

[78] Yasset Perez-Riverol et al. 'The PRIDE database at 20 years: 2025 update'. In: *Nucleic Acids Res.* 53 (D1 6th Jan. 2025), pp. D543–D553. DOI: 10.1093/nar/gkae1011.

# 5 Discussion & Conclusions

## 5.1 From Destruction to Divergence: Reframing Decomposition

The following sections present an integrated synthesis organised around five theme-level statements. Each begins with a concise declarative claim capturing a cross-paper pattern that emerges when the three data chapters are considered holistically (Sections 5.1.1 to 5.1.4). The fifth theme (Section 5.1.5) draws these strands together to articulate the conceptual advance this work contributes to the field, reshaping our current understanding of soft-tissue decomposition and preservation.

### 5.1.1 Brain preservation is systematic, not anomalous

> *Human brain preservation is widespread, correlates with climate, and is disproportionately persistent relative to other soft tissues, demonstrating that its preservation is not anomalous but reflects a reproducible, organ-specific taphonomic trajectory.*

Soft-tissue preservation in the archaeological record has traditionally been regarded as an exceptional, sporadic, and largely unpredictable phenomenon. This notion rests on two implicit assumptions: first, that internal organs follow a broadly uniform *post-mortem* trajectory of rapid, irreversible loss culminating in total destruction (what we might call a 'uniform decay' model) [1]; and second, that when soft tissues do persist, they do so primarily because decomposition has been

arrested wholesale by rare or extraordinary conditions [2]. Within this conceptual framework, preserved brains appear doubly improbable: among the fastest organs to autolyse and subsequently putrefy, their persistence on geological timescales – particularly beyond those of familiar mechanisms of preservation – has been viewed as exceedingly unlikely.

The evidence collated in this thesis forces a rethink of this traditional model of soft-tissue preservation. More than 4,400 preserved human brains are documented from every inhabited continent across the 12,000 years of the Holocene Epoch, which resolve into multiple preservation types whose distributions differ in space and time. Their prevalence and persistence varies systematically with geography and palaeoclimate, correlating with environmental variables like temperature, precipitation, elevation, and latitude, to such an extent that preservation types tend to correspond to a single present-day Köppen climate classification: for instance, dehydrated brains are found principally in hot deserts, frozen brains in polar tundras, and tanned brains in low-lying bogs.

Whereas internal organs are vanishingly rare in searchable bioarchaeological repositories, preserved brains are reported in numbers that markedly exceed those of other soft tissues documented over comparable time periods. The archive collated here, however, does not record brain preservation in isolation: for each site, it also documents the presence or absence of abdominal, thoracic, pelvic, muscular, retinal, collagenous, and keratinous tissues preserved in association with nervous tissues. The archive is therefore not simply a catalogue of finds; it is an empirical indication that, under certain conditions, certain soft tissues persist with sufficient regularity to be treated as anticipated rather than anomalous. These trends – in geographic and palaeoclimatic distribution, and in patterns of tissue co-occurrence – simultaneously support two inferences: preservation is systematic rather than sporadic, and internal organs do not share a single *post-mortem* fate.

These trends also suggest that 'soft tissue' does not constitute a chemically coherent umbrella term in molecular taphonomy, in the way that 'hard tissue' does. Bones and teeth are united by their high inorganic content and comparatively

constrained molecular composition [3, 4]; they comprise only a handful of cell types [5] and express only a fraction of the human proteome [6–8], being dominated by a narrow set of ECM proteins [9]. Internal organs, by contrast, lack unifying features that permit their grouping together in the same manner. They differ radically in biochemical composition, cellular architecture, and proteomic complexity [10–12], and there is no logical basis for assuming that they should share a uniform trajectory of decomposition. If organs begin from different molecular starting points, then multiple decay pathways are not only possible, but expected; and the tissue combinations observed across sites indicate that such divergence is realised in practice.

Further divergence is evident in the trends observed with archaeological age. The numbers of certain preservation types dwindle rapidly with time, while others persist in appreciable numbers over much longer periods of Earth history. This points to a distinction that remains underdeveloped in the taphonomic literature, between what might be termed 'preservation by inhibition' and 'preservation by transformation'. Inhibitory types of preservation are those in which decomposition is suppressed or arrested while environmental conditions persist (such as dehydration and freezing with extremes of temperature); when those conditions fluctuate, however, decay resumes and tissues are lost. Transformative types, by contrast, are those in which early *post-mortem* chemistry generates altered, stabilised products that can persist once formed, even if the initial environmental conditions are not maintained indefinitely.

The clearest illustration of preservation by transformation is the 'unknown' preservation type; referred to hereafter as the 'crosslinked' type, a working label reflecting the mechanistic hypothesis developed across the subsequent data chapters. Almost one-third of the archive falls into this category, exhibiting no co-occurrence with other soft tissues, but a longevity that exceeds the maximum age of other preservation types by several millennia. These observations cannot be reconciled with, for instance, the concession that brains may be preserved only incidentally, collateral to broader soft-tissue persistence. Rather, they point to the existence of

an organ-specific taphonomic trajectory; a pathway to preservation that the CNS accesses disproportionately, in depositional contexts where other internal organs are lost. Experimental decay data supports this inference: controlling water and oxygen availability in the burial environment yields reproducible divergence in molecular fate, consistent with multiple, discrete *post-mortem* trajectories rather than a single, shared route to destruction. Given, then, that soft tissues vary systematically at the archaeological level, the next question is whether that variation extends to the molecular level; and, more specifically, whether the observed divergence in preservation is encoded in patterns of molecular persistence.

### 5.1.2 Molecular persistence is probabilistic, not random

> *Peptide survival in preserved brains is not uniformly distributed across the proteome but biased toward specific residues, structures, cellular components and biological functions, demonstrating that intrinsic tissue chemistry shapes post-mortem fate without rendering it strictly deterministic.*

It is important to recognise that 'preserved' does not imply 'unchanged'. In archaeological contexts, elaborate recording systems exist to quantify and grade the preservation state of hard tissues (e.g., based on anatomical completeness, degree of fragmentation, cortical erosion, enamel abrasion, colour modification, etc.), but the preservation of soft tissues is often treated as a binary state: either soft tissue survived, or it did not. That framing frustrates much of the research that might have been conducted, and obscures the more fundamental question of what biomolecular data survives within a preserved soft tissue.

The uniform-decay model predicts that what remains at the molecular level is an isometrically reduced remnant of what was present at death. However, peptide-specific decay modelling resolves distinct labile and recalcitrant classes on the basis of their net loss (or lack thereof) over a six-month PMI, demonstrating differential decay trajectories within the same proteome and indicating that decomposition proceeds selectively at the molecular level, rather than as a wholesale collapse of information. This selectivity is systematically associated with specific residues, structural motifs, functional domains, and protein classes, indicating that recalcitrance is probabilistic

rather than stochastic. Independent support for that selectivity comes from the palaeoproteomic data, where extraction and identification of ancient brain proteins yields a subset of the original brain proteome whose composition reflects differential survival of peptides with specific bio- and physicochemical features. Together these observations reject the null model of uniform-decay with random peptide persistence, and suggest instead that decomposition at the molecular level is a structured phenomenon.

A useful way to conceptualise that structure is as selective filtering. Early decay erases large fractions of the proteome, but that erasure is neither homogeneous nor monotonous; it preferentially removes components that are readily hydrolysed, proteolysed, or otherwise solubilised, leaving behind (and relatively enriching) those that are conformationally constrained, aggregated, or embedded in resistant architectures. This filtering manifests as a directional shift in proteomic composition throughout the PMI: morphing from a comparatively life-like intracellular proteome on the order of weeks after death, to an enzyme-rich, membrane-associated proteome on the order of months after death. The end-state palaeoproteome, then, is an altered subset produced by predictable retentions as well as by predictable losses. The features associated with those retentions point to three primary axes shaping molecular survival: residue chemistry, local structure, and microenvironment.

In terms of the first axis, recalcitrant peptides are enriched in residues whose side chains participate in redox chemistry in ways that stabilise intermediates and dissipate oxidative flux, and are depleted in residues whose chemistry more readily promotes fragmentation, solubilisation, or chemically mediated scission under oxidative and hydrolytic stress. Independent support for such redox-mediated processes comes from the modification patterns these residues exhibit: aldehyde adduct formation, metal-catalysed oxidation, and di-oxidation are among the most frequent diagenetic PTMs observed across both palaeoproteomic and experimental taphonomic datasets, and their prevalence increases as decomposition progresses. The radical buffering capacity of a peptide's primary sequence might therefore increase its likelihood of long-term persistence, not only because reactive residues

can act as radical sinks that passively absorb oxidative flux [13–16], but because they can actively function as stabilising nodes, participating in covalent coupling reactions that convert short-lived intermediates into more stable, crosslinked products [17–19].

The second axis is local structure. It seems reasonable to expect that structures conferring resistance to turnover in life – for example, by stabilising polypeptide architecture, or favouring controlled aggregation – would also increase resistance to enzymatic cleavage and hydrolytic attack after death. Recalcitrant peptides are more likely to be $\beta$-sheet-dominant and possess lower intrinsic disorder than labile peptides: $\beta$-sheets are densely hydrogen-bonded and closely packed, and their architecture tends to resist both proteolysis and conformational disruption [20]. *In vivo*, the same structural tendencies underpin pathological protein stabilisation in ageing and neurodegenerative proteinopathies [21–23]. The contexts differ, but the mechanistic implication is consistent: structurally ordered regions have fewer accessible scission points and fewer conformational degrees of freedom, and that constraint increases the likelihood that they persist into the late PMI.

The third axis is the biochemical and spatial context in which these primary and secondary structures are embedded. Strong biases toward lipid-binding domains and membrane-associated components are evident in both the palaeoproteomic and experimental taphonomic data, indicating that persistence is disproportionately associated with peptides situated in hydrophobic or otherwise aggregation-prone interfaces, rather than in freely soluble intracellular compartments. Such contexts also impose spatial constraint: they restrict molecular diffusion, concentrate reactive partners, and reduce bulk exchange with the surrounding environment. These conditions increase the likelihood that generated radicals and chemically modified products persist locally, rather than dispersing.

Together, these patterns support the assertion that intrinsic tissue chemistry influences molecular persistence, which in turn implies that the chemical state of a tissue at death is not incidental to its preservation. Organs differ in their biochemical composition and cellular architecture [12, 24], but also in the chemical stresses that they manage in life [25], and the protective molecular systems they maintain

as a consequence [26]. That characteristic stress landscape – what we might call the tissue's 'reactive chemistry profile' – helps to determine what substrates and catalytic environments are present at the onset of decomposition. The brain, with its outsized oxygen consumption, abundance of lipid-rich membranes, and extensive redox-associated machinery, is primed for oxidative processes *in vivo* [27]. *Ex vivo*, preserved nervous tissue features particularly strong enrichment of oxidoreductases, peroxidases, and metalloproteases among protein classes contributing recalcitrant peptides, alongside selective retention of myelin- and membrane-associated components; interfaces that, in life, are major sites of lipid peroxidation and which, in death, remain abundant substrates for oxidative modification. Oxidative chemistry is thus a dominant axis of neural physiology, and its molecular infrastructure persists into the PMI, where it represents an ideal mixture of precursor reagents for diagenetic redox chemistry.

Once molecular survival is framed in probabilistic terms, it becomes reasonable to ask what might shift those survival likelihoods between individuals. The archive of preserved human brains hints at a life-history signal in this respect: juvenile individuals are rare ($< 1\%$) among brains of the crosslinked type. Several confounds preclude strong inference from this observation alone: juvenile individuals may be under-represented in waterlogged burial contexts for independent demographic and/or mortuary reasons, smaller crania may be less likely to retain intact tissue, and recognition of brain material in younger individuals may be less reliable. These factors are difficult to disentangle from any intrinsic difference in preservation potential. Setting them aside, however, a testable complementary hypothesis is that the progressive accumulation of oxidative modification, long-lived modified proteins, and altered metal homeostasis with normal ageing (Section 1.5.2) alters the molecular substrate available for stabilising chemistry after death, providing a credible route by which *ante-mortem* tissue chemistry modifies the *post-mortem* taphonomic trajectory. The current evidence does not justify a strong claim; it does, however, warrant the inference that an individual's life history is a further,

credible axis along which persistence probabilities could vary, and one that can be tested directly in future work.

In sum, the 'preservation potential' of an organ, tissue, protein, or even an individual peptide, can be understood as the integrated suite of intrinsic chemical, structural, and microenvironmental features that increase the probability of its participating in stabilising reactions during decay. The findings synthesised here support an interpretation of molecular survival as probabilistic, but not deterministic: intrinsic tissue chemistry biases *post-mortem* fate by shaping which residues, domains, compartments, and architectures persist, and by constraining the range of stabilising reactions available during decomposition. As a result, peptide persistence can be modelled as a calibrated probability distribution linked to measurable molecular features, providing a quantitative basis for estimating preservation likelihood at the molecular level. That distribution, however, is modulated by burial environment, which changes the fraction of peptides that occupy the high-probability tail and, by extension, the extent to which intrinsic preservation potential is realised.

### 5.1.3 Environmental constraint redirects decay chemistry

> *Water and oxygen availability together regulate whether post-mortem oxidation propagates through chain-amplified fragmentation or terminates through crosslinking, thereby selecting between destabilising and stabilising trajectories.*

The presence of moisture in the burial environment is widely accepted as an accelerant of soft-tissue loss [28–30], given the role of water in supporting hydrolysis, enzymatic activity, and oxygen diffusion (Section 1.3.3.3). By contrast, freezing and dehydrating conditions are considered favourable for soft-tissue preservation because extremes of temperature inhibit decay by immobilising or removing water, respectively (Sections 1.4.1 and 1.4.2). The evidence assembled in this thesis directly challenges that simple dichotomy. One-third of the archaeological archive correspond to brains preserved for millennia in a diverse array of wet, oxygen-poor depositional contexts, from river banks to lake shores, and from flooded caves to shipwrecks; and this crosslinked type is strongly correlated with temperate and continental climates characterised by year-round, frequently heavy rainfall. Rather

than biasing the record toward absence, wet depositional contexts disproportionately host the most temporally persistent type of brain preservation, and the data are more consistent with the proposition that, under specific constraints, water alters the mode of decomposition rather than merely its rate.

The experimental taphonomic data resolve those constraints by isolating water and oxygen as independent variables. As decomposition advances, late-stage proteomes separate clearly by oxygenation: oxic samples extend the early degradative trajectory toward increasing proteomic loss and high late-stage variability, whereas hypoxic samples converge into a distinct compositional cluster associated with greater retention. Protein recovery is lowest under wet–oxic burial, but wet–hypoxic burial yields both the largest pool and highest proportion of recalcitrant peptides. Moreover, the chemical signatures of modification diverge systematically. Whereas wet–oxic burial is characterised by extensive oxidative and alkylative modification, wet–hypoxic burial exhibits a different pattern of oxidative change: specifically aldehyde adduct formation, metal-catalysed oxidation, and di-oxidation of aromatic residues. These modification profiles demonstrate that oxidation is not wholly absent under low-oxygen conditions; rather, it proceeds *via* alternative reaction pathways. In this respect, the experimental taphonomic results mirror the archaeological trends: hydration is compatible with persistence, but only when coupled with restricted oxygen availability.

Given oxidation persists under both wet–oxic and wet–hypoxic regimes, then the decisive variable cannot be whether oxidative reactions occur, but whether they propagate or terminate. When oxygen is readily available in an aqueous environment, radical propagation is more easily sustained, increasing the likelihood of chain-amplified oxidative fragmentation and widespread molecular loss. When oxygen is restricted, radical propagation is less likely to proceed efficiently; oxidation becomes self-limiting, and termination is more likely to occur at the site of radical generation by quenching or covalent crosslinking. In other words, water primarily controls encounter probability, while oxygen controls chain length. Together, they

determine whether radical oxidation behaves as a self-amplifying cascade, or as a series of local initiation–termination events.

While the water–oxygen regime determines whether oxidation follows a stabilising or destabilising trajectory, the outcome of that selection depends on the substrate upon which it acts. Thus this framework also resolves a second observation that otherwise appears paradoxical: why crosslinked brains preserve in waterlogged, oxygen-poor environments where other organs perish. Sequestered within the cranial vault, nervous tissue contains an unusually dense network of oxidation-prone lipid–protein interfaces [31–33], redox-active metals [34, 35], and membrane-associated microenvironments [36–39] capable of generating, constraining, and terminating radical intermediates; conditions that favour stabilisation by crosslinking over destruction by fragmentation.

In effect then, the depositional context governs whether molecular features of preservation potential are amplified or erased. These findings collapse the long-standing assumption that environmental conditions can be classified according to inherently preservative or destructive effects. The role of water in preservation of the CNS is a particularly clear example: under disparate oxygen regimes it can select between competing oxidative pathways, such that stabilisation and destruction emerge as alternative outcomes of the same chemical system under different constraints. The remaining question is when that selection is made: that is, whether long-term persistence reflects prolonged transformation over millennia, or adoption of an early pathway that subsequently constrains the course of *post-mortem* alteration.

### 5.1.4 Long-term preservation is established early *post-mortem*

> *The taphonomic trajectory that enables millennial brain preservation is established during the early PMI, when shifts in molecular-loss dynamics constrain the subsequent course of decomposition.*

Long-term soft-tissue preservation has generally been attributed either to continuous diagenetic transformation [40], or a largely static state in which early decay

stabilises molecular profiles that reflect to the *ante-mortem* condition [41, 42]. The evidence assembled in this thesis, however, supports neither model. Although crosslinked brains persist for millennia, the taphonomic trajectory that permits such persistence is established during the early PMI, when autolysis and the first wave of putrefaction coincide. During this window of molecular reorganisation, partial degradation both alters the *ante-mortem* state, and generates the reactive intermediates and partially transformed biomolecular substrates from which long-term stabilisation ultimately arises.

The conventional stages into which taphonomists carve decomposition distinguish 'active decay' from 'post-decay', but the transition between these phases is defined descriptively (e.g., by changes in colour, odour, texture, etc.) and varies temporally with depositional context. The molecular changes that accompany this transition remain poorly understood; however, the time-resolved modelling approach employed in this thesis offers a quantitative means of examining that transition directly, at the scale of individual peptides. During the earliest phase of decomposition under wet–hypoxic burial, labile peptides exhibit no measurable net decline despite ongoing molecular alteration; only after an estimated breakpoint near the end of the first week after death does their depletion accelerate. The timing of this breakpoint is imprecise, but its significance lies in demonstrating that peptide transformation and peptide loss become transiently uncoupled under wet–hypoxic burial in the early PMI.

The most parsimonious interpretation of this slope behaviour is that early decay under wet–hypoxic burial involves a phase of molecular reorganisation in which diagenetic breakdown products are generated and retained within aqueous but oxygen-limited microenvironments. Under these conditions (Section 5.1.3), early cleavage and modification of labile peptides need not translate immediately into net loss, as observed in other water–oxygen regimes; rather, modified fragments and oxidised intermediates are more likely to remain locally confined and available for subsequent transformation to stable end-products, than to undergo further chain-amplified degradation. The apparent 'plateau' in peptide intensity is therefore consistent with a phase in which molecular conversion and retention balance

depletion. Over time, however, the labile fraction diminishes and the proteome becomes progressively enriched in recalcitrant components, producing the observed change in slope.

The importance of early diagenesis in stabilising biomolecules is not wholly unprecedented. Wiemann *et al.* [43] demonstrated that vertebrate hard-tissue proteins can undergo rapid oxidative crosslinking during fossilisation, producing ALE/AGE-derived N-heterocyclic polymers that resist further degradation (Section 1.4.5.2). In their study, chemically transformed soft tissues were observed only in specimens from oxidative depositional environments, with sediment colour and mineralogy used as proxies for redox conditions. Preservation was therefore interpreted as contingent upon burial in oxygen-rich settings, whereas reducing environments were considered incompatible with such transformation. The evidence collected in this thesis both corroborates and refines that framework. While it corroborates the central proposition that oxidative chemistry can contribute to long-term preservation by generating stabilised molecular products during early diagenesis, at the same time, it provides direct evidence that the molecular trajectories leading to preservation diverge during the early PMI, as peptide-loss kinetics and modification patterns begin to separate under different depositional contexts. Most importantly, it expands the range of environmental conditions under which such stabilisation can occur: the experimental data demonstrate that oxygen-poor burial can also yield stabilised molecular residues, provided that radical reactions terminate locally rather than propagating through chain-amplified oxidation. Long-term preservation therefore need not imply prolonged transformation over centuries; it can reflect early formation of stabilised products followed by slower subsequent change – an outcome that is rare only insofar as the necessary early conditions may rarely be met.

### 5.1.5 Preservation is a permissible outcome of decay

Schweitzer *et al.* [44] suggest that, for soft tissues and the proteins comprising them to preserve on geological timescales, 'a mode of preservation sufficiently rapid to outpace decay is required'. Indeed, across palaeontological, archaeological and

forensic discourse, decay and preservation are typically treated as opposing forces: decay is understood as progressive deterioration culminating in total destruction, whereas preservation is understood as its inhibition or arrest. That opposition is apposite for some forms of soft-tissue preservation, particularly those in which environmental extremes inhibit autolysis, putrefaction, or both; however, it is not appropriate for all of them.

The principal conceptual advance of this thesis is not simply that preservation can occur during decomposition, but that some types of preservation are generated by decomposition itself. In such cases, persistence reflects the formation of altered products that outlast the conditions under which they formed: what survives is not an unmodified residue spared from decay, but the chemically transformed outcome of it. The emphasis of taphonomic interpretation then shifts from whether decomposition was prevented, to how it proceeded: that is, which reaction pathways were available and realised during the early PMI, and whether they favoured suppression of decay, degradation, or transformation into more recalcitrant products. Decomposition is thus better understood not as a single route to destruction, but as a collection of branching chemical pathways whose possible endpoints include both destruction and stabilisation. Preservation, in this sense, is a chemically contingent outcome of decay rather than an anomalous departure from it.

## 5.2 Limitations

### 5.2.1 Of the archaeological archive

The principal limitation of the archive collated is, in part, a consequence of its scale and temporal breadth. Given its size (comprising more than 200 sources) and span of roughly four centuries of literature, it does not derive from standardised observation, but instead from heterogeneous reports produced across different languages, time periods, disciplines, and descriptive traditions. As a result, there is substantial variation in the amount of contextual detail provided, the extent and quality of associated metadata, the confidence with which preservation types are identified, and the terminology used to describe them. The archive therefore

supports the existence of several distinctive and recurring types of brain preservation, but cannot in isolation demonstrate that all cases assigned to each category represent equivalent end-members of a single taphonomic trajectory.

A related constraint is that the archive records broad environmental associations more effectively than it captures the immediate burial chemistry that would have governed decay. Variables such as Köppen climate classification, temperature, precipitation, latitude, and elevation are informative at regional scale, but they are only indirect, site-level proxies for the microenvironmental conditions in which *post-mortem* reactions actually occurred. Furthermore, while every effort was made to reconstruct these variables specifically for the interval of time in which deposition took place, in several instances – particularly in the pre-19$^{\text{th}}$ C. literature – the interval between deposition, excavation, and publication is uncertain. Regardless of the age of the report, parameters more proximal to *post-mortem* chemistry –such as pore-water composition, matric potential, diffusion dynamics, redox state, sediment mineralogy, iron speciation, microbial ecology, and coffin or container effects – are rarely recorded in sufficient detail, and entirely absent in most cases. The archive therefore identifies large-scale environmental correlations with preservation type, but those correlations must not be interpreted as evidence that an environmental variable acted as a driver of preservation in any individual case.

The archive also permits only an imprecise estimate of how frequent brain preservation may be relative to preservation of other soft tissues. The literature is strongly shaped by recognition and reporting bias: on the one hand, preserved brains may be preferentially reported because they are perceived as unusual, whereas other forms of soft-tissue preservation may receive less attention or fail to be recognised and recorded altogether. Conversely, preserved brains may be particularly prone to under-reporting, given their recovery depends upon recognition of an unexpected soft tissue concealed within the cranial cavity. Only a minority of reports quantify recovery frequency, and searchable bioarchaeological repositories remain heavily biased toward hard tissues and under-utilised for soft tissues. Thus, while the archive demonstrates convincingly that brain preservation is systematic rather than

anomalous, it cannot determine the true incidence of this phenomenon, nor how often comparable forms of selective soft-tissue preservation may have gone unrecognised.

### 5.2.2 Of the experimental design

Chapter IV provides strong evidence for the effects of water and oxygen availability on early *post-mortem* taphonomic trajectories, but it does so in a deliberately simplified system. Burial in sterile quartz sand under tightly controlled laboratory conditions was appropriate for isolating specific variables, yet necessarily excluded many features of the burial environment that may influence decomposition, including natural sediment heterogeneity, mineralogy, and mineral–organic interactions; variation in grain size and permeability; fluctuating hydrology and water retention; and pH variability and redox cycling mediated by the burial matrix. The experiment thus demonstrates that divergent molecular trajectories can be generated by controlled water–oxygen regimes, but cannot establish that these two variables alone account for the full complexity of CNS preservation in natural settings.

A further limitation is temporal, in that the experiment extended only to a six-month PMI. This was sufficient to demonstrate early divergence in peptide-loss dynamics, to identify decay-prone and decay-resistant molecular classes, and to support the hypothesis that long-term preservation is established soon after death. However, the archaeological and fossil records extend over many thousands to millions of years, and the experiment patently does not observe this subsequent diagenetic interval during which those early-formed products must remain stable.

The primary translational limitation is the use of mouse rather than human carcasses. Mice differ from humans in body size, body composition, lipid profile, skull geometry, and microbiome composition, all of which may influence the rate and mode of *post-mortem* molecular change. Skull geometry is particularly relevant: the degree to which the cranial cavity becomes effectively sealed after burial, and thereby develops an internally hypoxic microenvironment, will differ between rodents and humans, and may affect the rate and extent of oxygen depletion within the brain. Mouse models were used for practical and ethical reasons – whole-carcass

decay is rarely possible with human material – but the degree to which mouse brain taphonomy faithfully recapitulates the trajectories relevant to human archaeological brain preservation remains an open question.

Finally, although whole corpses were decayed, molecular analysis was restricted to the brain. The thesis demonstrates that nervous tissue can enter a stabilising *post-mortem* taphonomic trajectory under particular environmental conditions, but does not directly test whether other soft tissues or internal organs exposed to the same conditions would fail to do so, or whether they would follow equivalent or divergent trajectories.

### 5.2.3 Of the molecular evidence

The palaeoproteomic and experimental taphonomic data consistently support a model of radical-mediated oxidative crosslinking, through convergent evidence from peptide persistence, residue enrichment, structural bias, domain-level associations, and modification profiles, among other orthogonal sources. However, the crosslinked products themselves have not been isolated and structurally characterised in a way that would directly identify the specific inter- and intramolecular covalent linkages, or the resulting high-molecular-weight crosslinked products, responsible for long-term stabilisation.

Interpretation of molecular persistence is also constrained by the selectivity of analytical recovery and identification. Palaeoproteomic data do not provide a direct inventory of all molecules that persisted in the tissue; rather, they reflect the subset that persisted, remained extractable, produced detectable peptides, could be confidently identified by current workflows and reference databases, and met downstream confidence thresholds for retention in the analysed dataset. Chapter III demonstrates that extraction chemistry, clean-up strategy, and instrument configuration strongly influence which peptides and proteins are recovered, particularly for hydrophobic, membrane-associated, or otherwise recalcitrant analytes. Molecular recalcitrance must therefore be interpreted with care, given some components may be under-represented or absent for analytical reasons, rather than because they were not

preserved. This caveat has particular force at the most critical point of the argument: the highly crosslinked, insoluble, high-molecular-weight products proposed as the endpoint of stabilising chemistry are precisely those least amenable to tryptic digestion, solubilisation, and downstream detection by bottom-up proteomics. The molecular evidence for crosslinking is therefore necessarily indirect, assembled from the behaviour of soluble peptide fractions rather than from direct characterisation of the insoluble products themselves. That the convergent evidence from peptide persistence, residue enrichment, structural bias, and modification profiles nonetheless constitutes a coherent and internally consistent case for radical-mediated crosslinking is, in this light, a stronger result than it might otherwise appear: it is built from the fraction of the molecular record that is hardest to interpret, and argues from absence and pattern rather than from direct detection of the proposed products.

Finally, the methodological optimisation was conducted on a single archaeological brain, and without replicate extractions. That design was justified ethically by the human and irreplaceable nature of the material, and was appropriate for proof-of-concept development; however, it may constrain the method's generalisability. Different preserved brains may vary substantially in terms of the life history of the individual, and the taphonomic history of their remains, both of which may affect extraction efficiency and ultimately the palaeoproteome recovered. The optimised workflow is therefore a major methodological advance, but the extent to which it captures the full diversity of preserved brain palaeoproteomes remains to be established.

## 5.3 Further Work

The following section outlines targeted avenues for further work that address three specific limitations identified above: first, a within-body, multi-organ comparison required to resolve selective tissue persistence (Section 5.2.2); second, direct structural characterisation of the crosslinked products underpinning long-term stabilisation (Section 5.2.3); and third, establishing the generalisability of the optimised palaeoproteomic workflow (Section 5.2.3).

### 5.3.1 Experimental resolution of organ-specific taphonomic divergence

To resolve selective survival beyond the brain, the existing whole-carcass decay model should be expanded into a matched multi-organ time series under the same four burial regimes. Rather than analysing nervous tissue alone, other soft tissues and internal organs should be sampled alongside nervous tissue from the same individual carcasses at each PMI, and processed in parallel using the same extraction and acquisition pipeline. Peptide-level data should then be modelled with the analytical pipeline developed in Chapter IV – that is, estimation of peptide-specific decay slopes, classification of peptides into labile, intermediate, and recalcitrant classes, and evaluation of compositional, structural, and functional correlates of persistence – but with organ type included as a fixed effect in the regression model, and carcass treated as a random effect to account for within-individual dependence.

This expanded experimental design would allow direct testing of whether wet–hypoxic conditions generate a disproportionately large recalcitrant fraction in the brain relative to other organs, and whether this divergence increases through time as labile components are progressively lost, potentially resulting in a state in which nervous tissue is the only tissue retained. It would also allow evaluation of whether the same molecular features of recalcitrance (e.g., structurally-ordered, redox-active, and membrane-associated proteins) are uniquely enriched in the preserved CNS, or are preferentially retained in other soft tissues under comparable conditions. A valuable extension would be to pair proteomics with measurements of endogenous (tissue-derived) iron and copper by inductively coupled plasma–MS (ICP–MS), and with histology or immunohistochemistry targeting myelin-rich, pigmented, or ferritin-rich regions, so that any organ-level differences in recalcitrance can be related directly to metal loading, lipid architecture, and cellular organisation. This would move the thesis from inference about organ specificity to direct within-body comparison.

### 5.3.2 Direct characterisation of crosslinked products

To determine whether the radical-mediated oxidative crosslinking mechanism is underpinned by specific covalent products, direct characterisation would be required – and it is worth noting that this is analytically non-trivial for precisely the reasons identified above (Section 5.2.3): the products of interest are, by hypothesis, insoluble, high-molecular-weight, and refractory to the extraction and digestion workflows on which mass spectrometric characterisation depends. The following represents a pragmatic strategy for making inroads on that problem, designed for crosslink and adduct discovery rather than conventional bottom-up peptide recovery, and proceeding from the most accessible fractions toward the most recalcitrant.

A starting point would be sequential extraction of preserved brains of the crosslinked type in 8 M urea using the best-performing workflow identified in Chapter III, followed by high-speed centrifugation (e.g., $\geq$ 20,000 rcf, 10–20 min) to separate the urea-soluble fraction from an insoluble pellet. The pellet should then be washed repeatedly (e.g., with ammonium bicarbonate and organic solvents) to remove residual soluble material, and its insolubility verified empirically by monitoring protein yield across successive extraction steps (e.g., by BCA assay or LC–MS signal intensity), until no further recoverable material is detected in the supernatant. Material remaining after this step would constitute an operationally defined insoluble fraction for downstream analysis.

A second-stage extraction should then be applied to this insoluble fraction to test whether any component is conditionally insoluble rather than irreversibly crosslinked. This could involve re-extraction using stronger chaotropic conditions (e.g., 6 M GuHCl), ionic detergents (e.g., SDS), or limited chemical or enzymatic digestion (e.g., dilute acid hydrolysis or broad-specificity proteases). Any material brought back into solution at this stage should be retained as a separate 're-solubilised' fraction and analysed alongside the primary urea-soluble extract, given it may contain crosslinked or aggregated species that are refractory to standard extraction, but remain amenable to mass spectrometric characterisation. The residual material that remains insoluble after this second-stage treatment can

then be operationally defined as a highly recalcitrant fraction, likely enriched in extensively crosslinked and/or mineral-associated material.

Both soluble fractions should then be subjected to size-based separation (e.g., size-exclusion chromatography or ultrafiltration) to enrich high-molecular-weight species prior to LC–FAIMS–MS/MS. Data should be interrogated using crosslink-aware and open-modification search strategies (e.g., pLink [45, 46], XlinkX [47], or MSFragger [48] in open-search mode), rather than standard semi-tryptic workflows, to identify inter- and intramolecular peptide–peptide linkages, as well as peptide–lipid and other adduct masses. The insoluble fraction should be examined in parallel by solid-state or minimally destructive methods capable of resolving bulk product chemistry. For example, attenuated total reflectance–Fourier transform infrared (ATR–FTIR) spectroscopy and Raman microspectroscopy can be used to detect functional group transformations consistent with carbonylation, aromatic condensation, and heterocycle formation; pyrolysis–gas chromatography–MS (py–GC–MS) may be used to release diagnostic fragments from otherwise intractable macromolecular networks (e.g., ALEs/AGEs, or sulfur-linked species); and X-ray absorption spectroscopy (XAS) at the Fe and Cu K-edges, ideally coupled with micro-X-ray fluorescence (micro-XRF) mapping, may be used to determine whether transition metals are present in coordination environments consistent with incorporation into the stabilised residue.

### 5.3.3 Validation of the palaeoproteomic workflow across preserved brains

To establish whether the optimised palaeoproteomic workflow captures the diversity of preserved brain palaeoproteomes, it should next be tested across a deliberately stratified validation set. A pragmatic approach would be a multi-sample benchmarking study in which preserved brains are selected to span the five preservation types represented in the archive, with particular emphasis on multiple crosslinked brains from different archaeological sites and periods. Each specimen should be subsampled for technical replicates and processed using the current best-performing

urea-based workflow, alongside a small comparator panel of alternative extraction and clean-up strategies (e.g., urea with FASP, SDS with S-Trap, and SP3) to confirm that the preferred workflow remains optimal across a diverse set of preserved brains.

Acquisition should take the form of the Chapter III configuration that performed best, namely LC–FAIMS–MS/MS with the Orbitrap Ascend and DIA-NN-based [49] library-free analysis. Evaluation should build on the criteria established in Chapter III – such as recovery of non-tryptic and highly modified peptides, representation of intracellular domains, and contamination levels – while additionally assessing reproducibility across technical replicates, and concordance of palaeoproteomic profiles among samples from comparable depositional contexts. Consistent recovery of similar protein group identities, peptide modification spectra, and relative abundance distributions within preservation types would suggest that the recovered palaeoproteomes are shaped primarily by shared constraints on molecular survival under those conditions, rather than by stochastic loss, inter-individual or -site variability, or analytical variability. Conversely, systematic differences in the composition of recovered palaeoproteomes between extraction protocols applied to the same sample would indicate that method-dependent biases influence which components are retrieved, and therefore whether the full diversity of the palaeoproteome is captured by a given workflow. This approach would convert the Chapter III method development from a proof-of-concept optimised on one specimen into a generalisable analytical strategy for the preserved CNS.

## 5.4 Future Directions

### 5.4.1 Peptide-level decay profiling as a method of predictive taphonomy

The quantitative framework developed in Chapter IV suggests a route towards predictive taphonomy. By demonstrating that peptide persistence can be modelled and that recalcitrance is associated with distinct molecular features, the thesis establishes the basis for estimating preservation potential proactively, rather than describing preservation outcomes retrospectively. Applied within the multi-organ

experimental framework proposed (Section 5.3.1), peptide-level decay models could be developed for multiple tissues under controlled environmental conditions. Sequence, structural, domain, and modification features associated with recalcitrance could then be incorporated as explanatory variables to generate tissue-specific estimates of peptide survival under defined water–oxygen regimes. Mapped onto tissue-resolved reference proteomes [12], these models would permit estimation of the proportion of a tissue proteome expected to fall within a high-probability recalcitrant class; in effect, providing a quantitative measure of tissue-level preservation potential derived from underlying molecular properties. Comparisons among tissues could then identify those expected to retain the greatest fraction of their proteome under particular environmental conditions.

### 5.4.2 Preserved brains as a new archive for molecular palaeobiology and palaeopathology

The combination of the archaeological survey presented in Chapter II and the palaeoproteomic workflow developed in Chapter III establishes preserved brains as a previously underutilised archive for molecular palaeobiology. With more than 4,400 documented cases spanning the Holocene and the recovery of more than 1,200 proteins from a single specimen, preserved brains are both abundant and analytically tractable. Unlike bone and enamel [6–8], they provide access to a wide range of proteins associated with intracellular compartments, membranes, and core physiological processes, thereby extending palaeoproteomic investigation into biological systems that are largely inaccessible through mineralised tissues.

One immediate application is palaeopathology. Whereas human diseases number in the high tens of thousands [50], those with significant skeletal involvement number in the low hundreds [51]; as such, much of the human disease burden remains invisible within the hard-tissue bioarchaeological record. By contrast, a substantial proportion of diseases involve the CNS [52], either as a primary site of pathology or through secondary effects, and manifest at the molecular level through disruption of cellular homeostasis with altered protein expression and modification

[53–55]. Preserved brains thus permit the study of pathological conditions otherwise undetectable to bioarchaeologists. Crucially, realising this potential depends on distinguishing diagenetic modification and selective retention *post-mortem* from *ante-mortem* biological variation: the peptide-level taphonomic framework developed in Chapter IV provides a means of doing so in preserved brains, and Chapter III demonstrates that the resulting palaeoproteomes are of sufficient depth and breadth of composition to support such studies in practice.

Finally, the value of this archive extends beyond ancient disease alone. One of the most striking and consistent findings of this thesis is that the molecular features associated with long-term peptide persistence in the brain overlap with those implicated in pathological protein stabilisation, ageing, and NDDs. Preserved brains may therefore represent a unique opportunity to investigate the long-term consequences of these processes over timescales inaccessible to clinical or experimental neuroscientific studies, offering a complementary perspective on protein stability and the molecular biology of brain ageing.

## 5.5 Conclusions

Ancient, preserved human brains have long been treated as anomalous finds, yet this thesis demonstrates that their persistence in the archaeological record is neither rare nor inexplicable. By integrating a global archaeological survey, palaeoproteomic method development, and experimentally resolved, peptide-level decay modelling, it demonstrates that brain preservation reflects a reproducible, organ-specific taphonomic trajectory realised under particular environmental conditions. The archaeological archive establishes that preserved brains are widespread across the Holocene and that a substantial subset persists as the sole surviving soft tissue, especially in waterlogged, oxygen-poor depositional contexts. This distribution reflects a fundamental distinction between two modes of preservation: inhibitory preservation, in which decay is suppressed while particular environmental conditions persist, and transformative preservation, in which early *post-mortem* chemistry generates chemically altered products stable enough to outlast the conditions that

produced them. The crosslinked type belongs to the latter category, which explains both its temporal persistence and its independence from any single set of sustained environmental conditions. The methodological work then shows that such tissues can yield deep, information-rich palaeoproteomes, extending palaeoproteomics beyond mineralised substrates and rendering preserved internal organs analytically tractable as high-dimensional molecular archives.

Finally, the experimental taphonomic results resolve the paradox of selective brain preservation by showing that wet–hypoxic conditions divert the brain proteome onto a distinct taphonomic trajectory, characterised by radical-mediated oxidative crosslinking in membrane-associated microenvironments. Long-term preservation is established early, when intrinsic tissue chemistry and burial environment interact to constrain *post-mortem* molecular fate. Preservation potential – an intrinsic, probabilistic property of tissues that may be expressed as a distribution of survival likelihoods across molecular features – determines which components of the proteome are capable of participating in stabilising reactions; whereas environmental redox conditions, principally the interaction of water and oxygen availability, govern whether those reactions proceed *via* chain-propagating fragmentation or terminate through crosslinking. Soft-tissue preservation is therefore neither inevitable nor anomalous, but conditional: it emerges where intrinsic preservation potential is realised under environmental conditions that favour stabilising chemistry. By resolving how these intrinsic and extrinsic controls interact during the early PMI, this thesis reframes soft-tissue preservation as an explicable, chemically contingent outcome of decomposition: not a chance departure from decay, but a consequence of it, under defined physicochemical constraints.

## 5.6 References

[1] John Pless, Michael Worrell and Michael Clark. 'Postmortem changes in soft tissues'. In: *Forensic Taphonomy*. Ed. by W D Haglund and M H Sorg. Bosa Roca: CRC Press, 13th Dec. 1996, pp. 151–164. DOI: 10.1201/9781439821923.ch9.

[2] Thomas Clements and Sarah Gabbott. *Pers. comm.* 13th Apr. 2022.

[3] Liam C Palmer et al. 'Biomimetic systems for hydroxyapatite mineralization inspired by bone and enamel'. In: *Chem. Rev.* 108 (11 Nov. 2008), pp. 4754–4783. DOI: 10.1021/cr8004422.

[4] Jingxiao Zhong and Yo Shibata. 'The structural motifs of mineralized hard tissues from nano- to mesoscale: A future perspective for material science'. In: *Jpn. Dent. Sci. Rev.* 58 (Nov. 2022), pp. 348–356. DOI: 10.1016/j.jdsr.2022.11.001.

[5] Adele L Boskey and Rani Roy. 'Cell culture systems for studies of bone and tooth mineralization'. In: *Chem. Rev.* 108 (11 19th Nov. 2008), pp. 4716–4733. DOI: 10.1021/cr0782473.

[6] Rodrigo D A M Alves et al. 'Unraveling the human bone microenvironment beyond the classical extracellular matrix proteins: a human bone protein library'. In: *J. Proteome Res.* 10 (10 7th Oct. 2011), pp. 4725–4733. DOI: 10.1021/pr200522n.

[7] Ana Gil-Bona and Felicitas B Bidlack. 'Tooth Enamel and its Dynamic Protein Matrix'. In: *Int. J. Mol. Sci.* 21 (12 23rd June 2020), E4458. DOI: 10.3390/ijms21124458.

[8] Jacob P Rose et al. 'Deep coverage and quantification of the bone proteome provides enhanced opportunities for new discoveries in skeletal biology and disease'. In: *PLoS One* 18 (10 10th Oct. 2023), e0292268. DOI: 10.1371/journal.pone.0292268.

[9] Margalida Fontcuberta-Rigo, Miho Nakamura and Pere Puigbò. 'Phylobone: a comprehensive database of bone extracellular matrix proteins in human and model organisms'. In: *Bone Res.* 11 (1 15th Aug. 2023), p. 44. DOI: 10.1038/s41413-023-00281-w.

[10] Fredrik Pontén et al. 'A global view of protein expression in human cells, tissues, and organs'. In: *Mol. Syst. Biol.* 5 (1 22nd Dec. 2009), p. 337. DOI: 10.1038/msb.2009.93.

[11] Linn Fagerberg et al. 'Analysis of the human tissue-specific expression by genome-wide integration of transcriptomics and antibody-based proteomics'. In: *Mol. Cell. Proteomics* 13 (2 Feb. 2014), pp. 397–406. DOI: 10.1074/mcp.M113.035600.

[12] Mathias Uhlén et al. 'Proteomics. Tissue-based map of the human proteome'. In: *Science* 347 (6220 23rd Jan. 2015), p. 1260419. DOI: 10.1126/science.1260419.

[13] R L Levine, J Moskovitz and E R Stadtman. 'Oxidation of methionine in proteins: roles in antioxidant defense and cellular regulation'. In: *IUBMB Life* 50 (4-5 1st Oct. 2000), pp. 301–307. DOI: 10.1080/713803735.

[14] E R Stadtman and R L Levine. 'Free radical-mediated oxidation of free amino acids and amino acid residues in proteins'. In: *Amino Acids* 25 (3-4 Dec. 2003), pp. 207–218. DOI: 10.1007/s00726-003-0011-2.

[15] Earl R Stadtman, Jackob Moskovitz and Rodney L Levine. 'Oxidation of methionine residues of proteins: biological consequences'. In: *Antioxid. Redox Signal.* 5 (5 Oct. 2003), pp. 577–582. DOI: 10.1089/152308603770310239.

[16] Bethany F Laatsch et al. 'A review of methionine and cysteine: Their roles as sinks for reactive oxygen and nitrogen species, including bioinformatic analysis of their percent compositions in metabolic proteins'. In: *Indian J. Clin. Biochem.* 40 (4 Oct. 2025), pp. 551–562. DOI: 10.1007/s12291-024-01284-y.

[17] Michael J Davies. 'Protein oxidation and peroxidation'. In: *Biochem. J.* 473 (7 1st Apr. 2016), pp. 805–825. DOI: 10.1042/BJ20151227.

[18] Juan David Figueroa et al. 'Formation and characterization of crosslinks, including Tyr-Trp species, on one electron oxidation of free Tyr and Trp residues by carbonate radical anion'. In: *RSC Adv.* 10 (43 3rd July 2020), pp. 25786–25800. DOI: 10.1039/d0ra04051g.

[19] Eduardo Fuentes-Lemus et al. 'Oxidative crosslinking of peptides and proteins: Mechanisms of formation, detection, characterization and quantification'. In: *Molecules* 27 (1 21st Dec. 2021), p. 15. DOI: 10.3390/molecules27010015.

[20] James S Nowick. 'Exploring beta-sheet structure and interactions with chemical model systems'. In: *Acc. Chem. Res.* 41 (10 18th Oct. 2008), pp. 1319–1330. DOI: 10.1021/ar800064f.

[21] David Eisenberg and Mathias Jucker. 'The amyloid state of proteins in human diseases'. In: *Cell* 148 (6 16th Mar. 2012), pp. 1188–1203. DOI: 10.1016/j.cell.2012.02.022.

[22] Sylvain E Lesné et al. 'Brain amyloid- oligomers in ageing and Alzheimer's disease'. In: *Brain* 136 (Pt 5 9th May 2013), pp. 1383–1398. DOI: 10.1093/brain/awt062.

[23] Brandon H Toyama and Martin W Hetzer. 'Protein homeostasis: live long, won't prosper'. In: *Nat. Rev. Mol. Cell Biol.* 14 (1 Jan. 2013), pp. 55–61. DOI: 10.1038/nrm3496.

[24] Shuai He et al. 'Single-cell transcriptome profiling of an adult human cell atlas of 15 major organs'. In: *Genome Biol.* 21 (1 7th Dec. 2020), p. 294. DOI: 10.1186/s13059-020-02210-0.

[25] Klaudia Jomova et al. 'Reactive oxygen species, toxicity, oxidative stress, and antioxidants: chronic diseases and aging'. In: *Arch. Toxicol.* 97 (10 19th Oct. 2023), pp. 2499–2574. DOI: 10.1007/s00204-023-03562-9.

[26] Jorge Limón-Pacheco and María E Gonsebatt. 'The role of antioxidants and antioxidant-related enzymes in protective responses to environmentally induced oxidative stress'. In: *Mutat. Res.* 674 (1-2 31st Mar. 2009), pp. 137–147. DOI: 10.1016/j.mrgentox.2008.09.015.

[27] James Nathan Cobley, Maria Luisa Fiorello and Damian Miles Bailey. '13 reasons why the brain is susceptible to oxidative stress'. In: *Redox Biol.* 15 (May 2018), pp. 490–503. DOI: 10.1016/j.redox.2018.01.008.

[28] M S Archer. 'Rainfall and temperature effects on the decomposition rate of exposed neonatal remains'. In: *Sci. Justice* 44 (1 1st Jan. 2004), pp. 35–41. DOI: 10.1016/S1355-0306(04)71683-4.

[29] B B Dent, S L Forbes and B H Stuart. 'Review of human decomposition processes in soil'. In: *Environ. Geol.* 45 (4 1st Feb. 2004), pp. 576–585. DOI: 10.1007/s00254-003-0913-z.

[30] Arpad A Vass. 'The elusive universal post-mortem interval formula'. In: *Forensic Sci. Int.* 204 (1-3 30th Jan. 2011), pp. 34–40. DOI: 10.1016/j.forsciint.2010.04.052.

[31] Anju Singh et al. 'Oxidative stress: A key modulator in neurodegenerative diseases'. In: *Molecules* 24 (8 22nd Apr. 2019), E1583. DOI: 10.3390/molecules24081583.

[32] Mauricio G Martín and Carlos G Dotti. 'Plasma membrane and brain dysfunction of the old: Do we age from our membranes?' In: *Front. Cell Dev. Biol.* 10 (6th Oct. 2022), p. 1031007. DOI: 10.3389/fcell.2022.1031007.

[33] Mariona Jové et al. 'Lipid adaptations against oxidative challenge in the healthy adult human brain'. In: *Antioxidants (Basel)* 12 (1 12th Jan. 2023), p. 177. DOI: 10.3390/antiox12010177.

[34] James Everett et al. 'Biogenic metallic elements in the human brain?' In: *Sci. Adv.* 7 (24 June 2021), eabf6707. DOI: 10.1126/sciadv.abf6707.

[35] Alfredo Gonzalez-Alcocer et al. 'Unscrambling the role of redox-active biometals in dopaminergic neuronal death and promising metal chelation-based therapy for Parkinson's disease'. In: *Int. J. Mol. Sci.* 24 (2 9th Jan. 2023), p. 1256. DOI: 10.3390/ijms24021256.

[36] Brian A Tsui-Pierchala et al. 'Lipid rafts in neuronal signaling and function'. In: *Trends Neurosci.* 25 (8 Aug. 2002), pp. 412–417. DOI: 10.1016/s0166-2236(02)02215-4.

[37] Laura E Donovan et al. 'Analysis of a membrane-enriched proteome from postmortem human brain tissue in Alzheimer's disease'. In: *Proteomics Clin. Appl.* 6 (3-4 Apr. 2012), pp. 201–211. DOI: 10.1002/prca.201100068.

[38] Massimo Aureli et al. 'Lipid membrane domains in the brain'. In: *Biochim. Biophys. Acta* 1851 (8 1st Aug. 2015), pp. 1006–1016. DOI: 10.1016/j.bbalip.2015.02.001.

[39] Muthuraj Balakrishnan and Anne K Kenworthy. 'Lipid peroxidation drives liquid-liquid phase separation and disrupts raft protein partitioning in biological membranes'. In: *J. Am. Chem. Soc.* 146 (2 17th Jan. 2024), pp. 1374–1387. DOI: 10.1021/jacs.3c10132.

[40] Sarah E Gabbott, Robert S Sansom and Mark A Purnell. 'Systematic analysis of exceptionally preserved fossils: correlated patterns of decay and preservation'. In: *Palaeontology* 64 (6 Nov. 2021), pp. 789–803. DOI: 10.1111/pala.12571.

[41] Paul V Ullmann et al. 'Molecular tests support the viability of rare earth elements as proxies for fossil biomolecule preservation'. In: *Sci. Rep.* 10 (1 23rd Sept. 2020), p. 15566. DOI: 10.1038/s41598-020-72648-6.

[42] Elena R Schroeter et al. 'Soft-tissue, rare earth element, and molecular analyses of dreadnoughtus schrani, an exceptionally complete titanosaur from Argentina'. In: *Biology (Basel)* 11 (8 2nd Aug. 2022), p. 1158. DOI: 10.3390/biology11081158.

[43] Jasmina Wiemann et al. 'Fossilization transforms vertebrate hard tissue proteins into N-heterocyclic polymers'. In: *Nat. Commun.* 9 (1 9th Nov. 2018), p. 4741. DOI: 10.1038/s41467-018-07013-3.

[44] Mary H Schweitzer et al. 'A role for iron and oxygen chemistry in preserving soft tissues, cells and molecules from deep time'. In: *Proc. Biol. Sci.* 281 (1775 22nd Jan. 2014), p. 20132741. DOI: 10.1098/rspb.2013.2741.

[45] Sheng-Bo Fan et al. 'Using pLink to analyze cross-linked peptides: Using pLink to analyze cross-linked peptides'. In: *Curr. Protoc. Bioinformatics* 49 (1 9th Mar. 2015), pp. 8.21.1–8.21.19. DOI: 10.1002/0471250953.bi0821s49.

[46] Zhen-Lin Chen et al. 'A high-speed search engine pLink 2 with systematic evaluation for proteome-scale identification of cross-linked peptides'. In: *Nat. Commun.* 10 (1 30th July 2019), p. 3404. DOI: 10.1038/s41467-019-11337-z.

[47] Fan Liu et al. 'Proteome-wide profiling of protein assemblies by cross-linking mass spectrometry'. In: *Nat. Methods* 12 (12 28th Dec. 2015), pp. 1179–1184. DOI: 10.1038/nmeth.3603.

[48] Andy T Kong et al. 'MSFragger: ultrafast and comprehensive peptide identification in mass spectrometry-based proteomics'. In: *Nat. Methods* 14 (5 May 2017), pp. 513–520. DOI: 10.1038/nmeth.4256.

[49] Vadim Demichev et al. 'DIA-NN: neural networks and interference correction enable deep proteome coverage in high throughput'. In: *Nat. Methods* 17 (1 Jan. 2020), pp. 41–44. DOI: 10.1038/s41592-019-0638-x.

[50] C I Edvard Smith, Peter Bergman and Daniel W Hagey. 'Estimating the number of diseases - the concept of rare, ultra-rare, and hyper-rare'. In: *iScience* 25 (8 19th Aug. 2022), p. 104698. DOI: 10.1016/j.isci.2022.104698.

[51] Sheila Unger et al. 'Nosology of genetic skeletal disorders: 2023 revision'. In: *Am. J. Med. Genet. A* 191 (5 May 2023), pp. 1164–1209. DOI: 10.1002/ajmg.a.63132.

[52] Kyung-Yil Lee. 'Common immunopathogenesis of central nervous system diseases: the protein-homeostasis-system hypothesis'. In: *Cell Biosci.* 12 (1 16th Nov. 2022), p. 184. DOI: 10.1186/s13578-022-00920-5.

[53] Annika Höhn, Antonella Tramutola and Roberta Cascella. 'Proteostasis failure in neurodegenerative diseases: Focus on oxidative stress'. In: *Oxid. Med. Cell. Longev.* 2020 (27th Mar. 2020), p. 5497046. DOI: 10.1155/2020/5497046.

[54] Rohan Gupta et al. 'Post-translational modifications: Regulators of neurodegenerative proteinopathies'. In: *Ageing Res. Rev.* 68 (101336 1st July 2021), p. 101336. DOI: 10.1016/j.arr.2021.101336.

[55] Shahin Ramazi et al. 'Protein modification in neurodegenerative diseases'. In: *MedComm* 5 (8 1st Aug. 2024), e674. DOI: 10.1002/mco2.674.

# Appendices

# Glossary

**$\alpha$-Helix** A right-handed helical secondary structure element in which the peptide backbone forms hydrogen bonds between the carbonyl oxygen of residue $n$ and the amide nitrogen of residue $n+4$, generating 3.6 residues per helical turn with a rise of 1.5 Å per residue and a pitch of 5.4 Å. $\alpha$-Helices are stabilised by local intrachain hydrogen bonds running approximately parallel to the helical axis, rather than the extended interstrand hydrogen-bonding networks characteristic of $\beta$-sheets. Consequently, they are generally more conformationally flexible and accessible to solvent and proteases than $\beta$-sheet-rich regions.

**$\beta$-Oxidation** The principal catabolic pathway for fatty acid degradation in aerobic organisms, occurring in the mitochondrial matrix and peroxisomes, in which fatty acyl chains are progressively shortened by successive removal of two-carbon units as acetyl-CoA through repeated cycles of oxidation, hydration, oxidation, and thiolysis.

**$\beta$-Scission** A fragmentation reaction of alkoxyl radicals in which the C−C bond in the $\beta$-position (one bond removed from the radical centre) undergoes homolytic cleavage, generating a carbonyl-containing fragment (typically an aldehyde or ketone) and a smaller carbon-centred alkyl radical. In lipid systems, $\beta$-scission is a major pathway contributing to the formation of short-chain aldehydes (e.g., 4-HNE, MDA) and volatile organic compounds characteristic of *post-mortem* lipid oxidation.

**$\beta$-Sheet** A secondary structure element formed by the lateral association of extended $\beta$-strand backbone segments, linked by hydrogen bonds between the amide N−H groups of one strand and the carbonyl C=O groups of an adjacent strand; strands may be arranged in parallel (with the same N- to C-terminal directionality) or antiparallel (opposing directionality) configurations. $\beta$-Sheets form extended, closely packed hydrogen-bonding networks and occur as major structural elements in many membrane proteins, fibrous proteins, and amyloid fibrils. Their regular, tightly associated strand architecture restricts access of water and proteases to the peptide backbone, increasing resistance to hydrolytic and enzymatic degradation.

**4-Hydroxynonenal (4-HNE)** A reactive $\alpha,\beta$-unsaturated aldehyde produced during the $\beta$-scission of alkoxyl radicals derived from omega-6 PUFAs (particularly linoleic and arachidonic acids), representing one of the most abundant and biologically reactive secondary products of lipid peroxidation. 4-HNE reacts preferentially with nucleophilic amino-acid residues *via* Michael addition to its electrophilic $\beta$-carbon, with Cys reacting most rapidly, followed by His and Lys; the resulting covalent adducts alter protein conformation, impair enzymatic function, and can serve as bridging crosslinks when the aldehyde reacts with two nucleophilic sites. In the ageing brain, 4-HNE–protein adducts accumulate progressively in association with membranes and mitochondria, and modification of Lys contributes to the pre-existing burden of secondary carbonyl adducts present at death.

**Acetylation** An enzymatic, reversible (for Lys) PTM involving the transfer of an acetyl group ($-CO-CH_3$) from acetyl-CoA to the $\alpha$-amino group at the N-terminus or to the $\varepsilon$-amino group of Lys side chains, catalysed by specific acetyltransferases and reversed by deacetylases. Neutralisation of the positive charge on Lys alters electrostatic interactions, protein conformation, and protein–protein interactions, while also reducing the nucleophilicity of the $\varepsilon$-amino group and thereby its susceptibility to non-enzymatic glycation and other carbonyl-mediated modifications.

**Acrolein** An $\alpha,\beta$-unsaturated aldehyde ($CH_2{=}CH{-}CHO$), the smallest alkenal, generated principally as a secondary product of lipid peroxidation through decomposition of alkoxyl radicals derived from omega-3 and omega-6 PUFAs, and also by polyamine metabolism and microbial fermentation. Acrolein is among the most potent electrophilic Michael acceptors of the RCS class, reacting rapidly with Cys (thiol) > His (imidazole) > Lys ($\varepsilon$-amine) to form stable covalent adducts.

**Adipocere** A waxy, soap-like *post-mortem* transformation product formed from the lipid-rich tissues of the body – principally subcutaneous adipose – under conditions of persistent moisture, restricted oxygen, and alkaline or neutral-to-alkaline pH, commonly referred to as 'grave wax'. Its formation is initiated by endogenous lipase- and bacterial esterase-mediated hydrolysis of triglycerides to free fatty acids; under oxygen-limited conditions, unsaturated fatty acids are then transformed by microbial hydration of their double bonds, yielding hydroxy- and subsequently oxo-fatty acids (most characteristically 10-hydroxystearic and 10-hydroxypalmitic acids), while the alkalinity generated by proteolytic ammonia production promotes fatty-acid deprotonation and coordination with cations to form insoluble fatty-acid salts. The resulting semi-crystalline matrix is enriched in saturated and hydroxy fatty acids of high melting point, is poorly water-penetrable, and resists further microbial degradation as long as moist, anaerobic conditions are maintained.

**Advanced glycation end product (AGE)** A heterogeneous class of stable covalent adducts and crosslinks formed by the non-enzymatic Maillard reaction between reducing sugars (or reactive dicarbonyl intermediates derived therefrom) and nucleophilic groups on proteins, lipids, or nucleic acids, representing the terminal, irreversible products of glycation chemistry. The high chemical stability and crosslinking potential of AGEs render modified proteins increasingly resistant to proteolytic degradation.

**Advanced lipoxidation end product (ALE)** A heterogeneous class of stable covalent protein–lipid adducts formed by the reaction of nucleophilic amino-acid side chains – primarily Cys, His, and Lys – with RCS generated during lipid peroxidation, including $\alpha,\beta$-unsaturated aldehydes (e.g., acrolein, 4-HNE, 4-oxo-2-nonenal) and dialdehydes (e.g., MDA). ALEs are the lipoxidation-derived counterparts of AGEs and include both monoadducts and covalent crosslinks; together, these modifications promote protein stabilisation, aggregation, and increasing resistance to proteolytic degradation.

**Alanine (Ala, A)** An aliphatic amino acid with a methyl side chain ($-CH_3$), the smallest chiral amino acid and among the most abundant amino acids in proteins. Although its methyl side chain contributes less hydrophobic surface area than Leu, Val, or Ile, Ala participates in hydrophobic core packing while its small size and conformational flexibility confer a high propensity for $\alpha$-helical structures.

**Alkoxyl radical (RO·)** An oxygen-centred radical formed predominantly by metal-catalysed one-electron reduction of a hydroperoxide ($ROOH + Fe^{2+} \rightarrow RO\cdot + OH^- + Fe^{3+}$), representing a key reactive intermediate in the lipid peroxidation chain. Alkoxyl radicals can either propagate the radical chain by abstracting hydrogen from a neighbouring molecule (generating an alcohol and a new radical), or undergo $\beta$-scission, in which the C–C bond at the $\beta$-position relative to the radical centre undergoes homolytic cleavage, producing a carbonyl fragment (typically an aldehyde or ketone) and a smaller alkyl radical. The competition between propagation and $\beta$-scission determines whether alkoxyl radicals contribute to chain-amplified oxidative damage or to the formation of diffusible carbonyl species (e.g., 4-HNE, MDA) that participate in secondary protein crosslinking reactions.

**AlphaFold** A deep-learning protein structure prediction system developed by DeepMind that achieves near-experimental accuracy for many structured proteins by predicting three-dimensional structure from amino-acid sequence using evolutionary information derived from multiple sequence alignments. Sequence and pairwise residue representations are processed through the Evoformer attention architecture to predict atomic coordinates together with per-residue confidence estimates (pLDDT scores).

**Amadori product** The stable ketoamine formed by Amadori rearrangement of the initially formed Schiff base adduct between the carbonyl group of a reducing sugar and a protein $\varepsilon$-amino or $\alpha$-amino group, representing the first stable intermediate in the Maillard (glycation) reaction. Unlike the Schiff base, the Amadori product is a 1-amino-1-deoxy-2-ketose that persists for extended periods and serves as a branch point for multiple downstream glycation pathways: dehydration and fragmentation generate reactive $\alpha$-dicarbonyl intermediates (e.g., methylglyoxal, glyoxal, 3-deoxyglucosone), while glycoxidation and related carbonyl reactions produce carboxymethyl-Lys and other AGEs.

**Anaerobic glycolysis** The cytoplasmic metabolic pathway that converts glucose-6-phosphate to pyruvate through a series of 10 enzymatic steps, generating a net gain of two ATP and reducing two $NAD^+$ to two NADH per glucose molecule. Under anaerobic conditions (as occur rapidly *post-mortem* following cessation of oxidative phosphorylation), continued glycolysis depends on regeneration of $NAD^+$ by reduction of pyruvate to lactate *via* lactate dehydrogenase – a reaction that produces no additional ATP but replenishes the oxidised cofactor required to sustain glycolytic flux. The accumulation of lactate, together with ATP depletion and loss of proton homeostasis, contributes to progressive cytoplasmic acidification; promoting nuclear chromatin condensation, lysosomal enzyme activation, and eventually inhibition of glycolytic enzymes as pH falls below their optima.

**Anoxia** The complete absence of dissolved molecular oxygen from a tissue or burial medium, representing the extreme of hypoxic conditions and typically achieved in waterlogged, densely packed, or sealed burial environments after all available oxygen has been consumed by enzymatic and microbial activity. Under anoxic conditions, obligate and facultative anaerobic microorganisms predominate, using alternative terminal electron acceptors according to the classical redox sequence (where available): $NO_3^-$ > Mn(IV) > Fe(III) > $SO_4^{2-}$ > $CO_2$.

**Apoptosis** A regulated, caspase-mediated form of programmed cell death characterised by cell shrinkage, chromatin condensation (pyknosis), nuclear fragmentation (karyorrhexis), membrane blebbing into apoptotic bodies, and ultimately phagocytosis. It proceeds *via* intrinsic (mitochondrial) pathways – initiated by cytochrome *c* release and apoptosome assembly – or extrinsic (death receptor) pathways, both converging on activation of the executioner caspases 3, 6, and 7. Although apoptosis is a normal physiological process for removing damaged or superfluous cells, it is distinct from the enzymatic autolysis that drives *post-mortem* soft-tissue decomposition; however, mitochondrial apoptotic signalling pathways activated during the terminal stages of cellular stress before death (e.g., $Ca^{2+}$ overload and ROS-mediated cytochrome *c* release) may influence the chemical state of the tissue at the onset of the PMI.

**Arginine (Arg, R)** A basic amino acid with a guanidinium group side chain ($-NH-C[=NH_2^+]-NH_2$; p$K_a \sim 12.5$) that carries a positive charge across the full physiological and much of the acidic pH range, participating in salt bridges, hydrogen bonding (the guanidinium group can form up to five simultaneous hydrogen bonds), and metal coordination. Arg is susceptible to carbonylation by metal-catalysed oxidation to glutamic semialdehyde (converting the guanidinium group to an aldehyde, a $\sim$ 43 Da mass shift), and to non-enzymatic glycation through its guanidinium group, forming hydroimidazolone adducts with reactive dicarbonyls (e.g., methylglyoxal, glyoxal), as well as participating in certain AGE crosslinks (e.g., pentosidine).

**Asparagine (Asn, N)** An amidic amino acid with a neutral carboxamide side chain ($-CH_2-CO-NH_2$) that provides a non-ionisable hydrogen-bonding moiety and represents a common site of N-linked glycosylation. Asn is the primary residue susceptible to deamidation *via* the cyclic succinimide mechanism, particularly when the C-terminal neighbour is Gly or Ser.

**Aspartic acid (Asp, D)** An acidic amino acid with a $\gamma$-carboxylate side chain ($-CH_2-COOH$; p$K_a \sim 3.9$) that carries a negative charge at physiological pH and participates in salt bridges, metal coordination (particularly with $Ca^{2+}$, $Mg^{2+}$, and $Zn^{2+}$), and the active sites of aspartyl proteases. Asp is both a product and a substrate of deamidation: it arises from deamidation of Asn and undergoes the cyclic succinimide-mediated isomerisation that produces isoAsp and L/D-Asp mixtures.

**Astrocyte** The most abundant glial cell type in the CNS, serving critical support functions including regulation of extracellular ion composition (principally $K^+$ buffering), recycling of neurotransmitters (particularly glutamate *via* the Glu–Gln cycle), metabolic support of neurons (*via* the astrocyte–neuron lactate shuttle), and structural contribution to the blood–brain barrier (*via* astrocytic endfeet ensheathing blood vessels). *Post-mortem*, astrocytic processes take up water rapidly following ionic dysregulation, contributing to cytotoxic oedema and the early histological appearance of perivascular and pericellular rarefactions during nervous tissue autolysis.

**Autolysis** The 'self-digestion' of a cell by its own endogenous catabolic enzymes, initiated *post-mortem* when the failure of oxidative phosphorylation causes rapid ATP depletion, cessation of ATP-dependent ion transport, and progressive loss of membrane integrity. As intracellular $Ca^{2+}$ and $Na^+$ concentrations rise and pH declines through anaerobic glycolysis, lysosomal membrane integrity progressively fails and hydrolytic enzymes gain increasing access to their intracellular substrates under increasingly permissive conditions. Autolysis proceeds through an initial potentially reversible phase characterised by osmotic swelling and metabolic shift, followed by irreversible structural deterioration marked by mitochondrial matrix denaturation, cytoplasmic granular densities, progressive membrane dissolution, and widespread enzymatic degradation of cellular architecture.

**Autophagic cell death** A regulated form of cell death associated with extensive autophagic vacuolisation of the cytoplasm, in which double-membraned autophagosomes sequester cytoplasmic material for lysosomal degradation, typically in response to nutrient deprivation, metabolic stress, or developmental signalling. Autophagic cell death differs mechanistically from apoptosis (which involves caspase-dependent dismantling) and from necrosis (which involves passive membrane failure), although autophagy itself is generally regarded as a cytoprotective process and its direct role in executing cell death remains context-dependent.

**Autophagy–lysosomal pathway** A family of catabolic processes that deliver cytoplasmic contents to lysosomes for degradation, broadly classified as macroautophagy (in which double-membraned autophagosomes sequester bulk cytoplasmic material or specific cargo and fuse with lysosomes), microautophagy (direct engulfment of cytoplasmic material at the lysosomal membrane), and chaperone-mediated autophagy (in which specific substrates are translocated across the lysosomal membrane). Macroautophagy is the principal route for the turnover of organelles and protein aggregates, and contributes substantially to the degradation of long-lived proteins. Its decline in ageing neurons – manifested as reduced autophagic flux, accumulation of autolysosomes, and impaired cargo clearance – is associated with the accumulation of aggregation-prone proteins (e.g., amyloid-$\beta$, tau, $\alpha$-synuclein) that characterise neurodegenerative proteinopathies.

**Autoxidation** The spontaneous, radical-chain-propagating oxidation of unsaturated organic molecules by molecular oxygen, initiated by trace redox-active metal ions, decomposition of pre-existing hydroperoxides, or thermal bond homolysis. In lipid systems, autoxidation proceeds preferentially at allylic and bis-allylic positions of unsaturated fatty acyl chains, where C–H bond dissociation energies are reduced by the adjacent $\pi$-system; once initiated, the resulting peroxyl radicals propagate the chain reaction by abstracting hydrogen atoms from neighbouring unsaturated molecules.

***b*-Ion/*y*-ion** The two principal series of sequence-informative fragment ions generated by collision-induced dissociation (CID and HCD) of protonated peptide ions. *b*-Ions are N-terminal fragments produced by cleavage of the peptide (amide) bond, retaining the N-terminus and carrying the charge on the N-terminal portion; *y*-ions are complementary C-terminal fragments retaining the C-terminus and carrying the charge on the C-terminal portion. Where consecutive ions are observed, the mass difference between adjacent members of a *b*- or *y*-ion series corresponds to the mass of a single amino-acid residue, enabling reconstruction of the peptide sequence.

**Biomarker** A molecular species that retains diagnostic evidence of its biological precursor despite *post-mortem* alteration, enabling inference about the biology, taxonomy, ecology, or depositional environment of its source organism.

**Biostratinomy** The interval of an organism's taphonomic history between the moment of death and incorporation into its depositional environment, during which remains are exposed at or near the surface and subject to physical, biological, and early chemical modification.

**Bottom-up proteomics** A strategy for proteome analysis in which intact proteins are first cleaved into peptides by proteolytic enzymes (most commonly trypsin), and the resulting peptide mixture is separated by LC, ionised by ESI, and analysed by MS/MS; protein identities and quantities are then inferred computationally from peptide sequences and abundances. In palaeoproteomics, bottom-up analysis is effectively imposed by diagenesis: ancient proteins tend to persist as degraded, modified peptide mixtures rather than intact polypeptides.

**C18 stationary phase** The predominant reversed-phase sorbent material in proteomics chromatography, consisting of octadecylsilane groups ($-\mathrm{Si}-[\mathrm{CH_2}]_{17}-\mathrm{CH_3}$) covalently bonded to porous silica particles (1.7–3.0 µm diameter for analytical columns), providing a high-surface-area hydrophobic phase that retains peptides through hydrophobic partitioning according to their overall hydrophobicity. In addition to analytical separation columns, C18 sorbent is used in SPE for sample clean-up: peptide samples in aqueous solution are loaded onto equilibrated C18 material, polar contaminants (e.g., salts, detergents) are washed away, and retained peptides are eluted with a high proportion of organic solvent.

**C2 domain** A protein structural module ($\sim$ 120 amino acids) that mediates membrane binding, often in a $Ca^{2+}$-dependent manner, through interactions with anionic phospholipids (particularly phosphatidylserine and phosphatidylinositol phosphates). C2 domains adopt a $\beta$-sandwich fold and, in $Ca^{2+}$-dependent membranes, coordinate $Ca^{2+}$ ions through loops at one end of the $\beta$-sandwich, with the bound ions bridging the domain to the phospholipid head groups. In this thesis, $Ca^{2+}$-dependent phospholipid-binding C2 domains are the single strongest domain-level predictor of peptide recalcitrance under hypoxic burial conditions.

**Calpain** A family of calcium-dependent Cys proteases whose activity is tightly suppressed *in vivo* by the endogenous inhibitor calpastatin and by the low resting cytosolic $Ca^{2+}$ concentration ($\sim$ 100 nM). *Post-mortem* elevation of intracellular $Ca^{2+}$ above activation thresholds activates calpain-mediated proteolysis, promoting early cytoskeletal degradation.

**Carbonylation** An irreversible, non-enzymatic oxidative modification that introduces carbonyl groups (aldehydes and ketones) into proteins, representing one of the most extensively characterised forms of oxidative protein damage and a major marker of accumulated oxidative stress in ageing tissues. Carbonylation arises *via* three principal routes: (i) direct oxidation of susceptible residues (particularly Pro, Arg, Lys, and Thr) by metal-catalysed oxidation to yield primary carbonyls; (ii) nucleophilic addition of Lys $\varepsilon$-amines to RCS generated from lipid peroxidation (e.g., acrolein, 4-HNE, MDA) or glycation (e.g., methylglyoxal, glyoxal) to yield secondary carbonyl adducts; and (iii) oxidative cleavage of the peptide backbone by $\alpha$-amidation or diamide mechanisms. Extenively carbonylated proteins are often resistant to proteolytic degradation because carbonylation causes conformational alteration, aggregation, and crosslinking that sterically hinder protease access.

**Central nervous system (CNS)** The brain and spinal cord collectively, constituting the principal locus of information processing in vertebrates. The CNS is enclosed and protected by the cranial vault and vertebral column, surrounded by three meningeal membranes (dura, arachnoid, pia mater), bathed in CSF, and separated from the systemic circulation by the blood–brain barrier.

**Coagulative necrosis** A form of cell death in which structural proteins and hydrolytic enzymes denature more rapidly than enzymatic digestion can proceed, producing a coagulated, protein-rich mass in which the overall tissue architecture may be preserved for some time despite loss of cellular detail. It predominates in tissues where ischaemic injury causes rapid protein denaturation that limits proteolysis. In contrast to the liquefactive necrosis typical of brain tissue, coagulative necrosis produces a firmer, more resistant end product in the immediate PMI, though prolonged enzymatic and microbial activity ultimately leads to breakdown.

**Collision-induced dissociation (CID)** A fragmentation method in proteomics MS in which isolated precursor ions are accelerated through a collision cell containing an inert gas (typically $N_2$ or He) and undergo multiple low-energy collisions that convert kinetic energy into internal vibrational energy, activating the peptide toward dissociation. According to the mobile proton model, the deposited energy mobilises protons along the peptide backbone, promoting cleavage of amide bonds to generate complementary *b*- and *y*-ion series, which retain the N- and C-termini, respectively, and together encode the peptide sequence. CID (and its higher-energy variant HCD, implemented in Orbitrap™ instruments; Thermo Fisher Scientific) remains the dominant fragmentation method in palaeoproteomics because it produces abundant, predictable fragment-ion series that are well suited to database searching.

**Crosslinked preservation type** A category of human brain preservation defined in this thesis, in which the brain persists as the sole surviving soft tissue within otherwise skeletonised remains, forming a resilient, shrunken mass that most commonly occurs in waterlogged, low-oxygen depositional environments. The crosslinked preservation type is named on the basis of experimental taphonomic and palaeoproteomic evidence indicating that its longevity reflects radical-mediated oxidative crosslinking within membrane-associated microenvironments during the early PMI – a form of preservation by transformation rather than by inhibition.

**Crosslinking (enzymatic)** Covalent linkages within or between proteins catalysed by specific enzymes *in vivo*. Enzymatic crosslinks stabilise the structure and mechanical properties of ECMs by increasing molecular rigidity and resistance to proteolytic degradation. Extensive crosslinking of fibrillar collagens and elastin contributes to the exceptional longevity of these structural proteins.

**Crosslinking (non-enzymatic)** Covalent linkages forming stable (and largely irreversible) intra- or intermolecular bonds between amino-acid side chains or between proteins. Principal mechanisms include (i) oxidative coupling between radical intermediates of aromatic residues (producing dityrosine, ditryptophan, and Tyr–Trp crosslinks); (ii) Maillard chemistry involving reducing sugars and reactive carbonyl intermediates, generating AGE crosslinks; and (iii) reactions of bifunctional lipid-derived carbonyls (e.g., acrolein, 4-HNE, MDA) with two nucleophilic side chains *via* combined Michael addition and Schiff base pathways. Non-enzymatic crosslinking progressively reduces protein solubility, increases macromolecular rigidity, impairs proteolytic degradation, and promotes aggregation.

**Cuproptosis** A copper-dependent, non-apoptotic cell death pathway in which excess intracellular copper binds directly to lipoylated proteins in the tricarboxylic acid cycle, inducing their pathological aggregation. This aggregation promotes the destabilisation and loss of iron–sulfur cluster proteins involved in mitochondrial respiration, triggering proteotoxic stress, mitochondrial dysfunction, and ultimately cell death.

**Cyclic succinimide intermediate** A five-membered imide ring formed by intramolecular cyclisation of Asn (during deamidation) or Asp (during isomerisation) when the backbone amide nitrogen of the following residue, acting as a nucleophile, attacks the side-chain carbonyl carbon, displacing ammonia (from Asn) or water (from Asp). The resulting succinimide intermediate is highly strained and may undergo racemisation before ring opening, generating both L- and D-configurations. Subsequent hydrolysis yields either the canonical $\alpha$-linked Asp or the abnormal $\beta$-linked isoAsp, depending on which ring carbonyl is attacked by water, producing L- and D-forms of both residues if racemisation has occurred. Formation of isoAsp reroutes the peptide backbone through the side-chain $\beta$-carbon, perturbing backbone geometry, protein structure, and susceptibility to proteolytic cleavage.

**Cysteine (Cys, C)** A sulfur-containing amino acid with a thiol side chain ($-CH_2-SH$; $pK_a \sim 8.3$), among the most nucleophilic and redox-reactive of the canonical amino acids in typical protein environments. The Cys thiol is the principal site of disulfide bond formation (stabilising tertiary and quaternary structure), palmitoylation (membrane anchoring), S-nitrosylation, glutathionylation, and reaction with RCS *via* Michael addition to $\alpha,\beta$-unsaturated aldehydes (e.g., acrolein, 4-HNE). Its high sensitivity to oxidation means that Cys is rapidly modified *post-mortem*; in the presence of another thiol it readily forms disulfides, while further oxidation yields sulfenic acid ($-SOH$, reversible), sulfinic acid ($-SO_2H$, largely irreversible), and sulfonic acid ($-SO_3H$, irreversible).

**Cytosol** The aqueous cytoplasmic matrix of the cell – distinct from the contents of membrane-bound organelles – comprising $\sim 70\%$ water enriched in dissolved ions (principally $K^+$, with low $Na^+$ and $Ca^{2+}$), small metabolites (e.g., glucose-6-phosphate, amino acids, nucleotides), macromolecules (e.g., proteins at concentrations of 200–400 g/L, RNA), and macromolecular complexes (e.g., ribosomes, proteasomes, signal transduction complexes). The near-neutral pH ($\sim 7.2$) and low $Ca^{2+}$ concentration ($\sim 100$ nM) of the cytosol *in vivo* are tightly maintained; *post-mortem*, failure of ATP-dependent ion pumps collapses these gradients, causing $Ca^{2+}$ accumulation and cytosolic acidification through lactic acid production, altering the physicochemical environment, activating $Ca^{2+}$-dependent enzymes, and progressively converting the tightly regulated intracellular milieu into one permissive for autolytic degradation.

**Cytotoxic oedema** Cellular swelling arising from osmotic influx of water following failure of ATP-dependent ion homeostasis in the immediate PMI, principally through loss of $Na^+/K^+$-ATPase activity, allowing intracellular accumulation of $Na^+$ and $Cl^-$ and driving water into cells down its osmotic gradient. In the brain, cytotoxic oedema is associated with early histological changes including swelling of neuronal and glial somata, vacuolisation, and perivascular and pericellular rarefactions.

**Data-dependent acquisition (DDA)** A mass spectrometric acquisition strategy in which the instrument dynamically selects the most intense precursor ions detected in each MS1 survey scan for isolation and MS2 fragmentation, generating multiple MS2 spectra per duty cycle and $\sim 10 - 50$ MS2 spectra per second. DDA is biased toward high-abundance species (which trigger selection most frequently), stochastically samples medium-abundance species (which may or may not be selected in replicate analyses), and largely misses low-abundance species (which fall below the signal threshold for dynamic selection).

**Data-independent acquisition (DIA)** A mass spectrometric acquisition strategy in which all ions within predefined, sequentially scanned $m/z$ windows are fragmented simultaneously in each duty cycle, producing multiplexed MS2 spectra containing fragment ions from all co-eluting peptides within each window. Unlike DDA, DIA systematically fragments ions across the predefined $m/z$ range irrespective of precursor abundance, providing highly reproducible sampling across replicate analyses and enabling more consistent quantification of low-abundance peptides that would otherwise be sampled stochastically by DDA. The analytical challenge of DIA is the computational deconvolution of highly multiplexed MS2 spectra, which requires specialised algorithms that match experimental fragment-ion traces against predicted or measured reference spectra.

***De novo* sequencing** A peptide sequencing strategy in which the amino-acid sequence is inferred directly from the mass differences between adjacent fragment ions in the MS2 spectrum, without comparison to a protein sequence database or spectral library. The approach is particularly valuable when reference databases are incomplete or absent, or for heavily modified peptides bearing mass shifts not accommodated by standard database search parameters. Recent deep-learning approaches have substantially improved *de novo* sequence accuracy by learning to predict fragment-ion intensity patterns; however, *de novo* sequencing remains less robust than database searching for complex samples with spectral noise and chemical interference, and is most productively used as a complement to database search strategies for identifying novel sequences and uncharacterised modifications.

**Deamidation** A largely spontaneous, non-enzymatic hydrolytic process in which the neutral amide side chains of Asn or Gln residues are converted to negatively charged carboxylates – Asp/isoAsp and Glu, respectively – with a net mass change of $+0.984$ Da detectable by MS. Asn deamidation commonly proceeds *via* intramolecular cyclisation to a five-membered cyclic succinimide intermediate (formed by nucleophilic attack of the backbone amide nitrogen on the Asn side-chain carbonyl), which hydrolyses predominantly to isoAsp with lesser amounts of Asp. Gln deamidation proceeds predominantly by direct hydrolysis to Glu, although cyclisation through a six-membered glutarimide intermediate can also occur. The reaction rate depends strongly on the identity of the C-terminal neighbouring residue, the flexibility of local backbone conformation, temperature, pH, and water availability. In palaeoproteomics, site-specific deamidation of Asn and Gln is widely used as supporting evidence of protein antiquity and diagenetic alteration.

**Deamination (putrefactive)** The microbial enzymatic removal of the $\alpha$-amino group from amino acids during putrefaction, converting L-amino acids to their corresponding $\alpha$-keto acids with release of ammonia ($NH_3$), which is protonated to ammonium ($NH_4^+$) according to the prevailing pH. Deamination is carried out by bacterial deaminases and transaminases and represents a major pathway by which nitrogen is mobilised from proteinaceous substrates during decomposition; the resulting $\alpha$-keto acids may enter further fermentative pathways or undergo secondary chemical transformations. The accumulation of ammonia and other alkaline microbial metabolites contributes to the progressive rise in tissue pH during later stages of decomposition.

**Decarboxylation** The enzymatic or non-enzymatic removal of a carboxyl group (–COOH) from an organic molecule with release of carbon dioxide ($CO_2$), producing the corresponding decarboxylated product. In the context of putrefaction, amino-acid decarboxylation by bacterial amino-acid decarboxylases is a major pathway generating biogenic amines (e.g., Lys $\rightarrow$ cadaverine + $CO_2$; Trp $\rightarrow$ tryptamine + $CO_2$; Tyr $\rightarrow$ tyramine + $CO_2$).

**Decay experiment** A form of experimental taphonomy in which whole organisms, organs, or isolated tissues are allowed to decay under controlled biological and environmental conditions, with periodic sampling to track *post-mortem* transformation across a defined PMI.

**Dehydration** A mode of soft-tissue preservation in which the progressive removal of water from tissues suppresses hydrolytic degradation by removing the aqueous medium required for bond cleavage, reduces microbial activity below the threshold for proliferation ($A_w \lesssim 0.90$ for most non-extremophiles), and concentrates intracellular solutes to levels that may promote vitrification of the intracellular milieu. Dehydration is most effective in environmental settings where the rate of water loss from tissues exceeds the rate of replenishment from the surrounding medium, such as hyper-arid deserts, exposed high-altitude environments, well-ventilated crypts, or caves with low humidity.

**Denitrification** An anaerobic microbial respiratory pathway in which nitrate ($NO_3^-$) or nitrite ($NO_2^-$) serves as the terminal electron acceptor and is reduced, *via* nitric oxide (NO) and nitrous oxide ($N_2O$), to molecular nitrogen ($N_2$). Where nitrate is available, denitrification is typically the first major anaerobic respiratory pathway following oxygen depletion, carried out by facultative anaerobes such as *Pseudomonas*, *Paracoccus*, and related genera using nitrate present in soil pore waters. Although denitrification generally has relatively modest direct effects on tissue chemistry compared with later sulfate reduction and methanogenesis, it contributes to the progressive lowering of Eh and marks the transition from oxic to anaerobic microbial metabolism.

**Desulfhydration** An elimination reaction in which hydrogen sulfide ($H_2S$) is released from Cys through $\beta$-elimination, catalysed by bacterial enzymes during putrefaction. *Post-mortem*, Cys desulfhydration is a major source of $H_2S$ within decomposing tissues, contributing to the characteristic odour, discolouration, and reducing chemistry of putrefaction. Dehydroalanine, the product of Cys $\beta$-elimination, is a highly reactive electrophile that undergoes Michael addition with nucleophilic amino-acid side chains, yielding irreversible protein–protein crosslinks.

**Di-oxidation** The addition of two oxygen atoms to an amino-acid residue, most commonly Trp (producing mono-oxidised hydroxytryptophan and subsequently dihydroxytryptophan) or Met (producing mono-oxidised sulfoxide and subsequently sulfone), representing a more advanced or higher-flux radical modification than single oxidation events. Di-oxidation of Trp is associated with hydroxyl radical-mediated oxidation of the indole ring and can produce ring-opening products as intermediates; di-oxidation of Met to sulfone is essentially irreversible (unlike the reversible reaction to sulfoxide).

**DIA-NN** A deep-learning-based software package for the analysis of DIA LC–MS/MS data, using neural networks to predict MS2 fragment-ion intensities and retention times from protein sequences, and using these predictions to extract, score, identify, and quantify peptide signals directly from DIA data without requiring empirically measured spectral libraries. DIA-NN performs library-free DIA analysis (generating predictions directly from a FASTA database), implements sophisticated interference correction, decoy generation, and robust FDR control at peptide- and protein-levels across large datasets.

**Diagenesis** The suite of physicochemical and biological processes that alter the composition and structure of organic remains *post-mortem*, following the biostratinomic phase and during long-term residence within a depositional environment. Diagenetic processes include hydrolysis, oxidation, microbial metabolism, mineral dissolution and precipitation, ion exchange, and recrystallisation, governed by local physicochemical parameters such as temperature, water activity, pH, redox potential, and ionic strength. These parameters interact as a coupled and evolving system, in which each reaction modifies the local chemical environment and thereby influences the direction and rate of subsequent reactions.

**Diagenetic PTM** A chemical modification of a peptide or protein arising non-enzymatically during diagenesis; that is, *post-mortem* and as a consequence of the physicochemical conditions of the burial or storage environment, rather than *in vivo* enzymatic activity. Diagenetic modifications include deamidation (at Asn/Gln), isoaspartate formation (at Asp), racemisation (at multiple residues), oxidation (of Met, Trp, Tyr, Cys, and His), carbonylation (of Pro, Arg, Lys, and Thr), ALE/AGE adduct formation (on Lys, Arg, Cys, and His), and backbone fragmentation, among others. A central challenge of palaeoproteomics is distinguishing diagenetic modifications from biologically meaningful *ante-mortem* PTMs.

**Diagenetiform** A peptide or protein that has been diagenetically modified.

**Disulfide bond formation/rearrangement** A redox-dependent, reversible process encompassing both the formation and rearrangement of disulfide bonds, in which Cys thiol groups (−SH) are oxidised to form covalent disulfide linkages (−S−S−), while existing disulfide bonds undergo thiol–disulfide exchange to form new disulfide bonds; reduction by glutaredoxins, thioredoxins, or DTT restores free thiols. *In vivo*, disulfide bonds stabilise the tertiary/quaternary structures of secreted and membrane-associated proteins by constraining backbone conformation, and are introduced during oxidative protein folding in the ER lumen; intracellular (cytoplasmic) proteins are generally maintained in a reduced state. *Post-mortem*, loss of ATP-dependent reductive maintenance systems (e.g., NADPH, glutathione reductase, thioredoxin reductase) collapses the cytoplasmic redox poise, allowing formation of adventitious disulfide bonds between normally reduced Cys residues and scrambling of existing disulfide bonds to non-native configurations. Over longer timescales, oxidation of Cys to sulfenic, sulfinic, and sulfonic acids, together with reaction with lipid-derived electrophiles, progressively shifts sulfur chemistry from reversible thiol–disulfide exchange toward irreversible oxidative and electrophilic modifications.

**Ditryptophan** A covalent crosslink formed by radical-mediated coupling of two Trp indole rings, arising from one-electron oxidation to tryptophanyl radicals followed by radical recombination, and yielding a stable linkage capable of forming both intra- and intermolecular protein–protein crosslinks. Ditryptophan is widely used as a biomarker of radical-mediated oxidative protein damage and crosslinking.

**Dityrosine** A covalent biaryl crosslink formed by radical-mediated coupling of two tyrosyl radicals, generated by one-electron oxidation of Tyr residues by ROS, metal-centred oxidants, or oxidoreductase enzymes, *via* an ortho-carbon–ortho-carbon bond between the phenol rings. Dityrosine is widely used as a biomarker of radical-mediated oxidative protein damage and crosslinking.

**Electron transfer dissociation (ETD)** A fragmentation method in which multiply protonated peptide cations undergo gas-phase charge reduction by electron transfer from an anionic reagent (typically the fluoranthene radical anion), producing proton-reduced radical cations that dissociate *via* N−C$\alpha$ bond cleavage to yield *c*-type (N-terminal) and *z*-type (C-terminal) radical fragment ions. Unlike CID, ETD preserves labile PTMs (e.g., phosphorylation) because the fragmentation pathway does not involve proton-driven neutral loss of these substituents, making ETD valuable for characterising *in vivo* modification states. In ancient and diagenetically modified samples, ETD may be less effective than CID/HCD because its efficiency depends strongly on precursor charge state (typically performing best for $z \geq 3$), and short, singly or doubly charged peptides common in ancient digests fragment poorly under ETD conditions.

**Electron transport chain (ETC)** A series of four membrane-embedded multi-subunit protein complexes (Complex I: NADH–ubiquinone oxidoreductase; Complex II: succinate–ubiquinone oxidoreductase; Complex III: ubiquinol–cytochrome *c* oxidoreductase; Complex IV: cytochrome *c* oxidase) in the inner mitochondrial membrane, together with the mobile electron carriers ubiquinone (coenzyme Q) and cytochrome *c*, that collectively transfer electrons from NADH and $FADH_2$ to molecular oxygen, coupling the exergonic electron-transfer reactions to the endergonic pumping of protons across the membrane. Electron leakage from Complexes I and III generates superoxide ($\cdot O_2^-$), the principal mitochondrial source of ROS, and increases under conditions of mitochondrial dysfunction.

**Electrospray ionisation (ESI)** A soft ionisation technique for introducing analytes from solution into the gas phase for mass spectrometric analysis, by applying a high voltage to a liquid-filled capillary or spray tip to generate a fine mist of charged droplets; as solvent evaporates from the droplets under the influence of heat and drying gas, charge density increases until Coulombic fission produces progressively smaller droplets, ultimately yielding desolvated, multiply protonated gas-phase ions ($[M + zH]^{z+}$) that are transmitted into the mass spectrometer. ESI is 'soft' because it transfers intact analytes into the gas phase without extensive fragmentation; the multiply charged ions it generates for large peptides and proteins lower the observed $m/z$ into the detection range of most mass analysers, enabling analysis of species with molecular weights exceeding the nominal $m/z$ range of the instrument.

**Endoplasmic reticulum** An extensive intracellular membrane network forming a continuous sheet enclosing a lumenal space (the ER lumen) that communicates with the nuclear envelope; it exists in two functionally distinct domains: the rough ER (studded with ribosomes, the primary site of secretory and membrane protein synthesis and folding) and the smooth ER (involved in lipid synthesis and calcium storage). The ER is the principal intracellular $Ca^{2+}$ store in neurons (and is specialised as the sarcoplasmic reticulum in muscle); *post-mortem*, failure of ATP-dependent $Ca^{2+}$ pumps is among the earliest consequences of ATP depletion and contributes to the surge in cytosolic $Ca^{2+}$ that initiates calpain and phospholipase activation. ER dilation visible as vacuolisation on *post-mortem* histology is one of the earliest microscopic signs of autolysis in neurons.

**Ester hydrolysis** The cleavage of ester bonds ($-C[=O]-O-$) in triglycerides, phospholipids, and other acylglycerol lipids, yielding free fatty acids and glycerol (for triglycerides) or glycerophospholipid backbone components (for phospholipids). Ester bonds are susceptible to both enzymatic hydrolysis (by lipases and esterases) and non-enzymatic acid- or base-catalysed hydrolysis, with hydrolysis proceeding most rapidly under strongly alkaline conditions. *Post-mortem*, endogenous lipases released during autolysis and bacterial esterases secreted during putrefaction catalyse widespread ester hydrolysis.

**Exceptional preservation** The preservation of soft tissues, fine morphological detail, or biomolecular information beyond that expected under typical depositional conditions, in the archaeological or fossil record.

**Experimental taphonomy** The actualistic branch of taphonomy that reconstructs taphonomic trajectories by observing the transformation of organisms, organs, or isolated tissues under controlled laboratory conditions, over timescales accessible to direct observation.

**Extracellular matrix (ECM)** The organised, insoluble macromolecular network occupying the extracellular space of tissues, providing structural scaffolding, sequestering growth factors and signalling molecules, and modulating cell behaviour through mechanochemical interactions. In most tissues, the ECM is dominated by fibrillar collagens that provide tensile strength; in the brain, however, the ECM is largely devoid of fibrillar collagens and instead consists of a hydrated, proteoglycan-rich network dominated by hyaluronic acid and chondroitin sulfate proteoglycans. The sparsely fibrillar brain ECM maintains a compliant, high-water-content extracellular environment while regulating molecular diffusion, contributing to the brain's $\sim 20\%$ extracellular volume fraction. *Post-mortem*, alterations in ECM stiffness, crosslinking, and hydration arising from age-related remodelling modify the diffusion properties of the extracellular space.

**FAIMS** An atmospheric-pressure ion mobility separation device implementing high-field asymmetric-waveform ion mobility spectrometry, placed between the ion source and the mass spectrometer inlet, in which ions are separated according to the difference between their mobility under high and low electric fields in a carrier gas at atmospheric pressure. A user-defined CV selectively transmits ions with particular differential mobility characteristics: appropriately chosen CVs preferentially transmit multiply charged peptide ions while reducing transmission of many singly charged ions, including chemical noise, peptide contaminants, and other non-peptide species.

**False discovery rate (FDR)** The expected proportion of false positives (i.e., incorrect identifications) among all accepted identifications at a given score threshold, commonly estimated using the target–decoy strategy. In proteomics, FDR is typically controlled separately at the PSM, peptide, and protein levels. A 1% FDR threshold means that $\sim 1\%$ of accepted identifications are expected to be incorrect.

**Fenton reaction** The iron-catalysed reduction of hydrogen peroxide to generate a hydroxyl radical: $Fe^{2+} + H_2O_2 \rightarrow Fe^{3+} + \cdot OH + OH^-$. The hydroxyl radical produced is among the most reactive and non-selective of all ROS, reacting at or near diffusion-limited rates with virtually any organic molecule in its vicinity and initiating chain-propagating oxidative damage. In the brain, the Fenton reaction is driven by the unusually large and heterogeneous pool of iron, the continuous generation of $H_2O_2$ as a by-product of mitochondrial ETC leakage, and the presence of superoxide ($\cdot O_2{}^-$), which reduces $Fe^{3+}$ to $Fe^{2+}$, sustaining iron redox cycling.

**Fermentation** In the biochemical sense, an anaerobic catabolic process in which organic molecules serve as both electron donors and electron acceptors, generating ATP without an external terminal electron acceptor; in microbiological usage, the fermentation of carbohydrates by enteric bacteria that involves the conversion of sugars to a range of products (including lactic acid, acetic acid, propionic acid, butyric acid, ethanol, carbon dioxide, and hydrogen gas), depending on the organism and substrate. *Post-mortem*, fermentative metabolism is a major component of early putrefaction, during which enteric anaerobes catabolise autolysed cellular material before other anaerobic respiratory pathways become increasingly important as decomposition progresses.

**Ferroptosis** An iron-dependent, non-apoptotic form of regulated cell death driven by the accumulation of lethal levels of lipid hydroperoxides on cellular membranes. The critical role of iron distinguishes ferroptosis from other forms of regulated cell death: $Fe^{2+}$ in the labile iron pool catalyses the reductive decomposition of lipid hydroperoxides to lipid alkoxyl radicals that propagate membrane-damaging radical chains.

**Flocculent densities** Amorphous, electron-dense aggregates visible within mitochondrial matrices, associated with irreversible mitochondrial injury under conditions of ATP depletion, elevated intracellular $Ca^{2+}$, and progressive oxidative damage to the inner membrane. Their appearance is widely regarded as marking the transition from potentially reversible to irreversible cell injury.

**Freezing** A mode of soft-tissue preservation in which water is immobilised within an ice lattice, greatly reducing the availability of unfrozen liquid water required for diffusion, hydrolytic reactions, and microbial metabolism, while suppressing enzymatic and microbial activity through low temperature. Long-term preservation by freezing is conditional on sustained sub-zero temperatures: thawing reinstates liquid water, elevates enzyme and microbial activity (which may be enhanced by prior disruption of cellular compartmentation), and typically leads to rapid liquefactive decomposition. Environmental contexts include permafrost, glaciers, high-altitude snowfields, and thermally stable caves.

**Gene Ontology (GO) enrichment** A statistical analysis assessing whether a defined set of proteins is significantly enriched for proteins annotated to specific GO terms – biological processes (BP), molecular functions (MF), or cellular components (CC) – compared to a reference proteome background. The analysis compares the observed number of proteins annotated to each GO term with the number expected under the null hypothesis of random sampling from the background, assigning statistical significance using an appropriate enrichment test (commonly a Fisher's exact or hypergeometric test) with correction for multiple testing (typically Benjamini–Hochberg FDR).

**Generalised additive model** A semi-parametric regression model that extends the generalised linear model by allowing the relationship between each predictor and the response to be modelled by a smooth (typically spline-based) function rather than a fixed parametric form, enabling the detection of non-linear relationships without specifying their form *a priori*. GAMs are commonly fitted using penalised smoothers, with smoothing parameters selected to balance goodness of fit against model complexity.

**Glutamic acid (Glu, E)** An acidic amino acid with a longer $\gamma$-carboxylate side chain than Asp ($-CH_2-CH_2-COOH$; p$K_a \sim 4.3$). Glu is negatively charged at physiological pH and participates in salt bridges and hydrogen bonding. Its terminal carboxylate commonly coordinates metal ions including $Ca^{2+}$, $Zn^{2+}$, $Fe^{2+/3+}$, and $Cu^{+/2+}$ as part of protein metal-binding sites; when buried within a folded protein, this reduces local solvent access, whereas when solvent-exposed, the polar side chain promotes hydration and may increase the accessibility of neighbouring peptide bonds to hydrolysis.

**Glutamine (Gln, Q)** An amidic amino acid with a longer neutral carboxamide side chain than Asn ($-CH_2-CH_2-CO-NH_2$), capable of hydrogen bonding and serving as a nitrogen donor. Gln is susceptible to hydrolytic attack, and to spontaneous deamidation predominantly by direct hydrolysis to Glu (although cyclisation through a six-membered glutarimide intermediate can also occur).

**Glycine (Gly, G)** The smallest and only achiral amino acid, with hydrogen as its side chain, conferring exceptional backbone conformational flexibility by eliminating steric clashes that constrain dihedral angles in all other residues. This flexibility makes Gly abundant at structural turning points in proteins (e.g., loops, collagen triple-helical Gly–X–Y repeats) while reducing local conformational constraints on the peptide backbone.

**Glyoxal** A symmetric $\alpha$-dicarbonyl compound (OHC$-$CHO) produced during oxidative degradation of Amadori products, autoxidation of glucose, and ROS-mediated cleavage of glycated proteins. Like methylglyoxal, glyoxal is a potent electrophile that reacts with Lys and Arg residues to form stable AGE adducts and, less commonly, intermolecular protein–protein crosslinks.

**GRAVY score** The GRand AVerage of hydropathY score for a peptide or protein, calculated as the arithmetic mean of the Kyte–Doolittle hydropathy values of all constituent amino-acid residues; positive GRAVY scores indicate hydrophobicity, and negative scores indicate hydrophilicity. The GRAVY score is widely used in proteomics as a simple one-dimensional descriptor of the physicochemical character of a peptide, influencing chromatographic retention time, ionisation efficiency, and solubility in aqueous extraction buffers.

**Grey matter** The regions of the CNS enriched in neuronal cell bodies, proximal dendrites, synaptic connections, and associated glial cells (e.g., astrocytes, microglia), characterised by relatively high protein content ($\sim 60\%$ of dry weight from synaptic and cytoskeletal machinery) and substantial membrane-lipid content ($\sim 40\%$ of dry weight), but a lower lipid fraction than white matter. Grey matter has higher metabolic demand than white matter (i.e., consumes more oxygen per unit mass) and exhibits a greater oxidative burden with ageing, particularly in the frontal cortex and hippocampus relative to the less metabolically active cerebellum. *Post-mortem*, the high enzyme content and water-rich cytoplasm of grey matter render it more susceptible to rapid liquefactive autolysis than myelinated white matter structures.

**Haber–Weiss reaction** The net production of a hydroxyl radical from hydrogen peroxide and superoxide: $\cdot O_2^- + H_2O_2 \rightarrow \cdot OH + OH^- + O_2$, which is thermodynamically favourable but kinetically negligible in the absence of a catalyst. In the iron-catalysed Haber–Weiss reaction, the process proceeds in two steps: $Fe^{3+} + \cdot O_2^- \rightarrow Fe^{2+} + O_2$ (reduction of ferric iron by superoxide), followed by $Fe^{2+} + H_2O_2 \rightarrow Fe^{3+} + OH^- + \cdot OH$ (the Fenton reaction), with the net result that superoxide regenerates $Fe^{2+}$, sustaining Fenton-type hydroxyl radical production from the available iron pool. The Haber–Weiss cycle therefore links superoxide production (from ETC leakage and NADPH oxidase) with $H_2O_2$ generation (by superoxide dismutase) and hydroxyl radical production (*via* the Fenton reaction), providing an important mechanistic link between mitochondrial ROS generation and metal-catalysed oxidative damage.

**Histidine (His, H)** A basic aromatic amino acid with an imidazole side chain ($pK_a \sim 6.0$ in the free state, but variable in proteins from $\sim 4-9$ depending on environment), making His uniquely capable of switching between protonated (imidazolium) and neutral (imidazole) forms near physiological pH. This reversible protonation makes His a key participant in enzyme active sites (as a general acid–base catalyst), metal coordination centres (with $Zn^{2+}$, $Cu^{+/2+}$, $Fe^{2+/3+}$, and others, *via* the N$\delta$1 and/or N$\varepsilon$2 atoms of the imidazole ring), and in the mobile proton model of CID fragmentation. His is susceptible to metal-catalysed oxidation to 2-oxo-His, a primary carbonyl product.

**Holocene** The current geological epoch, beginning at the end of the Younger Dryas ($\sim 11{,}700$ y BP) and extending to the present day, representing the relatively climatically stable interglacial period in which human civilisation developed. It is the primary temporal framework of the archaeological record and encompasses virtually all documented human soft-tissue preservation.

**Humic substances** A heterogeneous family of complex, high-molecular-weight, partially oxidised organic compounds present in soil, peat, and water, arising from the microbial and chemical degradation of plant and animal remains; subdivided operationally by solubility into humin (insoluble at all pH), humic acid (soluble at pH $\gtrsim 2$), and fulvic acid (soluble at all pH). Humic substances contain a mixture of aromatic, aliphatic, and heteroatomic domains bearing carboxyl, carbonyl, hydroxyl, and phenolic functional groups, and are widely regarded as existing as amphiphilic supramolecular aggregates that adsorb to protein surfaces *via* hydrogen bonding, hydrophobic, and electrostatic interactions. In peat burial environments, adsorbed humic and fulvic aggregates form heterogeneous organic coatings on tissue surfaces that restrict diffusion, limit enzymatic access, and bind divalent metal ions required for microbial metabolism, thereby contributing to the chemical stabilisation of soft tissues alongside polyphenol-mediated crosslinking.

**Hydrogen peroxide ($H_2O_2$)** A relatively stable, membrane-permeable ROS produced *in vivo* principally by the dismutation of superoxide ($2{\cdot}O_2^- + 2\,H^+ \rightarrow H_2O_2 + O_2$) and by certain oxidase enzymes that reduce molecular oxygen by two electrons. Its chemical properties are intermediate between molecular oxygen and water: it is a weak oxidant for most organic molecules but a potent oxidant of $Fe^{2+}$ (*via* the Fenton reaction), generating highly reactive hydroxyl radicals. $H_2O_2$ oxidises Cys thiols to sulfenic acid by two-electron oxidation, and Met to sulfoxide.

**Hydrolysis** The cleavage of a covalent bond by reaction with water, incorporating the elements of water into the products. In biological systems, hydrolysis is the principal mechanism of polymer degradation: peptide bonds in proteins, ester bonds in lipids, glycosidic bonds in polysaccharides, and phosphodiester bonds in nucleic acids are all cleaved hydrolytically, either by specific enzymes or by the non-enzymatic action of water under acidic, alkaline, or elevated-temperature conditions.

**Hydroxyl radical (·OH)** The most reactive and least selective of all biologically relevant radical species, with a rate constant for reaction with organic molecules approaching the diffusion limit ($\sim 10^9$–$10^{10}$ $M^{-1}s^{-1}$) and essentially no substrate specificity: it reacts with whatever molecule it encounters within its extremely short diffusion distance in aqueous solution ($\sim 1$ nm). Generated principally by the Fenton reaction, ·OH initiates lipid peroxidation by hydrogen abstraction, oxidises all four DNA bases, attacks most amino-acid side chains, and causes protein backbone cleavage.

**Hypoxia** A condition of reduced oxygen availability below that required to sustain aerobic metabolism, arising in *post-mortem* tissues and burial environments when microbial and residual enzymatic oxygen consumption exceeds the rate of diffusion from the surrounding medium. Even in atmospherically exposed bodies, hypoxia develops rapidly within internal tissues following circulatory arrest, as the oxygen partial pressure ($pO_2$) declines steeply once residual dissolved oxygen is consumed. In waterlogged and submerged burial environments, hypoxia is particularly persistent because oxygen diffusion through water is approximately four orders of magnitude slower than in air.

**Intensity-based absolute quantification (iBAQ)** A protein quantification metric calculated by dividing the summed precursor-ion intensities of all detected peptides for a given protein by the number of theoretically observable tryptic peptides (typically those between $6 - 30$ amino acids), thereby approximately normalising protein abundance for protein length and enabling estimation of the relative molar abundances of different proteins within the same sample. Unlike LFQ intensity, which is optimised for comparing the abundance of the same protein across samples, iBAQ is intended to compare the relative abundances of different proteins within a single sample.

**Intrinsic disorder** The property of a protein or protein region that lacks a stable, folded three-dimensional structure under physiological conditions, and which instead adopts a heterogeneous ensemble of conformations; predicted computationally from amino-acid composition (e.g., low hydrophobicity, high charge, high Gly and Pro content) using tools such as IUPred. Disordered regions are more accessible to enzymatic cleavage and chemical modification than ordered regions.

**Ion trap** A mass analyser in which ions are trapped and stored in an oscillating electric field generated by hyperbolic (3D trap) or parallel plate (linear trap) electrodes, enabling mass-selective ejection of ions toward detectors by scanning the RF voltage. Ion traps offer the ability to isolate, accumulate, fragment (*via* resonance-excitation CID), and re-fragment ions in multiple stages ($MS^n$), making them powerful for detailed structural characterisation of complex modifications; however, their mass accuracy (typically 20–100 ppm) and resolving power are substantially lower than those of Orbitrap™ or TOF analysers. In hybrid instruments (e.g., the Orbitrap™ Tribrid, comprising a linear ion trap, Orbitrap™, and HCD cell), the linear ion trap is used for rapid, lower-resolution MS2 scans while the Orbitrap™ provides high-resolution MS1 and selective MS2 measurements in parallel, maximising information density per unit time.

**Ionic strength** A measure of the total concentration of ions in a solution, defined as one half of the sum of the product of each ion's molar concentration and the square of its charge number. Ionic strength governs the activity coefficients of dissolved species, the solubility of proteins and minerals, the activity of enzymes, and the speciation and precipitation behaviour of metal ions. In the burial context, elevated ionic strength (as in brackish or marine environments) can suppress certain enzymatic activities, alter metal complexation and precipitation equilibria, and select for halotolerant or halophilic microbial communities with distinct metabolic repertoires. *Post-mortem*, autolysis and microbial metabolism alter the ionic strength of tissue fluids through the release, consumption, and redistribution of dissolved ions and metabolites, contributing to the evolving physicochemical environment of decomposition.

**Isoelectric point (pI)** The pH at which a peptide or protein carries no net electrical charge: the number of positively charged groups (e.g., protonated amines and imidazolium groups) equals the number of negatively charged groups (e.g., deprotonated carboxylates, phosphates, and sulfates). The pI influences protein solubility (proteins are generally least soluble and most prone to aggregation near their pI), chromatographic behaviour, and charge state during electrospray ionisation.

**Isoleucine (Ile, I)** A branched-chain aliphatic hydrophobic amino acid with a branched side chain ($-CHCH_3-CH_2-CH_3$) that is among the most effective at stabilising hydrophobic protein cores through van der Waals interactions.

**Karyolysis** The complete dissolution of the cell nucleus during autolysis, driven primarily by endogenous DNase activity following loss of membrane integrity and organellar compartmentalisation. It represents an irreversible stage of autolytic cell death in which chromatin aggregation, nuclear envelope breakdown, and progressive enzymatic digestion of nucleoprotein complexes culminate in the loss of identifiable nuclear structure.

**Köppen climate classification** A widely used global climate classification system first published by Wladimir Köppen in 1884, which delineates climate zones based on monthly mean temperature and precipitation patterns into five major classes (tropical, arid, temperate, continental, and polar), each subdivided by temperature and precipitation seasonality.

**Label-free quantification (LFQ)** A proteomics quantification strategy in which the relative abundance of proteins or peptides across different samples is estimated from the intensity of peptide precursor ions (or their fragment ions) measured by MS, without the use of isotopic or isobaric labelling strategies (e.g., SILAC, TMT, iTRAQ). LFQ intensities are normalised across runs to correct for differences in sample loading, ionisation efficiency, and instrument performance; the MaxLFQ algorithm, implemented in MaxQuant, applies normalisation based on pairwise peptide intensity ratios across samples, weighted by detection consistency.

**Labile peptide** A decay-prone peptide characterised in this thesis by a peak of maximum intensity in the first six weeks *post-mortem*, followed by a steep negative trajectory of relative abundance; operationally defined by data-driven thresholds on peptide-specific decay slopes fit across the PMI.

**Lactic acidosis (autolytic)** The progressive acidification of the cytoplasm and surrounding tissue fluid accompanying anaerobic glycolysis *post-mortem* following the failure of oxidative phosphorylation, characterised by accumulation of lactate and a progressive decline in intracellular pH from $\sim 7.2$ toward $\sim 5.0$. As pH falls, nuclear chromatin aggregates, lysosomal hydrolase activity becomes increasingly permissive once enzymes escape their acidic compartments, and enzymatic degradation of cellular components accelerates. This *post-mortem* acidification is both a consequence of ATP depletion and an important contributor to autolytic tissue breakdown.

**Leucine (Leu, L)** A branched-chain aliphatic hydrophobic amino acid with an isobutyl side chain ($-CH_2-CHCH_3-CH_3$), and a key contributor to hydrophobic core packing in soluble proteins. When buried within a folded protein, Leu contributes to tight hydrophobic packing that limits local solvent accessibility and reduces exposure of adjacent peptide bonds to hydrolysis.

**Lipid peroxidation** Self-propagating, radical-mediated oxidation of PUFAs in membrane phospholipids and other lipid substrates, initiated when a ROS – most commonly a hydroxyl radical ($\cdot OH$) – abstracts a hydrogen atom from a bis-allylic position to generate a carbon-centred lipid radical ($L\cdot$). $L\cdot$ reacts with molecular oxygen to form a lipid peroxyl radical ($LOO\cdot$), which abstracts hydrogen from an adjacent lipid molecule, generating a lipid hydroperoxide (LOOH) and a new radical that continues the chain. LOOH decomposition, principally through metal-catalysed one-electron reduction, generates alkoxyl radicals ($LO\cdot$), which can either propagate the chain or undergo $\beta$-scission to yield aldehyde and ketone fragments (e.g., 4-HNE, MDA).

**Lipidation** The covalent attachment of hydrophobic lipid moieties to protein side chains, comprising several distinct enzymatic reactions: palmitoylation, the reversible attachment of palmitate (C16:0) to Cys thiols *via* a thioester bond; myristoylation, the irreversible N-terminal attachment of myristate (C14:0) to Gly *via* an amide bond; prenylation, the irreversible attachment of farnesyl (C15) or geranylgeranyl (C20) isoprenyl groups to Cys thiols *via* a thioether bond; and GPI anchor addition, the post-translational attachment of a glycosylphosphatidylinositol anchor to the C-terminus of targeted proteins following proteolytic processing. Lipidation regulates membrane affinity, protein trafficking, and protein–protein interactions. *Post-mortem*, palmitoyl thioester bonds are particularly susceptible to hydrolysis and thiol exchange, releasing fatty acids that may participate in subsequent lipid peroxidation; myristoyl amide bonds and prenyl thioether bonds are more stable but remain susceptible to oxidative modification of the lipid moiety.

**Liquefactive necrosis** A form of cell death characterised by extensive proteolytic activity that rapidly degrades cellular and extracellular components, producing a soft, (semi-)liquid, viscous mass that may undergo cavitation. It predominates in enzyme-rich tissues with high lytic capacity, of which the brain is the classical example given its abundance of lysosomal hydrolases, activation of cytosolic calpains following $Ca^{2+}$ dysregulation, and relatively low structural protein content, particularly within grey matter.

**Logistic regression** A statistical classification model that estimates the log-odds of a binary outcome as a linear combination of predictor variables, applying a logistic (sigmoid) function to map the linear predictor to a probability between 0 and 1. The fitted coefficients represent changes in log-odds associated with each predictor; exponentiation of these coefficients yields ORs that quantify the effect of each predictor on the odds of the outcome.

**Lysine (Lys, K)** A basic amino acid with a long aliphatic side chain terminating in a primary $\varepsilon$-amino group ($-[CH_2]_4-NH_2$; p$K_a \sim 10.5$), which is positively charged at physiological pH and represents the principal nucleophilic amine target for non-enzymatic covalent protein modifications, including Schiff base formation with reducing sugars (initiating AGE formation), Michael addition with $\alpha,\beta$-unsaturated aldehydes (e.g., acrolein, 4-HNE), side-chain oxidation to aminoadipic semialdehyde *via* metal-catalysed oxidation, and covalent crosslinking in the peat-tanning context *via* sphagnan carbonyl condensation.

**Lysosome** A membrane-bound acidic organelle (lumenal pH $\sim$ 4.5–5.0) containing more than 60 hydrolytic enzymes – including cathepsins, lipases, nucleases, glycosidases, and phosphatases – that together can degrade all major classes of biological macromolecules. *In vivo*, these acid hydrolases are sequestered within the lysosomal membrane at pH values well below the near-neutral pH of the cytosol; *post-mortem*, progressive membrane destabilisation driven by ATP depletion, osmotic stress, and lipid peroxidation increases lysosomal permeability, permitting hydrolases to access cytoplasmic substrates under conditions that become progressively more permissive for enzymatic activity, thereby accelerating autolytic degradation of cellular components and promoting the transition from reversible to irreversible cell injury.

**Maillard reaction** A cascade of non-enzymatic condensation reactions between carbonyl groups of reducing sugars and primary amino groups of amino acids, proteins, or other nitrogenous compounds. The reaction proceeds through the formation of Schiff bases, Amadori rearrangement to ketoamines, and subsequent fragmentation, cyclisation, oxidation, and polymerisation reactions that generate a heterogeneous mixture of AGEs, N-heterocyclic compounds, and high-molecular-weight crosslinked polymers known as melanoidins.

**Malondialdehyde (MDA)** A dialdehyde ($O{=}CH-CH_2-CH{=}O$) generated during the decomposition of lipid peroxidation products derived from PUFAs, representing one of the most widely used biomarkers of lipid peroxidation and oxidative stress. MDA reacts with primary amines – particularly the $\varepsilon$-amino group of Lys – to form reversible Schiff bases that can rearrange to more stable adducts or crosslink two amine-bearing molecules through bis-adduct formation.

**MaxQuant** An open-source computational proteomics platform for the analysis of DDA LC–MS/MS data, incorporating the Andromeda search engine for database searching. MaxQuant processes raw instrument files, detects precursor features in MS1, performs peptide-spectrum matching with configurable fixed and variable modifications, estimates FDRs using a target–decoy strategy, and assembles peptide- and protein-level identifications. It additionally provides LFQ (*via* the MaxLFQ algorithm), iBAQ, MBR (for transferring peptide identifications between aligned runs on the basis of precursor mass and retention time), and dependent-peptide searching (for open-modification discovery).

**Melanoidins** Heterogeneous, dark-pigmented, high-molecular-weight polymers formed by Maillard-type condensation reactions between carbonyl species (typically from reducing sugars or oxidised lipids) and primary amines (principally from amino acids and proteins), contributing to the brown-to-black discolouration of *post-mortem* tissues during active decay. Melanoidins share chemical characteristics with humic substances and arise from the same broad reaction network as ALEs/AGEs, being highly recalcitrant owing to their extensively crosslinked, aromatic-rich architecture.

**Membrane blebbing** The localised, irregular outward protrusion or 'blistering' of the plasma membrane caused by partial decoupling of the lipid bilayer from the underlying cytoskeletal network, driven by elevated intracellular $Ca^{2+}$, ATP depletion, and calpain-mediated cleavage of actin–spectrin attachments *post-mortem*. Unlike the membrane blebbing of apoptosis – which generates intact, membrane-bound apoptotic bodies – autolytic blebs are not phagocytosed and are followed by progressive membrane dissolution and cell lysis. Membrane blebbing is among the earliest ultrastructural manifestations of neuronal autolysis, while associated vacuolisation becomes detectable by light microscopy during the early PMI.

**Metal-catalysed oxidation** Site-specific oxidative modification of proteins catalysed by transition metal ions – principally $Fe^{2+}$ and $Cu^{+}$ – bound at protein metal-coordination sites, in which the metal participates in Fenton-type generation of highly reactive hydroxyl radicals. Because the radical is generated in the immediate vicinity of the bound metal, oxidative damage is highly localised rather than diffuse (as with exogenous radical sources): primary carbonyl formation occurs preferentially at nearby susceptible residues, like Lys, Arg, Pro, and Thr.

**Methanogenesis** The production of methane ($CH_4$) by methanogenic archaea (strict anaerobes) using $CO_2$ and $H_2$ or acetate as substrates in the final and most thermodynamically unfavourable step of anaerobic organic matter degradation, occurring only after $NO_3^-$, Mn(IV), Fe(III), and $SO_4^{2-}$ have been substantially depleted. In *post-mortem* environments, methanogenesis is characteristic of highly reducing, oxygen-depleted conditions and contributes to the late stages of organic matter degradation; methane production in burial sediments therefore serves as an indicator of strongly reducing diagenetic conditions.

**Methionine (Met, M)** A sulfur-containing amino acid with a thioether side chain ($-CH_2-CH_2-S-CH_3$) that is susceptible to oxidation – initially to sulfoxide (Met[O]; reversible two-electron oxidation), and subsequently to sulfone (Met[$O_2$]; irreversible) – and to demethylation and desulfurisation during microbial decomposition. In proteins, Met acts as a redox buffer to intercept oxidative flux before it can cause irreversible damage; *post-mortem*, this buffering capacity is retained during the early PMI but eventually exhausted.

**Methylglyoxal** A reactive, electrophilic $\alpha$-dicarbonyl compound ($CH_3-CO-CHO$) generated primarily by spontaneous degradation of glycolytic triose phosphates and secondarily during Amadori-product degradation in AGE formation. As a bifunctional carbonyl, methylglyoxal reacts with multiple nucleophilic sites on proteins, forming irreversible AGE adducts and, less commonly, intermolecular crosslinks; it reacts preferentially with Arg (forming hydroimidazolone adducts), with Lys $\varepsilon$-amines, and rapidly with Cys thiols. In the brain, methylglyoxal is detoxified principally by the glyoxalase I/II system, whose activity declines with age, permitting accumulation of methylglyoxal-derived AGEs on long-lived proteins.

**Michael addition** A 1,4-nucleophilic addition reaction in which a soft nucleophile attacks the $\beta$-carbon of an $\alpha,\beta$-unsaturated carbonyl compound (the Michael acceptor), forming a new covalent bond between the nucleophile and the $\beta$-carbon. In the context of protein oxidative modification, Michael addition is the principal mechanism by which Cys and His, and an important mechanism by which Lys, react with lipid-derived $\alpha,\beta$-unsaturated aldehydes (e.g., acrolein, 4-HNE, 4-oxo-2-nonenal), generating stable covalent protein–lipid adducts that modify local charge, conformation, and susceptibility to proteolysis. Bifunctional Michael acceptors (or sequential Michael/Schiff base reactions) can bridge two nucleophilic sites within or between proteins, producing intermolecular crosslinks that reduce solubility and increase resistance to enzymatic degradation.

**Microenvironment** The local physicochemical conditions – temperature, water activity, oxygen partial pressure, pH, redox potential, ionic composition, and the like – experienced by organic molecules at the (sub)cellular scale.

**Microglia** The resident immune cells of the CNS, constituting $\sim$ 5–15% of all brain cells and functioning as the primary mediators of immune surveillance, phagocytosis of cellular debris and pathogens, and synaptic pruning in the developing and adult brain. In the ageing brain, microglia shift toward a chronically activated (primed) state characterised by elevated basal production of pro-inflammatory cytokines, reduced phagocytic capacity, and increased generation of ROS and RNS; this neuroinflammatory milieu progressively alters the chemical composition of the extracellular space and accelerates the accumulation of oxidative and carbonyl modifications on extracellular and membrane-associated proteins.

**Mitochondria** Double-membrane organelles constituting the primary site of oxidative phosphorylation and the principal intracellular source of ROS generated by electron leakage from the ETC. *Post-mortem*, mitochondria are among the most sensitive organelles to the autolysis: $Ca^{2+}$ overload triggers opening of the mitochondrial permeability transition pore, collapsing the inner membrane potential, releasing cytochrome *c*, and swelling the organelle to the point of outer membrane rupture. Morphologically, swollen mitochondria with flocculent densities are among the earliest ultrastructural signs of irreversible autolysis.

**Molecular taphonomy** The study of taphonomic processes – degradation, transformation, and preservation – at the level of individual biomolecules and the chemical reactions that govern them. It focuses on how the chemistry of proteins, lipids, carbohydrates, and nucleic acids shifts from their *in vivo* states through *post-mortem* biostratinomy and diagenesis, and how environmental conditions modulate those shifts.

**Myelin** A highly specialised multilamellar membrane structure produced by oligodendrocytes in the CNS, forming concentric lipid bilayer lamellae that ensheath axons. The lamellae are compacted by extrusion of cytoplasm and stabilised by myelin-specific proteins, producing an insulating sheath with very high electrical resistance. Myelin is among the most lipid-rich biological membranes, comprising $\sim$ 70–85% lipid (e.g., cholesterol, galactocerebrosides, sulfatides, phosphatidylethanolamine) and $\sim$ 15–30% protein (e.g., MBP, PLP1) by dry weight.

**Myelin basic protein (MBP)** A peripheral membrane protein constituting $\sim$ 30% of CNS myelin protein, located on the cytoplasmic surface of compact myelin where it maintains close apposition of the cytoplasmic membrane leaflets. MBP is largely intrinsically disordered in solution, adopting a more ordered conformation upon membrane association, and is one of the most abundant proteins of the CNS, exhibiting slow turnover within compact myelin.

**Myelin proteolipid protein (PLP1)** The most abundant transmembrane protein of CNS myelin, accounting for $\sim$ 50% of myelin protein and $\sim$ 30% of total myelin dry weight, encoded by the *PLP1* gene. It is a highly hydrophobic integral membrane protein with four transmembrane domains and multiple palmitoylated Cys residues that anchor it within the lipid bilayer and contribute to myelin compaction.

**$Na^+/K^+$-ATPase pump** A plasma membrane-embedded, ATP-driven ion pump that transports three sodium ions ($Na^+$) out of and two potassium ions ($K^+$) into the cell per ATP molecule hydrolysed, maintaining the electrochemical gradients essential for membrane excitability, secondary active transport, and cell volume regulation. *Post-mortem*, the cessation of oxidative phosphorylation causes rapid ATP depletion; failure of the $Na^+/K^+$-ATPase allows intracellular $Na^+$ to rise and $K^+$ to fall, driving osmotic water influx and cytotoxic oedema. This ionic collapse is a pivotal early event in autolysis, triggering the cascade of membrane destabilisation, organellar swelling, and eventual lysis that characterises *post-mortem* cellular disintegration.

**Necrosis** A predominantly non-programmed form of cell death associated with acute physicochemical insult – including ATP depletion, ionic imbalance, osmotic stress, and oxidative damage – characterised by cellular and organellar swelling (oncosis), early plasma membrane rupture, and uncontrolled release of intracellular contents into the surrounding tissue, typically eliciting inflammatory responses. Necrosis follows a broadly defined sequence of cellular collapse: loss of membrane integrity, organellar dysfunction, and ultimate cellular lysis. In the *post-mortem* context, the autolytic cascade resembles necrotic cell death in its physicochemical drivers but occurs without the systemic inflammatory response that characterises necrosis in a living organism. Two major morphological subtypes relevant to taphonomy are coagulative necrosis (in which structural protein denaturation outpaces enzymatic degradation, potentially preserving gross tissue architecture) and liquefactive necrosis (in which enzymatic digestion rapidly degrades cellular components).

**Neuromelanin** A dark, insoluble pigment polymer synthesised by dopaminergic neurons in the substantia nigra pars compacta and noradrenergic neurons in the locus coeruleus, formed predominantly through oxidative polymerisation of dopamine and noradrenaline (catecholamines) that accumulate within lysosomes of these neurons over the lifespan. Neuromelanin is structurally related to eumelanin but includes additional lipid–protein components and is associated with a large repertoire of chelated metals – particularly $Fe^{2+}/Fe^{3+}$, $Cu^{+/2+}$, $Zn^{2+}$, and $Mn^{2+}$ – making it a major intracellular metal storage site in dopaminergic and noradrenergic neurons. Its iron-chelating capacity is normally protective, sequestering potentially toxic iron from the labile pool; however, in NDDs and *post-mortem* iron release, the neuromelanin-associated iron pool represents a concentrated source of redox-active metal that may catalyse localised Fenton-type radical chemistry.

**Neuron** The electrically excitable, post-mitotic, exceptionally long-lived primary signal-processing cell of the CNS, specialised for the generation, integration, and propagation of action potentials; morphologically polarised with a dendritic arbour receiving synaptic inputs, a soma integrating signals, and an axon conducting action potentials to presynaptic terminals where neurotransmitter release mediates chemical signalling at synapses. Most CNS neurons are post-mitotic from early development and do not normally undergo division or replacement in the adult, making their molecular maintenance critical over a lifespan of decades. The exceptional longevity of neurons means that their proteins accumulate spontaneous non-enzymatic modifications (e.g., deamidation, glycation, carbonylation, racemisation) to a greater extent than in rapidly turned-over cells.

**Non-enzymatic glycation** The spontaneous, non-enzymatic Maillard reaction in which the carbonyl group of a reducing sugar (most commonly glucose or fructose) reacts reversibly with nucleophilic primary amines on proteins – particularly the $\varepsilon$-amino group of Lys and the N-terminal $\alpha$-amino group – to form a labile Schiff base that rearranges to a more stable Amadori product (ketoamine). Through subsequent dehydration, fragmentation, and oxidation reactions, the Amadori product yields reactive $\alpha$-dicarbonyl intermediates (e.g., methylglyoxal, glyoxal, 3-deoxyglucosone) that form stable AGE adducts and, in some cases, covalent crosslinks.

**Oligodendrocyte** The glial cell responsible for the production and maintenance of myelin in the CNS. Oligodendrocytes are highly susceptible to oxidative stress because myelin production and maintenance require iron handling as well as high oxidative metabolism, and because these cells operate in a lipid-rich membrane environment with comparatively limited antioxidant defences. Age-related oligodendrocyte dysfunction therefore promotes myelin degeneration, lamellar disruption, and increased exposure of lipid-rich membrane domains to water and reactive species.

**Open-modification search** A database search strategy that removes or greatly relaxes the constraint on modification masses, allowing a wide range of precursor mass offsets between the theoretical unmodified peptide and the observed precursor to be considered as potential modifications without *a priori* specification of their chemical identities. This approach enables the identification of novel, unexpected, or uncharacterised modifications – including diagenetic PTMs – that would be missed by conventional database searching.

**Orbitrap™ mass analyser** A high-resolution, high-mass-accuracy Fourier transform mass analyser in which ions are injected tangentially into a spindle-shaped electrostatic field formed by an inner spindle electrode and an outer barrel electrode, and trapped in stable axial oscillations at frequencies inversely proportional to the square root of their $m/z$; the image current induced by these oscillating ion clouds is detected and Fourier-transformed to yield the mass spectrum. Orbitrap™ instruments achieve high mass resolving power and mass accuracy (typically $< 5\,\text{ppm}$, or $< 1\,\text{ppm}$ with internal calibration or lock-mass correction), enabling resolution of near-isobaric ions and reducing interference from co-eluting species.

**Oxidative phosphorylation** The principal aerobic pathway for cellular ATP synthesis, operating at the inner mitochondrial membrane and consisting of two coupled processes: electron transport, in which electrons derived from reduced cofactors (NADH and $FADH_2$) are passed along the ETC (a series of four multi-subunit protein complexes, I–IV), releasing energy that is used to pump protons from the matrix to the intermembrane space; and chemiosmosis, in which the resulting proton electrochemical gradient (the proton motive force) drives protons back through ATP synthase (Complex V), which harnesses the energy to attach a phosphate group to ADP, forming ATP. Molecular oxygen is the terminal electron acceptor at Complex IV (cytochrome *c* oxidase), accepting four electrons and four protons to form water. *Post-mortem*, cessation of oxidative phosphorylation due to oxygen depletion and loss of mitochondrial membrane potential initiates the cascade of ATP depletion and ionic dysregulation that drives autolytic cell death.

**Oxidative polymerisation** A set of radical-mediated reactions in which biomolecules – particularly unsaturated lipids and proteins – are converted from individual monomers or oligomers into crosslinked, high-molecular-weight macromolecular networks through partial oxidation and subsequent intermolecular bond formation. The process is initiated by hydrogen abstraction from an oxidisable site (generating a carbon-centred radical), propagated by sequential reaction with molecular oxygen to form peroxyl and alkoxyl radicals, and terminated by radical–radical recombination to form stable covalent crosslinks (predominantly C−C and C−O linkages). Under conditions of high oxygen availability, chain propagation dominates and the net effect is fragmentation; under oxygen-limited conditions, termination by crosslinking is favoured.

**Palaeoanthropology** The sub-discipline of biological anthropology concerned with the study of human evolution through the analysis of fossil hominins, including their morphology, phylogenetic relationships, behaviour, and ecology. Molecular palaeoanthropology – the application of ancient DNA, palaeoproteomics, and other biomolecular methods to hominin remains – has revolutionised our understanding of Late Pleistocene human evolution, revealing complex population histories and interbreeding between *Homo sapiens*, Neanderthals, and Denisovans.

**Palaeopathology** The study of disease, trauma, and other pathological conditions in ancient humans and other organisms, primarily through the analysis of morphological, histological, biochemical, and molecular evidence preserved in skeletal and soft-tissue remains.

**Palaeoproteome** The surviving peptide assemblage recovered from an archaeological or fossil specimen by mass spectrometric analysis; the subset of the original *in vivo* proteome that has persisted through taphonomic transformation, remained chemically accessible during extraction, produced detectable peptides during digestion, and could be confidently identified against a reference database. The palaeoproteome is therefore not equivalent to the *ante-mortem* proteome but represents its selectively filtered remnant, shaped by differential protein stability, diagenetic modification, burial environment, and the biases of the analytical workflow. Interpreting biological information from palaeoproteomic data requires explicit accounting for this cumulative filtering.

**Palaeoproteomics** The scientific discipline dedicated to the recovery, identification, and biological interpretation of proteins preserved in archaeological and fossil materials, typically using MS-based analytical workflows.

**Peptide bond (amide linkage)** The covalent bond formed by condensation between the $\alpha$-carboxyl group of one amino acid and the $\alpha$-amino group of the next, with loss of water, generating an amide linkage ($-$CO$-$NH$-$) that connects successive residues in the polypeptide chain. The peptide bond is planar and relatively rigid due to partial double-bond character arising from resonance delocalisation of the nitrogen lone pair into the carbonyl $\pi$-system, and exists predominantly in the trans configuration with the C$\alpha$ atoms on opposite sides of the C−N bond (although peptide bonds preceding Pro can also adopt the cis configuration). This planarity constrains rotation about the peptide bond, restricting backbone conformation and enabling the regular hydrogen-bonding patterns that define protein secondary structure.

**Peptide bond hydrolysis** The cleavage of the amide linkage ($-$CO$-$NH$-$) that connects adjacent amino-acid residues in a polypeptide chain, by nucleophilic attack of water on the carbonyl carbon, followed by collapse of the tetrahedral intermediate to reform the carbonyl and cleave the C−N bond, yielding a free carboxyl terminus on one fragment and a free amino terminus on the other. The peptide bond possesses partial double-bond character through resonance delocalisation of the nitrogen lone pair into the carbonyl, conferring kinetic stability; non-enzymatic hydrolysis is therefore slow under physiological conditions, but accelerated by enzymes, acid or base catalysis, elevated temperature, and metal ions.

**Peptide-level decay profiling** A quantitative analytical approach developed in this thesis in which individual peptide-specific decay trajectories – that is, the change in peptide abundance as a function of PMI across replicated burial conditions – are modelled to identify decay-prone and decay-resistant molecular classes. By fitting peptide-specific decay slopes and classifying peptides according to data-driven thresholds on those slopes, the approach resolves taphonomic heterogeneity within the palaeoproteome at a resolution inaccessible to protein-level analysis. The resulting classification into labile, putative, and recalcitrant peptide types enables statistical interrogation of the biochemical, structural, functional, and environmental correlates of molecular persistence.

**Peptide-spectrum match (PSM)** The assignment of an experimental MS2 tandem mass spectrum to a specific peptide sequence from a reference database, scored by the degree of agreement between the observed fragment-ion pattern and the theoretical fragmentation pattern predicted for that sequence. PSMs are the fundamental unit of identification in database-searching proteomics workflows; multiple PSMs for the same peptide sequence are aggregated to yield a peptide-level identification, and multiple peptide identifications are aggregated to yield a protein-level inference.

**Perivascular rarefaction** A region of reduced staining density appearing as optically clear spaces around blood vessels in *post-mortem* histological sections of the brain, associated primarily with swelling of astrocytic endfeet that ensheath cerebral vessels following the ionic dysregulation of autolysis. Perivascular rarefaction is among the earliest microscopic manifestations of cytotoxic oedema in the *post-mortem* brain.

**Permineralisation** A diagenetic process in which mineral-laden fluids percolate through pore spaces and intracellular spaces of buried organic remains, precipitating minerals (most commonly calcite, silica, pyrite, and iron oxides) within those spaces and thereby preserving the three-dimensional structure of the original tissue. Unlike replacement mineralisation, in which the original organic material is progressively replaced by mineral, permineralisation may preserve the external and internal morphology of the tissue by infilling void spaces within a mineral matrix that physically reinforces the original structure.

**Peroxyl radical (ROO·)** An oxygen-centred radical formed by the rapid addition of molecular oxygen to a carbon-centred radical ($\mathrm{R}\cdot + \mathrm{O_2} \rightarrow \mathrm{ROO}\cdot$), and the principal chain-carrying species in lipid peroxidation. Peroxyl radicals are more stable and selective than the hydroxyl radical but still sufficiently reactive to abstract hydrogen from bis-allylic positions in PUFAs (propagation), add to aromatic rings, or react with antioxidants (termination by reduction to a hydroperoxide). The formation of lipid peroxyl radicals from carbon-centred radicals is essentially irreversible under aerobic conditions due to the high concentration of dissolved oxygen.

**Phenylalanine (Phe, F)** An aromatic hydrophobic amino acid with a phenyl ring side chain ($-\mathrm{CH_2}-\mathrm{C_6H_5}$), contributing to hydrophobic core packing through van der Waals and $\pi$–$\pi$ interactions, but lacking the phenolic hydroxyl group that enables Tyr to form resonance-stabilised radicals and undergo efficient radical coupling. Phe is among the least reactive aromatic residues toward one-electron oxidation under mild conditions; however, its aromatic ring is susceptible to hydroxyl-radical addition under high radical flux, producing hydroxyphenylalanine (predominantly o-tyrosine).

**Phospholipid** A class of amphiphilic lipids comprising a glycerol backbone esterified with two fatty acyl chains and a phosphate head group further esterified to a polar alcohol (e.g., choline, ethanolamine, Ser, inositol), constituting the primary structural components of biological membranes. The two ester-linked fatty acyl chains are susceptible to enzymatic and non-enzymatic hydrolysis, yielding free fatty acids that are themselves susceptible to lipid peroxidation. *Post-mortem*, phospholipid hydrolysis by endogenous phospholipases (activated by elevated $\mathrm{Ca^{2+}}$) and bacterial esterases generates lysophospholipids and free fatty acids, contributing to membrane destabilisation and providing substrates for downstream oxidative and fermentative chemistry.

**Phospholipid bilayer** A two-layered sheet of phospholipid molecules in which the hydrophobic fatty acyl chains of each monolayer face inward – away from the aqueous environment – while the polar head groups face outward, forming a semipermeable barrier that defines the cell boundary (plasma membrane) and the membranes of all intracellular organelles. The bilayer is stabilised by the hydrophobic effect and van der Waals interactions between acyl chains, while its fluidity is governed by acyl chain length, degree of unsaturation, and cholesterol content. *Post-mortem*, failure of the $\mathrm{Na^+/K^+}$-ATPase and $\mathrm{Ca^{2+}}$-ATPase pumps initiates ionic imbalance and osmotic swelling; phospholipase activation by elevated $\mathrm{Ca^{2+}}$ hydrolyses the ester bonds linking fatty acyl chains to the glycerol backbone; and lipid peroxidation oxidatively fragments polyunsaturated acyl chains, collectively driving increased membrane permeability and membrane disintegration during autolysis.

**Phosphorylation** The most abundant and versatile reversible PTM, in which the $\gamma$-phosphate group of ATP is transferred to the hydroxyl group of Ser, Thr, or Tyr residues, introducing a bulky, negatively charged phosphate monoester ($-O-PO_3^{2-}$) that modulates local electrostatics, conformation, and protein–protein interactions. In the brain, phosphorylation is a major regulator of synaptic signalling, neuronal plasticity, and cell survival.

**Polyunsaturated fatty acid (PUFA)** A fatty acid containing two or more C=C double bonds along the aliphatic chain, the positions and geometries of which determine both the fluidity contribution to membranes and the susceptibility to oxidative attack. PUFAs are the primary substrates for lipid peroxidation because their bis-allylic methylene groups ($-CH=CH-CH_2-CH=CH-$) have particularly weak C–H bonds, making them highly susceptible to hydrogen abstraction by radical species. The brain is exceptionally enriched in PUFAs, particularly arachidonic acid (C20:4) and docosahexaenoic acid (C22:6).

***Post-mortem* interval (PMI)** The time elapsed between an organism's death and the point of sampling, representing the duration over which *post-mortem* biological, chemical, and physical processes have acted upon the remains.

**Precursor ion** The intact peptide ion (typically $[M + zH]^{z+}$ in positive-ion ESI) detected in the MS1 survey scan and selected for isolation and fragmentation in MS/MS. The precursor ion is characterised by its measured $m/z$ and charge state (inferred from isotope peak spacing in the MS1 spectrum), from which the monoisotopic or average neutral mass of the peptide is calculated. In DDA workflows, precursor ions exceeding a defined intensity threshold are dynamically selected for MS2 fragmentation; in DIA, all ions within predefined $m/z$ windows are fragmented simultaneously. MS1 precursor intensities provide the quantitative signal used by LFQ protein quantification methods.

**Preservation by inhibition** A class of soft-tissue preservation in which decomposition is suppressed or arrested while the environmental conditions responsible for that inhibition are maintained, preserving biomolecules with relatively little alteration to their intrinsic chemical reactivity.

**Preservation by transformation** A class of soft-tissue preservation in which decomposition proceeds through reactions that convert labile biomolecules into chemically altered, more recalcitrant products capable of long-term persistence. Such products include crosslinked macromolecular networks, mineral-associated organics, and other diagenetically stabilised derivatives. Unlike preservation by inhibition, preservation by transformation fundamentally alters the intrinsic chemical reactivity of biomolecules, generating stabilised products that can persist after the environmental conditions responsible for their formation have ceased.

**Preservation potential** The intrinsic properties of a molecule, cell, tissue, or organ that collectively increase the probability of its participating in stabilising reactions during decomposition and persisting into the archaeological or fossil record. In this thesis, preservation potential is operationalised at the peptide level as a calibrated probability score derived from a logistic regression model trained on compositional, structural, domain-level, and modification features associated with recalcitrant behaviour across burial conditions.

**Primary structure** The linear sequence of amino-acid residues in a polypeptide chain, defined by the covalent connectivity of peptide bonds from the N-terminus to the C-terminus and encoded directly by the gene.

**Principal component analysis (PCA)** A linear dimensionality reduction technique that transforms a high-dimensional dataset into a set of orthogonal principal components, each representing a linear combination of the original variables and successively capturing the greatest remaining variance in the data. The first few PCs summarise the dominant axes of variation among samples and are commonly visualised as score plots to reveal clustering, gradients, and outliers. PCA is an unsupervised method that captures linear patterns of covariance, making it a powerful exploratory tool but one that may not fully represent complex non-linear relationships.

**Proline (Pro, P)** An amino acid in which the side chain forms a covalent bond with the backbone nitrogen, creating a five-membered pyrrolidine ring that constrains backbone geometry, eliminates the backbone N–H hydrogen bond donor, and destabilises $\alpha$-helical and $\beta$-sheet structures. Pro is uniquely capable of both trans and cis isomerisation about the preceding peptide bond, which can slow folding and alter substrate recognition by enzymes; this modulates the susceptibility of adjacent peptide bonds to proteolytic cleavage.

**Protein group** In proteomics database searching, the minimal set of proteins that can explain the complete set of identified peptides for a group of related sequences, reported when peptide-to-protein assignment is ambiguous due to shared (degenerate) peptides among protein isoforms, homologues, or paralogues. The protein group concept reflects the fundamental parsimony principle: rather than asserting the presence of all proteins that could theoretically explain the observed peptides, only the minimal explanatory set is reported.

**Proteolytic cleavage** The hydrolysis of a peptide bond within a protein by proteolytic enzymes, generating an N-terminal fragment with a free carboxyl terminus and a C-terminal fragment with a free amino terminus. *In vivo*, proteolytic cleavage within proteins is highly specific, catalysed primarily by substrate-specific endoproteases; *post-mortem*, endogenous lysosomal cathepsins, cytoplasmic calpains, and exogenous microbial proteases execute an increasingly non-specific cascade of proteolysis that contributes to the abundance of semi- and non-tryptic peptides observed in palaeoproteomes.

**Proteostasis** Protein homeostasis – the maintenance of a functional, properly folded, correctly localised, and appropriately abundant cellular proteome – achieved by the integrated activity of molecular chaperones (that promote correct folding and prevent aggregation), the ubiquitin–proteasome system (which selectively degrades ubiquitylated short-lived, misfolded, or damaged proteins), autophagy–lysosomal pathways (which degrade long-lived proteins, protein aggregates, and organelles in bulk), and mitochondrial quality-control mechanisms. In neurons, proteostasis is under particular strain because post-mitotic cells containing long-lived proteins and extensive polarised architectures cannot dilute accumulated damage through cell division, making them reliant on maintenance systems that decline in efficiency with ageing.

**Putrefaction** The digestion of organic matter by the diverse microbial communities that colonise a decomposing body *post-mortem*, representing a fundamentally different chemical regime from autolysis in that microorganisms – principally the endogenous enteric microbiota and subsequently environmental xenobionts – are the primary agents. As oxygen is depleted and autolysis reaches its terminal stages, the large intestine's obligate anaerobes (dominated by *Clostridia* and *Bacteroidia*) proliferate and migrate into surrounding tissues, secreting exoenzymes that degrade complex biomolecules into amino acids, short-chain fatty acids, alcohols, and gases. Putrefaction is characterised by progressive reductive chemistry: as Eh falls, successive electron acceptors are utilised ($NO_3^-$ > Mn[IV] > Fe[III] > $SO_4^{2-}$ > $CO_2$), generating $H_2S$ and $CH_4$, together with fermentative products including $H_2$ and $NH_3$, and producing the malodour, discolouration, and gas accumulation characteristic of the bloat and active decay stages.

**Quadrupole mass analyser** A mass filter consisting of four parallel metallic rods arranged symmetrically around a central axis and connected in opposite pairs to combined radio frequency and direct current voltages. Ions travelling along the axis experience oscillating electric fields that produce stable trajectories only for ions within a defined $m/z$ range determined by the applied voltages; ions with unstable trajectories collide with the rods and are removed. In hybrid quadrupole–Orbitrap™ instruments (e.g., the Q Exactive™ Plus; Thermo Fisher Scientific), the quadrupole isolates precursor ions for fragmentation, after which the Orbitrap™ measures the masses of the resulting fragment ions with high resolution and mass accuracy.

**Quaternary structure** The association of two or more polypeptide chains (subunits) into a specific, symmetrically or asymmetrically organised higher-order assembly, stabilised primarily by the same non-covalent interactions that govern tertiary structure within individual chains and, in some proteins, by inter-subunit disulfide bonds or other covalent crosslinks.

**Quinone** A class of oxidised cyclic carbonyl compounds formed by the two-electron oxidation of hydroquinones, catechols, and related phenolic compounds by polyphenol oxidases, laccases, or peroxidases, or by autoxidation under partially aerobic conditions. In the context of tanning, quinones derived from the oxidation of phenolic compounds in peat pore waters react rapidly and irreversibly with nucleophilic amino acid side chains – principally Cys thiols *via* Michael addition and Lys $\varepsilon$-amines *via* nucleophilic addition – forming stable C–S and C–N bonds within and between proteins.

**Racemisation** The interconversion of L- and D-amino-acid configurations at the $\alpha$-carbon of an amino-acid residue, proceeding in proteins *via* a cyclic succinimide intermediate at Asn and Asp residues, and at other residues *via* base-catalysed abstraction of the $\alpha$-proton followed by reprotonation from either face of the planar intermediate. Because biological proteins are synthesised almost exclusively from L-amino acids, progressive accumulation of D-amino acids provides an approximate measure of protein age and long-term molecular alteration, although the rate of racemisation depends strongly on residue identity, temperature, and the microenvironment.

**Radical chain propagation** The sequential transfer of radical character through a population of molecules, in which each radical intermediate generates a new radical as a product, sustaining a self-amplifying cascade through continuous regeneration of radical intermediates. The length and extent of radical chain propagation – and therefore the cumulative degree of oxidative damage – is governed by the availability of molecular oxygen, the density and distribution of oxidisable substrates, and the availability of antioxidants or radical quenchers.

**Radical chain termination** The removal of radical intermediates from a propagation cascade through recombination or scavenging reactions that convert them into stable or comparatively unreactive products. Principal termination mechanisms in biological systems include radical–radical recombination ($\mathrm{R}\cdot + \mathrm{R}'\cdot \rightarrow \mathrm{R}{-}\mathrm{R}$), yielding covalent crosslinks; reaction of two peroxyl radicals with concerted elimination (Russell mechanism); and scavenging by low-molecular-weight antioxidants (e.g., ascorbate, tocopherols, polyphenols).

**Reactive carbonyl species (RCS)** A family of highly electrophilic carbonyl-containing molecules generated during lipid peroxidation, glycoxidation, carbohydrate degradation, and related oxidative processes, including $\alpha,\beta$-unsaturated aldehydes (e.g., acrolein, 4-HNE), dialdehydes (e.g., MDA), and $\alpha$-dicarbonyls (e.g., methylglyoxal, glyoxal, 3-deoxyglucosone). RCS are characterised by their reactivity toward nucleophilic functional groups on proteins (particularly Cys, His, Lys, and Arg) *via* Michael addition or Schiff base formation, generating stable covalent protein adducts and crosslinks, including ALEs and AGEs, that accumulate in chronically stressed and ageing tissues.

**Reactive nitrogen species (RNS)** A family of reactive nitrogen-containing molecules including nitric oxide (NO), peroxynitrite ($\mathrm{ONOO^-}$, formed by rapid reaction of NO with $\cdot\mathrm{O_2}^-$), nitrogen dioxide ($\mathrm{NO_2}$), and related compounds, generated primarily by nitric oxide synthase isoforms in neurons, endothelial cells, and inflammatory cells. RNS promote protein nitration (principally formation of 3-nitrotyrosine), S-nitrosylation of Cys thiols, and other oxidative modifications that alter protein conformation and promote aggregation.

**Reactive oxygen species (ROS)** A family of reactive, oxygen-containing molecules including the superoxide radical anion ($\cdot\mathrm{O_2}^-$), hydrogen peroxide ($\mathrm{H_2O_2}$), the hydroxyl radical ($\cdot\mathrm{OH}$), singlet oxygen ($^1\mathrm{O_2}$), and lipid peroxy and alkoxyl radicals, generated during aerobic metabolism (principally by mitochondrial electron transport at Complexes I and III) and by enzymes such as NADPH oxidases. In the brain, exceptionally high oxygen consumption, relatively modest antioxidant defences, and the abundance of PUFAs and redox-active metals together predispose the tissue to chronic oxidative stress.

**Recalcitrant peptide** A decay-resistant peptide characterised in this thesis by a peak of maximum intensity after the first six weeks *post-mortem*, followed by a shallow or positive trajectory of relative abundance; operationally defined by data-driven thresholds on peptide-specific decay slopes fit across the PMI.

**Redox cascade** The sequential utilisation of progressively lower-potential terminal electron acceptors by microbial communities as each preceding acceptor is exhausted, proceeding in order of decreasing free energy yield: $\mathrm{O_2} > \mathrm{NO_3}^- >$ Mn(IV) oxides > Fe(III) oxides > $\mathrm{SO_4}^{2-}$ > $\mathrm{CO_2}$. Each step in the cascade generates distinct reduced end-products – $\mathrm{N_2}/\mathrm{NH_4}^+$, $\mathrm{Mn}^{2+}$, $\mathrm{Fe}^{2+}$, $\mathrm{H_2S}$, and $\mathrm{CH_4}$ respectively – that further modify tissue chemistry and Eh, reinforcing the reducing conditions established by oxygen depletion. In *post-mortem* burial environments, the progression through this cascade is spatially and temporally heterogeneous, with different microenvironments supporting different metabolic guilds depending on local oxygen availability, organic substrate composition, and moisture.

**Redox potential (Eh)** The electrode potential of a solution relative to the standard hydrogen electrode, expressing the oxidising or reducing character of a chemical system. More positive Eh values indicate a greater tendency to accept electrons (i.e., more oxidising conditions), whereas more negative Eh values indicate a greater tendency to donate electrons (i.e., more reducing conditions).

**Reversed-phase liquid chromatography** A liquid chromatographic separation technique in which peptides are retained on a hydrophobic stationary phase (most commonly C18) through hydrophobic partitioning and eluted by an increasing proportion of organic solvent (typically acetonitrile) in an acidified water–organic mobile phase (typically 0.1% formic acid or 0.1% trifluoroacetic acid). Retention is governed primarily by peptide hydrophobicity, with shorter, more polar peptides eluting earlier and longer, while more hydrophobic peptides elute later. The solvent gradient is optimised to maximise chromatographic resolution by distributing peptide elution across the available retention-time window.

**Saponification** Strictly, the alkaline (base-catalysed) hydrolysis of ester bonds in triglycerides, yielding glycerol and the sodium or potassium salts of fatty acids (soaps). In *post-mortem* taphonomic usage, the term is applied more broadly to the transformation of body fat into adipocere, a process that proceeds primarily through enzyme-catalysed hydrolysis of triglycerides followed by secondary physicochemical transformation of the liberated fatty acids under the neutral-to-alkaline conditions that develop during putrefaction.

**Schiff base** A reversible imine linkage ($-\mathrm{C}{=}\mathrm{N}-$) formed by the condensation of a carbonyl group (aldehyde or ketone) with a primary amine, with loss of water. In proteins, Schiff bases are formed most commonly between reducing sugars, RCS, or lipid-derived aldehydes (e.g., MDA, 4-HNE) and the $\varepsilon$-amino group of Lys or the N-terminal $\alpha$-amino group. Schiff bases are inherently reversible and therefore generally represent transient intermediates under most conditions; however, they may undergo Amadori rearrangement or participate in subsequent crosslinking reactions, yielding more stable products including ALE/AGE adducts and intermolecular crosslinks.

**Secondary structure** Regular, locally repeating patterns of polypeptide backbone conformation stabilised by hydrogen bonds between backbone amide $\mathrm{N}-\mathrm{H}$ donor groups and backbone carbonyl $\mathrm{C}{=}\mathrm{O}$ acceptor groups, rather than by interactions involving amino-acid side chains. The two most common secondary structure elements are the $\alpha$-helix – in which hydrogen bonds form between residues $n$ and $n+4$, producing a right-handed helix with 3.6 residues per turn – and the $\beta$-sheet, in which extended backbone strands are arranged in parallel or antiparallel arrays with hydrogen bonds running approximately perpendicular to the strand direction.

**Serine (Ser, S)** A small polar amino acid with a primary alcohol side chain ($-\mathrm{CH_2}-\mathrm{OH}$) capable of hydrogen bonding, and a major substrate for enzymatic O-phosphorylation, O-glycosylation, and O-acetylation *in vivo*. *Post-mortem*, hydrolytic loss of these labile modifications can alter local polarity, hydrogen-bonding interactions, and protein conformation.

**SP3** Single-pot solid-phase-enhanced sample preparation. A bead-based sample-preparation method for proteomics in which proteins undergo solvent-induced aggregation (typically in $\sim 70\%$ v/v ethanol) and are captured on hydrophilic carboxylate-modified magnetic beads, enabling efficient removal of detergents, chaotropes, lipids, and other interfering compounds through magnetic washing, followed by on-bead proteolytic digestion and peptide recovery. SP3 is generally faster, simpler, and associated with lower sample losses than traditional SPE or FASP clean-up methods, particularly for low-input samples ($\lesssim 10\,\mu\mathrm{g}$ protein). Recovery is generally excellent for soluble proteins, although highly hydrophobic membrane proteins and large membrane-protein aggregates may be recovered less efficiently under standard solvent conditions.

**Sphagnan** A collective term for the acidic, water-retentive polysaccharide fraction derived from *Sphagnum* moss cell walls, characterised by abundant uronic acid residues, $\alpha$-keto-carboxylate groups, strong anionic character, and high cation-exchange capacity. Sphagnan contributes to preservation by tanning through three principal mechanisms: (i) its $\alpha$-keto-carboxylate moieties provide reactive carbonyl groups capable of Schiff base condensation with Lys $\varepsilon$-amino groups; (ii) its strong anionic character sequesters divalent metal ions required by many microbial metalloenzymes, suppressing microbial degradative activity; and (iii) its cation-exchange capacity maintains low ionic activity and regulates metal distribution within the peat microenvironment.

**Sulci and gyri** The characteristic folded surface morphology of the human cerebral cortex, produced by the coordinated outward growth of the cortical sheet against the mechanical constraint of the cranium: gyri are the outward-bulging ridges, while sulci are the inward-folding grooves between them. The folding dramatically increases the total cortical surface area ($\sim 25\,\mathrm{m}^2$ in a fully unfolded adult cortex) within the fixed volume of the skull.

**Sulfate reduction (microbial)** An anaerobic respiratory pathway in which sulfate-reducing microorganisms use sulfate ($SO_4^{2-}$) as the terminal electron acceptor in place of oxygen, producing hydrogen sulfide ($H_2S$) as the terminal reduced product.

**Superoxide ($\cdot O_2^-$)** A radical anion formed by the single-electron reduction of molecular oxygen, generated principally by electron leakage at Complexes I and III of the mitochondrial ETC, and also by NADPH oxidases. Superoxide has an extended lifetime in hydrophobic environments but undergoes rapid dismutation in aqueous solution to hydrogen peroxide ($H_2O_2$) and molecular oxygen; because of its negative charge it diffuses poorly across biological membranes, limiting its radius of action. Although relatively unreactive toward most organic molecules, superoxide is the principal precursor of hydrogen peroxide and, indirectly, hydroxyl radicals in biological systems. Its diffusion-limited reaction with nitric oxide generates peroxynitrite ($ONOO^-$), a potent oxidising and nitrating species.

**Tanning** A mode of soft-tissue preservation arising from the combined physicochemical effects of persistent waterlogging, low oxygen availability, acidic pH ($\sim$ 3.5–5), and the presence of reactive organic compounds derived from partially decomposed *Sphagnum* moss. The acidic, metal-binding aqueous phase generated during peat decomposition suppresses microbial activity while promoting chemical stabilisation of proteins through two principal mechanisms: (i) non-covalent polyphenol–protein interactions that reduce protein solubility and limit protease accessibility; and (ii) covalent crosslinking *via* carbonyl–amine (Schiff base) chemistry, in which reactive $\alpha$-keto-carboxylate-derived carbonyl groups associated with sphagnan condense with Lys $\varepsilon$-amino groups to form initially reversible imines that subsequently rearrange to more stable crosslinked products. Tanning produces characteristic selective preservation, stabilising collagen-rich soft tissues while progressively demineralising mineralised tissues under acidic conditions.

**Taphonomic filtering** The progressive and selective reduction in the information recoverable from organic remains in the archaeological and fossil records, imposed by the cumulative action of life, death, biostratinomy, diagenesis, excavation, curation, sampling, and analysis.

**Taphonomic history** The complete succession of biostratinomic, diagenetic, and post-excavation events experienced by organic remains from the moment of death through recovery, curation, and analysis. In molecular taphonomy, reconstructing taphonomic history is essential for distinguishing the *ante-mortem* state from *post-mortem* transformations.

**Taphonomic trajectory** The chemical pathway by which biological tissues are altered, degraded, or preserved from the moment of death to their eventual recovery, defined by the specific sequence of reactions that proceeds under a given set of environmental conditions.

**Taphonomy** The scientific study of organic remains after death, comprising all biological, chemical, and physical processes that govern their transformation, preservation, and eventual recovery. Taphonomy encompasses timescales from the immediate *post-mortem* period to geological deep time, and scales from individual molecules to entire fossil assemblages.

**Temperature coefficient $Q_{10}$** The multiplicative factor by which the rate of a chemical or biological process changes for every 10 °C change in temperature. Many biochemical reactions exhibit a $Q_{10} \approx 2$–3, corresponding to the empirical van 't Hoff 'rule of ten'.

**Tertiary structure** The three-dimensional fold of a single polypeptide chain, produced by the packing of secondary-structure elements and the arrangement of backbone and side-chain atoms in three-dimensional space. Tertiary structure is stabilised by the combined effects of hydrophobic interactions, hydrogen bonding, electrostatic interactions, van der Waals interactions, and, where present, covalent crosslinks such as disulfide bonds. It governs the functional properties of proteins by defining active-site geometry, ligand-binding pockets, and interaction interfaces, while also controlling solvent accessibility, susceptibility to proteolytic cleavage, and propensity for aggregation.

**Thiyl radical (RS$\cdot$)** A sulfur-centred radical formed by one-electron oxidation of the thiol group of Cys by hydroxyl radicals, peroxyl radicals, or metal-centred oxidants. Thiyl radicals are more selective and less oxidising than hydroxyl radicals, participating in hydrogen-atom abstraction, reversible oxygen addition, and radical recombination reactions that contribute to disulfide formation, thiol–disulfide exchange, and protein crosslinking.

**Threonine (Thr, T)** A polar amino acid with a branched side chain bearing a secondary hydroxyl group ($-\mathrm{CHOH}-\mathrm{CH_3}$), combining $\beta$-branching with hydrogen-bonding capacity. Thr is a substrate for enzymatic O-phosphorylation and O-glycosylation *in vivo*; *post-mortem*, hydrolytic loss of these labile modifications regenerates the free hydroxyl group, which remains susceptible to secondary oxidative modification. Thr is also particularly susceptible to direct carbonylation by metal-catalysed oxidation, yielding the primary carbonyl 2-amino-3-ketobutyric acid.

**Time-of-flight (TOF) analyser** A mass analyser in which ions are accelerated through a fixed potential difference and their $m/z$ determined from the time taken to traverse a field-free flight tube to a detector, with lower $m/z$ ions travelling faster and arriving before higher-$m/z$ ions. Modern TOF analysers achieve a mass accuracy typically $< 5$ ppm and have no theoretical $m/z$ upper limit, making them well suited to the analysis of large peptides, intact proteins, and other high-$m/z$ ions.

**Trapped ion mobility spectrometry (TIMS)** An ion mobility separation method implemented in TimsTOF instruments (Bruker), in which ions are accumulated and then sequentially released from a gas-flow-opposing electric field gradient in the TIMS tunnel by progressively reducing the retarding potential. Ions with lower mobility (typically corresponding to larger collision cross-sections for a given charge state) require a larger electric field to counteract the gas flow and are therefore released later. TIMS provides an orthogonal dimension of separation based on ion mobility, complementing chromatographic retention time and $m/z$, reducing spectral interference between co-eluting ions and improving peptide identification in complex mixtures. In the diaPASEF acquisition scheme, ion release from the TIMS analyser is synchronised with quadrupole isolation windows and TOF analysis, maximising fragmentation efficiency and achieving a near-100% duty cycle compared with $\sim$ 10–20% for conventional DDA methods.

**Trp-to-kynurenine conversion** An oxidative ring-opening of the indole ring of Trp producing N-formylkynurenine, which may subsequently be hydrolysed to kynurenine. The reaction is promoted by ROS – particularly hydroxyl radicals and singlet oxygen – which attack the electron-rich indole ring. Trp-to-kynurenine conversion therefore represents an alternative oxidative pathway for Trp that competes with radical recombination and covalent crosslink formation under conditions of oxidative stress.

**Trypsin** A Ser endopeptidase of the chymotrypsin family that cleaves peptide bonds on the C-terminal side of Lys and Arg residues (except when followed by Pro, which sterically hinders cleavage). The resulting peptides possess basic C-termini, readily acquire multiple charges under positive-ion ESI, and fragment efficiently by CID and HCD, making them well suited to sequence-database searching. Trypsin is the near-universal protease for bottom-up proteomics because its cleavage specificity is well characterised, its recognition sequence occurs frequently enough to generate peptides of suitable length ($\sim$ 7–25 residues), and its digestion products are highly predictable.

**Tryptophan (Trp, W)** An aromatic amino acid bearing a large bicyclic indole ring system, the most readily oxidised of the canonical aromatic residues owing to the high electron density and extended $\pi$-conjugation of the indole ring. One-electron oxidation generates a resonance-stabilised tryptophanyl radical that can undergo radical recombination with Tyr or Trp residues to form stable covalent crosslinks (e.g., Tyr–Trp, ditryptophan), or further oxidation to ring-opened products (e.g., N-formylkynurenine, kynurenine).

**Tyrosine (Tyr, Y)** An aromatic amino acid with a phenolic side chain (4-hydroxyphenyl group), whose para-hydroxyl group is capable of hydrogen bonding, ionisation ($\mathrm{p}K_\mathrm{a} \sim 10$), one-electron oxidation to a tyrosyl radical, and reaction with quinones during tanning. Tyrosyl radicals are relatively persistent because the unpaired electron is delocalised over the aromatic ring; they readily undergo radical recombination with other tyrosyl or tryptophanyl radicals to form dityrosine or Tyr–Trp crosslinks, respectively, providing a major mechanism of protein radical termination through formation of stable covalent crosslinks.

**Uniform manifold approximation and projection (UMAP)** A non-linear dimensionality reduction algorithm that constructs a fuzzy topological representation of the high-dimensional data manifold and optimises a low-dimensional embedding (typically two or three dimensions) by minimising the cross-entropy between the high- and low-dimensional representations. Unlike PCA, UMAP captures non-linear structure and is particularly effective at preserving local neighbourhood relationships while retaining meaningful global organisation. It is widely used in proteomics, transcriptomics, and other high-dimensional biological datasets for exploratory visualisation.

**Vacuolisation** The formation of rounded, optically clear spaces within cells or the surrounding neuropil during decomposition, attributable to organelle swelling, fluid accumulation, and physical separation of cellular components following failure of ion homeostasis. In the *post-mortem* brain, vacuolisation arises principally from swelling of astrocytic processes and perivascular endfeet as these cells take up water in response to the ionic imbalance of autolysis, and from dilation of the endoplasmic reticulum and mitochondria. The resulting appearance – optically clear pericellular and perivascular spaces on histological sections – is one of the earliest and most consistently reported microscopic changes in *post-mortem* brain tissue.

**Valine (Val, V)** A branched-chain aliphatic amino acid with an isopropyl side chain ($-\mathrm{CH}[\mathrm{CH}_3]_2$), highly hydrophobic and a major contributor to hydrophobic core packing. Val is $\beta$-branched (the first branch point occurs at the $\beta$-carbon), which increases its propensity for $\beta$-sheet conformations over $\alpha$-helices.

**Water activity ($\mathbf{A_w}$)** The ratio of the vapour pressure of water in a system to that of pure water at the same temperature and pressure, providing a thermodynamic measure of the availability of water to act as a solvent, hydrolytic reactant, or medium for microbial growth, rather than being bound to solutes or surfaces. Water activity ranges from 0 (anhydrous) to 1.0 (pure water), and in most living soft tissues is close to unity ($\sim 0.99$).

**White matter** The regions of the CNS composed predominantly of myelinated axons organised into fibre tracts that connect spatially separated grey matter regions, characterised by a high lipid fraction ($\sim$ 50–65% of dry weight) due to the abundance of myelin, and a substantially higher lipid-to-protein ratio than grey matter. In the *post-mortem* brain, myelinated fibre tracts are among the most structurally persistent features, reflecting the relative stability of the compact multilamellar myelin architecture.

# A

# Supplementary: Human Brains Preserve in Diverse Environments for at least 12,000 Years

Morton-Hayward, A.L., Anderson, R.P., Saupe, E.E., Larson G., & Cosmidis J.G.
*Human Brains Preserve in Diverse Environments for at least 12,000 Years.*
**Proc. Biol. Sci. 2024**, *291*(2019): 20232606.
doi.org/10.1098/rspb.2023.2606

## A.1 Co-Author Permissions

I, **Ross P. Anderson**, hereby give permission to Alexandra L. Seviour (formerly Morton-Hayward) to use our joint work, *Human brains persist in diverse environments for at least 12,000 years*, as a contribution towards her DPhil thesis, to be submitted for examination at the University of Oxford. I confirm that, to the best of my knowledge, the author contribution statement (Section 2.1) is accurate, and that Alexandra Seviour's overall contribution was greater than that of any other co-author.



Date: 11/03/2026

*A. Supplementary: Human Brains Preserve in Diverse Environments for at least 12,000 Years*

I, **Erin E. Saupe**, hereby give permission to Alexandra L. Seviour (formerly Morton-Hayward) to use our joint work, *Human brains persist in diverse environments for at least 12,000 years*, as a contribution towards her DPhil thesis, to be submitted for examination at the University of Oxford. I confirm that, to the best of my knowledge, the author contribution statement (Section 2.1) is accurate, and that Alexandra Seviour's overall contribution was greater than that of any other co-author.



Date: 11/03/2026

I, **Greger Larson**, hereby give permission to Alexandra L. Seviour (formerly Morton-Hayward) to use our joint work, *Human brains persist in diverse environments for at least 12,000 years*, as a contribution towards her DPhil thesis, to be submitted for examination at the University of Oxford. I confirm that, to the best of my knowledge, the author contribution statement (Section 2.1) is accurate, and that Alexandra Seviour's overall contribution was greater than that of any other co-author.



Date: 18/03/2026

I, **Julie G. Cosmidis**, hereby give permission to Alexandra L. Seviour (formerly Morton-Hayward) to use our joint work, *Human brains persist in diverse environments for at least 12,000 years*, as a contribution towards her DPhil thesis, to be submitted for examination at the University of Oxford. I confirm that, to the best of my knowledge, the author contribution statement (Section 2.1) is accurate, and that Alexandra Seviour's overall contribution was greater than that of any other co-author.



Date: 11/03/2026

## A.2 Dataset

We identified a total of 4,405 preserved human brains from 213 unique sources. This archive of archaeological human brains includes contextual (e.g., preservation type, number), geographical (e.g., latitude, longitude), temporal (e.g., date, age) and palaeoclimatic (e.g., temperature, precipitation) metadata, and is available online: `doi.org/10.1098/rspb.2023.2606`.

## A.3 Methods

We searched the literature reporting preservation of the brain in the archaeological record using scholarly libraries, online journals, academic search engines, and digital databases. Following the methodology of Brocke *et al.* [1], we employed both 'backward' and 'forward' search strategies (i.e., review of the references of a relevant article identified by keyword search, followed by review of additional sources citing that article) (Figure A.1). The search strategy proceeded in two stages: initially, literature reporting the preservation of biological soft tissue was sought using generalised terms (e.g., *archaeol-*, *bio-*, *preserv-*, *remains*, *soft tissue*, *organ*). Sources were screened for relevancy and later searched against more focused keywords pertaining specifically to the CNS (e.g., *brain*, *neuro-*, *nerv-*, *crani-*, *cerebellar*, *cerebr-*). Although English language material was targeted in the first instance, sources in languages other than English were identified by subsequent backward and forward search strategies; keywords were then adapted to the language of the source material (e.g., French, Spanish, German) using Google Translate.

Inclusion/exclusion criteria (Table A.1) were designed and applied to ensure both an efficient search strategy, and collation of a robust final dataset. Bias will be introduced in any search strategy when selection criteria are employed; however, the application of well defined selection criteria is nonetheless considered best practice [2], since the validity of the resulting meta-analysis is closely related to how systematically the data were retrieved [3]. After applying standard information synthesis procedures (e.g., identification of relevant information, critical assessment

of validity, evaluation of academic authority, determination of bias, etc.) [4], 213 unique sources remained from which data were extracted (Dataset S1). The literature was surveyed for common features of tissue appearance (e.g., colour, texture, volume, etc.) and of the depositional environment (e.g., soil type, moisture content, oxygenation, etc.). We identified five types of brain preservation (dehydrated, frozen, saponified, tanned and unknown) based on the descriptive terms and physical and biochemical features reported (Table A.2), and assigned brains to each type.

To assign latitude and longitude coordinates and elevation above sea level, we georeferenced each site using Google Earth Pro (v.7.3.6.9345). To determine the climatic conditions experienced for each preserved brain from the time of death through to excavation, we used estimates of palaeoclimate from climate models (including interactive vegetation) described in Singarayer *et al.* [5] and Davies-Barnard *et al.* [6], with details of climate model modifications in Saupe *et al.* [7], at 100 y temporal resolution and 1° spatial resolution from 12,000 y BP to Present, defined as AD 1950. Approximately one-quarter of terrestrial sites (26.4%, $n = 73/276$) fell on grid cells with no palaeoclimate data, and were therefore excluded from analysis. For each site with a grid cell for which climate data were available ($n = 203/276$), we calculated the maximum monthly temperature (°C) experienced by the remains during their taphonomic history, finding the maximum value from all maximum monthly temperature layers from the Present to the archaeological age of the material. Similarly, we calculated the mean annual precipitation (mm/d) experienced by each brain during their taphonomic history by averaging all mean annual precipitation values for all layers during the taphonomic history of each brain. Note the actual conditions experienced at a site may differ from those estimated, given the large spatial and temporal grain of the climate models ($\sim 100$ km at the equator; 100 y). We additionally assigned climate classifications to each preserved brain, to assess the present-day conditions associated with brain preservation. Based on a median date of source publication of AD 2000 ($n = 213$), we used Köppen–Geiger climate classifications [8] for the

period AD 1986–2010 for each site and created a climate map at 5′ resolution using the downscaling algorithms provided by Rubel *et al.* [9].

All subsequent analyses were performed using the R programming language (v.4.3.20) [10]. Summary statistics for archaeological age (i.e., PMI), elevation (i.e., height above sea level), latitude, maximum monthly temperature, and mean annual precipitation were computed for each brain, grouping by preservation type (Table A.4). These variables were tested for normality using Kolmogorov–Smirnov and Shapiro–Wilk tests, and for homogeneity of variance using Levene's test (Table A.5). Non-parametric, independent-sample Kruskal–Wallis tests with eta-squared effect sizes and *post hoc* Dunn pairwise comparisons (Holm-adjusted) (Tables A.6–A.10) were performed to determine whether there were significant differences between preservation types with respect to features of depositional context. To assess co-occurrence of nervous tissue with other tissue types (Figure A.2), a heatmap was generated from tissue presence–absence data after converting categorical observations (absent, undocumented, and present) to ordinal numeric values (1–3), averaging duplicate tissue–preservation type combinations, and hierarchically clustering both tissues and preservation types using Manhattan distances and complete-linkage with the `ComplexHeatmap` package (v.3.21) [11].

## A.4 Figures

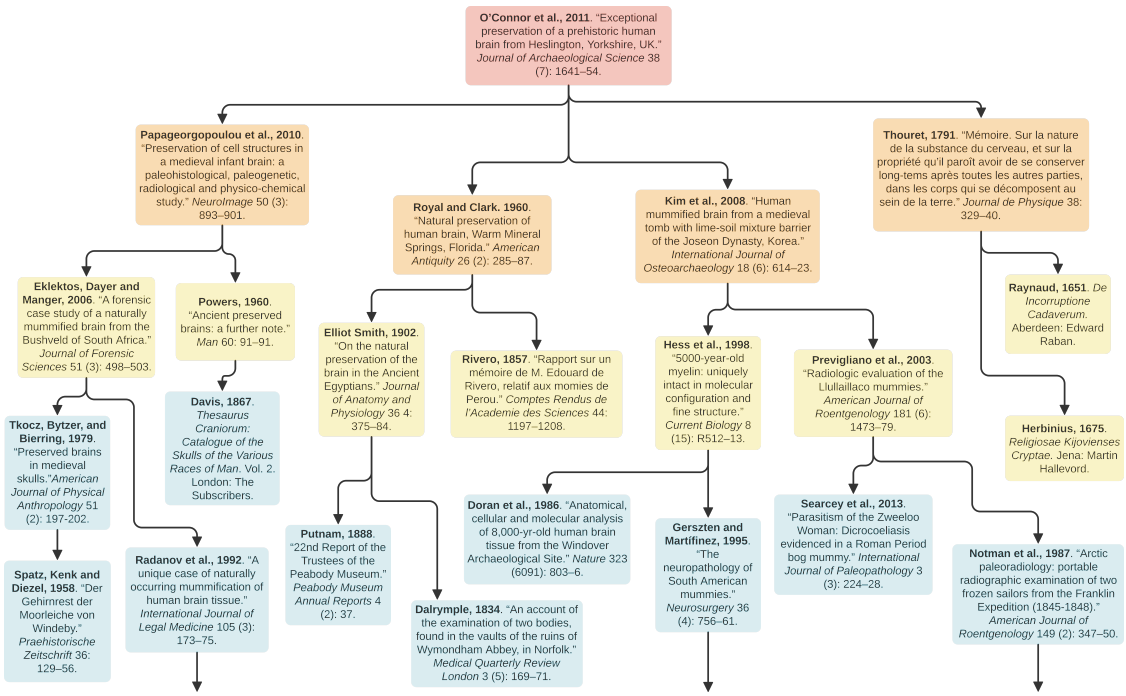



**Figure A.1 | Search strategy employed.** Conceptual flowchart illustrating the 'backward' search strategy [1] utilised in reviewing the extant archaeological literature on brain preservation. By sequentially mining the citations of each new reference discovered, progressively more arcane (though no less relevant) sources are unearthed.

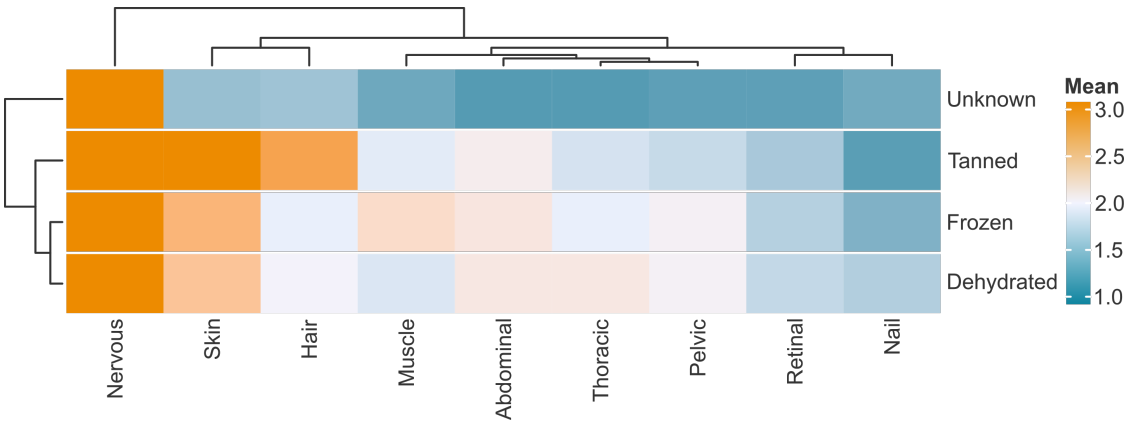



**Figure A.2 | Complex heatmap of co-occurrence of tissue types with integrated hierarchical clustering.** Cell colour represents the mean ordinal score for tissue occurrence (1 = absent, 2 = undocumented, 3 = present). Preservation types (*rows*) and tissue types (*columns*) are clustered using Manhattan distance with complete linkage. The saponified type was excluded from the analysis, given the small sample size ($n = 7$ sites).

# A.5 Tables

**Table A.1 | Selection (inclusion and exclusion) criteria applied in the literature search.**

| ✓ **Inclusion criteria** |
|---|
| Published work (e.g., books, journal articles, archaeological reports). |
| Proceedings of recognised academic conferences. |
| Direct personal communication of first-hand information. |
| **✗ Exclusion criteria** |
| Reports of non-human preserved brain tissue. |
| Reports of human preserved brain tissue post-dating AD 1950. |
| Anonymised forensic case studies (i.e., lacking contextual information, such as geographical location [e.g., 12–14]. |
| Direct personal communication of second-hand information. |

**Table A.2 | Types of brain preservation.** Five types of brain preservation identified, with descriptive terms frequently used in the literature.

| Preservation type | Description |
|---|---|
| **Dehydrated** | Generally a dry, brittle, dark-coloured mass; occasionally described as 'shiny' or 'resinous'.<br>**Keywords** \| *black*, *dark brown*, *dry*, *desiccated*, *hard*, *glassy*, *resin-like* |
| **Frozen** | Generally a spongiform mass with a 'buffy', granulose texture; prone to disintegration. Ice crystals may be present.<br>**Keywords** \| *brown*, *fragile*, *friable*, *crumbling*, *freeze-dried* |
| **Saponified** | Generally a greyish-white mass; of variable consistency, ranging from hard and crumbly to a soft, paste-like texture. Adipocere may be noted elsewhere on the corpse.<br>**Keywords** \| *white*, *grey*, *adipocerous*, *soap-like*, *waxy* |
| **Tanned** | Generally a resilient, slightly pliant, dark-coloured mass. Peat is almost universally recorded in the sedimentary matrix.<br>**Keywords** \| *black*, *dark brown*, *stained*, *leathery*, *peaty* |
| **Unknown** | Generally a resilient, slightly pliant mass of variable colouration, ranging from black to yellow; largely intact with recognisable macroscopic anatomy. Iron and clay are occasionally recorded in the sedimentary matrix.<br>**Keywords** \| *yellow*, *orange*, *dark red*, *brown*, *black*, *dense*, *insoluble*, *intact* |

**Table A.3 | Per-site frequency of brain preservation.** Number of brains preserved per site where frequency was noted at excavation ($n = 18$), expressed as a percentage of total individuals excavated.

| Name | Preservation type | No. of brains | No. of individuals | Frequency (%) |
|---|---|---|---|---|
| Atacama Desert [15] | Dehydrated | 8 | 16 | 50.0 |
| Svendborg [16] | Saponified | 56 | 75 | 74.7 |
| La Pedraja [17, 18] | Saponified | 45 | 104 | 43.3 |
| Seyitömer [19] | Unknown | 4 | 6 | 66.7 |
| Lithuanian POW Camps [20] | Unknown | N/A | N/A | 52.0 |
| Žhilkanal [21] | Unknown | 18 | 18 | 100.0 |
| Catacombe dei Cappuccini [22] | Unknown | 10 | 10 | 100.0 |

*Continued on next page*

| Name | Preservation type | No. of brains | No. of individuals | Frequency (%) |
|---|---|---|---|---|
| Dobrinishte [23] | Unknown | 7 | 39 | 17.9 |
| Cova des Pas [24, 25] | Unknown | 4 | 66 | 6.1 |
| Tottori [26] | Unknown | 3 | 92 | 3.3 |
| Gabriel Street [27] | Unknown | 3 | 16 | 18.8 |
| Kerkplein, Hoorn [28] | Unknown | 2 | 80 | 2.5 |
| Drybread [27] | Unknown | 2 | 9 | 22.2 |
| St John's [27] | Unknown | 2 | 27 | 7.4 |
| Warm Mineral Springs [29] | Unknown | 1 | 7 | 14.3 |
| Kanaljorden [30, 31] | Unknown | 1 | 10 | 10.0 |
| Royal Battleship Kronan [32] | Unknown | 1 | 2 | 50.0 |
| Ardrossan Street [27] | Unknown | 1 | 25 | 4.0 |

**Table A.4 | Summary statistics by preservation type.** Summary statistics for archaeological age, elevation, latitude, maximum monthly temperature, and mean annual precipitation by preservation type.

| | | Preservation type | | | | |
|---|---|---|---|---|---|---|
| | | **Dehydrated** | **Frozen** | **Saponified** | **Tanned** | **Unknown** |
| **Age (y BP)** | Mean (SEM) | 1,539 (138) | 608 (162) | 1,206 (527) | 1,938 (104) | 1,479 (289) |
| | Median | 438 | 464 | 562 | 1,960 | 400 |
| | Min. value | 50 | 11 | 14 | 418 | 5 |
| | Max. value | 8,970 | 5,180 | 3,900 | 2,790 | 12,000 |
| **Elevation (m)** | Mean (SEM) | 234 (52) | 2,920 (449) | 425 (219) | 44 (7) | 102 (20) |
| | Median | 78 | 2,700 | 94 | 27 | 37 |
| | Min. value | 2 | 1 | 7 | 4 | 0 |
| | Max. value | 3,414 | 6,739 | 1,186 | 175 | 848 |
| **Latitude (°)** | Mean (SEM) | 29.70 (1.53) | 20.52 (7.85) | 48.01 (2.34) | 54.71 (0.26) | 38.63 (2.91) |
| | Median | 35.18 | 46.63 | 48.43 | 54.45 | 43.61 |
| | Min. value | −23.86 | −66.22 | 39.61 | 52.83 | −46.13 |
| | Max. value | 65.85 | 80.21 | 55.06 | 57.36 | 58.54 |
| **Max. temp. (°C)** | Mean (SEM) | 33.52 (0.48) | 22.68 (1.11) | 26.89 (1.02) | 26.18 (0.33) | 27.75 (0.50) |
| | Median | 30.75 | 22.52 | 27.81 | 25.55 | 27.66 |
| | Min. value | 16.96 | 6.81 | 23.84 | 22.42 | 19.11 |
| | Max. value | 44.71 | 33.12 | 29.95 | 29.75 | 35.95 |
| **Mean precip. (mm/d)** | Mean (SEM) | 1.95 (0.16) | 1.57 (0.19) | 2.31 (0.48) | 2.16 (0.20) | 2.88 (0.17) |
| | Median | 1.89 | 1.13 | 1.76 | 1.82 | 2.41 |
| | Min. value | 0.02 | 0.38 | 1.64 | 1.44 | 1.25 |
| | Max. value | 6.71 | 3.42 | 4.55 | 5.17 | 6.36 |

**Table A.5 | Statistical testing by preservation type.** Results of Kolmogorov–Smirnov and Shapiro–Wilk tests for normality, Levene's tests for homogeneity of variance (centre = median; four degrees of freedom), and global Kruskal–Wallis rank sum tests (four degrees of freedom). Cells containing $p$-values are coloured according to significance thresholds.

| | | **Age** | **Elevation** | **Latitude** | **Max. temp.** | **Mean precip.** |
|---|---|---|---|---|---|---|
| **Kolmogorov–Smirnov** | $D$ statistic | 1.000 | 0.963 | 0.877 | 1.000 | 0.633 |
| | $p$-Value | $2.03 \times 10^{-238}$ | $1.24 \times 10^{-222}$ | $9.92 \times 10^{-185}$ | $1.28 \times 10^{-177}$ | $1.93 \times 10^{-71}$ |

*Continued on next page*

| | | Age | Elevation | Latitude | Max. temp. | Mean precip. |
|---|---|---|---|---|---|---|
| **Shapiro–Wilk** | $W$ statistic | 0.731 | 0.406 | 0.827 | 0.963 | 0.931 |
| | $p$-Value | $9.24 \times 10^{-21}$ | $3.90 \times 10^{-29}$ | $7.42 \times 10^{-17}$ | $3.30 \times 10^{-5}$ | $3.39 \times 10^{-8}$ |
| **Levene's** | $F$ value | 3.408 | 100.100 | 21.511 | 4.804 | 11.801 |
| | $p$-Value | $9.70 \times 10^{-3}$ | $3.35 \times 10^{-52}$ | $2.00 \times 10^{-15}$ | $1.01 \times 10^{-3}$ | $1.27 \times 10^{-8}$ |
| **Kruskal–Wallis** | $\chi^2$ | 24.863 | 41.116 | 86.320 | 84.490 | 14.336 |
| | $p$-Value | $5.36 \times 10^{-5}$ | $2.54 \times 10^{-8}$ | $7.96 \times 10^{-18}$ | $1.95 \times 10^{-17}$ | $6.30 \times 10^{-3}$ |

**Table A.6 | Archaeological age by preservation type.** Results of Kruskal–Wallis tests with eta-squared effect sizes and *post-hoc* Dunn pairwise comparisons (Holm-adjusted), for preservation type with respect to archaeological age ($\chi^2[4] = 24.86$, $p = 5.42 \times 10^{-5}$; $\eta^2_H = 0.078$). Cells containing $p$-values are coloured according to significance thresholds.

| Comparison | $Z$-statistic | Rank biserial correlation ($r$) | Cliff's $\delta$ (95% CI) | Adjusted $p$-value |
|---|---|---|---|---|
| Dehydrated – Frozen | 2.413 | 0.146 | 0.217 (0.005, 0.410) | $9.49 \times 10^{-2}$ |
| Dehydrated – Saponified | 1.065 | 0.064 | 0.244 (−0.294, 0.665) | $1.00 \times 10^{0}$ |
| Frozen – Saponified | −0.135 | 0.008 | −0.156 (−0.661, 0.446) | $8.93 \times 10^{-1}$ |
| Dehydrated – Tanned | −3.021 | 0.183 | −0.291 (−0.438, −0.123) | $2.01 \times 10^{-2}$ |
| Frozen – Tanned | −4.283 | 0.258 | −0.844 (−0.945, −0.596) | $1.84 \times 10^{-4}$ |
| Saponified – Tanned | −2.425 | 0.147 | −0.622 (−0.914, 0.096) | $1.07 \times 10^{-1}$ |
| Dehydrated – Unknown | 2.126 | 0.128 | 0.182 (0.012, 0.341) | $1.67 \times 10^{-1}$ |
| Frozen – Unknown | −0.727 | 0.044 | −0.081 (−0.521, 0.379) | $1.00 \times 10^{0}$ |
| Saponified – Unknown | −0.246 | 0.015 | −0.089 (−0.521, 0.379) | $1.00 \times 10^{0}$ |
| Tanned – Unknown | 4.242 | 0.256 | 0.532 (0.389, 0.649) | $1.99 \times 10^{-4}$ |

**Table A.7 | Elevation by preservation type.** Results of Kruskal–Wallis tests with eta-squared effect sizes and *post-hoc* Dunn pairwise comparisons (Holm-adjusted), for preservation type with respect to elevation ($\chi^2[4] = 41.12$, $p = 2.50 \times 10^{-8}$; $\eta^2_H = 0.137$). Cells containing adjusted $p$-values are coloured according to significance thresholds.

| Comparison | $Z$-statistic | Rank biserial correlation ($r$) | Cliff's $\delta$ (95% CI) | Adjusted $p$-value |
|---|---|---|---|---|
| Dehydrated – Frozen | −4.475 | 0.269 | −0.560 (−0.760, −0.264) | $6.11 \times 10^{-5}$ |
| Dehydrated – Saponified | −0.231 | 0.014 | −0.085 (−0.591, 0.470) | $8.17 \times 10^{-1}$ |
| Frozen – Saponified | 1.740 | 0.105 | 0.495 (0.127, 0.743) | $4.10 \times 10^{-1}$ |
| Dehydrated – Tanned | 2.869 | 0.173 | 0.355 (0.170, 0.516) | $2.88 \times 10^{-2}$ |
| Frozen – Tanned | 5.772 | 0.347 | 0.668 (0.357, 0.845) | $7.83 \times 10^{-8}$ |
| Saponified – Tanned | 1.483 | 0.089 | 0.297 (−0.376, 0.765) | $5.52 \times 10^{-1}$ |
| Dehydrated – Unknown | 2.053 | 0.124 | 0.192 (0.023, 0.351) | $2.41 \times 10^{-1}$ |
| Frozen – Unknown | 5.536 | 0.333 | 0.633 (0.352, 0.810) | $2.78 \times 10^{-7}$ |
| Saponified – Unknown | 0.939 | 0.057 | 0.237 (−0.357, 0.694) | $6.95 \times 10^{-1}$ |
| Tanned – Unknown | −1.217 | 0.073 | −0.178 (−0.393, 0.056) | $6.71 \times 10^{-1}$ |

**Table A.8 | Latitude by preservation type.** Results of Kruskal–Wallis tests with eta-squared effect sizes and *post-hoc* Dunn pairwise comparisons (Holm-adjusted), for preservation type with respect to latitude ($\chi^2[4] = 86.32$, $p = 7.96 \times 10^{-18}$; $\eta^2_H = 0.304$). Cells containing adjusted $p$-values are coloured according to significance thresholds.

| Comparison | $Z$-statistic | Rank biserial correlation ($r$) | Cliff's $\delta$ (95% CI) | Adjusted $p$-value |
|---|---|---|---|---|
| Dehydrated – Frozen | −1.958 | 0.118 | −0.065 (−0.345, 0.226) | $2.51 \times 10^{-1}$ |
| Dehydrated – Saponified | −2.886 | 0.174 | −0.855 (−0.923, −0.736) | $2.34 \times 10^{-2}$ |
| Frozen – Saponified | −1.857 | 0.112 | −0.212 (−0.525, 0.151) | $2.54 \times 10^{-1}$ |
| Dehydrated – Tanned | −8.582 | 0.517 | −0.924 (−0.966, −0.835) | $9.32 \times 10^{-17}$ |
| Frozen – Tanned | −5.265 | 0.317 | −0.447 (−0.698, −0.098) | $1.26 \times 10^{-6}$ |
| Saponified – Tanned | −1.084 | 0.065 | −0.635 (−0.904, −0.005) | $5.57 \times 10^{-1}$ |
| Dehydrated – Unknown | −5.092 | 0.306 | −0.520 (−0.656, −0.350) | $2.84 \times 10^{-6}$ |
| Frozen – Unknown | −1.761 | 0.106 | −0.076 (−0.351, 0.211) | $2.35 \times 10^{-1}$ |
| Saponified – Unknown | 1.060 | 0.064 | 0.239 (−0.122, 0.544) | $2.89 \times 10^{-1}$ |
| Tanned – Unknown | 4.365 | 0.263 | 0.758 (0.591, 0.863) | $8.89 \times 10^{-5}$ |

**Table A.9 | Maximum temperature by preservation type.** Results of Kruskal–Wallis tests with eta-squared effect sizes and *post-hoc* Dunn pairwise comparisons (Holm-adjusted), for preservation type with respect to maximum monthly temperature ($\chi^2[4] = 84.50$, $p = 1.95 \times 10^{-17}$; $\eta^2_H = 0.404$). Cells containing adjusted $p$-values are coloured according to significance thresholds.

| Comparison | $Z$-statistic | Rank biserial correlation ($r$) | Cliff's $\delta$ (95% CI) | Adjusted $p$-value |
|---|---|---|---|---|
| Dehydrated – Frozen | 6.857 | 0.480 | 0.765 (0.518, 0.895) | $7.02 \times 10^{-11}$ |
| Dehydrated – Saponified | 2.685 | 0.188 | 0.788 (0.591, 0.896) | $5.08 \times 10^{-2}$ |
| Frozen – Saponified | −0.781 | 0.055 | −0.455 (−0.751, −0.005) | $1.00 \times 10^{0}$ |
| Dehydrated – Tanned | 6.485 | 0.454 | 0.858 (0.739, 0.925) | $7.96 \times 10^{-10}$ |
| Frozen – Tanned | −0.725 | 0.051 | −0.461 (−0.725, −0.079) | $1.00 \times 10^{0}$ |
| Saponified – Tanned | 0.367 | 0.026 | 0.170 (−0.529, 0.732) | $7.14 \times 10^{-1}$ |
| Dehydrated – Unknown | 5.639 | 0.395 | 0.602 (0.436, 0.729) | $1.37 \times 10^{-7}$ |
| Frozen – Unknown | −2.557 | 0.179 | −0.498 (−0.723, −0.178) | $6.34 \times 10^{-2}$ |
| Saponified – Unknown | −0.563 | 0.039 | −0.142 (−0.546, 0.315) | $1.00 \times 10^{0}$ |
| Tanned – Unknown | −1.864 | 0.130 | −0.313 (−0.511, −0.084) | $3.12 \times 10^{-1}$ |

**Table A.10 | Precipitation by preservation type.** Results of Kruskal–Wallis tests with eta-squared effect sizes and *post-hoc* Dunn pairwise comparisons (Holm-adjusted), for preservation type with respect to mean annual precipitation ($\chi^2[4] = 14.34$, $p = 6.30 \times 10^{-3}$; $\eta^2_H = 0.052$). Cells containing adjusted $p$-values are coloured according to significance thresholds.

| Comparison | $Z$-statistic | Rank biserial correlation ($r$) | Cliff's $\delta$ (95% CI) | Adjusted $p$-value |
|---|---|---|---|---|
| Dehydrated – Frozen | 1.139 | 0.080 | 0.004 (−0.194, 0.201) | $1.00 \times 10^{0}$ |
| Dehydrated – Saponified | −0.453 | 0.032 | −0.137 (−0.496, 0.263) | $1.00 \times 10^{0}$ |
| Frozen – Saponified | −0.961 | 0.067 | −0.527 (−0.804, −0.062) | $1.00 \times 10^{0}$ |
| Dehydrated – Tanned | −0.417 | 0.029 | −0.068 (−0.271, 0.140) | $1.00 \times 10^{0}$ |
| Frozen – Tanned | −1.251 | 0.088 | −0.485 (−0.749, −0.087) | $1.00 \times 10^{0}$ |
| Saponified – Tanned | 0.240 | 0.017 | 0.059 (−0.464, 0.552) | $8.10 \times 10^{-1}$ |

*Continued on next page*

| Comparison | $Z$-statistic | Rank biserial correlation ($r$) | Cliff's $\delta$ (95% CI) | Adjusted $p$-value |
|---|---|---|---|---|
| Dehydrated – Unknown | −3.198 | 0.224 | −0.243 (−0.414, −0.056) | $1.25 \times 10^{-2}$ |
| Frozen – Unknown | −3.213 | 0.225 | −0.590 (−0.801, −0.249) | $1.31 \times 10^{-2}$ |
| Saponified – Unknown | −0.728 | 0.051 | −0.331 (−0.743, 0.263) | $1.00 \times 10^{0}$ |
| Tanned – Unknown | −1.931 | 0.135 | −0.413 (−0.630, −0.136) | $4.28 \times 10^{-1}$ |

## A.6 References


[1] J Brocke et al. 'Reconstructing the giant: On the importance of rigour in documenting the literature search process'. In: *ECIS* 161 (8th June 2009), pp. 2206–2217.

[2] Sebastian K Boell and Dubravka Cecez-Kecmanovic. 'On being 'systematic' in Literature Reviews in IS'. In: *J. Inf. Technol.* 30 (2 June 2015), pp. 161–173. DOI: 10.1057/jit.2014.26.

[3] Isabelle M Côté et al. '4. Gathering data: Searching literature and selection criteria'. In: *Handbook of Meta-analysis in Ecology and Evolution*. Ed. by Julia Koricheva, Jessica Gurevitch and Kerrie Mengersen. Princeton: Princeton University Press, 31st Dec. 2013, pp. 37–51. DOI: 10.1515/9781400846184-006.

[4] Robert B Frost and Chun Wei Choo. 'Revisiting the information audit: A systematic literature review and synthesis'. In: *Int. J. Inf. Manage.* 37 (1 Feb. 2017), pp. 1380–1390. DOI: 10.1016/j.ijinfomgt.2016.10.001.

[5] Joy S Singarayer, Paul J Valdes and William H G Roberts. 'Ocean dominated expansion and contraction of the late Quaternary tropical rainbelt'. In: *Sci. Rep.* 7 (1 24th Aug. 2017), p. 9382. DOI: 10.1038/s41598-017-09816-8.

[6] Taraka Davies-Barnard et al. 'Quantifying the influence of the terrestrial biosphere on glacial-interglacial climate dynamics'. In: *Clim. Past Discuss.* (10th Feb. 2017), pp. 1–22. DOI: 10.5194/cp-2017-12.

[7] Erin E Saupe et al. 'Spatio-temporal climate change contributes to latitudinal diversity gradients'. In: *Nat. Ecol. Evol.* 3 (10 Oct. 2019), pp. 1419–1429. DOI: 10.1038/s41559-019-0962-7.

[8] Markus Kottek et al. 'World Map of the Köppen-Geiger climate classification updated'. In: *Meteorol. Z.* 15 (3 10th July 2006), pp. 259–263. DOI: 10.1127/0941-2948/2006/0130.

[9] Franz Rubel et al. 'The climate of the European Alps: Shift of very high resolution Köppen-Geiger climate zones 1800–2100'. In: *Meteorol. Z.* 26 (2 25th Apr. 2017), pp. 115–125. DOI: 10.1127/metz/2016/0816.

[10] R Core Team. *R: A language and environment for statistical computing*. Vienna, Austria: R Foundation for Statistical Computing, 2023.

[11] Zuguang Gu. 'Complex heatmap visualization'. In: *Imeta* 1 (3 1st Sept. 2022), e43. DOI: 10.1002/imt2.43.

[12] M Graw, H J Weisser and S Lutz. 'DNA typing of human remains found in damp environments'. In: *Forensic Sci. Int.* 113 (1-3 11th Sept. 2000), pp. 91–95. DOI: 10.1016/s0379-0738(00)00221-8.

[13] Christian Jackowski et al. 'Adipocere in postmortem imaging using multislice computed tomography (MSCT) and magnetic resonance imaging (MRI)'. In: *Am. J. Forensic Med. Pathol.* 26 (4 Dec. 2005), pp. 360–364. DOI: 10.1097/01.paf.0000188091.11225.38.

[14] Mario Giusiani, Silvio Chericoni and Ranieri Domenici. 'Identification and quantification of phenobarbital in a mummified body 10 years after death: Identification and quantification of phenobarbital'. In: *J. Forensic Sci.* 57 (5 Sept. 2012), pp. 1384–1387. DOI: 10.1111/j.1556-4029.2012.02147.x.

[15] Arthur C Aufderheide. *The Scientific Study of Mummies*. Cambridge, England: Cambridge University Press, 13th Jan. 2011. 634 pp.

[16] Izabella Tkocz, Peter Bytzer and Franz Bierring. 'Preserved brains in medieval skulls'. In: *Am. J. Phys. Anthropol.* 51 (2 Aug. 1979), pp. 197–202. DOI: 10.1002/ajpa.1330510206.

[17] Fernando Serrulla et al. 'Preserved brains from the Spanish Civil War mass grave (1936) at La Pedraja1, Burgos, Spain'. In: *Sci. Justice* 56 (6 Dec. 2016), pp. 453–463. DOI: 10.1016/j.scijus.2016.08.001.

[18] Francisco Etxeberria and Fernando Serrulla. 'El caso de los cerebros de la Pedraja: Ciencias forenses y memoria histórica en España'. In: *Mètode Rev. difus. investig.* (10 8th Jan. 2020), pp. 109–117. DOI: 10.7203/metode.10.13295.

[19] M A Altinoz et al. 'Human brains found in a fire-affected 4000-years old Bronze Age tumulus layer rich in soil alkalines and boron in Kutahya, Western Anatolia'. In: *Homo* 65 (1 Feb. 2014), pp. 33–50. DOI: 10.1016/j.jchb.2013.08.005.

[20] Ingrida Čičiurkaitė and Rokas Kraniauskas. 'Investigating two mass grave sites of WWII POW camps in Lithuania'. In: *Scand. J. Forensic Sci.* 28 (s1 1st Dec. 2022), pp. 20–31. DOI: 10.2478/sjfs-2022-0014.

[21] G Pilleri and H Schwab. 'Morphological structures in 2100-year old Celtic brains'. In: *Man (Lond.)* 5 (4 1970), pp. 701–702.

[22] Stephanie Panzer, Albert R Zink and Dario Piombino-Mascali. 'Scenes from the past: Radiologic evidence of anthropogenic mummification in the Capuchin catacombs of Palermo, Sicily'. In: *Radiographics* 30 (4 July 2010), pp. 1123–1132. DOI: 10.1148/rg.304095174.

[23] S Radanov et al. 'A unique case of naturally occurring mummification of human brain tissue'. In: *Int. J. Legal Med.* 105 (3 1992), pp. 173–175. DOI: 10.1007/bf01625172.

[24] Gemma Prats-Muñoz et al. 'A paleoneurohistological study of 3,000-year-old mummified brain tissue from the mediterranean bronze age'. In: *Pathobiology* 79 (5 21st June 2012), pp. 239–246. DOI: 10.1159/000334353.

[25] Gemma Prats-Muñoz et al. 'Human soft tissue preservation in the Cova des Pas site (Minorca Bronze Age)'. In: *J. Archaeol. Sci.* 40 (12 Dec. 2013), pp. 4701–4710. DOI: 10.1016/j.jas.2013.07.022.

[26] Constance Holden. 'Probing the brains of ancient Japanese'. In: *Science* 292 (5517 27th Apr. 2001), pp. 635–635. DOI: 10.1126/science.292.5517.635d.

[27] Brittany Moller et al. 'Preservation of brain material in the archaeological record: A case study in the New Zealand colonial context'. In: *J. Archaeol. Sci.* 156 (105774 Aug. 2023), p. 105774. DOI: 10.1016/j.jas.2023.105774.

[28] A Pijpelink. *Pers. comm.* 2020.

[29] William Royal and Eugenie Clark. 'Natural preservation of human brain, Warm Mineral Springs, Florida'. In: *Am. Antiq.* 26 (2 Oct. 1960), pp. 285–287. DOI: 10.2307/276213.

[30] F Hallgren. 'Mesolithic skull depositions at Kanaljorden, Motala, Sweden'. In: *Curr. Swed. Archaeol.* 19 (2011), pp. 244–246.

[31] Sara Gummesson, Fredrik Hallgren and Anna Kjellström. 'Keep your head high: skulls on stakes and cranial trauma in Mesolithic Sweden'. In: *Antiquity* 92 (361 Feb. 2018), pp. 74–90. DOI: 10.15184/aqy.2017.210.

[32] J Bergquist. *Pers. comm.* 2002.

# B

# Supplementary: Deep Palaeoproteomic Profiling of Archaeological Human Brains

Morton-Hayward, A.L., Flannery, S., Vendrell, I., & Fischer, R. (2025).
*Deep Palaeoproteomic Profiling of Archaeological Human Brains.*
**PLoS One 2025**, *20*(5): e0324246.
doi.org/10.1371/journal.pone.0324246

## B.1 Co-Author Permissions

I, **Sarah Flannery**, hereby give permission to Alexandra L. Seviour (formerly Morton-Hayward) to use our joint work, *Deep palaeoproteomic profiling of archaeological human brains*, as a contribution towards her DPhil thesis, to be submitted for examination at the University of Oxford. I confirm that, to the best of my knowledge, the author contribution statement (Section 3.1) is accurate, and that Alexandra Seviour's overall contribution was greater than that of any other co-author.



Date: 16/03/2026

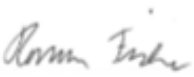
I, **Iolanda Vendrell**, hereby give permission to Alexandra L. Seviour (formerly Morton-Hayward) to use our joint work, *Deep palaeoproteomic profiling of archaeological human brains*, as a contribution towards her DPhil thesis, to be submitted for

examination at the University of Oxford. I confirm that, to the best of my knowledge, the author contribution statement (Section 3.1) is accurate, and that Alexandra Seviour's overall contribution was greater than that of any other co-author.



Date: 11/03/2026

I, **Roman Fischer**, hereby give permission to Alexandra L. Seviour (formerly Morton-Hayward) to use our joint work, *Deep palaeoproteomic profiling of archaeological human brains*, as a contribution towards her DPhil thesis, to be submitted for examination at the University of Oxford. I confirm that, to the best of my knowledge, the author contribution statement (Section 3.1) is accurate, and that Alexandra Seviour's overall contribution was greater than that of any other co-author.



Date: 13/03/2026

## B.2 Methods

### B.2.1 In-solution

#### B.2.1.1 PreOmics® BeatBox iST

**Table B.1** | Reagents from the iST Sample Preparation Kit (v.4.0; PreOmics®) [1] required for the PreOmics® BeatBox iST method.

| Reagent | Description |
|---|---|
| DIGEST | Trypsin/LysC mix to digest proteins. |
| RESUSPEND | Reconstitutes lyophilized proteolytic enzymes. |
| LYSE | Denatures, reduces and alkylates proteins. |
| STOP | Stops enzymatic activity. |
| WASH 1 | Cleans peptides from hydrophobic contaminants. |
| WASH 2 | Cleans peptides from hydrophilic contaminants. |
| ELUTE | Elutes peptides from the cartridge. |
| LC–LOAD | Loads peptides on reversed-phase LC–MS columns. |

1. Transfer 50 mg of brain to a 2 mL collection tube. Add 50 mg glass beads to the sample.
2. Add 100 µL LYSE. Shear the sample by BeatBox sonication for 10 cycles of 30 s.

3. Place the sample in a heating block at 95 °C and 1,000 rpm for 10 min.
4. Centrifuge at 20 °C and 300 rcf for 10 s.
5. Add 210 µL RESUSPEND to DIGEST. Shake at 20 °C and 500 rpm for 10 min; pipette up and down to mix.
6. Add 50 µL DIGEST and place in a preheated heating block at 37 °C and 500 rpm for 3 h.
7. Add 100 µL STOP. Shake at 20 °C and 500 rpm for 1 min; pipette up and down to mix.
8. Centrifuge at 16,000 rcf for 1 min.
9. Use the iST adapter to place the iST cartridge (both PreOmics®) in a new 2 mL waste tube.
10. Transfer the supernatant to the cartridge.
11. Centrifuge at 20 °C and 4,000 rcf for 1 min, or until all the liquid has passed through.
12. Add 200 µL WASH 1 to the cartridge, and repeat step 11.
13. Add 200 µL WASH 2 to the cartridge, and repeat step 11. (*Optional*: To assess sample loss, transfer the flow-through to a new 1.5 mL collection tube and store at −20 °C prior to analysis.)
14. Use the adapter to place the cartridge in a new 1.5 mL collection tube.
15. Add 100 µL ELUTE to the cartridge, and repeat step 11.
16. Repeat step 15.
17. Discard the cartridge and dehydrate the sample in a vacuum concentrator at 45 °C. Store eluted peptides at −20 °C prior to analysis.
18. For LC–MS analysis, add 50 µL LC–LOAD.
19. Shake at 20 °C and 500 rpm for 5 min.

#### B.2.1.2 Urea with SPE

**Table B.2** | Reagents required for the urea with SPE method.

| Reagent | Preparation |
|---|---|
| Urea lysis buffer | For 10 mL total volume, dissolve 4.8 g 8 M urea ($NH_2CONH_2$; Sigma–Aldrich) in ∼ 8 mL high-performance liquid chromatography (HPLC)-grade $H_2O$. Add 1 mL 1 M TEAB (triethylammonium bicarbonate [$C_7H_{17}NO_3$]; Sigma–Aldrich), and bring to 10 mL with HPLC-grade $H_2O$. Vortex to mix. |
| 0.5 M TCEP | For 300 µL total volume, dissolve 43.0 mg TCEP (tris[2-carboxyethyl]phosphine [$C_9H_{15}O_6P$]; Sigma–Aldrich) in 300 µL HPLC-grade $H_2O$. Vortex to mix. |
| 0.5 M IAA | For 300 µL total volume, dissolve 27.8 mg IAA (iodoacetamide [$ICH_2CONH_2$]; Sigma–Aldrich) in 30 µL 100 mM TEAB with 270 µL HPLC-grade $H_2O$. Vortex to mix and store at 4 °C until use. |
| 50 mM TEAB | For 10 mL total volume, combine 500 µL 1 M TEAB and 9.5 mL HPLC-grade $H_2O$. Vortex to mix. |
| Buffer A (0.1% TFA, 2% ACN) | For 10 mL total volume, combine 10 µL TFA (trifluoroacetic acid [$C_2HF_3O_2$]; Sigma–Aldrich) and 200 µL ACN (acetonitrile [$C_2H_3N$]; Sigma–Aldrich) with 9.8 mL HPLC-grade $H_2O$. Vortex to mix. |
| Buffer B (0.1% TFA, 65% ACN) | For 10 mL total volume, combine 10 µL TFA and 6.5 mL ACN with 3.5 mL HPLC-grade $H_2O$. Vortex to mix. |

1. Transfer 50 mg of brain to a 2 mL hard-tissue grinding Precellys® lysing tube (Bertin Technologies).
2. Add 200 µL urea lysis buffer.
3. Use the Precellys® 24 Touch homogeniser (Bertin Technologies) to lyse at 5,500 rpm for 30 s. Repeat twice for a total of three cycles, cooling on ice between cycles.
4. Incubate in the dark at 20 °C and 1,000 rpm for 30 min.
5. Add 4.1 µL 0.5 M TCEP for a final concentration of 10 mM TCEP.
6. Add 22.7 µL 0.5 M IAA for a final concentration of 50 mM IAA. Incubate in the dark at 20 °C and 1,000 rpm for 30 min.
7. Add 840 µL 50 mM TEAB for a final concentration of 1.5 M urea.
8. Add 1 µg MS-grade trypsin (Promega). Incubate at 37 °C and 1,250 rpm overnight.
9. Add 10.7 µL TFA for a final concentration of 1%. Vortex briefly to mix, and confirm pH $< 2.0$.
10. Pipette the supernatant into a new 2 mL Eppendorf Protein LoBind® tube (Thermo Fisher Scientific). Centrifuge at 20 °C and 22,000 rcf for 10 min.
11. Pipette the supernatant into a 10 mL Corning® centrifuge tube (Sigma–Aldrich) of buffer A. Vortex briefly to mix.

12. Insert a SOLA™ SPE C18 cartridge (Thermo Fisher Scientific) into a new 2 mL waste tube.
13. Add 500 µL buffer B to activate the cartridge, plunging the syringe to filter liquid through the column. Ensure that the C18 membrane does not dry out.
14. Add 1 mL buffer A to equilibrate the cartridge, plunging the syringe to filter liquid through the column. Ensure that the C18 membrane does not dry out. Dispose of the flow-through.
15. Slowly load the sample onto the cartridge, 1 mL at a time, plunging the syringe to filter liquid through the column. Ensure that the C18 membrane does not dry out. Dispose of the flow-through.
16. Wash with 1 mL buffer A, plunging the syringe to filter liquid through the column. Ensure that the C18 membrane does not dry out. Dispose of the flow-through and tube. (*Optional*: To assess sample loss, transfer the flow-through to a new 1.5 mL LoBind® tube and store at −20 °C prior to analysis.)
17. Transfer the cartridge to a new 1.5 mL LoBind® tube.
18. Add 100 µL buffer B to the cartridge to elute peptides, plunging the syringe to filter all the liquid through the column. Discard the cartridge.
19. Dehydrate in a vacuum concentrator at 30 °C. Store eluted peptides at −20 °C prior to analysis.

#### B.2.1.3 Urea with SPE + iST

**Table B.3** | Reagents required for the urea with SPE + iST method.

| Reagent | Preparation |
|---|---|
| Urea lysis buffer | For 10 mL total volume, dissolve 4.8 g 8 M urea in ∼ 8 mL HPLC-grade $H_2O$. Add 1 mL 1 M TEAB, and bring to 10 mL with HPLC-grade $H_2O$. Vortex to mix. |
| 0.5 M IAA | For 300 µL total volume, dissolve 27.8 mg IAA in 30 µL 100 mM TEAB with 270 µL HPLC-grade $H_2O$. Vortex to mix and store at 4 °C until use. |
| 50 mM TEAB | For 10 mL total volume, combine 500 µL 1 M TEAB and 9.5 mL HPLC-grade $H_2O$. Vortex to mix. |
| Buffer A (0.1% TFA, 2% ACN) | For 10 mL total volume, combine 10 µL TFA and 200 µL ACN with 9.8 mL HPLC-grade $H_2O$. Vortex to mix. |
| Buffer B (0.1% TFA, 65% ACN) | For 10 mL total volume, combine 10 µL TFA and 6.5 mL ACN with 3.5 mL HPLC-grade $H_2O$. Vortex to mix. |
| Buffer C (0.1% TFA, 50% ACN) | For 1 mL total volume, combine 1 µL TFA and 500 µL ACN with 499 µL HPLC-grade $H_2O$. Vortex to mix. |

*Continued on next page*

| Reagent | Preparation |
|---|---|
| **From the iST Sample Preparation Kit (v.4.0; PreOmics®) [1]:** | |
| WASH 1 | Cleans peptides from hydrophobic contaminants. |
| WASH 2 | Cleans peptides from hydrophilic contaminants. |
| ELUTE | Elutes peptides from the cartridge. |
| LC–LOAD | Loads peptides on reversed-phase LC–MS columns. |

Complete steps 1–18 as for the urea with SPE protocol (Section B.2.1.2), and proceed as follows:

1. Reconstitute the sample by adding 100 µL buffer A. Sonicate at 4 °C for 5 min.
2. Incubate at 20 °C and 1,250 rpm for 5 min.
3. Insert the iST cartridge into a new 2 mL waste tube. Add 200 µL buffer C to activate the cartridge. Centrifuge at 20 °C and 4,000 rcf for 1 min, or until all the liquid has passed through.
4. Add 200 µL buffer A to equilibrate the cartridge. Centrifuge at 20 °C and 4,000 rcf for 1 min, or until all the liquid has passed through. Dispose of the flow-through.
5. Add 50 µL of sample and 150 µL buffer A to the cartridge.
6. Centrifuge at 20 °C and 4,000 rcf for 1 min, or until all the liquid has passed through.
7. Add 200 µL WASH 1 to the cartridge, and repeat step 6.
8. Add 200 µL WASH 2 to the cartridge, and repeat step 6. Dispose of the flow-through. (*Optional*: To assess sample loss, transfer the flow-through to a new 1.5 mL LoBind® tube and store at −20 °C prior to analysis.)
9. Transfer the iST cartridge to a new 1.5 mL collection tube.
10. Add 100 µL ELUTE to the cartridge, and repeat step 6.
11. Repeat step 10.
12. Discard the cartridge and dehydrate the sample in a vacuum concentrator at 45 °C. Store eluted peptides at −20 °C prior to analysis.
13. For LC–MS analysis, add 50 µL LC–LOAD.
14. Shake at 20 °C and 500 rpm for 5 min.

#### B.2.1.4 Sodium laurate with SPE

**Table B.4** | Reagents required for the sodium laurate with SPE method.

| Reagent | Preparation |
|---|---|
| 0.5 M TCEP | For 300 µL total volume, dissolve 43.0 mg TCEP in 300 µL HPLC-grade $H_2O$. Vortex to mix. |
| 0.5 M IAA | For 300 µL total volume, dissolve 27.8 mg IAA in 30 µL 100 mM TEAB with 270 µL HPLC-grade $H_2O$. Vortex to mix and store at 4 °C until use. |
| 50 mM TEAB | For 10 mL total volume, combine 500 µL 1 M TEAB and 9.5 mL HPLC-grade $H_2O$. Vortex to mix. |
| 100 mM TEAB | For 10 mL total volume, combine 1 mL 1 M TEAB and 9 mL HPLC-grade $H_2O$. Vortex to mix. |
| 1% sodium laurate | For 1 mL total volume, combine 10 mg sodium laurate ($CH_3[CH_2]_{10}CO_2Na$; Sigma–Aldrich) and 1 mL of HPLC-grade $H_2O$. Vortex to mix. |
| Buffer A (0.1% TFA, 2% ACN) | For 10 mL total volume, combine 10 µL TFA and 200 µL ACN with 9.8 mL HPLC-grade $H_2O$. Vortex to mix. |
| Buffer B (0.1% TFA, 65% ACN) | For 10 mL total volume, combine 10 µL TFA and 6.5 mL ACN with 3.5 mL HPLC-grade $H_2O$. Vortex to mix. |

1. Transfer 50 mg of brain to a 2 mL hard-tissue grinding Precellys® lysing tube (Bertin Technologies).
2. Add 50 µL 1% sodium laurate.
3. Use the Precellys® 24 Touch homogeniser (Bertin Technologies) to lyse at 5,500 rpm for 30 s. Repeat twice for a total of three cycles, cooling on ice between cycles.
4. Sonicate at 4 °C for 10 min.
5. Vortex for 1 min.
6. Add 1 µL 0.5 M TCEP for a final concentration of 10 mM.
7. Add 2 µL 0.5 M IAA for a final concentration of 20 mM. Incubate in the dark at 20 °C for 30 min.
8. Dilute to 150 µL total volume with 97 µL 1% sodium laurate.
9. Add 1 µg MS-grade trypsin (Promega). Incubate at 37 °C and 1,000 rpm for 3 h.
10. Add 1.5 µL TFA to a final concentration of 1%. Vortex briefly to mix, and confirm pH $< 2.0$.
11. Centrifuge at 20 °C and 22,000 rcf for 10 min. Transfer the supernatant to a new 2 mL Eppendorf Protein LoBind® tube (Thermo Fisher Scientific). Note the volume recovered.

12. Add a volume of ethyl acetate equal to the volume of supernatant recovered, and vortex for 1 min.
13. Centrifuge at 20 °C and 15,700 rcf for 10 min.
14. Transfer the lower phase to a new 1.5 mL Eppendorf Protein LoBind® tube (Thermo Fisher Scientific).
15. Repeat steps 12–14.
16. Insert a SOLA™ SPE C18 cartridge (Thermo Fisher Scientific) into a new 2 mL waste tube.
17. Add 500 µL buffer B to activate the cartridge, plunging the syringe to filter liquid through the column. Ensure that the C18 membrane does not dry out.
18. Add 1 mL buffer A to equilibrate the cartridge, plunging the syringe to filter liquid through the column. Ensure that the C18 membrane does not dry out. Dispose of the flow-through.
19. Load the sample onto the cartridge.
20. Wash with 1 mL buffer A, plunging the syringe to filter liquid through the column. Ensure that the C18 membrane does not dry out. Dispose of the flow-through and tube. (*Optional*: To assess sample loss, transfer the flow-through to a new 1.5 mL LoBind® tube and store at −20 °C prior to analysis.)
21. Transfer the cartridge to a new 1.5 mL LoBind® tube.
22. Add 100 µL buffer B to the cartridge to elute peptides, plunging the syringe to filter all the liquid through the column. Repeat and discard the cartridge.
23. Dehydrate in a vacuum concentrator at 30 °C. Store eluted peptides at −20 °C prior to analysis.

## B.2.2 In-gel

### B.2.2.1 SDS–PAGE

**Table B.5 |** Reagents required for the SDS–PAGE method.

| Reagent | Preparation |
|---|---|
| 5% SDS lysis buffer | For 1 mL total volume, combine 250 µL 20% SDS (sodium dodecyl sulfate [$C_{12}H_{25}NaO_4S$]; Sigma–Aldrich) and 100 µL 100 mM TEAB with 650 µL HPLC-grade $H_2O$. Vortex to mix. |
| NuPAGE™ LDS (4×) sample buffer (Invitrogen™, Thermo Fisher Scientific) | A basic solution (pH 8.5) mixed in a 1:3 ratio with the sample that stains the moving ion front for PAGE. Contains 141 mM Tris (Tris[hydroxymethyl]aminomethane [$NH_2C(CH_2OH)_3$]), 106 mM Tris-HCl (Tris[hydroxymethyl]aminomethane hydrochloride [$NH_2C(CH_2OH)_3 \cdot HCl$]), 2% LDS (lithium dodecyl sulfate [$CH_3(CH_2)_{11}OSO_3Li$]), 0.51 mM EDTA (ethylenediaminetetraacetic acid [$(HO_2CCH_2)_2NCH_2CH_2N(CH_2CO_2H)_2$]), 0.22 mM SERVA™ Blue G-250, and 0.175 mM Phenol Red. |
| NuPAGE™ MES SDS (20×) running buffer (Invitrogen™, Thermo Fisher Scientific) | A neutral solution (pH 7.3) that facilitates ion migration during PAGE. Contains 50 mM MES (2-[n-morpholino]ethanesulfonic acid [$C_6H_{13}NO_4S$]), 50 mM Tris, 0.1% SDS, and 1 mM EDTA. |
| 5% acetic acid | For 20 mL total volume, combine 10 mL methanol ($CH_3OH$; Sigma–Aldrich), 1 mL glacial acetic acid ($CH_3CO_2H$; Sigma–Aldrich) and 9 mL HPLC-grade $H_2O$. Vortex to mix and store at 4 °C until use. |
| 100 mM ambic | For 1 mL total volume, dissolve 7.9 mg ambic (ammonium bicarbonate [$NH_4HCO_3$]; Sigma–Aldrich) in 1 mL HPLC-grade $H_2O$. Vortex to mix and vacuum-filter with a 0.22 µm filter. |
| 0.5 M DTT | For 1 mL total volume, dissolve 77.1 mg DTT (dithiothreitol [$C_4H_{10}O_2S_2$]; Sigma–Aldrich) in 1 mL HPLC-grade $H_2O$. Vortex to mix and store at −20 °C until use. |
| 200 mM DTT | For 1 mL total volume, combine 400 µL 0.5 M DTT with 600 µL ambic. Vortex to mix and store at −20 °C until use. |
| 10 mM DTT | For 1 mL total volume, combine 50 µL 200 mM DTT with 950 µL 100 mM ambic. Vortex to mix and store at −20 °C until use. |
| 50 mM IAA | For 1 mL total volume, dissolve 9.3 mg IAA in 1 mL HPLC-grade $H_2O$. Vortex to mix and store at 4 °C until use. |
| 50 mM ambic | For 1 mL total volume, combine 500 µL 100 mM ambic and 500 µL HPLC-grade $H_2O$. Vortex to mix and vacuum-filter with a 0.22 µm filter. |
| Digestion buffer | For 200 µL total volume, combine 200 µL 50 mM ambic with 1 µg trypsin. Pipette gently to mix. |
| Buffer A (5% FA, 50% ACN) | For 10 mL total volume, combine 500 µL FA (formic acid [$CH_2O_2$]; Sigma–Aldrich) and 5 mL ACN with 4.5 mL HPLC-grade $H_2O$. Vortex to mix. |
| Buffer B (5% FA, 85% ACN) | For 10 mL total volume, combine 500 µL FA and 8.5 mL ACN with 1 mL HPLC-grade $H_2O$. Vortex to mix. |

1. Transfer 50 mg of brain to a 2 mL hard-tissue grinding Precellys® lysing tube (Bertin Technologies).
2. Add 100 µL 5% SDS lysis buffer.
3. Use the Precellys® 24 Touch homogeniser (Bertin Technologies) to lyse at 5,500 rpm for 30 s. Repeat twice for a total of three cycles, cooling on ice between cycles.

4. Centrifuge at 20 °C and 4,000 rcf for 5 min.
5. Pipette the supernatant into a 2 mL Eppendorf Protein LoBind® tube (Thermo Fisher Scientific). Centrifuge at 20 °C and 22,000 rcf for 5 min.
6. Pipette the supernatant into a new 2 mL LoBind® tube. Add 33.3 µL NuPAGE™ LDS (4×) sample buffer (Invitrogen™, Thermo Fisher Scientific).
7. Add 44.4 µL 200 mM DTT to a final concentration of 50 mM.
8. Incubate at 20 °C and 2,000 rpm for 1 h.
9. Centrifuge at 20 °C and 22,000 rcf for 2 min.
10. Insert a 1.0 mm NuPAGE™ Bis-Tris gel into a Mini Gel Tank and load with enough NuPAGE™ MES SDS (20×) running buffer (all Invitrogen™, Thermo Fisher Scientific) to fill the tank. Remove and discard the comb.
11. Load 20 µL of sample into each of six gel lanes.
12. Cover the chamber and connect the electrodes. Run the gel at a constant voltage of 120 V for 10 min.
13. Disconnect the electrodes and remove the cover. Remove the gel and place in a sterile petri dish. Cover the gel with InstantBlue™ staining dye (Sigma–Aldrich), and place in a rocker for 10 min.
14. Wash the gel of the dye with HPLC-grade $H_2O$.
15. Using a sterile scalpel, excise each gel lane and cut into approximately 1 $mm^2$ cubes. Transfer each lane to a new 1.5 mL LoBind™ tube and add 1 µL 5% acetic acid.
16. Incubate at 20 °C and 1,000 rpm overnight.
17. Remove the supernatant from the gel pieces.
18. Add 200 µL ACN and vortex. Allow to dehydrate at 20 °C for 5 min.
19. Remove the supernatant and repeat step 18.
20. Add 30 µL 10 mM DTT and incubate at 20 °C for 30 min.
21. Remove the supernatant and add 30 µL 50 mM IAA. Incubate in the dark at 20 °C for 30 min.
22. Remove the supernatant and add 200 µL ACN. Allow to dehydrate at 20 °C for 5 min.

23. Remove the supernatant and add 200 µL 100 mM ambic. Allow to rehydrate at 20 °C for 10 min.
24. Repeat step 22.
25. Add 100 µL digestion buffer. Place the tubes on ice with shaking at 500 rpm for 10 min.
26. Centrifuge at 20 °C and 4,000 rcf for 1 min.
27. Remove the supernatant and add 15 µL 50 mM ambic.
28. Incubate at 37 °C overnight.
29. Add 50 µL of 50 mM ambic and incubate at 20 °C for 10 min, gently vortexing every 2–3 min.
30. Transfer the supernatant to a new 1.5 mL LoBind® tube.
31. Add 50 µL of buffer A to the gel pieces and incubate at 20 °C for 10 min, gently vortexing every 2 min.
32. Transfer the supernatant to the collection tube.
33. Add 50 µL of buffer B to the gel pieces and incubate at 20 °C for 10 min, gently vortexing every 2 min.
34. Repeat step 32.
35. Combine the gel pieces in a new 1.5 mL LoBind® tube. Dehydrate in a vacuum concentrator at 30 °C. Store eluted peptides at −20 °C prior to analysis.

## B.2.3 On-filter

### B.2.3.1 PreOmics® BeatBox with S-Trap micro

**Table B.6 |** Reagents required for the PreOmics® BeatBox with S-Trap micro method.

| Reagent | Preparation |
|---|---|
| 0.5 M TCEP | For 300 µL total volume, dissolve 43.0 mg TCEP in 300 µL HPLC-grade $H_2O$. Vortex to mix. |
| 5% SDS lysis buffer | For 5 mL total volume, combine 1.25 mL 20% SDS, 100 µL 0.5 M TCEP and 500 µL 100 mM TEAB in 3.15 mL HPLC-grade $H_2O$. Vortex to mix. |
| 0.5 M IAA | For 300 µL total volume, dissolve 27.8 mg IAA and 30 µL 100 mM TEAB with 270 µL HPLC-grade $H_2O$. Vortex to mix and store at 4 °C until use. |
| 12% phosphoric acid | For 1 mL total volume, combine 141 µL 85% phosphoric acid ($H_3PO_4$; Sigma–Aldrich) and 859 µL HPLC-grade $H_2O$. Vortex to mix. |
| S-Trap buffer | For 5 mL total volume, combine 4.5 mL methanol and 500 µL 100 mM TEAB. Vortex to mix. |

*Continued on next page*

| **Reagent** | **Preparation** |
|---|---|
| 50 mM TEAB | For 10 mL total volume, combine 500 µL 1 M TEAB and 9.5 mL HPLC-grade $H_2O$. Vortex to mix. |
| Buffer A (0.2% TFA) | For 1 mL total volume, combine 2 µL TFA and 998 µL HPLC-grade $H_2O$. Vortex to mix. |
| Buffer B (0.2% TFA, 50% ACN) | For 1 mL total volume, combine 2 µL TFA and 500 µL ACN with 498 µL HPLC-grade $H_2O$. Vortex to mix. |

1. Transfer 50 mg of brain to a 2 mL Eppendorf Protein LoBind® tube (Thermo Fisher Scientific). Add 50 mg 1.0 mm glass beads to the sample.
2. Add 1 mL of 5% SDS lysis buffer.
3. Shear the sample by BeatBox sonication for 10 cycles of 30 s.
4. Centrifuge at 20 °C and 4,000 rcf for 1 min.
5. Transfer the supernatant to a new 2 mL LoBind® tube and centrifuge at 20 °C and 22,000 rcf for 10 min.
6. Add 41.7 µL 0.5 M IAA for a final concentration of 20 mM. Incubate in the dark at 20 °C for 30 min.
7. Add 116 µL 12% phosphoric acid for a final concentration of 1.2%.
8. Add 3 mL of S-Trap buffer.
9. Place the S-Trap micro (Protifi, Biosys Technologies, Inc.) into a 2 mL S-Trap collection tube and slowly load the sample onto the membrane, 500 µL at a time. After each load, centrifuge at 20 °C and 4,000 rcf for 30 s, and discard the flow-through. Repeat the process until all the sample has been loaded.
10. Add 400 µL S-Trap buffer, and centrifuge at 20 °C and 4,000 rcf for 30 s. Discard the flow-through and repeat this step.
11. Transfer the S-Trap micro to a new 2 mL LoBind® tube. Repeat step 10 twice, for a total of four washes.
12. Transfer the S-Trap micro to a new 1.5 mL LoBind® tube. Add 125 µL 50 mM TEAB.
13. Add 1 µg MS-grade trypsin (Promega). Incubate at 37 °C overnight.
14. Add 80 µL 50 mM TEAB.
15. Add 80 µL buffer A. Confirm pH $< 2.0$.
16. Add 80 µL buffer B. Discard the S-Trap micro.

17. Dehydrate in a vacuum concentrator at 30 °C. Store eluted peptides at −20 °C prior to analysis.

#### B.2.3.2 SDS with S-Trap micro

**Table B.7** | Reagents required for the SDS with S-Trap micro method.

| Reagent | Preparation |
|---|---|
| 0.5 M TCEP | For 300 µL total volume, dissolve 43.0 mg TCEP in 300 µL HPLC-grade $H_2O$. Vortex to mix. |
| 5% SDS lysis buffer | For 5 mL total volume, combine 1.25 mL 20% SDS, 100 µL 0.5 M TCEP and 500 µL 100 mM TEAB in 3.15 mL HPLC-grade $H_2O$. Vortex to mix. |
| 0.5 M IAA | For 300 µL total volume, dissolve 27.8 mg IAA and 30 µL 100 mM TEAB with 270 µL HPLC-grade $H_2O$. Vortex to mix and store at 4 °C until use. |
| 12% phosphoric acid | For 1 mL total volume, combine 141 µL 85% phosphoric acid ($H_3PO_4$; Sigma–Aldrich) and 859 µL HPLC-grade $H_2O$. Vortex to mix. |
| S-Trap buffer | For 5 mL total volume, combine 4.5 mL methanol and 500 µL 100 mM TEAB. Vortex to mix. |
| 50 mM TEAB | For 10 mL total volume, combine 500 µL 1 M TEAB and 9.5 mL HPLC-grade $H_2O$. Vortex to mix. |
| Buffer A (0.2% TFA) | For 1 mL total volume, combine 2 µL TFA and 998 µL HPLC-grade $H_2O$. Vortex to mix. |
| Buffer B (0.2% TFA, 50% ACN) | For 1 mL total volume, combine 2 µL TFA and 500 µL ACN with 498 µL HPLC-grade $H_2O$. Vortex to mix. |

1. Transfer 50 mg of brain to a 2 mL hard-tissue grinding Precellys® lysing tube (Bertin Technologies).
2. Add 1 mL of 5% SDS lysis buffer.
3. Use the Precellys® 24 Touch homogeniser (Bertin Technologies) to lyse at 5,500 rpm for 30 s. Repeat twice for a total of three cycles, cooling on ice between cycles.
4. Centrifuge at 20 °C and 4,000 rcf for 1 min.
5. Transfer the supernatant to a 2 mL Eppendorf Protein LoBind® tube (Thermo Fisher Scientific) and centrifuge at 20 °C and 22,000 rcf for 10 min.
6. Add 41.7 µL 0.5 M IAA for a final concentration of 20 mM. Incubate in the dark at 20 °C for 30 min.
7. Add 116 µL 12% phosphoric acid for a final concentration of 1.2%.
8. Add 3 mL of S-Trap buffer.
9. Place the S-Trap micro (Protifi, Biosys Technologies, Inc.) into a 2 mL S-Trap collection tube and slowly load the sample onto the membrane, 500 µL at a

time. After each load, centrifuge at 20 °C and 4,000 rcf for 30 s, and discard the flow-through. Repeat the process until all the sample has been loaded.

10. Add 400 µL S-Trap buffer, and centrifuge at 20 °C and 4,000 rcf for 30 s. Discard the flow-through and repeat this step.
11. Transfer the S-Trap micro to a new 2 mL LoBind® tube. Repeat step 10 twice, for a total of four washes.
12. Transfer the S-Trap micro to a new 1.5 mL LoBind® tube. Add 125 µL 50 mM TEAB.
13. Add 1 µg MS-grade trypsin (Promega). Incubate at 37 °C overnight.
14. Add 80 µL 50 mM TEAB.
15. Add 80 µL buffer A. Confirm pH < 2.0.
16. Add 80 µL buffer B. Discard the S-Trap micro.
17. Dehydrate in a vacuum concentrator at 30 °C. Store eluted peptides at −20 °C prior to analysis.

#### B.2.3.3 Urea with FASP

**Table B.8** | Reagents required for the urea with FASP method.

| Reagent | Preparation |
|---|---|
| Urea lysis buffer | For 10 mL total volume, dissolve 4.8 g 8 M urea in ∼ 8 mL HPLC-grade $H_2O$. Add 1 mL 1 M TEAB, and bring to 10 mL with HPLC-grade $H_2O$. Vortex to mix. |
| Buffer A (0.1% TFA, 50% ACN) | For 1 mL total volume, combine 1 µL TFA and 500 µL ACN with 499 µL HPLC-grade $H_2O$. Vortex to mix. |
| 0.5 M TCEP | For 300 µL total volume, dissolve 43.0 mg TCEP in 300 µL HPLC-grade $H_2O$. Vortex to mix. |
| 0.5 M IAA | For 300 µL total volume, combine 27.8 mg IAA and 30 µL 100 mM TEAB with 270 µL HPLC-grade $H_2O$. Vortex to mix and store at 4 °C until use. |
| 50 mM TEAB | For 10 mL total volume, combine 500 µL 1 M TEAB and 9.5 mL HPLC-grade $H_2O$. Vortex to mix. |
| Buffer B (0.1% TFA) | For 1 mL total volume, combine 1 µL TFA and 999 µL HPLC-grade $H_2O$. Vortex to mix. |

1. Transfer 50 mg of brain to a 2 mL hard-tissue grinding Precellys® lysing tube (Bertin Technologies).
2. Add 200 µL urea lysis buffer.
3. Use the Precellys® 24 Touch homogeniser (Bertin Technologies) to lyse at 5,500 rpm for 30 s. Repeat twice for a total of three cycles, cooling on ice between cycles.

4. Centrifuge at 20 °C and 4,000 rcf for 1 min.
5. Insert a Sartorius Vivacon™ 500 30 kDa MWCO filter (Thermo Fisher Scientific) into a 2 mL adapter tube.
6. Add 200 µL buffer A. Centrifuge at 20 °C and 14,300 rcf for 10 min, or until all the liquid has passed through the filter. Discard the flow-through. (*Optional*: To assess sample loss, transfer the flow-through to a 1.5 mL Eppendorf Protein LoBind® tube (Thermo Fisher Scientific) and store at −20 °C prior to analysis.)
7. Load the sample on the filter. Centrifuge at 20 °C and 14,300 rcf for 10 min, or until all the liquid has passed through. Transfer the flow-through to a 2 mL LoBind® tube.
8. Add 200 µL urea lysis buffer to the filter.
9. Add 4.1 µL 0.5 M TCEP for a final concentration of 10 mM TCEP.
10. Add 22.7 µL 0.5 M IAA for a final concentration of 50 mM IAA. Incubate in the dark at 20 °C for 30 min.
11. Centrifuge at 20 °C and 14,300 rcf for 10 min, or until all the liquid has passed through.
12. Add 200 µL 50 mM TEAB. Centrifuge at 20 °C and 14,300 rcf for 10 min, or until all the liquid has passed through.
13. Repeat step 12 twice, for a total of three washes with 50 mM TEAB. Discard the flow-through.
14. Transfer the filter to a new 2 mL adapter tube.
15. Add 200 µL 50 mM TEAB, and 1 µg MS-grade trypsin (Promega). Incubate at 37 °C overnight.
16. Centrifuge at 20 °C and 14,300 rcf for 10 min to elute peptides. Transfer the flow-through to a 2 mL LoBind® tube and keep on ice.
17. Add 200 µL buffer B to the filter. Centrifuge at 20 °C and 14,300 rcf for 10 min, or until all the liquid has passed through.
18. Add 200 µL buffer A. Centrifuge at 20 °C and 14,300 rcf for 10 min, or until all the liquid has passed through.
19. Combine the flow-through from steps 16–18. Discard the filter.

20. Dehydrate in a vacuum concentrator at 30 °C. Store eluted peptides at −20 °C prior to analysis.

#### B.2.3.4 SDS with FASP

**Table B.9** | Reagents required for the SDS with FASP method.

| Reagent | Preparation |
|---|---|
| 5% SDS lysis buffer | For 1 mL total volume, combine 250 µL 20% SDS and 100 µL 100 mM TEAB with 650 µL HPLC-grade $H_2O$. Vortex to mix. |
| Buffer A (0.1% TFA, 50% ACN) | For 1 mL total volume, combine 1 µL TFA and 500 µL ACN with 499 µL HPLC-grade $H_2O$. Vortex to mix. |
| 0.5 M TCEP | For 300 µL total volume, dissolve 43.0 mg TCEP in 300 µL HPLC-grade $H_2O$. Vortex to mix. |
| Urea lysis buffer | For 10 mL total volume, dissolve 4.8 g 8 M urea in ∼ 8 mL HPLC-grade $H_2O$. Add 1 mL 1 M TEAB, and bring to 10 mL with HPLC-grade $H_2O$. Vortex to mix. |
| 0.5 M IAA | For 300 µL total volume, combine 27.8 mg IAA and 30 µL 100 mM TEAB with 270 µL HPLC-grade $H_2O$. Vortex to mix and store at 4 °C until use. |
| 50 mM TEAB | For 10 mL total volume, combine 500 µL 1 M TEAB and 9.5 mL HPLC-grade $H_2O$. Vortex to mix. |
| Buffer B (0.1% TFA) | For 1 mL total volume, combine 1 µL TFA and 999 µL HPLC-grade $H_2O$. Vortex to mix. |

1. Transfer 50 mg of brain to a 2 mL hard-tissue grinding Precellys® lysing tube (Bertin Technologies).
2. Add 200 µL 5% SDS lysis buffer.
3. Use the Precellys® 24 Touch homogeniser (Bertin Technologies) to lyse at 5,500 rpm for 30 s. Repeat twice for a total of three cycles, cooling on ice between cycles.
4. Centrifuge at 20 °C and 4,000 rcf for 1 min.
5. Insert a Sartorius Vivacon™ 500 30 kDa MWCO filter (Thermo Fisher Scientific) into a 2 mL adapter tube.
6. Add 200 µL buffer A. Centrifuge at 20 °C and 14,300 rcf for 10 min, or until all the liquid has passed through the filter. Discard the flow-through. (*Optional*: To assess sample loss, transfer the flow-through to a 1.5 mL Eppendorf Protein LoBind® tube (Thermo Fisher Scientific) and store at −20 °C prior to analysis.)
7. Load the sample on the filter. Centrifuge at 20 °C and 14,300 rcf for 10 min, or until all the liquid has passed through. Transfer the flow-through to a 2 mL LoBind® tube (Thermo Fisher Scientific).

8. Add 200 µL urea lysis buffer to the filter.
9. Add 4.1 µL 0.5 M TCEP for a final concentration of 10 mM TCEP.
10. Add 22.7 µL 0.5 M IAA for a final concentration of 50 mM IAA. Incubate in the dark at 20 °C for 30 min.
11. Centrifuge at 20 °C and 14,300 rcf for 10 min, or until all the liquid has passed through.
12. Add 200 µL 50 mM TEAB. Centrifuge at 20 °C and 14,300 rcf for 10 min, or until all the liquid has passed through.
13. Repeat step 12 twice, for a total of three washes with 50 mM TEAB. Discard the flow-through.
14. Transfer the filter to a new adapter tube.
15. Add 200 µL 50 mM TEAB, and 1 µg MS-grade trypsin (Promega). Incubate at 37 °C overnight.
16. Centrifuge at 20 °C and 14,300 rcf for 10 min to elute peptides. Transfer the flow-through to a new 2 mL LoBind® tube and keep on ice.
17. Add 200 µL buffer B to the filter. Centrifuge at 20 °C and 14,300 rcf for 10 min, or until all the liquid has passed through.
18. Add 200 µL buffer A. Centrifuge at 20 °C and 14,300 rcf for 10 min, or until all the liquid has passed through.
19. Combine the flow-through from steps 16–18. Discard the filter.
20. Dehydrate in a vacuum concentrator at 30 °C. Store eluted peptides at −20 °C prior to analysis.

## B.2.4 On-bead

### B.2.4.1 SP3

**Table B.10** | Reagents required for the SP3 method.

| Reagent | Preparation |
|---|---|
| 0.5% SDS lysis buffer | For 1 mL total volume, combine 25 µL 20% SDS and 975 µL HPLC-grade $H_2O$. Vortex to mix. |
| 200 mM DTT | For 1 mL total volume, dissolve 30.9 mg DTT in 1 mL HPLC-grade $H_2O$. Vortex to mix and store at −20 °C until use. |

*Continued on next page*

| **Reagent** | **Preparation** |
|---|---|
| 0.5 M IAA | For 300 µL total volume, combine 27.8 mg IAA and 30 µL 100 mM TEAB with 270 µL HPLC-grade $H_2O$. Vortex to mix and store at 4 °C until use. |
| 50 mM TEAB | For 10 mL total volume, combine 500 µL 1 M TEAB and 9.5 mL HPLC-grade $H_2O$. Vortex to mix. |

1. Transfer 50 mg of brain to a 2 mL hard-tissue grinding Precellys® lysing tube (Bertin Technologies).
2. Add 50 µL 0.5% SDS.
3. Use the Precellys® 24 Touch homogeniser (Bertin Technologies) to lyse at 5,500 rpm for 30 s. Repeat twice for a total of three cycles, cooling on ice between cycles.
4. Centrifuge at 20 °C and 22,000 rcf for 5 min. Transfer the supernatant to a 1.5 mL Eppendorf Protein LoBind® tube (Thermo Fisher Scientific).
5. Add 1.3 µL 200 mM DTT to a final concentration of 5 mM. Incubate at 20 °C for 30 min.
6. Add 2.1 µL 0.5 M IAA to a final concentration of 20 mM. Incubate in the dark at 20 °C for 30 min.
7. Centrifuge at 20 °C and 22,000 rcf for 5 min.
8. Transfer the supernatant to a new 1.5 mL LoBind® tube containing 3 µL of SP3 beads in a 1:1 hydrophobic:hydrophilic ratio.
9. Add 125 µL ACN to a final concentration of 70%. Mix at 20 °C and 1,000 rpm for 18 min.
10. Place the sample on the magnetic rack and leave for 2 min, to allow all beads to migrate to the plate.
11. Pipette off and discard the supernatant. Keep the sample on the magnetic rack until steps 12–15 are complete.
12. Rinse with 200 µL 70% ethanol. Leave for 15 s, then pipette off and discard the supernatant.
13. Rinse with 200 µL 100% ACN. Leave for 15 s, then pipette off and discard the supernatant.
14. Repeat step 12.

15. Repeat step 13.
16. Remove the tube from the magnetic rack and allow the beads to settle to the bottom.
17. Add 150 µL 50 mM TEAB, or enough of this digestion buffer to ensure all beads are covered.
18. Add 1 µg MS-grade trypsin (Promega). Incubate at 37 °C and 1,000 rpm overnight.
19. Transfer the supernatant to a new 1.5 mL LoBind® tube.
20. Add 1.5 µL TFA to a final concentration of 1%. Vortex briefly to mix, and confirm pH $< 2.0$.
21. Dehydrate in a vacuum concentrator at 30 °C. Store eluted peptides at −20 °C prior to analysis.

## B.3 Results

The LC–(FAIMS)–MS/MS data have been deposited to the ProteomeXchange Consortium *via* the PRIDE [2] partner repository with the dataset identifier, PXD062254. Supplementary Data are available online: `doi.org/10.1371/journal.pone.0324246`.

# B.4 Figures

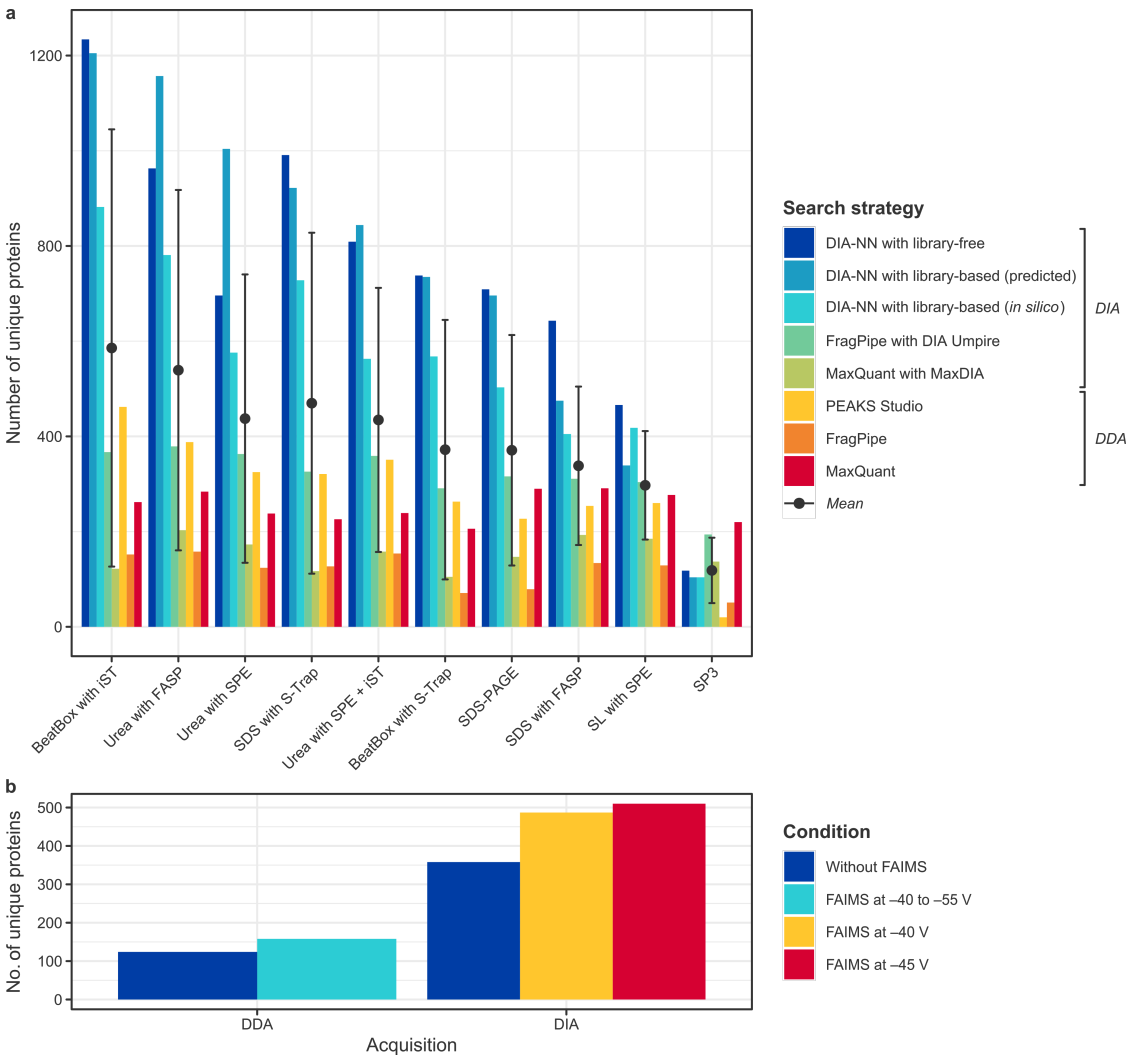



**Figure B.1 | Proteins retrieved with each search strategy, and impact of FAIMS on protein identification. (a)** Bar chart of the numbers of unique proteins identified at 1% FDR and $q$-value $\leq .01$ in the DIA and DDA data, summed per and coloured by search strategy (*left to right*, highest to lowest total proteins). Black dots represent mean values per protocol, with error bars reflecting the SD. **(b)** Bar chart of the numbers of unique proteins identified at 1% FDR and $q$-value $\leq .01$ in the pooled samples analysed in DDA and DIA modes, summed per and coloured by the use of a FAIMS source with associated negative CV.

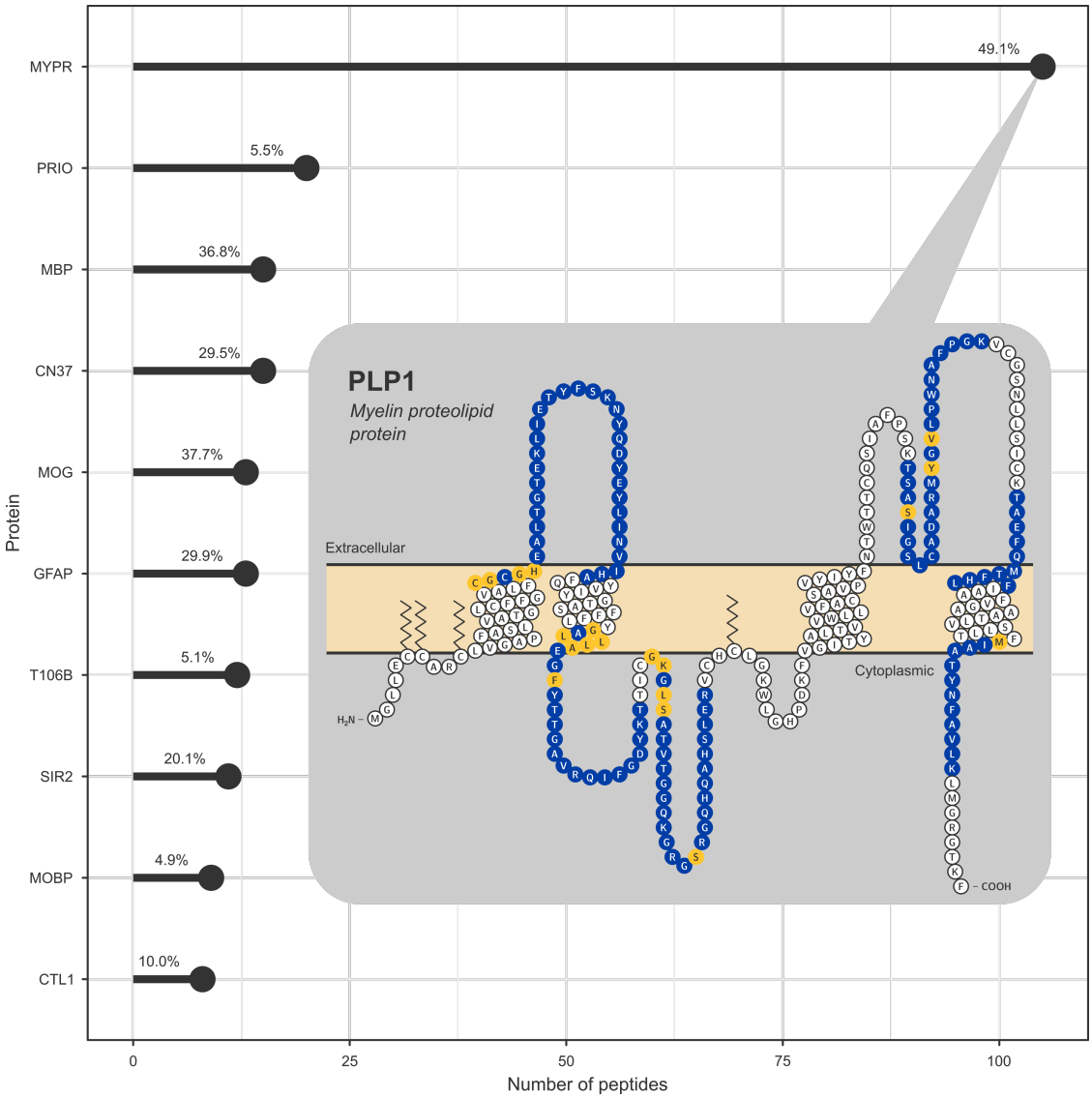



**Figure B.2 | Nature of non-tryptic peptides.** Proteins associated with the 10 highest numbers of non-tryptic peptides, and their percentage sequence coverage. Myelin proteolipid protein (PLP1), the most abundant and the major transmembrane protein of the CNS, is illustrated by its proteoform, with (*top to bottom*) the extracellular, transmembrane and cytoplasmic spaces; created with Protter (v.1.0)[3]. Solid colours represent recovered peptides, with yellow residues reflecting non-tryptic cleavage sites.

## B.5 Tables

**Table B.11 | DDA and DIA search strategies.** Protein identification and quantification analyses conducted with associated software packages.

| Data type | Search strategy |
|---|---|
| **DIA** | DIA-NN (v.1.9) [4] with library-free search.<br>DIA-NN (v.1.9) [4] with spectral library search, based on library-free generation.<br>DIA-NN (v.1.9) [4] with spectral library search, based on *in silico* generation.<br>FragPipe (v.22.0) [5] with spectral deconvolution using DIA-Umpire Signal Extraction (v.2.0) [6], and quantification with DIA-NN (v.1.8.2) [4].<br>MaxQuant (v.2.6.1.0) [7] with MaxDIA [8] for spectral library search, based on DDA library generation. |
| **DDA** | FragPipe (v.22.0) [9] with LFQ–MBR.<br>MaxQuant (v.2.4.3.0) [7] with LFQ–MBR and dependent peptide search.<br>PEAKS® Studio 13 (Bioinformatics Solutions, Inc.). |

**Table B.12 | DIA identification results for each protocol.** Total numbers of proteotypic precursors, peptides, and proteins identified per protocol at 1% FDR and $q$-value $\leq 0.1$, with total quantities.

| Protocol | Precursors identified | Peptides identified | Proteins identified | Total quantity |
|---|---|---|---|---|
| BeatBox with iST | 2840 | 2645 | 1205 | $2.88 \times 10^9$ |
| Urea with FASP | 2679 | 2506 | 1157 | $5.48 \times 10^9$ |
| Urea with SPE | 2433 | 2259 | 1004 | $1.26 \times 10^9$ |
| SDS with S-Trap | 2402 | 2274 | 922 | $7.16 \times 10^9$ |
| Urea with SPE + iST | 2178 | 2042 | 844 | $1.07 \times 10^9$ |
| BeatBox with S-Trap | 2029 | 1900 | 735 | $1.45 \times 10^9$ |
| SDS–PAGE | 1953 | 1820 | 696 | $6.94 \times 10^8$ |
| SDS with FASP | 1500 | 1369 | 475 | $1.97 \times 10^9$ |
| SL with SPE | 1139 | 1066 | 339 | $1.89 \times 10^9$ |
| SP3 | 328 | 303 | 104 | $1.68 \times 10^8$ |

**Table B.13 | Statistical over-representation of protein classes.** Over-representation test results for proteins recovered by every protocol ($n = 98$). Only statistically significant results (i.e., Bonferroni-corrected for $p \leq 0.5$) for classified proteins are shown. Parent classes (*italics*) are indented below subclasses to illustrate hierarchical relationships. Cells containing $p$-values are coloured according to significance thresholds.

| Protein class | No. of reference genes | No. of queried genes | No. of expected genes | Fold enrichment | $p$-Value |
|---|---|---|---|---|---|
| Tubulin | 17 | 3 | 0.11 | 26.68 | $3.35 \times 10^{-2}$ |
| Intermediate filament | 25 | 4 | 0.17 | 24.19 | $3.85 \times 10^{-3}$ |
| Small GTPase | 112 | 9 | 0.74 | 12.15 | $9.82 \times 10^{-6}$ |
| ↪ *G-protein* | 166 | 13 | 1.10 | 11.84 | $1.21 \times 10^{-8}$ |
| ↪ *Protein-binding activity modulator* | 673 | 15 | 4.45 | 3.37 | $6.36 \times 10^{-3}$ |

**Table B.14 | Nature of dependent peptides.** Total numbers per protocol of annotated modifications to ≥ 2 unique peptides, identified by dependent peptide search. Fixed modifications (i.e., those explicitly searched for) are italicised.

| Modification | BB w/ iST | Urea w/ FASP | Urea w/ SPE | SDS w/ S-Trap | Urea w/ SPE + iST | BB w/ S-Trap | SDS–PAGE | SDS w/ FASP | SL w/ SPE | SP3 | Total |
|---|---|---|---|---|---|---|---|---|---|---|---|
| *Deamidation* | *9* | *4* | *7* | *5* | *7* | *2* | *3* | *4* | *9* | *1* | *51* |
| Comp: 12 C−13 C | 7 | 5 | 4 | 3 | 3 | 1 | 1 | 2 | 2 | 0 | 28 |
| *Oxidation* | *6* | *4* | *1* | *3* | *5* | *0* | *2* | *0* | *1* | *0* | *22* |
| *Carbamidomethylation* | *0* | *0* | *7* | *0* | *10* | *0* | *0* | *1* | *0* | *0* | *18* |
| Loss of water | 6 | 1 | 1 | 1 | 3 | 0 | 0 | 0 | 2 | 0 | 14 |
| Acetaldehyde | 0 | 1 | 5 | 0 | 1 | 0 | 0 | 0 | 4 | 0 | 11 |
| Comp: O−$NH_3$ | 4 | 0 | 1 | 1 | 1 | 0 | 0 | 1 | 0 | 0 | 8 |
| Comp: −$H_5C_2NOS$ | 1 | 0 | 1 | 1 | 1 | 0 | 0 | 1 | 1 | 1 | 7 |
| Comp: 13 C−12 C | 1 | 2 | 2 | 0 | 2 | 0 | 0 | 0 | 0 | 0 | 7 |
| Comp: O−$H_2$ | 3 | 1 | 0 | 0 | 0 | 0 | 0 | 2 | 1 | 0 | 7 |
| Didehydro | 1 | 1 | 1 | 0 | 1 | 0 | 0 | 2 | 1 | 0 | 7 |
| Loss of ammonia | 2 | 0 | 2 | 0 | 2 | 0 | 0 | 1 | 0 | 0 | 7 |
| Reduction | 0 | 1 | 2 | 0 | 1 | 0 | 0 | 2 | 0 | 0 | 6 |
| Comp: O−$CH_2$ | 1 | 0 | 1 | 0 | 0 | 0 | 1 | 0 | 1 | 0 | 4 |
| Comp: S−$C_4$ | 3 | 0 | 0 | 0 | 0 | 0 | 1 | 0 | 0 | 0 | 4 |
| Formylation | 1 | 1 | 1 | 0 | 1 | 0 | 0 | 0 | 0 | 0 | 4 |
| Comp: C−$N_3$ | 2 | 0 | 0 | 0 | 1 | 0 | 0 | 0 | 0 | 0 | 3 |
| Sulfide | 0 | 0 | 1 | 0 | 0 | 0 | 0 | 1 | 1 | 0 | 3 |
| Comp: C | 0 | 1 | 1 | 0 | 0 | 0 | 0 | 0 | 0 | 0 | 2 |
| Comp: NO−$CH_3$ | 0 | 2 | 0 | 0 | 0 | 0 | 0 | 0 | 0 | 0 | 2 |
| Carboxymethylation | 0 | 0 | 0 | 0 | 2 | 0 | 0 | 0 | 0 | 0 | 2 |

**Table B.15 | Summary of hydropathy by protocol.** Summary statistics for GRand AVerage of hydropathY (GRAVY) score for proteins retrieved in all protocols (the 'common proteome', italicised; $n = 98$), and peptides corresponding to the same proteins retrieved by each protocol.

| Protocol | Mean | Standard deviation | Median |
|---|---|---|---|
| *Common proteome* | *−0.262* | *0.416* | *−0.322* |
| BeatBox with iST | −0.395 | 0.848 | −0.340 |
| Urea with FASP | −0.413 | 0.809 | −0.422 |
| Urea with SPE | −0.341 | 0.783 | −0.300 |
| SDS with S-Trap | −0.326 | 0.852 | −0.262 |
| Urea with SPE + iST | −0.318 | 0.799 | −0.267 |
| BeatBox with S-Trap | −0.344 | 0.876 | −0.259 |
| SDS–PAGE | −0.341 | 0.846 | −0.300 |
| SDS with FASP | −0.600 | 0.863 | −0.668 |
| SL with SPE | −0.517 | 0.838 | −0.514 |
| SP3 | −0.345 | 0.820 | −0.300 |

**Table B.16 | Hydropathic profiles retrieved by each protocol.** Results of *post-hoc* pairwise comparisons ($n = 55$) with Bonferroni correction at 95% CI for a linear mixed effects model with Satterthwaite $t$-tests ($n_{obs}= 4,383$) with respect to GRAVY score, for proteins shared across all protocols (the 'common proteome', CP) and for peptides corresponding to the same proteins retrieved by each protocol. Cells containing $p$-values are coloured according to significance thresholds.

| Comparison | Estimate ($E$) | Standard error (SE) | $t$-Ratio | $p$-Value |
|---|---|---|---|---|
| CP – BB w/ iST | 0.14753 | 0.09069 | 1.62685 | $1.00 \times 10^{0}$ |
| CP – Urea w/ FASP | 0.16504 | 0.09052 | 1.82327 | $1.00 \times 10^{0}$ |
| CP – Urea w/ SPE | 0.09395 | 0.09085 | 1.03411 | $1.00 \times 10^{0}$ |
| CP – SDS w/ S-Trap | 0.07719 | 0.09214 | 0.83774 | $1.00 \times 10^{0}$ |
| CP – Urea w/ SPE + iST | 0.07047 | 0.09170 | 0.76855 | $1.00 \times 10^{0}$ |
| CP – BB w/ S-Trap | 0.09551 | 0.09276 | 1.02971 | $1.00 \times 10^{0}$ |
| CP – SDS–PAGE | 0.09261 | 0.09186 | 1.00815 | $1.00 \times 10^{0}$ |
| CP – SDS w/ FASP | 0.35140 | 0.09248 | 3.79980 | $8.08 \times 10^{-3}$ |
| CP – SL | 0.26677 | 0.09345 | 2.85464 | $2.38 \times 10^{-1}$ |
| CP – SP3 | 0.08802 | 0.10115 | 0.87019 | $1.00 \times 10^{0}$ |
| BB w/ iST – Urea w/ FASP | 0.01750 | 0.05048 | 0.34672 | $1.00 \times 10^{0}$ |
| BB w/ iST – Urea w/ SPE | −0.05358 | 0.05109 | −1.04885 | $1.00 \times 10^{0}$ |
| BB w/ iST – SDS w/ S-Trap | −0.07035 | 0.05341 | −1.31716 | $1.00 \times 10^{0}$ |
| BB w/ iST – Urea w/ SPE + iST | −0.07706 | 0.05262 | −1.46444 | $1.00 \times 10^{0}$ |
| BB w/ iST – BB w/ S-Trap | −0.05202 | 0.05450 | −0.95440 | $1.00 \times 10^{0}$ |
| BB w/ iST – INGEL | −0.05493 | 0.05291 | −1.03818 | $1.00 \times 10^{0}$ |
| BB w/ iST – SDS w/ FASP | 0.20387 | 0.05401 | 3.77454 | $8.94 \times 10^{-3}$ |
| BB w/ iST – SL | 0.11924 | 0.05571 | 2.14044 | $1.00 \times 10^{0}$ |
| BB w/ iST – SP3 | −0.05951 | 0.06815 | −0.87325 | $1.00 \times 10^{0}$ |
| Urea w/ FASP – Urea w/ SPE | −0.07109 | 0.05078 | −1.39976 | $1.00 \times 10^{0}$ |
| Urea w/ FASP – SDS w/ S-Trap | −0.08785 | 0.05312 | −1.65386 | $1.00 \times 10^{0}$ |
| Urea w/ FASP – Urea w/ SPE + iST | −0.09456 | 0.05233 | −1.80717 | $1.00 \times 10^{0}$ |
| Urea w/ FASP – BB w/ S-Trap | −0.06952 | 0.05422 | −1.28221 | $1.00 \times 10^{0}$ |
| Urea w/ FASP – SDS–PAGE | −0.07243 | 0.05261 | −1.37662 | $1.00 \times 10^{0}$ |
| Urea w/ FASP – SDS w/ FASP | 0.18637 | 0.05372 | 3.46893 | $2.90 \times 10^{-2}$ |
| Urea w/ FASP – SL | 0.10173 | 0.05543 | 1.83542 | $1.00 \times 10^{0}$ |
| Urea w/ FASP – SP3 | −0.07702 | 0.06793 | −1.13384 | $1.00 \times 10^{0}$ |
| Urea w/ SPE – SDS w/ S-Trap | −0.01676 | 0.05369 | −0.31223 | $1.00 \times 10^{0}$ |
| Urea w/ SPE – Urea w/ SPE + iST | −0.02348 | 0.05290 | −0.44376 | $1.00 \times 10^{0}$ |
| Urea w/ SPE – BB w/ S-Trap | 0.00156 | 0.05478 | 0.02856 | $1.00 \times 10^{0}$ |
| Urea w/ SPE – SDS–PAGE | −0.00134 | 0.05319 | −0.02527 | $1.00 \times 10^{0}$ |
| Urea w/ SPE – SDS w/ FASP | 0.25745 | 0.05429 | 4.74232 | $1.20 \times 10^{-4}$ |
| Urea w/ SPE – SL | 0.17282 | 0.05597 | 3.08747 | $1.12 \times 10^{-1}$ |
| Urea w/ SPE – SP3 | −0.00593 | 0.06837 | −0.08674 | $1.00 \times 10^{0}$ |
| SDS w/ S-Trap – Urea w/ SPE + iST | −0.00671 | 0.05511 | −0.12183 | $1.00 \times 10^{0}$ |
| SDS w/ S-Trap – BB w/ S-Trap | 0.01833 | 0.05689 | 0.32218 | $1.00 \times 10^{0}$ |
| SDS w/ S-Trap – SDS–PAGE | 0.01542 | 0.05537 | 0.27846 | $1.00 \times 10^{0}$ |
| SDS w/ S-Trap – SDS w/ FASP | 0.27422 | 0.05641 | 4.86075 | $7.00 \times 10^{-5}$ |
| SDS w/ S-Trap – SL | 0.18958 | 0.05804 | 3.26649 | $6.04 \times 10^{-2}$ |
| SDS w/ S-Trap – SP3 | 0.01083 | 0.07007 | 0.15459 | $1.00 \times 10^{0}$ |
| Urea w/ SPE + iST – BB w/ S-Trap | 0.02504 | 0.05617 | 0.44582 | $1.00 \times 10^{0}$ |
| Urea w/ SPE + iST – SDS–PAGE | 0.02213 | 0.05462 | 0.40520 | $1.00 \times 10^{0}$ |

*Continued on next page*

| Comparison | Estimate ($E$) | Standard error (SE) | $t$-Ratio | $p$-Value |
|---|---|---|---|---|
| Urea w/ SPE + iST – SDS w/ FASP | 0.28093 | 0.05569 | 5.04437 | $3.00 \times 10^{-5}$ |
| Urea w/ SPE + iST – SL | 0.19629 | 0.05734 | 3.42358 | $3.43 \times 10^{-2}$ |
| Urea w/ SPE + iST – SP3 | 0.01755 | 0.06949 | 0.25249 | $1.00 \times 10^{0}$ |
| BB w/ S-Trap – SDS–PAGE | −0.00291 | 0.05643 | −0.05155 | $1.00 \times 10^{0}$ |
| BB w/ S-Trap – SDS w/ FASP | 0.25589 | 0.05744 | 4.45511 | $4.70 \times 10^{-4}$ |
| BB w/ S-Trap – SL | 0.17125 | 0.05902 | 2.90162 | $2.05 \times 10^{-1}$ |
| BB w/ S-Trap – SP3 | −0.00750 | 0.07089 | −0.10573 | $1.00 \times 10^{0}$ |
| SDS–PAGE – SDS w/ FASP | 0.25880 | 0.05596 | 4.62513 | $2.10 \times 10^{-4}$ |
| SDS–PAGE – SL | 0.17416 | 0.05759 | 3.02410 | $1.38 \times 10^{-1}$ |
| SDS–PAGE – SP3 | −0.00459 | 0.06970 | −0.06580 | $1.00 \times 10^{0}$ |
| SDS w/ FASP – SL | −0.08464 | 0.05858 | −1.44480 | $1.00 \times 10^{0}$ |
| SDS w/ FASP – SP3 | −0.26338 | 0.07052 | −3.73489 | $1.05 \times 10^{-2}$ |
| SL – SP3 | −0.17875 | 0.07179 | −2.48992 | $7.05 \times 10^{-1}$ |

**Table B.17 | Summary of isoelectric point by protocol.** Summary statistics for pI for proteins retrieved in all protocols (the 'common proteome', italicised; $n = 98$), and peptides corresponding to the same proteins retrieved by each protocol.

| Protocol | Mean | Standard deviation (SD) | Median |
|---|---|---|---|
| *Common proteome* | *6.596* | *1.770* | *6.086* |
| BeatBox with iST | 5.928 | 1.943 | 6.067 |
| Urea with FASP | 5.983 | 1.997 | 5.993 |
| Urea with SPE | 6.045 | 2.029 | 6.089 |
| SDS with S-Trap | 6.233 | 2.053 | 6.213 |
| Urea with SPE + iST | 5.808 | 1.850 | 5.461 |
| BeatBox with S-Trap | 6.339 | 2.081 | 6.327 |
| SDS–PAGE | 6.296 | 2.039 | 6.234 |
| SDS with FASP | 5.860 | 1.952 | 5.410 |
| SL with SPE | 6.039 | 2.074 | 5.910 |
| SP3 | 6.029 | 1.955 | 6.108 |

**Table B.18 | Isoelectric profiles retrieved by each protocol.** Results of *post-hoc* pairwise comparisons ($n = 55$) with Bonferroni correction at 95% CI for a linear mixed effects model with Satterthwaite $t$-tests ($n_{obs}$= 4,383) with respect to average pI, for proteins shared across all protocols (the 'common proteome', CP) and for peptides corresponding to the same proteins retrieved by each protocol. Cells containing $p$-values are coloured according to significance thresholds.

| Comparison | Estimate ($E$) | Standard error (SE) | $t$-Ratio | $p$-Value |
|---|---|---|---|---|
| CP – BB w/ iST | 0.87582 | 0.21640 | 4.04738 | $2.90 \times 10^{-3}$ |
| CP – Urea w/ FASP | 0.82091 | 0.21602 | 3.80025 | $8.06 \times 10^{-3}$ |
| CP – Urea w/ SPE | 0.76014 | 0.21678 | 3.50658 | $2.52 \times 10^{-2}$ |
| CP – SDS w/ S-Trap | 0.56754 | 0.21971 | 2.58318 | $5.40 \times 10^{-1}$ |
| CP – Urea w/ SPE + iST | 0.99562 | 0.21870 | 4.55244 | $3.00 \times 10^{-4}$ |
| CP – BB w/ S-Trap | 0.45951 | 0.22113 | 2.07802 | $1.00 \times 10^{0}$ |
| CP – SDS–PAGE | 0.50468 | 0.21906 | 2.30378 | $1.00 \times 10^{0}$ |
| CP – SDS w/ FASP | 0.93976 | 0.22049 | 4.26218 | $1.14 \times 10^{-3}$ |

*Continued on next page*

| Comparison | Estimate ($E$) | Standard error (SE) | $t$-Ratio | $p$-Value |
|---|---|---|---|---|
| CP – SL | 0.75526 | 0.22272 | 3.39111 | $3.86 \times 10^{-2}$ |
| CP – SP3 | 0.70020 | 0.24045 | 2.91208 | $1.99 \times 10^{-1}$ |
| BB w/ iST – Urea w/ FASP | −0.05495 | 0.11958 | −0.45951 | $1.00 \times 10^{0}$ |
| BB w/ iST – Urea w/ SPE | −0.11572 | 0.12102 | −0.95621 | $1.00 \times 10^{0}$ |
| BB w/ iST – SDS w/ S-Trap | −0.30832 | 0.12667 | −2.43400 | $8.24 \times 10^{-1}$ |
| BB w/ iST – Urea w/ SPE + iST | 0.11976 | 0.12476 | 0.95991 | $1.00 \times 10^{0}$ |
| BB w/ iST – BB w/ S-Trap | −0.41635 | 0.12933 | −3.21923 | $7.13 \times 10^{-2}$ |
| BB w/ iST – SDS–PAGE | −0.37119 | 0.12546 | −2.95868 | $1.71 \times 10^{-1}$ |
| BB w/ iST – SDS w/ FASP | 0.06390 | 0.12814 | 0.49867 | $1.00 \times 10^{0}$ |
| BB w/ iST – SL | −0.12060 | 0.13224 | −0.91200 | $1.00 \times 10^{0}$ |
| BB w/ iST – SP3 | −0.17567 | 0.16226 | −1.08264 | $1.00 \times 10^{0}$ |
| Urea w/ FASP – Urea w/ SPE | −0.06077 | 0.12032 | −0.50505 | $1.00 \times 10^{0}$ |
| Urea w/ FASP – SDS w/ S-Trap | −0.25337 | 0.12601 | −2.01072 | $1.00 \times 10^{0}$ |
| Urea w/ FASP – Urea w/ SPE + iST | 0.17407 | 0.12409 | 1.40702 | $1.00 \times 10^{0}$ |
| Urea w/ FASP – BB w/ S-Trap | −0.36140 | 0.12868 | −2.80844 | $2.75 \times 10^{-1}$ |
| Urea w/ FASP – SDS–PAGE | −0.31624 | 0.12479 | −2.53419 | $6.22 \times 10^{-1}$ |
| Urea w/ FASP – SDS w/ FASP | 0.11885 | 0.12749 | 0.93223 | $1.00 \times 10^{0}$ |
| Urea w/ FASP – SL | −0.06566 | 0.13161 | −0.49888 | $1.00 \times 10^{0}$ |
| Urea w/ FASP – SP3 | −0.12072 | 0.16174 | −0.74637 | $1.00 \times 10^{0}$ |
| Urea w/ SPE – SDS w/ S-Trap | −0.19260 | 0.12731 | −1.51286 | $1.00 \times 10^{0}$ |
| Urea w/ SPE – Urea w/ SPE + iST | 0.23547 | 0.12541 | 1.87768 | $1.00 \times 10^{0}$ |
| Urea w/ SPE – BB w/ S-Trap | −0.30063 | 0.12996 | −2.31331 | $1.00 \times 10^{0}$ |
| Urea w/ SPE – SDS–PAGE | −0.25547 | 0.12610 | −2.02590 | $1.00 \times 10^{0}$ |
| Urea w/ SPE – SDS w/ FASP | 0.17962 | 0.12877 | 1.39485 | $1.00 \times 10^{0}$ |
| Urea w/ SPE – SL | −0.00489 | 0.13285 | −0.03677 | $1.00 \times 10^{0}$ |
| Urea w/ SPE – SP3 | −0.05995 | 0.16276 | −0.36834 | $1.00 \times 10^{0}$ |
| SDS w/ S-Trap – Urea w/ SPE + iST | 0.42808 | 0.13056 | 3.27880 | $5.78 \times 10^{-2}$ |
| SDS w/ S-Trap – BB w/ S-Trap | −0.10803 | 0.13479 | −0.80146 | $1.00 \times 10^{0}$ |
| SDS w/ S-Trap – SDS–PAGE | −0.06286 | 0.13117 | −0.47926 | $1.00 \times 10^{0}$ |
| SDS w/ S-Trap – SDS w/ FASP | 0.37220 | 0.13364 | 2.78516 | $2.96 \times 10^{-1}$ |
| SDS w/ S-Trap – SL | 0.18772 | 0.13758 | 1.36444 | $1.00 \times 10^{0}$ |
| SDS w/ S-Trap – SP3 | 0.13266 | 0.16664 | 0.79608 | $1.00 \times 10^{0}$ |
| Urea w/ SPE + iST – BB w/ S-Trap | −0.53611 | 0.13314 | −4.02660 | $3.17 \times 10^{-3}$ |
| Urea w/ SPE + iST – SDS–PAGE | −0.49094 | 0.12938 | −3.79458 | $8.26 \times 10^{-3}$ |
| Urea w/ SPE + iST – SDS w/ FASP | −0.05586 | 0.13198 | −0.42322 | $1.00 \times 10^{0}$ |
| Urea w/ SPE + iST – SL | −0.24036 | 0.13597 | −1.76778 | $1.00 \times 10^{0}$ |
| Urea w/ SPE + iST – SP3 | −0.29542 | 0.16531 | −1.78710 | $1.00 \times 10^{0}$ |
| BB w/ S-Trap – SDS–PAGE | 0.04517 | 0.13374 | 0.33769 | $1.00 \times 10^{0}$ |
| BB w/ S-Trap – SDS w/ FASP | 0.48025 | 0.13606 | 3.52972 | $2.31 \times 10^{-2}$ |
| BB w/ S-Trap – SL | 0.29575 | 0.13984 | 2.11485 | $1.00 \times 10^{0}$ |
| BB w/ S-Trap – SP3 | 0.24068 | 0.16851 | 1.42830 | $1.00 \times 10^{0}$ |
| SDS–PAGE – SDS w/ FASP | 0.43508 | 0.13259 | 3.28150 | $5.73 \times 10^{-2}$ |
| SDS–PAGE – SL | 0.25058 | 0.13655 | 1.83506 | $1.00 \times 10^{0}$ |
| SDS–PAGE – SP3 | 0.19552 | 0.16579 | 1.17932 | $1.00 \times 10^{0}$ |
| SDS w/ FASP – SL | −0.18450 | 0.13883 | −1.32902 | $1.00 \times 10^{0}$ |
| SDS w/ FASP – SP3 | −0.23956 | 0.16767 | −1.42881 | $1.00 \times 10^{0}$ |

*Continued on next page*

| Comparison | Estimate ($E$) | Standard error (SE) | $t$-Ratio | $p$-Value |
|---|---|---|---|---|
| SL – SP3 | −0.05506 | 0.17059 | −0.32278 | $1.00 \times 10^{0}$ |

## B.6 References


[1] PreOmics. *iST Sample Preparation Kit 8x*. Version 4.0. 2025.

[2] Yasset Perez-Riverol et al. 'The PRIDE database at 20 years: 2025 update'. In: *Nucleic Acids Res.* 53 (D1 6th Jan. 2025), pp. D543–D553. DOI: 10.1093/nar/gkae1011.

[3] Ulrich Omasits et al. 'Protter: interactive protein feature visualization and integration with experimental proteomic data'. In: *Bioinformatics* 30 (6 15th Mar. 2014), pp. 884–886. DOI: 10.1093/bioinformatics/btt607.

[4] Vadim Demichev et al. 'DIA-NN: neural networks and interference correction enable deep proteome coverage in high throughput'. In: *Nat. Methods* 17 (1 Jan. 2020), pp. 41–44. DOI: 10.1038/s41592-019-0638-x.

[5] Fengchao Yu et al. 'Analysis of DIA proteomics data using MSFragger-DIA and FragPipe computational platform'. In: *Nat. Commun.* 14 (1 12th July 2023), p. 4154. DOI: 10.1038/s41467-023-39869-5.

[6] Chih-Chiang Tsou et al. 'DIA-Umpire: comprehensive computational framework for data-independent acquisition proteomics'. In: *Nat. Methods* 12 (3 Mar. 2015), 258–64, 7 p following 264. DOI: 10.1038/nmeth.3255.

[7] Stefka Tyanova, Tikira Temu and Juergen Cox. 'The MaxQuant computational platform for mass spectrometry-based shotgun proteomics'. In: *Nat. Protoc.* 11 (12 Dec. 2016), pp. 2301–2319. DOI: 10.1038/nprot.2016.136.

[8] Pavel Sinitcyn et al. 'MaxDIA enables library-based and library-free data-independent acquisition proteomics'. In: *Nat. Biotechnol.* 39 (12 Dec. 2021), pp. 1563–1573. DOI: 10.1038/s41587-021-00968-7.

[9] Fengchao Yu, Sarah E Haynes and Alexey I Nesvizhskii. 'IonQuant enables accurate and sensitive label-free quantification with FDR-controlled match-between-runs'. In: *Mol. Cell. Proteomics* 20 (100077 2nd Apr. 2021), p. 100077. DOI: 10.1016/j.mcpro.2021.100077.

# C

# Supplementary: Molecular Solution to the Paradox of Ancient Brain Preservation

Morton-Hayward, A.L., Flannery, S., Berry, P., Vendrell, I.,
Johansen, A., Hansen, M., & Fischer, R.
*Molecular Solution to the Paradox of Ancient Brain Preservation.*
**J. Proteome Res. 2026**, *25*(7): 6c00200.
doi.org/10.1021/acs.jproteome.6c00200

## C.1 Co-Author Permissions

I, **Sarah Flannery**, hereby give permission to Alexandra L. Seviour (formerly Morton-Hayward) to use our joint work, *Molecular solution to the paradox of ancient brain preservation*, as a contribution towards her DPhil thesis, to be submitted for examination at the University of Oxford. I confirm that, to the best of my knowledge, the author contribution statement (Section 4.1) is accurate, and that Alexandra Seviour's overall contribution was greater than that of any other co-author.



Date: 16/03/2026

I, **Peter Berry**, hereby give permission to Alexandra L. Seviour (formerly Morton-Hayward) to use our joint work, *Molecular solution to the paradox of ancient*

*brain preservation*, as a contribution towards her DPhil thesis, to be submitted for examination at the University of Oxford. I confirm that, to the best of my knowledge, the author contribution statement (Section 4.1) is accurate, and that Alexandra Seviour's overall contribution was greater than that of any other co-author.



Date: 15/04/2026

I, **Iolanda Vendrell**, hereby give permission to Alexandra L. Seviour (formerly Morton-Hayward) to use our joint work, *Molecular solution to the paradox of ancient brain preservation*, as a contribution towards her DPhil thesis, to be submitted for examination at the University of Oxford. I confirm that, to the best of my knowledge, the author contribution statement (Section 4.1) is accurate, and that Alexandra Seviour's overall contribution was greater than that of any other co-author.



Date: 11/03/2026

I, **Anders Johansen**, hereby give permission to Alexandra L. Seviour (formerly Morton-Hayward) to use our joint work, *Molecular solution to the paradox of ancient brain preservation*, as a contribution towards her DPhil thesis, to be submitted for examination at the University of Oxford. I confirm that, to the best of my knowledge, the author contribution statement (Section 4.1) is accurate, and that Alexandra Seviour's overall contribution was greater than that of any other co-author.



Date: 12/03/2026

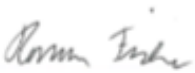
I, **Martin Hansen**, hereby give permission to Alexandra L. Seviour (formerly Morton-Hayward) to use our joint work, *Molecular solution to the paradox of ancient brain preservation*, as a contribution towards her DPhil thesis, to be submitted for

examination at the University of Oxford. I confirm that, to the best of my knowledge, the author contribution statement (Section 4.1) is accurate, and that Alexandra Seviour's overall contribution was greater than that of any other co-author.



Date: 11/03/2026

I, **Roman Fischer**, hereby give permission to Alexandra L. Seviour (formerly Morton-Hayward) to use our joint work, *Molecular solution to the paradox of ancient brain preservation*, as a contribution towards her DPhil thesis, to be submitted for examination at the University of Oxford. I confirm that, to the best of my knowledge, the author contribution statement (Section 4.1) is accurate, and that Alexandra Seviour's overall contribution was greater than that of any other co-author.



Date: 12/03/2026

## C.2 Results

The LC–MS/MS data have been deposited to the ProteomeXchange Consortium *via* the PRIDE [1] partner repository with the dataset identifier, PXD074190. Supplementary Data are available online: `doi.org/10.1021/acs.jproteome.6c00200`.

### C.2.1 Divergent taphonomic trajectories under oxic and hypoxic burial

The mean number of identified proteins decreased as decomposition progressed (Supplementary Data S1; Table C.1). The mean protein concentration at 72 hours (mean [SD] = 8.74 [0.79]µg/µL) was slightly higher than at 24 hours (8.64 [1.26]µg/µL; Figure C.1), which may reflect accumulation of degraded cellular and molecular components during early autolysis [2]; however, the difference was non-significant ($p = .817$). The number of proteins recovered declined over time (Figure C.3a), with

the highest mean at 24 hours ($n = 3,607$ [78]) and the lowest at six months ($n = 1,409$ [1,007]). The > 10-fold increase in SD between these two time points suggested increasing variation with advancing decay. Most unique proteins (69.6%, $n = 2,722/3,910$) were identified at every time point (Figure C.3b), but statistically significant differences were observed between 'early' (< six weeks) and 'late' (≥ six weeks) PMIs (Table C.2). Intersections spanning non-adjacent time points were rare (8.5%, $n = 7/82$; e.g., two proteins identified only at 72 hours and six months), indicating that sampling intervals were sufficient to resolve the majority of proteomic changes. Significant pairwise differences in protein recovery between burial environments were confined to comparisons involving the wet–oxic condition (Table C.3): this condition yielded the lowest mean number of proteins ($n = 2,231$ [1,411]) and the dry–hypoxic condition the highest ($n = 2,939$ [693]; Figure C.2a), yet almost all unique proteins were identified in every condition (93.8%, $n = 3,667/3,910$; Figure C.2b). Temporal profiles of each condition suggested an apparent 'pseudo-enrichment' of proteins at the latest PMI under hypoxia (Chapter IV, Figure 4.2a), with mean counts at six months approximately one-tenth higher than at three months (wet–hypoxic: mean [SD] = 2,024 [105] *vs.* 1,813 [80]; dry–hypoxic: 2,312 [374] *vs.* 2,048 [69]). Under oxia, the opposite pattern was observed: in dry–oxic conditions the mean at six months was approximately half that at three months (1,220 [967] *vs.* 2,346 [393]), whereas in wet–oxic samples it was an order of magnitude lower (81 [70] *vs.* 1,016 [503]).

Complementary ordination approaches further elucidated both the temporal shifts in proteomic profiles during decomposition, and the environmental factors shaping them. PCA demonstrated a clear separation between early and late PMIs (Chapter IV, Figure 4.2b), with decomposition progression (PC1) explaining almost three-quarters of the variation in the dataset (73.7%). Early time points (24 hours, 72 hours, and one week) clustered tightly, pointing to a relatively stable proteomic landscape, whereas late time points (six weeks, three months, and six months) were more dispersed, suggesting increased variability with advancing decay. UMAP recapitulated this temporal trend, and additionally highlighted the influence of

oxygen availability (Chapter IV, Figure 4.2c): at late PMI, oxic samples followed the continuous trajectory of early PMI samples, indicating a gradual proteomic shift, whereas hypoxic samples diverged into a distinct cluster, consistent with an alternate taphonomic trajectory. Correlation analysis with unsupervised hierarchical clustering corroborated these observations, splitting later PMIs into two major groupings by burial oxygenation (Chapter IV, Figure 4.2d): hypoxic samples evidenced strong within-group correlations (e.g., wet–hypoxic *vs.* dry–hypoxic at 6 months: $\rho_{mean} = 0.77$), whereas oxic samples were more variable (e.g., wet–oxic *vs.* dry–oxic at 6 months: $\rho_{mean} = 0.13$).

### C.2.2 *Post-mortem* shifts in brain proteome composition

Linear modelling with $k$-means and hierarchical clustering identified two major groups (Figure C.4). The first ($n = 1,886$) comprised proteins generally more abundant at early PMI in all conditions; the second ($n = 1,112$) evidenced a more complex pattern, with proteins in hypoxic conditions relatively more abundant at late PMI. These trends were confirmed by per-condition analyses (Figures C.5–C.8). GO enrichment of global $k$-means clusters revealed significant decay-associated shifts in biological process (Figure C.9), molecular function (Figure C.10), and cellular component (Figure C.11) terms. Proteins peaking at early PMI were characterised by mRNA- and translation-related processes (e.g., peptide biosynthesis, ribonucleoprotein complex biogenesis), with molecular functions reflecting (m)RNA binding, GTPase regulator activity, and structural constituents of the ribosome. Cellular component annotations were dominated by ribonucleoprotein assemblies, nuclear bodies, and chromosomal regions. By contrast, proteins peaking at late PMI were associated with energy and nucleotide metabolism (e.g., aerobic respiration, ATP metabolic process) and redox chemistry. Molecular functions centered on oxidoreductase (including peroxidase) activities, cytoskeletal protein binding, chaperone/heat-shock protein binding, and receptor binding. Cellular component terms localised to membrane protein complexes – particularly mitochondrial and organelle inner membranes – as well as neuronal structures (e.g., glutamatergic

synapse, axon, myelin sheath) and supramolecular fibres. Together, these results indicate a clear *post-mortem* progression from a relatively life-like, regulatory- and translation-focused intracellular proteome, to an enzyme-rich, membrane- and extracellular-associated proteome with advancing PMI.

### C.2.3 Environment-specific peptide decay trajectories and recalcitrance

The recalcitrance (i.e., decay resistance) of proteomic profiles was investigated by determining peptide-specific decay rates (Supplementary Data S2), which varied by experimental condition. No wet–oxic peptides met the quality criteria and were excluded from investigation; however, their low late-PMI abundance (detection frequency $< 90^{\text{th}}$ percentile) and high variability (SE $> 90^{\text{th}}$ percentile) were inconsistent with stability. Across other conditions, labile peptides decayed rapidly (mean slope [SD] $= -1.73 \times 10^{-2}$ [$7.08 \times 10^{-3}$]), losing approximately five $\log_2$ units of intensity (18.1–13.4) across the PMI (Chapter IV, Figure 4.3a). Peptides of putative preservation type exhibited a shallower decline, losing two $\log_2$ units during the same period ($16.4 - 14.4$). Recalcitrant peptides showed little net loss overall ($4.28 \times 10^{-3}$ [$5.36 \times 10^{-3}$]): in wet–hypoxic and dry–oxic conditions, their relative abundance increased with PMI ($3.47 \times 10^{-3}$ [$5.43 \times 10^{-3}$]), and in dry–hypoxic conditions, an initial modest decrease in intensity from early- to mid-PMI was followed by a rebound to levels exceeding those at 24 hours ($15.0 - 17.1$ $\log_2$ units). In wet–hypoxic samples, labile peptides exhibited an early phase of relative stability not evident in other conditions: segmented regression identified a breakpoint at approximately one week *post-mortem* ($\psi$ [SE] $= 0.84[0.44]$ $\log_{10}$ PMI, corresponding to 6.9 days), although uncertainty around the timing was considerable (95% CI $= 0.95 - 49.5$ days). Regardless of the precise moment of inflection, the slope before this breakpoint did not differ from zero (estimated slope $\pm$ SE $= -0.05 \pm 1.25$, $p = .97$), whereas after the breakpoint it became strongly negative ($-2.09 \pm 0.40$, $p = 1.28 \times 10^{-7}$), suggesting accelerated peptide loss. Thus, although the overall

stability hierarchy (labile $\ll$ putative $\ll$ recalcitrant) was conserved, peptide decay trajectories were modulated by burial environment.

Logistic regression was employed to estimate peptide-specific probabilities of recalcitrance, with bootstrap resampling ($n = 1000$) to assess calibration and overall fit (Figures C.12 and C.13). The calibration intercept was essentially zero (median [95% CI] = $-2.85 \times 10^{-16}$ [$-7.75 \times 10^{-15}$, $7.76 \times 10^{-15}$]) and the slope was unity (1.000 [1.000, 1.000]), indicating no systematic mis-, over-, or under-prediction. The median Brier score – measuring mean squared error of the predicted probabilities, and thus ideally zero – was 0.113 [0.110, 0.117], consistent with strong overall accuracy. Spiegelhalter's $Z$-statistic for perfect calibration was also essentially zero (median [95% CI] = $-3.32 \times 10^{-12}$ [$-1.67 \times 10^{-11}$, $-6.29 \times 10^{-13}$], $p = 1.00$), and the calibration plot (Chapter IV, Figure 4.3b) yielded a high coefficient of determination ($R^2 = 0.975$). The predicted probability distribution was strongly right-skewed (Chapter IV, Figure 4.3c): whereas half of all peptides (50.1%) had low recalcitrance probability ($P < 0.25$), a distinct peak at high probabilities ($P > 0.75$) pinpointed a subpopulation (19.6%) with strong preservation potential. Hypoxic peptides were enriched in this high-probability tail (mean $\geq 0.75 = 20.7\%$) compared to oxic peptides (13.6%; Chapter IV, Figure 4.3d).

### C.2.4 Environmental controls on recalcitrant peptide classes

Wet–hypoxic conditions yielded the largest pool ($n = 2,647$) and highest proportion (37.4%) of recalcitrant peptides, as well as the largest number identified in a single context ($n = 922$; Chapter IV, Figure 4.4a). Hypoxic samples evidenced the most extensive pairwise overlap ($n = 1,166$), almost four times the number identified exclusively in oxic samples ($n = 294$). Over-representation analysis indicated that the classes of proteins corresponding to recalcitrant peptides differed across water- and oxygen-availability regimes (Chapter IV, Figure 4.4b; Tables C.4–C.6). Although $> 90\%$ of proteins were identified in all conditions (Figure C.2b), only 414 peptides were recalcitrant in every burial environment: this shared set was enriched for oxidoreductases (mean FE = 2.88, $p = 5.57 \times 10^{-3}$), proteases (2.80,

$n = 5.87 \times 10^{-5}$), and metabolite interconversion enzymes (2.15, $p = 5.73 \times 10^{-6}$). Hypoxic conditions evidenced four times as many enriched classes as oxic conditions (12 *vs.* 3), with the strongest enrichment for peroxidases (7.74, $p = 1.61 \times 10^{-2}$), followed by calcium-binding proteins (5.24, $p = 1.18 \times 10^{-4}$), and metalloproteases (4.79, $p = 2.37 \times 10^{-6}$).

### C.2.5 Physicochemical, sequence, and structural predictors of peptide recalcitrance

A range of physicochemical properties were investigated as potential correlates of peptide decay resistance. In terms of hydropathy, all preservation types exhibited negative mean GRAVY scores, indicative of hydrophilicity (Figure C.14); under hypoxia, however, labile peptides were slightly more hydrophobic than recalcitrant peptides in wet conditions (mean [SD] = −0.26 [0.70], $p = 2.16 \times 10^{-2}$), but more hydrophilic in dry conditions (−0.34 [0.72], $p = 4.36 \times 10^{-4}$). Despite these pairwise differences reaching statistical significance, effect sizes were negligible (mean $\eta^2_H = 0.003$; Table C.7), indicating that decay resistance accounted for little variation in hydropathy. No significant differences between preservation types were detected in terms of net charge (Table C.8) or isoelectric point (Table C.9).

Peptide-recovery metrics also exhibited limited discriminatory power. Mean peptide length and protein sequence coverage differed only weakly between preservation types ($p \leq 10^{-2}$; Table C.10). Putative peptides had marginally shorter mean chain lengths (mean [SD] = 13.9 [4.7] amino acids) than labile (14.3 [4.2], $p = 1.86 \times 10^{-2}$) and recalcitrant peptides (14.4 [4.8], $p = .394$), but labile and recalcitrant peptides did not differ ($p = .208$), and all pairwise effect sizes were negligible ($\delta < 0.002$). Putative peptides also exhibited lower mean sequence coverage (9.2%) than labile (11.4%, $p = 2.38 \times 10^{-4}$) and recalcitrant peptides (12.3%, $p = 7.94 \times 10^{-4}$), which again did not differ from one another other ($p = 1.00$), with an overall negligible effect ($\eta^2_H = 0.006$). When analyses were stratified by burial environment (Tables C.11–C.12), wet–oxic conditions yielded the strongest contrast between labile and recalcitrant peptides (mean peptide length:

$p = 1.60 \times 10^{-4}$; sequence coverage: $p = 6.26 \times 10^{-10}$), with recalcitrant peptides evidencing the highest coverage (Figure C.15a) with a long right-tailed distribution (Figure C.15b). However, effect sizes remained small ($\delta < 0.039$), and cumulative distribution curves converged rapidly across preservation types and conditions (Figure C.15c), with only minor divergence at low coverage, consistent with small effect sizes despite statistically significant contrasts.

Primary structure, however, differed markedly between preservation types (Chapter IV, Figure 4.4c). Recalcitrant peptides were strongly enriched for Trp ($\log_2$FC = 0.476, $p = 2.12 \times 10^{-55}$), Tyr (0.181, $4.55 \times 10^{-29}$), and Met (0.161, $1.17 \times 10^{-13}$); relatively enriched in Gly (0.123, $2.02 \times 10^{-26}$) and Pro (0.084, $4.16 \times 10^{-9}$); and modestly enriched for Ser (0.043, $2.74 \times 10^{-4}$), Thr (0.028, $2.42 \times 10^{-2}$), and Lys (0.043, $5.75 \times 10^{-5}$). Recalcitrant peptides were strongly depleted in Gln (–0.222, $4.27 \times 10^{-53}$) and His (–0.198, $1.67 \times 10^{-17}$), and modestly depleted in Phe (–0.088, $3.31 \times 10^{-9}$), Ala (–0.075, $8.78 \times 10^{-11}$), Ile (–0.069, $1.84 \times 10^{-8}$), Val (–0.028, $1.40 \times 10^{-2}$), and Glu (–0.030, $5.57 \times 10^{-3}$).

To assess whether these differences reflected site-specific biases near peptide ends, the analysis was repeated by position at peptide termini (Chapter IV, Figure 4.4d). At the N-terminus (N1), recalcitrant peptides were enriched in Glu ($\log_2$FC = 0.008, $p = 4.77 \times 10^{-4}$) and Trp (0.005, $3.87 \times 10^{-10}$), and depleted in Gln (–0.006, $7.78 \times 10^{-6}$) and Lys (–0.007, $1.04 \times 10^{-7}$). N2 evidenced enrichment of Thr (0.015, $1.26 \times 10^{-17}$), Tyr (0.014, $3.62 \times 10^{-23}$), and Glu (0.116, $1.47 \times 10^{-10}$), with depletion of Ala (–0.020, $1.75 \times 10^{-23}$). N3 was enriched for Gly (0.015, $6.07 \times 10^{-14}$), Thr (0.007, $5.11 \times 10^{-5}$), Pro (0.007, $5.69 \times 10^{-5}$) and Tyr (0.007, $4.19 \times 10^{-6}$), and evidenced depletion of Asp (–0.019, $3.79 \times 10^{-19}$) and Ile (–0.010, $2.94 \times 10^{-7}$). The C-terminus (C1) of recalcitrant peptides was dominated by Lys (0.018, $6.07 \times 10^{-6}$) and depleted in Arg (–0.018, $6.07 \times 10^{-6}$), consistent with tryptic termini. C2 evidenced enrichment of Gly (0.016, $9.69 \times 10^{-16}$), Pro (0.009, $9.04 \times 10^{-10}$), Met (0.007, $5.53 \times 10^{-10}$), and Ala (0.007, $6.98 \times 10^{-4}$), and depletion of Gln (–0.008, $1.42 \times 10^{-6}$). C3 evidenced enrichment of Asp (0.015, $1.89 \times 10^{-17}$), Tyr (0.008, $1.82 \times 10^{-8}$), Pro (0.005, $5.94 \times 10^{-4}$), and Met (0.005,

$1.86 \times 10^{-5}$), and depletion of Leu (–0.016, $3.34 \times 10^{-10}$). Positional $\log_2$-fold changes were small but reproducible ($n = 77,508$ peptides), indicating subtle, site-specific primary-structure biases associated with decay resistance.

Secondary structure differed substantially between preservation categories (chi-squared association: $\chi^2[4] = 741.83$, $p = 3.06 \times 10^{-159}$). 57.8% of labile peptides were $\alpha$-helix-dominant (standardised residuals, $|r| = +26.80$) and 40.8% $\beta$-sheet-dominant (–26.22). Conversely, recalcitrant peptides were enriched in $\beta$-sheets (50.2%, +20.58) and depleted in $\alpha$-helices (48.3%, –20.44). Coil-dominant peptides were rare in both groups (recalcitrant: 1.5%, –0.38; labile: 1.4%, –2.58). Logistic regression of peptide recalcitrance as a function of secondary-structure composition, mean residue-level confidence scores (by means of predicted local distance difference testing [pLDDT]), and peptide length ($\beta$-sheet as reference; $n_{obs} = 96,768$) confirmed a strong negative association of $\alpha$-helical content with recalcitrance (coefficient $\pm$ SE $= -0.539 \pm 0.025$, $p = 1.91 \times 10^{-106}$), a weaker negative effect of peptide length ($0.027 \pm 0.002$, $1.05 \times 10^{-38}$), and a strong positive effect of mean pLDDT ($0.027 \pm 0.001$, $1.96 \times 10^{-190}$). Coil fraction exhibited a weak positive effect ($0.186 \pm 0.070$, $7.86 \times 10^{-3}$) that became non-significant when restricting to high-confidence predictions (mean pLDDT $> 70$). All other effects persisted after controlling for model confidence and sampling noise (Table C.13). Kruskal–Wallis tests likewise indicated that the $\alpha$-helix and $\beta$-sheet weighted fractions and mean pLDDT differed significantly between labile and recalcitrant peptides in every burial condition ($p \leq 10^{-6}$; Tables C.14–C.16). Together, these analyses indicated that peptides with higher $\alpha$-helical content (and, to a lesser extent, greater length) are less likely to persist, whereas those with higher $\beta$-sheet content and greater predicted structural confidence are most strongly associated with *post-mortem* stability.

Although 97% of all peptides exhibited high predicted model confidence (mean pLDDT $\geq 70$; $n = 87,588$), recalcitrant peptides evidenced significantly higher scores (mean pLDDT [SD]: 93.4 [7.5]) than either putative (92.0 [9.1], $p = 2.44 \times 10^{-62}$) or labile (91.4 [9.5], $p = 5.30 \times 10^{-284}$) peptides, suggestive of greater predicted

structural order. To assess whether this difference in pLDDT corresponded to differences in intrinsic disorder, peptide-level mean IUPred scores were compared among preservation categories. Median scores were low ($< 0.170$) across all categories, consistent with an overall predominance of ordered structure, but recalcitrant peptides evidenced significantly lower mean disorder (mean [SD] = 0.222 [0.170]) than putative (0.240 [0.186], $p = 7.27 \times 10^{-17}$) and labile peptides (0.244 [0.184], $p = 2.64 \times 10^{-71}$; Table C.17). When stratified by environment, the labile–recalcitrant separation in disorder was present under hypoxia ($p \leq 10^{-13}$) but not in the oxic treatment ($p = .742$; Table C.18), suggesting that peptide recalcitrance was associated with lower predicted disorder only under low-oxygen conditions. Analyses of the fraction of residues exceeding the disorder threshold ($\geq 0.5$) yielded congruent results (Table C.19), indicating that these findings were robust to how disorder propensity was summarised.

### C.2.6 Protein topology, domains, and modifications associated with recalcitrance

Peptide features also differed between preservation categories. At broad annotation levels, nearly all UniProt features evidenced significant associations ($p \leq 10^{-3}$; Tables C.20 and C.21), but effect sizes were small overall (Cramér's $V < 0.10$), indicating widespread but modest biases across protein topology, domains, regions, and PTMs. Descriptor-level analyses were performed on UniProt features meeting a minimum observation threshold ($n = 72$; Supplementary Data S3): although many associations were nominally significant (a consequence of the large sample size; $n_{obs} = 215,088$), a restricted subset ($n = 18$) exhibited large and statistically robust effects ($p \leq 10^{-6}$, $V \geq 0.10$, odds ratio [OR] $\geq 2$). Extracellular domains were three-fold enriched in recalcitrant peptides ($n = 8,724$, $p = 5.47 \times 10^{-260}$, $V = 0.28$, OR = 3.42), whereas cytoplasmic and mitochondrial domains were three-fold enriched in labile peptides (cytoplasmic: $n = 3,642$, $p = 2.82 \times 10^{-193}$, $V = 0.24$, OR = 3.08; mitochondrial matrix: $n = 708$, $p = 9.19 \times 10^{-41}$, $V = 0.11$, OR = 2.77). Calcium-dependent phospholipid-binding domains evidenced the

largest domain-level differences, being approximately four- to 16-fold more common in recalcitrant than labile peptides (C2: $n = 354$, $p = 2.11 \times 10^{-50}$, $V = 0.10$, OR = 6.08; C2 1: $n = 258$, $p = 1.35 \times 10^{-20}$, $V = 0.06$, OR = 3.77; C2 2: $n = 342$, $p = 3.31 \times 10^{-87}$, $V = 0.13$, OR = 15.68).

Finally, protein modification was investigated by estimating ORs for a given PTM at late PMI relative to early PMI (Figure C.16). In wet–oxic conditions – those least conducive to preservation – the odds of oxidative replacement of a methylene group (O–$CH_2$, +1.98 Da) were nearly six times higher at late PMI (mean OR [95% CI] = 5.67 [1.56, 20.64]), and those of $C_2H_3NO$ alkylation (+57.02 Da) were more than four times higher (4.09 [1.44, 11.6]). The odds of methylation (+14.02 Da) were also elevated (2.42 [1.60, 3.65]), whereas those of sodium ($Na^+$, +21.98 Da) and calcium adduction ($Ca^{2+}$, +37.95 Da) were decreased ($Na^+$: 0.62 [0.51, 0.76]; $Ca^{2+}$: 0.60 [0.41, 0.90]). Sodium adduction also exhibited reduced odds at late PMI in wet–hypoxic conditions, whereas the odds of Trp-to-kynurenine conversion (+4.00 Da) were almost three-fold higher (2.82 [1.45, 5.50]). In dry–hypoxic conditions, the odds of di-oxidation (+31.99 Da) were approximately twice as high at late PMI (2.04 [1.44, 2.89]), with two-thirds of all di-oxidation events (66.1%, $n = 37/56$) localised to Trp.

# C.3 Discussion

## C.3.1 Role of water in enabling radical-mediated oxidative crosslinking under hypoxia

Water availability appears to be a necessary co-determinant of the taphonomic trajectory identified here. In biological tissues, oxidative radical chemistry and subsequent crosslinking typically occur in aqueous media, such as the cellular environment [3]. More generally, the initiation, propagation, and termination of radical processes depend on proton-coupled electron transfer, metal coordination, and short-range molecular mobility [4]: these requirements are expected to be attenuated as water availability decreases, given dehydration suppresses the local transport and solvent-mediated interactions that facilitate the formation, persistence,

and encounter with suitable reaction partners of reactive species on relevant timescales [5, 6].

Crucially, water and oxygen availability together can influence whether oxidation proceeds as a chain-propagating process that progressively accumulates damage, or as a self-limiting sequence of local initiation–termination events (Table C.22). Aqueous environments can sustain limited oxidative chemistry even when oxygen is restricted [3]: residual dissolved oxygen, endogenous peroxides, and metal-mediated redox cycling (e.g., $Fe^{2+}/Fe^{3+}$ interconversion [7]) can persist in water and generate short-lived radical intermediates capable of oxidising redox-active residues such as Trp, Tyr, and Met [8]. When oxygen availability is low, however, radical oxidation is less likely to proceed efficiently *via* oxygen-dependent chain propagation [9]. Under such conditions, oxidation is more likely to take the form of spatially localised radical events whose dominant fate is termination, either by electron transfer to nearby sinks [8] or by covalent coupling with nearby reactive groups [10].

Water also modulates this balance between stabilising and destructive oxidation by controlling oxygen transport. In waterlogged substrates, oxygen diffusion is orders of magnitude slower than in air, promoting steep redox gradients and localised depletion [11]; such conditions would be expected to further suppress sustained chain propagation, which requires continuous access to molecular oxygen, and to favour isolated initiation–termination events [9]. By contrast, in wet–oxic environments, continued radical regeneration and peroxyl-radical formation are more readily sustained [3], increasing the likelihood of secondary reactions (such as backbone cleavage) that promote more widespread molecular loss [8]. Together, these considerations are consistent with wet–hypoxic environments occupying an intermediate chemical regime in which oxidation is neither fully absent, nor catastrophically destructive.

In addition to enabling redox chemistry, water supports limited conformational flexibility and local molecular rearrangement [5]. Partial hydration can permit side-chain reorientation and transient exposure of reactive groups [12], increasing the likelihood of encounter between short-lived radical intermediates and suitable

coupling partners; in fully desiccated systems, however, such mobility is strongly suppressed [6]. In fully hydrated but oxygenated systems, radical lifetimes and effective chain length can be extended by continuous regeneration, favouring diffusion, interception by quenchers, and chain-propagating oxidation [3]. In fully hydrated but hypoxic systems, molecular mobility would be expected to facilitate radical termination by coupling [10], and low oxygen to limit propagation and promote local stabilisation [9].

Taken together, these considerations suggest that water is not merely permissive, but likely mechanistically important for the taphonomic trajectory described here. Radical-mediated oxidative crosslinking is most plausibly supported by an aqueous phase that enables redox cycling, molecular encounter, and termination by coupling, while low oxygen availability restricts escalation into chain-propagating fragmentation. The selective preservation of brain tissue in waterlogged, oxygen-poor environments may therefore reflect a chemically constrained regime in which hydration permits radical chemistry, while hypoxia prevents its escalation into wholesale molecular loss.

### C.3.2 Role of reactive residues in radical-mediated oxidative crosslinking

The enrichment of Trp, Tyr, and Met in recalcitrant peptides is chemically consistent with their redox activity, and their propensity to form relatively stable oxidation products and radicals capable of secondary reactions, including radical-mediated oxidative crosslinking (Table C.23). These residues are readily oxidised because their side chains contain high-electron-density functional groups – the indole ring of Trp, the phenolic ring of Tyr, and the thioether group of Met – with low ionisation potentials that facilitate electron donation to ROS [13, 14]. The ensuing oxidation products, however, tend to promote stabilisation rather than fragmentation [10, 15]. Trp, with its conjugated indole system, undergoes stepwise one-electron oxidations yielding indoxyl, kynurenine, and quinonoid intermediates [16] that act as radical sinks, and can couple to neighbouring aromatic or carbonyl groups to

form crosslinks and other stable adducts [17]. The almost three-fold increased odds of Trp-to-kynurenine conversion at late PMI under waterlogged, hypoxic burial conditions is consistent with preservation *via* Trp-centred oxidation pathways that generate comparatively stable products and long-lived radical intermediates.

Tyr's phenolic oxygen stabilises tyrosyl radicals by delocalisation over the aromatic ring, forming dityrosine and higher-order crosslinks [18, 19] that are chemically robust, hindering enzymatic cleavage [20] and accumulating as markers of oxidative ageing [21, 22]. Met is easily oxidised because the sulfur atom's lone pairs participate in soft electrophilic interactions, forming sulfoxides or sulfones [23]; *post-mortem*, these reactions allow Met to act as a sacrificial redox buffer [24, 25] that can modulate local radical availability. Transient sulfoxides can also generate thiyl radicals that might participate in secondary oxidative crosslinking with aromatic or carbonyl moieties [26]. Collectively, these reactions provide a plausible route by which oxidative energy is dissipated into radical quenching and oxidative crosslinking, increasing resistance to proteolysis and thereby favouring preservation.

Structural evidence supports this interpretation. Met–aromatic motifs are widespread in oxidoreductases, where Met, Trp, and Tyr cluster in defined geometries around redox-active metal centres [27, 28]. *In vivo*, these motifs mediate electron transfer and regulate controlled oxidation [13]; *ex vivo*, analogous geometries may instead promote intra- and intermolecular radical chemistry, increasing the probability of oxidative crosslinking when reactive side chains are exposed by partial degradation, and reaction products have accumulated locally (e.g., within partially unfolded and diffusion-limited microenvironments). The prevalence of oxidoreductases and peroxidases among recalcitrant peptides is consistent with this model, as these classes are both metal-associated and structurally enriched in redox-active residues.

By contrast, residues depleted in recalcitrant peptides are chemically disposed either to destructive oxidation, or to inertness that disfavours stabilising reactions. The imidazole ring of His co-ordinates transition metals such as $Fe^{2+}$ and $Cu^{2+}$, catalysing Fenton-like reactions that generate hydroxyl radicals [29]; these oxidise

His to 2-oxo-histidine or ring-cleaved imidazolone derivatives [30], promoting peptide scission. Gln deamidates by direct hydrolysis in acidic conditions, and *via* cyclic imide intermediates in neutral or alkaline conditions [31]; the process converts a neutral amide into a negatively-charged carboxyl group, increasing solubility and susceptibility to hydrolytic cleavage. Phe, though aromatic, lacks heteroatoms capable of stabilising radicals and therefore does not readily support crosslink formation analogous to Trp and Tyr [32]. Small aliphatic residues (Ala, Val, Ile) undergo slow oxidation *via* peroxyl-radical intermediates, yielding unstable hydroperoxides [33] that decompose by $\beta$-scission to RCS and other fragments [34]. Their under-representation in recalcitrant peptides likely reflects both this vulnerability to fragmentation, and their limited capacity for the oxidative crosslinking that stabilises surviving peptides.

## C.4 Methods

### C.4.1 Experimental taphonomy

All experimental procedures complied with the Danish Animal Experimentation Inspectorate (2020-15-0201-00432), and ethical approval was obtained from the Central University Research Ethics Committee at the University of Oxford (R80617/RE001). Male, specific pathogen-free mice ($n = 72$; C57BL/6JRj, Janvier Laboratories) were reared and sacrificed under identical conditions for the purposes of other scientific research [35], and were donated to our study. Mice were weaned 25 d after birth, then fed on a low-fat defined control diet (D12328, Research Diets, Inc.), with body weight measured weekly. Mice were maintained in individually ventilated cages at 22 ± 1 °C on a standard 12 h light–dark cycle with *ad libitum* access to water and food. Mice were euthanised five months after birth by sedation with inhalation of isoflurane followed by cervical dislocation. Immediately after death, whole carcasses were flash-frozen in liquid $N_2$ and stored at −80 °C. Immediately prior to beginning the decay experiment, carcasses were allowed to thaw to 20 °C over the course of approximately 2 h.

*C. Supplementary: Molecular Solution to the Paradox of Ancient Brain Preservation*

All equipment underwent dry heat sterilisation at 160 °C overnight prior to use. For each carcass, 500 g of inert quartz sand (210–297 µg granularity; Sigma–Aldrich), hereafter referred to as 'matrix', was measured into a glass beaker using a mass balance. A 500 mL glass Kilner jar was filled with approximately 200 g of matrix, and a strip of nylon mesh (50–100 µm pore size; Streno), cut to approximately 15 cm × 30 cm with sterile scissors, was laid over the 200 g of matrix within the jar. The carcass was placed in the centre of the nylon strip perpendicular to its length, with the rostral aspect of the body oriented toward the lock of the jar to facilitate discriminating the head region during advanced decay. The remaining 300 g of matrix was poured into the jar to completely cover the carcass. The ends of the nylon strip were exposed above the surface to facilitate removing the carcass during sampling.

Four experimental conditions were created to mimic degrees of waterlogging and oxygenation: wet–oxic (HWHO), wet–hypoxic (HWLO), dry–oxic (LWHO), and dry–hypoxic (LWLO). Three mice (designated replicates A, B, and C) were decayed in each of the four conditions at each of six time points – 24 hours ($T_1$), 72 hours ($T_2$), one week ($T_3$), six weeks ($T_4$), three months ($T_5$) and six months ($T_6$) – for a total of 12 mice at each time point. It should be noted that, in an ideal longitudinal experiment, one would sample the brain of a single individual at each time point (i.e., one carcass six times); however, this would necessitate repetitive exhumation and reburial, disturbing both the decaying tissues and the microenvironment, and introduce additional sources of variation. Given every effort was made to minimise interindividual variation in animal samples, coupled with our triplication of each condition, it was determined that exhuming an individual at every time point (i.e., sampling six carcasses once) was likely a more robust experimental design.

To determine the volume of water appropriate for wet and dry conditions, a test Kilner jar with 500 g of matrix was filled slowly with ultrapure Milli-Q® $H_2O$ (Sigma–Aldrich) until a layer of clear water (> 5 mm) was established above the surface, simulating waterlogged burial contexts. The amount of water used was measured and determined to be 180 mL. Thus, 180 mL of Milli-Q® $H_2O$ was used for wet conditions, and half this volume (90 mL) for dry conditions. Oxic conditions (i.e.,

with atmospheric exchange and oxygen replenishment) were simulated by leaving the lid of the jar open, allowing air to circulate; hypoxic conditions (i.e., without atmospheric exchange and oxygen replenishment) were simulated by fastening the lid of the jar, and an airtight seal ensured by the use of a silicon gasket. All jars ($n = 72$) were placed together in a fume hood with controlled temperature (20 °C), ambient laboratory lighting, and air circulation. Water levels were monitored at each time point by comparing the mass of the dry jars with the equivalent wet jars, and the mass difference ($\Delta$M, accounted for by the loss of water) determined. No difference was observed at $T_1$, $T_2$, or $T_3$. At $T_4$, the $\Delta$M was determined to be 140 g between wet–oxic and wet–hypoxic conditions, and 100 g between dry–oxic and dry–hypoxic conditions; thus, 140 mL of Milli-Q® $H_2O$ was added to each of the remaining replicates in the wet–oxic condition, and 100 mL Milli-Q® $H_2O$ to each of the replicates in the dry–oxic condition. At $T_5$, the $\Delta$M was determined to be 200 g between wet–oxic and wet–hypoxic conditions, and 100 g between dry–oxic and dry–hypoxic conditions; thus, 200 mL of Milli-Q® $H_2O$ was added to each of the remaining replicates in the wet–oxic condition, and 100 mL Milli-Q® $H_2O$ to replicates in the dry–oxic condition.

Sterile, single-use, disposable equipment (e.g., scalpel blades, petri dishes) were used for sampling wherever possible. All non-disposable surgical equipment (e.g., scissors, spatulae) underwent dry heat sterilisation at 160 °C overnight prior to use, and were treated with 70% ethanol prior to and immediately after each use. At each time point, 12 jars (replicates A, B, and C for each of the four experimental conditions) were removed from the fume hood. The carcass was removed from the jar by carefully lifting out the nylon strip. Matrix was loosened to expose the carcass with minimal disturbance. Using large scissors, the carcass was decapitated caudal to the skull (at the level of the cervical vertebrae) and the head placed on a petri dish. Using fine scissors, the skin of the scalp was incised toward the snout and peeled apart and forward to expose the skull, which was cut along the midline. Holding the head steady by the snout, the two halves of the skull were pulled apart with fine tweezers to expose the brain. The brain was removed from the

endocranial cavity using a spatula, briefly homogenised by mechanical action, and divided evenly into five samples of approximately 80 mg each. The five sample sets ($n = 360$) were collected in 0.5 mL Eppendorf Safe-Lock® tubes (Thermo Fisher Scientific), immediately flash-frozen in liquid $N_2$, and stored at −80 °C.

## C.4.2 Proteomics

### C.4.2.1 Data-dependent acquisition

Samples for DDA ($n = 72$) were lysed in 100 mM ambic (Sigma–Aldrich) with 2% SDS (Sigma–Aldrich) and 1× Halt™ protease inhibitor cocktail (Thermo Fisher Scientific), using a Precellys® 24 Touch homogeniser (Bertin Technologies) for 12 cycles of 15 s at 5,500 rpm, followed by one cycle of 30 s at 5,500 rpm. Samples were placed on ice between cycles to reduce heating. Protein concentration was estimated using BCA assay with bovine serum albumin (BSA) standards (Table C.24). 2.5 µg of protein from each sample was diluted to a total volume of 40 µL using 50 mM ambic, and added to a 96-well plate. Cys reduction was performed at 60 °C and 1,000 rpm for 10 min with 4 mM DTT solution. Alkylation was performed in the dark at 20 °C for 30 min with 10 mM IAA. Each sample was combined with 40 ng SP3 beads (1:1 hydrophobic:hydrophilic) [36] and ACN added to a final concentration of 80%. The solution was gently mixed by pipetting and incubated at 20 °C and 1,000 rpm for 30 min. The plate was placed on a magnetic rack and the beads allowed to settle for 5 min, before three washes with 100% ACN. Beads were resuspended in 100 mM ambic, and the plate sonicated at 4 °C for 2 min. Digestion was performed with 0.2 µg/µL trypsin (MS-grade, Promega) at 37 °C and 1,000 rpm overnight. Each sample was acidified with TFA to 1%, and incubated at 37 °C without shaking for 30 min, followed by 30 min on ice. Eluted peptides were dried by vacuum centrifugation at 30 °C for storage at −20 °C prior to analysis.

LC–MS/MS was performed on a Dionex UltiMate™ 3000 Rapid Separation LC system coupled to a Q Exactive™ Plus Hybrid Quadrupole-Orbitrap™ mass spectrometer (both Thermo Fisher Scientific). To determine injection volumes (target base peak intensity [BPI]: $1–2 \times 10^8$), survey runs of 15 min gradient (30 min

program) were performed on each sample; based on the BPI obtained, the final injection volume of samples varied between 4–15 µL. The sample was loaded onto an Acclaim™ PepMap™ 100 C18 HPLC cartridge (5 mm × 300 µm) using partial loop injection for 7 min at a flow rate of 12 µL/min with 0.1% (v/v) TFA, and resolved on an EASY-Spray™ PepMap™ C18 HPLC column (500 mm × 75 µm, both Thermo Fisher Scientific) using a 90 min linear gradient of 96.2% buffer A (0.1% FA) and 3.8% buffer B (80% ACN, 19.9% $H_2O$, 0.1% FA), to 50% A to 50% B at 300 nL/min flow rate. In DDA mode, MS1 spectra were acquired in the Orbitrap™ at 70K resolution between 300–2000 $m/z$, with an AGC target of $1 \times 10^6$ ions, and a maximum injection time of 250 ms. Precursor ions associated with the five most abundant peaks were fragmented using HCD with 30% NCE. MS2 spectra were acquired at 35K resolution with a quad isolation window of 2.0 Da and a maximum injection time of 300 ms, and a 20 s dynamic exclusion window to avoid repeated selection of precursors for MS2.

#### C.4.2.2 Data-independent acquisition

Samples for DIA ($n = 72$) were lysed in Pierce® RIPA buffer (Thermo Fisher Scientific), using a Precellys® 24 Touch homogeniser (Bertin Technologies) for three cycles of 45 s at 5,000 rpm. Samples were placed on ice between cycles to reduce heating. Protein concentration was estimated using BCA assay with BSA standards (Table C.25). 10 µg of protein from each sample was diluted to a total volume of 15 µL using RIPA buffer, and added to a 96-well plate. Cys reduction was performed at 60 °C and 1,000 rpm for 10 min with 5 mM DTT solution. Alkylation was performed in the dark at 20 °C for 30 min with 20 mM IAA. Each sample was combined with 2 µL SP3 beads (1:1 hydrophobic:hydrophilic) and ACN added to a final concentration of 70%. The solution was gently mixed by pipetting and incubated at 20 °C and 1,000 rpm for 18 min. The plate was placed on a magnetic rack and the beads allowed to settle for 5 min, before two washes with 70% ethanol and two washes with 100% ACN. Beads were resuspended in 50 mM ambic, and digestion performed with 8 ng/µL trypsin (MS-grade, Promega) at 37 °C and

1,000 rpm overnight. Each sample was acidified with TFA to 1%. Eluted peptides were dried by vacuum centrifugation at 30 °C for storage at −20 °C prior to analysis.

LC–MS/MS was performed on a TimsTOF Pro mass spectrometer (Bruker) equipped with trapped ion mobility spectrometry (TIMS). Peptides were reconstituted in 0.1% FA and an estimated 200 ng loaded onto Evotips (Evosep Biosystems) according to the manufacturer's instructions, then chromatographically separated on an Evosep One (Evosep Biosystems) using the 60 spd standard method. Peptides were eluted onto the TimsTOF Pro, which was operated in parallel accumulation–serial fragmentation combined with DIA (diaPASEF) mode [37] with eight diaPASEF scans per TIMS–MS scan. The ion mobility range ($1/K_0$) was set to 0.64–1.41 V s/cm$^2$. Each mass window isolated was 25 $m/z$ wide, ranging from 475–1000 $m/z$ with an ion mobility-dependent collision energy that increased linearly from 20 eV to 59 eV between 0.6–1.6 V s/cm$^2$. All LC–MS/MS data have been deposited to the ProteomeXchange Consortium *via* the PRIDE [1] partner repository with the dataset identifier, PXD074190.

## C.4.3 Data analysis

### C.4.3.1 Protein identification

Both DDA and DIA raw data files ($n = 144$) were searched against the *Mus musculus* brain proteome retrieved from Korovesi *et al.* [38]. Mapping one-protein-per-gene identified in normal mouse brain regions and having removed duplicates (i.e., those expressed in more than one region), 6,252 proteins remained corresponding to the mouse brain proteome, which were downloaded as a FASTA file. In all cases, data were searched against this FASTA with semi-specific tryptic digestion and the fixed modification of carbamidomethylation of Cys, and the following variable PTMs: oxidation of Met and Pro; deamidation of Asn, Gln, and Arg; and protein N-terminal acetylation.

A search of DDA raw data files ($n = 72$) based on *in silico* FASTA digest with LFQ–MBR in MaxQuant (v.2.4.3.0) [39] yielded the fewest unique proteins identified at 1% FDR, but the most information in terms of protein modification.

Search criteria included a first, fully tryptic search with up to three missed cleavages allowed [40] and a peptide tolerance of 20 ppm, followed by a main, semi-specific tryptic search and a peptide tolerance of 4.5 ppm, followed by a final dependent peptide search for covalently-modified peptides. All subsequent analyses were performed on the DDA dataset using the R programming language (v.2026.01.0) [41]: global peptide and protein lists were removed of potential contaminants, reversed identifications, and identifications with $< 2$ unique peptides, then filtered for $q$-value and PEP $\leq 0.01$. Modified specific and dependent peptide lists were removed of unannotated modifications and those corresponding to $< 2$ unique peptides, then filtered for $q$-value and PEP $\leq 0.05$.

A library-free search of all DIA raw data files ($n = 72$) was performed with DIA-NN (v.2.0) [42]. Search criteria included a semi-specific tryptic search with one missed cleavage and up to three variable PTMs allowed, and both a mass and MS1 accuracy of 15 ppm. All subsequent analyses were performed on the DIA dataset using R (v.2026.01.1) [41]. Precursors were filtered using the following parameters: precursor $q$-value $\leq 0.01$, protein $q$-value $\leq 0.01$, and protein- and gene-group $q$-values $\leq 1$. Peptides and protein groups were filtered with the same parameters, and removed of potential contaminants, reversed identifications, and identifications with $< 2$ unique peptides. Data were preprocessed using `DIAgui` (v.1.4.2) [43], which integrates the `iq` package (v.1.9.12) [44] to perform proteome-wide LFQ *via* delayed normalisation and maximal peptide ratio extraction (*aka.* MaxLFQ) [45], and the `imputeLCMD` package (v.2.1.0) for missing value imputation *via* QRILC [46, 47]. Precursors were filtered using the following parameters: precursor $q$-value $\leq 0.01$, protein $q$-value $\leq 0.01$, and protein- and gene-group $q$-values $\leq 1$. Peptides and protein groups were filtered with the same parameters, and removed of potential contaminants, reversed identifications, and identifications with $< 2$ unique peptides. Protein intensities were summarised as iBAQ values at the protein-group level; calculated as the sum of peptide intensities divided by the number of theoretically-observable tryptic peptides per protein [48]. This length-normalised metric constitutes a proxy for molar protein abundance and reduces the

dependence of raw LFQ intensities on protein size. Given the aim of the DIA analysis was to characterise shifts in the composition of the brain proteome and to compare the relative representation of protein classes across PMIs and burial environments, $\log_2$-transformed iBAQ values were used for ordination, differential expression analysis (DEA), and downstream clustering, while peptide-level analyses of decay trajectories were performed separately on peptide intensities. $\text{Log}_2$ transformation was used to stabilise variance and facilitate interpretation of abundance differences and decay slopes in terms of fold change. Batch effects associated with MS run were corrected using the `sva` package (v.3.2.1) [49] *via* the ComBat algorithm. All subsequent analyses were performed on the DIA dataset, unless otherwise stated.

#### C.4.3.2 Ordination and differential expression analysis

PCA and UMAP were conducted on the $\log_2$-transformed iBAQ intensity matrix with the `factoextra` (v.3.1.2) [50] and `uwot` packages (v.0.2.3) [51], respectively. Prior to analysis, protein abundances were mean-centred and scaled to unit variance (i.e., $z$-scored per protein across samples). PCA employed a covariance-based approach, while UMAP was implemented with 10 nearest neighbours, a minimum distance of 0.05, and a cosine similarity metric, using a fixed random seed to ensure reproducibility. Based on the results of dimension reduction, PMI was divided into two periods corresponding to 'early' ($< 6$ weeks) and 'late' ($\geq 6$ weeks) decay. DEA was performed using the `limma` package (v.3.2.1) [52]: iBAQ data were modelled using a design matrix with additive main effects for experimental condition and PMI. Empirical-Bayes-moderated statistics were computed, and proteins considered differentially expressed for PMI if FDR-adjusted $p < 0.05$ and $\log_2\text{FC} > 1$ (coefficient: late PMI). Significant proteins were standardised by per-protein $z$-scoring across samples, and clustered by $k$-means: the elbow and average silhouette width were inspected for $k = 1 - 10$, and $k = 2$ chosen for downstream analysis (Figure C.17). GO enrichment of resulting clusters was performed using `clusterProfiler` (v.3.10.1) [53] and visualised using `enrichplot` (v.1.10.1) [54]. A composite heat map of $z$-scored modelled expression was generated with

`ComplexHeatmap` (v.3.21) [55], using $k$-means cluster assignment and hierarchical clustering to order rows and columns.

#### C.4.3.3 Peptide preservation modelling and classification

Peptide preservation was assessed on the basis of per-peptide decay trajectories, computed from $\log_2$-transformed, batch effect-corrected peptide intensities. Each peptide's time of maximum intensity ($t_{max}$) was identified and used to define early-peaking ($t_{max} \leq 1$ week) and late-peaking ($t_{max} \geq 6$ weeks) groups as proxies for 'labile' (relatively decay-prone) and 'recalcitrant' (relatively decay-resistant) behaviour. Peptide-specific decay rates were then estimated by fitting ordinary least squares regressions of $\log_2$-intensity on PMI, from which slope estimates, SEs, $p$-values, and residual degrees of freedom were extracted. To ensure robust trend estimation, peptides with SEs $> 90^{\text{th}}$ percentile and/or detection frequencies $< 90^{\text{th}}$ percentile were excluded; given no peptides detected in the wet–oxic condition met these criteria, these samples were omitted from the analysis. To determine a target positive predictive value (PPV) for early- and late-peaking calls, candidate slope thresholds ($\tau$; $n = 200$) spanning the observed slope range were evaluated by computing precision and recall at each threshold, and precision–recall (Pareto) frontiers generated. Two per-condition classification thresholds were derived based on (i) weighted-mean and (ii) median slopes: the sensitivity and specificity of each were compared *via* balanced accuracy, and an additive margin $\delta$ was grid-searched ($\delta \in [0, 0.020]$) with bootstrapping resamples ($n = 200$) to achieve a target PPV for recalcitrant calls $\geq 0.80$. Final classification employed an optimised weighted mean-based threshold to designate peptides as recalcitrant (slope $\geq \tau_{mean} + \delta$), labile (slope $< \tau_{mean} - \delta$), or putative (otherwise), with bootstrap resamples ($n = 1,000$) yielding 95% CIs for PPV and negative predictive value (NPV). Calibration was assessed by decile binning of observed slopes and predicted probabilities, and by fitting a logistic regression with Spiegelhalter's $Z$-statistic, Brier score, and receiver operating characteristic–area under the curve (ROC–AUC) goodness-of-fit

tests quantifying performance. Smoothed-mean decay trajectories were fit using a generalised additive model with the package `mgcv` (v.1.9.3) [56].

#### C.4.3.4 Biochemical correlates of peptide preservation

For each experimental condition, over- and under-representation of protein classes associated with peptides of each preservation category (i.e., the difference between the number of observed *vs.* expected) was investigated using a Fisher's exact test and Bonferroni correction for multiple comparisons with the PANTHER classification system (v.19.0) [57]. GRAVY scores were calculated in R for all peptides using the Kyte–Doolittle hydrophobicity scale [58]. For each experimental condition the distribution of GRAVY scores across preservation categories was assessed non-parametrically: a Kruskal–Wallis test with eta-squared effect sizes ($\eta^2_H$) was performed to detect any overall differences, and $\eta^2_H$ values interpreted using conventional thresholds ($\eta^2_H < 0.01$ negligible; 0.01–0.06 small; 0.06–0.14 moderate; $\geq 0.14$ strong) [59]. Where the omnibus test indicated differences, pairwise *post-hoc* comparisons were conducted using Dunn's test with Holm (family-wise) $p$-value adjustment, and a rank biserial correlation ($r$) for each pairwise contrast reported ($|Z|/\sqrt{n}$). pI was estimated for all peptides using the `Peptides` package (v.2.4.6) [60] in R. For each sequence, theoretical pI values were first computed under nine standard pK scales (Bjellqvist, EMBOSS, Murray, Sillero, Solomon, Stryer, Lehninger, Dawson, and Rodwell) and averaged to obtain a consensus experimental estimate. These preliminary estimates were refined by incorporating machine-learning predictions from IPC 2.0 [61], to produce a final predicted pI for each peptide. For each experimental condition, Kruskal–Wallis with pairwise Dunn tests (Holm-adjusted) were used to assess category-wise differences in pI.

#### C.4.3.5 Compositional and structural correlates of peptide preservation

Sequence coverage and amino-acid composition were computed in R. Groupwise differences in coverage and fragmentation were tested non-parametrically with Kruskal–Wallis and pairwise Dunn tests (Holm-adjusted). Effect magnitudes were reported as Cliff's $\delta$ and interpreted using conventional thresholds ($\delta < 0.147$

negligible; 0.147–0.330 small; 0.330–0.474 moderate; $\geq 0.474$ strong) [62]. Empirical cumulative distribution functions (ECDFs) were plotted with 95% bootstrap CIs ($n = 1,000$ resamples, grid 0–100% in 0.5% steps) and median CIs ($n = 2,000$ resamples); bootstrap seeds were fixed for reproducibility. Amino-acid composition was compared at two scales: (i) global within-peptide relative frequencies were contrasted between preservation categories using empirical-Bayes-moderated linear models (primary contrast: recalcitrant *vs.* labile) with Benjamini–Hochberg adjustment, and (ii) terminal positional composition (three N-terminal and three C-terminal residues) assessed by one-hot encoding of terminal residues (excluding amino acids with $< 5$ observations at a given position) followed by moderated contrasts.

Secondary structure was assessed using a model-based approach. Prediction files for the *Mus musculus* proteome ($n = 21,452$) were downloaded from AlphaFold (accessed 07.10.2025) [63], and processed in R using the `bio3d` package [64]. Per-atom B-factors were averaged to yield per-residue pLDDT estimates, and backbone torsions computed. Per-residue $\phi/\psi$ were converted to conservative secondary-structure calls ($\alpha$-helix, $\beta$-sheet, or coil) by angular windows on $\phi/\psi$. For each peptide the subset of per-residue rows spanning its mapped coordinates was extracted and used to compute fractional $\alpha$-helix, $\beta$-sheet, and coil composition; dominant structural class (i.e., largest fractional component); peptide length, and mean pLDDT. Association between structure class and preservation type was tested by Pearson's $\chi^2$ with standardised residuals to identify over- and under-represented combinations. Binomial logistic regression modelled peptide recalcitrance (binary outcome) as a function of helix and coil fractions, mean pLDDT, and peptide length, with the $\beta$-sheet fraction as the implicit reference (based on the results of dominant structure frequencies). The model was repeated after excluding peptides with low ($< 70$) and very low ($< 50$) mean pLDDT scores to confirm stability against low-confidence regions. Finally, helix, coil, and sheet fractions were all recalculated after weighting by per-peptide structural confidence (fraction $\times$ [pLDDT/100]): group means were summarised by preservation category, and global differences assessed using Kruskal–Wallis tests with pairwise Dunn tests (Holm-adjusted).

Both (i) excluding low-confidence peptides and (ii) reweighting by confidence yielded distributions and between-category differences that were indistinguishable from the unweighted analysis. Intrinsic disorder was investigated using AIUPred [65]: disorder scores were parsed and joined to peptide coordinates in R, and tested non-parametrically with Kruskal–Wallis and pairwise Dunn tests (Holm-adjusted) for (i) mean IUPred score (reflecting the overall strength of disorder tendencies), and (ii) the fraction of residues exceeding the disorder threshold ($\geq 0.5$; reflecting the extent of confidently disordered regions).

#### C.4.3.6 Functional feature analyses

Peptide features were annotated in R by retrieving the UniProtKB JSON record for each unique protein accession (accessed 14.10.2025) [66], parsing these into numeric feature ranges, and overlapping them with peptide intervals to identify intersecting annotated regions. Peptide–feature association testing followed a three-tier hierarchical workflow (UniProt section $\rightarrow$ feature type $\rightarrow$ descriptor). Secondary-structure annotations were removed before testing ($n = 288$ annotated peptides), given these were analysed previously (Section C.4.3.5). For each section, and then for each type within sections that evidenced significant overall associations, contingency testing was performed using Pearson's $\chi^2$ tests ($n = 215,088$ peptide–UniProt feature observations corresponding to 94,296 unique peptides) and overall effect size quantified with Cramér's $V$. To reduce underpowered descriptor tests, a conservative minimum-occurrence threshold was computed from the observed category proportions using Cohen's $w$ (0.3) with high target power (0.95), inflated for multiple testing and converted into expected positive counts under several presence rate scenarios; descriptors were tested only if they met peptide- and protein-count minima ($\geq 2$ unique peptides/proteins). Benjamini–Hochberg adjustment was applied globally and, for significant descriptors, pairwise comparisons with ORs and 95% CIs reported.

### C.4.3.7 Post-translational modification analysis

PTM analysis was performed in R on the results of MaxQuant's dependent peptide search of the DDA data. Identifications were removed where (i) the PEP $> 0.05$, (ii) the score $< 50$, or where the modification type was (iii) unclassified or (iv) unmodified. Ratios of modified to base intensities were $\log_2$-transformed. To screen for between-condition differences in modification frequency, a $4 \times 2$ contingency table (four burial conditions $\times$ modification present/absent) was constructed per modification for each PMI group, and tested with Pearson's $\chi^2$ when expected counts $\geq 5$ or with Fisher's exact test otherwise; $p$-values were adjusted within each PMI group by the Benjamini–Hochberg method. Modifications with (i) $\geq 10$ observations total, (ii) $\geq 5$ observations per PMI group, and (iii) an adjusted $p$-value $\leq .05$ were designated 'target modifications'. For each target, within-condition early *vs.* late PMI comparisons were performed using binomial generalised linear models, with problematic fits (e.g., non-finite SEs) refit using Firth's penalised logistic regression in the `logistf` package (v.1.26.1) [67]. Model coefficients, SEs, ORs, and 95% CIs were reported, and $p$-values corrected within each condition by Benjamini–Hochberg. PTMs were validated by inspecting per-peptide site-localisation probabilities to ensure that each reported modification was chemically consistent with the pool of potentially affected sites; the most frequently affected residues were computed as the percentage of that pool with localisation probabilities ($P_{loc}$) $\geq 0.75$.

## C.5 Figures

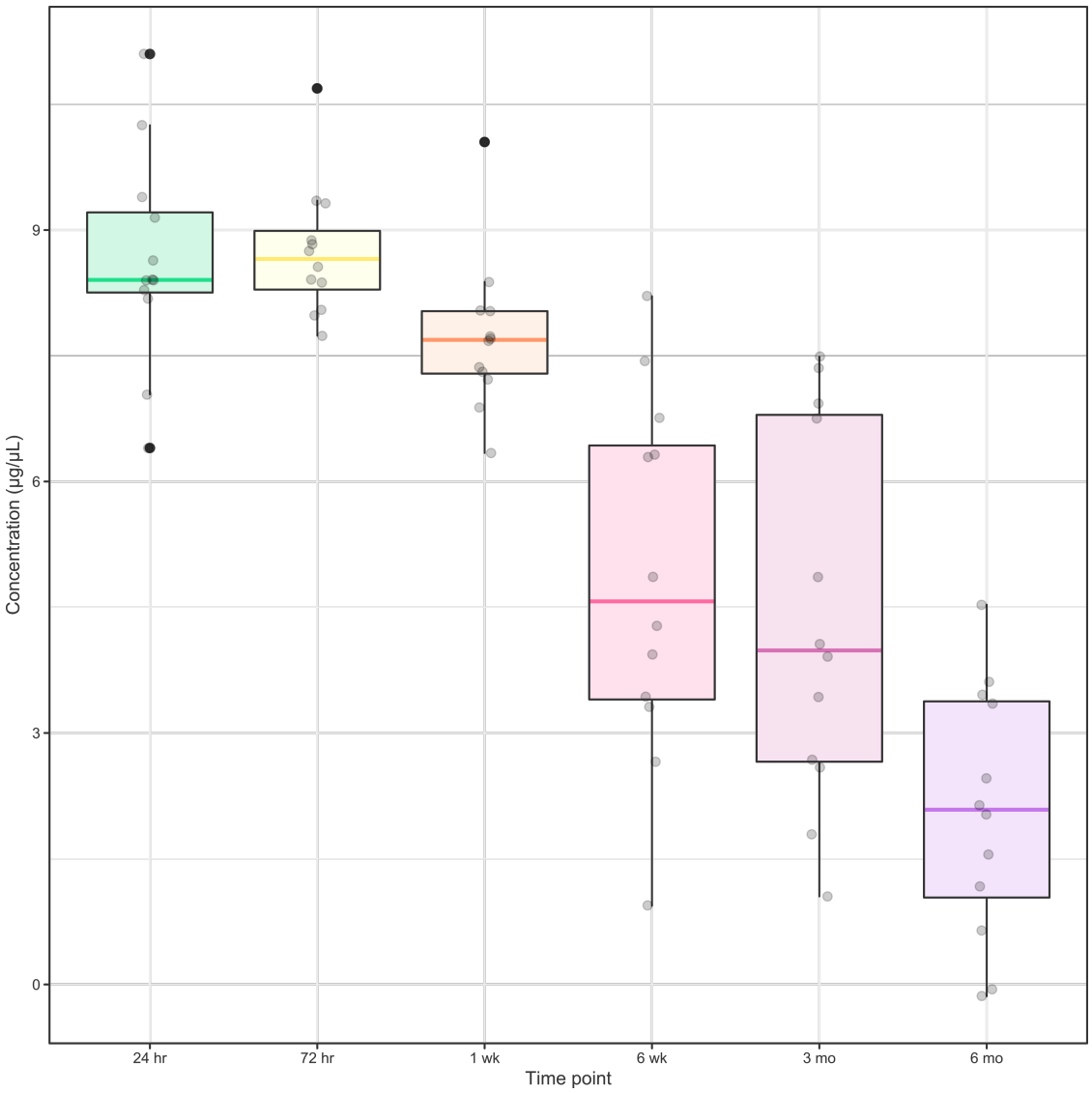



**Figure C.1 | Protein concentration during decomposition.** Jittered box plots of mean protein concentrations (estimated by BCA assay) recovered from samples ($n = 72$) at six time points. Solid black dots represent statistical outliers.

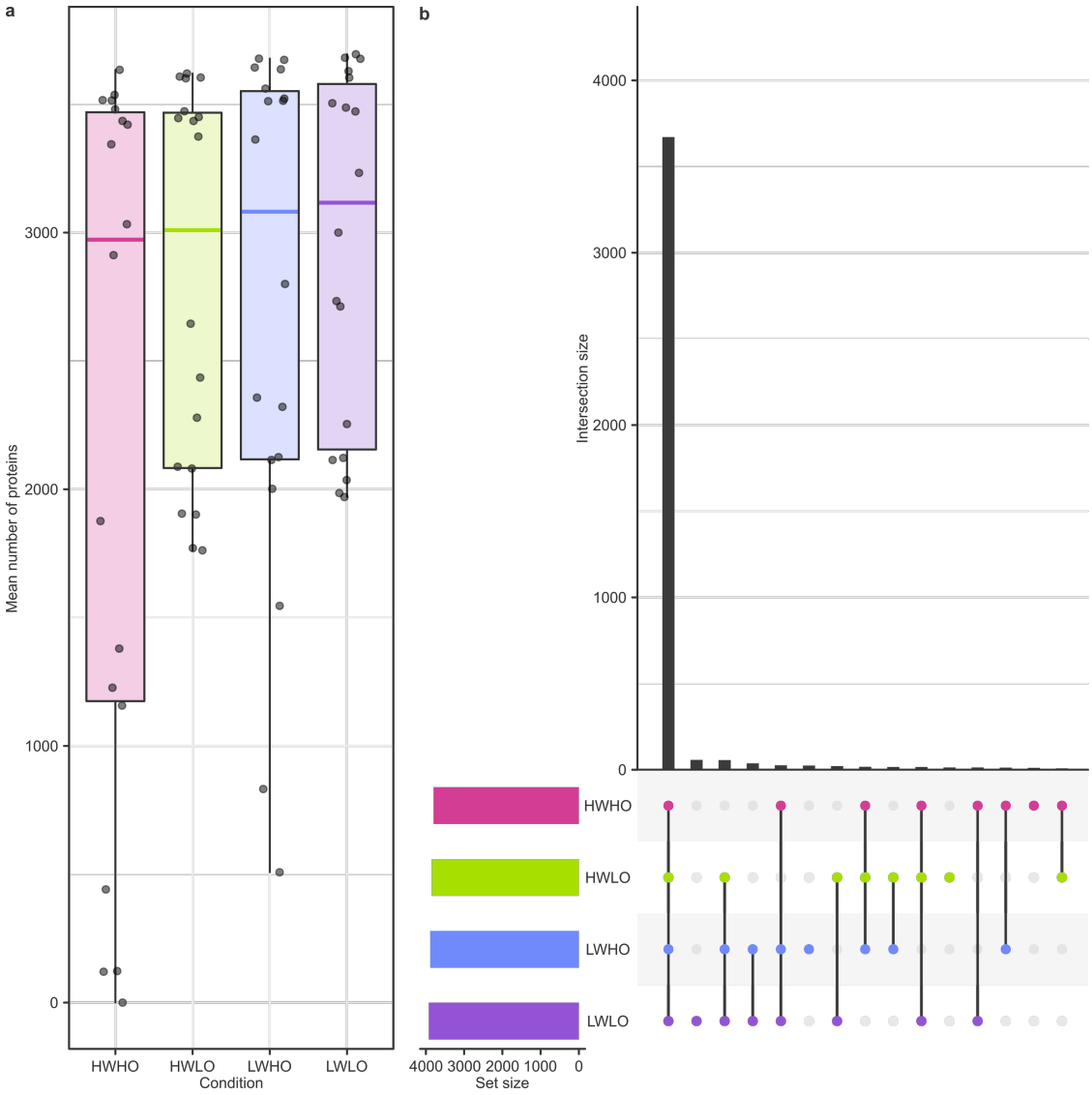



**Figure C.2 | Proteomic profiles by burial environment. (a)** Jittered box plot of mean number of proteins at 1% FDR and $q$-value $\leq .01$ recovered in each experimental condition, and **(b)** upset plot of the number of unique proteins at 1% FDR and $q$-value $\leq .01$ recovered in each experimental condition. Horizontal bars indicate the total peptides per individual condition; connected dots denote the condition(s) contributing to each intersection, and vertical bars indicate intersection sizes.

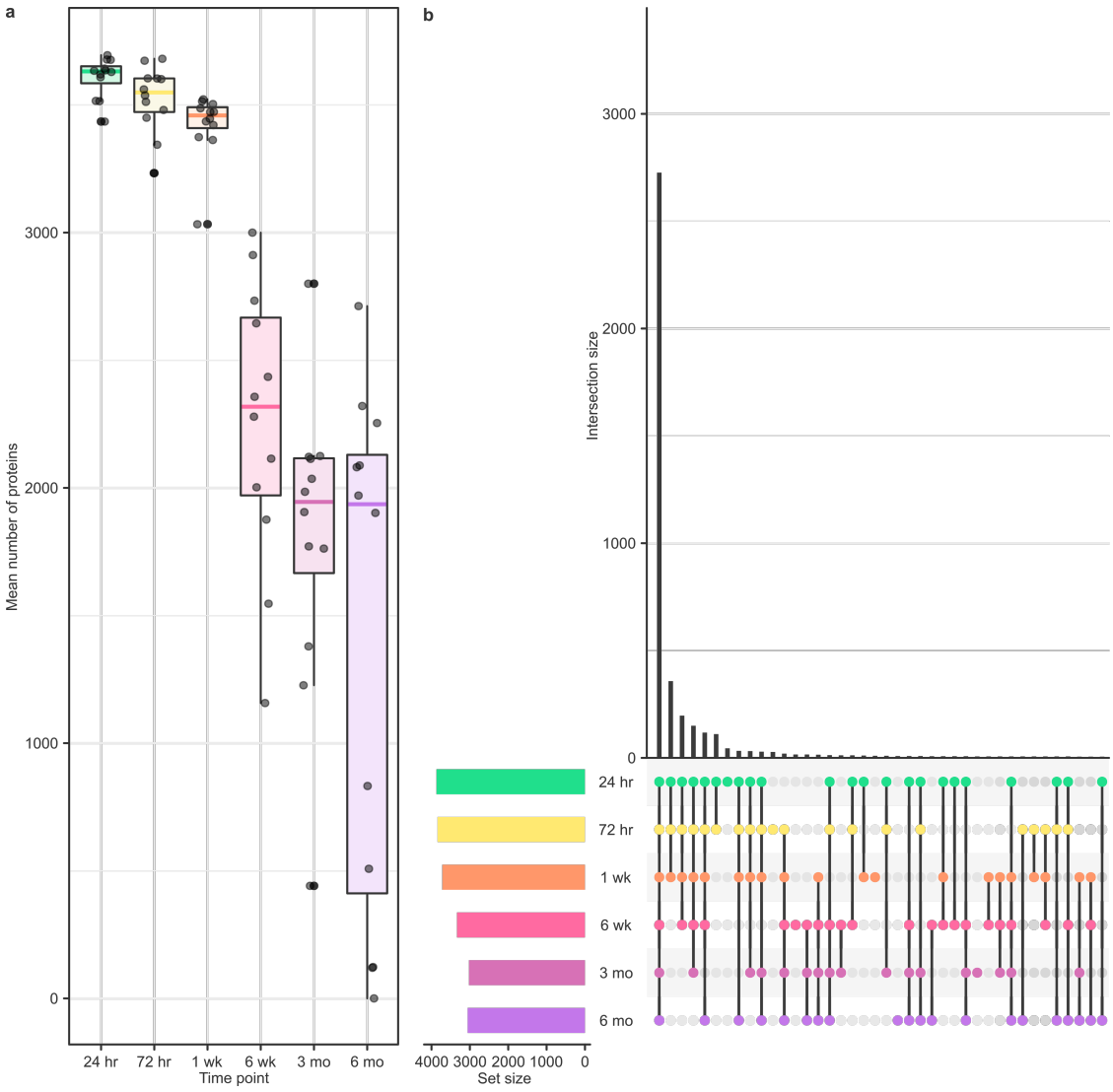



**Figure C.3 | Proteomic profiles by time point. (a)** Jittered box plot of mean number of proteins at 1% FDR and $q$-value $\leq .01$ recovered at each time point (solid black points represent statistical outliers), and **(b)** upset plot of the number of unique proteins at 1% FDR and $q$-value $\leq .01$ recovered at each time point. Horizontal bars indicate the total peptides per individual time point; connected dots denote the time point(s) contributing to each intersection, and vertical bars indicate intersection sizes.

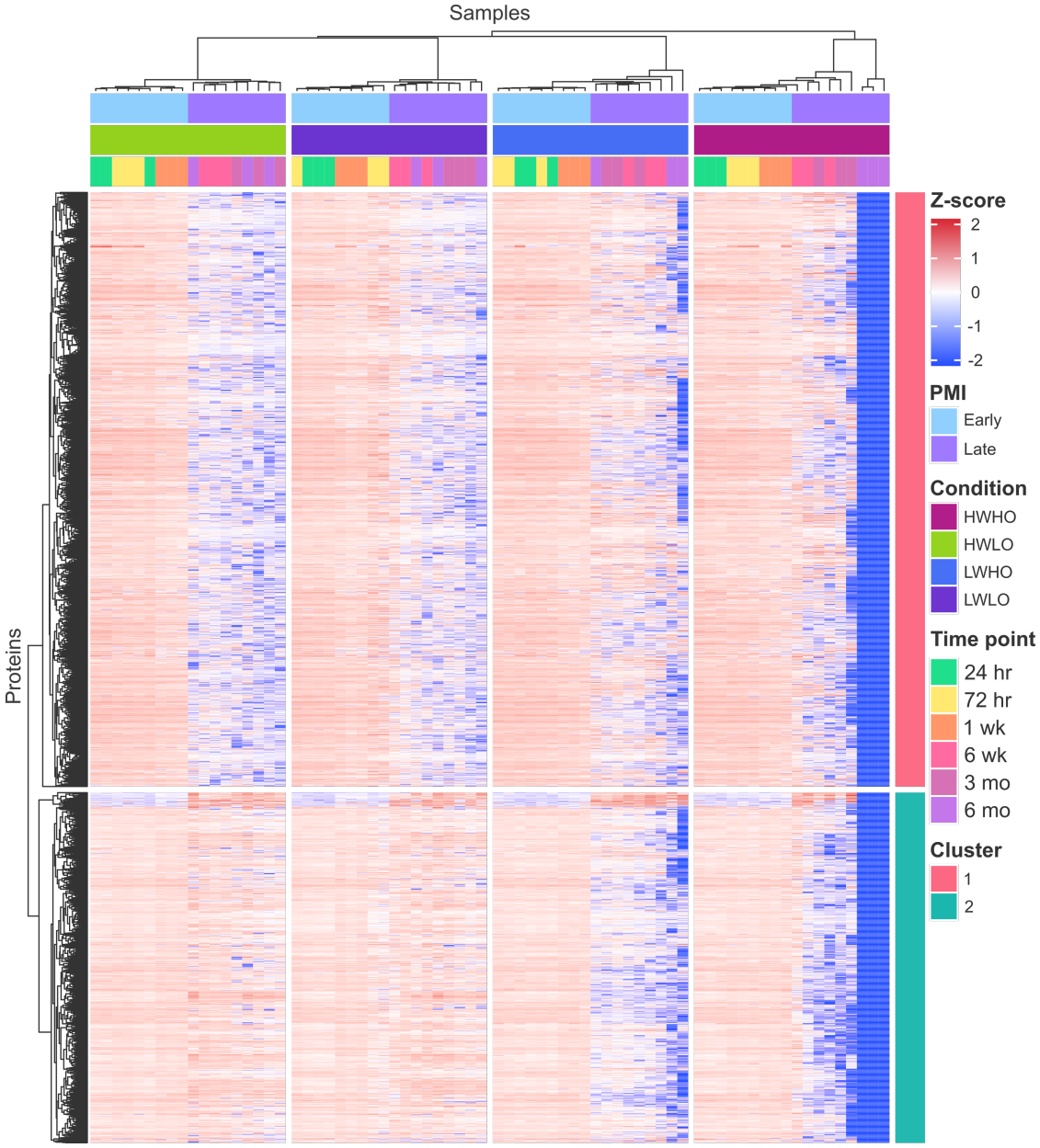



**Figure C.4 | Complex heatmap of scaled protein iBAQ data with integrated linear modelling, $k$-means and hierarchical clustering of proteins globally.** Complex heatmap of scaled protein iBAQ data with integrated linear modelling, $k$-means and hierarchical clustering. iBAQ data were $\log_2$-transformed and missing values imputed using QRILC, and fit to a linear model including PMI (main effect) and burial condition (covariate only) to identify proteins with a consistent late–*vs.*–early change in protein abundance across all conditions. Proteins significantly differentially abundant at late PMI relative to early PMI ($n = 2,998$) were $z$-score normalised and partitioned into two groups by $k$-means clustering. Within each protein cluster, hierarchical clustering using Manhattan distance with complete linkage was applied to resolve differential abundance trends. Columns represent all samples ($n = 72$), split by the four burial conditions and clustered using Manhattan distance with complete linkage.

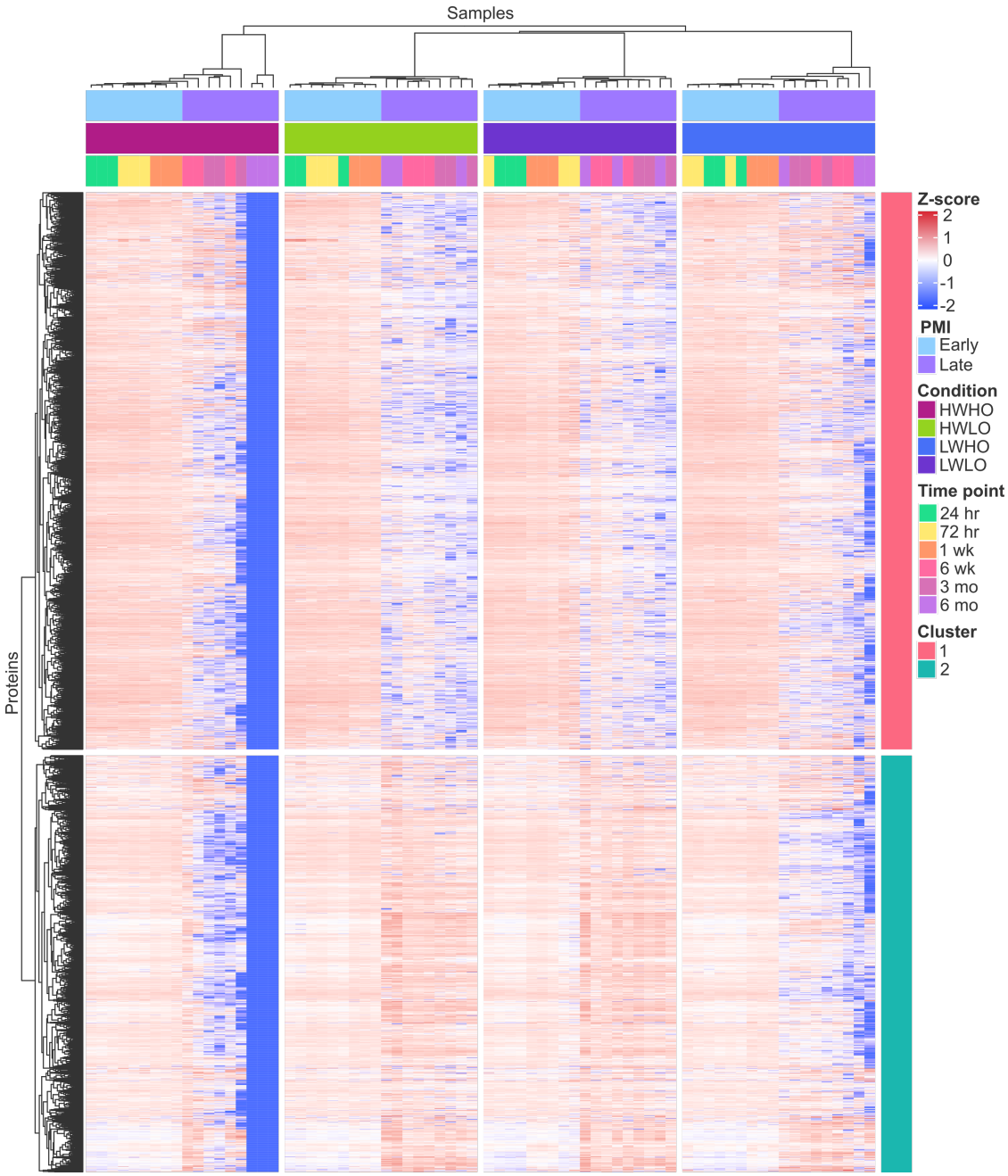



**Figure C.5 | Complex heatmap of scaled protein iBAQ data with integrated linear modelling, $k$-means and hierarchical clustering of proteins in wet–oxic conditions.** iBAQ data were $\log_2$-transformed and missing values imputed using QRILC, and fit to a linear model with a condition–PMI interaction to identify proteins with a consistent late–*vs.*–early change in protein abundance in the wet–oxic condition. Proteins significantly differentially abundant at late PMI relative to early PMI ($n = 3,791$) were $z$-score normalised, and partitioned into two groups by $k$-means clustering. Within each protein cluster, hierarchical clustering using Manhattan distance with complete linkage was applied to better resolve differential abundance trends. Columns represent all samples ($n = 72$), split by the four experimental conditions and clustered using Manhattan distance with complete linkage.

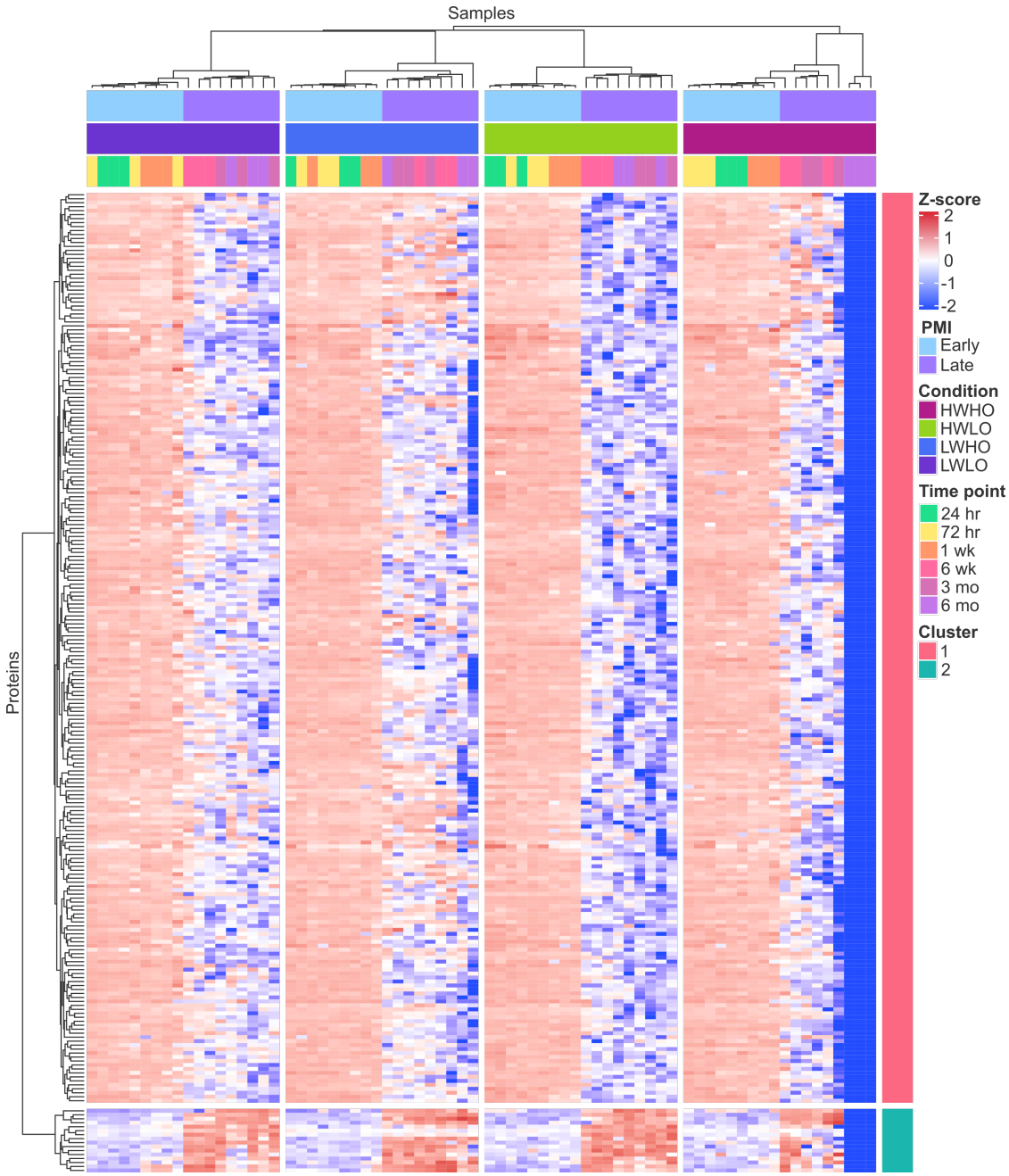



**Figure C.6 | Complex heatmap of scaled protein iBAQ data with integrated linear modelling, $k$-means and hierarchical clustering of proteins in wet–hypoxic conditions.** iBAQ data were $\log_2$-transformed and missing values imputed using QRILC, and fit to a linear model with a condition–PMI interaction to identify proteins with a consistent late–*vs.*–early change in protein abundance in the wet–hypoxic condition. Proteins significantly differentially abundant at late PMI relative to early PMI ($n = 245$) were $z$-score normalised, and partitioned into two groups by $k$-means clustering. Within each protein cluster, hierarchical clustering using Manhattan distance with complete linkage was applied to better resolve differential abundance trends. Columns represent all samples ($n = 72$), split by the four experimental conditions and clustered using Manhattan distance with complete linkage.

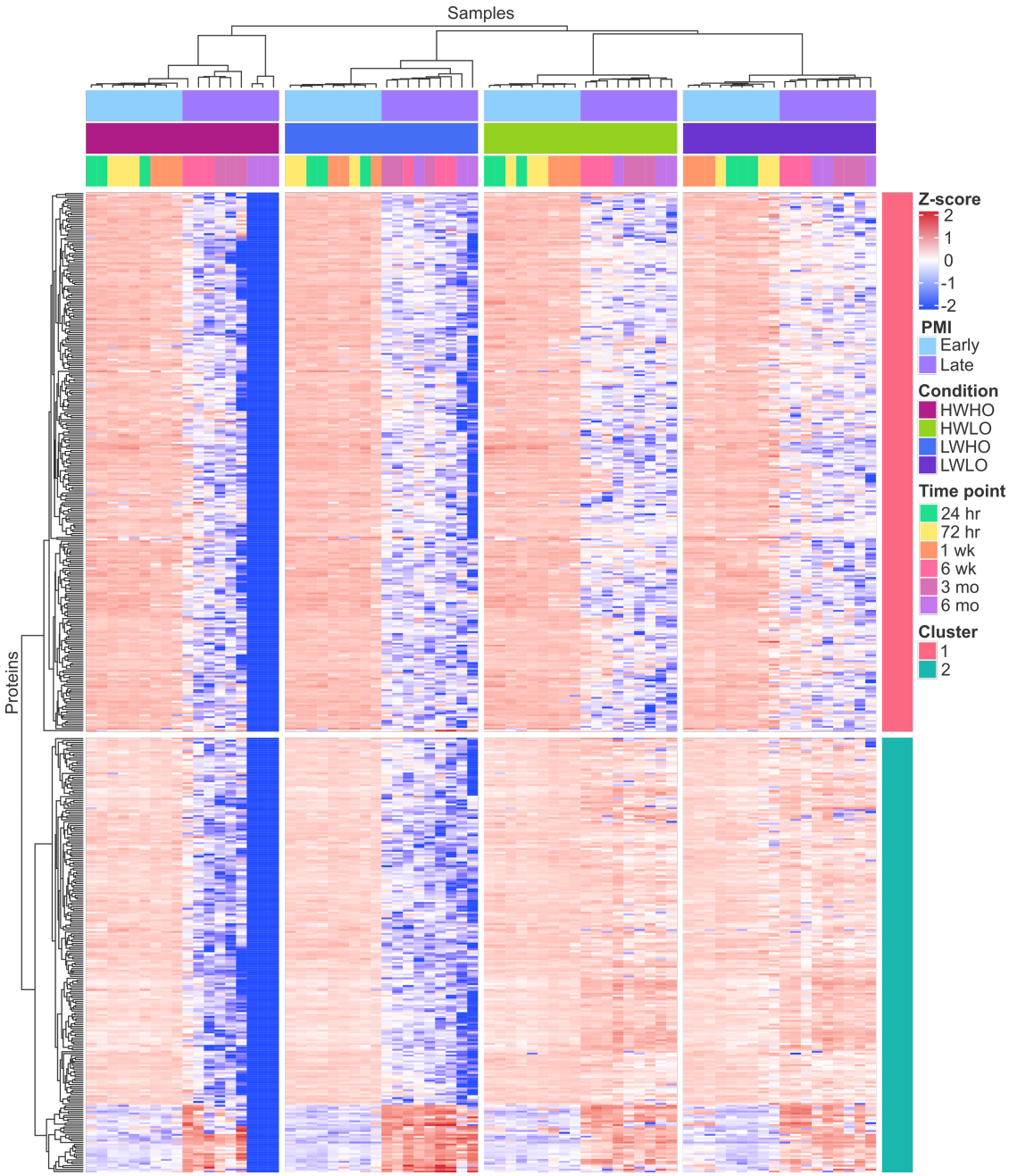



**Figure C.7 | Complex heatmap of scaled protein iBAQ data with integrated linear modelling, $k$-means and hierarchical clustering of proteins in dry–oxic conditions.** iBAQ data were $\log_2$-transformed and missing values imputed using QRILC, and fit to a linear model with a condition–PMI interaction to identify proteins with a consistent late–*vs.*–early change in protein abundance in the dry–oxic condition. Proteins significantly differentially abundant at late PMI relative to early PMI ($n = 245$) were $z$-score normalised, and partitioned into two groups by $k$-means clustering. Within each protein cluster, hierarchical clustering using Manhattan distance with complete linkage was applied to better resolve differential abundance trends. Columns represent all samples ($n = 72$), split by the four experimental conditions and clustered using Manhattan distance with complete linkage.

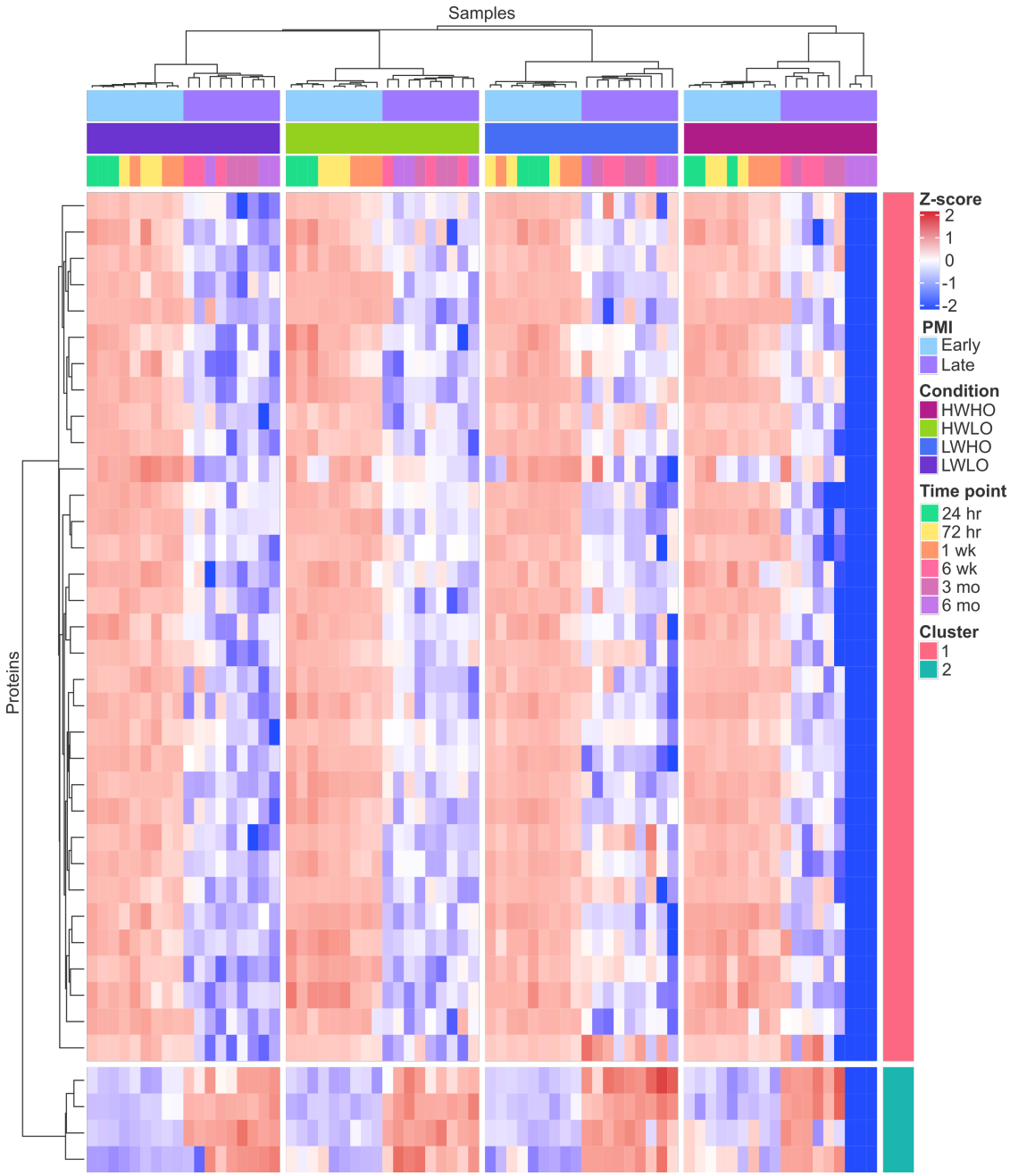



**Figure C.8 | Complex heatmap of scaled protein iBAQ data with integrated linear modelling, $k$-means and hierarchical clustering of proteins in dry–hypoxic conditions.** iBAQ data were $\log_2$-transformed and missing values imputed using QRILC, and fit to a linear model with a condition–PMI interaction to identify proteins with a consistent late–*vs.*–early change in protein abundance in the dry–hypoxic condition. Proteins significantly differentially abundant at late PMI relative to early PMI ($n = 245$) were $z$-score normalised, and partitioned into two groups by $k$-means clustering. Within each protein cluster, hierarchical clustering using Manhattan distance with complete linkage was applied to better resolve differential abundance trends. Columns represent all samples ($n = 72$), split by the four experimental conditions and clustered using Manhattan distance with complete linkage.

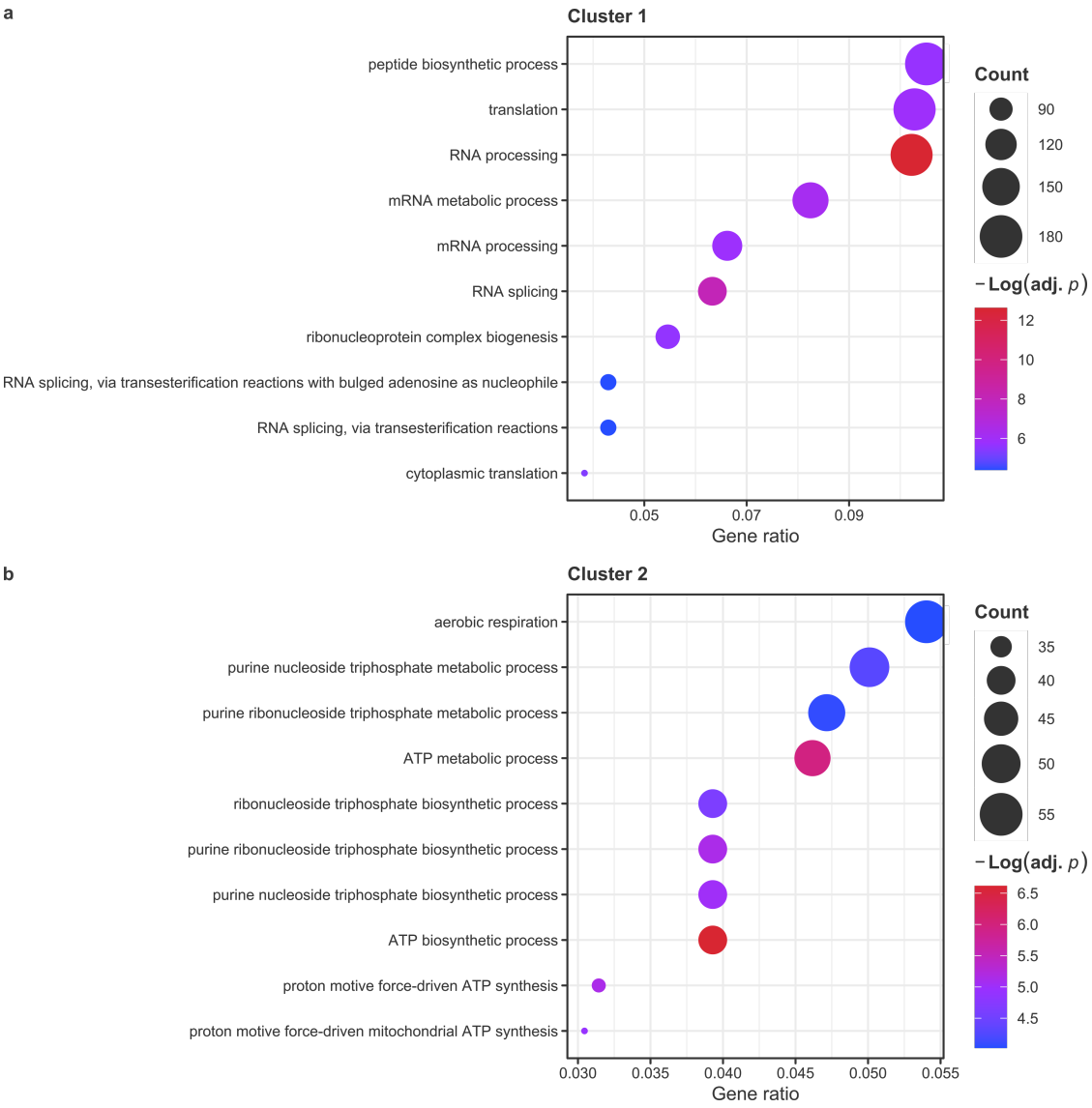



**Figure C.9 | Biological process enrichment of proteins at early and late PMI.** Enrichment analysis (GO Biological Process) of significantly differentially abundant proteins clustered by $k$-means ($n = 2,998$). Top 10 most significant GO terms with $> 3$ genes per term for **(a)** cluster 1 ($n = 1,886$), representing proteins more abundant in the early PMI, and for **(b)** cluster 2 ($n = 1,112$), proteins more abundant in the late PMI. Point size represents the number of unique proteins at 1% FDR and $q$-value $\leq .01$ associated with a GO term, and point colour represents the $-\log_{10}$ of adjusted $p$-value.

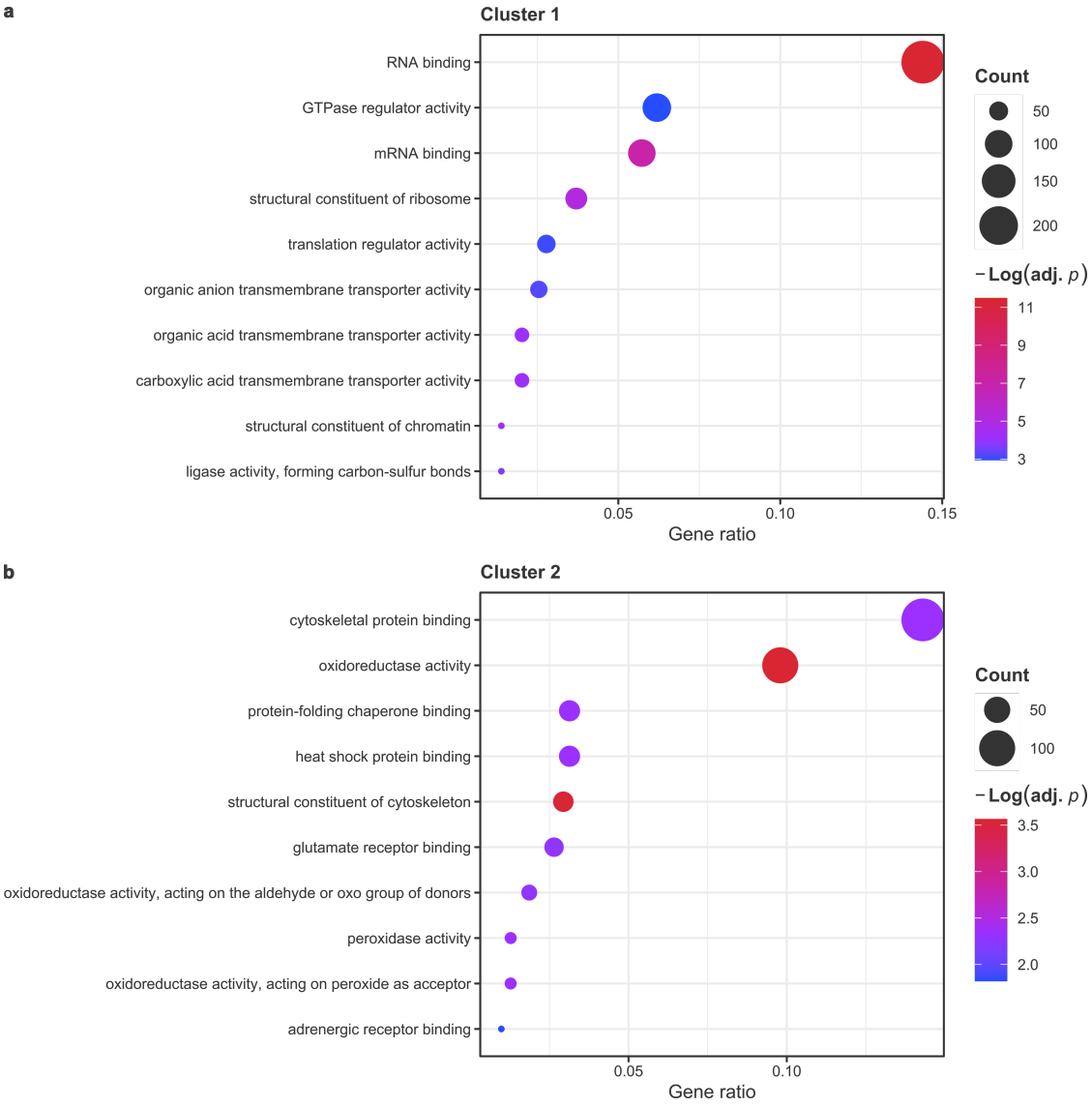



**Figure C.10 | Molecular function enrichment of proteins at early and late PMI.** Enrichment analysis (GO Molecular Function) of significantly differentially abundant proteins clustered by $k$-means ($n = 2,998$). Top 10 most significant GO terms with $> 3$ genes per term for **(a)** cluster 1 ($n = 1,886$), representing proteins more abundant in the early PMI, and for **(b)** cluster 2 ($n = 1,112$), proteins more abundant in the late PMI. Point size represents the number of unique proteins at 1% FDR and $q$-value $\leq .01$ associated with a GO term, and point colour represents the $-\log_{10}$ of adjusted $p$-value.

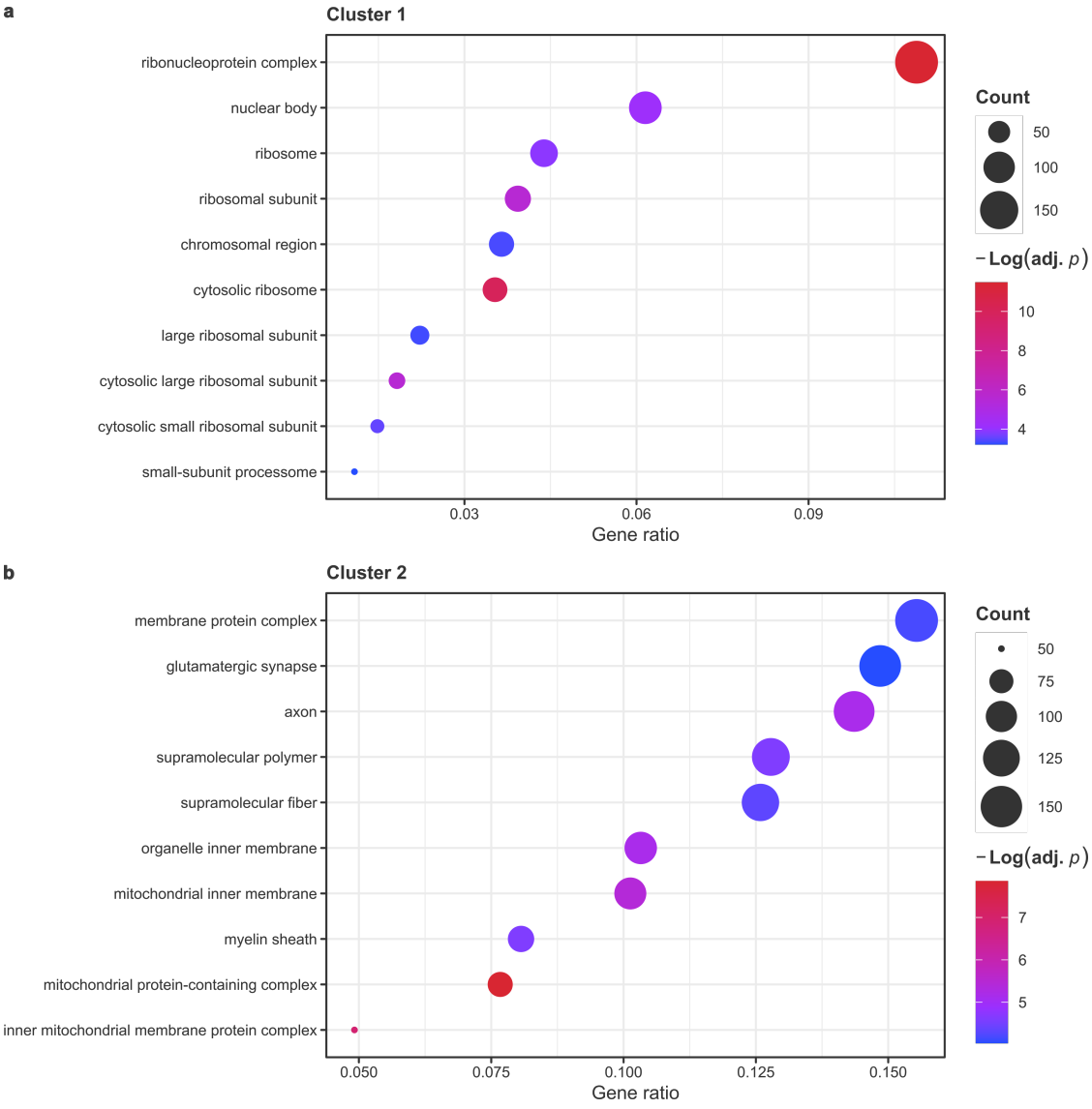



**Figure C.11 | Cellular component enrichment of proteins at early and late PMI.** Enrichment analysis (GO Cellular Component) of significantly differentially abundant proteins clustered by $k$-means ($n = 2,998$). Top 10 most significant GO terms with $> 3$ genes per term for **(a)** cluster 1 ($n = 1,886$), representing proteins more abundant in the early PMI, and for **(b)** cluster 2 ($n = 1,112$), proteins more abundant in the late PMI. Point size represents the number of unique proteins at 1% FDR and $q$-value $\leq .01$ associated with a GO term, and point colour represents the $-\log_{10}$ of adjusted $p$-value.

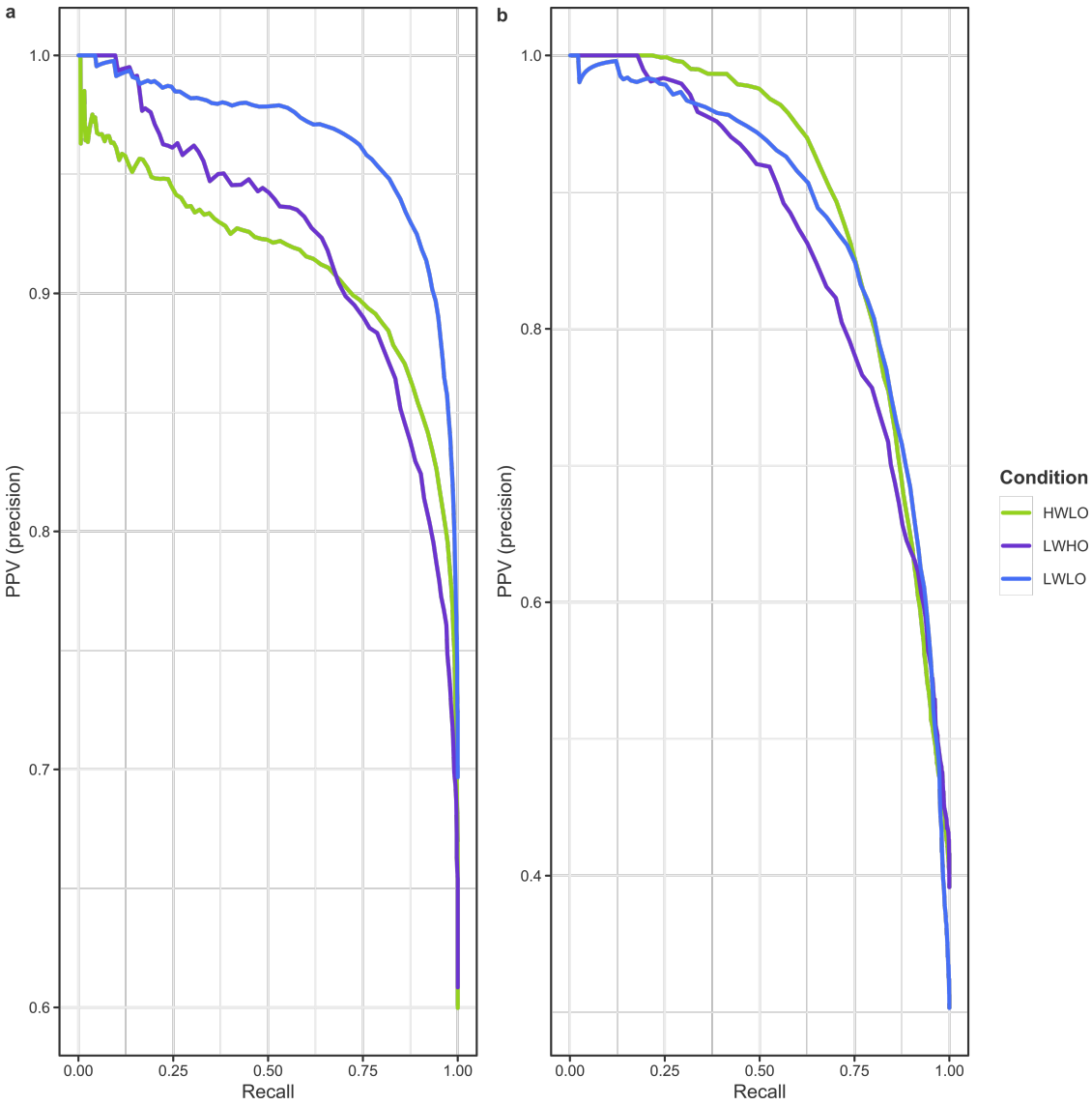



**Figure C.12 | Precision–recall for early- and late-peaking peptide classifiers across conditions.** Performance when predicting **(a)** early-peaking peptides, and **(b)** late-peaking peptides. Lines show the convex hull ('Pareto frontier') of PPV (precision) *vs.* recall for peptide classification in each condition. No peptides detected in the wet–oxic condition met quality criteria, and were excluded from analysis.

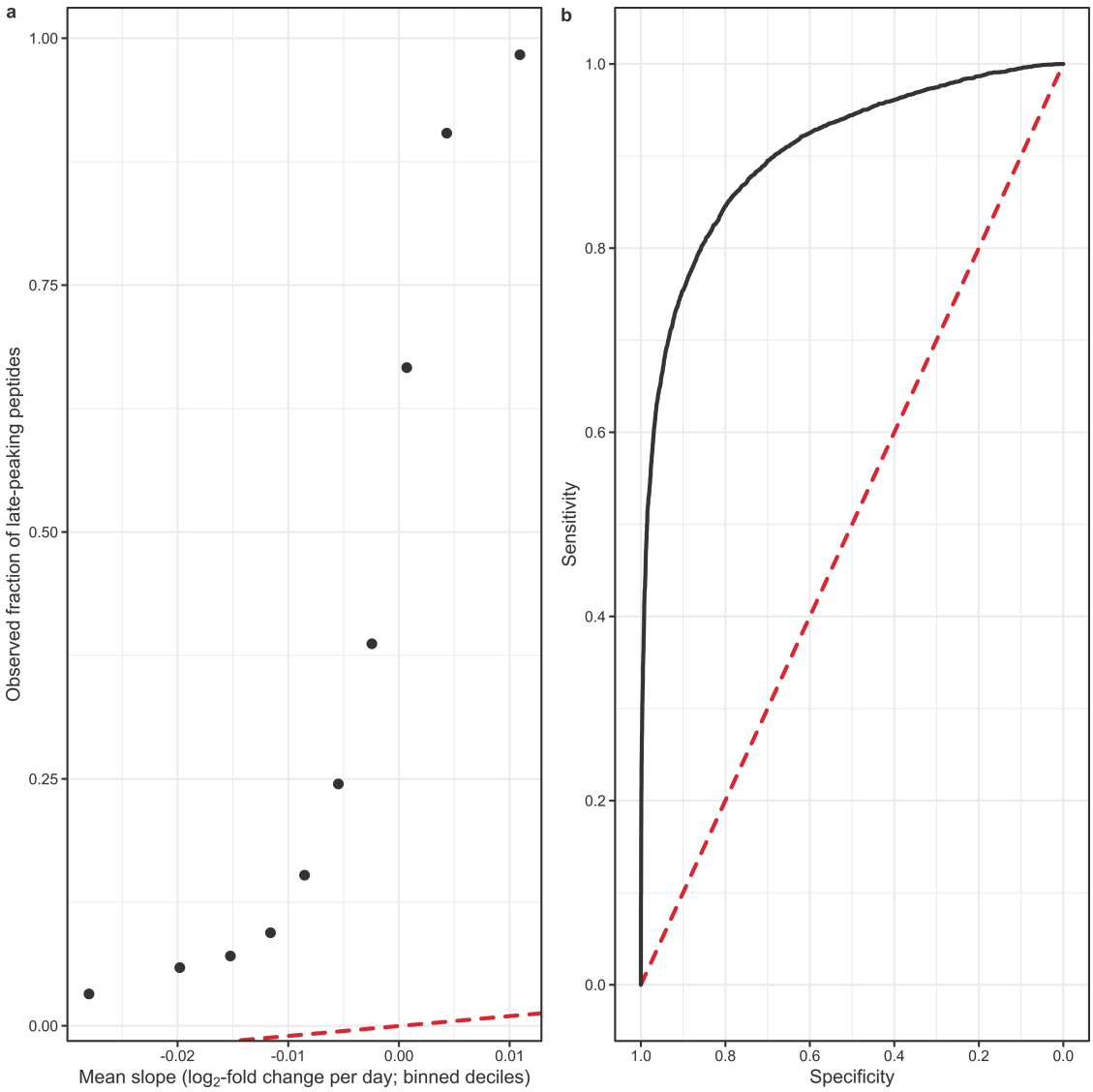



**Figure C.13 | Calibration and discrimination of the peptide-level recalcitrance classifier. (a)** Calibration plot showing the observed fraction of late-peaking peptides *vs.* the mean predicted $\log_2$-fold change slope per day, binned into deciles. Points indicate the empirical late-peaking peptide rate in each bin; the red dashed line marks the ideal (no-bias) relationship. The upward trend demonstrates that peptides with higher predicted mean slopes are increasingly likely to exhibit late-peaking behaviour. **(b)** ROC curve for distinguishing early- *vs.* late-peaking peptides. The solid black line is the classifier performance across all thresholds, and the red dashed line represents random chance. The pronounced convexity of the curve indicates the strong discriminative ability of the model.

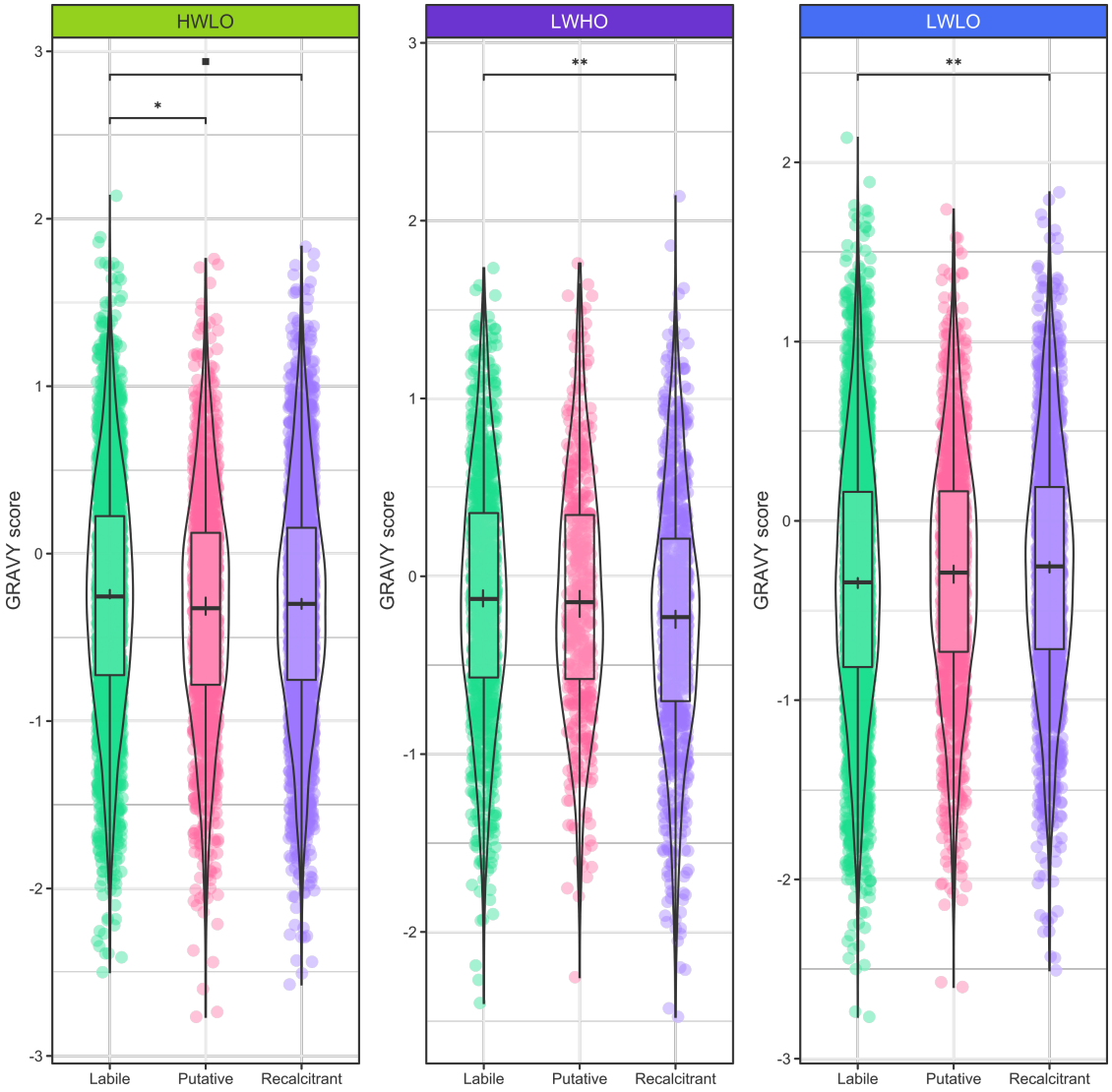



**Figure C.14 | Hydropathy by burial environment.** Results of Kruskal–Wallis tests ($n_{obs}$= 16, 128) with eta-squared effect sizes ($\eta^2_H$) and *post-hoc* Dunn pairwise comparisons (Holm-adjusted), for peptide preservation with respect to GRAVY score. Higher GRAVY scores are more hydrophobic, and lower scores more hydrophilic. Vertical black lines intersecting the median indicate bootstrapped 95% CIs. Only statistically significant comparisons are shown (for all other comparisons, see Table C.7), and adjusted significance indicated by the following codes: $***$ = $p$-value $<$ .0001; $**$ = $p$-value $\leq$ .001; $*$ = $p$-value $\leq$ .01; ■ = $p$-value $\leq$ .05. No peptides detected in the wet–oxic condition met quality criteria, and were excluded from analysis.

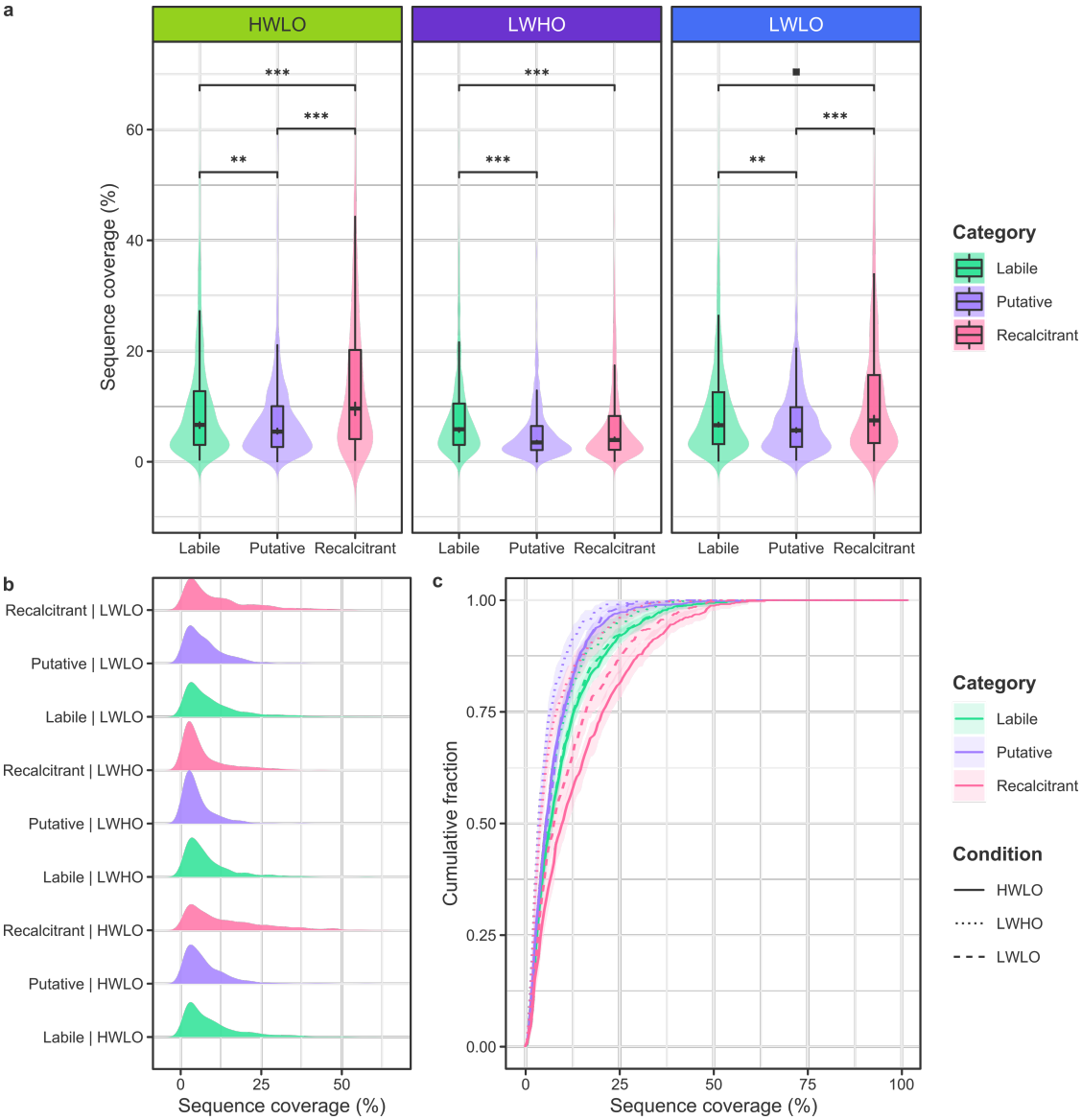



**Figure C.15 | Sequence coverage distributions by preservation category within burial environments. (a)** Violin–box plots illustrate distributions of sequence coverage (%) across proteins for labile, putative, and recalcitrant peptides in each burial condition ($n = 5,445$). Vertical black lines intersecting the median indicate bootstrapped 95% CIs. Only statistically significant comparisons are shown (for all other comparisons, see Table C.12), and adjusted significance indicated by the following codes: $***$ = $p$-value $< .0001$; $**$ = $p$-value $\leq .001$; $*$ = $p$-value $\leq .01$; ■ = $p$-value $\leq .05$. No peptides detected in the wet–oxic condition met quality criteria, and were excluded from analysis. **(b)** Ridgeline density plots illustrate the coverage distributions for each category–condition combination. **(c)** ECDFs depict cumulative fractions of sequence coverage with 95% CIs, coloured by preservation category and styled by condition.

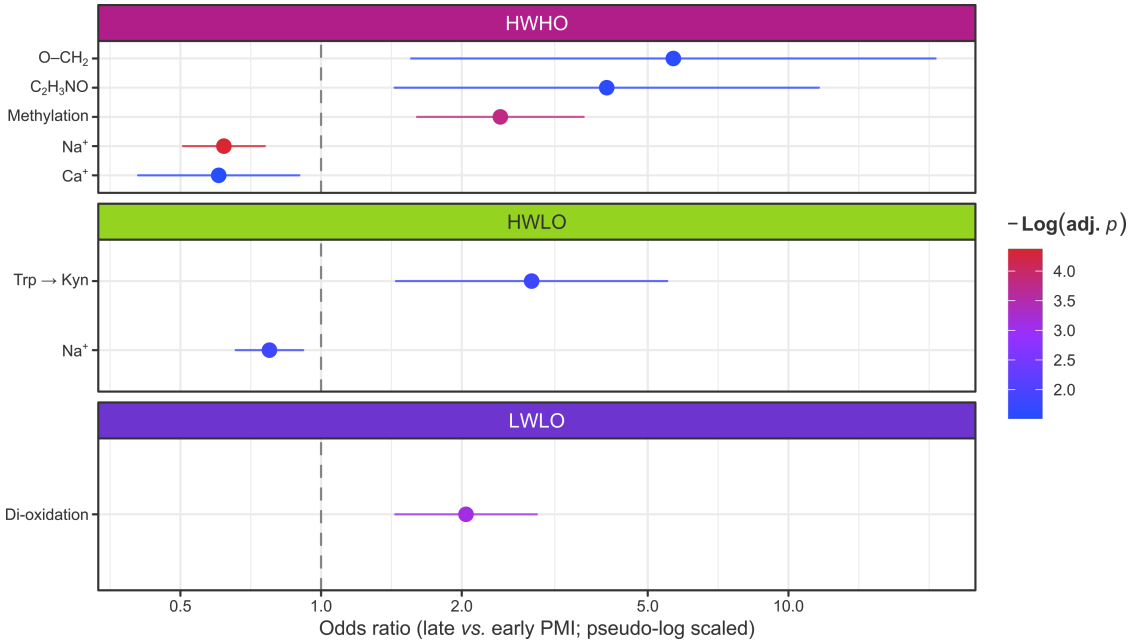



**Figure C.16 | Odds of modification at late *vs.* early PMI by burial environment.** Forest plots of ORs (pseudo-log scaled) of PTMs at late *vs.* early PMI within each experimental condition, estimated by mixed-effects logistic regression or, when convergence criteria were not met, by Firth's penalised logistic regression. Each point illustrates the direction and magnitude of the PMI effect, with horizontal lines representing 95% CIs and colour intensity corresponding to $-\log_{10}$ of adjusted $p$-value. The vertical dashed line marks OR = 1 (no effect), such that a point left of the dashed line indicates that PTM is more likely in the early PMI, and right of the dashed line in the late PMI. Only modifications with 95% CIs excluding 1 and $p$-value $< .05$ were considered statistically significant, and only significant results are shown. No PTMs in the dry–oxic condition met these criteria.

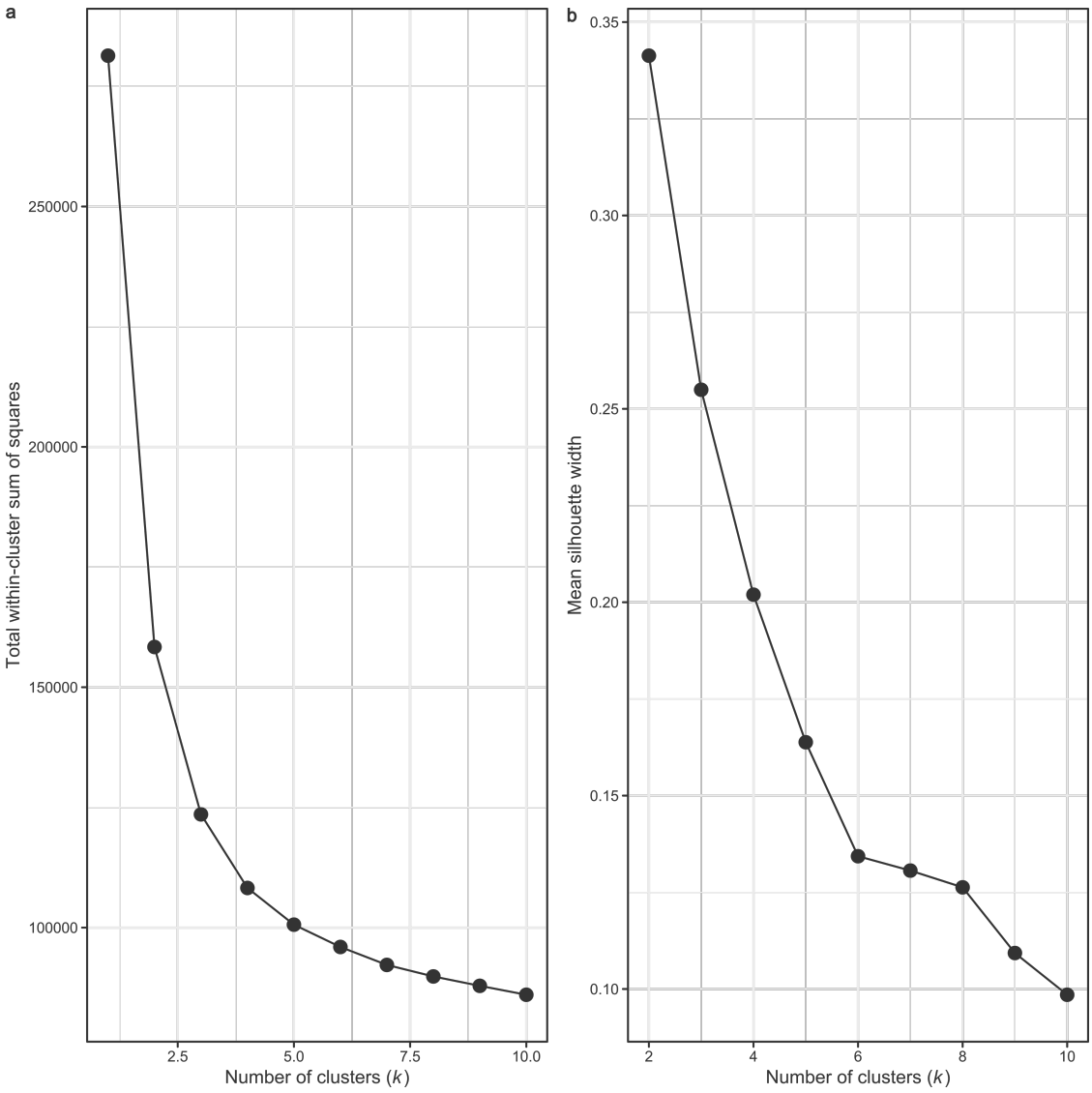



**Figure C.17 | Determination of optimal number of clusters for hierarchical clustering analysis of iBAQ data. (a)** Elbow method plot depicting total within-cluster sum of squares against the number of clusters ($k$). **(b)** Silhouette analysis illustrating the mean silhouette width against $k$.

## C.6 Tables

**Table C.1 | Proteins recovered by experimental condition and time point.** Summary statistics for numbers of proteins at 1% FDR and $q$-value $\leq .01$ recovered in the DIA dataset ($n = 192,244$), grouped by time point and experimental condition.

| Time point | Total | Mean | Standard deviation | Median | Min. value | Max. value |
|---|---|---|---|---|---|---|
| 24 hours | 43,286 | 3,607 | 78 | 3,632 | 3,435 | 3,695 |
| 72 hours | 42,280 | 3,523 | 132 | 3,549 | 3,233 | 3,681 |
| 1 week | 41,044 | 3,420 | 132 | 3,459 | 3,033 | 3,522 |
| 6 weeks | 27,056 | 2,255 | 552 | 2,318 | 1,157 | 3,000 |
| 3 months | 21,667 | 1,806 | 585 | 1,945 | 441 | 2,800 |
| 6 months | 16,911 | 1,409 | 1,007 | 1,936 | 0 | 2,712 |
| **Condition** | **Total** | **Mean** | **Standard deviation** | **Median** | **Min. value** | **Max. value** |
| HWHO | 40,150 | 2,231 | 1,411 | 2,973 | 0 | 3,634 |
| HWLO | 50,479 | 2,804 | 761 | 3,010 | 1,762 | 3,620 |
| LWHO | 48,707 | 2,706 | 1,026 | 3,082 | 508 | 3,678 |
| LWLO | 52,908 | 2,939 | 693 | 3,117 | 1,970 | 3,695 |

**Table C.2 | Protein abundance at different time points.** Results of a linear mixed effects model (random intercept by condition) with type-III ANOVA (Satterthwaite method) and Bonferroni-adjusted pairwise contrasts ($n = 72$) for the number of proteins identified at 1% FDR and $q$-value $\leq .01$ across time points. Cells containing $p$-values are coloured according to significance thresholds.

| Comparison | Estimate ($E$) | Standard error | $t$-Ratio | $p$-Value |
|---|---|---|---|---|
| 24 hours – 72 hours | 83.83333 | 189.61470 | 0.44212 | $1.00 \times 10^{0}$ |
| 24 hours – 1 week | 186.83333 | 189.61470 | 0.98533 | $1.00 \times 10^{0}$ |
| 24 hours – 6 weeks | 1352.50000 | 189.61470 | 7.13289 | $1.76 \times 10^{-8}$ |
| 24 hours – 3 months | 1801.58333 | 189.61470 | 9.50129 | $1.33 \times 10^{-12}$ |
| 24 hours – 6 months | 2197.91667 | 189.61470 | 11.59149 | $4.32 \times 10^{-16}$ |
| 72 hours – 1 week | 103.00000 | 189.61470 | 0.54321 | $1.00 \times 10^{0}$ |
| 72 hours – 6 weeks | 1268.66667 | 189.61470 | 6.69076 | $1.03 \times 10^{-7}$ |
| 72 hours – 3 months | 1717.75000 | 189.61470 | 9.05916 | $7.67 \times 10^{-12}$ |
| 72 hours – 6 months | 2114.08333 | 189.61470 | 11.14937 | $2.27 \times 10^{-15}$ |
| 1 week – 6 weeks | 1165.66667 | 189.61470 | 6.14756 | $8.92 \times 10^{-7}$ |
| 1 week – 3 months | 1614.75000 | 189.61470 | 8.51596 | $6.73 \times 10^{-11}$ |
| 1 week – 6 months | 2011.08333 | 189.61470 | 10.60616 | $1.80 \times 10^{-14}$ |
| 6 weeks – 3 months | 449.08333 | 189.61470 | 2.36840 | $3.14 \times 10^{-1}$ |
| 6 weeks – 6 months | 845.41667 | 189.61470 | 4.45860 | $5.20 \times 10^{-4}$ |
| 3 months – 6 months | 396.33333 | 189.61470 | 2.09020 | $6.10 \times 10^{-1}$ |

**Table C.3 | Protein abundance in different burial environments.** Results of a linear mixed effects model (random intercept by time point) with type III-ANOVA (Satterthwaite method) and Bonferroni-adjusted pairwise contrasts ($n = 72$) for the number of proteins identified at 1% FDR and $q$-value $\leq .01$ across experimental conditions. Cells containing $p$-values are coloured according to significance thresholds.

| Comparison | Estimate ($E$) | Standard error | $t$-Ratio | $p$-Value |
|---|---|---|---|---|
| HWHO – HWLO | −573.83333 | 154.81970 | −3.70646 | $2.67 \times 10^{-3}$ |
| HWHO – LWHO | −475.38889 | 154.81970 | −3.07060 | $1.89 \times 10^{-2}$ |
| HWHO – LWLO | −708.77778 | 154.81970 | −4.57808 | $1.36 \times 10^{-4}$ |
| HWLO – LWHO | 98.44444 | 154.81970 | 0.63587 | $1.00 \times 10^{0}$ |
| HWLO – LWLO | −134.94444 | 154.81970 | −0.87162 | $1.00 \times 10^{0}$ |
| LWHO – LWLO | −233.38889 | 154.81970 | −1.50749 | $8.20 \times 10^{-1}$ |

**Table C.4 | Protein classes recalcitrant in wet–hypoxic conditions.** Over-representation test results for PANTHER protein class corresponding to recalcitrant peptides ($n = 2,647$) identified in wet–hypoxic conditions. Subclasses (*italics*) are indented below parent classes to illustrate hierarchical relationships. Only statistically significant results (i.e., Bonferroni-corrected for $p < .05$) for classified proteins are shown, and cells containing $p$-values are coloured according to significance thresholds.

| Protein class | No. referenced | No. queried | No. expected | Fold enrichment | $p$-Value |
|---|---|---|---|---|---|
| Metabolite interconversion enzyme | 737 | 127 | 53.58 | 2.37 | $1.83 \times 10^{-21}$ |
| ↪ *Oxidoreductase* | 228 | 54 | 16.58 | 3.26 | $1.63 \times 10^{-13}$ |
| ↪ *Peroxidase* | 9 | 5 | 0.65 | 7.64 | $3.18 \times 10^{-2}$ |
| Protease | 178 | 32 | 12.94 | 2.47 | $1.76 \times 10^{-4}$ |
| ↪ *Metalloprotease* | 44 | 16 | 3.20 | 5.00 | $4.56 \times 10^{-6}$ |
| Calcium-binding protein | 43 | 21 | 3.13 | 6.72 | $2.78 \times 10^{-11}$ |
| ↪ *Calmodulin-related* | 29 | 10 | 2.11 | 4.74 | $3.41 \times 10^{-3}$ |
| Lyase | 54 | 15 | 3.93 | 3.82 | $6.47 \times 10^{-4}$ |
| Dehydrogenase | 82 | 22 | 5.96 | 3.69 | $6.97 \times 10^{-6}$ |
| Translational protein | 184 | 2 | 13.38 | 0.15 | $3.49 \times 10^{-2}$ |
| RNA metabolism protein | 242 | 1 | 17.59 | 0.06 | $5.23 \times 10^{-5}$ |

**Table C.5 | Protein classes recalcitrant in dry–oxic conditions.** Over-representation test results for PANTHER protein class corresponding to recalcitrant peptides ($n = 908$) identified in dry–oxic conditions. Subclasses (*italics*) are indented below parent classes to illustrate hierarchical relationships. Only statistically significant results (i.e., Bonferroni-corrected for $p < .05$) for classified proteins are shown, and cells containing $p$-values are coloured according to significance thresholds.

| Protein class | No. referenced | No. queried | No. expected | Fold enrichment | $p$-Value |
|---|---|---|---|---|---|
| Protease | 178 | 39 | 13.53 | 2.88 | $1.09 \times 10^{-7}$ |
| Metabolite interconversion enzyme | 737 | 94 | 56.04 | 1.68 | $1.72 \times 10^{-3}$ |
| ↪ *Oxidoreductase* | 228 | 34 | 17.34 | 1.96 | $1.67 \times 10^{-2}$ |

**Table C.6 | Protein classes recalcitrant in dry–hypoxic conditions.** Over-representation test results for PANTHER protein class corresponding to recalcitrant peptides ($n = 1,977$) identified in dry–hypoxic conditions. Subclasses (*italics*) are indented below parent classes to illustrate hierarchical relationships. Only statistically significant results (i.e., Bonferroni-corrected for $p < .05$) for classified proteins are shown, and cells containing $p$-values are coloured according to significance thresholds.

| Protein class | No. referenced | No. queried | No. expected | Fold enrichment | $p$-Value |
|---|---|---|---|---|---|
| Metabolite interconversion enzyme | 737 | 176 | 73.08 | 2.41 | $3.70 \times 10^{-32}$ |
| ↪ *Oxidoreductase* | 228 | 77 | 22.61 | 3.41 | $5.58 \times 10^{-22}$ |
| ↪ *Peroxidase* | 9 | 7 | 0.89 | 7.84 | $4.45 \times 10^{-4}$ |
| Protease | 178 | 54 | 17.65 | 3.06 | $1.29 \times 10^{-12}$ |
| ↪ *Metalloprotease* | 44 | 20 | 4.36 | 4.58 | $1.74 \times 10^{-7}$ |
| Dehydrogenase | 82 | 33 | 8.13 | 4.06 | $4.00 \times 10^{-11}$ |
| Lyase | 54 | 21 | 5.35 | 3.92 | $2.08 \times 10^{-6}$ |
| Calcium-binding protein | 43 | 16 | 4.26 | 3.75 | $2.35 \times 10^{-4}$ |
| Protein-binding activity modulator | 292 | 12 | 28.95 | 0.41 | $4.08 \times 10^{-2}$ |
| RNA metabolism protein | 242 | 1 | 24.00 | 0.04 | $5.14 \times 10^{-8}$ |

**Table C.7 | Hydropathy by preservation category.** Results of Kruskal–Wallis tests with eta-squared effect sizes and *post-hoc* Dunn pairwise comparisons (Holm-adjusted), for peptide preservation with respect to GRAVY score. Cells containing $p$-values are coloured according to significance thresholds.

| Condition | Comparison | $Z$-statistic | Rank biserial correlation ($r$) | Cliff's $\delta$ (95% CI) | Adjusted $p$-value |
|---|---|---|---|---|---|
| **HWLO** $n_{obs} = 7{,}076$, $\chi^2[2] = 12.33$, $p = 2.10 \times 10^{-3}$, $\eta^2_H = 0.001$ | Labile – Putative | 3.2074 | 0.0381 | 0.0599 (0.0235, 0.0962) | $4.01 \times 10^{-3}$ |
| | Labile – Recalcitrant | 2.5485 | 0.0303 | 0.0391 (0.0091, 0.0692) | $2.16 \times 10^{-2}$ |
| | Putative – Recalcitrant | –1.0878 | 0.0129 | –0.0208 (–0.0582, 0.0166) | $2.77 \times 10^{-1}$ |
| **LWHO** $n_{obs} = 2{,}467$, $\chi^2[2] = 15.63$, $p = 4.03 \times 10^{-4}$, $\eta^2_H = 0.006$ | Labile – Putative | 0.0951 | 0.0019 | 0.0032 (–0.0586, 0.0649) | $9.24 \times 10^{-1}$ |
| | Labile – Recalcitrant | 3.7026 | 0.0745 | 0.0961 (0.0454, 0.1464) | $6.40 \times 10^{-4}$ |
| | Putative – Recalcitrant | 2.8518 | 0.0574 | 0.0934 (0.0298, 0.1562) | $5.74 \times 10^{-2}$ |
| **LWLO** $n_{obs} = 6{,}585$, $\chi^2[2] = 14.98$, $p = 5.58 \times 10^{-4}$, $\eta^2_H = 0.002$ | Labile – Putative | –1.9589 | 0.0241 | –0.0368 (–0.0728, –0.0007) | $1.00 \times 10^{-1}$ |
| | Labile – Recalcitrant | –3.7988 | 0.0468 | –0.0624 (–0.0942, –0.0305) | $4.36 \times 10^{-4}$ |
| | Putative – Recalcitrant | –1.2630 | 0.0156 | –0.0259 (–0.0659, 0.0141) | $2.07 \times 10^{-1}$ |

**Table C.8 | Net charge by preservation category.** Results of Kruskal–Wallis tests with eta-squared effect sizes and *post-hoc* Dunn pairwise comparisons (Holm-adjusted), for peptide preservation with respect to weighted mean net charge. Cells containing $p$-values are coloured according to significance thresholds.

| Condition | Comparison | $Z$-statistic | Rank biserial correlation ($r$) | Cliff's $\delta$ (95% CI) | Adjusted $p$-value |
|---|---|---|---|---|---|
| **HWLO** $n_{obs} = 7{,}076$, $\chi^2[2] = 2.33$, $p = 3.11 \times 10^{-1}$, $\eta^2_{\mathrm{H}} = 0.000$ | Labile – Putative | 0.7481 | 0.0089 | 0.0141 (–0.0227, 0.0509) | $4.54 \times 10^{-1}$ |
| | Labile – Recalcitrant | –0.9439 | 0.0112 | –0.0145 (–0.0447, 0.0156) | $6.90 \times 10^{-1}$ |
| | Putative – Recalcitrant | –1.4890 | 0.0177 | –0.0284 (–0.0657, 0.0091) | $4.09 \times 10^{-1}$ |
| **LWHO** $n_{obs} = 2{,}467$, $\chi^2[2] = 5.46$, $p = 6.52 \times 10^{-2}$, $\eta^2_{\mathrm{H}} = 0.001$ | Labile – Putative | –0.5941 | 0.0120 | –0.0192 (–0.0809, 0.0427) | $5.52 \times 10^{-1}$ |
| | Labile – Recalcitrant | 1.8753 | 0.0378 | 0.0489 (–0.0021, 0.0997) | $1.22 \times 10^{-1}$ |
| | Putative – Recalcitrant | 2.0685 | 0.0416 | 0.0672 (0.0034, 0.1305) | $1.16 \times 10^{-1}$ |
| **LWLO** $n_{obs} = 6{,}585$, $\chi^2[2] = 9.37$, $p = 9.22 \times 10^{-3}$, $\eta^2_{\mathrm{H}} = 0.001$ | Labile – Putative | –1.9329 | 0.0238 | –0.0361 (–0.0726, 0.0004) | $1.06 \times 10^{-1}$ |
| | Labile – Recalcitrant | –2.8803 | 0.0355 | –0.0474 (–0.0795, –0.0153) | $1.19 \times 10^{-2}$ |
| | Putative – Recalcitrant | –0.5473 | 0.0067 | –0.0111 (–0.0511, 0.0289) | $5.84 \times 10^{-1}$ |

**Table C.9 | Isoelectric point by preservation category.** Results of Kruskal–Wallis tests with eta-squared effect sizes and *post-hoc* Dunn pairwise comparisons (Holm-adjusted), for peptide preservation with respect to predicted pI. Cells containing $p$-values are coloured according to significance thresholds.

| Condition | Comparison | $Z$-statistic | Rank biserial correlation ($r$) | Cliff's $\delta$ (95% CI) | Adjusted $p$-value |
|---|---|---|---|---|---|
| **HWLO** $n_{obs} = 7{,}076$, $\chi^2[2] = 3.36$, $p = 1.86 \times 10^{-1}$, $\eta^2_{\mathrm{H}} = 0.000$ | Labile – Putative | 0.5709 | 0.0068 | 0.0107 (–0.0260, 0.0473) | $5.68 \times 10^{-1}$ |
| | Labile – Recalcitrant | –1.3913 | 0.0165 | –0.0214 (–0.0514, 0.0087) | $3.28 \times 10^{-1}$ |
| | Putative – Recalcitrant | –1.6763 | 0.0200 | –0.0320 (–0.0694, 0.0054) | $2.81 \times 10^{-1}$ |
| **LWHO** $n_{obs} = 2{,}467$, $\chi^2[2] = 4.32$, $p = 1.15 \times 10^{-1}$, $\eta^2_{\mathrm{H}} = 0.001$ | Labile – Putative | –1.0083 | 0.0203 | –0.0322 (–0.0944, 0.0304) | $3.13 \times 10^{-1}$ |
| | Labile – Recalcitrant | 1.3111 | 0.0264 | 0.0341 (–0.0168, 0.0849) | $3.80 \times 10^{-1}$ |
| | Putative – Recalcitrant | 2.0225 | 0.0407 | 0.0659 (0.0013, 0.1299) | $1.29 \times 10^{-1}$ |
| **LWLO** $n_{obs} = 6{,}585$, $\chi^2[2] = 3.97$, $p = 1.37 \times 10^{-1}$, $\eta^2_{\mathrm{H}} = 0.000$ | Labile – Putative | –1.6524 | 0.0204 | –0.0309 (–0.0677, 0.0061) | $2.95 \times 10^{-1}$ |
| | Labile – Recalcitrant | –1.5997 | 0.0197 | –0.0264 (–0.0586, 0.0059) | $2.19 \times 10^{-1}$ |
| | Putative – Recalcitrant | 0.2268 | 0.0028 | 0.0047 (–0.0354, 0.0448) | $8.21 \times 10^{-1}$ |

**Table C.10 | Mean peptide length and sequence coverage by preservation category.** Results of Kruskal–Wallis tests with eta-squared effect sizes and *post-hoc* Dunn pairwise comparisons (Holm-adjusted), for peptide preservation with respect to mean peptide length and sequence coverage (%). Cells containing $p$-values are coloured according to significance thresholds.

| Metric | Comparison | $Z$-statistic | Rank biserial correlation ($r$) | Cliff's $\delta$ (95% CI) | Adjusted $p$-value |
|---|---|---|---|---|---|
| **Mean peptide length** $n_{obs} = 2{,}954$, $\chi^2[2] = 7.52$, $p = 2.33 \times 10^{-2}$, $\eta^2_H = 0.002$ | Labile – Putative | 2.7365 | 0.0503 | 0.0704 (0.0208, 0.1197) | $1.86 \times 10^{-2}$ |
| | Labile – Recalcitrant | 1.2589 | 0.0232 | 0.0314 (–0.0211, 0.0836) | $2.08 \times 10^{-1}$ |
| | Putative – Recalcitrant | –1.2900 | 0.0237 | –0.0341 (–0.0893, 0.0213) | $3.94 \times 10^{-1}$ |
| **Sequence coverage** $n_{obs} = 2{,}954$, $\chi^2[2] = 19.15$, $p = 6.95 \times 10^{-5}$, $\eta^2_H = 0.006$ | Labile – Putative | 3.9460 | 0.0726 | 0.1010 (0.0518, 0.1496) | $2.38 \times 10^{-4}$ |
| | Labile – Recalcitrant | –0.1453 | 0.0027 | –0.0052 (–0.0573, 0.0469) | $8.84 \times 10^{-1}$ |
| | Putative – Recalcitrant | –3.6824 | 0.0678 | –0.1015 (–0.1562, –0.04612) | $4.62 \times 10^{-4}$ |

**Table C.11 | Mean peptide length by preservation category.** Results of Kruskal–Wallis tests with eta-squared effect sizes and *post-hoc* Dunn pairwise comparisons (Holm-adjusted), for peptide preservation with respect to mean peptide length. Cells containing $p$-values are coloured according to significance thresholds.

| Condition | Comparison | $Z$-statistic | Rank biserial correlation ($r$) | Cliff's $\delta$ (95% CI) | Adjusted $p$-value |
|---|---|---|---|---|---|
| **HWLO** $n_{obs} = 2{,}113$, $\chi^2[2] = 17.25$, $p = 1.80 \times 10^{-5}$, $\eta^2_H = 0.007$ | Labile – Putative | –0.5915 | 0.0129 | –0.0189 (–0.0783, 0.0406) | $5.54 \times 10^{-1}$ |
| | Labile – Recalcitrant | –4.0410 | 0.0878 | –0.1220 (–0.1812, –0.0620) | $1.60 \times 10^{-4}$ |
| | Putative – Recalcitrant | –3.0606 | 0.0666 | –0.1064 (–0.1725, –0.0393) | $4.42 \times 10^{-3}$ |
| **LWHO** $n_{obs} = 1{,}186$, $\chi^2[2] = 15.22$, $p = 4.95 \times 10^{-4}$, $\eta^2_H = 0.011$ | Labile – Putative | 3.6898 | 0.1070 | 0.1566 (0.0739, 0.2372) | $6.73 \times 10^{-4}$ |
| | Labile – Recalcitrant | 2.7326 | 0.0792 | 0.1055 (0.0275, 0.1821) | $1.26 \times 10^{-2}$ |
| | Putative – Recalcitrant | –1.0825 | 0.0314 | –0.0441 (–0.1283, 0.0407) | $2.79 \times 10^{-1}$ |
| **LWLO** $n_{obs} = 2{,}139$, $\chi^2[2] = 3.97$, $p = 1.38 \times 10^{-1}$, $\eta^2_H = 0.001$ | Labile – Putative | 1.8576 | 0.0401 | 0.0565 (–0.0027, 0.1153) | $1.90 \times 10^{-1}$ |
| | Labile – Recalcitrant | –0.0250 | 0.0005 | –0.0017 (–0.0650, 0.0614) | $9.80 \times 10^{-1}$ |
| | Putative – Recalcitrant | –1.6251 | 0.0351 | –0.0547 (–0.1227, 0.0137) | $2.08 \times 10^{-1}$ |

**Table C.12 | Sequence coverage by preservation category.** Results of Kruskal–Wallis tests with eta-squared effect sizes and *post-hoc* Dunn pairwise comparisons (Holm-adjusted), for peptide preservation with respect to sequence coverage (%). Cells containing $p$-values are coloured according to significance thresholds.

| Condition | Comparison | $Z$-statistic | Rank biserial correlation ($r$) | Cliff's $\delta$ (95% CI) | Adjusted $p$-value |
|---|---|---|---|---|---|
| **HWLO** $n_{obs} = 2{,}113$, $\chi^2[2] = 83.35$, $p = 7.95 \times 10^{-19}$, $\eta^2_H = 0.039$ | Labile – Putative | 3.8465 | 0.0836 | 0.1179 (0.0594, 0.1756) | $1.20 \times 10^{-4}$ |
| | Labile – Recalcitrant | –6.2921 | 0.1368 | –0.1921 (–0.2508, –0.1320) | $6.26 \times 10^{-10}$ |
| | Putative – Recalcitrant | –9.0066 | 0.1958 | –0.3080 (–0.3700, –0.2433) | $6.37 \times 10^{-19}$ |
| **LWHO** $n_{obs} = 1{,}186$, $\chi^2[2] = 47.60$, $p = 4.61 \times 10^{-11}$, $\eta^2_H = 0.038$ | Labile – Putative | 6.5139 | 0.1889 | 0.2781 (0.1985, 0.3542) | $2.20 \times 10^{-10}$ |
| | Labile – Recalcitrant | 4.8550 | 0.1408 | 0.1870 (0.1096, 0.2621) | $2.41 \times 10^{-6}$ |
| | Putative – Recalcitrant | –1.8832 | 0.0546 | 0.0756 (–0.0090, –0.1592) | $5.97 \times 10^{-2}$ |
| **LWLO** $n_{obs} = 2{,}139$, $\chi^2[2] = 30.92$, $p = 1.93 \times 10^{-7}$, $\eta^2_H = 0.014$ | Labile – Putative | 3.9322 | 0.0850 | 0.1191 (0.0613, 0.1760) | $1.68 \times 10^{-4}$ |
| | Labile – Recalcitrant | –2.3134 | 0.0500 | –0.0728 (–0.1344, –0.0106) | $2.07 \times 10^{-2}$ |
| | Putative – Recalcitrant | –5.4499 | 0.1178 | –0.1871 (–0.2522, –0.1204) | $1.51 \times 10^{-7}$ |

**Table C.13 | Secondary structure by preservation category.** Results of linear regression for secondary-structure composition *vs.* preservation category, with $\beta$-sheet as the reference term and sensitivity analyses across mean pLDDT confidence thresholds. Cells containing $p$-values are coloured according to significance thresholds.

| Sensitivity | Term | Coefficient ($\beta$) | SE | $Z$-statistic | Adjusted $p$-value |
|---|---|---|---|---|---|
| **No filtering on mean pLDDT** $n_{obs} = 96{,}768$ | $\beta$-Sheet fraction | –2.5823 | 0.0935 | –27.6244 | $5.66 \times 10^{-168}$ |
| | $\alpha$-Helix fraction | –0.5389 | 0.0246 | –21.9140 | $1.91 \times 10^{-106}$ |
| | Coil fraction | 0.1864 | 0.0701 | 2.6582 | $7.86 \times 10^{-3}$ |
| | Mean pLDDT | 0.0274 | 0.0009 | 29.4351 | $1.96 \times 10^{-190}$ |
| | Peptide length | –0.0271 | 0.0021 | –13.0115 | $1.05 \times 10^{-38}$ |
| **Peptides with mean pLDDT $\geq$ 50** $n_{obs} = 89{,}976$ | $\beta$-Sheet fraction | –2.7695 | 0.1021 | –27.1222 | $5.39 \times 10^{-162}$ |
| | $\alpha$-Helix fraction | –0.5384 | 0.0247 | –21.8309 | $1.81 \times 10^{-105}$ |
| | Coil fraction | 0.1327 | 0.0710 | 1.8691 | $6.16 \times 10^{-2}$ |
| | Mean pLDDT | 0.0294 | 0.0010 | 28.4751 | $2.38 \times 10^{-178}$ |
| | Peptide length | –0.0265 | 0.0021 | –12.6940 | $6.38 \times 10^{-37}$ |
| **Peptides with mean pLDDT $\geq$ 70** $n_{obs} = 87{,}588$ | $\beta$-Sheet fraction | –3.4722 | 0.1273 | –27.2779 | $7.75 \times 10^{-164}$ |
| | $\alpha$-Helix fraction | –0.5662 | 0.0250 | –22.6635 | $1.03 \times 10^{-113}$ |
| | Coil fraction | 0.0668 | 0.0727 | 0.9187 | $3.58 \times 10^{-1}$ |
| | Mean pLDDT | 0.0371 | 0.0013 | 28.0529 | $3.68 \times 10^{-173}$ |
| | Peptide length | –0.0270 | 0.0021 | –12.7827 | $2.05 \times 10^{-37}$ |

**Table C.14 | Weighted $\alpha$-helix fraction by preservation category and burial environment.** Results of Kruskal–Wallis tests with eta-squared effect sizes and *post-hoc* Dunn pairwise comparisons (Holm-adjusted), for peptide preservation with respect to weighted $\alpha$-helix fraction. Cells containing $p$-values are coloured according to significance thresholds.

| Condition | Comparison | $Z$-statistic | Rank biserial correlation ($r$) | Cliff's $\delta$ (95% CI) | Adjusted $p$-value |
|---|---|---|---|---|---|
| **HWLO** $n_{obs} = 39{,}594$, $\chi^2[2] = 301.16$, $p = 4.01 \times 10^{-66}$, $\eta^2_H = 0.007$ | Labile – Putative | 11.1684 | 0.0542 | 0.0881 (0.0724, 0.1038) | $1.16 \times 10^{-28}$ |
| | Labile – Recalcitrant | 16.5508 | 0.0803 | 0.1075 (0.0948, 0.1200) | $4.74 \times 10^{-61}$ |
| | Putative – Recalcitrant | 2.2536 | 0.0194 | 0.0175 (0.0015, 0.0334) | $2.42 \times 10^{-2}$ |
| **LWHO** $n_{obs} = 14{,}178$, $\chi^2[2] = 72.32$, $p = 1.98 \times 10^{-16}$, $\eta^2_H = 0.005$ | Labile – Putative | 2.4830 | 0.0204 | 0.0311 (0.0046, 0.0576) | $1.30 \times 10^{-2}$ |
| | Labile – Recalcitrant | 8.4734 | 0.0696 | 0.0929 (0.0714, 0.1143) | $7.25 \times 10^{-17}$ |
| | Putative – Recalcitrant | 4.3507 | 0.0358 | 0.0573 (0.0309, 0.0835) | $2.71 \times 10^{-5}$ |
| **LWLO** $n_{obs} = 36{,}882$, $\chi^2[2] = 313.32$, $p = 9.18 \times 10^{-69}$, $\eta^2_H = 0.008$ | Labile – Putative | 13.4031 | 0.0674 | 0.1064 (0.0907, 0.1219) | $1.16 \times 10^{-40}$ |
| | Labile – Recalcitrant | 15.3895 | 0.0774 | 0.1065 (0.0930, 0.1199) | $5.78 \times 10^{-53}$ |
| | Putative – Recalcitrant | –0.0090 | 0.0000 | –0.0003 (–0.0172, 0.0166) | $9.93 \times 10^{-1}$ |

**Table C.15 | Weighted $\beta$-sheet fraction by preservation category and burial environment.** Results of Kruskal–Wallis tests with eta-squared effect sizes and *post-hoc* Dunn pairwise comparisons (Holm-adjusted), for peptide preservation with respect to weighted $\beta$-sheet fraction. Cells containing $p$-values are coloured according to significance thresholds.

| Condition | Comparison | $Z$-statistic | Rank biserial correlation ($r$) | Cliff's $\delta$ (95% CI) | Adjusted $p$-value |
|---|---|---|---|---|---|
| **HWLO** $n_{obs} = 39{,}594$, $\chi^2[2] = 428.29$, $p = 9.96 \times 10^{-94}$, $\eta^2_H = 0.010$ | Labile – Putative | –9.6179 | 0.0467 | –0.0754 (–0.0910, –0.0598) | $1.34 \times 10^{-21}$ |
| | Labile – Recalcitrant | –20.6120 | 0.1000 | –0.1334 (–0.1459, –0.1209) | $6.42 \times 10^{-94}$ |
| | Putative – Recalcitrant | –7.0190 | 0.0341 | –0.0557 (–0.0716, –0.0399) | $2.23 \times 10^{-12}$ |
| **LWHO** $n_{obs} = 14{,}178$, $\chi^2[2] = 26.09$, $p = 2.16 \times 10^{-6}$, $\eta^2_H = 0.002$ | Labile – Putative | –0.9482 | 0.0078 | –0.0107 (–0.0368, 0.0154) | $3.43 \times 10^{-1}$ |
| | Labile – Recalcitrant | –5.0117 | 0.0412 | –0.0552 (–0.0764, –0.0339) | $1.62 \times 10^{-6}$ |
| | Putative – Recalcitrant | –3.0775 | 0.0253 | –0.0396 (–0.0660, –0.0132) | $4.17 \times 10^{-3}$ |
| **LWLO** $n_{obs} = 36{,}882$, $\chi^2[2] = 558.49$, $p = 5.31 \times 10^{-122}$, $\eta^2_H = 0.014$ | Labile – Putative | –15.7725 | 0.0793 | –0.1237 (–0.1391, –0.1083) | $9.63 \times 10^{-56}$ |
| | Labile – Recalcitrant | –21.8714 | 0.1100 | –0.1516 (–0.1645, –0.1383) | $1.46 \times 10^{-105}$ |
| | Putative – Recalcitrant | –3.0115 | 0.0152 | –0.0239 (–0.0408, –0.0070) | $2.60 \times 10^{-3}$ |

**Table C.16 | Predicted secondary structure model confidence by preservation category.** Results of Kruskal–Wallis tests with eta-squared effect sizes and *post-hoc* Dunn pairwise comparisons (Holm-adjusted), for peptide preservation with respect to mean pLDDT. Cells containing $p$-values are coloured according to significance thresholds.

| Condition | Comparison | $Z$-statistic | Rank biserial correlation ($r$) | Cliff's $\delta$ (95% CI) | Adjusted $p$-value |
|---|---|---|---|---|---|
| **HWLO** $n_{obs} = 39{,}594$, $\chi^2[2] = 732.48$, $p = 8.78 \times 10^{-160}$, $\eta^2_H = 0.019$ | Labile – Putative | –2.9912 | 0.0150 | –0.0219 (–0.0377, –0.0062) | $2.78 \times 10^{-3}$ |
| | Labile – Recalcitrant | –25.9883 | 0.1306 | –0.1691 (–0.1816, –0.1567) | $2.01 \times 10^{-148}$ |
| | Putative – Recalcitrant | –17.8178 | 0.0895 | –0.1423 (–0.1580, –0.1265) | $1.03 \times 10^{-70}$ |
| **LWHO** $n_{obs} = 14{,}178$, $\chi^2[2] = 65.71$, $p = 5.39 \times 10^{-15}$, $\eta^2_H = 0.005$ | Labile – Putative | 4.0015 | 0.0336 | 0.0528 (0.0270, 0.0786) | $1.26 \times 10^{-4}$ |
| | Labile – Recalcitrant | 8.0322 | 0.0675 | 0.0872 (0.0660, 0.1083) | $2.87 \times 10^{-15}$ |
| | Putative – Recalcitrant | 2.5275 | 0.0212 | 0.0344 (0.0079, 0.0609) | $1.15 \times 10^{-2}$ |
| **LWLO** $n_{obs} = 36{,}882$, $\chi^2[2] = 1237.90$, $p = 1.54 \times 10^{-269}$, $\eta^2_H = 0.034$ | Labile – Putative | –18.7200 | 0.0975 | –0.1482 (–0.1635, –0.1328) | $6.81 \times 10^{-78}$ |
| | Labile – Recalcitrant | –34.3453 | 0.1788 | –0.2378 (–0.2508, –0.2249) | $4.97 \times 10^{-258}$ |
| | Putative – Recalcitrant | –10.3126 | 0.0537 | –0.0879 (–0.1047, –0.0710) | $6.18 \times 10^{-25}$ |

**Table C.17 | Intrinsic disorder by preservation category.** Results of Kruskal–Wallis tests with eta-squared effect sizes and *post-hoc* Dunn pairwise comparisons (Holm-adjusted), for peptide preservation with respect to mean IUPred score and fraction disordered. Cells containing $p$-values are coloured according to significance thresholds.

| Metric | Comparison | $Z$-statistic | Rank biserial correlation ($r$) | Cliff's $\delta$ (95% CI) | Adjusted $p$-value |
|---|---|---|---|---|---|
| **Mean IUPred score** $n_{obs} = 96{,}708$, $\chi^2[2] = 74.83$, $p = 5.63 \times 10^{-17}$, $\eta^2_H = 0.003$ | Labile – Putative | 6.2308 | 0.0200 | 0.0306 (0.0207, 0.0404) | $4.64 \times 10^{-10}$ |
| | Labile – Recalcitrant | 17.9162 | 0.0576 | 0.0754 (0.0672, 0.0836) | $2.64 \times 10^{-71}$ |
| | Putative – Recalcitrant | 8.4241 | 0.0271 | 0.0434 (0.0331, 0.0537) | $7.27 \times 10^{-17}$ |
| **Fraction disordered** $n_{obs} = 96{,}708$, $\chi^2[2] = 416.09$, $p = 4.45 \times 10^{-91}$, $\eta^2_H = 0.004$ | Labile – Putative | 3.7054 | 0.0119 | 0.0120 (0.0054, 0.0186) | $2.11 \times 10^{-4}$ |
| | Labile – Recalcitrant | 19.2469 | 0.0619 | 0.0529 (0.0477, 0.0582) | $4.50 \times 10^{-82}$ |
| | Putative – Recalcitrant | 11.8974 | 0.0383 | 0.0406 (0.0340, 0.0472) | $2.44 \times 10^{-32}$ |

**Table C.18 | Mean IUPred score by preservation category and burial environment.** Results of Kruskal–Wallis tests with eta-squared effect sizes and *post-hoc* Dunn pairwise comparisons (Holm-adjusted), for peptide preservation with respect to mean IUPred score. Cells containing $p$-values are coloured according to significance thresholds.

| Condition | Comparison | $Z$-statistic | Rank biserial correlation ($r$) | Cliff's $\delta$ (95% CI) | Adjusted $p$-value |
|---|---|---|---|---|---|
| **HWLO** $n_{obs} = 42{,}438$, $\chi^2[2] = 74.83$, $p = 5.63 \times 10^{-17}$, $\eta^2_H = 0.002$ | Labile – Putative | –1.5054 | 0.0073 | –0.0121 (–0.0272, 0.0030) | $1.32 \times 10^{-1}$ |
| | Labile – Recalcitrant | 7.2916 | 0.0354 | 0.0460 (0.0338, 0.0583) | $6.12 \times 10^{-13}$ |
| | Putative – Recalcitrant | 7.3321 | 0.0356 | 0.0565 (0.0410, 0.0719) | $6.74 \times 10^{-13}$ |
| **LWHO** $n_{obs} = 14{,}784$, $\chi^2[2] = 66.92$, $p = 2.94 \times 10^{-15}$, $\eta^2_H = 0.004$ | Labile – Putative | 7.7054 | 0.0634 | 0.1012 (0.0759, 0.1263) | $3.91 \times 10^{-14}$ |
| | Labile – Recalcitrant | 0.3293 | 0.0027 | 0.0028 (–0.0180, 0.0237) | $7.42 \times 10^{-1}$ |
| | Putative – Recalcitrant | –7.2270 | 0.0594 | –0.0949 (–0.1204, –0.0693) | $9.88 \times 10^{-13}$ |
| **LWLO** $n_{obs} = 39{,}486$, $\chi^2[2] = 416.09$, $p = 4.45 \times 10^{-91}$, $\eta^2_H = 0.011$ | Labile – Putative | 6.6022 | 0.0332 | 0.0501 (0.0352, 0.0650) | $4.05 \times 10^{-1}$ |
| | Labile – Recalcitrant | 20.3975 | 0.1026 | 0.1373 (0.1244, 0.1501) | $5.28 \times 10^{-92}$ |
| | Putative – Recalcitrant | 10.3746 | 0.0522 | 0.0860 (0.0700, 0.1023) | $6.47 \times 10^{-25}$ |

**Table C.19 | Fraction disordered by preservation category and burial environment.** Results of Kruskal–Wallis tests with eta-squared effect sizes and *post-hoc* Dunn pairwise comparisons (Holm-adjusted), for peptide preservation with respect to fraction disordered. Cells containing $p$-values are coloured according to significance thresholds.

| Condition | Comparison | $Z$-statistic | Rank biserial correlation ($r$) | Cliff's $\delta$ (95% CI) | Adjusted $p$-value |
|---|---|---|---|---|---|
| **HWLO** $n_{obs} = 42{,}438$, $\chi^2[2] = 94.19$, $p = 3.52 \times 10^{-21}$, $\eta^2_H = 0.002$ | Labile – Putative | –2.9217 | 0.0142 | –0.0155 (–0.0261, –0.0049) | $3.48 \times 10^{-3}$ |
| | Labile – Recalcitrant | 7.4294 | 0.0361 | 0.0318 (0.0236, 0.0400) | $2.18 \times 10^{-13}$ |
| | Putative – Recalcitrant | 8.8288 | 0.0429 | 0.0464 (0.0359, 0.0569) | $3.17 \times 10^{-18}$ |
| **LWHO** $n_{obs} = 14{,}784$, $\chi^2[2] = 42.77$, $p = 5.12 \times 10^{-10}$, $\eta^2_H = 0.003$ | Labile – Putative | 5.4736 | 0.0450 | 0.0383 (0.0260, 0.0506) | $8.82 \times 10^{-8}$ |
| | Labile – Recalcitrant | –1.2751 | 0.0105 | –0.0074 (–0.0189, 0.0041) | $2.02 \times 10^{-1}$ |
| | Putative – Recalcitrant | –6.3343 | 0.0521 | –0.0448 (–0.0576, –0.0320) | $7.15 \times 10^{-10}$ |
| **LWLO** $n_{obs} = 39{,}486$, $\chi^2[2] = 509.05$, $p = 4.45 \times 10^{-91}$, $\eta^2_H = 0.011$ | Labile – Putative | 5.9168 | 0.0298 | 0.0301 (0.0198, 0.0404) | $3.28 \times 10^{-9}$ |
| | Labile – Recalcitrant | 22.5031 | 0.1132 | 0.1007 (0.0925, 0.1088) | $1.16 \times 10^{-111}$ |
| | Putative – Recalcitrant | 12.6989 | 0.0639 | 0.0705 (0.0602, 0.0808) | $1.20 \times 10^{-36}$ |

**Table C.20 | UniProt feature section by preservation category.** Chi-squared association tests were conducted on 215,088 peptide–UniProt feature observations corresponding to 94,296 unique peptides. Pairwise comparisons are omitted because section-level labels serve only as hierarchical groupings of feature types; reported statistics therefore describe global compositional bias rather than individual feature effects. Cells containing $p$-values are coloured according to significance thresholds.

| Section | $\chi^2$ [2] statistic | Cramér's $V$ | Adjusted $p$-value |
|---|---|---|---|
| Topology | 768.61 | 0.09028322679 | $1.00 \times 10^{-166}$ |
| Repeats | 222.52 | 0.0485782804 | $1.91 \times 10^{-48}$ |
| Domains and regions | 220.92 | 0.04840298907 | $2.84 \times 10^{-48}$ |
| PTM | 208.65 | 0.04703917137 | $9.86 \times 10^{-46}$ |
| Molecule processing | 133.12 | 0.03757236843 | $1.99 \times 10^{-29}$ |
| Variants/mutagenesis | 60.94 | 0.0254216548 | $7.80 \times 10^{-14}$ |
| Sites | 13.71 | 0.01205916729 | $1.20 \times 10^{-3}$ |
| Other | 5.39 | 0.00755911831 | $6.80 \times 10^{-2}$ |

**Table C.21 | UniProt feature type by preservation category.** Chi-squared association tests were conducted on 215,088 peptide–UniProt feature observations corresponding to 94,296 unique peptides. Pairwise comparisons are omitted because type-level labels serve only as hierarchical groupings of feature descriptors; reported statistics therefore describe global compositional bias rather than individual feature effects. Cells containing $p$-values are coloured according to significance thresholds.

| Section | Type | $\chi^2$ [2] statistic | Cramér's $V$ | Adjusted $p$-value |
|---|---|---|---|---|
| Domains and regions | Region | 797.35 | 0.1527306007 | $2.16 \times 10^{-173}$ |
| | Domain | 591.93 | 0.1315937602 | $4.37 \times 10^{-129}$ |
| | Motif | 16.03 | 0.02165634928 | $3.30 \times 10^{-4}$ |
| Molecule processing | Transit peptide | 32.29 | 0.01867474088 | $4.86 \times 10^{-7}$ |
| | Chain | 22.13 | 0.0154597819 | $2.61 \times 10^{-5}$ |
| | Signal | 22.26 | 0.01550450353 | $2.61 \times 10^{-5}$ |
| | Propeptide | 15.96 | 0.01313020300 | $3.51 \times 10^{-4}$ |
| | Peptide | 15.91 | 0.0131084283 | $3.51 \times 10^{-4}$ |
| PTM | Disulfide bond | 1699.23 | 0.2723176685 | $< 2.22 \times 10^{-354}$ |
| | Modified residue | 1396.35 | 0.2468572707 | $1.53 \times 10^{-303}$ |
| | Cross-link | 135.55 | 0.07691361418 | $6.12 \times 10^{-30}$ |
| | Lipidation | 27.28 | 0.0345024968 | $1.49 \times 10^{-6}$ |
| | Glycosylation | 0.22 | 0.003068974986 | $8.98 \times 10^{-1}$ |
| Sites | DNA binding | 66.87 | 0.08375045275 | $1.51 \times 10^{-14}$ |
| | Zinc finger | 30.25 | 0.05632493097 | $6.76 \times 10^{-7}$ |
| | Active site | 16.80 | 0.04197409596 | $3.75 \times 10^{-4}$ |
| | Binding site | 12.69 | 0.03648514223 | $2.19 \times 10^{-3}$ |
| | Site | 5.09 | 0.02311053736 | $7.84 \times 10^{-2}$ |
| Topology | Transmembrane | 51.75 | 0.05602203651 | $1.74 \times 10^{-11}$ |
| | Topological domain | 29.83 | 0.04253202092 | $3.34 \times 10^{-7}$ |
| | Intramembrane | 30.16 | 0.04253202092 | $3.34 \times 10^{-7}$ |
| Variants/mutagenesis | Alternative sequence | 25.45 | 0.04932749288 | $1.19 \times 10^{-5}$ |
| | Mutagenesis | 21.64 | 0.04548693962 | $4.00 \times 10^{-5}$ |

*Continued on next page*

| Section | Type | $\chi^2$ [2] statistic | Cramér's $V$ | Adjusted $p$-value |
|---|---|---|---|---|
| | Natural variant | 10.72 | 0.03201004823 | $6.28 \times 10^{-3}$ |
| | Sequence conflict | 6.07 | 0.02409030952 | $4.81 \times 10^{-2}$ |

**Table C.22 | Dominant radical oxidation pathways under contrasting hydration and oxygen regimes.** The table presents mechanistic pathways inferred from the experimental results and established radical oxidation chemistry (Appendix C.3), summarising how water and oxygen availability jointly control radical initiation, chain propagation, and termination: water primarily governs molecular mobility and encounter probability, whereas oxygen controls chain length and the balance between propagation, regeneration, and termination. $H_2O_2$ = hydrogen peroxide; $OH^-$ = hydroxide; $\cdot OH$ = hydroxyl radical; R–H = oxidisable protein site; $R\cdot$ = protein-centred radical; $ROO\cdot$ = peroxyl radical; ROOH = hydroperoxide; $RO\cdot$ = alkoxyl radical; $R'\cdot$ = new radical created after bond cleavage; R–R = crosslink; A–H = local electron or hydrogen donor (e.g., Trp, Tyr, Met); $A\cdot$ = corresponding donor-centred radical.

| Condition | Initiation | Propagation | Termination | Net molecular consequence |
|---|---|---|---|---|
| HWHO | Primary radical generation (Fenton-type): $Fe^{2+} + H_2O_2 \rightarrow Fe^{3+} + OH^- + \cdot OH$<br><br>Secondary radical generation (H-abstraction): $\cdot OH + R{-}H \rightarrow H_2O + R\cdot$ | $O_2$ addition: $R\cdot + O_2 \rightarrow ROO\cdot$<br><br>Chain propagation (peroxyl H-abstraction): $ROO\cdot + R{-}H \rightarrow ROOH + R'\cdot$<br><br>Radical regeneration (metal-mediated): $ROOH + Fe^{2+} \rightarrow RO\cdot + OH^- + Fe^{3+}$<br><br>Chain-amplifying fragmentation ($\beta$-scission): $RO\cdot \rightarrow$ carbonyl-containing fragments $+ R''\cdot$ | Late peroxyl termination after extended chain propagation: $ROO\cdot + ROO\cdot \rightarrow$ non-radical products ($\pm O_2$)<br><br>Crosslinking possible, but competes with ongoing propagation: $R\cdot + R'\cdot \rightarrow R{-}R$ | Maximal chain-propagating oxidation with repeated radical regeneration and accumulation of ROOH and/or $RO\cdot$, favouring backbone and side-chain cleavage, generation of successive radicals ($R\cdot$, $R'\cdot$, $R''\cdot$, etc.), and thus extensive molecular loss. |
| HWLO | Primary radical generation (Fenton-type): $Fe^{2+} + H_2O_2 \rightarrow Fe^{3+} + OH^- + \cdot OH$<br><br>Secondary radical generation (H-abstraction): $\cdot OH + R{-}H \rightarrow H_2O + R\cdot$ | $H_2O$ availability maintains molecular mobility and permits continued radical transfer and turnover, but reduced $O_2$ availability limits chain length and radical regeneration. | Termination dominates at the site of radical generation, by:<br><br>Electron-transfer quenching: $R\cdot + A{-}H \rightarrow R{-}H + A\cdot$<br><br>Crosslinking: $R\cdot + R'\cdot \rightarrow R{-}R$ | Repeated, spatially localised initiation –termination oxidation events with high probability of crosslinking per initiated radical, and preferential preservation *via* cumulative crosslinking. |

*Continued on next page*

*C. Supplementary: Molecular Solution to the Paradox of Ancient Brain Preservation*

| **Condition** | **Initiation** | **Propagation** | **Termination** | **Net molecular consequence** |
|---|---|---|---|---|
| LWHO | Initiation rate-limited by reduced molecular mobility. If initiation occurs:<br><br>Primary radical generation (Fenton-type): $Fe^{2+} + H_2O_2 \rightarrow Fe^{3+} + OH^- + \cdot OH$<br><br>Secondary radical generation (H-abstraction): $\cdot OH + R{-}H \rightarrow H_2O + R\cdot$ | Propagation rate-limited by reduced molecular mobility.<br><br>$O_2$ addition occurs, but is encounter-limited. Chain propagation and radical regeneration are limited by restricted ion diffusion. | Termination dominates at the site of radical generation, most often by electron-transfer quenching: $R\cdot + A{-}H \rightarrow R{-}H + A\cdot$<br><br>Peroxyl termination possible, if generated locally: $ROO\cdot + ROO\cdot \rightarrow$ non-radical products ($\pm O_2$)<br><br>Crosslinking possible, but only if radicals generated in proximity: $R\cdot + R'\cdot \rightarrow R{-}R$ | Slow, heterogeneous oxidation dominated by mobility-limited kinetics, producing fewer long chains than HWHO and fewer crosslinks than HWLO. Net effect is partial oxidation rather than extensive fragmentation or stabilisation. |
| LWLO | Initiation most strongly rate-limited, with limited metal cycling, peroxide turnover, and substrate mobility. If initiation occurs:<br><br>Primary radical generation (H-abstraction): $\cdot OH + R{-}H \rightarrow H_2O + R\cdot$ | Propagation rate-limited by reduced $O_2$ availability and reduced molecular mobility.<br><br>$O_2$ addition is suppressed. Chain propagation and radical regeneration are relatively rare and limited by restricted ion diffusion. | Termination dominates at the site of radical generation, most often by electron-transfer quenching: $R\cdot + A{-}H \rightarrow R{-}H + A\cdot$<br><br>Crosslinking possible, but only if radicals generated in proximity: $R\cdot + R'\cdot \rightarrow R{-}R$ | Minimal oxidation due to low radical flux. Chemical change is limited and spatially restricted; preservation arises primarily from suppression of oxidative chemistry rather than from stabilising crosslink formation. |

**Table C.23 | Reactivity and preservation potential of key amino-acid residues.** The table summarises how specific side-chain chemistries govern modification pathways: residues forming delocalised, stabilising radicals (e.g., Trp, Tyr, Met) promote crosslinking, whereas those yielding destructive or inert products (e.g., His, Gln, Ala, Ile, Leu) accelerate degradation.

| Amino acid | Key reactive group(s) | Typical modification pathway | Principal product(s) and/or effect(s) | Likely consequence for preservation |
|---|---|---|---|---|
| Trp | Indole ring with weakly basic nitrogen; highly electron-rich $\pi$ system. | One-electron oxidation *via* indolyl radical intermediate, followed by hydroxylation, oxidative ring cleavage, or radical coupling. | Stable oxidised aromatics (e.g., Trp–Trp, Trp–Tyr, hydroxyindoles, kynurenines) capable of further radical coupling and intermolecular crosslinking. | Acts as a radical sink and nucleation site for polymerisation; promotes formation of insoluble aggregates; stabilising. |
| Tyr | Phenolic ring; moderately electron-rich $\pi$ system. | Reversible one-electron oxidation *via* tyrosyl radical intermediate, followed by dimerisation. | Dityrosine and higher-order covalent crosslinks. | Produces covalently crosslinked networks resistant to hydrolysis and proteolysis; stabilising. |
| Met | Thioether sulfur; soft redox centre. | One-electron oxidation to transient thiyl radicals, followed by oxidation to sulfoxide or sulfone. | Stable, non-fragmenting products that persist unchanged or slowly condense with RCS or neighbouring sulfur groups; reversible redox cycling. | Buffers oxidative flux; can mediate secondary crosslinking; stabilising. |
| His | Imidazole ring with two nitrogen donors; weakly electron-rich (amphoteric) $\pi$ system. | Metal coordination leading to Fenton-type radical generation and self-oxidation. | 2-oxo-His, ring-cleaved or fragmented products. | Generates local ROS; self-oxidising and locally destabilising, but may promote system-level preservation *via* promotion of oxidative crosslinking. |
| Gln | Terminal amide group. | Redox-inactive; hydrolytic deamidation or *via* cyclic imide intermediate. | Carboxylate and either Glu or iso-Glu plus ammonia; increases hydrophilicity. | Promotes peptide cleavage and solubilisation; destabilising. |
| Phe | Benzyl ring lacking heteroatoms; electron-neutral $\pi$ system. | Slow peroxidation at benzylic C−H *via* benzylic radical intermediates with limited radical stability. | Unstable (hydro)peroxides decompose to RCS, leading to side-chain or backbone cleavage. | Chemically inert toward crosslinking; prone to fragmentation; destabilising. |

*Continued on next page*

| **Amino acid** | **Key reactive group(s)** | **Typical modification pathway** | **Principal product(s) and/or effect(s)** | **Likely consequence for preservation** |
|---|---|---|---|---|
| Aliphatic residues (Ala, Val, Ile) | Saturated C−H bonds. | Hydrogen abstraction and oxidation at tertiary carbons *via* peroxyl radical intermediates, followed by $\beta$-scission. | Unstable (hydro)peroxides decompose to RCS, leading to side-chain or backbone cleavage. | Promotes fragmentation; destabilising. |
| Small/ flexible residues (Gly, Pro, Thr) | Minimal side chains; conformational freedom. | Limited redox chemistry; hydrolysis, dehydration, and condensation reactions enabling secondary crosslinking. | Confer flexibility or steric protection at or near termini; stabilise fragments and promote aggregation *via* hydrogen bonding or condensation. | Protects N-termini from cleavage; aids aggregation by bringing reactive groups into proximity; moderately stabilising. |
| Lys | Primary $\varepsilon$-amine. | Limited redox chemistry; Schiff-base formation and carbonyl condensation with oxidised lipids or sugars. | Crosslinks with RCS; ALE/AGEs, imines, and Michael adducts. | Participates in secondary condensation; moderately stabilising. |
| Acidic residues (Asp, Glu) | Carboxylate. | Redox-inactive; metal coordination, acid/base-catalysed hydrolysis. | Metal complexes or salt bridges; potential peptide cleavage. | Generally destabilising, but may confer local stability through ionic or metal-mediated interactions. |

**Table C.24 | Sample mass and protein concentration for the DDA dataset.** Starting mass, volume of SDS lysis buffer, and protein concentration of samples ($n = 72$) post-lysis, estimated using BCA assay with BSA standards, followed by normalised volumes of sample and buffer for reduction, alkylation and digestion.

| **Time point** | **Sample ID** | **Sample mass** (mg) | **Buffer volume** (µL) | **Concentration** (µg/µL) |
|---|---|---|---|---|
| $\mathbf{T}_1$ | HWHO_24hr_A | 89.5 | 1600 | 4.05 |
| | HWHO_24hr_B | 89.2 | 1600 | 2.61 |
| | HWHO_24hr_C | 105.6 | 1600 | 3.53 |
| | HWLO_24hr_A | 124.5 | 1600 | 3.97 |
| | HWLO_24hr_B | 86.3 | 1553 | 0.66 |
| | HWLO_24hr_C | 102.3 | 1600 | 0.43 |
| | LWHO_24hr_A | 63.9 | 1150 | 0.14 |
| | LWHO_24hr_B | 76.6 | 1379 | 3.09 |
| | LWHO_24hr_C | 87.1 | 1568 | 3.09 |
| | LWLO_24hr_A | 94.5 | 1600 | 3.43 |
| | LWLO_24hr_B | 75.1 | 1352 | 3.04 |
| | LWLO_24hr_C | 88.0 | 1584 | 3.69 |
| $\mathbf{T}_2$ | HWHO_72hr_A | 74.9 | 1348 | 3.63 |
| | HWHO_72hr_B | 119.3 | 1600 | 4.90 |
| | HWHO_72hr_C | 83.1 | 1496 | 2.91 |
| | HWLO_72hr_A | 96.3 | 1600 | 3.58 |

*Continued on next page*

| Time point | Sample ID | Sample mass (mg) | Buffer volume (µL) | Concentration (µg/µL) |
|---|---|---|---|---|
| | HWLO_72hr_B | 102.0 | 1600 | 3.16 |
| | HWLO_72hr_C | 118.9 | 1600 | 4.90 |
| | LWHO_72hr_A | 86.5 | 1557 | 2.34 |
| | LWHO_72hr_B | 95.2 | 1600 | 0.64 |
| | LWHO_72hr_C | 78.3 | 1409 | 3.97 |
| | LWLO_72hr_A | 84.5 | 1521 | 8.27 |
| | LWLO_72hr_B | 109.7 | 1600 | 3.52 |
| | LWLO_72hr_C | 92.8 | 1600 | 3.16 |
| | HWHO_1wk_A | 100.5 | 1600 | 0.37 |
| | HWHO_1wk_B | 99.7 | 1600 | 7.39 |
| | HWHO_1wk_C | 104.3 | 1600 | 7.39 |
| | HWLO_1wk_A | 71.3 | 1283 | 2.58 |
| | HWLO_1wk_B | 84.5 | 1521 | 2.72 |
| $\mathbf{T}_3$ | HWLO_1wk_C | 101.2 | 1600 | 3.85 |
| | LWHO_1wk_A | 66.8 | 1202 | 2.61 |
| | LWHO_1wk_B | 78.6 | 1415 | 3.18 |
| | LWHO_1wk_C | 86.7 | 1561 | 3.71 |
| | LWLO_1wk_A | 77.6 | 1397 | 3.40 |
| | LWLO_1wk_B | 78.9 | 1420 | 3.30 |
| | LWLO_1wk_C | 85.8 | 1544 | 4.12 |
| | HWHO_6wk_A | 80.6 | 1451 | 0.06 |
| | HWHO_6wk_B | 88.5 | 1593 | 0.14 |
| | HWHO_6wk_C | 39.9 | 718 | 0.35 |
| | HWLO_6wk_A | 98.4 | 1600 | 2.25 |
| | HWLO_6wk_B | 55.9 | 1006 | 2.14 |
| $\mathbf{T}_4$ | HWLO_6wk_C | 60.1 | 1082 | 3.39 |
| | LWHO_6wk_A | 41.6 | 749 | 3.51 |
| | LWHO_6wk_B | 34.8 | 626 | 0.33 |
| | LWHO_6wk_C | 38.7 | 697 | 1.93 |
| | LWLO_6wk_A | 77.1 | 1388 | 2.44 |
| | LWLO_6wk_B | 49.8 | 896 | 1.27 |
| | LWLO_6wk_C | 95.3 | 1600 | 2.77 |
| | HWHO_3mo_A | 39.6 | 713 | 1.13 |
| | HWHO_3mo_B | 51.5 | 927 | 1.49 |
| | HWHO_3mo_C | 62.0 | 1116 | 0.28 |
| | HWLO_3mo_A | 62.0 | 1116 | 1.28 |
| | HWLO_3mo_B | 92.2 | 1600 | 2.31 |
| $\mathbf{T}_5$ | HWLO_3mo_C | 62.3 | 1121 | 1.35 |
| | LWHO_3mo_A | 33.9 | 610 | 1.58 |
| | LWHO_3mo_B | 43.6 | 785 | 4.82 |
| | LWHO_3mo_C | 43.5 | 783 | 1.65 |
| | LWLO_3mo_A | 64.7 | 1165 | 1.43 |
| | LWLO_3mo_B | 59.9 | 1078 | 5.03 |
| | LWLO_3mo_C | 47.3 | 851 | 0.90 |
| | HWHO_6mo_A | 32.2 | 580 | 3.11 |
| | HWHO_6mo_B | 43.7 | 787 | 2.17 |
| | HWHO_6mo_C | 33.6 | 605 | 4.41 |
| | HWLO_6mo_A | 85.2 | 1534 | 0.49 |
| $\mathbf{T}_6$ | HWLO_6mo_B | 96.7 | 1600 | 1.23 |
| | HWLO_6mo_C | 81.4 | 1465 | 0.52 |
| | LWHO_6mo_A | 28.7 | 517 | 0.76 |
| | LWHO_6mo_B | 28.2 | 508 | 0.79 |
| | LWHO_6mo_C | 98.0 | 1600 | 0.38 |

*Continued on next page*

| Time point | Sample ID | Sample mass (mg) | Buffer volume (µL) | Concentration (µg/µL) |
|---|---|---|---|---|
| | LWLO_6mo_A | 40.6 | 731 | 1.69 |
| | LWLO_6mo_B | 30.0 | 540 | 0.15 |
| | LWLO_6mo_C | 30.3 | 545 | 0.33 |

**Table C.25 | Sample mass and protein concentration for the DIA dataset.** Starting mass, volume of RIPA lysis buffer, and protein concentration of samples ($n = 72$) post-lysis, estimated using BCA assay with BSA standards, followed by normalised volumes of sample and buffer for reduction, alkylation and digestion.

| Time point | Sample ID | Sample mass (mg) | Buffer volume (µL) | Conc. (µg/µL) | Normalised vol. of sample (µL) for 10 µg protein | Normalised vol. of buffer (µL) for 15 µL total |
|---|---|---|---|---|---|---|
| $\mathbf{T}_1$ | HWHO_24hr_A | 8 | 80 | 11.10 | 0.90 | 14.10 |
| | HWHO_24hr_B | 13 | 130 | 8.41 | 1.19 | 13.81 |
| | HWHO_24hr_C | 32 | 320 | 8.40 | 1.19 | 13.81 |
| | HWLO_24hr_A | 17 | 170 | 8.40 | 1.19 | 13.81 |
| | HWLO_24hr_B | 27 | 270 | 8.28 | 1.21 | 13.79 |
| | HWLO_24hr_C | 17 | 170 | 8.18 | 1.22 | 13.78 |
| | LWHO_24hr_A | 17 | 170 | 6.40 | 1.56 | 13.44 |
| | LWHO_24hr_B | 37 | 370 | 9.15 | 1.09 | 13.91 |
| | LWHO_24hr_C | 45 | 450 | 7.04 | 1.42 | 13.58 |
| | LWLO_24hr_A | 18 | 180 | 9.39 | 1.06 | 13.94 |
| | LWLO_24hr_B | 24 | 240 | 8.64 | 1.16 | 13.84 |
| | LWLO_24hr_C | 22 | 220 | 10.25 | 0.98 | 14.02 |
| $\mathbf{T}_2$ | HWHO_72hr_A | 20 | 200 | 10.69 | 0.94 | 14.06 |
| | HWHO_72hr_B | 22 | 220 | 8.05 | 1.24 | 13.76 |
| | HWHO_72hr_C | 37 | 370 | 8.41 | 1.19 | 13.81 |
| | HWLO_72hr_A | 13 | 130 | 8.37 | 1.19 | 13.81 |
| | HWLO_72hr_B | 47 | 470 | 7.74 | 1.29 | 13.71 |
| | HWLO_72hr_C | 39 | 390 | 8.88 | 1.13 | 13.87 |
| | LWHO_72hr_A | 56 | 560 | 8.75 | 1.14 | 13.86 |
| | LWHO_72hr_B | 34 | 340 | 8.83 | 1.13 | 13.87 |
| | LWHO_72hr_C | 47 | 470 | 9.35 | 1.07 | 13.93 |
| | LWLO_72hr_A | 36 | 360 | 7.98 | 1.25 | 13.75 |
| | LWLO_72hr_B | 36 | 360 | 8.56 | 1.17 | 13.83 |
| | LWLO_72hr_C | 22 | 220 | 9.32 | 1.07 | 13.93 |
| $\mathbf{T}_3$ | HWHO_1wk_A | 15 | 150 | 7.36 | 1.36 | 13.64 |
| | HWHO_1wk_B | 48 | 480 | 8.38 | 1.19 | 13.81 |
| | HWHO_1wk_C | 9 | 90 | 7.22 | 1.39 | 13.61 |
| | HWLO_1wk_A | 40 | 400 | 8.03 | 1.25 | 13.75 |
| | HWLO_1wk_B | 50 | 500 | 7.31 | 1.37 | 13.63 |
| | HWLO_1wk_C | 33 | 330 | 7.73 | 1.29 | 13.71 |
| | LWHO_1wk_A | 18 | 180 | 8.04 | 1.24 | 13.76 |
| | LWHO_1wk_B | 26 | 260 | 6.88 | 1.45 | 13.55 |
| | LWHO_1wk_C | 42 | 420 | 7.70 | 1.30 | 13.70 |
| | LWLO_1wk_A | 59 | 590 | 7.68 | 1.30 | 13.70 |
| | LWLO_1wk_B | 26 | 260 | 6.34 | 1.58 | 13.42 |
| | LWLO_1wk_C | 46 | 460 | 10.05 | 1.00 | 14.00 |
| $\mathbf{T}_4$ | HWHO_6wk_A | 3 | 30 | 4.28 | 2.34 | 12.66 |
| | HWHO_6wk_B | 37 | 370 | 0.94 | 10.68 | 4.32 |

*Continued on next page*

| Time point | Sample ID | Sample mass (mg) | Buffer volume (µL) | Conc. (µg/µL) | Normalised vol. of sample (µL) for 10 µg protein | Normalised vol. of buffer (µL) for 15 µL total |
|---|---|---|---|---|---|---|
| | HWHO_6wk_C | 7 | 70 | 6.76 | 1.48 | 13.52 |
| | HWLO_6wk_A | 46 | 460 | 2.66 | 3.76 | 11.24 |
| | HWLO_6wk_B | 24 | 240 | 3.31 | 3.02 | 11.98 |
| | HWLO_6wk_C | 29 | 290 | 3.43 | 2.91 | 12.09 |
| | LWHO_6wk_A | 16 | 160 | 6.29 | 1.59 | 13.41 |
| | LWHO_6wk_B | 9 | 90 | 8.21 | 1.22 | 13.78 |
| | LWHO_6wk_C | 6 | 60 | 6.32 | 1.58 | 13.42 |
| | LWLO_6wk_A | 20 | 200 | 4.86 | 2.06 | 12.94 |
| | LWLO_6wk_B | 20 | 200 | 7.44 | 1.34 | 13.66 |
| | LWLO_6wk_C | 15 | 150 | 3.94 | 2.54 | 12.46 |
| | HWHO_3mo_A | 25 | 250 | 1.79 | 5.60 | 9.40 |
| | HWHO_3mo_B | 4 | 40 | 4.86 | 2.06 | 12.94 |
| | HWHO_3mo_C | 5 | 50 | 1.05 | 9.50 | 5.50 |
| | HWLO_3mo_A | 5 | 50 | 2.59 | 3.87 | 11.13 |
| | HWLO_3mo_B | 6 | 60 | 3.91 | 2.56 | 12.44 |
| $\mathbf{T}_5$ | HWLO_3mo_C | 7 | 70 | 2.68 | 3.73 | 11.27 |
| | LWHO_3mo_A | 12 | 120 | 6.75 | 1.48 | 13.52 |
| | LWHO_3mo_B | 4 | 40 | 7.35 | 1.36 | 13.64 |
| | LWHO_3mo_C | 7 | 70 | 7.49 | 1.34 | 13.66 |
| | LWLO_3mo_A | 2 | 30 | 6.93 | 1.44 | 13.56 |
| | LWLO_3mo_B | 14 | 140 | 3.43 | 2.91 | 12.09 |
| | LWLO_3mo_C | 21 | 210 | 4.06 | 2.46 | 12.54 |
| | HWHO_6mo_A | 1 | 30 | 0.64 | 15.0 | 0.00 |
| | HWHO_6mo_B | 1 | 30 | 0.06 | 15.0 | 0.00 |
| | HWHO_6mo_C | 9 | 90 | 2.14 | 4.67 | 10.33 |
| | HWLO_6mo_A | 18 | 180 | 1.17 | 8.55 | 6.45 |
| | HWLO_6mo_B | 14 | 140 | 2.46 | 4.06 | 10.94 |
| $\mathbf{T}_6$ | HWLO_6mo_C | 26 | 260 | 1.55 | 6.44 | 8.56 |
| | LWHO_6mo_A | 3 | 30 | 0.14 | 15.0 | 0.00 |
| | LWHO_6mo_B | 8 | 80 | 2.03 | 4.94 | 10.06 |
| | LWHO_6mo_C | 5 | 50 | 3.61 | 2.77 | 12.23 |
| | LWLO_6mo_A | 13 | 130 | 3.35 | 2.99 | 12.01 |
| | LWLO_6mo_B | 7 | 70 | 4.53 | 2.21 | 12.79 |
| | LWLO_6mo_C | 7 | 70 | 3.46 | 2.89 | 12.11 |

# C.7 References


[1] Yasset Perez-Riverol et al. 'The PRIDE database at 20 years: 2025 update'. In: *Nucleic Acids Res.* 53 (D1 6th Jan. 2025), pp. D543–D553. DOI: 10.1093/nar/gkae1011.

[2] Robert H Powers. 'The decomposition of human remains'. In: *Forensic Medicine of the Lower Extremity*. Totowa, NJ: Humana Press, 2005, pp. 3–15. DOI: 10.1385/1-59259-897-8:003.

[3] Clemens von Sonntag and Heinz-Peter Schuchmann. 'The elucidation of peroxyl radical reactions in aqueous solution with the help of radiation-chemical methods'. In: *Angew. Chem., Int. Ed. Engl.* 30 (10 Oct. 1991), pp. 1229–1253. DOI: 10.1002/anie.199112291.

[4] Chryssostomos Chatgilialoglu, Sebastian Barata-Vallejo and Thanasis Gimisis. 'Radical reactions in organic synthesis: Exploring in-, on-, and with-water methods'. In: *Molecules* 29 (3 23rd Jan. 2024), p. 569. DOI: 10.3390/molecules29030569.

[5] Agostino Migliore et al. 'Water-mediated electron transfer between protein redox centers'. In: *J. Phys. Chem. B* 111 (14 12th Apr. 2007), pp. 3774–3781. DOI: 10.1021/jp068773i.

[6] Marco Malferrari, Francesco Francia and Giovanni Venturoli. 'Retardation of protein dynamics by trehalose in dehydrated systems of photosynthetic reaction centers. Insights from electron transfer and thermal denaturation kinetics'. In: *J. Phys. Chem. B* 119 (43 29th Oct. 2015), pp. 13600–13618. DOI: 10.1021/acs.jpcb.5b02986.

[7] Konstantin O Muranov. 'Fenton Reaction in vivo and in vitro. Possibilities and Limitations'. In: *Biochemistry (Mosc.)* 89 (Suppl 1 8th Jan. 2024), S112–S126. DOI: 10.1134/S0006297924140074.

[8] Michael J Davies. 'Protein oxidation and peroxidation'. In: *Biochem. J.* 473 (7 1st Apr. 2016), pp. 805–825. DOI: 10.1042/BJ20151227.

[9] Eugene Pliss et al. 'Kinetic analysis of the reactivity of peroxyl radicals in chain oxidation of unsaturated compounds'. In: *React. Kinet. Mech. Catal.* 137 (1 16th Nov. 2023), pp. 53–76. DOI: 10.1007/s11144-023-02524-7.

[10] Juan David Figueroa et al. 'Formation and characterization of crosslinks, including Tyr-Trp species, on one electron oxidation of free Tyr and Trp residues by carbonate radical anion'. In: *RSC Adv.* 10 (43 3rd July 2020), pp. 25786–25800. DOI: 10.1039/d0ra04051g.

[11] Petra Marschner. 'Processes in submerged soils – linking redox potential, soil organic matter turnover and plants to nutrient cycling'. In: *Plant Soil* 464 (1 16th June 2021), pp. 1–12. DOI: 10.1007/s11104-021-05040-6.

[12] Giorgio Schirò and Martin Weik. 'Role of hydration water in the onset of protein structural dynamics'. In: *J. Phys. Condens. Matter* 31 (46 20th Nov. 2019), p. 463002. DOI: 10.1088/1361-648X/ab388a.

[13] Lin Zheng et al. 'Radical scavenging activities of Tyr-, Trp-, Cys- and Met-Gly and their protective effects against AAPH-induced oxidative damage in human erythrocytes'. In: *Food Chem.* 197 (Pt A 15th Apr. 2016), pp. 807–813. DOI: 10.1016/j.foodchem.2015.11.012.

[14] Lin Zheng et al. 'Structure–activity relationship of antioxidant dipeptides: Dominant role of Tyr, Trp, Cys and Met residues'. In: *J. Funct. Foods* 21 (Mar. 2016), pp. 485–496. DOI: 10.1016/j.jff.2015.12.003.

[15] Eduardo Fuentes-Lemus et al. 'Oxidative crosslinking of peptides and proteins: Mechanisms of formation, detection, characterization and quantification'. In: *Molecules* 27 (1 21st Dec. 2021), p. 15. DOI: 10.3390/molecules27010015.

[16] Marilyn Ehrenshaft, Leesa J Deterding and Ronald P Mason. 'Tripping up Trp: Modification of protein tryptophan residues by reactive oxygen species, modes of detection, and biological consequences'. In: *Free Radic. Biol. Med.* 89 (21st Dec. 2015), pp. 220–228. DOI: 10.1016/j.freeradbiomed.2015.08.003.

[17] Stephanie Bellmaine, Alisa Schnellbaecher and Aline Zimmer. 'Reactivity and degradation products of tryptophan in solution and proteins'. In: *Free Radic. Biol. Med.* 160 (20th Nov. 2020), pp. 696–718. DOI: 10.1016/j.freeradbiomed.2020.09.002.

[18] Lisa K Folkes et al. 'The effects of nitric oxide or oxygen on the stable products formed from the tyrosine phenoxyl radical'. In: *Free Radic. Res.* 55 (2 2nd Feb. 2021), pp. 141–153. DOI: 10.1080/10715762.2020.1870684.

[19] Anouchka Gatin et al. 'Oxidative radicals ($HO^{\bullet}$ or $N3^{\bullet}$) induce several di-tyrosine bridge isomers at the protein scale'. In: *Free Radic. Biol. Med.* 162 (1st Jan. 2021), pp. 461–470. DOI: 10.1016/j.freeradbiomed.2020.10.324.

[20] Soumya Mukherjee et al. 'Characterization and identification of dityrosine cross-linked peptides using tandem mass spectrometry'. In: *Anal. Chem.* 89 (11 6th June 2017), pp. 6136–6145. DOI: 10.1021/acs.analchem.7b00941.

[21] J M Souza et al. 'Dityrosine cross-linking promotes formation of stable alpha -synuclein polymers. Implication of nitrative and oxidative stress in the pathogenesis of neurodegenerative synucleinopathies: Implication of nitrative and oxidative stress in the pathogenesis of neurodegenerative synucleinopathies'. In: *J. Biol. Chem.* 275 (24 16th June 2000), pp. 18344–18349. DOI: 10.1074/jbc.M000206200.

[22] Mahmoud B Maina, Youssra K Al-Hilaly and Louise C Serpell. 'Dityrosine cross-linking and its potential roles in Alzheimer's disease'. In: *Front. Neurosci.* 17 (22nd Mar. 2023), p. 1132670. DOI: 10.3389/fnins.2023.1132670.

[23] Adrian Drazic and Jeannette Winter. 'The physiological role of reversible methionine oxidation'. In: *Biochim. Biophys. Acta* 1844 (8 1st Aug. 2014), pp. 1367–1382. DOI: 10.1016/j.bbapap.2014.01.001.

[24] R L Levine, J Moskovitz and E R Stadtman. 'Oxidation of methionine in proteins: roles in antioxidant defense and cellular regulation'. In: *IUBMB Life* 50 (4-5 1st Oct. 2000), pp. 301–307. DOI: 10.1080/713803735.

[25] Geumsoo Kim, Stephen J Weiss and Rodney L Levine. 'Methionine oxidation and reduction in proteins'. In: *Biochim. Biophys. Acta* 1840 (2 Feb. 2014), pp. 901–905. DOI: 10.1016/j.bbagen.2013.04.038.

[26] Christian Schöneich. 'Thiyl radicals and induction of protein degradation'. In: *Free Radic. Res.* 50 (2 2016), pp. 143–149. DOI: 10.3109/10715762.2015.1077385.

[27] Esam A Orabi and Ann M English. 'Predicting structural and energetic changes in Met-aromatic motifs on methionine oxidation to the sulfoxide and sulfone'. In: *Phys. Chem. Chem. Phys.* 20 (35 12th Sept. 2018), pp. 23132–23141. DOI: 10.1039/c8cp03277g.

[28] David S Weber and Jeffrey J Warren. 'A survey of methionine-aromatic interaction geometries in the oxidoreductase class of enzymes: What could Met-aromatic interactions be doing near metal sites?' In: *J. Inorg. Biochem.* 186 (Sept. 2018), pp. 34–41. DOI: 10.1016/j.jinorgbio.2018.05.008.

[29] Can Wang et al. 'Fenton-like reaction of the iron(II)-histidine complex generates hydroxyl radicals: implications for oxidative stress and Alzheimer's disease'. In: *Chem. Commun. (Camb.)* 57 (92 19th Nov. 2021), pp. 12293–12296. DOI: 10.1039/d1cc05000a.

[30] Yahua Liu et al. 'Model studies on the metal-catalyzed protein oxidation: structure of a possible His-Lys cross-link'. In: *Chem. Res. Toxicol.* 17 (1 Jan. 2004), pp. 110–118. DOI: 10.1021/tx034167s.

[31] Xiaojuan Li, Cheng Lin and Peter B O'Connor. 'Glutamine deamidation: differentiation of glutamic acid and gamma-glutamic acid in peptides by electron capture dissociation'. In: *Anal. Chem.* 82 (9 1st May 2010), pp. 3606–3615. DOI: 10.1021/ac9028467.

[32] Sahin Uyaver. 'Tyrosine, phenylalanine, and tryptophan undergo self-aggregation in similar and different manners'. In: *Atmosphere (Basel)* 13 (9 7th Sept. 2022), p. 1448. DOI: 10.3390/atmos13091448.

[33] Jessica Saladino et al. 'Aliphatic peptidyl hydroperoxides as a source of secondary oxidation in hydroxyl radical protein footprinting'. In: *J. Am. Soc. Mass Spectrom.* 20 (6 June 2009), pp. 1123–1126. DOI: 10.1016/j.jasms.2009.02.004.

[34] S Gebicki and J M Gebicki. 'Formation of peroxides in amino acids and proteins exposed to oxygen free radicals'. In: *Biochem. J.* 289 ( Pt 3) (3 1st Feb. 1993), pp. 743–749. DOI: 10.1042/bj2890743.

[35] Sigri Kløve et al. 'Early-life *Helicobacter pylori* infection worsens metabolic state in mice receiving a high-fat diet'. In: *bioRxiv* biorxiv;2025.04.27.650497v1 (30th Apr. 2025). DOI: 10.1101/2025.04.27.650497.

[36] Christopher S Hughes et al. 'Single-pot, solid-phase-enhanced sample preparation for proteomics experiments'. In: *Nat. Protoc.* 14 (1 Jan. 2019), pp. 68–85. DOI: 10.1038/s41596-018-0082-x.

[37] Florian Meier et al. 'diaPASEF: parallel accumulation-serial fragmentation combined with data-independent acquisition'. In: *Nat. Methods* 17 (12 30th Dec. 2020), pp. 1229–1236. DOI: 10.1038/s41592-020-00998-0.

[38] Artemis G Korovesi et al. 'Normal mouse brain proteome II: Analysis of brain regions by high-resolution mass spectrometry'. In: *Cancer Genomics Proteomics* 17 (6 Nov. 2020), pp. 757–767. DOI: 10.21873/cgp.20230.

[39] Stefka Tyanova, Tikira Temu and Juergen Cox. 'The MaxQuant computational platform for mass spectrometry-based shotgun proteomics'. In: *Nat. Protoc.* 11 (12 Dec. 2016), pp. 2301–2319. DOI: 10.1038/nprot.2016.136.

[40] Siri Hildonen, Trine Grønhaug Halvorsen and Léon Reubsaet. 'Why less is more when generating tryptic peptides in bottom-up proteomics'. In: *Proteomics* 14 (17-18 1st Sept. 2014), pp. 2031–2041. DOI: 10.1002/pmic.201300479.

[41] R Core Team. *R: A language and environment for statistical computing*. R Foundation for Statistical Computing, 2025.

[42] Vadim Demichev et al. 'DIA-NN: neural networks and interference correction enable deep proteome coverage in high throughput'. In: *Nat. Methods* 17 (1 Jan. 2020), pp. 41–44. DOI: 10.1038/s41592-019-0638-x.

[43] Marc-Antoine Gerault, Luc Camoin and Samuel Granjeaud. 'DIAgui: a Shiny application to process the output from DIA-NN'. In: *Bioinform. Adv.* 4 (1 13th Jan. 2024), vbae001. DOI: 10.1093/bioadv/vbae001.

[44] Thang V Pham, Alex A Henneman and Connie R Jimenez. 'iq: an R package to estimate relative protein abundances from ion quantification in DIA-MS-based proteomics'. In: *Bioinformatics* 36 (8 15th Apr. 2020), pp. 2611–2613. DOI: 10.1093/bioinformatics/btz961.

[45] Jürgen Cox et al. 'Accurate proteome-wide label-free quantification by delayed normalization and maximal peptide ratio extraction, termed MaxLFQ'. In: *Mol. Cell. Proteomics* 13 (9 Sept. 2014), pp. 2513–2526. DOI: 10.1074/mcp.M113.031591.

[46] Cosmin Lazar et al. 'Accounting for the multiple natures of missing values in label-free quantitative proteomics data sets to compare imputation strategies'. In: *J. Proteome Res.* 15 (4 1st Apr. 2016), pp. 1116–1125. DOI: 10.1021/acs.jproteome.5b00981.

[47] Mingyi Liu and Ashok Dongre. 'Proper imputation of missing values in proteomics datasets for differential expression analysis'. In: *Brief. Bioinform.* 22 (3 20th May 2021), bbaa112. DOI: 10.1093/bib/bbaa112.

[48] Björn Schwanhäusser et al. 'Global quantification of mammalian gene expression control'. In: *Nature* 473 (7347 19th May 2011), pp. 337–342. DOI: 10.1038/nature10098.

[49] Jeffrey T Leek et al. 'The sva package for removing batch effects and other unwanted variation in high-throughput experiments'. In: *Bioinformatics* 28 (6 15th Mar. 2012), pp. 882–883. DOI: 10.1093/bioinformatics/bts034.

[50] Alboukadel Kassambara. *Pers. comm.* 2020.

[51] Leland McInnes et al. 'UMAP: Uniform Manifold Approximation and Projection'. In: *J. Open Source Softw.* 3 (29 2nd Sept. 2018), p. 861. DOI: 10.21105/joss.00861.

[52] Matthew E Ritchie et al. 'limma powers differential expression analyses for RNA-sequencing and microarray studies'. In: *Nucleic Acids Res.* 43 (7 20th Apr. 2015), e47. DOI: 10.1093/nar/gkv007.

[53] Guangchuang Yu et al. 'clusterProfiler: an R package for comparing biological themes among gene clusters'. In: *OMICS* 16 (5 May 2012), pp. 284–287. DOI: 10.1089/omi.2011.0118.

[54] Tianzhi Wu et al. 'clusterProfiler 4.0: A universal enrichment tool for interpreting omics data'. In: *Innovation (Camb.)* 2 (3 28th Aug. 2021), p. 100141. DOI: 10.1016/j.xinn.2021.100141.

[55] Zuguang Gu. 'Complex heatmap visualization'. In: *Imeta* 1 (3 1st Sept. 2022), e43. DOI: 10.1002/imt2.43.

[56] Simon N Wood. 'Fast stable restricted maximum likelihood and marginal likelihood estimation of semiparametric generalized linear models: Estimation of Semiparametric Generalized Linear Models'. In: *J. R. Stat. Soc. Series B Stat. Methodol.* 73 (1 1st Jan. 2011), pp. 3–36. DOI: 10.1111/j.1467-9868.2010.00749.x.

[57] Paul D Thomas et al. 'PANTHER: Making genome-scale phylogenetics accessible to all'. In: *Protein Sci.* 31 (1 Jan. 2022), pp. 8–22. DOI: 10.1002/pro.4218.

[58] J Kyte and R F Doolittle. 'A simple method for displaying the hydropathic character of a protein'. In: *J. Mol. Biol.* 157 (1 5th May 1982), pp. 105–132. DOI: 10.1016/0022-2836(82)90515-0.

[59] Jacob Cohen. *Statistical power analysis for the behavioral sciences*. 2nd ed. New York, NY: Routledge Member of the Taylor and Francis Group, 12th Aug. 1988. 400 pp.

[60] Daniel Osorio, Paola Rondón-Villarreal and Rodrigo Torres. 'Peptides: A package for data mining of antimicrobial peptides'. In: *R J.* 7 (1 4th Feb. 2015), p. 4. DOI: 10.32614/rj-2015-001.

[61] Lukasz Pawel Kozlowski. 'IPC 2.0: prediction of isoelectric point and pKa dissociation constants'. In: *Nucleic Acids Res.* 49 (W1 2nd July 2021), W285–W292. DOI: 10.1093/nar/gkab295.

[62] Norman Cliff. 'Dominance statistics: Ordinal analyses to answer ordinal questions'. In: *Psychol. Bull.* 114 (3 Nov. 1993), pp. 494–509. DOI: 10.1037/0033-2909.114.3.494.

[63] John Jumper et al. 'Highly accurate protein structure prediction with AlphaFold'. In: *Nature* 596 (7873 Aug. 2021), pp. 583–589. DOI: 10.1038/s41586-021-03819-2.

[64] Barry J Grant et al. 'Bio3d: an R package for the comparative analysis of protein structures'. In: *Bioinformatics* 22 (21 1st Nov. 2006), pp. 2695–2696. DOI: 10.1093/bioinformatics/btl461.

[65] Gábor Erdős and Zsuzsanna Dosztányi. 'AIUPred: combining energy estimation with deep learning for the enhanced prediction of protein disorder'. In: *Nucleic Acids Res.* 52 (W1 5th July 2024), W176–W181. DOI: 10.1093/nar/gkae385.

[66] Shadab Ahmad et al. 'The UniProt website API: facilitating programmatic access to protein knowledge'. In: *Nucleic Acids Res.* 53 (W1 7th July 2025), W547–W553. DOI: 10.1093/nar/gkaf394.

[67] Georg Heinze et al. 'Firth's bias-reduced logistic regression with logistf'. In: *CRAN* (16th Apr. 2025). DOI: 10.32614/CRAN.package.logistf.